ISSN 2301-1092 • ISSN (en línea) 2301-1106

MEMORIA

INVESTIGACIONES EN INGENIERÍA

Nº 26

FACULTAD DE INGENIERÍA

UM
UNIVERSIDAD DE MONTEVIDEO

MEMORIA

Investigaciones en Ingeniería

ISSN 2301-1092 • ISSN (en línea) 2301-1106

Núm. 26 (2024)

Sumario

Págs.

Editorial – Innovación y Sostenibilidad en la Ingeniería.

Nos complace presentar la Edición 26 de Memoria Investigaciones en Ingeniería, un esfuerzo continuo de la Universidad de Montevideo por más de dos décadas. Este volumen reúne una colección de investigaciones que reflejan el compromiso y la excelencia en el campo de la ingeniería y la tecnología, abarcando una variedad de temas relevantes y actuales.

La edición actual destaca la importancia de la eficiencia energética y la sostenibilidad, con estudios innovadores que buscan reducir el consumo de energía y optimizar sistemas existentes. Desde el diseño de sistemas energéticamente eficientes para auditorios universitarios hasta la reducción del consumo de energía en compresores de refrigeradores mediante el uso de nanopartículas, estos trabajos muestran el avance hacia un futuro más sostenible.

También se presentan investigaciones en el ámbito de la ingeniería civil, como la utilización de ceniza de aserrín como aditivo en hormigón y el análisis sísmico de edificaciones multifamiliares, que subrayan la búsqueda de soluciones constructivas más resistentes y sostenibles. Además, se exploran las técnicas avanzadas en el análisis estructural y el impacto del envejecimiento estructural en edificios educativos.

La incorporación de tecnologías emergentes es otro tema clave de esta edición. Estudios sobre el uso de materiales de cambio de fase para mejorar la eficiencia de módulos fotovoltaicos, y soluciones de IoT para el monitoreo en tiempo real de la salud de baterías de plomo-ácido, demuestran cómo la innovación tecnológica puede abordar desafíos actuales en la energía y la sostenibilidad.

Además, la edición incluye desarrollos en el campo de la telemedicina con el diseño de electrocardiógrafos portátiles de bajo costo, resaltando la intersección entre la ingeniería y la salud pública, y cómo estas innovaciones pueden mejorar la calidad de vida en comunidades remotas.

La colaboración internacional y el rigor académico son pilares fundamentales de nuestra revista. Agradecemos a todos los autores y revisores que han contribuido con su tiempo y conocimientos, y que provienen de diversos países, enriqueciendo la calidad y diversidad de nuestro contenido.

Con esta nueva edición, esperamos seguir inspirando a nuestros lectores y fomentando el intercambio de conocimientos que impulsen el progreso en el campo de la ingeniería y la tecnología.

Agradecemos a la Lic. Valentina Morandi y al M.Sc. Ing. Fernando Hernández por su invaluable dedicación y profesionalismo, esenciales para la realización de cada edición de Memoria Investigaciones en Ingeniería.

Dr. Ing. Rafael Sotelo
Editor en Jefe
Facultad de Ingeniería
Universidad de Montevideo

https://doi.org/10.36561/ING.26.1
ISSN 2301-1092 • ISSN (en línea) 2301-1106

Revitalizing Comfort: Designing an Energy–Efficient HVAC System for the University Auditorium

Comodidad revitalizante: Diseño de un Sistema HVAC Energéticamente Eficiente para el Auditorio Universitario

Revitalizando o Conforto: Projeto de um Sistema HVAC com Eficiência Energética para o Auditório Universitário

Abdul Samad Khan[1(*)], Muhammad Ehtesham ul Haque[2], Adeel Ahmed Khan[3], Syed Izhar ul haque[4], Syed Obaidullah[5], Muhammad Umer Khan[6]

Recibido: 29/07/2023 Aceptado: 13/04/2024

Summary. - Nowadays, thermal comfort is becoming a major problem for people due to increasing global warming and climatic changes, but it can be resolved by the concept of Heating, Ventilation, and Air Conditioning (HVAC) systems. The purpose of HVAC is to provide occupants with a comfort zone so that they can feel comfortable according to their thermal comfort. The core objective of this study is to design and propose an HVAC system as per actual design conditions for the University Auditorium located in Karachi, Pakistan. A direct Expansion (DX – Type) system is installed in the Auditorium that has exceeded the lifespan of twenty years, refrigerant R-22 which is currently being used has been obsolete due to its high GWP (Global Warming Potential) and ODP (Ozone Depletion Potential) values which are 1810 and 0.05 respectively. To achieve the objective of this study, two approaches are employed. Cooling Load Temperature Difference (CLTD) method & Hourly Analysis Program (HAP) software. The cooling load calculated from the CLTD method is 202 kW equivalent to 57.5 Ton of Refrigeration (TR). On the other side, the cooling load calculated from HAP software is 192.8 kW equivalent to 55 TR. By considering the calculated cooling load for the University Auditorium, two different HVAC systems are proposed, based on Water cooled and Air-cooled Vapor Compression Cycle. After this study, engineers will be able to design an HVAC system for any facility as per design conditions. Also, they can propose different cost-effective and energy-efficient HVAC systems for that particular space.

Keywords: HVAC; Auditorium; Duct sizing; Cooling load; Piping.

(*) Corresponding Author

[1] Lecturer, Department of Mechanical Engineering, NED University of Engineering and Technology (Pakistan), abdulsamadkhan@neduet.edu.pk, ORCID iD: https://orcid.org/0009-0005-5449-635X

[2] Assistant Professor. Department of Mechanical Engineering, NED University of Engineering and Technology (Pakistan),, mehaque@neduet.edu.pk, ORCID iD: https://orcid.org/0000-0001-8751-348X

[3] Assistant Professor. Department of Mechanical Engineering, NED University of Engineering and Technology (Pakistan), adeelahmedk@neduet.edu.pk, ORCID iD: https://orcid.org/0009-0004-6790-8176

[4] Senior Undergraduate Student. *Department of Mechanical Engineering, NED University of Engineering and Technology (Pakistan),* izharmumshad97@hotmail.com, ORCID iD: https://orcid.org/0009-0002-5693-5879

[5] Senior Undergraduate Student. Department of Mechanical Engineering, NED University of Engineering and Technology (Pakistan), syedobaid2121@gmail.com, ORCID iD: https://orcid.org/0009-0000-0168-6196

[6] Senior Undergraduate Student. Department of Mechanical Engineering, NED University of Engineering and Technology (Pakistan), engineerumerkhan@gmail.com, ORCID iD: https://orcid.org/0009-0001-7173-6395

Memoria Investigaciones en Ingeniería, núm. 26 (2024). pp. 2-37
https://doi.org/10.36561/ING.26.2
ISSN 2301-1092 • ISSN (en línea) 2301-1106 – Universidad de Montevideo, Uruguay

Resumen. - *Hoy en día, el confort térmico se está convirtiendo en un gran problema para las personas debido al aumento del calentamiento global y los cambios climáticos, pero puede ser resuelto por el concepto de sistemas de Calefacción, Ventilación y Aire Acondicionado (HVAC). El objetivo de HVAC es proporcionar a los ocupantes una zona de confort para que puedan sentirse cómodos de acuerdo con su confort térmico. El objetivo central de este estudio es diseñar y proponer un sistema HVAC según las condiciones de diseño reales para el Auditorio Universitario ubicado en Karachi, Pakistán. En el Auditorio se encuentra instalado un sistema de Expansión Directa (Tipo DX) que ha superado la vida útil de veinte años, el refrigerante R-22 que se utiliza actualmente ha quedado obsoleto por su alto GWP (Global Warming Potential) y ODP (Ozone Depletion Potencial) valores que son 1810 y 0.05 respectivamente. Para lograr el objetivo de este estudio, se emplean dos enfoques. Método de diferencia de temperatura de carga de enfriamiento (CLTD) y software de programa de análisis por hora (HAP). La carga de refrigeración calculada a partir del método CLTD es de 202 kW equivalente a 57,5 Toneladas de Refrigeración (TR). Por otro lado, la carga de refrigeración calculada a partir del software HAP es de 192,8 kW equivalente a 55 TR. Al considerar la carga de enfriamiento calculada para el Auditorio Universitario, se proponen dos sistemas HVAC diferentes, basados en el ciclo de compresión de vapor enfriado por agua y enfriado por aire. Después de este estudio, los ingenieros podrán diseñar un sistema HVAC para cualquier instalación según las condiciones de diseño. Además, pueden proponer diferentes sistemas HVAC rentables y energéticamente eficientes para ese espacio en particular.*

Palabras clave: *HVAC; Auditorio; Dimensionamiento de ductos; Carga de enfriamiento; Piping.*

Resumo. ***-*** *Hoje em dia, o conforto térmico está a tornar-se um grande problema para as pessoas devido ao aumento do aquecimento global e às alterações climáticas, mas pode ser resolvido pelo conceito de sistemas de Aquecimento, Ventilação e Ar Condicionado (HVAC). O objetivo do HVAC é proporcionar aos ocupantes uma zona de conforto para que se sintam confortáveis de acordo com o seu conforto térmico. O objetivo principal deste estudo é projetar e propor um sistema HVAC de acordo com as condições reais de projeto para o Auditório Universitário localizado em Karachi, Paquistão. No Auditório está instalado um sistema de Expansão Direta (Tipo DX) que ultrapassou sua vida útil de vinte anos. O refrigerante R-22 atualmente utilizado tornou-se obsoleto devido ao seu alto GWP (Potencial de Aquecimento Global) e ODP (Depleção de Ozônio). Potencial) valores que são 1810 e 0,05 respectivamente. Para atingir o objetivo deste estudo, duas abordagens são utilizadas. Método de diferença de temperatura de carga de resfriamento (CLTD) e software de programa de análise horária (HAP). A carga de resfriamento calculada a partir do método CLTD é de 202 kW equivalente a 57,5 toneladas de refrigeração (TR). Por outro lado, a carga de refrigeração calculada a partir do software HAP é de 192,8 kW equivalente a 55 TR. Ao considerar a carga de refrigeração calculada para o Auditório Universitário, são propostos dois sistemas HVAC diferentes, baseados no ciclo de compressão de vapor refrigerado a água e arrefecido a ar. Após este estudo, os engenheiros serão capazes de projetar um sistema HVAC para qualquer instalação com base nas condições de projeto. Além disso, eles podem propor diferentes sistemas HVAC econômicos e energeticamente eficientes para esse espaço específico.*

Palavras-chave: *AVAC; Público; Dimensionamento de dutos; Carga de resfriamento; Tubulação.*

Nomenclature:

A	Area
ACH	Air Changes per Hour
$CLTD_{adj}$	Cooling Load Temperature Difference Adjusted
D	Diameter
E	Efficiency
F_b	Ballast Factor
F_u	Utilization Factor
g	Acceleration due to gravity
h_i	Inside Relative Humidity
h_L	Head Loss
h_M	Mixed air enthalpy
h_o	Outside air enthalpy
h_R	Recirculated air enthalpy
l	Length
L_{eq}	Equivalent Length
m_M	Mixed air flowrate
m_o	Outdoor air flowrate
m_R	Recirculated air flowrate
N	No. of Occupant
$\dot{Q}$	Heat Gain
$\dot{Q}_{il}$	Latent Heat Gain by Infiltration
$\dot{Q}_{is}$	Sensible Heat Gain by Infiltration
$\dot{Q}_{latent}$	Latent Heat Gain
$\dot{Q}_{sensible}$	Sensible Heat Gain
$\dot{Q}_{vl}$	Latent Heat Gain by Ventilation
$\dot{Q}_{vs}$	Sensible Heat Gain by Ventilation
t_a	Temperature below the floor of the Auditorium
t_{avg}	Outside average temperature
t_i	Inside design temperature
T_M	Mixed air temperature
t_0	Outside design temperature
T_S	Supply air temperature
R	Thermal Resistance
R_A	Area Outdoor Air rate
R_P	People's Outdoor Air rate
U	Thermal Transmittance
V	Volume
v	Velocity
$\dot{V}_i$	Infiltration Air Flowrate
$\dot{V}_m$	Minimum Outdoor Air Flowrate
$\dot{V}_o$	Outside Air Flowrate
$\dot{V}_r$	Recirculation Air Flowrate
$\dot{V}_v$	Ventilation Air Flowrate
W	Wattage
W_i	Inside Humidity Ratio
W_0	Outside Humidity Ratio

Greek Symbols:

ρ	Density
ΔP	Pressure drop
$\emptyset$	Relative Humidity
$q_{e,\theta}$	Heat gain through wall or roof, at calculation hour θ
θ	Time
δ	Time interval
$t_{e,\theta-n\delta}$	Sol-air temperature at time $\theta - n\delta$
$t_{r,c}$	Constant indoor room temperature
b_n, c_n, d_n	Conduction transfer function coefficients

Subscripts:

a	adjacent space
adj	adjusted
avg	average
i	inside
il	infiltration latent
is	infiltration sensible
M	mixed
m	minimum outdoor air
n	summation index (each summation has as many terms as there are non-negligible values of coefficients)
o	outside
P	people
R	recirculated
r	recirculation
S	supply
vl	ventilation latent
vs	ventilation sensible

Acronyms

AHU	Air Handling Unit
ASHRAE	American Society of Heating, Refrigeration & Air Conditioning Engineers
CLF	Cooling Load Factor
CLTD	Cooling Load Temperature Difference
DX	Direct Expansion
EER	Energy Efficiency Ratio
GWP	Global Warming Potential
HAP	Hourly Analysis Program
HFC	Hydrofluorocarbons
HVAC	Heating Ventilation and Air Conditioning
IAQ	Indoor Air Quality
LHG	Latent Heat Gain
ODP	Ozone Depletion Potential
PET	Polyethylene terephthalate
SCL	Solar Cooling Load Factor
SEER	Seasonal Energy Efficiency Ratio
SHG	Sensible Heat Gain
TFM	Transfer Function Method
TR	Ton of Refrigeration
VCC	Vapor Compression Cycle

1. Introduction. - Nowadays, global warming become one of the major issues. If temperature, pressure, and relative humidity in the ambient atmospheric conditions are observed, there is an uncomfortable situation for the people. There are many regions in the World where outside ambient conditions are too hot and humid. So, in this situation, people can't perform daily life activities and tasks due to their lower thermal comfort. Due to the environmental changes, the term "climate" comes into play [1]. Pakistan, the country in this World is now tolerating the summer season extending from April to November. At the global scale, it is significantly observed there was a greater number of hot days as compared to cold days over the past decade which is evident the frequency of hot and humid days is higher. Also, from the study conducted by the Pakistan Meteorological Department, a significant increase in heatwave days is observed which is now a major issue for Pakistan especially the occupants living in different cities due to thermal comfort zones [2].

Without people's thermal comfort, the occupants can't feel comfortable, and they can't perform daily activities. By considering the mentioned situation and conditions related to human comfort, especially in hot climatic conditions, scientists developed the concept of an HVAC system which is the most important requirement for people.
The concept of thermal comfort is a state of mind, the essential parameter for the occupant's comfort zone that provides satisfaction to the occupant so that one can perform his tasks in a comfortable environment [3-5]. The comfort zone for an occupant is predicted by relative humidity, air velocity, air & radiant temperatures, clothing insulation, and metabolic rate [6], it can be defined by a range of operative temperatures that will provide acceptable thermal conditions for a person's state of mind [7].

An HVAC system is mainly responsible for maintaining the desired IAQ by supplying adequate and acceptable fresh air [8, 9]. HVAC systems need to be much more efficient as it consumes around 60% of the building's total energy consumption [10]. In Pakistan, it is observed that the systems which are installed for human comfort are not designed on standard conditions. Either the system is overdesigned in that it produces too much cooling effect and is not economically feasible or the system is under designed so that the occupants are not thermally comfortable [11].
Heat gain is the heat generated by material or equipment in space. HVAC system performance depends on the heat generated by several pieces of equipment. Heat gain ultimately depends on several factors such as room orientation relative to solar radiation, electric devices or appliances, wall and roof materials, and the number of occupants present in a space [12].

Nowadays, due to increasing heat-generating sources and hot & humid climatic conditions, the need for an air conditioning system is a must. On a domestic level, air conditioning requirement is fulfilled by split air conditioners [13] but in large buildings, offices, or auditoriums, these are not feasible due to insufficient supply of air flowrate. So, to resolve this issue, the HVAC system plays an important role to supply adequate fresh air and maintain IAQ within the facility. Researchers and designers introduced some software to make energy-efficient systems. But the problem with this software is it doesn't completely fit the real-time data and the real-time data is something else that is different from the built-in values of the software. This is the reason why when researchers design a particular system that is only based on software and no manual method is used, there must be an error [14].

There are several ways to determine the cooling load of space. Some methods such as CLTD, CLF, SCL, and HAP (Transfer Function) are being used for cooling load calculation. Each of these methods possesses a different and unique methodological approach for calculating space cooling load. CLTD and HAP methods will be discussed in this paper [15].
CLTD is widely used for manual cooling load calculation, as proposed by ASHRAE. This method is used to calculate space cooling loads in which heat-dissipating devices are present. It is also used to calculate the load due to heat dissipation from the walls, windows, and roofs in the space [16]. For walls and roofs, CLTD uses the concept of heat transfer temperature difference but for internal load and windows, it uses CLF [17]. The tabulated CLTD and CLF data were calculated using the transfer function method, which yielded cooling loads for standard environmental conditions and zone types. The cooling loads for each component are then summed to obtain the total zone cooling load [18]. The cooling load of an auditorium space is determined using the CLTD/CLF method, developed as a manual calculation technique relying on tabulated CLTD and CLF values. These tabulated data were derived using the transfer function method, providing cooling load estimates for typical environmental conditions and zone types. These loads were subsequently standardized for easy hourly calculation by designers through normalization. Total zone cooling load is computed by summing the cooling loads of individual components.
HAP is a powerful computer-based tool developed by Carrier Corporation, designed for consulting engineers, HVAC contractors, facility engineers, and other professionals involved in the design and analysis of commercial building HVAC systems. The HAP uses the ASHRAE Transfer Function Method (TFM) for system load calculations and detailed 8,760 hour-by-hour simulation techniques for energy analysis. The TFM uses transfer functions to model transient heat transfer equations [19].

The two major functions of HAP are:

1. Estimating load and designing systems
2. Performing Energy and Cost analysis

The HAP software uses a specific built-in program called the "HAP System Design Load" program to calculate, design, and size the HVAC system. The following are some features of this program:

- ✓ Calculates design cooling and heating loads for spaces, zones, and coils in the HVAC system.
- ✓ Determines required airflow rates for spaces, zones, and the system.
- ✓ Sizes cooling and heating coils.
- ✓ Sizes air circulation fans.
- ✓ Sizes chillers and boilers.

Some previous case studies were performed by different researchers for cooling load calculation of particular facilities by different methods and there is a significant result variation after validation by researchers which leads to an inappropriate design of the HVAC system. ALameen awad Alameen et al. [20] performed a study related to the designing of an Air Conditioning System for a Sports Hall, with a capacity of 1000 occupants in Sudan by using CLTD and HAP methods. The results obtained from CLTD and HAP were 116 TR and 103 TR respectively, with a percentage error of 13%. Khakre et al. [21] conducted a study for cooling load calculation that incorporates the CLTD method for an evaporative cooling system. The cooling load obtained from the CLTD method was 42.35 TR and from the HAP program, it was 38.6 TR, contributing an error of 9% which is not allowed to design an accurate HVAC system. These

variations of calculated cooling load from two different methods make it impossible to design an accurate HVAC system.

Based on cooling load calculation, all previous research studies are focused on designing of HVAC system for any facility by using the CLTD method and HAP software. The purpose of this research study is to design and propose different possible HVAC systems for the University Auditorium. A Central Air Conditioning system is already installed in the Auditorium which is DX – type system. An HVAC system that is currently being operated has exceeded the lifespan of twenty years and Refrigerant R-22 (Chloro-Difluoro-Methane) is currently being used and has been obsolete due to high GWP and ODP values. In the existing HVAC system, R-22 enters AHU and cools the air without the need for secondary refrigerant but it's a danger zone for occupants if the refrigerant piping leaks for some reason, it will directly be mixed with cool air and goes into the space where potential health hazards for occupants will be taken place. So, R-22 (Freon) is not suitable for the cause rather it will be harmful to the occupants. To the knowledge of the authors, no study is available that proposed new HVAC systems with the refrigerant R-410 (A) for the University Auditorium. R-410 (A) is a zeotropic and its ODP is zero due to the absence of chlorine. Although it has a higher GWP than R-22 due to its higher SEER rating, and by reducing the power consumption of the system, it is overall more environmentally friendlier than R-22. The novelty of this research work is to fill this research gap. In this paper, the cooling load of the University Auditorium is calculated via the CLTD method and HAP software. The calculated cooling load is then used to select new equipment like Chillers for both proposed systems which are water-cooled and air-cooled. Other equipment like AHU, cooling towers, and pumps are also selected for both systems as per available data and calculations.

2. The University Auditorium. - The analysis involves the designing of an HVAC system for the University Auditorium located in Karachi. The Auditorium contains electrical equipment and devices that are dissipating continuous heat for which proper temperature control is necessary and IAQ must be maintained. The audience or working staff can't feel comfortable in such an environment when there is no proper control of inside dry bulb temperature and relative humidity due to occupants present at that particular time. DX – Type system has already been installed in the Auditorium and this system provides both air-conditioning as well as ventilation through a ducting network in which refrigerant directly enters AHU and cools the air without the need for any secondary refrigerant. This system has exceeded the lifespan of twenty years with the usage of R-22 which is now obsolete due to its high GWP and ODP values which are 1810 and 0.05 respectively. Montreal and Kyoto Protocols introduced HFCs for the replacement of chlorofluorocarbons (CFCs) and hydrochlorofluorocarbons (HCFCs) because of the low ODP of HCFCs [22]. However, the qualifying criteria for the selection of refrigerant is not only based on ODP but the potential alternative refrigerant has been selected based on a high energetic performance and GWP [23, 24]. Table I represents the specification of components installed in the HVAC system of the University Auditorium.

Components	**Specifications**
Compressor	Company: Carlyle Carrier *Type: Open-Drive Reciprocating* *Model: 5H66*
Condenser	Shell & Tube Type
Evaporator	DX - Type
Expansion device	Thermal Expansion Valve
Air Handling Unit	Size: 400 x 300 x 175 cm Coil Area: 300 x 170 cm
Cooling Tower	Induced draft Counter Flow
Refrigeration cycle	Vapor Compression
Refrigerant	R-22 (Chloro-Difluoro Methane)
Other capacities	Compressor: 75 hp AHU fan: 15 hp Cooling tower pump: 1.5 hp Condenser water pump: 9.8 hp

Table I. *Existing HVAC system of the University Auditorium*

The occupancy schedule is taken as 6 hours (from 0800 hours to peak time of 1400 hours). The geographical location of the Auditorium is as: Latitude is 24.9 °N, Longitude is 67.1 °E and Elevation is 51 meters. The orientation of all four walls of the Auditorium in a cardinal direction is shown in Figure I.

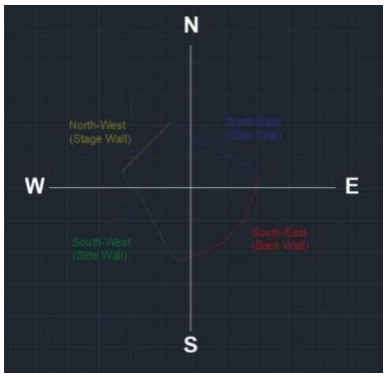

Figure I.- *Walls orientation of the University Auditorium*

The Auditorium consists of a Hall with roof and floor areas are 615.25 m^2 & 615.24 m^2 respectively. It consists of four walls South East (Back wall), South West (Sidewall), North East (Sidewall), and North West (Stage wall) with areas of 67.23 m^2, 168.84 m^2, 168.84 m^2 & 103.79 m^2 respectively. Although there is no window in the Auditorium, its cooling load won't be calculated. The outside weather data condition for the University Auditorium is obtained by keeping Jinnah International Airport as a reference [25]. The weather data shows an outside design temperature of 38.9 ℃ and an average humidity ratio of 19.8 g/kgda [25]. Figure II depicts how the existing HVAC system of the Auditorium works while Figure III shows the 3D model drawn on Autodesk Revit.

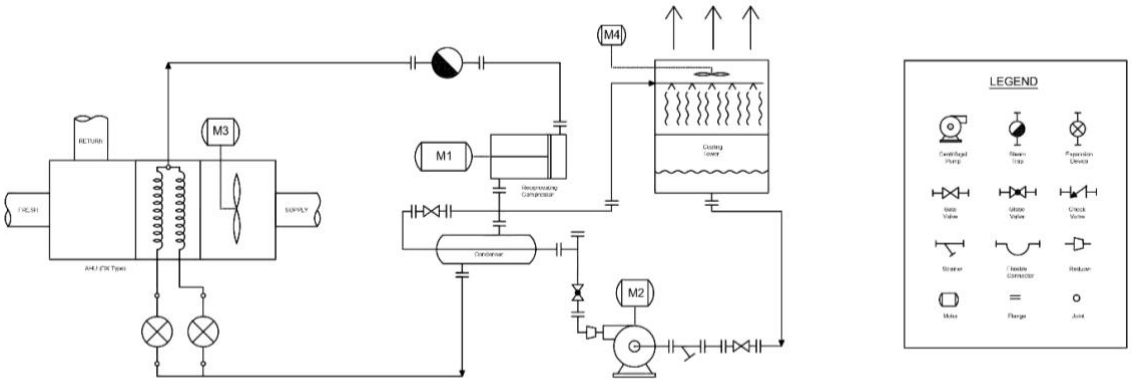

Figure II.- *Process flow diagram of the existing HVAC system of the University Auditorium*

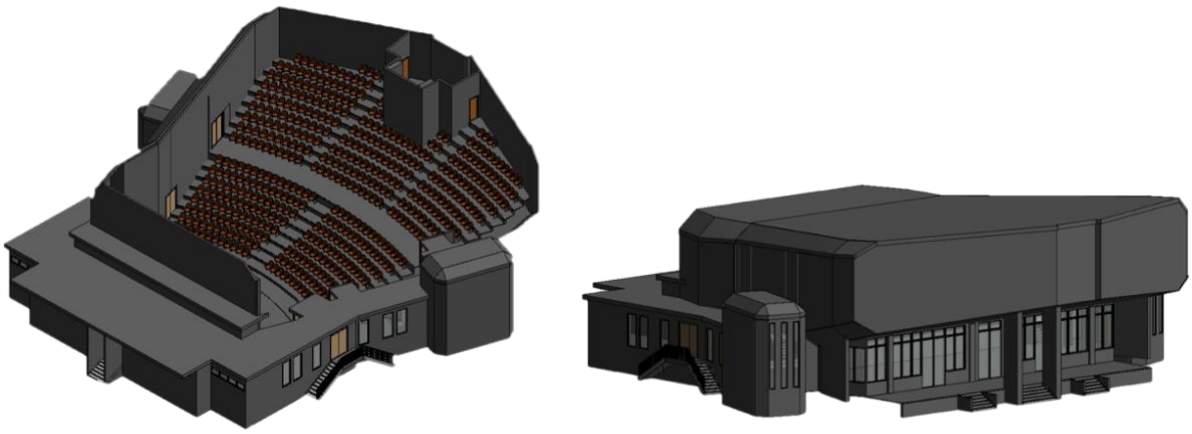

(a) ***(b)***

Figure III.- *3D Revit model of the University Auditorium*

Figures IV, V, VI & VII represent the front view, back view, top view, and section view of the Auditorium.

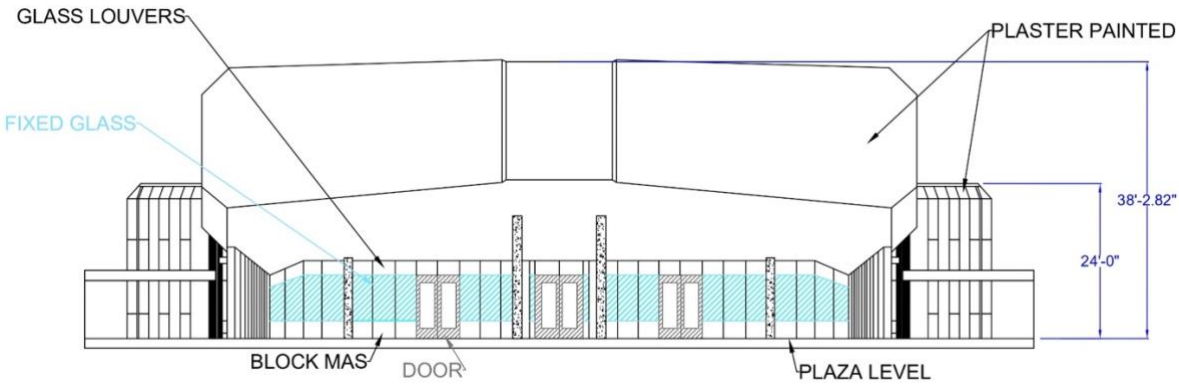

Figure IV.- *Front side view of the University Auditorium*

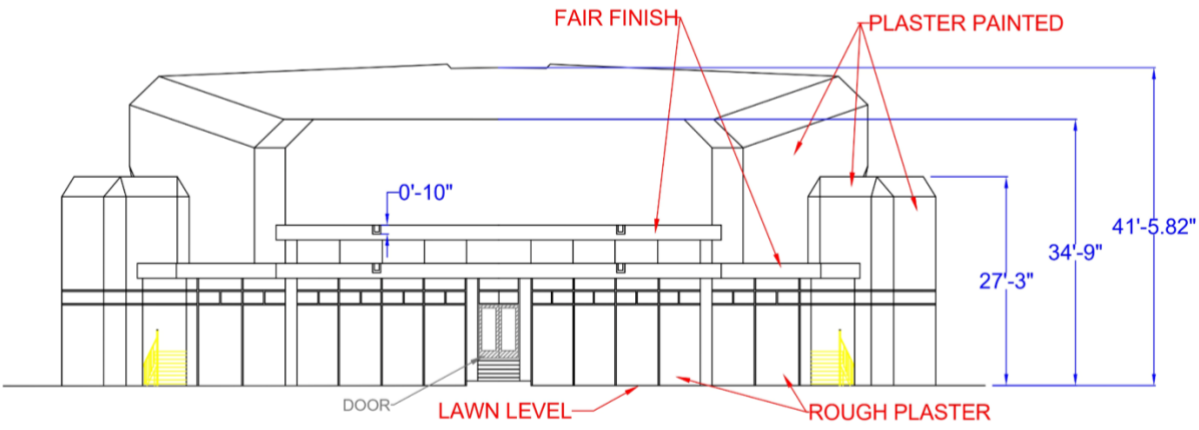

Figure V.- *Back view of the University Auditorium*

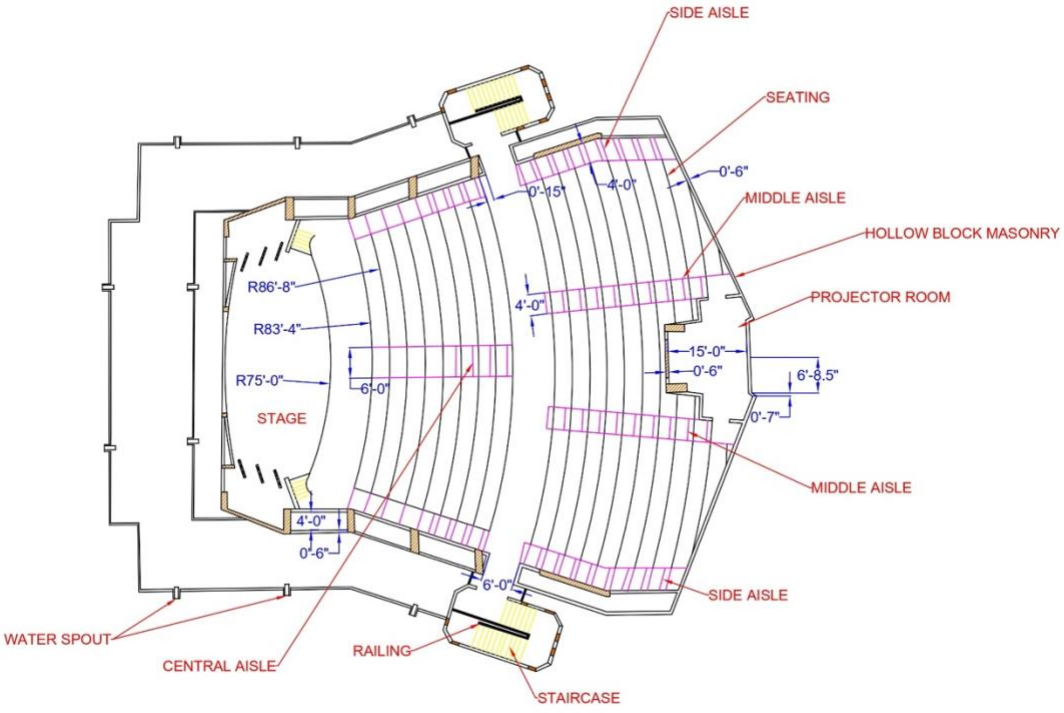

Figure VI.- *Top view of the University Auditorium*

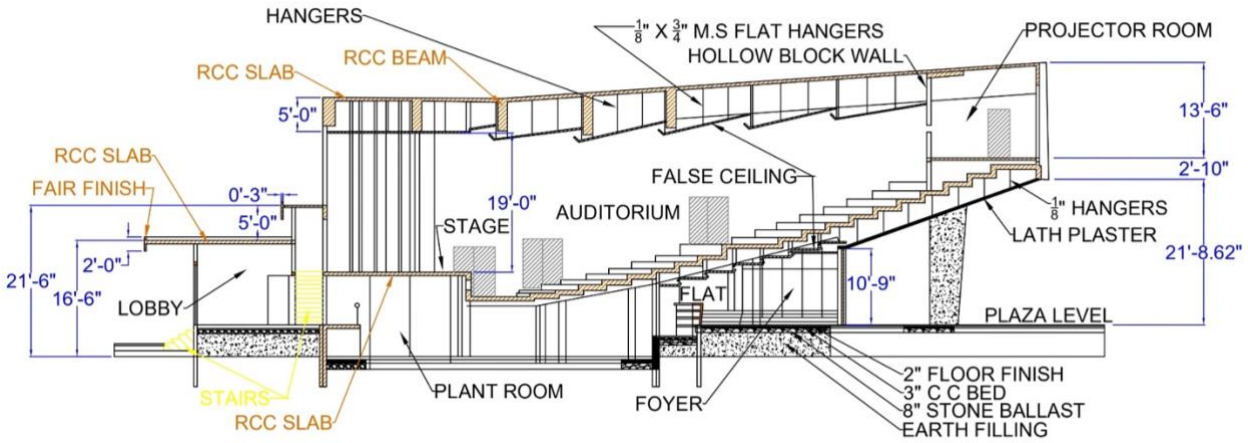

Figure VII.- *Section view of the University Auditorium*

3. Methodology. - This section consists of the calculations of the Roof, walls, and floor areas of the Auditorium manually. Inside weather conditions of the University Auditorium will be selected as per design conditions [26]. Figure VIII represents the methodological flow chart.

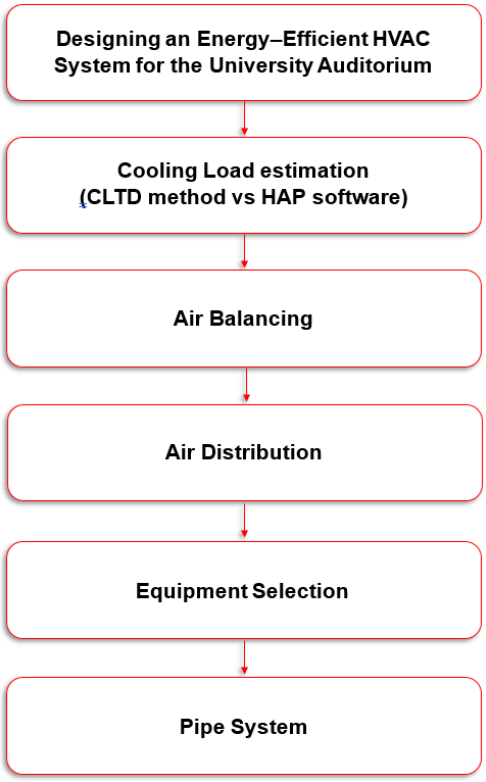

Figure VIII.- *Methodological approach*

3.1 Manual Cooling Load Estimation (CLTD Method). - Table II depicts the important design conditions for cooling load calculation.

Inside Condition	Symbols	Values	References
Dry bulb temperature	t_i	22 °C	[26]
Relative Humidity	∅	60 %	[26]
Humidity Ratio	W_i	9.9 g/kgda	[26]

Outside Condition	Symbols	Values	References
Dry bulb temperature	t_o	38.9 °C	[25]
Average temperature	t_{avg}	36 °C	[25]
Humidity Ratio	W_o	19.8 g/kgda	[25]

Table II. *Inside and outside weather conditions*

Table III represents surface film coefficients/resistances [25]. Table IV represents the thermal resistances of Auditorium structural materials.

Table III. *Thermal Resistances of Surface Films*

Position of surface	The direction of heat flow	Thermal Resistance at Emissivity (90%) (m^2 k/W)	References
Indoor			
Vertical	Horizontal	0.12	[25]
Horizontal	Downward	0.16	[25]
Horizontal	Upward	0.11	[25]
Outdoor			
(any position for summer at 3.4 m/s)	Any	0.044	[25]

Material	Thermal Conductivity (W/ m.k)	Thickness of material (L)	Thermal Resistance (m^2 k/W)	Ref
The air between the roof and ceiling	26.24	60''	0.058	[27]
The air between the side walls	26.24	54''	0.052	[27]
Plaster	0.72	1''	0.035	[25]
Concrete Slab	1.818	6''	0.0825	[28]
Acoustic Tiles	0.052	5/8''	0.288	[25]
Hardwood	0.18	1''	0.141	[25]
Hollow Block	0.88	6''	0.172	[29]

Table IV. *Thermal Resistances of Structure Materials*

3.1.1 Roof. - The cooling load from the roof can be calculated by eq (1) [28].

$$\dot{Q} = U\ A\ CLTD_{adj} \qquad (1)$$

U-value for the surface of the roof can be calculated by eq (2). Figure IX shows the thermal network diagram for the construction material of the roof.

$$U = \frac{1}{\sum Resistance} \qquad (2)$$

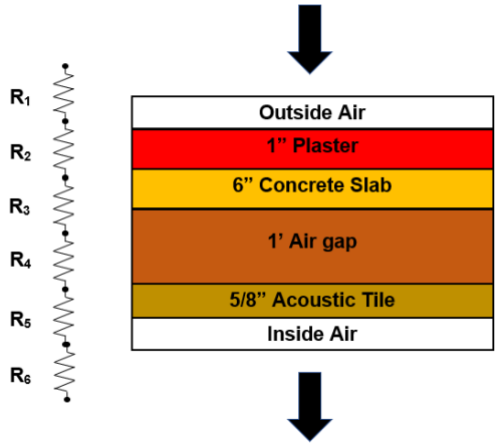

Figure IX.- *Thermal network diagram for the roof's construction*

Table V depicts the thermal resistance values of the material used in the construction of the Roof.

Resistance	Description	Value (m^2 k/W)	References
R_1	Outside Air Resistance	0.044	[25]
R_2	Plaster	0.035	[25]
R_3	Concrete Slab	0.083	[28]
R_4	Air Gap	0.058	[27]
R_5	Acoustic tile	0.288	[25]
R_6	Inside Air Resistance	0.160	[25]

Table V. *Thermal Resistances for Roof Material*

The total area of the roof is 615.25 m^2. Solar time of 1400 hours with Type-4 roof with suspended ceiling is selected. The CLTD value obtained is 16 ℃ [28]. $CLTD_{adj}$ value is determined from eq (3) [28].

$$CLTD_{adj} = CLTD + (25 - t_i) + (t_{avg} - 29) \qquad (3)$$

3.1.2 Walls. - The cooling load from the wall can be calculated from eq (1) [28]. U-value can be calculated for the surface of the wall by eq (2). Figures X, XI, XII, and XIII illustrate thermal network diagrams for walls oriented in the southeast, southwest, northeast, and northwest directions, respectively.

3.1.2.1 South East (Back Wall). - Table VI represents the thermal resistance values of the material used in the construction of South East (Back Wall).

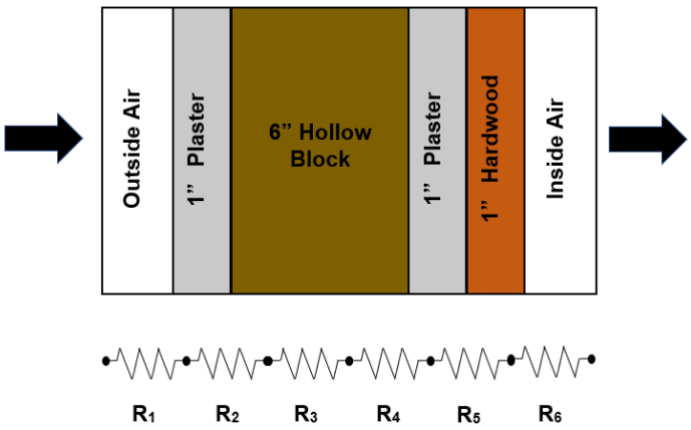

Figure X.- *Thermal network diagram for South East wall construction*

Resistance	Description	Value (m^2 k/W)	References

R_1	Outside Air Resistance	0.044	[25]
R_2	Plaster	0.035	[25]
R_3	Hollow block	0.172	[29]
R_4	Plaster	0.035	[25]
R_5	Hardwood	0.141	[25]
R_6	Inside Air Resistance	0.120	[25]

Table VI. *Thermal Resistances for South East material*

3.1.2.2 South West (Side Wall). - Table VII represents the thermal resistance values of the material used in the construction of South West (Side Wall).

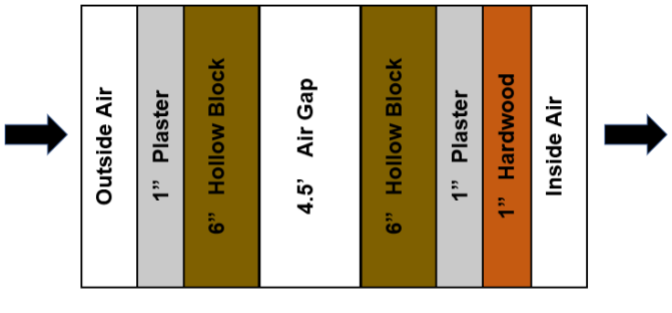

Figur *on*

Resistance			References
R_1	Outside Air Resistance	0.044	[25]
R_2	Plaster	0.035	[25]
R_3	Hollow block	0.172	[29]
R_4	Air gap	0.052	[27]
R_5	Hollow block	0.172	[29]
R_6	Plaster	0.035	[25]
R_7	Hardwood	0.141	[25]
R_8	Inside Air Resistance	0.120	[25]

Table VII. *Thermal Resistances for South West (Side Wall) material*

3.1.2.3 North East (Side Wall). - Table VIII represents the thermal resistance values of the material used in the construction of North East (Side Wall).

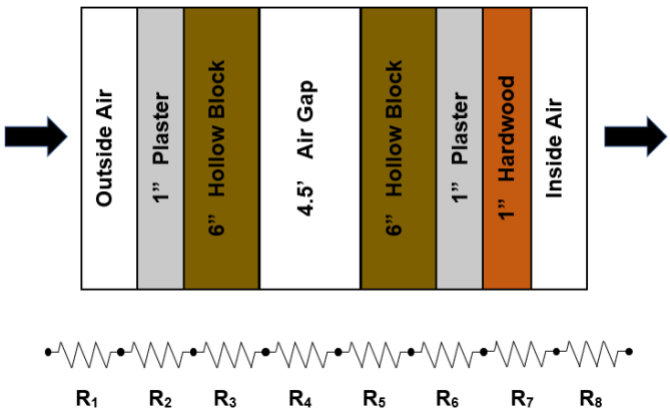

Figure XII.- *Thermal network diagram for North East wall construction*

Resistance	Description	Value (m^2 k/W)	References

R_1	Outside Air Resistance	0.044	[25]
R_2	Plaster	0.035	[25]
R_3	Hollow block	0.172	[29]
R_4	Air gap	0.052	[27]
R_5	Hollow block	0.172	[29]
R_6	Plaster	0.035	[25]
R_7	Hardwood	0.141	[25]
R_8	Inside Air Resistance	0.120	[25]

Table VIII. *Thermal Resistances for North East (Side Wall) material*

3.1.2.4 North West (Stage Wall). - Table IX represents the thermal resistance values of the material used in the construction of North West (Stage Wall).

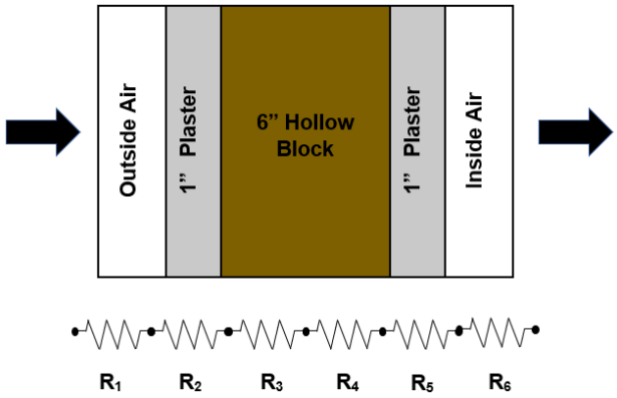

Figure XIII.- *Thermal network diagram for North West wall construction*

Resistance	Description	Value (m^2 k/W)	References
R_1	Outside Air Resistance	0.044	[25]
R_2	Plaster	0.035	[25]
R_3	Hollow block	0.172	[29]
R_4	Plaster	0.035	[25]
R_5	Inside Air Resistance	0.120	[25]

Table IX. *Thermal Resistances for North West (Stage Wall) Material*

Solar time of 1400 hours with Wall Type - E is selected. $CLTD_{adj}$ value is determined from eq (3). Table X depicts the CLTD value of different walls along with their surface areas.

Wall orientations	CLTD (°C) [28]	Wall Area (m^2)
South East	20	67.23
South West	10	168.84
North East	14	168.84
North West	7	103.79

Table X. *Wall Areas & CLTD values*

3.1.3 Floor. - The cooling load from the floor can be calculated by eq (4) [28]. U-value is calculated for floor surface by eq (2). t_a is the temperature below the floor of University Auditorium, taken as 30 °C. The floor area is 615.24 m^2. Table XI represents the thermal resistance values of the material used in the construction of the Floor. Figure XIV

represents the thermal network diagram for the construction material of the floor.

$$\dot{Q} = U\ A\ (t_a - t_i) \qquad (4)$$

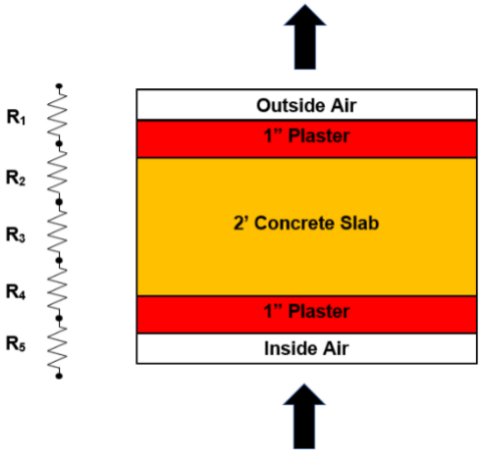

Figure XIV.- *Thermal network diagram for Floor Construction*

Resistance	Description	Value (m^2 k/W)	References
R_1	Inside Air Resistance	0.11	[25]
R_2	Plaster	0.035	[25]
R_3	Concrete Slab	0.335	[25]
R_4	Plaster	0.035	[25]
R_5	Outside Air Resistance	0.11	[25]

Table XI. *Thermal Resistances for Floor Material*

3.1.4 Occupants. - The sum of latent and sensible heat is the total heat generated by the people present within the space. Sensible Heat Gain (SHG) is the heat gained via conduction, convection, or radiation and can be calculated by eq (5) [28]. If the water molecules are incorporated, then the heat gain in this condition is Latent Heat Gain (LHG) and can be calculated by eq (6) [28].

$$\dot{Q}_{sensible} = No.of\ people\ (SHG)\ CLF \qquad (5)$$

$$\dot{Q}_{latent} = No.of\ people\ (LHG) \qquad (6)$$

The values of SHG & LHG are taken as per the desired condition whereas the CLF is selected for 8 hours in space (0800 hours to 1600 hours) and entry time is taken as 6 hours (from 0800 hours to peak time of 1400 hours). Table XII depicts the values of SHG & LHG by seated and unseated persons present within the Auditorium.

No. of people who are seated = 550

No. of people who are unseated = 25

Load	Seated (W / person)	Unseated	References
Sensible load	60	75	[28]
Latent load	40	75	[28]

Table XII. *Sensible & Latent heat gain by a person*

3.1.5 Lights. - The lighting load within the space can be calculated by eq (7) [28].

$$\dot{Q} = W.F_u.F_b.CLF \qquad (7)$$

Light is assumed to be operating for 10 hours and the duration of light between turning on and peak time is taken as 6 hours (from 0800 hours to peak time of 1400 hours). Table XIII represents the wattage calculation of lights installed in the Auditorium while Table XIV depicts the parameters of lighting load calculation.

Type of light	Quantity	Wattage per light	Total Wattage
Energy saver	25	25	625
Recessed light	16	60	960
		Total	1590

Table XIII. *Wattage of lights*

Parameters	Symbol	Value	Reference
Utilization factor	F_u	1	[28]
Ballast factor	F_b	1.2	[28]
Cooling Load factor	CLF	0.78	[28]
Wattage	W	1590	--

Table XIV. *Lighting load parameters*

3.1.6 Infiltration. - Infiltration is the uncontrolled introduction of outside air into a building and is represented by $\dot{V}_i$. The ACH (Air Changes per Hour) method is used to determine the ventilation requirement of the Auditorium. ACH value is taken for medium-construction buildings at an outside temperature condition of 38℃ [30]. V is the volume of the University Auditorium calculated from the drawing.

$$\dot{V}_i = \frac{V\ (ACH)}{3600} \qquad (8)$$

$\dot{Q}_{is}$ is the sensible heat gain while $\dot{Q}_{il}$ is the latent heat gain due to infiltration. These values can be calculated by eq (9) and (10) [28].

$$\dot{Q}_{is} = 1.23\ \dot{V}_i(t_o - t_i) \qquad (9)$$

$$\dot{Q}_{il} = 3000\ \dot{V}_i(W_o - W_i) \qquad (10)$$

The volume of the Auditorium (m^3)	ACH [30]
2876.5	0.52

Table XV. *Air Change Method Parameters*

3.1.7 Ventilation. - Ventilation air comprises a combination of fresh and recirculated air [28] and plays a crucial role in ensuring IAQ reaches acceptable levels, meaning the air contains no harmful concentrations of known contaminants [31]. This system functions by delivering fresh air to indoor areas while concurrently eliminating stagnant air [32]. Fresh outdoor air enters the building through ventilation ducts, where it undergoes filtration and conditioning via a cooling coil to meet comfort and health requirements. The conditioned air is then dispersed throughout the building via ductwork and strategically placed vents. Stale air, containing pollutants and excess moisture, is extracted from the building through exhaust vents, usually directed outside. Some of the air may be recirculated during the exhaust phase to mix with fresh air before being reintroduced into the space, completing the cycle. This entire process is depicted in Figure XV.

$\dot{V}_v$ is the supply air rate for ventilation purposes which can be calculated by eq (11) [28], $\dot{V}_r$ is the recirculation air rate can be calculated by eq (12) [28] and $\dot{V}_m$ is the minimum outdoor air rate.

$$\dot{V}_v = \dot{V}_r + \dot{V}_m \qquad (11)$$

$$\dot{V}_r = \frac{\dot{V}_o - \dot{V}_m}{E} \qquad (12)$$

$\dot{V}_o$ is the outdoor air rate and E is the efficiency of contaminant removal by cleaning device. $\dot{Q}_{vs}$ is the sensible heat gain while $\dot{Q}_{vl}$ is the latent heat gain due to ventilation. These values can be calculated by eq (13) and (14) [28].

$$\dot{Q}_{vs} = 1.23\ \dot{V}_v(t_o - t_i) \qquad (13)$$

$$\dot{Q}_{vl} = 3000\ \dot{V}_v(W_o - W_i) \qquad (14)$$

Parameters	Values	Reference
$\boldsymbol{V_o}$	2.7	[33]
$\boldsymbol{V_m}$	2.5	[33]

Table XVI. *Ventilation Load Parameters*

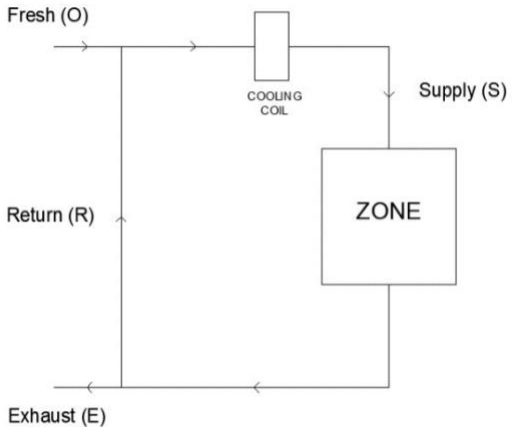

Figure XV.- *Airflow schematic diagram*

3.2 Cooling Load estimation using HAP (Transfer Function method)

The software used for the verification of cooling load calculation is Carrier's HAP version 4.9 as it has a user-friendly interface, uses the ASHRAE transfer function method for load calculations, and is the fastest way to get a solution and results rather than doing a manual calculation technique.

The weather properties such as design temperatures and humidity conditions are by default fed in HAP. The only selection will be of the desired location [34].

The distribution of the desired building into multiple units or sections for thermal comfort is known as Space in which further parameters like external cooling loads, internal cooling loads, infiltration, and ventilation loads are inserted [16].

As far as the schedule is concerned, it's the time and concern day for any activity that is to be performed in any section. There are some schedules made for lighting purposes, occupants, and other required conditions. Light is assumed to be operating for 10 hours and the duration of light between turning on and peak time is taken as 6 hours (from 0800 hours to peak time of 1400 hours).

For walls, its construction and structural details for the University Auditorium have been inserted and the R-value for each material to be used gives out the overall U-value of the wall. Similarly, for the roof, its construction and structural details have also been inserted, and the R-value for each material to be used gives out the overall U-value of the roof [35].

The transfer function method (TFM) is especially suitable for computer applications. It provides a straightforward calculation of the heat gain through a wall or roof, given by the eq (16) [36]:

$$q_{e,\theta} = A\left[\sum_{n=0} b_n\left(t_{e,\theta-n\delta}\right) - \sum_{n=0}\frac{d_n(q_{e,\theta-n\delta})}{A} - t_{r,c}\sum_{n=0} c_n\right] \qquad (15)$$

3.3 Air Balancing

3.3.1 Fresh / Exhaust air flowrate (Ventilation). - Flow rates of fresh / exhaust air can be determined by eq (15) [33]. Table XVII represents ventilation rates and related parameters.

$$Outdoor\ Air = R_p\ (N) + R_A\ (Zone\ Area) \quad (16)$$

Parameters	Symbol	Values	Units	Reference
People's outdoor air rate	R_P	5	cfm / person	[33]
Area outdoor air rate	R_A	0.06	cfm / ft^2	[33]
No of occupants	N	575	No.	--
Zone area (Area of Auditorium)	--	6619	m^2	--

Table XVII. *Ventilation rates in the breathing zone*

3.3.1.1 Condition of air at different stages. - Concerning the Figure XV, the condition of air at different stages can be categorized as:

- Outside Air - fresh air coming from outside.
- Mixed Air - this state is achieved when outside air is mixed with return air from the space.
- Supply Air - this state is achieved after mixed air passes through the cooling coil.
- Zone Air - this is the state of air inside the conditioned zone.

The supply air flow rate has been taken from HAP software. Eq (17) & (18) are used to find properties at the mixing state. Table XVIII represents the condition of air at different stages.

$$m_M = m_O + m_R \quad (17)$$

$$m_M h_M = m_O h_O + m_R h_R \quad (18)$$

Parameters	Symbol	Values	Units
Total cooling load	Q_T	202	kW
Sensible load	Q_S	119	kW
Latent load	Q_L	82	kW
Fresh air rate	V_O	1.54	m^3/s
Supply air rate	V_S	7.59	m^3/s

Table XVIII. *Different Parameters for different stages of Air*

3.3.2 Supply & Return Air Flowrate (Heat Removal Method). - The supply & return air flow rate is calculated by eq (19) [28] and eq (20) respectively. Here T_M and T_S are the temperatures at mixed and supply air condition respectively.

$$Supply\ air\ flowrate = \frac{Q_{sensible}}{1.08\ (T_M - T_S)} \quad (19)$$

$$Return\ air\ flowrate = Supply\ air\ flowrate - Fresh\ air\ flowrate \quad (20)$$

3.4 Air Distribution

3.4.1 Diffuser / Return Grill Selection & Duct Routing. - Diffusers are selected based on flow requirements and the noise criteria permissible for the room [37]. To select a diffuser and return air grill, the flow rate of discharge and intake air respectively is required. The diffusers and return air grills were selected as per the catalog for price diffusers [38] and price louvered grilles [39] respectively. Return and Supply air diffusers are divided in such a way that they provide air to an equal number of outlets. Figure XVI depicts the placement of diffusers and routing of duct from AHU to Space.

Figure XVI.- *Duct Routing*

3.4.2 Duct Losses. - Duct pressure drop is calculated by using the Equal Friction method. The value of pressure drop per unit length must be determined from the friction chart [36] and kept constant among all segments. Major loss & minor loss in pipe segment is calculated by eq (21) & (22) respectively.

$$\Delta P = \left(\frac{\Delta P}{l}\right)_{seg} . l_{seg} \quad (21)$$

$$\Delta P = (sum\ of\ joint\ losses).\frac{1}{2}\ \rho v_{seg}^2 \quad (22)$$

Table XIX shows the loss coefficient values of some common joints [36].

Joint	Loss Coefficient
$K_{entrance}$	0.82
$K_{tee-through}$	0.04
$K_{tee-branch}$	0.73
K_{90°	1.27
K_{45°	0.37
$K_{wye-branch}$	0.52
$K_{wye-through}$	0.05
Pressure drop across supply diffuser	16 Pascals
Pressure drop across return grills	17 Pascals

Table XIX. *Loss coefficients*

Table XX represents the flow, dimensions, and head losses for each segment in the index run of the Supply air duct.

	Major				**Minor (K_L)**						
					No. of Fittings						
Segment	$\frac{\Delta P}{l}$ (Pa/m)	Flow rate (L/s)	Velocity (m/s)	Length (m)	Entrance	Wye - through	Wye - branch	Tee - through	Tee - branch	K90	K45
A	0.15	8307	5.0	4.93	1	--	--	--	--	--	--
B	0.15	4153	4.2	13.47	--	1	--	--	--	1	--
B1	0.15	4153	4.2	10.01	--	--	--	--	--	1	--
D	0.15	4153	4.2	15.24	--	--	--	--	--	2	--
G	0.15	2076	3.6	6.83	--	1	--	--	--	--	--
I	0.15	1038	3.0	4.85	--	1	1	--	--	1	--
I1	0.15	519.2	2.5	0.30	--	--	--	--	--	--	--

Table XX. *Pressure losses in different Supply air duct segments of the Index run*

Table XXI represents the flow, dimensions, and head losses for each segment in the index run of the Return air duct.

	Major				**Minor (K_L)**						
					No. of Fittings						
Segment	$\frac{\Delta P}{l}$ (Pa/m)	Flow rate (L/s)	Velocity (m/s)	Length (m)	Entrance	Wye - through	Wye - branch	Tee - through	Tee - branch	K90	K45
A	0.08	6570	3.8	0.58	1	--	--	--	--	--	--
C	0.08	3285	3.3	5.08	--	--	--	--	--	1	--
G	0.08	2190	2.8	7.85	--	--	--	--	1	1	--
G1	0.08	2190	2.8	11.64	--	--	--	--	--	1	--
K	0.08	1095	2.4	1.04	--	--	--	--	--	1	--
K1	0.08	1095	2.4	1.65	--	--	--	--	--	1	--
K2	0.08	1095	2.4	10.98	--	--	--	--	--	1	--
K3	0.08	1095	2.4	0.66	--	--	--	--	--	1	--
K4	0.08	1095	2.4	1.65	--	--	--	--	--	1	--
K5	0.08	1095	2.4	0.66	--	--	--	--	--	1	--

Table XXI. *Pressure losses in different Return air duct segments of the Index run*

3.4.4 Duct Sizing. - A rectangular duct for our design (except at the discharge where the cross-section will be circular) is selected, equivalent diameter is calculated by eq (23) [28].

$$D_h = \frac{1.3\,(ab)^{0.625}}{(a+b)^{0.25}} \qquad (23)$$

3.5 Equipment Selection. - We are proposing two different HVAC systems for the University Auditorium which are based on water cooled chiller and an air-cooled chiller.

3.5.1 Proposed System # 1. - This system primarily relies on a water-cooled chiller. Its main components consist of a compressor, condenser, expansion valve, and evaporator. Chilled water from the evaporator is directed to the AHU via two chilled water pumps (one operational and the other on standby). The AHU comprises various elements, including filters, a supply air duct, a fresh air duct, a return air duct, an air mixing chamber, and a cooling coil. Chilled water

flows through the coil while air passes over it, becoming cooled in the process. The cooled air is then distributed into the space. Another essential part is the condenser water circuit. Hot water from the condenser is conveyed to the cooling tower through two condenser water pumps (one operational and the other on standby). After heat rejection, the water returns to the condenser, completing the cycle. The term "water-cooled" refers to the condenser water being cooled by the cooling tower. The entire system is illustrated in Figure XVII for reference.

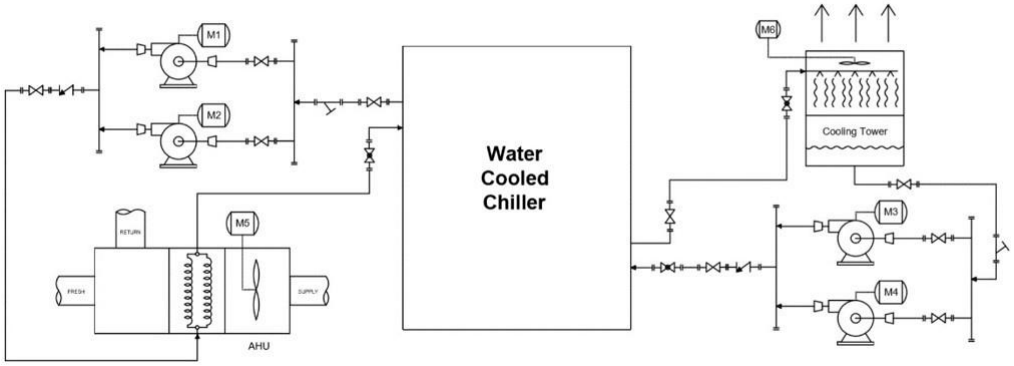

Figure XVII.- *Proposed System # 1*

3.5.2 Proposed System # 2. - This system operates on an air-cooled chiller. Its main components are identical to those of a water-cooled chiller, except for the absence of a cooling tower. Instead, an air-cooled condenser is used, eliminating the need for a cooling tower as the condenser water is cooled naturally by air. This system configuration is depicted in Figure XVIII.

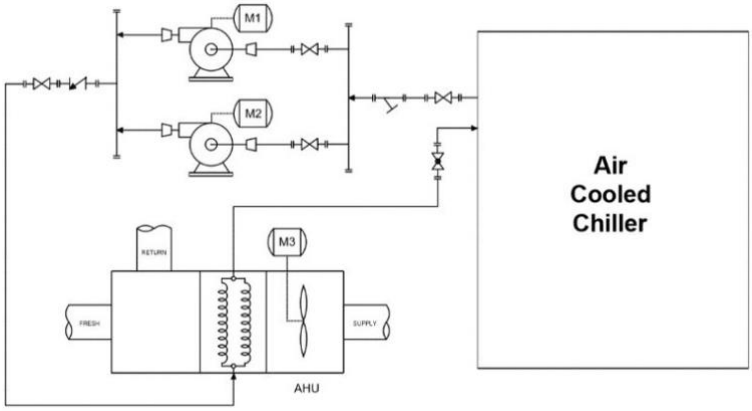

Figure XVIII.- *Proposed System # 2*

3.5.3 Chiller & AHU selection. - Typically, the chiller supplies chilled water at around 7 °C which makes the return water temperature 12 °C. The chilled water flow rate will be taken from water cooled chiller's datasheet. The supply, return, and fresh air flow rates have been taken from the Air Balancing section. The fan selection performed in the AHU is based on the external and internal pressure drops. Internal pressure drop is due to the losses inside AHU while external pressure drop is the sum of pressure drop in the damper, ducting, and diffusers.

3.5.4 Cooling Tower & Pump selection. - The condenser water flow rate will be taken from the chiller's datasheet. Cooling tower inlet and outlet water temperatures depend upon the selection of chiller because the condenser's inlet and outlet water conditions vary with different chillers. For wet bulb temperature, outside air data will be used. We will select two pumps each for the condenser and chilled water circuits. One pump is working while the other is for backup. The cooling tower's height, condenser & evaporator losses (from the chiller datasheet), pipes, fittings, and valve losses will be considered for the head. The flow rate will be taken from the selected water-cooled chiller datasheet.

3.6 Piping System

3.6.1 Water Cooled System. - For the application of HVAC, steel pipes are commonly used. We are selecting steel pipe of Schedule 40 for condenser and chilled water piping. For pipe sizing, we are using Carrier's friction charts [36]

for Schedule 40 Pipe. Table XXII depicts the Pipe design parameters for the cool and chilled water circuit.

Parameters	Condenser water	Chilled water	Unit	Ref
Velocity	5	6	Ft/sec	[40]
Flowrate	205	156	US gpm	[40]
Pipe size	4	3.5	inch	[40]
Friction loss	3.6	2.5	Ft of water per 100 ft	[40]

Table XXII. *Pipe design parameters for Cool and chilled water system*

The total piping length in the condenser and chilled water system is 161 ft & 79 ft respectively. Head losses due to valves and fittings for condenser and chilled water lines are taken [40] for 4" & 3.5" pipe diameters respectively. Table XXIII shows the equivalent lengths of the head, no. of valves, and fittings in the condenser and chilled water line.

Designing Criteria		Condenser water line			Chilled water line		
		L/D	Quantity	L_{eq} (ft)	L/D	Qty	L_{eq} (ft)
Fittings	Elbow 90°	10	20	66.7	9	16	48
	Tee (flow thru branch)	21	4	28	18	4	24
Valves	Gate	4.5	4	6	4	3	4
	Globe	120	2	80	100	1	33.3
	60° Strainer	60	1	20	48	1	16
	Swing Check	40	1	13.3	35	1	11.7
			Total	214			137
		Total equivalent length		375			216

Table XXIII. *Pipe fittings, valves & equivalent length in condenser & chilled water line*

Head loss due to piping is given by eq (24) [40].

$$h_L = f\frac{L}{D}\frac{v^2}{2g} \qquad (24)$$

The pressure loss in the condenser and evaporator is calculated by eq (25) [40].

$$h_L = \frac{P}{\rho g} \qquad (25)$$

3.6.2 Air Cooled System. - Steel pipe of Schedule 40 for Chilled Water Piping is selected. For pipe sizing, we select Schedule 40 Pipe [40]. Table XXIV depicts the Pipe design parameters for the chilled water circuit.

Parameters	Chilled water	Unit	Reference
Velocity	6	Ft/sec	[40]
Flowrate	168	US gpm	[40]
Pipe size	3.5	inch	[40]
Friction loss	3.6	Ft of water per 100 ft	[40]

Table XXIV. *Pipe design parameters for chilled water system*

The total piping length in a chilled water system is 112 ft. Head losses due to valves and fittings for chilled water lines are taken [40] for a 3.5" pipe diameter. Table XXV depicts the equivalent lengths of the head, no. of valves, and fittings in the chilled water line.

Designing Criteria		Chilled water line		
		L/D	Quantity	L_{eq} (ft)
Fittings	Elbow 90°	9	20	60

	Tee (flow thru branch)	18	4	24
Valves	Gate	4	3	4
	Globe	100	1	33.3
	60° Strainer	48	1	16
	Swing Check	35	1	11.7
			Total	149
			Total equivalent length	261

Table XXV. *Pipe fittings, valves & equivalent length in a chilled water line*

3.6.3 Duct & Piping Layout. - Figure XIX & XX shows the ducting and piping layouts for the two proposed HVAC systems for the Auditorium while Figure XXI depicts a ducting layout of the plant room for both the proposed HVAC systems.

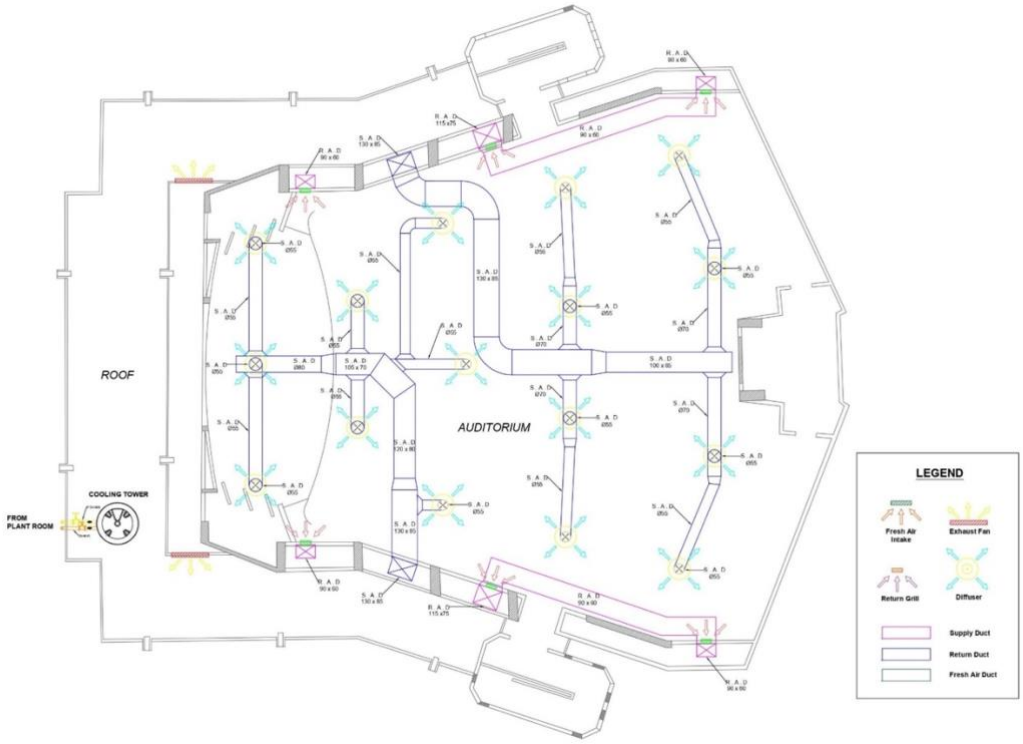

Figure XIX.- *Duct & Pipe Layout for Proposed System # 1*

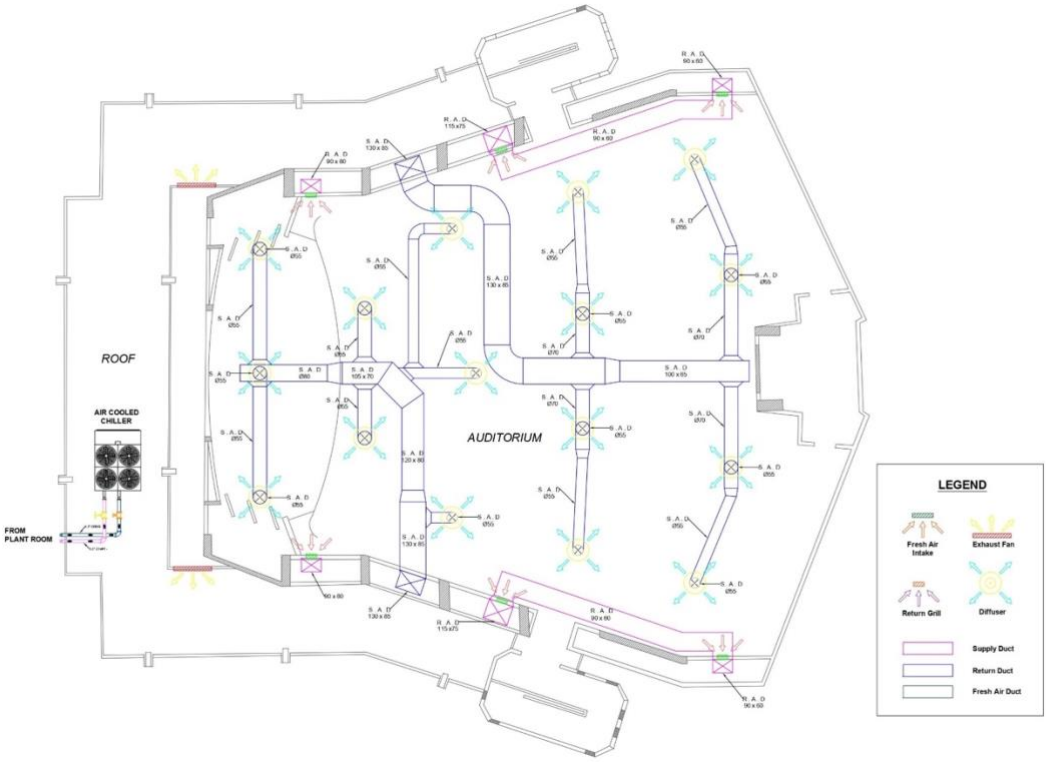

Figure XX.- *Duct & Pipe Layout for Proposed System # 2*

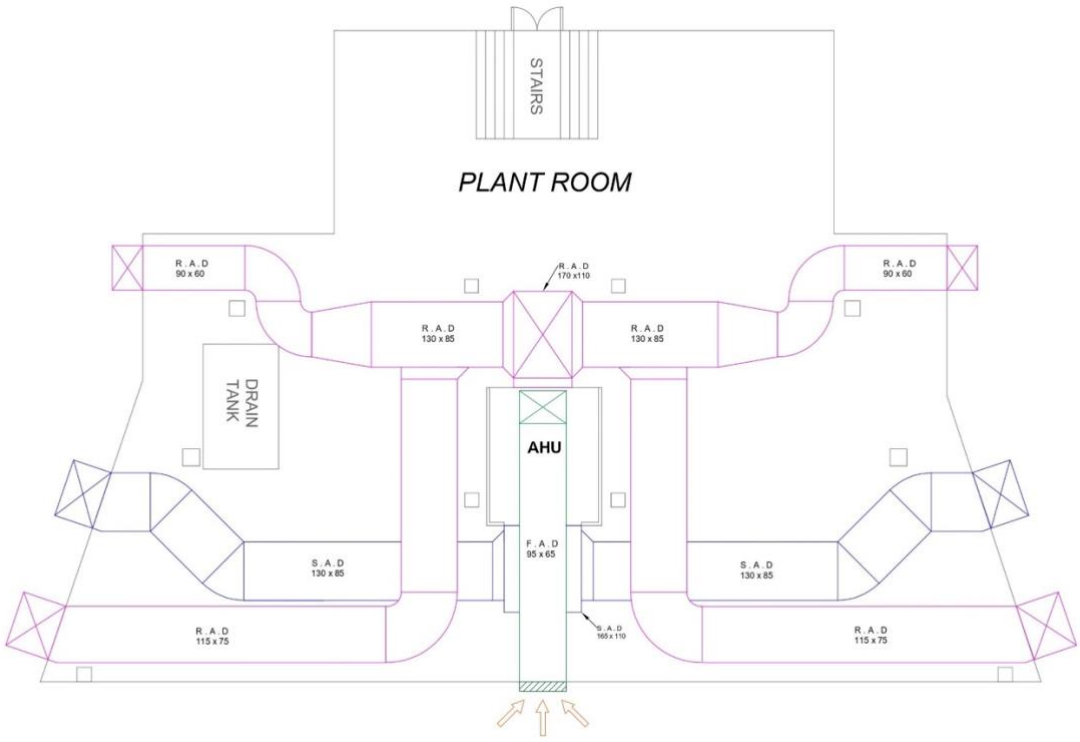

Figure XXI.- *Duct Layout of Plant Room for Proposed Systems # 1 & 2*

4. Results. - In this study, we calculated the cooling load of the University Auditorium first by manual calculation using the CLTD method then the results obtained were validated by using CARRIER's HAP (version 4.9) software.

4.1 Cooling Load by CLTD Results. - The results of the cooling load obtained after calculation by using CLTD methods are listed in Table XXVI. All the cooling loads are taken in kW.

External Cooling Load		**Roof**	23.96
	Walls	**South East (Back wall)**	3.7
		South West (Sidewall)	4.4
		North East (Sidewall)	5.28
		North West (Stage wall)	4.37
		Floor	7.87
Internal Cooling Load		**Occupant**	51.78
		Lights	1.48
		Infiltration Load	20.98
		Ventilation Load	78.38
		Total Cooling Load of the Auditorium	**202**

Table XXVI. *Cooling Load (CLTD method)*

The cooling load obtained from the CLTD-based calculation was 202 kW which is equivalent to around 57 TR. Figure XXII shows the condition of air at different stages on a psychrometric chart calculated by the CLTD method.

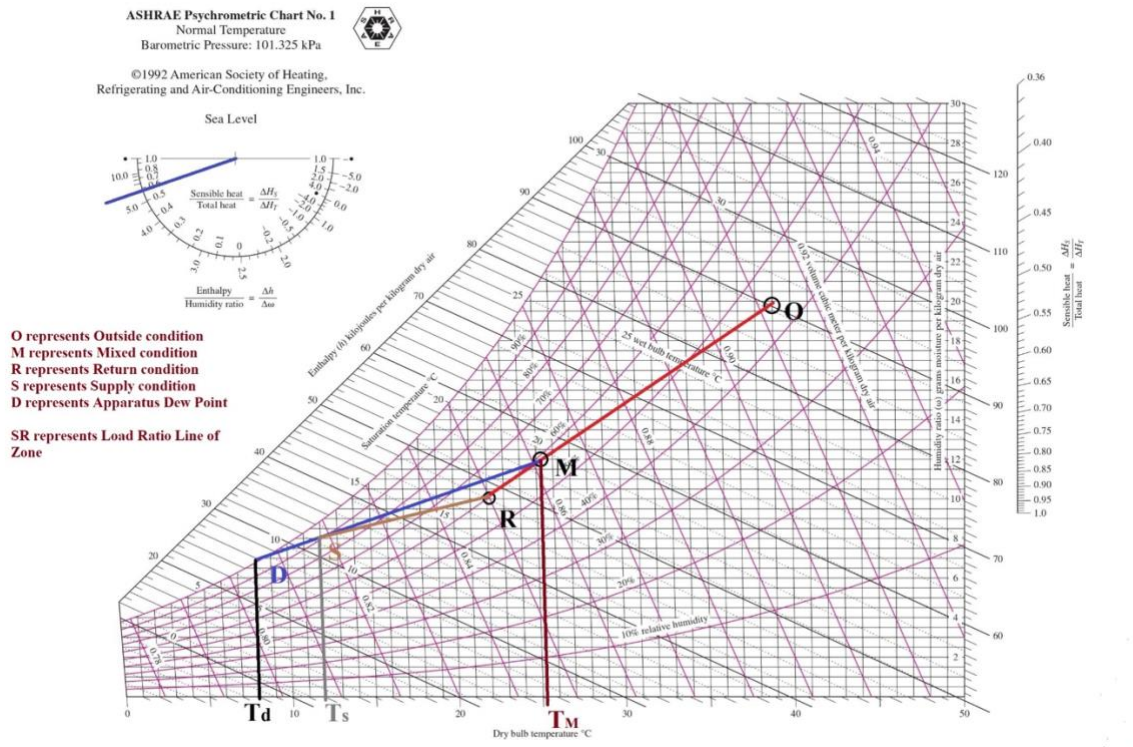

Figure XXII.- *Psychrometric Chart (CLTD Results)*

4.2 Cooling Load by HAP Results

- The HAP result depicts the cooling load of the University Auditorium as 192.8 kW which is equivalent to around 55 TR.
- The calculated ventilation (fresh air) rate for desired air conditioning in the air balancing section is 3273 cfm which is close to the value determined from the HAP result which is 1622 L/s (3436 cfm).
- The calculated supply air flow rate from the Heat Removal method is 16071 cfm which is close to the value given by the HAP result as 7589 L/s (16080 cfm).

- Figure XXIII & XXIV shows the results obtained by HAP.

Project Name: University

Air System Sizing Summary for University

Air System Information

Air System Name	Auditorium		Number of zones	1	
Equipment Class	CW AHU		Floor Area	615.0	m²
Air System Type	SZCAV		Location	Karachi, Pakistan	

Sizing Calculation Information

Calculation Months	Jan to Dec	Zone L/s Sizing	Peak zone sensible load
Sizing Data	Calculated	Space L/s Sizing	Zone L/(s-m²)

Central Cooling Coil Sizing Data

Total coil load	192.8	kW	Load occurs at	Jun 1600	
Sensible coil load	117.2	kW	OA DB / WB	38.1 / 27.7	°C
Coil L/s at Jun 1600	7589	L/s	Entering DB / WB	25.9 / 20.1	°C
Max block L/s at Jul 1700	7589	L/s	Leaving DB / WB	13.1 / 12.6	°C
Sum of peak zone L/s	7589	L/s	Coil ADP	11.7	°C
Sensible heat ratio	0.608		Bypass Factor	0.100	
m²/kW	3.2		Resulting RH	61	%
W/m²	313.5		Design supply temp.	12.0	°C
Water flow @ 5.6 °K rise	8.31	L/s	Zone T-stat Check	1 of 1	OK
			Max zone temperature deviation	0.0	°K

Supply Fan Sizing Data

Actual max L/s at Jul 1700	7589	L/s	Fan motor BHP	0.00	BHP
Standard L/s	7585	L/s	Fan motor kW	0.00	kW
Actual max L/(s-m²)	12.34	L/(s-m²)	Fan static	0	Pa

Outdoor Ventilation Air Data

Design airflow L/s	1622	L/s	L/s/person	2.82	L/s/person
L/(s-m²)	2.64	L/(s-m²)			

Figure XXIII.- *HAP Results*

Air System Design Load Summary for University

Project Name: University

	DESIGN COOLING			DESIGN HEATING		
	COOLING DATA AT Jun 1600 COOLING OA DB / WB 38.1 °C / 27.7 °C			HEATING DATA AT DES HTG HEATING OA DB / WB 9.4 °C / 5.1 °C		
ZONE LOADS	Details	Sensible (W)	Latent (W)	Details	Sensible (W)	Latent (W)
Window & Skylight Solar Loads	0 m²	0	-	0 m²	-	-
Wall Transmission	510 m²	14748	-	510 m²	10439	-
Roof Transmission	615 m²	25465	-	615 m²	12242	-
Window Transmission	0 m²	0	-	0 m²	0	-
Skylight Transmission	0 m²	0	-	0 m²	0	-
Door Loads	24 m²	610	-	24 m²	479	-
Floor Transmission	615 m²	6789	-	615 m²	0	-
Partitions	0 m²	0	-	0 m²	0	-
Ceiling	0 m²	0	-	0 m²	0	-
Overhead Lighting	1902 W	1559	-	0	0	-
Task Lighting	0 W	0	-	0	0	-
Electric Equipment	0 W	0	-	0	0	-
People	575	30106	20240	0	0	0
Infiltration	-	9670	12998	-	0	0
Miscellaneous	-	0	0	-	0	0
Safety Factor	0% / 0%	0	0	0%	0	0
>> Total Zone Loads	-	88949	33238	-	23160	0
Zone Conditioning	-	86802	33238	-	-6085	0
Plenum Wall Load	0%	0	-	0	0	-
Plenum Roof Load	0%	0	-	0	0	-
Plenum Lighting Load	0%	0	-	0	0	-
Return Fan Load	7589 L/s	0	-	7589 L/s	0	-
Ventilation Load	1622 L/s	30390	42381	1622 L/s	6310	0
Supply Fan Load	7589 L/s	0	-	7589 L/s	0	-
Space Fan Coil Fans	-	0	-	-	0	-
Duct Heat Gain / Loss	0%	0	-	0%	0	-
>> Total System Loads	-	117193	75619	-	224	0
Central Cooling Coil	-	117193	75621	-	0	0
>> Total Conditioning	-	117193	75621	-	0	0
Key:	Positive values are clg loads Negative values are htg loads			Positive values are htg loads Negative values are clg loads		

Figure XXIV.- *Sensible & Latent heat gains*

Figure XXV depicts the HAP result which shows a psychrometric diagram of the Air conditioning process for the University Auditorium.

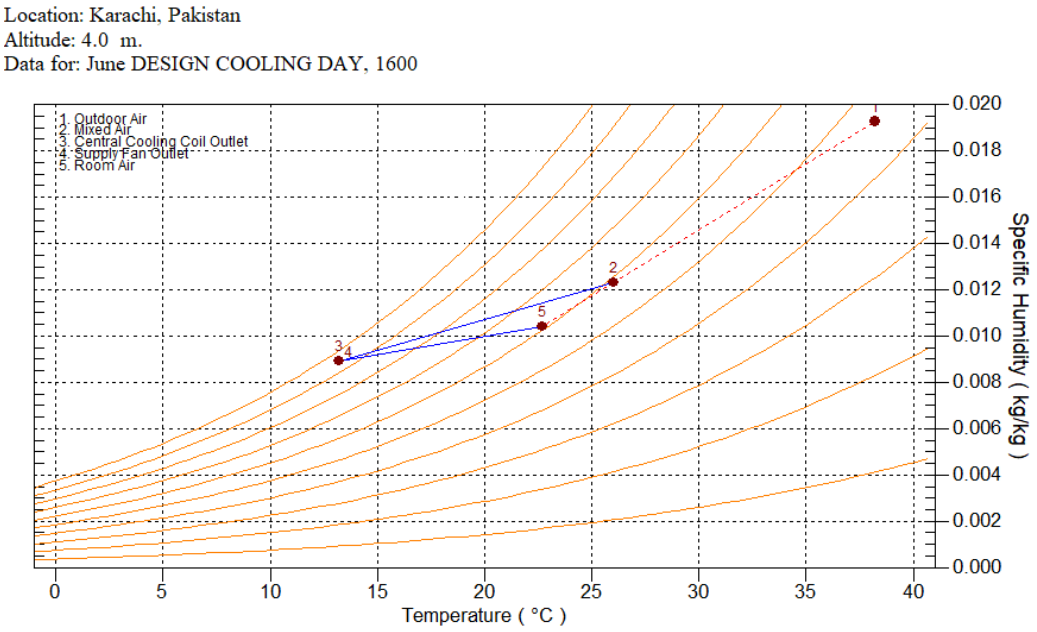

Figure XXV.- *Psychrometric chart obtained from HAP software*

Figure XXVI shows the comparison of the University Auditorium cooling loads between CLTD and HAP. Figure XXVII depicts the comparison of Total Heat Gain by CLTD & HAP software.

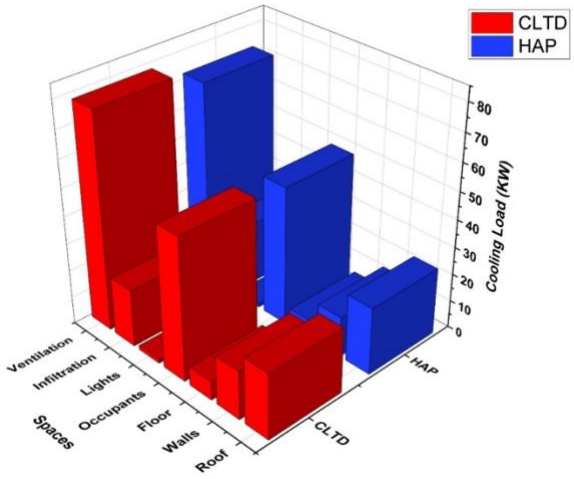

Figure XXVI.- *Cooling load (CLTD vs HAP)*

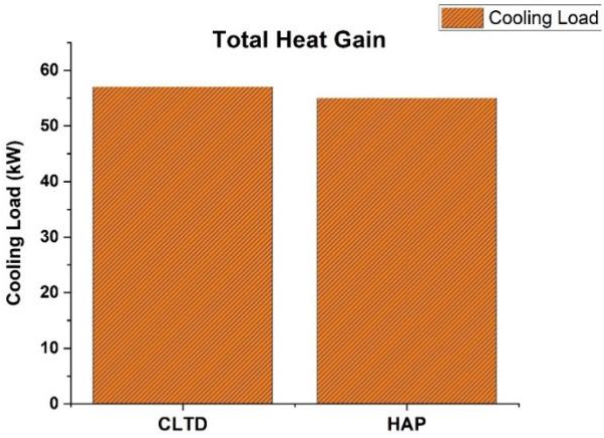

Figure XXVII.- *Total Heat Gain (CLTD vs HAP)*

4.3 Air Balancing. - Figure XXVIII shows the Fresh air, return air & Supply air flow rates by using the CLTD method.

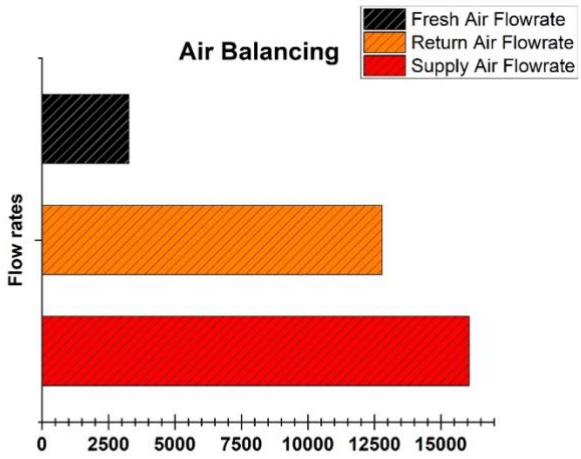

Figure XXVIII.- *Air Balancing Flowrates*

4.4 Diffuser & Return Air Grill Selection. - A total sixteen number of diffusers in the University Auditorium have been calculated. We have selected Round Diffusers [38] because they meet the low NC requirement for the Auditorium. The diffuser that meets our requirement is Price's 20" Round Cone Diffuser (RCD) providing supply air of 1100 cfm at a minimal NC value of 15. Air velocity is 500 fpm whereas the throw at 150 mm is 14 ft.
Similarly, we will install six return air grills in the Auditorium space and select Price's 40" x 16" Rectangular Louvered Grille, whose intake flow rate is 2320 cfm [39].

4.5 Duct Losses. - Table XXVII represents the results obtained for the major and minor losses through different Supply air duct segments of the Index run. Table XXVIII represents the results obtained for the major and minor losses through different Return air duct segments of the Index run.

Segment	Major Loss (Pa)	Minor Loss (Pa)	Head Loss (Pa)	Total Pressure Drop (Pa)
A	0.72	12.7	--	13.43
B	1.98	14.43	--	16.41
B1	1.47	13.88	120.29	135.65
D	2.24	27.76	--	30.00
G	1.00	0.39	--	1.39
I	0.71	7.36	--	8.07
I1	0.04	2.01	--	2.06
		Pressure drop across supply diffuser		16
			Total	223.01

Table XXVII. *Supply air duct losses*

Segment	Major Loss (Pa)	Minor Loss (Pa)	Total Pressure Drop (Pa)
A	0.05	7.34	7.39
C	0.41	8.31	8.73
G	0.64	9.37	10.01
G1	0.95	5.95	6.90
K	0.09	4.35	4.43
K1	0.13	4.35	4.48
K2	0.90	4.35	5.24
K3	0.05	4.35	4.40
K4	0.13	4.35	4.48
K5	0.05	4.35	4.40
		Pressure drop across the return grill	17
		Total	77.46

Table XXVIII. *Return air duct losses*

4.6 Duct Sizing. - Supply & return air duct sizing results for an aspect ratio of 1.5 are shown in Table XXIX & Table XXX respectively.

Segment	Dia. (cm)	Size		Duct Shape
		a (cm)	b (cm)	
A	144	164	109	Rectangular
B	111	126	84	Rectangular
B1	111	126	84	Rectangular
C	111	126	84	Rectangular
C1	111	126	84	Rectangular

D	111	126	84	Rectangular
E	66	75	50	Circular
E1	51	59	39	Circular
E2	51	59	39	Circular
F	66	75	50	Circular
F1	51	59	39	Circular
F2	51	59	39	Circular
G	86	98	65	Rectangular
H	66	75	50	Circular
H1	51	59	39	Circular
H2	51	59	39	Circular
I	66	75	50	Circular
I1	51	59	39	Circular
I2	51	59	39	Circular
J	111	126	84	Rectangular
J1	51	59	39	Circular
J2	106	120	80	Rectangular
K	93	105	70	Rectangular
L	66	75	50	Circular
M	51	59	39	Circular
N	51	59	39	Circular
O	51	59	39	Circular
P	51	59	39	Circular
Q	77	89	59	Circular
R	51	59	39	Circular
S	51	59	39	Circular
T	51	59	39	Circular
Fresh	82	93	62	Rectangular

Table XXIX. *Supply air duct sizing*

Segment	**Dia. (cm)**	**Size**	
		a (cm)	**b (cm)**
A	147	166	110
B	112	127	84
C	112	127	84
D	76	86	57
D1	76	86	57
D2	76	86	57
E	76	86	57
E1	76	86	57
E2	76	86	57
F	100	112	75
F1	100	112	75
G	100	112	75
G1	100	112	75
H	76	86	57
I	76	86	57

J	76	86	57
J1	76	86	57
J2	76	86	57
J3	76	86	57
J4	76	86	57
J5	76	86	57
K	76	86	57
K1	76	86	57
K2	76	86	57
K3	76	86	57
K4	76	86	57
K5	76	86	57

Table XXX. *Return air duct sizing*

4.7 Chiller Selection

4.7.1 Proposed System # 1. - As per the design requirement and the consultant's provided design condition datasheet, the chiller we have selected is YORK's 65-ton scroll compressor-type water-cooled chiller.

YORK's 65 tons scroll compressor type water-cooled chiller specification	
Model	YCWL0261HE
Refrigerant	R-410 (A)
EER	14.90 (Btu/W·h)
Chilled water supply/return temp.	7 °C / 12 °C (44 °F / 54 °F)
Condenser water supply/return temp.	32 °C /38 °C (90 °F /100 °F)
Condenser / chilled water flow rates	205 / 156 US gpm
Condenser/evaporator pressure drop	8.01 / 5.74 ft. of water
Maximum operating power	52 kW

Table XXXI. *Specification of Water-cooled chiller*

This chiller consists of four scroll compressors which provide a part load condition. All four compressors are operating at maximum cooling load conditions but as the cooling requirement of the zone decreases, the system automatically turns off one of the compressors. Therefore, the number of compressors in operation depends on the zone cooling requirement resulting in saving power. Moreover, even at the maximum capacity, the system operating power is still lower than the existing installed system whose compressor's operating power is 55 kW. GWP of R-410 (A) is 2088.

4.7.2 Proposed System # 2. - Another chiller that is nearest to our design capacity and as per the consultant's provided design condition datasheet is YORK's 71 tons Air-cooled Scroll Chiller.

YORK's 71 tons Air-cooled Scroll Chiller specification	
Model	YLAA0286SE
Refrigerant	R-410 (A)
EER	7.47 (Btu/W·h)
Chilled water supply/return temp.	7 °C / 12 °C (44 °F /54 °F)
Chilled water flow rates	168 US gpm
Pressure loss	10.6 ft. of water
Maximum operating power	115 kW

Table XXXII. *Specification of Air-cooled chiller*

This chiller consists of six scroll compressors, R-410 (A) as a refrigerant, and works on the same part load condition as water cooled chiller does. As compared to water cooled chiller, this chiller has a lower value of energy efficiency and its power input is more than double that of the water-cooled chiller. The chiller has an approx. size of 3400 mm x

2250 mm x 2400 mm. The roof of the University Auditorium where the current cooling tower is installed has sufficient space to accommodate this chiller.

4.8 AHU Selection. - Table XXXIII depicts the important parameters for selection of AHU which we have previously calculated.

AHU Selection	
Supply air flow rate	16071 cfm
Return air flow rate	12800 cfm
Fresh air flow rate	3272 cfm
Off-coil temperature (dbt / wbt)	26 °C / 20 °C
On coil temperature (dbt / wbt)	13 °C / 11 °C
External press. drop	223 x 1.25 (Factor of safety) = 277 Pa
Chilled water flow rate	156 / 168 US gpm
Chilled water supply/return temperature	7 °C / 12 °C

Table XXXIII. *AHU selection parameters*

By considering the above parameters and as per the consultant's provided datasheet, we have selected AHU from YORK, having Model # YMA(T)1730H-2450W. This AHU provides a supply air flow rate of 8.30 m^3/s (17600 cfm approx.) having a size of 3000 mm x 2450 mm x 1830 mm (smaller than the AHU of an existing system whose dimensions are 3940 mm x 3090 mm x 1740 mm) and will easily be fitted inside the plant room. The fan must overcome a total pressure drop of 750 Pa. (internal Pressure Drop = 277 Pa, external Pressure Drop = 473 Pa). For this purpose, a fan of 15 kW of nominal power is selected. This AHU model is applicable for both proposed System # 1 and System # 2.

4.9 Cooling Tower Selection. - Table XXXIV depicts the important parameters for the selection of a cooling tower which we have previously calculated.

Cooling Tower Selection	
System capacity	65 tons
Condenser water flow rate	205 US gpm
Cooling tower inlet/outlet temperatures	32 °C / 38 °C (90 °F /100 °F)
Design wet bulb temperature	23.2 °C (73 °F)

Table XXXIV. *Cooling tower selection parameters*

By considering the above parameters and as per the consultant's design condition datasheet, we have selected Liang Chi's bottle type counter flow induced draft cooling tower of Model # LBC-60-S. This model can provide a flow rate at 205 US gpm and meets the required condenser temperatures. It has a direct motor drive axial-flow fan that runs at 750 rpm with a motor input power of 2 hp. Furthermore, the inlet and outlet connection have a 3" dia. so a reducer must be required for the installation of the condenser water pipe. The roof of the University Auditorium is a suitable place for its installation.

4.10 Pump Selection. - Table XXXV depicts the important parameters for the selection of Chilled/condenser water pumps which we have previously calculated.

Parameters	Unit	Water cooled system		Air-cooled system
		Chilled water pump	Condenser water pump	Chilled water pump
Flowrate	US gpm	156	205	168
Pressure head	Ft	32.43	36.37	51.26
Pipe dia.	inch	3.5	4	3.5

Table XXXV. *Pump selection parameters*

By considering the above parameters and as per the consultant's design condition datasheet, we have selected KSB's low-pressure centrifugal pumps. Table XXXVI depicts the model numbers and quantity of selected chilled & cool water pumps for both proposed systems.

System	Pump	Quantity	Model No.
Water cooled system	Chilled Water Pump	2	ETN 065-050-200 GBSAA11GD200224B
	Condenser Water Pump	2	ETN 080-065-200 GBSAA11GD200224B
Air-cooled system	Chilled Water Pump	2	ETN 080-065-200 GBSAA11GD200404B

Table XXXVI. *Pumps Model Number*

These models meet our required head and flow rates. Motor input power and speed of chilled water and condenser water pumps are 2.95 hp each & 1400 rpm for water cooled system. The motor input power and speed of the chilled water pump are 5.36 hp & 1400 rpm for the air-cooled system.

4.11 Piping System. - Table XXXVII depicts the head loss from the water-cooled and air-cooled chilled & cool water piping system. All losses are measured in ft.

Head Loss	Water cooled system		Air-cooled system
	Condenser water circuit	Chilled water circuit	Chilled water circuit
Pipe Friction	15.72	7.19	18.01
Condenser / Evaporator	8.03 / --	-- / 5.75	-- / 10.62
Cooling Tower / AHU	6.56 / --	-- / 14.09	-- / 14.09
Total Head Loss (with 20% Factor of Safety)	36.4	32.43	51.26

Table XXXVII. *Piping head loss*

4.12 Piping Layout. - Figure XXIX & XXX depicts the piping layout of the plant room for both the proposed HVAC systems.

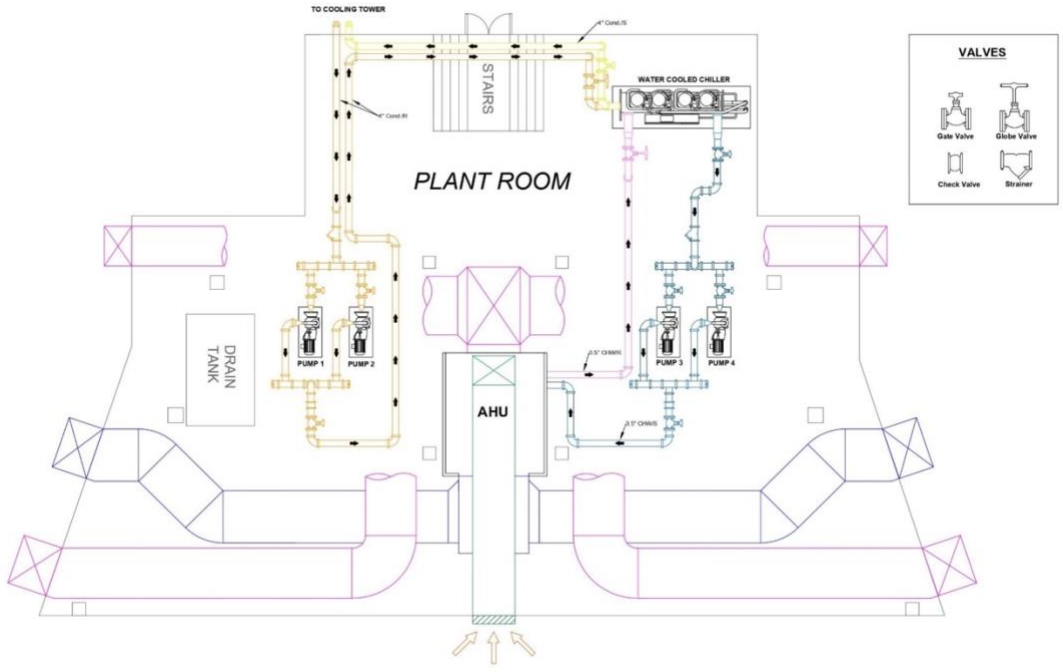

Figure XXIX.- *Pipe Layout of Plant Room for Proposed System # 1*

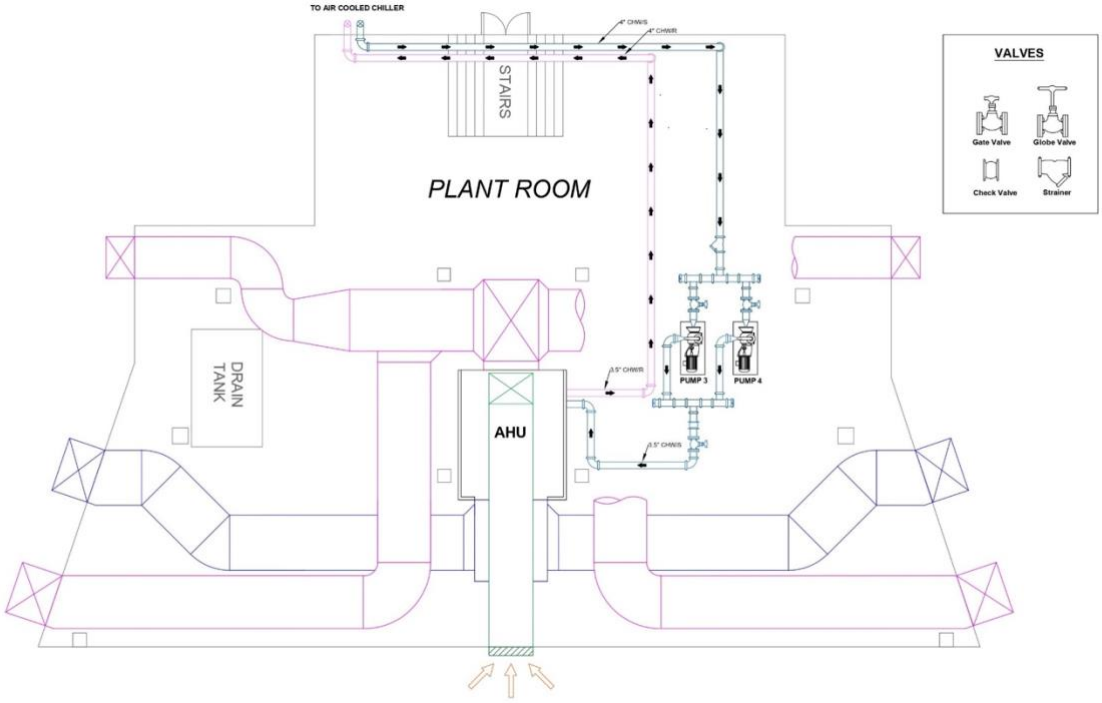

Figure XXX.- *Pipe Layout of Plant Room for Proposed System # 2*

5. Conclusion & Discussion. - This study outlines the design of HVAC systems for the University Auditorium, proposing both water-cooled and Air-Cooled Vapor Compression systems. Cooling loads were calculated using the CLTD method and HAP software, resulting in 57 TR and 55 TR respectively, with a small discrepancy of only 3.5%. The fresh air flow rate was manually calculated at 3272 cfm, closely matching HAP's 3436 cfm, while for the Supply air flow rate, the manual calculation (Heat Removal method) yielded 16071 cfm compared to HAP's 16080 cfm. Equipment selections include sixteen Price's 20-inch Round Cone Diffusers, six Price's 40" x 16" Rectangular Louvered Grille, YORK's 65 tons scroll compressor type water-cooled chiller, YORK's 71 tons Air-cooled Scroll Chiller, YORK's AHU, and Liang Chi's bottle type counter flow induced draft cooling tower, along with two KSB's centrifugal pumps. The study highlights the importance of designing cost-effective and energy-efficient HVAC systems, addressing the increasing demand driven by global warming and humid climates, and offering guidance for engineers and researchers to propose new systems for spaces, including replacing obsolete ones, based on selection criteria and research findings.

References.

[1] M. H. A. R. B. F. U. R. A. S. I. A. R. B. Yousaf, "A comprehensive review of climate change impacts, adaptation, and mitigation on environmental and natural calamities in Pakistan," 2019, doi: https://doi.org/10.1007/s10661-019-7956-4.

[2] D. G. R. Dr. Qamar uz Zaman Chaudhry, Ahmad Kamal, Munir Ahmad Mangrio and Shahbaz Mahmood, "Technical Report on Karachi Heat wave June 2015," 2015.

[3] A. Yatim, I. Pamuntjak, and F. Yudhi, "Thermal Comfort Analysis of Art Centre Auditorium Utilizing R290 Refrigerant Chiller," *International Journal on Advanced Science, Engineering and Information Technology,* vol. 11, p. 1246, 06/30 2021, doi: 10.18517/ijaseit.11.3.14485.

[4] J. Hoof, M. Mazej, and J. Hensen, "Thermal comfort: Research and practice," *Frontiers in Bioscience,* vol. 15, pp. 765-788, 01/01 2010, doi: 10.2741/3645.

[5] P. Thirumal, K. S. Amirthagadeswaran, and S. Jayabal, "Optimization of Indoor Air Quality Characteristics in an Air-Conditioned Car Using Multi-objective Genetic Algorithm," *Arabian Journal for Science and Engineering,* vol. 39, no. 11, pp. 8307-8317, 2014/11/01 2014, doi: 10.1007/s13369-014-1392-0.

[6] O. M. Al-Rabghi, A. S. Al-Ghamdi, and M. M. Kalantan, "Thermal Comfort Around the Holy Mosques," *Arabian Journal for Science and Engineering,* vol. 42, no. 5, pp. 2125-2139, 2017/05/01 2017, doi: 10.1007/s13369-017-2464-8.

[7] *Thermal Environmental Conditions for Human Occupancy*, A. A. S. 55-2010, 2010. [Online]. Available: http://arco-hvac.ir/wp-content/uploads/2015/11/ASHRAE-55-2010.pdf

[8] R. Lathia and J. Mistry, "Process of designing efficient, emission free HVAC systems with its components for 1000 seats auditorium," *Pacific Science Review A: Natural Science and Engineering,* vol. 18, no. 2, pp. 109-122, 2016.

[9] S. M. Hussain, W. Jamshed, and M. R. Eid, "Solar-HVAC Thermal Investigation Utilizing (Cu-AA7075/C6H9NaO7) MHD-Driven Hybrid Nanofluid Rotating Flow via Second-Order Convergent Technique: A Novel Engineering Study," *Arabian Journal for Science and Engineering,* vol. 48, no. 3, pp. 3301-3322, 2023/03/01 2023, doi: 10.1007/s13369-022-07140-6.

[10] K. Rabhi, C. Ali, R. Nciri, and H. Ben Bacha, "Novel Design and Simulation of a Solar Air-Conditioning System with Desiccant Dehumidification and Adsorption Refrigeration," *Arabian Journal for Science and Engineering,* vol. 40, no. 12, pp. 3379-3391, 2015/12/01 2015, doi: 10.1007/s13369-015-1839-y.

[11] M. W. Ellis and E. H. Mathews, "Needs and trends in building and HVAC system design tools," *Building and Environment,* vol. 37, pp. 461-470, 05/01 2002, doi: 10.1016/S0360-1323(01)00040-3.

[12] S. Mat Dahan, S. N. Nina, M. Taib, and A. A. S. Basirul, "Analysis of heat gain in computer laboratory and excellent centre by using CLTD/CLF/SCL method," *Procedia Engineering,* vol. 53, pp. 655–664, 11/20 2012, doi: 10.1016/j.proeng.2013.02.085.

[13] M. Ramzan, M. S. Kamran, M. W. Saleem, H. Ali, and M. I. M. Zeinelabdeen, "Energy Efficiency Improvement of the Split Air Conditioner Through Condensate Assisted Evaporative Cooling," *Arabian Journal for Science and Engineering,* vol. 46, no. 8, pp. 7719-7727, 2021/08/01 2021, doi: 10.1007/s13369-021-05494-x.

[14] T. Nadeem *et al.*, "Designing of Heating, Ventilation, and Air Conditioning (HVAC) System for Workshop Building in Hot and Humid Climatic Zone Using CLTD Method and HAP Analysis: A Comparison," *Arabian Journal for Science and Engineering,* vol. 47, 01/30 2022, doi: 10.1007/s13369-021-06428-3.

[15] S. Saragasan, "The Comparison Of Cooling Load Calculation Using Manual Method And Hourly Analysis Program," *Research Progress in Mechanical and Manufacturing Engineering,* vol. 2, no. 2, pp. 972-981, 2021.

[16] R. Sirwan and A. Mohammed, "Comparison between hand calculation and HAP programs for estimating total cooling load for buildings," *Zanco Journal of Pure and Applied Sciences,* vol. 28, pp. 90-96, 10/10 2016.

[17] C. Mao, J. Baltazar, and J. Haberl, "Comparison of ASHRAE peak cooling load calculation methods," *Science and Technology for the Built Environment,* vol. 25, pp. 1-45, 08/13 2018, doi: 10.1080/23744731.2018.1510240.

[18] G. Acharya, G. Yewale, M. Tendolkar, and S. Kulkarni, "Estimation and Analysis of Cooling Load for Indian Subcontinent by CLD/SCL/CLF method at part load conditions," *Journal of Physics: Conference Series,* vol. 1240, p. 012031, 07/01 2019, doi: 10.1088/1742-6596/1240/1/012031.

[19] K. Mahmud, U. Amin, M. Hossain, and J. Ravishankar, "Computational tools for design, analysis, and management of residential energy systems," *Applied Energy,* vol. 221, pp. 535-556, 2018.

[20] A. A. A. Ahmed, A. A. A. Mohammed, and M. A. H. Elnoor, "Design of Air Conditioning System for Sport Hall for 1000 Occupant," Sudan University of Science and Technology, 2017.

[21] V. Khakre, A. Wankhade, and M. Ali, "Cooling load estimation by CLTD method and hap 4.5 for an evaporative cooling system," *International Research Journal of Engineering and Technology,* vol. 4, no. 1, pp. 1457-1460, 2017.

[22] K. Salhi, K. Mohamed Ramadan, M. M. Hadjiat, and A. Hamidat, "Energetic and Exergetic Performance of Solar-Assisted Direct Expansion Air-Conditioning System with Low-GWP Refrigerants in Different Climate Locations," *Arabian Journal for Science and Engineering,* vol. 45, no. 7, pp. 5385-5398, 2020/07/01 2020, doi: 10.1007/s13369-020-04426-5.

[23] T. Aized and A. Hamza, "Thermodynamic Analysis of Various Refrigerants for Automotive Air Conditioning System," *Arabian Journal for Science and Engineering,* vol. 44, no. 2, pp. 1697-1707, 2019/02/01 2019, doi: 10.1007/s13369-018-3646-8.

[24] J. U. Ahamed, R. Saidur, and H. H. Masjuki, "Investigation of Environmental and Heat Transfer Analysis of Air Conditioner Using Hydrocarbon Mixture Compared to R-22," *Arabian Journal for Science and Engineering,* vol. 39, no. 5, pp. 4141-4150, 2014/05/01 2014, doi: 10.1007/s13369-014-0961-6.

[25] *Fundamentals, ASHRAE–American society of heating, Ventilating and Air-Conditioning Engineers*, A. Handbook, 2017.

[26] *American Society of Heating, Refrigerating and Air-Conditioning Engineers, Inc. (ASHRAE)*, A. Handbook, 2013.

[27] "Air - Thermal Conductivity vs. Temperature and Pressure." https://www.engineeringtoolbox.com/air-properties-viscosity-conductivity-heat-capacity-d_1509.html (accessed.

[28] W. F. S. J. W. Jones, *Refrigeration and Air Conditioning*. Mcgraw Hill Higher Education, 1982, p. 440.

[29] "Hollow Dense Concrete Block." https://source.thenbs.com/product/hollow-dense-concrete-block/77i2jw4eN9TZCzQooqeZJq/ua2LtG5fr28yKnpspdabHt (accessed.

[30] *Fundamentals, ASHRAE–American society of heating, Ventilating and Air-Conditioning Engineers*, A. Handbook, 2001.

[31] B. Chenari, J. Dias Carrilho, and M. Gameiro da Silva, "Towards sustainable, energy-efficient and healthy ventilation strategies in buildings: A review," *Renewable and Sustainable Energy Reviews,* vol. 59, pp. 1426-1447, 2016/06/01/ 2016, doi: https://doi.org/10.1016/j.rser.2016.01.074.

[32] A. M. Elsaid and M. S. Ahmed, "Indoor Air Quality Strategies for Air-Conditioning and Ventilation Systems with the Spread of the Global Coronavirus (COVID-19) Epidemic: Improvements and Recommendations," *Environmental Research,* vol. 199, p. 111314, 2021/08/01/ 2021, doi: https://doi.org/10.1016/j.envres.2021.111314.

[33] *Ventilation for Acceptable Indoor Air Quality*, A. Handbook, 2015.

[34] J. Ligade and A. Razban, "Investigation of Energy Efficient Retrofit HVAC Systems for a University: Case Study," *Sustainability,* vol. 11, no. 20, p. 5593, 2019.

[35] S. A. Hashmi, C. R. Prasad, S. Faheem, S. O. U. Rahman, and S. M. Ali, "Cooling Load Calculation during Summer & Duct Design and Duct Drafting for Commercial Project," *Int. J. Sci. Res. Sci. Eng. Technol.,* vol. 3, no. 2, pp. 501-508, 2017.

[36] *Fundamentals, ASHRAE–American society of heating, Ventilating and Air-Conditioning Engineers*, A. Handbook, 1997.

[37] S. Agarwal and D. Gera, "Study and optimisation of supply duct bend and diffuser in HVAC system for a classroom," *International Journal of Innovative Science and Research Technology,* vol. 5, no. 7, pp. 988-995, 2020.

[38] *Price - Round cone diffuser*, 2021. [Online]. Available: https://www.priceindustries.com/content/uploads/assets/literature/catalogs/catalog-pages/section%20c/rcd-round-cone-diffuser-catalog.pdf.

[39] *Price - Louvered Grille*, 2019. [Online]. Available: https://www.priceindustries.com/content/uploads/assets/literature/catalogs/catalog-pages/section%20d/500600700-louvered-grille-catalog.pdf.

[40] C. C. C. A. C. Company, *Handbook of Air Conditioning System Design* (no. v. 1). McGraw-Hill, 1965.

Nota contribución de los autores:

1. Concepción y diseño del estudio
2. Adquisición de datos
3. Análisis de datos
4. Discusión de los resultados
5. Redacción del manuscrito
6. Aprobación de la versión final del manuscrito

ASK ha contribuido en: 1, 2, 3, 4, 5 y 6.
MEUH ha contribuido en: 1, 2, 3, 4, 5 y 6.
AAK ha contribuido en: 1, 2, 3, 4, 5 y 6.
SIUH ha contribuido en: 1, 2, 3, 4, 5 y 6.
SO ha contribuido en: 1, 2, 3, 4, 5 y 6.
MUK ha contribuido en: 1, 2, 3, 4, 5 y 6.

Nota de aceptación: Este artículo fue aprobado por los editores de la revista Dr. Rafael Sotelo y Mag. Ing. Fernando A. Hernández Gobertti.

Reducing Energy Consumption of Refrigerator Compressor using Aluminum Oxide Nanoparticles

Reducción del Consumo de Energía del Compresor de Refrigerador mediante Nanopartículas de Óxido de Aluminio

Reduzindo o Consumo de Energia do Compressor de Refrigeradores usando Nanopartículas de Óxido de Alumínio

Adeel Ahmed Khan[1(*)], Muhammad Ehtesham ul Haque[2], Farjad Siddiqui[3], Syed Muhammad Taha Nasir[4], Talha Shafique[5], Hassan Khalid[6]

Recibido: 24/08/2023 Aceptado: 08/03/2024

Summary. - Refrigeration has become an integral part of our daily lives and can be regarded as a process whose replacement is nearly impossible. Therefore, the only way of making this process efficient is by reducing the energy consumed by the components of refrigerators. One way of doing this is to reduce the power consumption of compressor by the addition of nanoparticles either in a refrigerant or in a lubricant. This study focusses on producing nanolubricant (Al2O3/Synthetic lubricant) and dispersing the nanolubricant into R-134a compressor. This study investigates that how much power can be reduced when Aluminum oxide (Al2O3) nanoparticles dispersed in SL-32 lubricant (base fluid). A comparison between SL-32 lubricant with and without the addition of Aluminum oxide nanoparticles was done and it showed a reduction of 0.913% in current consumption and 2.74% in power at the same initial temperature of 31°C in both cases. Hence it can be concluded that Alumina nanoparticles can be utilized to reduce the energy utilized by compressors by creating a nanolubricant with SL-32 lubricant.

Keywords: Refrigeration, Nanoparticles, Lubricant, Compressor, Energy.

(*) Corresponding Author

[1] Assistant Professor, Department of Mechanical Engineering, NED University of Engineering and Technology (Pakistan), adeelahmedk@neduet.edu.pk, ORCID iD: https://orcid.org/0009-0004-6790-8176

[2] PhD, Assistant Professor, Department of Mechanical Engineering, NED University of Engineering and Technology (Pakistan), mehaque@neduet.edu.pk, ORCID iD: https://orcid.org/0000-0001-8751-348X

[3] Senior Undergrad Student, Department of Mechanical Engineering, NED University of Engineering and Technology (Pakistan), siddiqui4103227@cloud.neduet.edu.pk, ORCID iD: https://orcid.org/0009-0006-7494-556X

[4] Senior Undergrad Student, Department of Mechanical Engineering, NED University of Engineering and Technology (Pakistan), nasir4101034@cloud.neduet.edu.pk, ORCID iD: https://orcid.org/0009-0008-5545-0179

[5] Senior Undergrad Student, Department of Mechanical Engineering, NED University of Engineering and Technology (Pakistan), shafique4102210@cloud.neduet.edu.pk, ORCID iD: https://orcid.org/0009-0008-6002-8298

[6] Senior Undergrad Student, Department of Mechanical Engineering, NED University of Engineering and Technology (Pakistan), khalid4106343@cloud.neduet.edu.pk, ORCID iD: https://orcid.org/0009-0004-2923-1854

Resumen. - *La refrigeración se ha convertido en una parte integral de nuestra vida diaria y puede considerarse como un proceso cuya sustitución es casi imposible. Por tanto, la única forma de hacer eficiente este proceso es reduciendo el consumo energético de los componentes de los frigoríficos. Una forma de hacerlo es reducir el consumo de energía del compresor mediante la adición de nanopartículas en un refrigerante o en un lubricante. Este estudio se centra en la producción de nanolubricante (Al2O3/lubricante sintético) y la dispersión del nanolubricante en el compresor R-134a. Este estudio investiga cuánta energía se puede reducir cuando las nanopartículas de óxido de aluminio (Al2O3) se dispersan en el lubricante SL-32 (líquido base). Se realizó una comparación entre el lubricante SL-32 con y sin la adición de nanopartículas de óxido de aluminio y mostró una reducción del 0,913% en el consumo de corriente y del 2,74% en la potencia a la misma temperatura inicial de 31°C en ambos casos. Por lo tanto, se puede concluir que las nanopartículas de alúmina se pueden utilizar para reducir la energía utilizada por los compresores mediante la creación de un nanolubricante con lubricante SL-32.*

Palabras clave: *Refrigeración, Nanopartículas, Lubricante, Compresor, Energía*.

Resumo. ***-*** *A refrigeração tornou-se parte integrante do nosso dia a dia e pode ser considerada um processo quase impossível de substituir. Portanto, a única forma de tornar esse processo eficiente é reduzir o consumo de energia dos componentes do refrigerador. Uma maneira de fazer isso é reduzir o consumo de energia do compressor adicionando nanopartículas a um refrigerante ou lubrificante. Este estudo tem como foco a produção de nanolubrificante (Al2O3/lubrificante sintético) e a dispersão do nanolubrificante no compressor R-134a. Este estudo investiga quanta energia pode ser reduzida quando nanopartículas de óxido de alumínio (Al2O3) são dispersas em lubrificante SL-32 (líquido base). Foi feita uma comparação entre o lubrificante SL-32 com e sem adição de nanopartículas de óxido de alumínio e mostrou uma redução de 0,913% no consumo de corrente e 2,74% na potência na mesma temperatura inicial de 31° C em ambos os casos. Portanto, pode-se concluir que nanopartículas de alumina podem ser utilizadas para reduzir a energia utilizada pelos compressores, criando um nanolubrificante com lubrificante SL-32.*

Palavras-chave: *Refrigeração, Nanopartículas, Lubrificante, Compressor, Energia*.

1. Introduction. - Thermal systems like air conditioners and refrigerators use a lot of electricity; therefore, research into producing energy-efficient refrigeration with environmentally benign refrigerants is necessary. The characteristics of a preferable refrigeration system include system efficiency [1]. Due to increasing demands for energy, innovative approaches are being adopted by engineers to improve the efficiency of refrigeration systems [2]. Improving system efficiency is a key to save energy and make the system more energy efficient. It conserves available energy resource and has environmental benefits such as reduced greenhouse gas emission and other pollutants. Improving insulation and upgrading to energy efficient system are the two main traditional methods of improving energy efficiency. As opposed to the traditional methods, addition of nanoparticles provides a new means to improve system efficiency and hence the energy conservation. A refrigeration system usually comprises a condenser, evaporator, expansion device and compressor. Without these components, heat cannot flow from a colder region to a warmer region [3].
The thermal conductivities of fluids that contain suspended solid metallic particles are expected to be significantly more enhanced when compared with conventional heat transfer fluids. Nano fluids are engineered by suspending ultrafine metallic or nonmetallic particles of nanometer dimensions in traditional heat transfer fluids such as water, engine oil, and ethylene glycol. [4]

One way of using nanoparticles is by adding them to the lubricant utilized in the compressor [5]. By dispersion of metal or metallic oxide nanoparticles into a chosen base fluid, such as water, oils, or ethylene glycol, nanofluids can be created. After adding nanoparticles, the base fluid's density, viscosity, specific heat, and thermal conductivity can be altered, this results in improved compressor performance. [6]. The primary purpose of oil is to improve the lubrication of the compressor along with cooling. The main characteristic of a good lubricant is that it should be chemically stable, produces no wax deposits, has excellent performance at low temperatures and is compatible with the material used in the compressor [7]. Nanofluids can be prepared in two steps: Firstly, nanoparticles are produced in the form of dry powder then they are dispersed in the base fluid using a magnetic force agitation. In two step method Nanoparticles, Nanofibers, Nanotubes or any other nanomaterial are produced in a form of dry powder using chemical or any physical method. In the second step, they are dispersed in the fluid by the use of magnetic force agitation, ultrasonic agitation, high shear mixing, homogenizing, and ball milling. On the large scale, this method is more economical because they have been scaled up to the industrial level. In one step method, the making and dispersing of nanoparticles in the fluid are done simultaneously. The processes such as drying, transportation, storage and dispersion are eliminated. The nanoparticle's agglomeration is reduced as the nanoparticles are uniformly dispersed in the fluid and stably suspended in it. This method cannot be used for large-scale synthesis, and it is more expensive than the two-step method [8].

Several studies have shown that nanofluids help in reducing the energy consumed by the compressor. A study conducted in 2019 used an R-12 household refrigerator tested under certain ambient temperature conditions with a 40g R-600a charge enhanced with different TiO_2 nano-lubricant concentrations (0 g/L and 0.2 g/L nano-lubricants) which shows that reduction in energy consumption was in the range of 3.42 to 4.52% when compared to the base fluid [9]. In 2011, a comparison was done between three lubricants POE oil, SUNISO 3GS and SUNISO 3GS mixed with nanoparticles while the refrigerant was R-134a. Compared to POE oil, the power consumption was reduced up to 18% when SUNISO 3GS was used and this reduction in energy consumption increased to 25% when nanoparticles were mixed in SUNISO 3GS [10].

An experimental investigation was done with R-134a refrigerant and a nano-oil mixture of Polyalkylene glycol in which Al_2O_3 nanoparticles were dispersed. The comparison was done between PAG oil and nano-oil mixture. It was found that the COP of the systems improved up to 6.5% and sub-cooling was also improved at the exit of the condenser [11]. In a study conducted in 2009, 0.1 % by weight of Al_2O_3 nanoparticles were added to mineral refrigeration oil and the power consumption was reduced by an amount of 2.4% while the COP increased by 4.4%. The primary refrigerant used was R-134a [12]. R-600a refrigerant with TiO_2 nanolubricant and LPG refrigerant were compared in a study. Titanium dioxide was dissolved in mineral oil to create a nanolubricant. There were three different concentrations: 0.2 g/l, 0.4 g/l, and 0.6 g/l. In comparison to baseline LPG refrigerant, the power used by the system for all charges of R-600a refrigerant and 0.2 g/L of TiO_2 nano-lubricant was 1.94-33.33% lower [13]. In 2008, a study was done to compare how much energy is reduced if HFC134a/nano-oil mixture is used instead of HFC134a/Polyester oil. Nano-oil was a mixture of mineral oil in which Titanium oxide was dispersed with a 0.1% mass fraction. The results showed a 26.1% decrease in energy consumption and also nanoparticles helped in improving the solubility of HFC134a and mineral oil which was shown clearly by the higher oil return ratio [14].

In 2009, a study was conducted in which 1% mass fraction of Copper Oxide nanoparticles of 50nm size was utilized in POE oil to reduce the compressor work by 21.37% [15]. A reduction was showed in compressor work of 11% when a combination of TiO_2 nanolubricant and R134a refrigerant was tested and a boost in COP of 24% was observed when SiO_2/PAG nanolubricant was used instead of TiO_2 with R134a refrigerant. The influence of nano refrigerants and nano lubricants on heat transfer, refrigerant-oil combination, and tribology improved the overall performance of Vapor

Compression Refrigeration Systems [16]. It is anticipated that nano refrigerants and nano lubricants will be the greatest candidates for increasing the effectiveness of the Vapor Compression Refrigeration System. A test was done using Polyalkaline glycol (PAG) compressor oil and modifying it with a 1.0% volume fraction of Titanium dioxide nanoparticles with R134a refrigerant and the COP improved by 21.42% [17]. CuO/SiO_2 nano-lubricants was used in vapour compression refrigeration systems in place of pure mineral oil. In this study, experiments are conducted with hybrid nano-lubricants made by dispersing two distinct nanoparticles, namely CuO and SiO_2, at concentrations of 0.2 g/L and 0.4 g/L and 40 and 60 g of R-600a refrigerant, respectively. CuO and SiO_2 hybrid nano-lubricants result in a 35% increase in performance efficiency, an 18% increase in cooling capacity, and a 75W reduction in compressor power consumption [18]. When employing R-290 with TiO_2 nanoparticle in the lubricants, the air conditioner's input power falls by about 3.1%, while the cooling capacity and the coefficient of performance (COP) rise by about 5.1% and 8.4%, respectively, in comparison to the system without nanoparticle in the lubricant [19]. When SiO_2 nano-oil was added to compressor oil at particular concentrations of 1%, 2%, and 2.5% (by a mass fraction), it enhanced the system's coefficient of performance (COP) by 7.61%, 14.05%, and 11.90% when used in place of pure oil, respectively [20]. In an experimental investigation, the performance of an R-134a refrigerant vapour compression refrigeration system was examined utilizing nanolubricant with various volume percentages of Al_2O_3 to mineral oil (MO) (0.05%, 0.075%, 0.1%, and 0.2%). The outcome indicates a maximum improvement in COP of almost 85% for a volume percentage of 0.075%. Comparing nanolubricant to base fluid, the use of nanolubricant reduces compressor power usage by about 27% [21].

This research is focused on a method that can help in decreasing the overall energy consumed by a refrigerating system by utilizing an approach that is environment-friendly and cost-effective. The presence of a nanolayer at the solid-liquid interface is the primary cause of the thermal conductivity enhancement, however particle clustering may also play a significant role. The liquid or oil molecules that are closer to the particle are referred to as forming layered structures because they behave like solid surfaces and serve as a thermal bridge between the oil molecules and the particle. Additionally, compared to oil, particles have a higher heat conductivity and hence higher heat transfer [22]. Most of the research on improving heat transfer of thermal fluid is done on either water or ethyl glycol. In this research a novel thermal fluid is investigated which is made by adding aluminum oxide nanoparticles to lubricant compressor oil. Keeping all the factors in mind SL-32 lubricant was considered as a base fluid (See Table I. Properties of Suniso SL-32 lubricant). It is a synthetic ester lubricant. This research utilizes a test rig and compares a synthetic lubricant i.e., SL-32 with and without any addition of Alumina Nanoparticles. The solvent SL-32 is being utilized as it is already an effective lubricant, and the addition of nanoparticles will reveal how much improvement can further be made in its properties.

In this study we will investigate how much power can Aluminum oxide nanoparticles reduce when dispersed in SL-32 lubricant (base fluid).

2. Methodology. -

2.1 Preparation of Nanofluid. - One way to create nanofluids is to mix metal or metallic oxide nanoparticles with a chosen base fluid, like ethylene glycol, water, or oil. By adding nanoparticles, the base fluid's density, viscosity, specific heat, and thermal conductivity can all be altered, improving compressor performance. Using nanoparticles in lubricants or thermal fluids has three key benefits presently. By increasing the solubility of the refrigerant in the lubricant and decreasing wear and friction coefficient through dispersion, nanoparticles can improve the lubricant's thermal conductivity and heat transfer properties. Increased heat transfer rate from nano-lubricant may result in refrigeration systems using less electricity and smaller compressors.

SL-32 lubricant properties are mentioned in **Error! Reference source not found..** Al_2O_3 nanoparticles were used to prepare the nanofluid by dispersing it in SL-32 lubricant. Al_2O_3 nanoparticle had an average class size of 100nm. Nanofluid is not just a simple mixture of solid (powder) and liquid. It requires some special guidelines which include stable and durable suspension, negligible agglomeration of particles, and no chemical change of the fluid. For the preparation of Nanolubricant, we first take a sample of 100ml Suniso SL-32 in the beaker and measure its weight on a digital scale and put a 0.06% mass fraction of Aluminum Oxide (Al_2O_3) in the beaker as it is the only mass fraction of Al_2O_3 that passed the sedimentation test (See Section 0). Then a magnetic stir bar was added to the beaker and the mixture was stirred. The beaker is then placed on the hot plate stirrer and a mixture of nanoparticles and lubricant is allowed to heat and stirred for 30 minutes at 70 ºC and 400 rpm (See figure I). After that Nano lubricant is allowed to cool. Then the nano lubricant is shifted from the beaker to the glass bottle. Then Ultrasonication is performed to ensure the proper mixing of lubricant with nanoparticles for 30 minutes in and kept under observation for the sedimentation process.

Density at 15 ºC	0.980

Viscosity at 40 ºC	32.0 cSt
Viscosity at 100 ºC	5.8 cSt
Viscosity index	125
Flash Point ºC	235 ºC
Pour Point ºC	-48 ºC
Color	L0.5
Cu Corrosion at 100 ºC x 3hrs	1a

Table I. *Properties of Suniso SL-32 lubricant*

Figure I.- *Beaker with magnetic stirrer placed on Hot plate*

2.2 Sedimentation Test. - The sedimentation test is done to check the settling down of suspended particles after a period of time. Images displayed were taken on the 4th day, 8th day, 12th day and 16th day respectively. The complete time period of observation was 16 days. After 12 days, 0.06% was the only sample which did not settle while all the other samples did not pass the test.

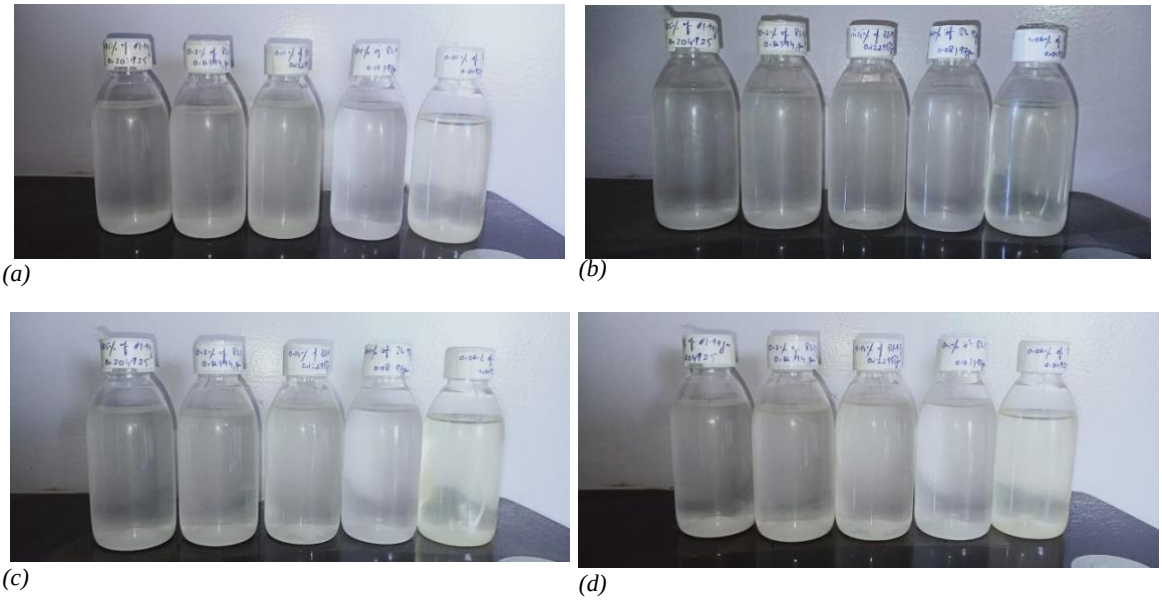

(a) *(b)*

(c) *(d)*

Figure II.- *Samples on 4th, 8th, 12th and 16th day*

In order to find out the number of nanoparticles that would pass the sedimentation test trial and error method was

adopted. The volume is converted into kilograms by weighing with electronic balance. 0.06% was the number of nanoparticles that was added in the lubricant.

2.3 Test Rig. - The refrigerator we used for this experiment is a defrost, double-door refrigerator from the Haier brand as shown in Figure III. The specifications of the refrigerator were shown in Table II.

Model	HRF-368J
Storage Volume	329L
Freezer Volume	68L
Power	180W
Voltage	200-240V (50 Hz)
Refrigerant	R-134A(190g)
Freezing Power	4Kg/24h
Overall Dimensions	620x600x1700(mm)

Table II. *Refrigerator specifications*

Figure III.*- Refrigerator with Data logger Sensors*

The test rig was modified by placing the compressor outside the refrigerator as shown in **Error! Reference source not found.**V for easily changing the lubricant and refrigerant. The refrigerant circuit was rebuilt with the proper facilitation to measure pressure and temperature. A leak check was carried out to make sure that there is no leakage of refrigerant and pressure drop because of that.

***Figure IV**.- Modified location of Compressor*

2.4 Changing Lubricant in Hermetic Compressor. - First, we have to evacuate the mineral oil present in the system. For this operate the charging nozzle to drain out the entire refrigerant and shut off the suction and discharge line of compressor by untighten the copper coupling. Dismantle the compressor out of the body and unplug the charging nozzle and then place the compressor upside down to drain out the lubricant in the pot. Leave the compressor for 24 hours to drain out every single drop of lubricant. Install the compressor in the refrigerator body. The amount of oil added to the compressor is 250 ml. Measure the correct quantity of lubricant in a beaker. Fix the rubber pipe to the charging nozzle and immerse the other side of the pipe in the lubricant. Switch on the compressor to displace the lubricant. Screw the Non-Return Valve to charging nozzle and plug the charging cap. Couple the suction and discharge line of refrigerant.

***Figure V**.- Draining out lubricant*

Figure VI.- *Charging Lubricant*

2.5 System Evacuation. - The evacuation procedure is used to get rid of incondensable materials like air, water, moisture, and inert gases from the refrigeration system. The most popular pieces of equipment for evacuation are a charging manifold and a vacuum pump. A tst-215 model 2-stages vacuum pump (see figure VII) and a three-hose charging manifold with low-side and high- side pressure gauges are used in this experiment to evacuate the system. Check the pressure gauge manifold make sure that both suction and discharge valves are closed. Connect the low-pressure hose pipe of pressure gauge manifold to Vacuum Pump. Attach the other hose pipe to compressor charging point. Switch on the vacuum pump and observe the suction pressure gauge and make sure it reaches to -30 psi for complete air removal. Switch off the vacuum pump and close the suction pressure valve of pressure Gauge manifold and disconnect the low-pressure hose pipe.

Figure VII.- *Vacuum Pump for system evacuation*

2.6 Charging R-134a Refrigerant in Hermetic Compressor. - The refrigerator (Figure III) can be fully charged with 190 g of refrigerant. R-134a. Connect the low-pressure hose pipe with Refrigerant R-134a cylinder. Open the valve of Refrigerant cylinder and open the pressure gauge valve and then Switch on the Refrigerator. Close the valve of refrigerant cylinder and check the discharge pressure if it decreases then again opens the valve of refrigerant cylinder until discharge pressure is not decreasing. Disconnect the hose pipe from compressor charging point and plug the Charging cap. Refrigerator is ready to operate.

Figure VIII.- *Charging R-134a Refrigerant*

As safety precaution personal protective equipment (PPE) such as gloves, safety goggles, and respirator masks made especially for working with refrigerants has been used. This guards against coming into direct touch with the refrigerant and keeps dangerous fumes from entering the lungs. To disperse any possible refrigerant leaks or vapors that may emerge during installation made sure the workspace has enough ventilation. It's important to follow fire safety procedures since refrigerants have the potential to catch fire, therefore, smoking and open fires in locations where refrigerant handling takes place should be avoided.

2.7 Experimental Procedure. - The compressor was charged with lubricant and then readings of current, voltage, temperature and time were obtained using data logger. The temperature sensors were installed in the refrigerator and freezer compartment (see figure IX) and connected to data logger. The voltage and current sensors were connected with compressor. The temperature sensors which we utilized are DS18B20 in our analysis. They have a measuring range -55°C to 125°C.Then, power (P) was calculated using the relation P= IV, where current (I) is in amperes and voltage (V) is in volts. Graphs were plotted between Power versus Time and Current versus Time. Comparison between the reduction in power and compressor was done by calculating the amount of percentage reduced by replacing nanolubricant instead of SL-32 lubricant. The data was collected for several days.

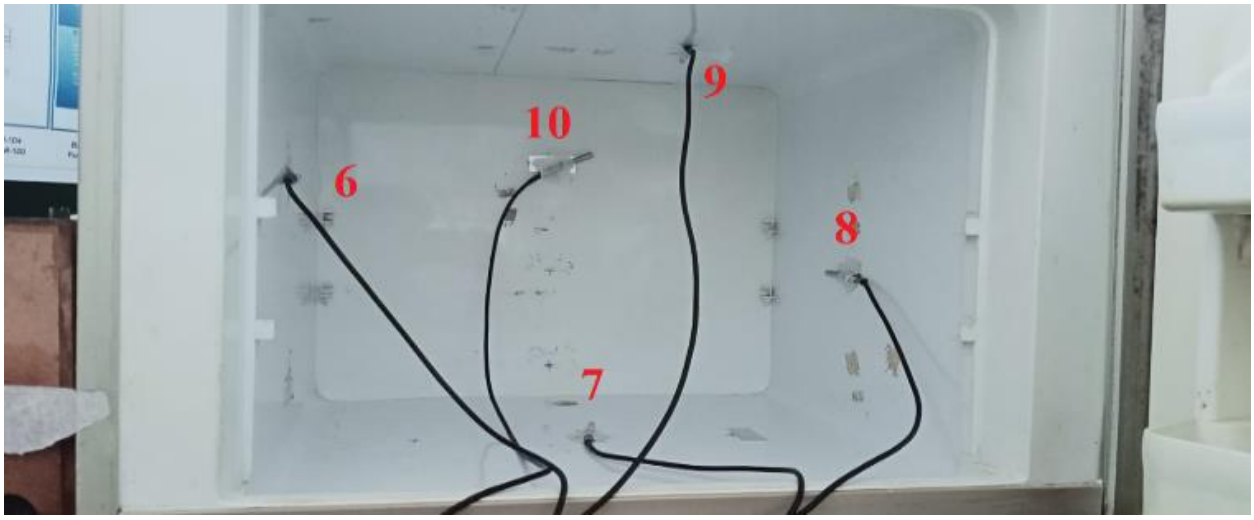

Figure IX.- Sensors in Freezer compartment

3. Results & Discussions. - The power consumption with and without nanofluid versus time graph plotted in figure X. As shown in figure X power consumption decreases with addition of Al_2O_3 nanoparticles. The power dropped down to approximately zero at the 270-minute mark due to the thermostat shutting off the current supply when lubricant SL-32 is used without nano particles. The maximum power in the whole process is 447.635 Watts. As shown in figure X with the addition of nano particles in SL-32 lubricant the power dropped down to approximately zero at the 260-minute mark that means the compressor is shutting down 10 minutes early with the addition of nanolubricant which is saving power. The actual difference in the power consumption with and without nanoparticles is magnified in figure XI which clearly shows that power consumption is less with nanoparticles. The average power consumed without nanoparticles is 407.98 Watts and with nano particles it is reduced to 396.809 Watts as shown if figure XII. The maximum power consumed by the compressor throughout the operation is 434.99 Watts while the average power consumed is 396.809 Watts.

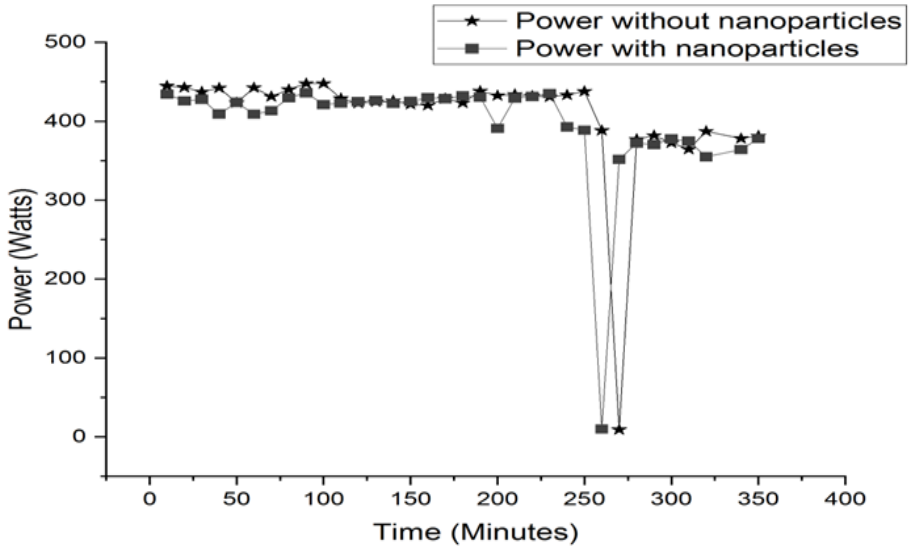

Figure X.- *Power versus Time graph*

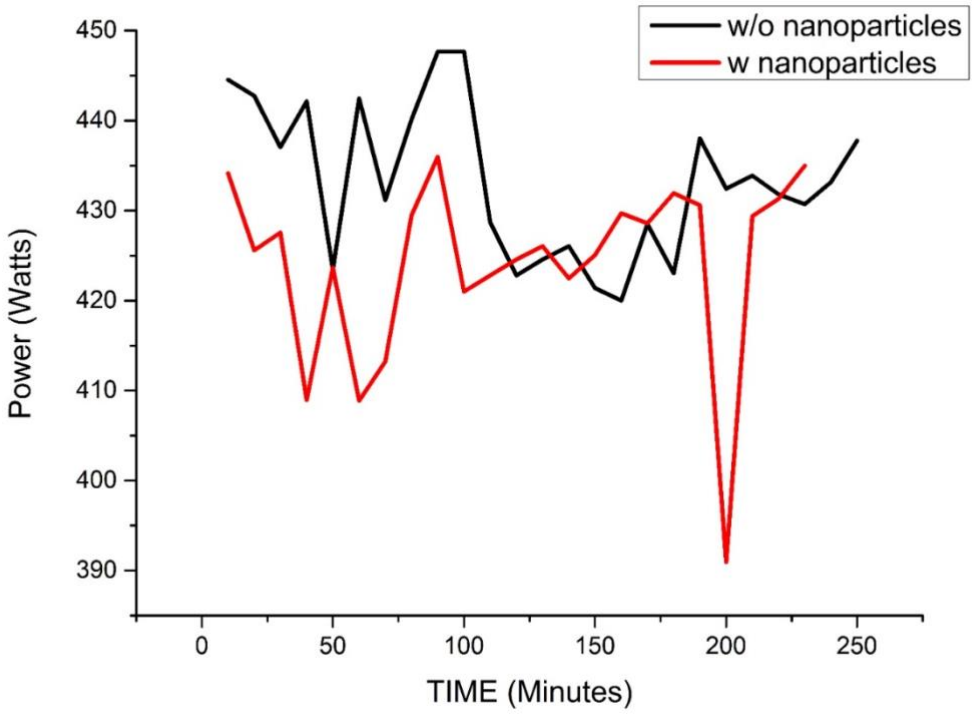

Figure XI.- *Magnified Power versus Time graph*

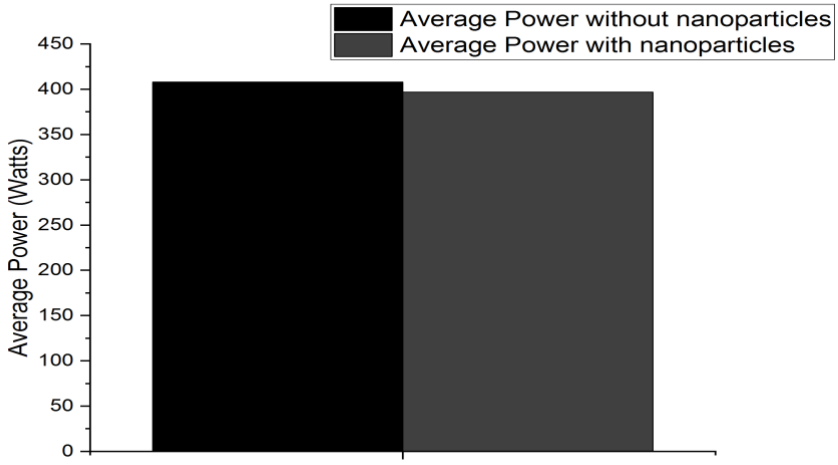

Figure XII.- *Reduction in power due to nanoparticles*

The current consumption with and without addition of Al_2O_3 nanoparticles versus time graph plotted in Figure XIII. As shown in figure current consumption decreases with addition of Al_2O_3 nanoparticles. The actual difference in the current consumption with and without nanoparticles is magnified in figure XIV which clearly shows that current consumption is less with nanoparticles. The average current consumed by the compressor without nanoparticles is 1.643 amperes while it is 1.628 amperes with nanoparticles as shown if figure XV.

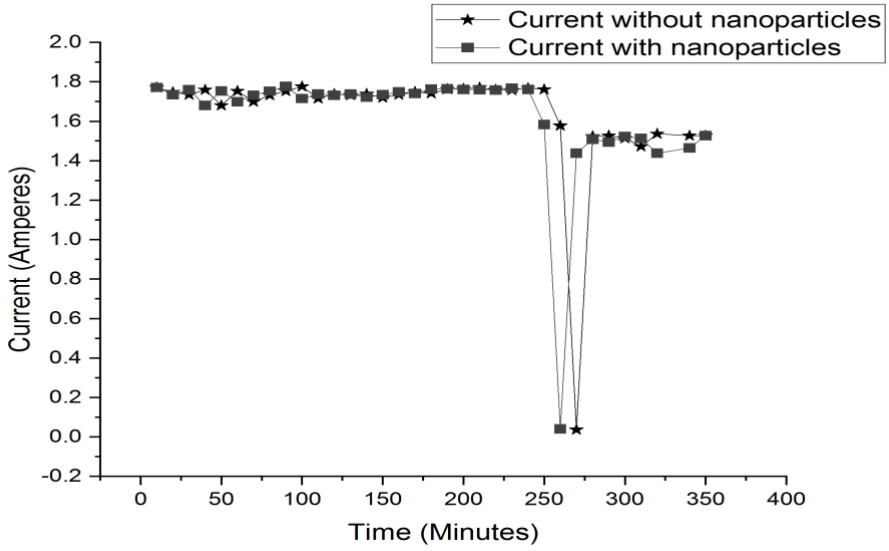

Figure XIII.- *Magnifed Current versus Time comparison Graph*

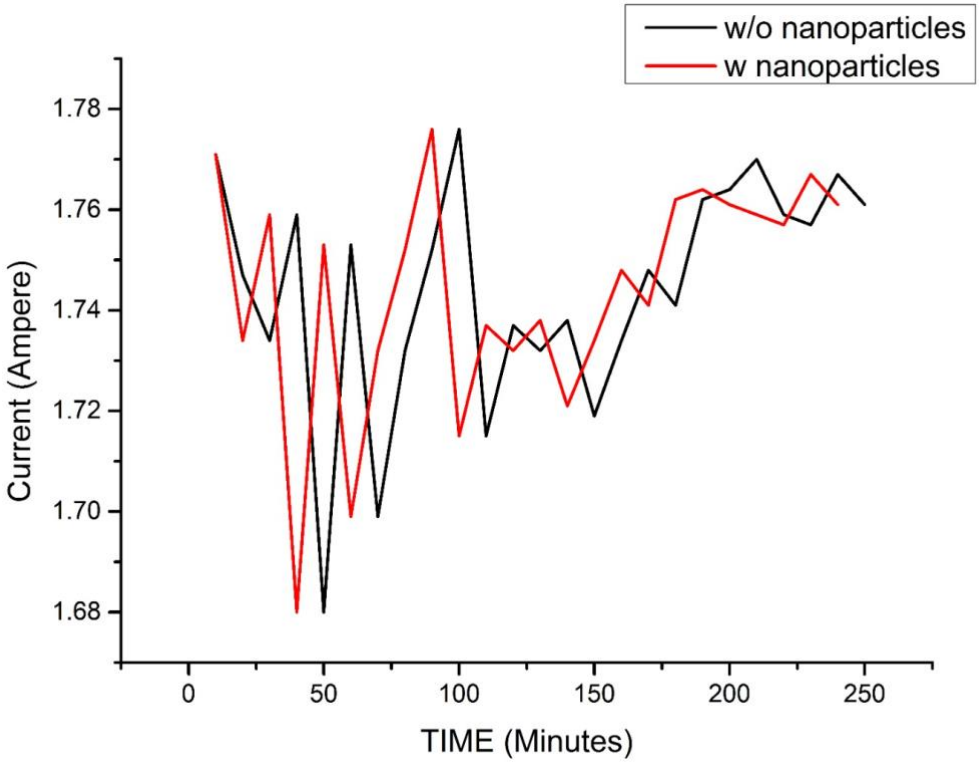

Figure XIV.- *Magnifed Current versus Time comparison Graph*

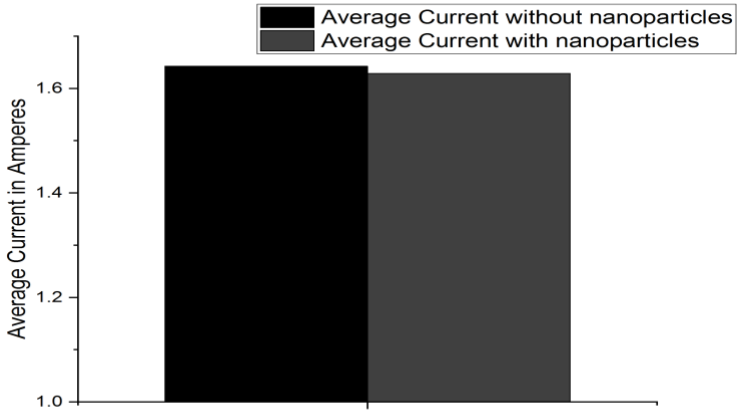

Figure XV.- *Reduction in current due to nanoparticles*

The Average values of power and current with and without nanolubricant is shown in Table III.

Parameters	Power	Current
Average value without nanoparticles	407.98 Watts	1.643 amperes
Average value with Nanoparticles	396.809 Watts	1.628 amperes
Percentage reduction in average consumption	2.74	0.913
Maximum value without nanoparticles	447.635 Watts	1.776 amperes
Maximum value with nanoparticles	434.99 Watts	1.776 amperes
Percentage reduction in maximum value	2.82	0

Table III. *Reduction in Current and Power because of nanoparticles*

4. Conclusions. - The compressor was charged with lubricant and then readings of current, voltage, temperature and time were obtained. Then, power (P) was calculated using the relation P= IV, where current (I) is in amperes and voltage (V) is in volts. Graphs were plotted between Power versus Time and Current versus Time. Comparison between the reduction in power and compressor was done by calculating the amount of percentage reduced by replacing nanolubricant instead of SL-32 lubricant. The data was collected for several days with the same initial temperature of 31°C. The average current consumption was reduced by 0.913% while the power consumption was effectively reduced by 2.74% while keeping the operating time of the refrigerator same. These results conclude that Al_2O_3 nanoparticles can be utilized to reduce the energy utilized by compressors by creating a nanolubricant with SL-32 lubricant. This could be because the lubricant's friction and heat transfer properties are both improved by the nanoparticles. The decrease in friction power loss is explained by the fact that while an increase in nanoparticle concentration is shown to enhance viscosity, it also decreases the friction coefficient.

References

[1] S. Comstock, "HALOCARBON REFRIGERATION SYSTEMS," in *ASHRAE HANDBOOK*, Atlanta, Stephen Comstock, 2014, p. 1.

[2] W. F. Stoecker, "Applications of Refrigeration and Airconditioning," in *Refrigeration and Air conditioning (2nd Edition)*, McGraw-Hill, 1986, p. 12.

[3] Y. A. Cengel, "THE SECOND LAW OF THERMODYNAMICS," in *Thermodynamics: An Engineering Approach (5th Ed)*, McGraw-Hill, 2006, p. 287.

[4] Stephen U. S. Choi and J. A.Eastman, "Enhancing thermal conductivity of fluids with nano particles," *ASME International Mechanical Engineering Congress & Exposition*, 1995.

[5] A. Majgaonkar, "Use of nanoparticles in refrigeration systems: a literature review paper," in *International Refrigeration and Air Conditioning Conference*, 2016.

[6] M. Hatami and D. Jing, Nanofluids: Mathematical, Numerical, and Experimental Analysis, Elsevier, 2020.

[7] G. H. Hundy, A. R. Trott and T. C. Welch, "Oil in Refrigerant Circuits," in *Refrigeration and air-conditioning*, Butterworth-Heinemann, 2008, pp. 89-98.

[8] W. Yu and H. Xie, "A review on nanofluids: preparation, stability mechanisms, and applications," *Journal of nanomaterials*, 2012.

[9] L. J. Akinlesi, D. S. Adelekan, O. S. Ohunakin, O. E. Atiba, J. Gill and A. A. Atayero, "Experimental performance of a domestic refrigerator with TiO2-nanoparticles operating within selected ambient temperature," *Journal of Physics*, vol. 1378, no. 4, 2019.

[10] N. Subramani and M. J. Prakash, "Experimental studies on a vapour compression system using nanorefrigerants," *International Journal of Engineering, Science and Technology*, vol. 3, no. 9, pp. 95-102, 2011.

[11] V. Nair, A. D. Parekh and P. R. Tailor, "Experimental investigation of a vapour compression refrigeration system using R134a/Nano-oil mixture," *International Journal of Refrigeration*, vol. 112, pp. 21-36, 2020.

[12] C. S. Jwo, L. Y. Jeng, T. P. Teng and H. Chang, "Effects of nanolubricant on performance of hydrocarbon refrigerant system," *Journal of Vacuum Science & Technology B: Microelectronics and Nanometer Structures Processing, Measurement, and Phenomena*, vol. 27, no. 3, pp. 1473-1477, 2009.

[13] G. Jatinder, O. S. Ohunakin, D. S. Adelekan, O. E. Atiba, A. B. Daniel, J. Singh and A. A. Atayero, "Performance of a domestic refrigerator using selected hydrocarbon working fluids and TiO2–MO nanolubricant," *Applied Thermal Engineering*, vol. 160, p. 114004, 2019.

[14] S. S. Bi, L. Shi and L. L. Zhang, "Application of nanoparticles in domestic refrigerators," *Applied Thermal Engineering*, vol. 28, no. 14-15, pp. 1834-1843, 2008.

[15] A. S. Husainy, P. Chougule, S. Hasure, A. Patil, S. Tukshetti and K. Badade, "Performance improvement of ducted air-conditioning system with different mass fraction of CuO nanoparticles mixed in POE oil," *Int. Res. J. Eng. Technol.*, vol. 6, no. 4, pp. 1003-1007, 2019.

[16] M. Sharif, W. H. Azmi, R. Mamat and A. I. M. Shaiful, "Mechanism for improvement in refrigeration system performance by using nanorefrigerants and nanolubricants–A review," *International Communications in Heat and Mass Transfer*, vol. 92, pp. 56-63, 2018.

[17] T. B. F. Selimefendigil, "Experimental investigation of nano compressor oil effect on the cooling performance of a vapor-compression refrigeration system," *Journal of Thermal Engineering*, vol. 5, no. 1, pp. 100-104, 2019.

[18] A. Senthilkumar, P. V. Abhishek, M. Adithyan and A. Arjun, "Experimental investigation of CuO/SiO2 hybrid nano-lubricant in R600a vapour compression refrigeration system," *Materials Today: Proceedings*, vol. 45, pp. 6083-6086, 2021.

[19] T. P. Pramudantoro, F. N. Ani and H. Nasution, "Enhancing air conditioning performance using TiO2 nanoparticles in compressor lubricant," *Advanced Materials Research*, vol. 1125, pp. 556-560, 2015.

[20] N. S. Desai and P. R. Patil, "Application of SiO2 nanoparticles as lubricant additive in VCRS: an experimental investigation," *Asian Review of Mechanical Engineering*, vol. 4, no. 1, pp. 1-6, 2015.

[21] D. G. Subhedar, J. Z. Patel and B. M. Ramani, "Experimental studies on vapour compression refrigeration system using Al2O3/mineral oil nano-lubricant," *Australian Journal of Mechanical Engineering*, vol. 20, no. 4, pp. 1136-1141, 2022.

[22] Subramani Narayanasarma and Biju T. Kuzhiveli, "Evaluation of the properties of POE/SiO2 nanolubricant for an energy-efficient refrigeration system – An experimental assessment," *Powder Technology*, vol. 356, no. November, p. 1029–1044, 2019.

Nota contribución de los autores:

1. Concepción y diseño del estudio
2. Adquisición de datos
3. Análisis de datos
4. Discusión de los resultados
5. Redacción del manuscrito
6. Aprobación de la versión final del manuscrito

AAK ha contribuido en: 1, 2, 3, 4, 5 y 6.
MEUH ha contribuido en: 1, 2, 3, 4, 5 y 6.
FS ha contribuido en: 1, 2, 3, 4, 5 y 6.
SMTN ha contribuido en: 1, 2, 3, 4, 5 y 6.
TS ha contribuido en: 1, 2, 3, 4, 5 y 6.
HK ha contribuido en: 1, 2, 3, 4, 5 y 6.

Nota de aceptación: Este artículo fue aprobado por los editores de la revista Dr. Rafael Sotelo y Mag. Ing. Fernando A. Hernández Gobertti.

Utilization of Sawdust Ash as an additive of cement in concrete and study of its mechanical properties

Utilización de Ceniza de Aserrín como aditivo del cemento en hormigón y estudio de sus propiedades mecánicas

Utilização da Cinza de Serragem como aditivo de cimento em concreto e estudo de suas propriedades mecânicas

Ifrah Asif[1(*)], Muhammad Ubair Hussain[2], Abdul Arham Khan[3], Muhammad Ashar[4], Muhammad Usman[5], Zain Shahid[6]

Recibido: 24/08/2023 Aceptado: 08/03/2024

Summary. - The sustainability of the concrete industry is in jeopardy because it is one of the biggest consumers of natural resources. Environmental and monetary issues are the main difficulties the concrete industry is currently dealing with. In this study, the potential substitution of sawdust ash for cement in the production of concrete is explored. In this project, the potential substitution of sawdust ash for cement in concrete production was explored, a typical carpentry waste, and then we utilize several testing techniques to examine how it impacts the mechanical characteristics of concrete. In an experiment, the compressive, tensile, and flexural strengths of concrete samples made with various ratios of sawdust ash and cement were examined. The samples were made following ASTM C-109, ASTM C-496 and ASTM C-78 for compression, tensile and flexural testing. In place of cement, saw dust ash was added to the M-15 (M indicates 'mix' and 15 indicates compressive strength of 15MPA) sample in weight percentages of 5%, 10%, 15%, 20%, and 25%. The concrete samples were tested to ascertain their compressive, tensile, and flexural strengths after 14 days. Comparisons between the results and untreated concrete were done. In this study, the behavior of concrete was investigated when sawdust ash was replaced for cement to weight-based extents of 0%, 5%, 10%, 20%, and 25%. This could address the problem of how to dispose of sawdust ash while also enhancing the properties of concrete.

Keywords: Tensile strength, compressive strength, flexural strength of concrete, sawdust ash, concrete cubes, sustainable construction.

(*) Corresponding Author

[1] Lecturer, Department of Mechanical Engineering, NED University of Engineering and Technology (Pakistan), ifrahasif@neduet.edu.pk, ORCID iD: https://orcid.org/0000-0001-7551-2199

[2] Senior Undergrad Student, Department of Mechanical Engineering, NED University of Engineering and Technology (Pakistan), ubairhussain130@gmail.com, ORCID iD: https://orcid.org/0009-0001-4120-8559

[3] Senior Undergrad Student, Department of Mechanical Engineering, NED University of Engineering and Technology (Pakistan), khanarham123@gmail.com, ORCID iD: https://orcid.org/0009-0005-8487-4235

[4] Senior Undergrad Student, Department of Mechanical Engineering, NED University of Engineering and Technology (Pakistan), asharmuhammad196@gmail.com, ORCID iD: https://orcid.org/0009-0002-4686-0412

[5] Senior Undergrad Student, Department of Mechanical Engineering, NED University of Engineering and Technology (Pakistan), usmanahmed5987@gmail.com, ORCID iD: https://orcid.org/0009-0007-2267-6385

[6] Lecturer, Department of Mechanical Engineering, NED University of Engineering and Technology (Pakistan), zainshahid@neduet.edu.pk, ORCID iD: https://orcid.org/0009-0003-4447-0143

Memoria Investigaciones en Ingeniería, núm. 26 (2024). pp. 54-69
https://doi.org/10.36561/ING.26.4
ISSN 2301-1092 • ISSN (en línea) 2301-1106 – Universidad de Montevideo, Uruguay

Resumen. - *La sostenibilidad de la industria del hormigón está en peligro porque es uno de los mayores consumidores de recursos naturales. Las cuestiones medioambientales y monetarias son las principales dificultades a las que se enfrenta actualmente la industria del hormigón. En este estudio se explora la potencial sustitución de cenizas de aserrín por cemento en la producción de hormigón. En este proyecto, se exploró la posible sustitución de cenizas de aserrín por cemento en la producción de concreto, un desperdicio típico de carpintería, y luego utilizamos varias técnicas de prueba para examinar cómo afecta las características mecánicas del concreto. En un experimento, se examinaron las resistencias a la compresión, la tracción y la flexión de muestras de hormigón elaboradas con diversas proporciones de ceniza de aserrín y cemento. Las muestras se fabricaron siguiendo las normas ASTM C-109, ASTM C-496 y ASTM C-78 para ensayos de compresión, tracción y flexión. En lugar de cemento, se añadió ceniza de aserrín a la muestra M-15 (M indica "mezcla" y 15 indica resistencia a la compresión de 15 MPA) en porcentajes en peso de 5%, 10%, 15%, 20% y 25%. Las muestras de concreto fueron ensayadas para determinar sus resistencias a compresión, tracción y flexión después de 14 días. Se realizaron comparaciones entre los resultados y el hormigón sin tratar. En este estudio, se investigó el comportamiento del concreto cuando se reemplazó la ceniza de aserrín por cemento en proporciones basadas en peso de 0%, 5%, 10%, 20% y 25%. Esto podría abordar el problema de cómo eliminar las cenizas de aserrín y al mismo tiempo mejorar las propiedades del hormigón.*

Palabras clave: *Resistencia a la tracción, resistencia a la compresión, resistencia a la flexión del hormigón, cenizas de aserrín, cubos de hormigón, construcción sostenible.*

Resumo. *- A sustentabilidade da indústria do betão está em perigo porque é um dos maiores consumidores de recursos naturais. As questões ambientais e monetárias são as principais dificuldades com que a indústria do betão enfrenta actualmente. Neste estudo, é explorada a potencial substituição da cinza de serragem por cimento na produção de concreto. Neste projeto, foi explorada a potencial substituição da cinza de serragem por cimento na produção de concreto, um típico resíduo de carpintaria, e em seguida utilizamos diversas técnicas de testes para examinar como isso impacta às características mecânicas do concreto. Em um experimento, foram examinadas as resistências à compressão, tração e flexão de amostras de concreto feitas com diversas proporções de cinza de serragem e cimento. As amostras foram confeccionadas seguindo ASTM C-109, ASTM C-496 e ASTM C-78 para ensaios de compressão, tração e flexão. No lugar do cimento, cinza de serragem foi adicionada à amostra M-15 (M indica 'mistura' e 15 indica resistência à compressão de 15MPA) em porcentagens em peso de 5%, 10%, 15%, 20% e 25%. As amostras de concreto foram testadas para verificar suas resistências à compressão, tração e flexão após 14 dias. Foram feitas comparações entre os resultados e o concreto não tratado. Neste estudo, o comportamento do concreto foi investigado quando a cinza de serragem foi substituída por cimento em extensões de peso de 0%, 5%, 10%, 20% e 25%. Isto poderia resolver o problema de como descartar as cinzas de serragem e, ao mesmo tempo, melhorar as propriedades do concreto.*

Palavras-chave: *Resistência à tração, resistência à compressão, resistência à flexão do concreto, cinza de serragem, cubos de concreto, construção sustentável.*

1. Introduction. - Concrete, the most common building material globally, is composed of cement, water, and aggregate. Its production requires significant energy and carbon, generating 5-10% of annual anthropogenic CO_2 emissions. Efforts to reduce cement emissions and make it greener have been ongoing due to the environmental impacts of global warming.[1]. Since sawdust is a byproduct of the timber industry and is frequently seen as waste, using sawdust composite in buildings is relevant since it can function as a sustainable resource. However, it offers a sustainable substitute for conventional building materials like steel or concrete by incorporating sawdust into composite materials. It is also feasible to modify the construction process' carbon footprint by using sawdust[2].While scientists, researchers, people, and governments are sincerely trying to find solutions for these top global concerns, they pose a serious threat to our ecosystem on a worldwide scale [3].

One of the main causes of climate change is human activity, which has detrimental effects on the environment such as increasing sea levels, heat waves, global temperatures, and the melting of permafrost. The most widely used building material, concrete, is overused worldwide and accounts for 7% of emissions of carbon dioxide from human activity. The issue is exacerbated by the growing population and demand for concrete, which in turn affects cement output. Building expenses have gone up as a result of this, especially in developing countries. [4].Cement production, a major contributor to global CO_2 emissions, also depletes limestone reserves. In the past, river sand was the most often used option for the fine aggregate component of concrete, but overuse of the material has raised environmental hazards, lowered the availability of trustworthy river sand sources, and increased the material's cost [5].

One of the most often utilized building materials is concrete. Cement, fine aggregate, coarse aggregate, and water are the components of concrete. One of the greatest adhesives for concrete is cement, which is harmful to the environment. During the production of Portland cement, more carbon dioxide and other potentially hazardous greenhouse gases are emitted into the atmosphere. [4] Manufacturing releases carbon dioxide, which adds to global warming and other environmental problems like dust pollution and ozone layer thinning [6]. Almost 3 billion tons of Portland cement are consumed each year, and for every 600 kg of cement manufactured, 400 kg of carbon dioxide gas is created.

On the other hand, as a result of present expansion and housing demands, consumption of the individual components of concrete has gradually improved. The cement business works around the clock to supply the demand from consumers. Moreover, quarrying for natural aggregates is problematic. Natural aggregates' natural sources are quickly vanishing, according to a recent analysis of their use. Alternative means of maintaining natural aggregates should be investigated to avoid damage to the environment from aggregate quarrying and the effects on the cement industry [7]. The effective plan to reduce environmental impact while also lowering energy, cost, and waste emission is to use extra cementitious materials as a partial replacement for cement mortar and concrete [5]. Many trials on extra binders or cement replacement are ongoing to address the aforementioned. As a result, municipal, industrial, commercial, and agricultural wastes with significant cementitious properties were utilized as potential non-conventional building materials [8].

Communities should consider using locally available materials for building houses, as demand for cement and natural sand increases. Waste materials, like fly ash, slag, limestone powder, siliceous minerals, and saw dust ash, can reduce production costs, increase concrete strength, and reduce environmental impact[4]. Researchers from all over the world have used a range of various materials to partially or completely replace the components of concrete. Nonetheless, the contradictory results show that more research is still needed to enhance the general public's understanding of the use of such items. This study suggests switching some of the cement with sawdust ash. Several sawdust ash volumes are used. To assess the impact of using sawdust ash as a partial replacement for cement, the compressive and tensile strengths of concrete specimens are assessed [7].

Sawdust is produced as a byproduct or waste during several stages of the production of timber, including as sawing, planning, routing, drilling, sanding, and joinery. Small, irregular wood chips or merely microscopic wood particles make up this waste stream. Sawdust is frequently spilled, fired, or landfilled in an open area [9]. Sawdust burning increases greenhouse gas emissions and adds to the burden in landfills [10]. Sawdust, an organic waste, is a result of the mechanical shaping and size of wood (timber). The dust is often burned for home heating. The final result is a kind of pozzolana called saw-dust ash (SDA). Concrete made from dry sawdust is 30% lighter than regular concrete and features insulate similar qualities to those of wood. When the ratios of cement to sawdust are right, it is not combustible. The use of sawdust concrete as a key building material provide a purpose [11].

Sawdust, which is made up of tiny pieces of wood, is a result of using a saw or other tool to cut, compress, or otherwise process another material. Moreover, it is a side effect of some animals that reside in wooded area. The daily process of chopping wood results in additional wood waste being produced. The sawdust exhibits both pozzolanic and cementitious abilities [12]. It is possible to replace conventional cement with sawdust ash, which is created when sawdust burns at a high temperature and contains a considerable portion of silicate and aluminate. A few studies have

looked into the use of sawdust ash (SDA) as a partial substitute for cement in concrete mixtures [9], [13], [14].

This study indicates changing some of the cement with sawdust ash. Several sawdust ash doses are applied. In a bid to assess the impact of using sawdust ash as a partial replacement for cement, the compressive and tensile strengths of concrete specimens are assessed [7]. Inappropriate handling of wood ash could result in adverse effects on the environment and human health. Since cement is the most expensive component of concrete, using it instead of SDA might save a lot of money on construction. [12]. The sawdust for this investigation was gathered from sawmills. To prevent sand and sawdust from mixing, the Sample was carefully assembled. The acquired sample was open burned in a metal container until it was burnt to ash. After cooling, the sawdust ash (SDA) was ground in a mortar and pestle. To determine the yield and conduct tests to measure the compressive, tensile, and flexural strength of saw dust ash-containing concrete [15].

In this study, cement was replaced with sawdust ash in weight-based proportions of 5%, 10%, 15%, 20%, and 25%. The compressive, tensile, and flexural strengths of concrete specimens were examined. Implementing eco-friendly practices and technologies can reduce the carbon footprint of cement production, which contributes to 5-10% of annual CO_2 emissions, promoting sustainable development, and responsible resource management.

2. Methodology. –

2.1 Cement and Aggregates. - The entire project was built with regular Portland cement. Clean river sand that had been put through a no.4 sieve and was kept on a no. 200 screen was used to make the fine aggregates used throughout the project. The stone that had been physically crushed and stored on no. 4 sieves was used to make the coarse aggregates.

2.2 Saw Dust Ash. - Sawdust Ash is a by-product created when the wood is sawed, ground, drilled, sanded, or otherwise processed into powder. Little pieces of wood are present inside. For this project, sawdust from a local workshop had to be collected. To minimize sand contamination, samples were painstakingly taken by tightly stuffing fresh sawdust ash samples into bags. To speed up the burning process, the obtained sawdust was exposed to the sun for ten days. The gathered sawdust samples were burned to ashes in a drum. After cooling, the ash was pulverized and is being used in research. Table 1 lists the chemical makeup of sawdust, and Table 2 lists its physical traits.

Chemical Property	SDA% by weight
Ph	11.12
SiO_2	50.20
AL_2O_3	1.02
Fe_2O_3	14.23
CaO	5.45
MgO	0.09
MnO	5.60
Na_2O	0.07
K_2O	9.57
P_2O_5	0.56
SO_3	0.58

Table I. Chemical Composition of Sawdust ash [11]

Property	Values
Specific Gravity	2.19
Loose bulk Density (kg/m³)	1040
Loss in Ignition (%)	4.30
Yield (%)	3.00
Moisture Content (%)	0.30

Table II. Physical Properties of Saw dust ash [12]

2.3 Mixture Design and Sample Preparation. - The six concrete combinations that will be the subject of this study will each have a specific composition that is detailed in Table 2. Sawdust ash (SDA) will substitute for Portland cement (PC) at 0%, 5%, 10%, 15%, 20%, and 25% SDA. One of the mixtures is referred to as (0SDA), which denotes the

absence of SDA. The mixture ID indicates the percentage of PC that have been replaced with SDA. As an example, the term 20SDA refers to a concrete mixture in which 20% of the Portland cement is replaced by SDA. In each of the combinations water was used for mixing and curing the concrete.

The dry ingredients were mixed for 4 minutes for each formulation before the water was added gradually while the mixture was still going on. After all the water was added, the mixture was again mixed. When the fresh properties of the mixtures were tested, the fresh mixture was poured into the pre-oiled mold for various tests to be performed. After around 24 hours, the samples were demolded, and they were then cured in water for 14 days. The whole data is displayed in Table 3.

The concrete grade that was used was M-15, which used cement, fine aggregates, and coarse aggregates in ratios of 1:2:4 (1 part of cement, 2 parts of sand, and 4 parts of coarse aggregate) under ASTM C-109 and had a water to cement ratio of 0.65.

Concrete Mix Design					
Saturated Surface Dry Aggregates					
%	**Cement**		**Fine Aggregates**	**Course Aggregates**	**Water**
	Pure Cement	**Saw Dust Ash**			
	kg	kg	kg	kg	ml
0%	1.375	0	2.75	5.5	893.75
5%	1.30625	0.06875	2.75	5.5	893.75
10%	1.2375	0.1375	2.75	5.5	893.75
15%	1.16875	0.20625	2.75	5.5	893.75
20%	1.1	0.275	2.75	5.5	893.75
25%	1.03125	0.34375	2.75	5.5	893.75

Table III. Concrete Mix Design

2.4 Casting of Specimens. - Different types of specimens are casted for this experimental research study.

2.4.1 Concrete Specimens for Compressive Testing. - 18 concrete specimens in the shape of 6”x 6” cubes were prepared for compressive strength testing. The specimens included varying levels of sawdust ash replacement for cement, specifically at 0%, 5%, 10%, 15%, 20%, and 25**%.** The concrete specimens prepared for Compressive testing has volume of $216in^3$, $205.2in^3$, $194.4in^3$, $183.6in^3$, $172.8in^3$ and $162in^3$ at 0 %, 5%, 10%, 15%, 20%, and 25% respectively when using these percentages of cement.

Concrete Specimens (Cube)	
Mixture Type	**Compressive Strength Testing Specimen**
	No. of Specimen for 14 Days of Curing
0%	3
5%	3
10%	3
15%	3
20%	3
25%	3

Table IV. Number of concrete specimens for compressive testing

Figure I. Representation of concrete for compressive testing

2.4.2 Concrete Specimens for Tensile Testing. -18 concrete specimens in the shape of 6"x 6" cylinders were prepared for tensile strength testing. The specimens included varying levels of sawdust ash replacement for cement, specifically at 0%, 5%, 10%, 15%, 20%, and 25%. The concrete specimens prepared for tensile strength testing has volume of $200.74in^3$, $190.703in^3$, $180.666in^3$, $170.629in^3$, $160.592in^3$ and $150.555in^3$ at 0 %, 5%, 10%, 15%, 20%, and 25% respectively when using mentioned percentages of cement.

Concrete Specimens (Cylinder)	
Mixture Type	**Tensile Strength Testing Specimen**
	No. of Specimen For 14 Days of Curing
0%	3
5%	3
10%	3
15%	3
20%	3
25%	3

Table V. Number of concrete specimens for tensile testing

Figure II. Representation of concrete for tensile testing

2.4.3 Concrete Specimens for Flexural Testing. - 18 concrete specimens in the shape of beams were prepared for flexural strength testing. The specimens included varying levels of sawdust ash replacement for cement, specifically at 0%, 5%, 10%, 15%, 20%, and 25%. The concrete specimens prepared for flexural strength testing has volume of $320in^3$, $304in^3$, $288in^3$, $272in^3$, $256in^3$ and $240in^3$ at 0 %, 5%, 10%, 15%, 20%, and 25% respectively when using mentioned percentages of cement.

Concrete Specimens (Beam)	
Mixture Type	**Flexural Strength Testing Specimen**
	No. of Specimen For 14 Days of Curing
0%	3
5%	3
10%	3
15%	3
20%	3
25%	3

Table VI. Number of concrete specimens for flexural testing

Figure III. Representation of concrete for flexural testing

2.5 Tests on Fresh Concrete. - The slump test, following ASTM C143, assesses the workability of concrete by measuring the difference between initial height and final settlement. It helps adjust mix design and placement techniques, ensuring proper construction processes and better-quality structures.

2.6 Tests on Hardened Concrete. - Split tensile, compressive, and flexural strength tests were conducted for hardened concrete.

2.6.1 Compressive Strength Test. - The compressive strength test is a fundamental mechanical test used to determine the ability of a material to withstand compressive loads without failing or undergoing deformation. It is a critical property for materials that are subjected to compressive forces, such as concrete, masonry, rocks, ceramics, and metals. The compressive strength of the material was calculated by dividing the total load on the specimens by the area of the specimen. The following equation can be used to find the Compressive Strength (ASTM C-109).

$$\text{Compressive Strength} = P/A$$

Where, P = Optimum Weight in Pounds. A= Area of Cross Section.

To calculate Compressive Strength in kPa:

$$\underset{\text{(in kPa)}}{\text{Compressive Strength}} = \underset{\text{(in Psi)}}{\text{Compressive Strength}} \times 6.895$$

Figure IV. Experimental Setup of Compression Test of Concrete Specimens by UTM

2.6.2 Tensile Strength Test. - The tensile strength test is a mechanical test used to determine the maximum amount

of tensile (pulling) force a material can withstand before it breaks or deforms. It is an essential test in materials science and engineering to evaluate the strength and quality of various materials. The following equation was used to get the Splitting Tensile Strength (ASTM C 496).

$$\text{Tensile Strength} = (2P)/(\pi ld)$$

Where,
T = Tested specimen's tensile strength.
P = Maximum Load in Pounds.
L = Specimen's Length.
d = Specimen's Diameter.
To calculate Tensile Strength in kPa :
Tensile Strength = Tensile Strength x 6.895

Figure V. Experimental Setup of Tensile Strength Test of Concrete Specimens by UTM.

2.6.3 Flexural Strength Test. - The flexural strength test, also known as the modulus of rupture test or bending strength test, is a mechanical test used to determine the strength and behavior of a material when subjected to bending forces. It is commonly performed on brittle materials such as ceramics, concrete, glass, and some types of polymers. The test involves applying a three-point or four-point bending load to a rectangular or cylindrical specimen. The below mentioned equation of rupture modulus (ASTM C-78) was used:

$$R = (Pl)/ (bd^2)$$

Where,
R = Rupture modulus of the tested specimen.
P = Force exerted on tested specimen.
L = Specimen's length.
B = Specimen's width at the fracture of the test specimen.
D = Specimen's depth at the fracture of the test specimen.

Figure VI. Experimental Setup of Flexural Strength Test of Concrete Specimens by UTM.

3. Results and Discussions

3.1 Fresh Concrete. - As the levels of sawdust ash rose, the slump values also rose. Because they don't absorb as much water as cement, the sawdust ash particles in the concrete mix are more workable than cement.

3.2 Compressive Strength Results of Concrete. - Compressive strength tests on the concrete sample were performed after 14 days of curing. Specimens were created of a 6" x 6" cube and kept inside the curing container of water following ASTM C-109. The cubical specimens have a height of 6 inches (152.4mm) and a width of 6 inches (152.4mm). Three Specimens of each of the different percentages (0%, 5%, 10%, 15 %, 20%, and 25%) were evaluated on a compression testing machine at 14 days of curing. The compressive strength of the material was calculated by dividing the total load on the specimens by the area of the specimen. There were 4 samples of 6" cubes for every mixture type (0%, 5%, 10%, 15%, 20%, and 25% of SDA). In this research, the specimen has a 36 in^2 cross-sectional area. Table 7 presents the experimental result of compressive strength of concrete for 14 days respectively.

S. No	Replacement with Saw Dust Ash (%)	Strength (psi)			Average	
		Specimen 1	Specimen 2	Specimen 3	psi	kPa
1	0%	1530	1373.90	1498.80	1467.56	10118.8
2	5%	1312.5	1500	1343.75	1385.41	9552.44
3	10%	1812.5	1781.25	1718.75	1770.83	12209.9
4	15%	1312.5	1250	1281.25	1281.25	8834.2
5	20%	1200	1156.25	1281.25	1212.5	8360.18
6	25%	1093.75	1137.5	1156.25	1129.16	7785.6

Table VII. Compressive strength of concrete at 14 days.

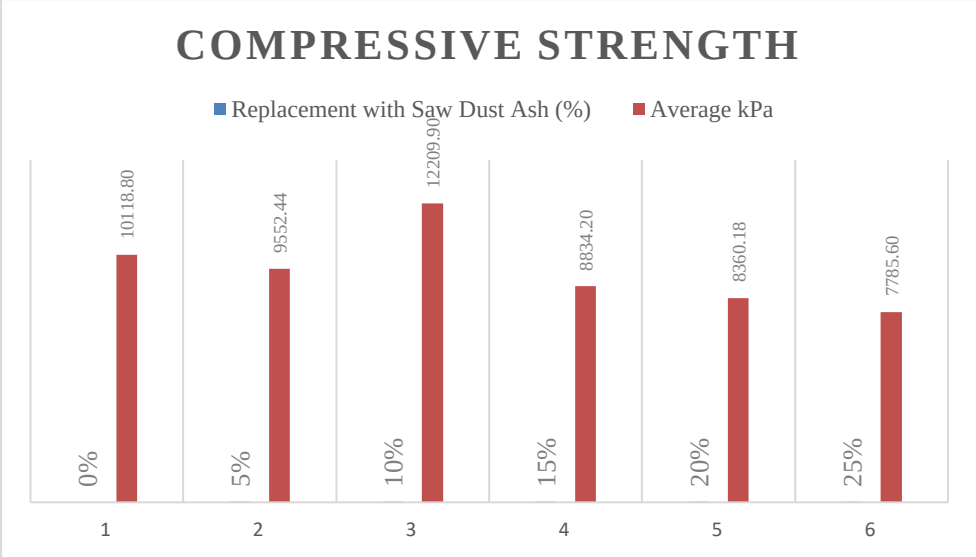

Figure VII. Graphical representation of compressive strength of concrete at 14 days.

The compressive strength of concrete is influenced by factors such as water demand, particle size distribution, chemical reactions, and aggregate-paste bonding. Higher SDA content can lead to increased water demand, reducing compressive strength. Unfavorable particle size distribution can mix compactness and strength. Chemical interactions between SDA and cement can either improve or damage compressive strength. The bond between aggregates and paste is crucial for overall concrete strength, and SDA can negatively affect it. A balance of factors, such as water demand, particle size, beneficial chemical reactions, and strong aggregate-paste bonding, can result in better compressive strength after 14 days, exhibiting maximum compressive strength at 10 % and continues declination at increasing % of SDA.

3.3 Tensile Strength Results of Concrete. - At 14 days of curing, the concrete specimens of the split tensile strength test were evaluated. The split tensile strength test specimens of 4in. (102 mm) in diameter and 8 in. (203 mm) in length respectively were cast. According to ASTM C 496, the specimens were tested using a compression testing machine. There were 3 samples of 4x8-inch cylinders for every mixture type (0%, 5%, 10%, 15%, 20%, and 25% of SDA). In this research, the specimen has a 12.5 cross-sectional area, 0.65 water-cement ratio, and 1:2:4 cement sand and coarse aggregate ratio. Table 8 represents the experimental result of the concrete strength of split tensile cylinders for 14 days respectively.

S. No	Replacement with Saw Dust Ash (%)	Strength (psi)			Average	
		Specimen 1	Specimen 2	Specimen 3	psi	kPa
1	0%	223.62	232.566	219.149	225.11	1552.13
2	5%	192.31	199.02	183.36	191.56	1320.80
3	10%	174.42	176.88	170.62	173.97	1199.52
4	15%	165.47	164.136	152.06	160.55	1107
5	20%	143.11	134.172	144.90	140.72	970.26
6	25%	122.99	129.70	119.86	124.18	856.22

Table VIII. Tensile strength of concrete at 14 days.

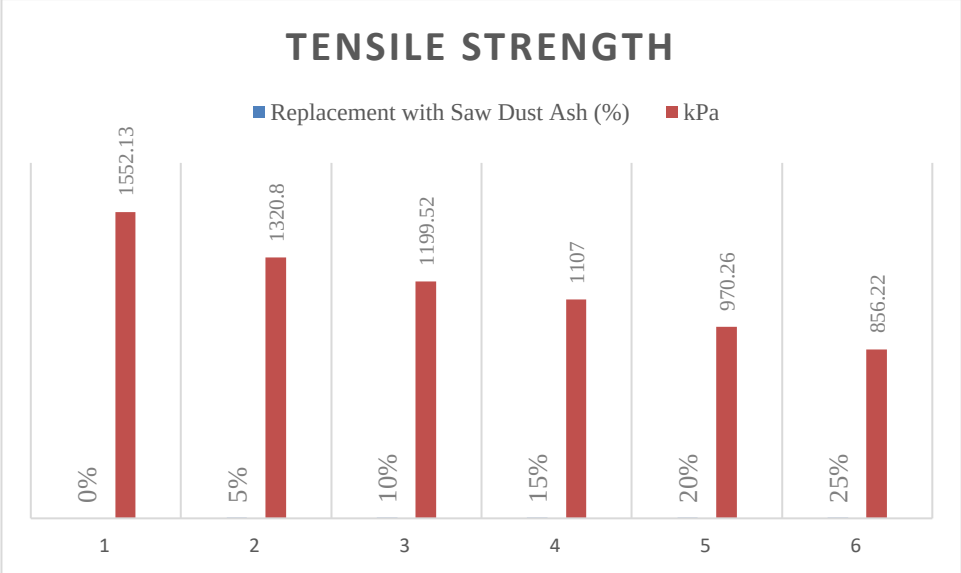

Figure VIII. Graphical representation of tensile strength of concrete at 14 days.

The causes behind the strength trends in concrete with altered SDA replacement levels include factors like water demand and mix properties. Higher SDA content may increase water demand, affecting workability and hydration, which lowers strength. The particle size distribution of SDA influences mix compactness and uniformity, impacting workability and strength. Additionally, the interaction between sawdust ash and cement can disrupt crucial hydration and pozzolanic reactions, affecting overall strength. Lastly, the bond between aggregates and paste in the concrete mix can be impacted by SDA content, contributing to the observed trend of declination in tensile strength.

3.4 Flexural Strength Results of Concrete. - For the flexural strength test, the rupture modulus was evaluated after 14 days of curing. Three specimens for each mixture type were molded at the time of casting. Beam samples were 20 inches long and had a cross-sectional dimension of 4 inches by 4 inches (101.6 mm × 101.6 mm × 508 mm). Samples were kept in a water container for storage. In accordance with ASTM C 78, specimens were tested utilizing 3rd-point loading, and the rupture modulus was obtained. There were two beams for every mixture (0%, 5%, 10%, 15%, 20%, and 25% of SDA) that were cast to test at 14 days of curing. In this research, the specimen has 16 in 2 cross-sectional areas, 0.65 water-cement ratio, and 1:2:4 cement sand and coarse aggregate ratio. Table 9 represents the experimental result of beams of flexural for 14 curing days.

S. No	Replacement with Saw Dust Ash (%)	Strength (kPa)			Average
		Specimen 1	Specimen 2	Specimen 3	kPa
1	0%	3350	3310	3400	3353
2	5%	3046	3075	2950	3023
3	10%	3800	3831	3940	3857
4	15%	3010	2915	2960	2961
5	20%	2460	2550	2390	2466
6	25%	1970	2050	1925	1981

Table IX. Flexural strength of concrete at 14 days.

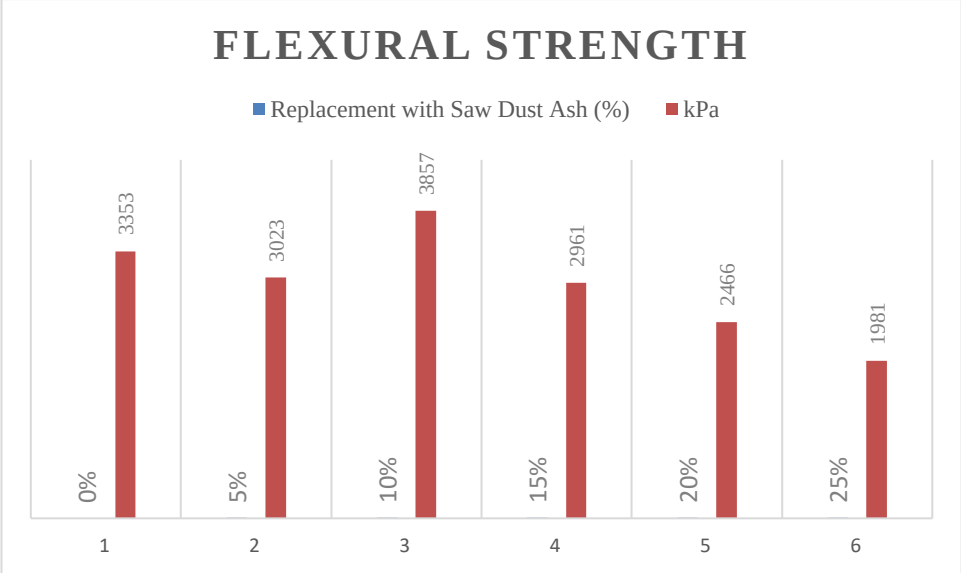

Figure IX. Graphical representation of flexural strength of concrete at 14 days

Concrete strength trends vary with different levels of Sawdust Ash (SDA) due to reasons like water demand, particle size distribution, chemical reactions, and aggregate-paste bonding. Higher SDA content can increase water demand, affecting workability and hydration, and reducing strength. Particle size distribution affects mix compactness and uniformity. Chemical interactions between SDA and cement can either improve or decrease strength, with pozzolanic reactions potentially improving it and disrupting hydration processes potentially reducing it. The bond between aggregates and paste is crucial for overall flexural strength, showing maximum strength at 10% and further declines with increasing % of SDA.

4. Conclusion. - Following are the concluding remarks from this research study.

- The use of sawdust ash in concrete provides additional environmental as well as other technical benefits for all related industries. Partial replacement of cement with sawdust ash reduces the cost of concrete manufacturing.
- The results of the compressive test have indicated that the strength of concrete has shown a reduction of 5.60 %, 12.70 %, 17.38 % and 23.06 % at 5 %, 15 %, 20 % and 25 % of SDA with concrete mix respectively. While, the compressive strength has increased to 20.67 % at 10 % of the concrete mix. Therefore, 10% gives the best result for the compressive strength test after 14 days of curing of the specimens.
- The results of the split tensile strength test have indicated that the strength of concrete decreases as the amount of percentage of SDA increases in the concrete mix. That is 0% gives the best result for the split tensile strength test after 14 days of curing of the specimens.
- The results of the flexural strength test have indicated that the strength of concrete has exhibited a reduction of 9.84 %, 11.69 %, 26.45 % and 40.92 % at 5 %, 15 %, 20 % and 25 % of SDA with concrete mix respectively. However, the flexural strength has increased to 15.03 % at 10 %. Hence 10% gives the best result for the flexural strength test after 14 days of curing of the specimen.
- There is a significant reduction in the density of concrete with the increase in the percentage of sawdust in the concrete.
- Sawdust ash can be used as a cement replacement due to its pozzolanic properties as seen in some of the strength tests conducted. Thus, sawdust ash can replace cement in the concrete up to a certain degree without compromising the concrete strength.

To summarize it can be stated that adding SDA to a fresh concrete mix allows for an increase in both compressive and flexural strength at a rate of 10%. Tensile strength, on the other hand, declines as SDA levels in the concrete mix rise.

References

[1] B. Meko and J. O. Ighalo, "Utilization of Cordia Africana wood sawdust ash as partial cement replacement in C 25 concrete," *Cleaner Materials*, vol. 1, p. 100012, Dec. 2021, doi: 10.1016/j.clema.2021.100012.

[2] B. C. Olaiya, M. M. Lawan, and K. A. Olonade, "Utilization of sawdust composites in construction—a review," *SN Appl. Sci.*, vol. 5, no. 5, p. 140, May 2023, doi: 10.1007/s42452-023-05361-4.

[3] T. Skytt, S. N. Nielsen, and B.-G. Jonsson, "Global warming potential and absolute global temperature change potential from carbon dioxide and methane fluxes as indicators of regional sustainability – A case study of Jämtland, Sweden," *Ecological Indicators*, vol. 110, p. 105831, Mar. 2020, doi: 10.1016/j.ecolind.2019.105831.

[4] A. O. I. and T. E. O. F. C. Onyeka, "Design and Production of Concrete Kerbs for Pavement Construction Made with Saw Dust Ash as Partial Replacement of Cement," Sep. 2023, doi: 10.5281/ZENODO.8353259.

[5] S. N. C. Deraman, M. A. D. A. Rashid, S. A. Saad, N. Md. Husain, and S. A. Masjuki, "Effects of durian sawdust as a partial replacement of fine aggregate in concrete," *IOP Conf. Ser.: Mater. Sci. Eng.*, vol. 1144, no. 1, p. 012027, May 2021, doi: 10.1088/1757-899X/1144/1/012027.

[6] S. Praveenkumar and G. Sankarasubramanian, "Mechanical and durability properties of bagasse ash-blended high-performance concrete," *SN Appl. Sci.*, vol. 1, no. 12, p. 1664, Dec. 2019, doi: 10.1007/s42452-019-1711-x.

[7] A. Mwango and C. Kambole, "Engineering Characteristics and Potential Increased Utilisation of Sawdust Composites in Construction—A Review," *JBCPR*, vol. 07, no. 03, pp. 59–88, 2019, doi: 10.4236/jbcpr.2019.73005.

[8] O. Arowojolu, E. Fanijo, and A. Ibrahim, "Behavior of kernelrazzo floor finish in aggressive chloride environment," *Case Studies in Construction Materials*, vol. 11, p. e00256, Dec. 2019, doi: 10.1016/j.cscm.2019.e00256.

[9] B. C. Olaiya, M. M. Lawan, and K. A. Olonade, "Utilization of sawdust composites in construction—a review," *SN Appl. Sci.*, vol. 5, no. 5, p. 140, May 2023, doi: 10.1007/s42452-023-05361-4.

[10] U. Udokpoh and C. Nnaji, "Reuse of Sawdust in Developing Countries in the Light of Sustainable Development Goals," *Recent Prog Mater*, vol. 05, no. 01, pp. 1–33, Jan. 2023, doi: 10.21926/rpm.2301006.

[11] B. N. AL-Kharabsheh, M. M. Arbili, A. Majdi, J. Ahmad, A. F. Deifalla, and A. Hakamy, "A Review on Strength and Durability Properties of Wooden Ash Based Concrete," *Materials*, vol. 15, no. 20, p. 7282, Oct. 2022, doi: 10.3390/ma15207282.

[12] W. M. Tawfeeq, H. Alaisaee, Y. Almoqbali, A. Alsaadi, and K. Almaqbaliy, "Structural Performance of Reinforced Cement Concrete Beam with Sawdust," *KEM*, vol. 913, pp. 155–167, Mar. 2022, doi: 10.4028/p-70t5ev.

[13] P. O. Awoyera, A. Adesina, and R. Gobinath, "Role of recycling fine materials as filler for improving performance of concrete - a review," *Australian Journal of Civil Engineering*, vol. 17, no. 2, pp. 85–95, Jul. 2019, doi: 10.1080/14488353.2019.1626692.

[14] A. Sivakrishna, A. Adesina, P. O. Awoyera, and K. Rajesh Kumar, "Green concrete: A review of recent developments," *Materials Today: Proceedings*, vol. 27, pp. 54–58, 2020, doi: 10.1016/j.matpr.2019.08.202.

[15] E. E. Teker Ercan, L. Andreas, A. Cwirzen, and K. Habermehl-Cwirzen, "Wood Ash as Sustainable Alternative Raw Material for the Production of Concrete—A Review," *Materials*, vol. 16, no. 7, p. 2557, Mar. 2023, doi: 10.3390/ma16072557.

Nota contribución de los autores:

1. Concepción y diseño del estudio
2. Adquisición de datos
3. Análisis de datos
4. Discusión de los resultados
5. Redacción del manuscrito
6. Aprobación de la versión final del manuscrito

IA ha contribuido en: 1, 2, 3, 4, 5 y 6.
MUH ha contribuido en: 1, 2, 3, 4, 5 y 6.
AAK ha contribuido en: 1, 2, 3, 4, 5 y 6.
MA ha contribuido en: 1, 2, 3, 4, 5 y 6.
MU ha contribuido en: 1, 2, 3, 4, 5 y 6.
ZS ha contribuido en: 1, 2, 3, 4, 5 y 6.

Nota de aceptación: Este artículo fue aprobado por los editores de la revista Dr. Rafael Sotelo y Mag. Ing. Fernando A. Hernández Gobertti.

Diseño de un sistema de control para el tratamiento de aguas de enfriamiento de un formador de azufre

Design of a control system for the treatment of cooling water from a sulfur former

Projeto de um sistema de controle para tratamento de água de resfriamento proveniente de um formador de enxofre

Urimare Campos[1], Yordi González-Rondón[2(*)]

Recibido: 08/11/2023 Aceptado: 08/03/2024

Resumen. - Se presenta el diseño de un sistema de control para el tratamiento de aguas de enfriamiento de un formador de azufre en un mejorador de crudo, para mantener la conductividad del agua de enfriamiento en rangos establecidos y de esta manera evitar la acumulación de minerales en las tuberías, lo cual deteriora el sistema de enfriamiento. En el desarrollo, se determinaron las propiedades fisicoquímicas a controlar, como la conductividad, sus agentes biológicos y los sólidos disueltos (TDS) presentes en el agua, tratándose la conductividad mediante purgas controladas y los microorganismos y TDS mediante la dosificación de productos químicos. También, se diseñó el sistema de control de conductividad y dosificación de químicos utilizando un Controlador Lógico Programable, se seleccionaron los diferentes componentes como sensores, bombas, válvulas, medidor de nivel y medidor de conductividad y posteriormente se validó el sistema de control mediante simulación del proceso con en el software LOGO SOFT confort. Los resultados demostraron el correcto funcionamiento de encendido y apagado de las bombas y válvulas, y se concluyó que el diseño es capaz de mantener controlado todos los parámetros ante cualquier cambio en las variables de entradas.

Palabras clave: Sistema de control, formador de azufre, Simulación.

(*) Autor Corresponsal

[1] Bachiller en Ingeniería. Universidad de Oriente, Núcleo de Anzoátegui, Centro de Termofluidodinámica y Mantenimiento, Barcelona, Estado Anzoátegui (Venezuela), urimarecampos@gmail.com, ORCID iD: https://orcid.org/0009-0004-7025-8442

[2] Ingeniería Mecánica. Universidad de Oriente, Instituto de Investigaciones en Biomedicina y Ciencias Aplicadas, IIBCAUDO "Dra. Susan Tai", Cumaná, Estado Sucre (Venezuela), yordygonzalez@hotmail.com, ORCID iD: https://orcid.org/0000-0002-4769-75682

https://doi.org/10.36561/ING.26.5
ISSN 2301-1092 • ISSN (en línea) 2301-1106 – Universidad de Montevideo, Uruguay

Summary. - *The design of a control system for the treatment of cooling water of a sulfur former in a crude oil upgrader is presented, to maintain the conductivity of the cooling water in established ranges, and in this way avoid the accumulation of minerals in the pipes which deteriorates the cooling system. In the development, the physicochemical properties to be controlled were determined, such as conductivity, its biological agents and the dissolved solids (TDS) present in the water, treating the conductivity through controlled purges and the microorganisms and TDS through the dosage of chemical products. Also, the conductivity and chemical dosing control system was designed using a Programmable Logic Controller, the different components such as sensors, pumps, valves, level meter and conductivity meter were selected and subsequently the control system was validated through simulation of the process within the LOGO SOFT comfort software. The results demonstrated the correct on and off operation of the pumps and valves, and it was concluded that the design is capable of keeping all the parameters controlled in the event of any change in the input variables.*

Keywords: *Control system, sulfur former, Simulation.*

Resumo. ***-*** *É apresentado o projeto de um sistema de controle para o tratamento da água de resfriamento de um formador de enxofre em um melhorador de petróleo bruto, para manter a condutividade da água de resfriamento em faixas estabelecidas, e desta forma evitar o acúmulo de minerais nas tubulações que se deterioram. o sistema de refrigeração. No desenvolvimento foram determinadas as propriedades fisicoquímicas a serem controladas, como a condutividade, seus agentes biológicos e os sólidos dissolvidos (TDS) presentes na água, tratando a condutividade através de purgas controladas e os microrganismos e TDS através da dosagem de produtos químicos. Além disso, o sistema de controle de condutividade e dosagem de produtos químicos foi projetado utilizando um Controlador Lógico Programável, os diferentes componentes como sensores, bombas, válvulas, medidor de nível e condutivímetro foram selecionados e posteriormente o sistema de controle foi validado através de simulação do processo dentro do LOGO Software de conforto SOFT. Os resultados demonstraram o correto funcionamento liga e desliga das bombas e válvulas, e concluiu-se que o projeto é capaz de manter todos os parâmetros controlados caso ocorra alguma alteração nas variáveis de entrada.*

Palavras-chave: *Sistema de controle, formador de enxofre, Simulação.*

1. Introducción. - Un mejorador de crudo tiene como propósito procesar crudo extrapesado para transformarlo en un crudo mucho más liviano. En este proceso, uno de los subproductos que se obtiene es el azufre, el cual se genera en la unidad formadora de azufre y posteriormente se almacena en pilas en los patios del mejorador. Esta unidad formadora recibe el mineral en estado líquido a 150 °C aproximadamente, y luego lo transforma en estado sólido a 45 °C. Para lograr la solidificación del azufre, es fundamental la acción de aguas de enfriamiento, las cuales circulan a través de un sistema que consta de líneas de tuberías, intercambiador de calor, tanque de almacenamiento de agua de acero inoxidable y bomba de recirculación [1].

Todo sistema de enfriamiento recirculante que utiliza agua como medio refrigerante debe contar con algún tipo de tratamiento ya sea físico o químico [2], para evitar el aumento de ciclos de concentración, es decir, la concentración de iones en el agua (conductividad), la cantidad de minerales, los sólidos disueltos y la dureza en dichas aguas durante la recirculación [3-5]. A pesar de lo anterior, en las unidades formadoras de azufre no se trata el agua de ninguna forma, lo que se hace es suministrar agua constantemente al sistema de enfriamiento para impedir que aumente de manera exacerbada de estos ciclos, y para reponer el volumen del flujo evaporado [6].

Al respecto, la estrategia de suministrar agua constantemente en los formadores de azufre no es lo más adecuado, ya que se desperdicia en exceso el fluido, y además, esta agua de reposición generalmente viene asociada con bacterias, conjuntamente con carbonatos, bicarbonatos, sulfatos, entre otros minerales [7,8], que con el transcurrir del tiempo tienden a depositarse en las paredes internas de la tubería, lo que ocasiona severos daños como corrosión. Asimismo, se produce un aumento del espesor de pared del sistema hidráulico, lo que causa una disminución en la tasa de transferencia de calor del intercambiador, y un incremento en las pérdidas de carga del sistema de bombeo [9,10]. Por otra parte, las bacterias que se encuentran en el agua crean algas que causan obstrucción en las boquillas de aspersión de los sistemas de enfriamiento. Todos estos factores disminuyen la eficiencia en el proceso de formación de azufre lo que se traduce en pérdidas económicas [11].

Para darle solución a la problemática presentada, en esta investigación se planteó hacer modificaciones a las condiciones operacionales del sistema de tratamiento de agua de una unidad formadora de azufre de un Complejo Petroquímico, tomando como estrategia el uso de químicos y purgas controladas. Para esto se propuso el diseño de un sistema de control con la finalidad de mantener en el agua de enfriamiento la conductividad, y a su vez dosificar las cantidades adecuadas de químicos dentro de parámetros que no afecten el proceso. Asimismo, se realiza la simulación del sistema de control propuesto, y se describe la selección de accesorios y equipos necesarios para el funcionamiento correcto del sistema.

2. Materiales y métodos.-

2.1 Descripción del sistema formador de azufre. - Un complejo de mejoramiento de crudo tiene como propósito procesar crudo extrapesado para transformarlo en un crudo más liviano. Como subproductos de este proceso se obtiene coke y azufre. Este último es bombeado en forma líquida desde un tanque de almacenamiento de la unidad (ver figura I) por medio de tuberías enchaquetadas hacia la unidad de solidificación de azufre, constituida por dos trenes en paralelo, como se muestra uno de ellos en la figura II. En el proceso, el azufre pasa por un filtro de malla de acero inoxidable de 150 mesh, y es solidificado de acuerdo al proceso Rotoformer®, que consiste en un estator cilíndrico y un cilindro hueco perforado. El azufre líquido llega al interior del estator cilíndrico y sale a la superficie de este por medio de boquillas, fluyendo de forma controlada por la acción de una barra distribuidora. Asimismo, el cilindro hueco perforado que rodea al estator gira concéntricamente depositando gotas de azufre sobre una banda transportadora metálica de acero inoxidable donde son enfriadas.

En la superficie de la banda transportadora se aplica una película muy delgada de antiadherente tipo polimérica (solución de Tegopren) mediante un rodillo, con la finalidad de evitar que se pegue el azufre a la correa y se mantenga la forma del producto de azufre (en forma de pastillas). La banda transportadora absorbe el calor del azufre mediante conducción, haciendo que el azufre solidifique a temperaturas inferiores de 45 °C. En el proceso, la velocidad de rotación del Rotoformer se sincroniza con la velocidad de la correa metálica, haciendo que las gotas se depositen sobre la correa sin deformación, y posterior a la solidificación, resulten en pastillas regulares con forma y/o aspecto óptimo. La forma de las pastillas es importante para las características de manejo y generación de polvo, debido a que una relación apropiada de diámetro y altura, le daría la cualidad de forma semiesférico.

Figura I. Tanque de almacenamiento de azufre.

Figura II. Tren de formación de azufre.

Para que ocurra con éxito la solidificación, en la parte inferior de la banda metálica se encuentran dispuestos varios aspersores que expulsan agua hacia la banda con el fin de retirar el calor de la misma. En el enfriamiento se pierde parte del líquido refrigerante por evaporación, y la otra parte de agua que no es evaporada, se recoge por gravedad en una bandeja, la cual converge en el tanque de almacenamiento del proceso de enfriamiento. La parte del agua que se evapora ocasiona un aumento en la cantidad de solidos disueltos en el agua de enfriamiento. Este proceso de enfriamiento está constituido por dos (2) bombas centrífugas de 15 Hp (una en Stand Bie), las cuales se encargan de la recirculación de las aguas de enfriamiento, un intercambiador de calor de tiro forzado de 1.736 m^2, donde el agua de enfriamiento disminuye su temperatura de 45 °C a 30 °C y un tanque de almacenamiento, construido en acero inoxidable, el cual puede albergar un volumen de 2.700 L.

Durante el proceso de enfriamiento se producen emanaciones de vapor de azufre, el cual es tóxico e irritante, razón por la cual existe un sistema de extracción o escape provisto de un ventilador de extracción de aire. La parte final del proceso que cumple la unidad 32 concluye con el transporte del azufre solidificado por un sistema de bandas transportadoras hacia el patio de manejo de sólidos, donde es almacenado en grandes pilas. La descripción anterior de la unidad formadora de azufre sugiere que se trata de proceso es muy complejo, pues en ella se involucran diferentes variables que se interrelacionan y deben ser controladas. Para resolver el problema planteado, en esta investigación se realizó una búsqueda detallada de información sobre las unidades de formadores de azufre en manuales, libros,

artículos, proyectos, revisión de diagramas de instrumentación y tuberías, todo esto con la finalidad de conocer el proceso y recorrido de las aguas de enfriamiento, así como también los accesorios, equipos, metalografía y el ambiente con que está en contacto el fluido refrigerante.

2.2 Propiedades fisicoquímicas y concentración apropiada de químicos para la dosificación en las aguas de enfriamiento. - Para conocer las propiedades fisicoquímicas que guardan relación con los diferentes problemas existentes en el sistema de enfriamiento, se realizaron entrevistas a expertos en sistemas de aguas industriales, también se realizaron inspecciones *in situ* de unidades formadores de azufre para determinar los posibles problemas del sistema de enfriamiento. Se realizaron toma de muestras del agua de enfriamiento con instrucciones y recomendaciones del personal de aguas industriales. Las muestras fueron analizadas en laboratorio a fin de seleccionar y analizar los productos químicos que mejor se adapten a las características dichas aguas, y así poder determinar la concentración del químico elegido, de igual manera esta concentración fue verificada mediante la prueba de jarras.

2.3 Sistema de control de conductividad y dosificación de químicos para el tratamiento del agua de enfriamiento en el formador de azufre. - El control de purgas controladas y la dosificación de productos químicos que se desarrolla en esta investigación, se realiza mediante la implementación de un controlador lógico programable (PLC). Para el cálculo de las purgas, se define primeramente el punto de ajuste (*set point*) que determina el encendido de una válvula, luego se determina el volumen de purga el cual será igual al volumen de reposición, y dependerá del volumen evaporado durante el proceso de refrigeración. Posteriormente se verifica, mediante la aplicación de un balance de masa en concentraciones, que el volumen de purga garantiza las sugerencias de expertos en operaciones. Por otra parte, la dosificación de químicos se diseña en base al volumen de agua de reposición y de la dosis de cada producto seleccionado. El punto de ajuste o *set point* que determina el encendido de las bombas se fija en función al nivel del tanque de almacenamiento y el tiempo de encendido de las mismas se determina respecto al volumen y al caudal de dosificación.
Para la dosificación de químicos y la medición de las variables es necesario diseñar un baypass siguiendo recomendaciones del personal de operaciones, con la finalidad que no fluya un caudal mayor a 1,955 m^3/hr. Para esto se siguen las normas PDVSA 90616.1.024 y PDVSA MDP-02-FF-03, asumiendo un diámetro de tubería y un factor de fricción, se realizan iteraciones, y se verifica que los resultados obtenidos satisfagan las normas antes mencionadas. Igualmente se verifica que el espesor correspondiente al diámetro escogido soporte las sobrepresiones de diseño, esto mediante la norma MDP-02-FF-03. Luego se especifica la disposición de los equipos y accesorios necesarios para el funcionamiento de la propuesta de control y así definir la lógica de control que regirá el proceso. El lenguaje de programación que más se adapta a las necesidades de la organización y a las características del software de programación se eligió cumpliendo con la norma IEC 1131-3. El procedimiento incluye la conexión de los distintos componentes al PLC, así como los ajustes de los sensores de conductividad y nivel en función al rango de entrada.

2.4 Componentes y simulación del sistema de control. - Según los requerimientos necesarios para llevar a cabo el proceso de tratamiento de agua de enfriamiento, se realiza la selección de la instrumentación mediante matrices de comparación y en otros casos se seleccionan en base a las marcas que manejan los formadores de azufre. Respecto a la simulación del proceso, se elige el lenguaje de programación adecuado a las necesidades del proceso, y a las características del software de programación cumpliendo con la norma IEC 1131-3. Se especifica la conexión de los distintos componentes al PLC, además se realizan los ajustes de los sensores (conductividad y nivel) en función al rango de entrada. Todo con el fin de conocer la relación existente entre los valores de entrada y salida de cada sensor, ya que el PLC interpreta la entrada de valores en esta unidad, para luego realizar el acondicionamiento de esta señal de entrada al rango de lectura del Software.

3. Resultados y discusión.-

3.1 Propiedades fisicoquímicas a controlar.- Se identificó que las propiedades a tratar en el agua del proceso de enfriamiento corresponden a la conductividad, el carbonato de calcio y minerales asociados al proceso, así como también los microrganismos, debido a que se evidenció la existencia de algas en las boquillas de aspersión y tendencia a la corrosión galvánica en algunos tramos de tubería por la acumulación de sedimentos en la misma, provenientes de la acumulación del carbonato de calcio, sílice, fosfatos, entre otros.
Para resolver la problemática, se decidió mantener bajo control el incremento de los minerales producidos por la recirculación y la evaporación en el proceso de la solidificación del azufre mediante la aplicación de purgas controladas. Respecto a los minerales que pudieran encontrase en el agua de reposición, se implementa un tratamiento por medio de la dosificación de un inhibidor de corrosión para la dispersión del carbonato de calcio y los demás minerales, de tal manera que se reducirá al máximo la acumulación de estos agentes en la tubería. Asimismo, para el control de seres vivos muy pequeños formados por una sola célula (microorganismos) que bloquean el flujo de agua, reducen la transferencia de calor y aumentan las tasas de corrosión, se decidió utilizar una agente biosida no oxidante, esto conllevaría a preservar el tanque de almacenamiento, faja metálica, tuberías, intercambiador de calor, entre otros.

3.2 Relación de la dosificación de químicos. - La relación de dosificación de los productos químicos que se requiere para la solución del problema antes descrito, se determinó según las características de cada producto; y adicionalmente se realizó la prueba de jarra [12] en laboratorio. El ensayo consistió en someter a prueba la acción de determinada concentración de químico sobre una solución para corroborar el buen funcionamiento de los productos químicos. Los resultados obtenidos fueron satisfactorios en cada caso pertinente, pudiéndose observar que el agua no alteraba su color y los minerales no formaron flóculos de mayor tamaño, esto debido a la acción de inhibidor de corrosión el cual le proporciona una carga eléctrica a los minerales para que éstos se rechacen entre sí, y así impedir que éstos se adhieran a las paredes de las tuberías.
Posteriormente a esto, se examinó los análisis de laboratorio, y se sugirió la dosificación de un inhibidor de corrosión de acción media para el valor referente a la dureza total, la dureza cálcica y la conductividad del agua del proceso. Los productos químicos seleccionados en base a los agentes presentes en el agua de enfriamiento fueron LIPESA 131 y Biocida, y para controlar los agentes biológicos se especificó un Biocida no oxidante, LIPESA 100, por la existencia de acero inoxidable en el sistema [13].

3.3 Propuesta de control para las aguas de enfriamiento de la unidad 32.- En la industria se acostumbra a mantener la conductividad en los procesos de enfriamiento mediante purgas controladas [14], lo que conlleva a una reposición de las aguas de enfriamiento. Esta agua fresca de reposición al poseer una conductividad menor a la del proceso influirá directamente en dichas aguas, disminuyendo la concentración del carbonato de calcio, y por ende sobre la conductividad, ya que esta es directamente proporcional a dichos minerales.
En el estudio se determinó mantener en las aguas de enfriamiento una conductividad menor a quinientos siemens (500 µS), como se muestra en la tabla I, ya que por encima de este valor se podrían presentar inconvenientes en el proceso, tales como: problemas de transferencias de calor en el intercambiador del sistema, aumentaría la tendencia a la corrosión en las tuberías y/o daría lugar para la formación de depósitos y/o el taponamiento de las tuberías por la alta concentración de minerales en las aguas de enfriamiento.

Tabla I. Clasificación de las aguas en función a su conductividad [15]

Conductividad y dureza del agua			
ppm	**µS/cm (Siemens)**	**ºF**	**Dureza**
0-70	0-140	0-7	muy blanda
70-150	140-300	7-15	blanda
150-250	300-500	15-25	ligeramente dura
250-320	500-640	25-32	moderadamente dura
320-420	640-840	32-42	dura
superior a 420	superior a 840	superior a 42	muy dura

Debido a que en el proceso de formación de azufre existe evaporación de las aguas de enfriamiento, se producirá un descenso del nivel en el tanque de almacenamiento, disminuyendo un centímetro y medio (1,5 cm) aproximadamente por hora de operación, según la lectura de los datos registrados por el medidor de nivel en dicho tanque. También se conoció que la conductividad en las aguas de enfriamiento en un día de operación promedio alcanza un incremento de sesenta y cinco (65) µS aproximadamente. Al respecto, se propone realizar las purgas en función al volumen evaporado en un día de operación para así realizar un encendido diario de las válvulas y bombas dosificadoras, lo cual se llevará a cabo de manera automatizada mediante la utilización de un control lógico programable (PLC).

3.3.1. Volumen evaporado (VEP). - En el estudio se dio a conocer que la altura de evaporación/h es de 1,5 cm, en un promedio de operación diaria de 11 h. El volumen de evaporación es de 0,093 m^3 en un área de 6,206 m^2 y para las once horas de operación se obtuvo un total de:

$$V_{ep} = 6{,}206m^2 * 0{,}015\frac{m}{h} = \frac{0{,}093m^3}{h} * \ 11h = 1{,}024\ m^3\ (1.024\ L)$$

3.3.2. Conductividad resultante. - Del mismo modo, se conoció que el sistema de transporte y almacenamiento de agua posee un diámetro y longitud de tubería de 4 pulgadas y 93 cm respectivamente, con volumen del tanque de 2.700 L y volumen de tubería de 3,454 m^3. Sabiendo que una vez implementado el sistema de control, la conductividad en

las aguas de enfriamiento no superará los $500\ \mu S$ (considerando que las características no varían) debido a la realización de las purgas controladas, la cual permitirá introducir siempre el mismo volumen de $1.024\ L$ de agua fresca al sistema, y conociendo que esta posee una conductividad promedio de $220\ \mu S$, se pudo calcular la conductividad resultante (C_f) en el proceso, siendo de $414\ \mu S$ lo que satisface las exigencias de mantener la conductividad de las aguas de enfriamiento por debajo de los $500\ \mu S$.

$$C_f = 500\mu S + \frac{996{,}1\ \frac{Kg}{m^3}\,1024\ L}{990{,}2\ \frac{Kg}{m^3}\,3.454\ L}(211 - 500)\mu S \approx 414\ \mu S$$

3.3.3. Evaporación en el tanque de almacenamiento. - La apertura y cierre de las válvulas, y el encendido de las bombas, dependerán del nivel existente en el tanque de almacenamiento. La altura que representa el volumen de evaporación y la altura referente al volumen de químicos dosificados en dicho tanque se conoció basado en el volumen evaporado de $1.024\ L$ y la ecuación de volumen evaporado, por lo que la altura del punto de ajuste (*set point*) quedo determinado por A_{sp}:

$$A_{sp} = \frac{V_{ep}}{Ancho * largo} = \frac{1{,}024\ m^3}{1{,}372\ \text{m} * 4{,}523\ \text{m}} = 165\ mm$$

3.3.4. Volumen de productos químicos a dosificar. - La relación de dosificación que dictan los dos (2) productos químicos seleccionados es de 6 L de producto por cada 1.000 L de agua de reposición, por lo que el volumen de cada uno de los dos químicos a dosificar por cada 1.024 L es de 6,144 L/Bomba. Dado a que la relación de dosificación será igual para el inhibidor de corrosión y el biocida, se estarán inyectando al tanque de almacenamiento un total de 12,288 L de productos químicos, y una altura de productos químicos en el tanque de 2 mm. De tal manera, que la altura menor del *set point*, quedó definida por la sustracción de la altura de evaporación y la altura de productos de químicos a la altura máxima de llenado en el tanque de almacenamiento. Este *set point* activará la apertura de la válvula que permitirá el cierre o paso de las aguas de reposición.

$$SP = 435\ mm - 165\ mm - 2\ mm = 268\ mm$$

Respecto a las bombas dosificadoras, estas serán encendidas y apagadas por un temporizador, el cual se programa según el tiempo en el cual este estará enviando la señal de encendido a las bombas dosificadoras. Este tiempo (td) depende del caudal de dosificación 0,0091 L/s y el volumen de dosificación por bomba de 6,144 L:

$$td = \frac{V}{Q} = \frac{6{,}144\ L}{0{,}0091\ L/s} = 675\ seg$$

3.4. Filosofía de operación de la unidad formadora de azufre. - En la figura III se muestra la disposición de los elementos y las diferentes alturas de control en el tanque de almacenamiento, y en la figura IV se muestra el diagrama de flujo que define el sistema de control. Para iniciar el proceso se suplirá en su totalidad el sistema de enfriamiento con agua fresca hasta una altura de cuatrocientos treinta y tres (433) mm en el tanque de almacenamiento, y posteriormente se le agregarán veinte (20) litros de biocida LIPESA 100 y veinte (20) litros de inhibidor LIPESA 131 y se activará el proceso de control automatizado [16].

Una vez que el proceso de enfriamiento esté en funcionamiento y comience a evaporarse el fluido refrigerante, se abrirá la válvula de entrada (Q2), cuando el nivel del tanque alcance los 268 mm, la válvula de entrada (Q2) estará abierta hasta que el nivel del tanque llegue a los 433 mm, Las bombas dosificadoras se encenderán cuando los temporizadores lo indiquen, los cuales enviarán la señal de encendido durante 675 s a dichas bombas. Los temporizadores se activarán cuando el nivel en el tanque haya alcanzado los 433 mm, si y soló si, la altura anterior en el tanque sea menor a dicha altura, y se apagarán cuando el temporizador lo indique. Cuando la conductividad de las aguas de enfriamiento sea mayor o igual a 500 µS, se abrirá la válvula de purga (Q1). Una vez drenado el volumen necesario para llegar a los 268 mm de altura, la válvula de purga se cerrará y entraran en accionamiento el control de nivel y dosificación de químicos descritos anteriormente.

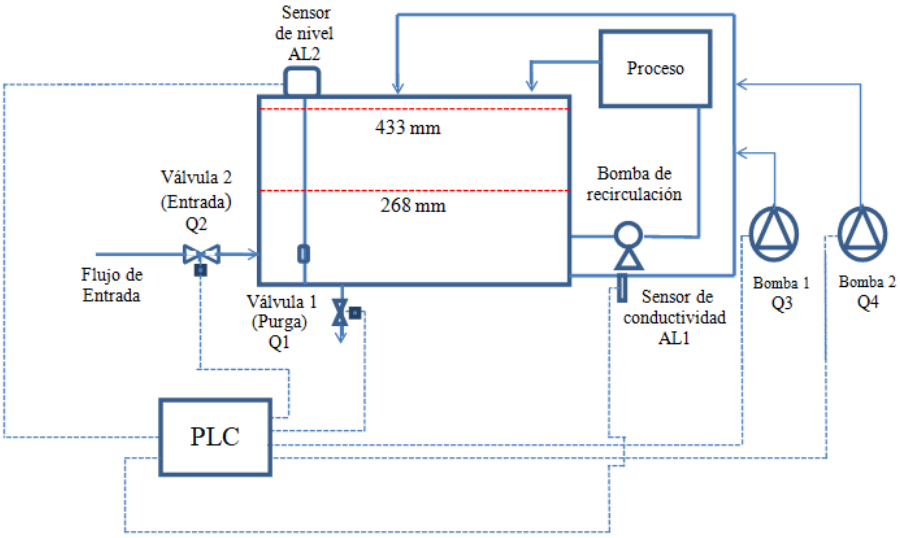

Figura III. Esquema de los elementos de control propuesto en el sistema de enfriamiento de la unidad formadora de azufre (unidad 32).

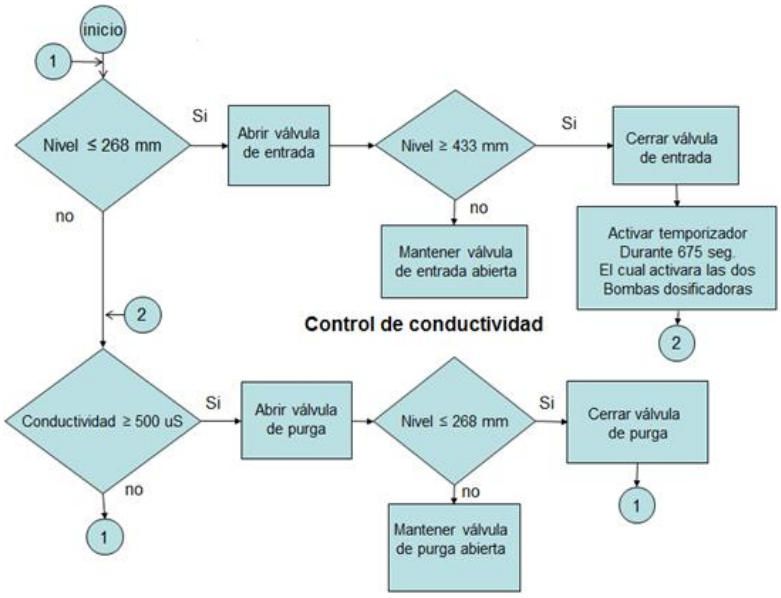

Figura IV. Diagrama de flujo para el control del agua de enfriamiento de la unidad 32, (control de nivel y dosificación de químicos).

3.5. Diseño hidráulico de tubería bypass. - Debido a que tanto las mediciones de variables como las modificaciones sólo se realizaran en la línea de tubería, fue necesario el diseño de un bypass [17] que se describe en la figura V con una longitud total de 9,50 m. El bypass se diseñó en función de un caudal no mayor del 5 % del caudal de recirculación, debido a que el sistema de enfriamiento fue diseñado para operar con un flujo no menor al 90 % del caudal de recirculación, quedando así un 5 % del caudal de recirculación para futuras modificaciones. Al respecto, el caudal de recirculación del sistema de enfriamiento cuenta con 39,1 m^3/h, de tal manera que el caudal del bypass se define por:

$$caudal\ de\ bypass < \frac{5\%}{100\%} * \frac{39{,}1 m^3}{h} = 0{,}5\ L/s$$

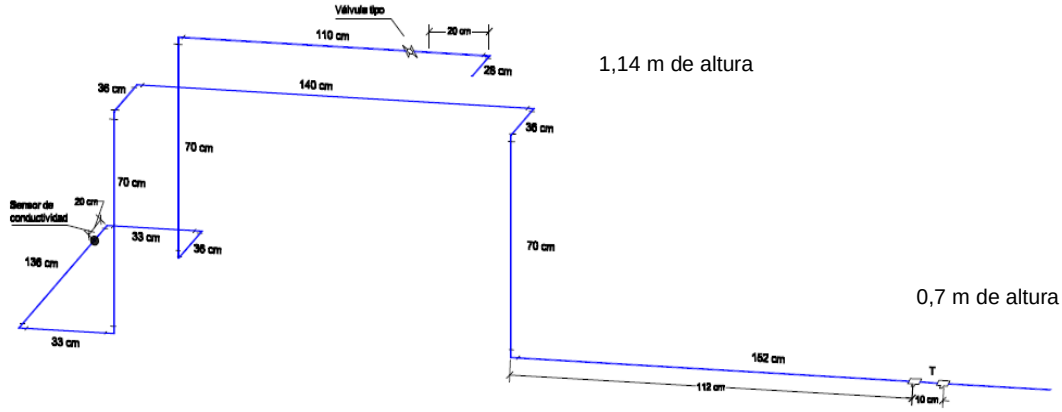

Figura V. Geometría del bypass.

Asimismo, para el dimensionamiento de la tubería basándose en ciertos criterios de velocidad y caída de presión, se utilizó la ecuación de caudal [16], y se determinó que el diámetro en función de la velocidad de erosión y a un caudal menor del especificado anteriormente, resultando $D \leq 0{,}027\ m\ (1\ plg)$. Se seleccionó un diámetro de 3/4 plg. con un diámetro interior de 18,9 mm, tomando en cuenta que se debe garantizar un caudal menor a $0{,}5\ L/s$.

3.6. Selección de componentes. - Fue necesario un sensor de conductividad GF modelo 3-2820-1 con transmisor GF Signet 8850-1 de visualización directa de lectura para instalación en panel [18]. Para la medición de nivel en el tanque de almacenamiento un sensor modelo NORMIX 190122111 con salida 4 – 20 mA, y dos (2) válvulas solenoides on/off del tipo normalmente cerradas. Una de las válvulas se coloca en la tubería que suministra agua al tanque de almacenamiento (válvula de entrada) y la segunda válvula para la realización de purgas (válvula de purga) montada en niple en la parte inferior del tanque de almacenamiento [19]. Las bombas dosificadoras que integran el sistema de control corresponden al tipo PROMINENT y línea Gamma/L por existir en los procesos del mejorador. Las bombas son de tipo electromecánica de membrana modelo GALa0232. Los PLC modelo SIMATIC S7-200 Siemens se ajustaron a las exigencias del proceso.

3.7. Programación del controlador y modelo de montaje. - La programación se basó en el PLC S7 SIEMENS con el software LOGO Soft Comfort, mediante el leguaje normalizado escalera. El modelo de montaje consistió en el PLC montado en campo, conectado a la sala de control de la unidad 32 por medio de la interfaz de comunicación Ethernet, para permitir la visualización del proceso control ejercido sobre las aguas de enfriamiento. La válvula de entrada, válvula de salida y bombas dosificadoras se alimentan desde el PLC por medio de los penetradores, los cuales son activados digitalmente mediante selenoides. El sensor de conductividad y sensor de nivel de tipo analógico fueron ajustados según las respuestas de los mismos, en función a su escala de medición y su rango de salida que es de 4-20 mA para ambos sensores. En las figuras VI y VII se muestra la disposición de los pines de la CPU 224 XP para la conexión de los elementos finales de control y los sensores, respectivamente.

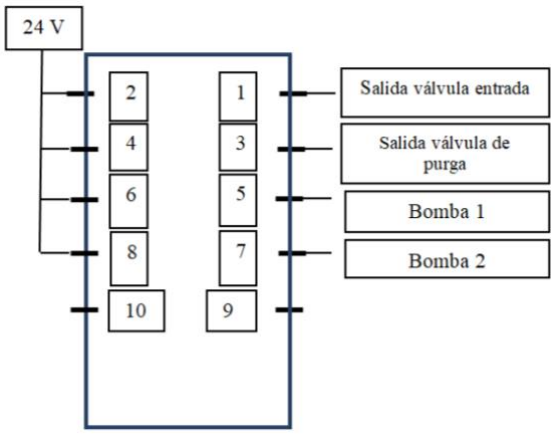

Figura VI. Esquema de conexión de los elementos finales de control en el pinado de la CPU 224 XP.

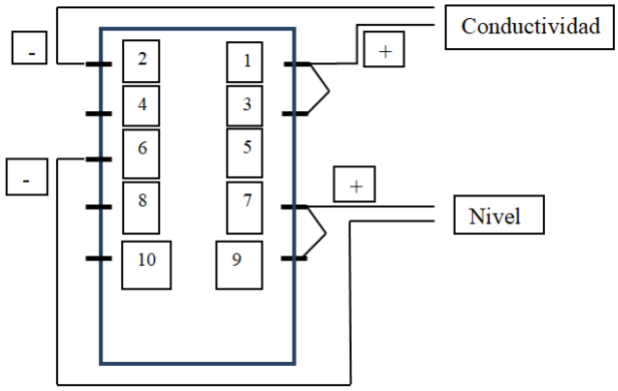

Figura VII. Esquema de conexión de los sensores en el pinado de la CPU 224 XP.

3.8. Simulación del diseño. - Para validar el funcionamiento del diseño, se tomaron ejemplos representativos de acciones de control en funcionamiento, comprobándose que las entradas y salidas se comportan de manera esperada según las perturbaciones [20]. En la figura VIII se muestra la pantalla de la simulación en condiciones de trabajo, pudiéndose observar en el cuadro de monitoreo una conductividad de 450 µS y un llenado total del tanque. También se le han ingresado valores de entrada de 450 µS al sensor de conductividad AI1 y 435 mm al sensor de nivel AI2, los cuales equivalen a 454 y 857,45 respectivamente, en la escala interna del PLC.

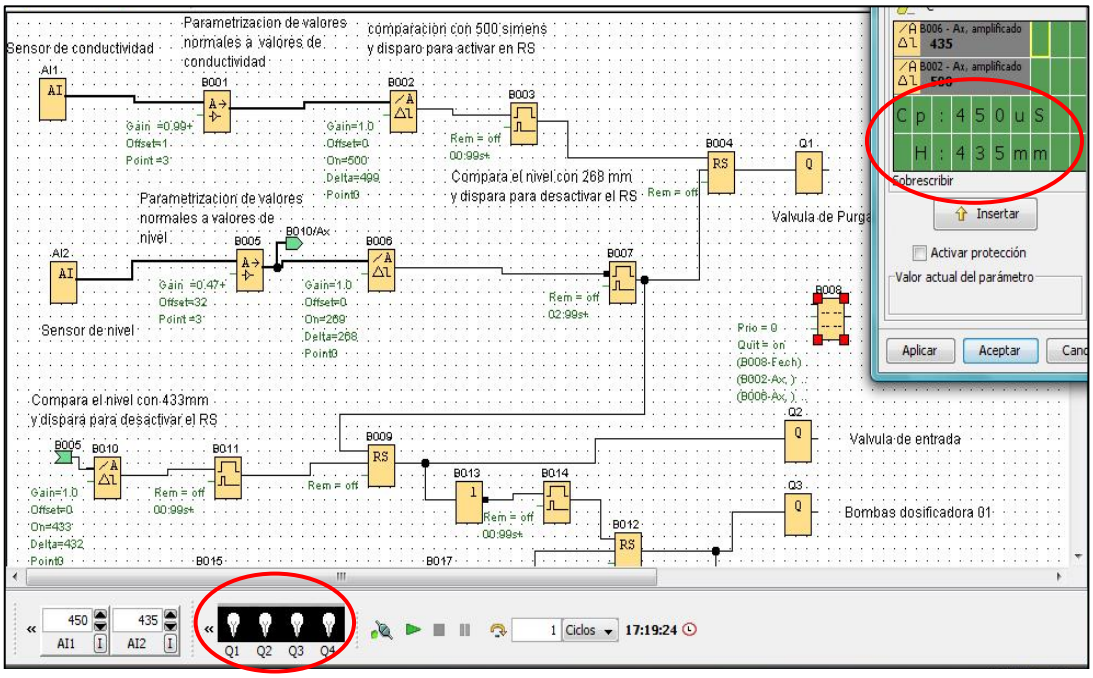

Figura VIII. Simulación del bloque de monitoreo.

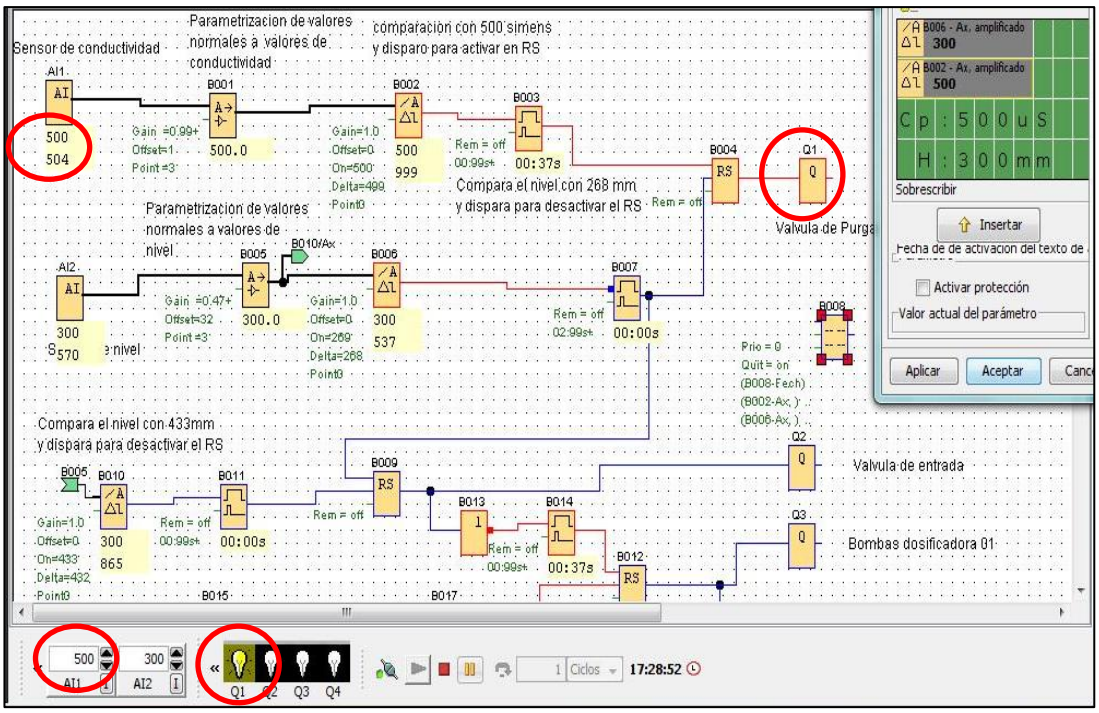

Figura IX. Simulación de la alarma de alta conductividad.

Como se explicó en la filosofía, el sistema de control del agua de enfriamiento del formador de azufre consta de dos procesos paralelos: el control de conductividad del agua del proceso y el control de nivel del tanque de almacenamiento. En esta parte de la simulación se muestra cómo actúa el sistema de control cuando la conductividad sale del rango deseado (menor a 500 µS) y alcanza los quinientos (500) µS equivalente a quinientos cuatro (504) en la escala interna del PLC, este valor de entrada arrojado por el medidor de conductividad (AI1) enciende la válvula de purga Q1, lo cual se puede apreciar en la figura IX. Luego que se da la apertura de la válvula de purga (Q1), el nivel en el tanque empieza a disminuir y cuando este haya alcanzado los doscientos sesenta y ocho (268) mm, lo cual equivale a quinientos dos con trece (502,13) en la escala interna del PLC, la alarma se encenderá; El PLC al leer dicho valor enviará un impulso a la válvula de entrada (Q2) para dar paso a la entrada del flujo de reposición, como se observa en la figura X.

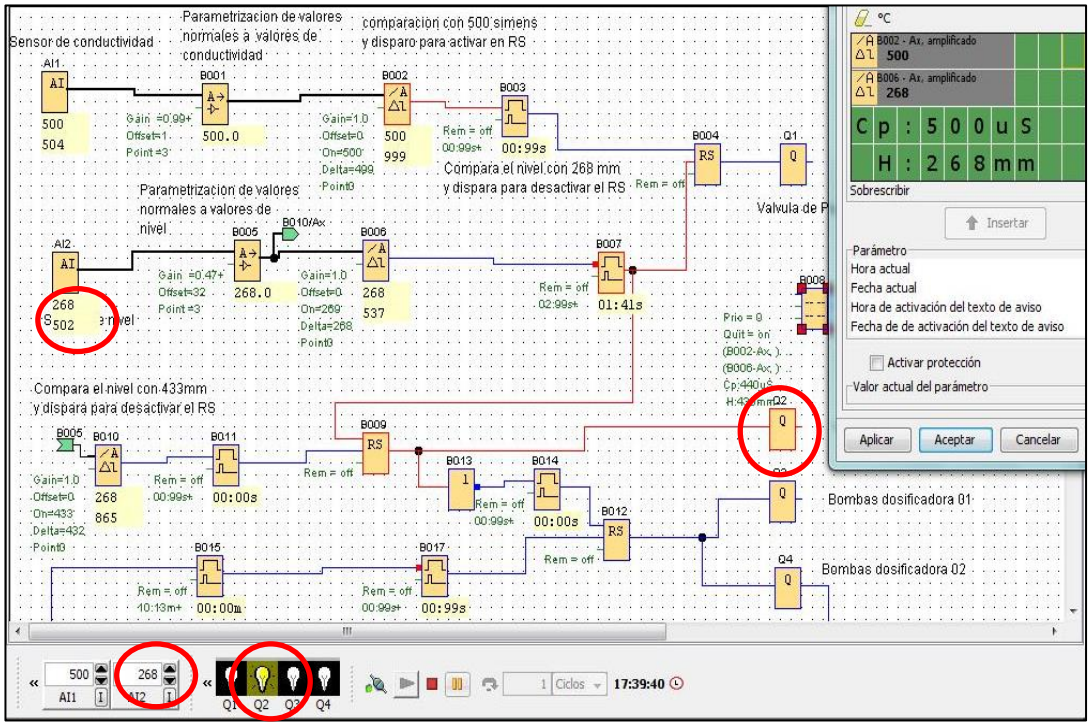

Figura X. Simulación de alerta del encendido de la válvula de entrada.

Con la apertura de la válvula de entrada (Q2) empieza el ascenso del nivel del tanque, al llegar a los cuatrocientos treinta y cinco (435) mm equivalente a ochocientos cincuenta y siete con cuarenta y cinco (857,45) de lectura interna del PLC, la misma será interpretada por el PLC para enviar una señal ordenando el cierre de la válvula de entrada (ver figura XI). La señal de cierre de la válvula de entrada servirá para el encendido de las dos (2) bombas dosificadoras, las cuales estarán encendidas durante diez minutos con catorce segundos (10 min.14 s) por medio de la utilización de un bloque funcional de relé de barrido.

El proceso de la activación de las alertas anteriormente descritas se activará cada vez que la conductividad de las aguas del proceso de enfriamiento alcance los quinientos (500) µS. Para el control del nivel en el tanque de almacenamiento, por motivo de la evaporación existente en el proceso, se cumplirán de manera análoga la activación de la alerta de encendido de la válvula de entrada y la alerta del encendido de las bombas dosificadoras.

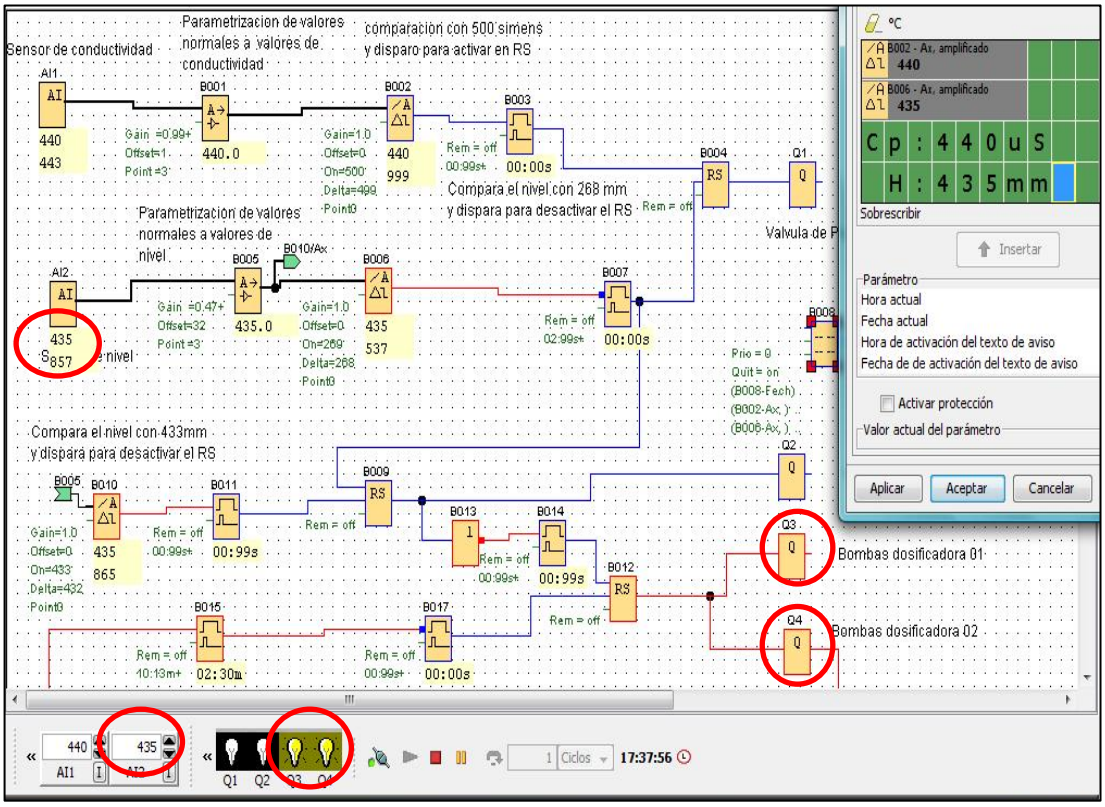

Figura XI. Simulación de alerta del encendido de las bombas dosificadoras.

3.9. Análisis de la simulación del proceso.- Luego de validar mediante simulación el correcto funcionamiento del sistema de control diseñado en esta investigación, se sugiere que su implementación repercutirá positivamente en los aspectos que fueron considerados en los objetivos planteados según se describen a continuación: Se mantendrá el control de los minerales que aparecen en el sistema de enfriamiento producto de la recirculación y evaporación del agua durante el proceso de solidificación del azufre. La aplicación del tratamiento al agua de recirculación a base de LIPESA 131, Biocida, y LIPESA 100 permitirá la dispersión del carbonato de calcio y otros minerales, reduciendo al máximo la acumulación de estos agentes en el sistema hidráulico. También se mantendrá controlada la aparición de pequeños seres vivos unicelular, microorganismos, que tienden normalmente a obstruir el flujo de agua en los aspersores de refrigeración. Asimismo, este control permitirá que la eficiencia del sistema de transferencia de calor se mantenga en niveles más altos, y la tasa de corrosión en todo el sistema permanezca en los niveles más bajos, alargando la vida útil del tanque de almacenamiento, tuberías, intercambiador de calor, entre otros.

4. Conclusiones. - Se diseñó un sistema de control para el tratamiento de aguas de enfriamiento de un formador de azufre que evitara el deterioro del mejorador de crudo, traduciéndose en menor impacto ambiental y económico causado por el agotamiento de los recursos, labores de mantenimiento, reemplazos de equipos y paradas del proceso. Con el estudio de la filosofía de operación se conocieron los complejos procesos que intervienen en él, desde la entrada del azufre en estado líquido hasta la solidificación de este por acción refrigerante. Se establecieron como propiedades a controlar en el tratamiento del agua de enfriamiento la conductividad, los minerales disueltos y los microorganismos, a partir de estudios de laboratorio. Se determinaron las adecuadas concentraciones de químicos que repercute en una mejor actuación de los productos sobre el agua de enfriamiento. Asimismo, se estableció el tiempo de encendido de

las bombas que dosifican dichos químicos.
Se seleccionó la instrumentación necesaria para censar las variables nivel y conductividad, y un controlador lógico programable con entradas y salidas integradas para mantener la acción de dos bombas dosificadoras electromecánicas y dos válvulas on/off. El sistema de control diseñado fue validado mediante simulación con el software computacional LOGO SOFT confort. Para esto se verificó el correcto funcionamiento de encendido y apagado de las bombas y válvulas, las cuales dependen de diferentes valores de *set point*, es decir, el encendido y apagado de las válvulas al igual que el encendido de las bombas dosificadoras se establecieron con un *set point* referente al nivel del tanque y el apagado de éstas en función a un *set point* que solo guarda relación con el volumen y el caudal de dosificación.

Referencias

[1] NALCO, (1990). Manual Técnico de Agua de Enfriamiento. Sección 1 y 3, Illinois: Naperville S.A. URL
[2] González – Rondón, Y. Rengel, J. & Martínez, J. (2021). Simulación termofluidodinámica en un molde de colada continua de acero. Revista Memoria Investigaciones en Ingeniería. No. 21. https://doi.org/10.36561/ING.21.4
[3] Guan, C., Yicheng, Y., Nan, Y., Nanyan, H., Jie, Z., Yang, H. (2021). A critical review of prevention, treatment, reuse, and resource recovery from acid mine drainage, Journal of Cleaner Production, Volume 329.
[4] Jun, L., Salma, T. (2022). Synergism of hydrolytic acidification and sulfate reducing bacteria for acid production and desulfurization in the anaerobic baffled reactor: High sulfate sewage wastewater treatment, Chemical Engineering Journal, Volume 444.
[5] Macías, M., Padilla, H., Jordy, L. (2021). Evaluación del tiempo de retención hidráulico de la planta de tratamiento de aguas residuales en base a lodos activados como posible causante de la contaminación odorífera en la ciudadela Puerto Seymour. Guayaquil. ULVR. Facultad de Ingeniería, Industria y Construcción Carrera de Ingeniería Civil. 109 p.
[6] Colomo, A. (2001). Instructivo de la unidad Formadora de Azufre "Trenes Solidificadores".Operadora Petroanzoategui C.A.
[7] Yanhui, L., Shaoming, D., Zhouyang, B., Shuzhong, W., Fan, Z., Jie, Z., Donghai, X., Jianqiao, Y. (2022). Corrosion characteristics and mechanisms of typical iron/nickel-based alloys in reductive supercritical water environments containing sulfides, The Journal of Supercritical Fluids, Volume 187.
[8] Zhao, Z., Chunhui, Z., Yang, Y., Zhuowei, Z., Yuanhui, T., Peidong, S., Zhiwei, L. (2022). A review of sulfate-reducing bacteria: Metabolism, influencing factors and application in wastewater treatment, Journal of Cleaner Production, Volume 376.
[9] Hong-Cheng, W., Ying, L., Yu-Meng, Y., Ying-Ke, F., Shuang, L. Hao-Vi, C. Ai-Jie, W. (2022). Element sulfur-based autotrophic denitrification constructed wetland as an efficient approach for nitrogen removal from low C/N wastewater, Water Research, Volume 226.
[10] Nallakukkala, S., Rehman, A., Zaini, D.B., Lal, B. (2022). Gas Hydrate-Based Heavy Metal Ion Removal from Industrial Wastewater: A Review. Water, 14, 1171. https://doi.org/10.3390/w14071171.
[11] Elis, W., Nogueira, L., Augusto, G., Lauren, N., Márcia, R. (2021). Sulfate and metal removal from acid mine drainage using sugarcane vinasse as electron donor: Performance and microbial community of the down-flow structured-bed bioreactor, Bioresource Technology, Volume 330.
[12] Suárez, V. y Trujillo, D. (2011). Diseño y Construcción de un Equipo de Prueba de Jarras para la Tratabilidad de Aguas Residuales. Escuela Superior Politécnica de Chimborazo. Riobamba.
[13] LIPESA, (2003). Manual Técnico de Sistemas de Enfriamiento. Sección 3 y 5. Barcelona. URL
[14] Rigola, M. (2001). Tratamiento de aguas industriales: aguas de procesos y residuales. Barcelona, España: Alfaomega Marcombo S.A.
[15] INFOAGRO (2009). Informe de conductividad. URL
[16] González – Rondón, Y. (2022). Automatización del sistema de medición de parámetros en un compresor centrífugo de pruebas experimental ARMFIELD FM 12. Revista Servolab Science. Volumen 1, No. 2. URL
[17] American National Standards Institute. Committee B31, Code for Pressure Piping. (2002). Pipeline Transportation Systems for Liquid Hydrocarbons and Other Liquids: ASME Code for Pressure Piping, B31. American Society of Mechanical Engineers. URL
[18] Creus, A. (2005). Instrumentación Industrial. Barcelona, España: Alfaomega Marcombo S.A.
[19] Mora, K. B. (2013). Conceptualización del sistema de separación y transporte de los fluidos producidos en la zona sur del campo el salto. Universidad de Oriente. Tesis de Grado. URL
[20] Lugo, J. G. C., Ybarra, J. J. P., y Romero, E. (2005). Metodología para realizar una automatización utilizando PLC. Impulso, 18. URL

Nota contribución de los autores:

1. Concepción y diseño del estudio
2. Adquisición de datos
3. Análisis de datos
4. Discusión de los resultados
5. Redacción del manuscrito
6. Aprobación de la versión final del manuscrito

UC ha contribuido en: 1, 2, 3, 4, 5 y 6.

YGR ha contribuido en: 1, 2, 3, 4, 5 y 6.

Nota de aceptación: Este artículo fue aprobado por los editores de la revista Dr. Rafael Sotelo y Mag. Ing. Fernando A. Hernández Gobertti.

Use of Phase Change Material to enhance the Effectiveness of the Photovoltaic Module

Uso de Material de Cambio de Fase para potenciar la Efectividad del Módulo Fotovoltaico

Uso de Material de Mudança de Fase para aumentar a Eficácia do Módulo Fotovoltaico

Muhammad Farhan[1], Asad Akhter Naqvi[2], Muhammad Uzair[3(*)]

Recibido: 26/11/2023 Aceptado: 29/03/2024

Summary. - The usefulness and productivity of photovoltaic (PV) panels are significantly impacted by ambient and operating temperatures. However, the negative influence of hot climates on PV panel performance can be mitigated through innovative cooling techniques. This research work aims to investigate the implementation of phase change material (PCM) on the backside of solar modules to reduce panel temperature and enhance energy production. A hybrid system utilizing soy wax for cooling is applied to the rear of the panel. Comparative data have been collected on various days, and the outcomes have been analyzed. The outcomes reveal that the usage of phase change material reduced panel temperature by up to 18°C, causing a 10.89% rise in electricity generation compared to panels without cooling systems.

Keywords: Photovoltaics; Solar irradiance; Cell temperature; Phase change material; Solar Energy.

(*) Corresponding Author

[1] Senior Undergrad Student, Department of Mechanical Engineering, NED University of Engineering and Technology (Pakistan), 3820232027@bit.edu.cn, ORCID iD: https://orcid.org/0009-0004-6984-5287

[2] Assistant Professor, Department of Mechanical Engineering, NED University of Engineering and Technology (Pakistan), asadakhter@cloud.neduet.edu.pk, ORCID iD: https://orcid.org/0000-0001-6290-3115

[3] Associate Professor, Department of Mechanical Engineering, NED University of Engineering and Technology (Pakistan), uzair@neduet.edu.pk, ORCID iD: https://orcid.org/0000-0002-2033-6244

Memoria Investigaciones en Ingeniería, núm. 26 (2024). pp. 85-97
https://doi.org/10.36561/ING.26.6
ISSN 2301-1092 • ISSN (en línea) 2301-1106 – Universidad de Montevideo, Uruguay

Resumen. - *La utilidad y productividad de los paneles fotovoltaicos (PV) se ven significativamente afectadas por las temperaturas ambiente y de funcionamiento. Sin embargo, la influencia negativa de los climas cálidos en el rendimiento de los paneles fotovoltaicos se puede mitigar mediante técnicas de refrigeración innovadoras. Este trabajo de investigación tiene como objetivo investigar la implementación de material de cambio de fase (PCM) en la parte posterior de módulos solares para reducir la temperatura del panel y mejorar la producción de energía. En la parte posterior del panel se aplica un sistema híbrido que utiliza cera de soja para enfriar. Se han recopilado datos comparativos en varios días y se han analizado los resultados. Los resultados revelan que el uso de material de cambio de fase redujo la temperatura del panel hasta 18°C, provocando un aumento del 10,89% en la generación de electricidad en comparación con los paneles sin sistemas de refrigeración.*

Palabras clave: *Fotovoltaica; Radiacion solar; Temperatura celular; Material de cambio de fase; Energía solar.*

Resumo. ***-*** *A utilidade e a produtividade dos painéis fotovoltaicos (PV) são significativamente afetadas pelas temperaturas ambiente e de operação. No entanto, a influência negativa dos climas quentes no desempenho dos painéis fotovoltaicos pode ser mitigada através de técnicas inovadoras de arrefecimento. Este trabalho de pesquisa tem como objetivo investigar a implementação de material de mudança de fase (PCM) na parte traseira de módulos solares para reduzir a temperatura do painel e aumentar a produção de energia. Um sistema híbrido que utiliza cera de soja para resfriamento é aplicado na parte traseira do painel. Dados comparativos foram coletados em vários dias e os resultados foram analisados. Os resultados revelam que o uso de material de mudança de fase reduziu a temperatura do painel em até 18°C, causando um aumento de 10,89% na geração de eletricidade em comparação com painéis sem sistemas de refrigeração.*

Palavras-chave: *Fotovoltaica; Irradiância solar; Temperatura celular; Material de mudança de fase; Energia solar.*

1. Introduction . - The depletion of natural resources, especially fossil fuels, has become a significant worry for both developed and developing nations. Due to this, researchers are now trying to harvest energy through renewable energy sources with maximum efficiency [1]. Considering all renewable sources, solar energy has garnered the greatest attention [2]–[4]. Solar energy, an infinite and sustainable renewable resource, offers the potential for generating both thermal energy through a solar thermal (ST) system and electrical energy through a photovoltaic (PV) system [5]. Photovoltaic (PV) technology is experiencing rapid progress among all renewable energy sources due to its simplicity and cost-effectiveness in operation [6]. PV cells, unfortunately, can only transform 15 to 20 percent of solar irradiation into power [7]. The unutilized energy is dissipated as heat, leading to a surge in cell temperature. The performance of the photovoltaic module is notably influenced by its operating temperature [8]. The tendency of PV cells to transform solar radiation into electrical energy decreases as the working temperature upsurges, which has a direct relation with the ambient temperature. Consequently, the efficiency of the PV cell experiences a substantial reduction on hotter days [9]. The electrical efficiency of a PV cell decreases by almost 0.5% for every single 1°C rise in temperature [10].

By integrating a heat recovery system at the backside of the panel, the electrical efficiency can be better. This transformation turns the conventional PV system into a hybrid Photovoltaic/Thermal (PVT) scheme, capable of simultaneously generating electricity as well as heat from a solo integrated system. Various researchers have explored different cooling methods for PV panels, involving the use of diverse working fluids such as air, water, and PCM. Uzair et al. [11]–[13] researched optimizing PV panels and performed numerical simulations to analyze the ideal tilt angles for enhanced performance. Kim et al. [14] researched improving the overall efficiency of PV units by implementing air cooling. Their findings indicated that, on average, the system attained a thermal efficiency of approximately 20% and an electrical efficiency of 15%. Diwania et al. [15] performed a experiments to boost the overall efficiency of PV modules using a V-type air channel. Their research was specifically carried out for the climate conditions of Ghaziabad, India. The findings revealed that the hybrid system was capable of converting approximately 10.3% of sunlight into electricity and 41.5% into heat, resulting in an overall system efficiency of around 52%. In our previous study [7], we achieved an enhancement in the efficiency of PV modules by transforming them into hybrid PVT modules. This was achieved by integrating a wooden air duct at the backside of the module. As a result of this implementation, the electrical efficiency was measured at 14.8%, while the thermal efficiency reached an impressive 65.6%.

Indeed, water can be a more effective option for heat removal than air due to its higher thermal conductivity. Water's ability to conduct heat more efficiently allows for improved cooling of PV modules, making it a favourable choice for certain cooling systems. According to Aste et al. [16], who utilized a specially designed PVT water collector, water-cooled PV systems displayed more electrical efficiency when performance was compared with air-cooled PV systems. Sardouei et al. [17] explored the effects of water flow rate on the production of PVT systems. They experimented with flow rates varies in the range of 30 L/h and 90 L/h and found that a water flow rate of 90 L/h led to a remarkable thermal efficiency of 56%. Yazdanpanahi et al. [18] conducted a comprehensive investigation into the energy efficiency of water-cooled PV systems using both experimental and computational approaches. Their research demonstrated a strong agreement among the computational and investigational results. Furthermore, they found that a flow velocity of 2 g/s resulted in a extreme electrical efficiency of 14 percent.

In recent times, PV cooling by Phase Change Material (PCM) has garnered significant attention [19]–[22] due to its distinct advantages over air- and water-cooling methods. Indeed, Phase Change Material (PCM) can absorb more heat compared to air and water, leading to a greater reduction in cell temperature. This characteristic makes PCM-based cooling an attractive option for enhancing the efficiency and performance of PVs. In both air- and water-cooled PV systems, the need for pumping devices to maintain a continuous flow of fluid results in energy consumption. According to Najjar et al. [23], the utilization of metal foam as a PCM can effectively reduce the cell temperature by approximately 12°C. To boost the productivity of PV systems, Hasan et al. [24] conducted a study that involved investigating five different PCMs, namely capric-lauric acid (C-L), capric-palmitic acid (C-P), paraffin wax (RT20), commercial mix (SP22) and a pure salt hydrate (CaCl2.6H2O). Their discoveries revealed that the utilization of PCM successfully dropped the temperature of PVs by an impressive 18°C. According to Indartono et al. [25], petroleum jelly can be effectively employed as a Phase Change Material (PCM) for the heat management of PVs. When applied to the rare surface of the PV plate, petroleum jelly effectively absorbs thermal energy from the plate. The study found that petroleum jelly was particularly effective in reducing cell temperature, resulting in an impressive increase in electrical efficiency of approximately 7.3%. In a comparative study conducted by Stropnik and Stritih [26], they examined a standard PV module and a customized PV module integrated with an RT28HC PCM. The results exposed that the cell temperature in the simple PV plate was approximately 36°C more when compared with the plate having PCM cooling.

Additionally, they found that the PCM-cooled PV system generated power at a rate that was 7.3% higher than the simple PV module. This suggests that the incorporation of PCM cooling can meaningfully enhance the efficiency and presentation of PV systems. In an attempt to progress the overall efficiency of PV systems, Xu et al. [27] utilized fatty

acids as PCM. The study revealed that this approach led to a remarkable increase in electrical efficiency by 22.2%. The use of fatty acids as PCM proved to be a promising method for enhancing the performance of PV modules and optimizing their energy output.

Indeed, the explanations provided earlier highlight the standing of cooling PV units to improve the overall effectiveness of the system. While air and water can also be used for cooling, PCM stands out as the most efficient approach to increase electrical efficiency and lower cell temperature. The usage of PCM as a cooling method had demonstrated significant advantages, making it a preferred choice for enhancing the performance and efficiency of PV systems. In this study, soya wax is being utilized as a Phase Change Material (PCM) for the first time to enhance the electrical efficiency of PV panels. Since soya wax is derived from natural materials and extracted from soybeans, its use poses no risk to the environment. The investigation involves two panels: one is cooled by incorporating soy wax on the back side of the plate, while the other remains unmodified. The cell temperature and electrical efficiency of both panels are measured on different days to analyze and compare the effects of using soya wax as PCM. This research aims to assess the potential of soya wax as an efficient and eco-friendly cooling method to advance the performance of PV systems.

2. Methodology. - For the investigation, two monocrystalline PV modules, each rated at 30 Watts, were sourced from the local electrical market in Karachi. The modules' specifications are detailed in Table 1.

Maximum Rated Power (P_{max})	30 W
Output Tolerance	±3.0 %
Current at Maximum Power (I_{mp})	1.93 Amps
Voltage at Maximum Power (V_{mp})	17.5 Volts
Short Circuit Current (I_{sc})	1.93 Amps
Open Circuit Voltage (V_{oc})	21.07 Volts
Nominal Operating Cell Temperature (NOCT)	47º C

Table I. Specifications of PV module used.

To improve their electrical efficiency, Soya Wax, with a melting point of approximately 45°C, was utilized as the Phase Change Material (PCM) at the rear side of the solar plate. For this setup, 4 kg of Soya Wax had been used as PCM. To support and hold the Soya Wax in place, an aluminum sheet was utilized. Approximately 10% of the space was left unfilled to accommodate thermal expansion during the phase change process. Figure 1 illustrates the actual experimental setup, while Figure 2 showcases the backside of the panel equipped with PCM.

Both panels were positioned at a tilt of approximately 25°, which is roughly equivalent to the latitude of city Karachi. This angle is chosen to capture the maximum possible solar radiation efficiently.

Experiments were conducted on 10 different days throughout the calendar year. These experiments aim to gather data and observe the performance of the PV panels equipped with Soya Wax as PCM under varying weather and solar radiation conditions throughout the year in Karachi. During the experiments, the instantaneous solar radiations were measured using a Pyranometer, which provided real-time data on the solar energy received by the PV plates. Simultaneously, the instantaneous cell temperature of both panels was monitored to judge the impression of Soya Wax as PCM on temperature reduction. To understand the electrical performance, the power output from both PV modules was determined by employing a variable load. Figure 3 displays the solar radiation data collected on the experimental days.

Figure I. Two panels, the right one is equipped with PCM while the left is without PCM.

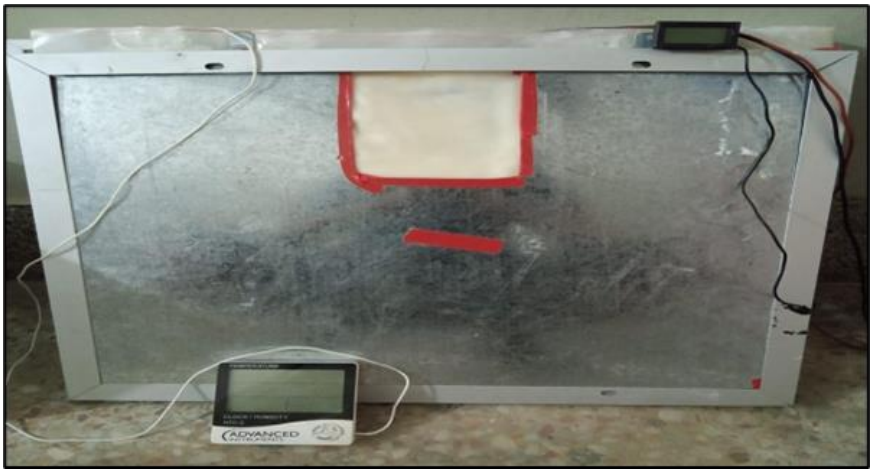

Figure II. Back side of the PV plate is equipped with an Aluminum sheet.

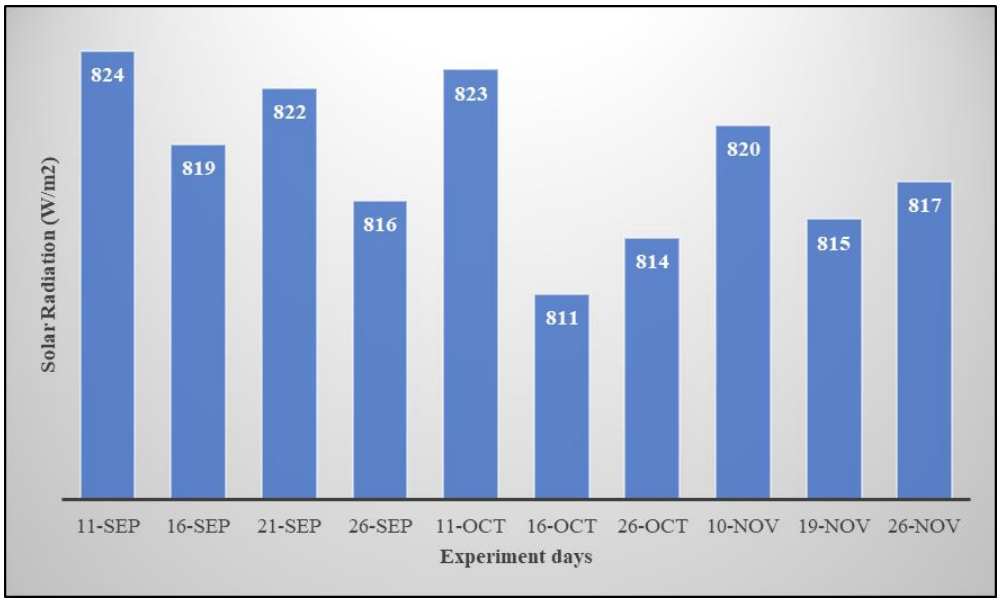

Figure III. Solar irradiance on different days

The cell temperature of the PV plate was calculated by using the following relation

$$T_{cell} = T_{amb} + \left(\frac{NOCT-20}{0.8}\right) \quad \text{Equation 1}$$

Where T_{cell} is the cell temperature, T_{amb} is the ambient temperature and NOCT is the Nominal Operating Cell Temperature, which is given in Table 1.

The temperature-adjusted power from the PV module was calculated by

$$P_T = P_R(1 - C_T(T_{cell} - 25)) \quad \text{Equation 2}$$

Here, P_T is the temperature-adjusted power, P_R is the rated power given in Table 1 and C_T is the temperature coefficient taken to be 0.5%/ºC [28]

The actual power drawn from both panels had been determined by

$$P = I \times V \quad \text{Equation 3}$$

Here, P is the actual power produced by the panel, I is the current from PV while V is the voltage produced by the PV plate

The efficiency of the PVs had been determined by

$$\eta = \frac{P\ electrical}{P\ irradiance} = \frac{I \times V}{E \times A} \times 100\% \quad \text{Equation 4}$$

Here, E is the solar radiation incident on the panel, which is given in Figure 3 while, A is the area of the collector.

3. Result and Analysis. - During the experiments conducted on 10 different days throughout the calendar year, both PV panels were placed side by side at a tilt of approximately 25°, which corresponds to the latitude of Karachi. This angle was chosen to maximize solar energy incident on the PV plates. The temperature of both panels was measured using an infrared thermometer and compared, as shown in Figure 4. The outcomes indicate that the PV plates' temperature is highly dependent on the surrounding temperature. Theoretical temperature calculations of the PV plate were performed using Equation 1. Figure 4 clearly illustrates that the PV panel equipped with Soya Wax as PCM exhibits lower temperatures compared to the plate without PCM cooling. This temperature difference arises from the efficient heat transfer among the PV plate and the PCM. When the PV module's temperature increases, the high-temperature difference facilitates the transfer of heat to the PCM, causing a cut in the PV panel's temperature while rising the PCM temperature. On the other hand, the PV panel without PCM lacks a heat sink mechanism, resulting in significantly higher temperatures compared to the PV panel with PCM cooling. On average, the temperature of the PV panel with PCM is approximately 22°C lower than that of the panel without PCM, as depicted in Figure 5. These findings emphasize the significant cooling effect of Soya Wax as PCM.

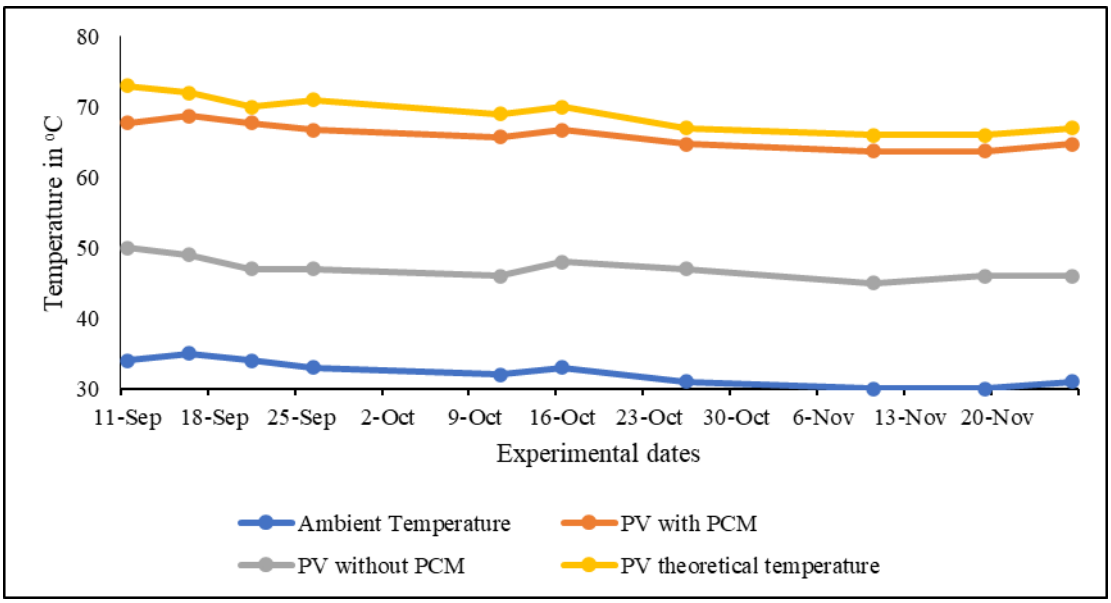

Figure IV. Temperature distribution of panels on experimental days

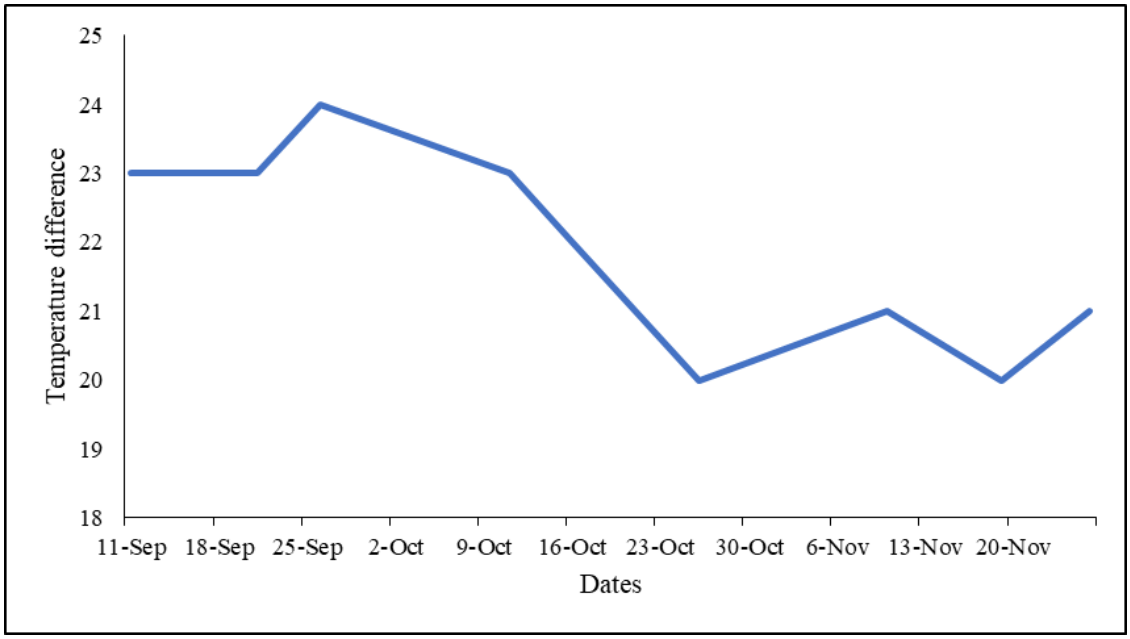

Figure V. The temperature difference between panels

In addition to measuring the actual cell temperature, the theoretical power generated by the PV plates was also computed using equation 2, considering both the theoretical cell temperature and the actual cell temperature. The results of this calculation are presented in Figure 6. From where it is evident that the PV panel equipped with Soya Wax as PCM extracts the maximum power. On average, the PV panel with PCM can generate approximately 14% more power compared to the panel without PCM. This notable difference in power generation is attributed to the cooling effect provided by Soya Wax as PCM. While both the panels are subjected to the identical ambient conditions, the PV plate equipped with PCM has the advantage of continuously transferring heat to the PCM, leading to a reduction in its temperature. Consequently, this cooling effect results in higher power production as compared to that of plate without PCM. On the other hand, the panel without PCM is producing less power than the temperature-adjusted power of the PV module. This discrepancy occurs because the genuine temperature of the PV plate without PCM is more than the theoretic temperature, as observed in Figure 4. Overall, the results from Figure 6 underscore the significant impact of Soya Wax cooling on the electrical performance of the PV panels, showcasing its ability to enhance power production and increase the total effectiveness of the PV system.

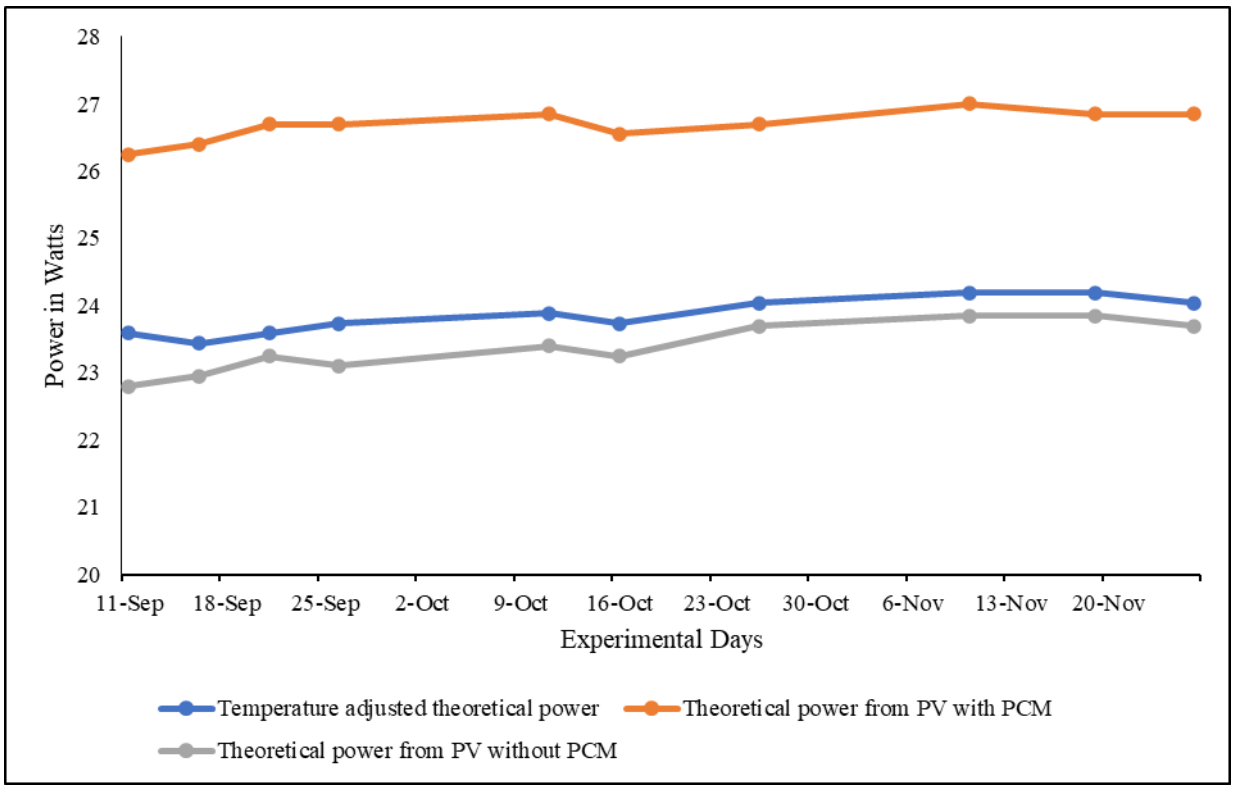

Figure VI. Theoretical power from panels

Using equation 3, the electric power generated by both panels was calculated based on the measured voltage and current at experimental dates, obtained using a Multimeter. Figure 7 illustrates the outcomes, clearly displaying that the PV plate equipped with Soya Wax as PCM produces more power compared to the plate without PCM. On average, the PV plate with PCM generates approximately 9.7% more power than the panel without PCM. This notable increase in power output is directly attributed to the cooling effect provided by Soya Wax as PCM. The cooling mechanism enabled by the PCM significantly decreases the operating temperature of the PV plate, leading to upgraded electrical efficiency and enhanced power generation.

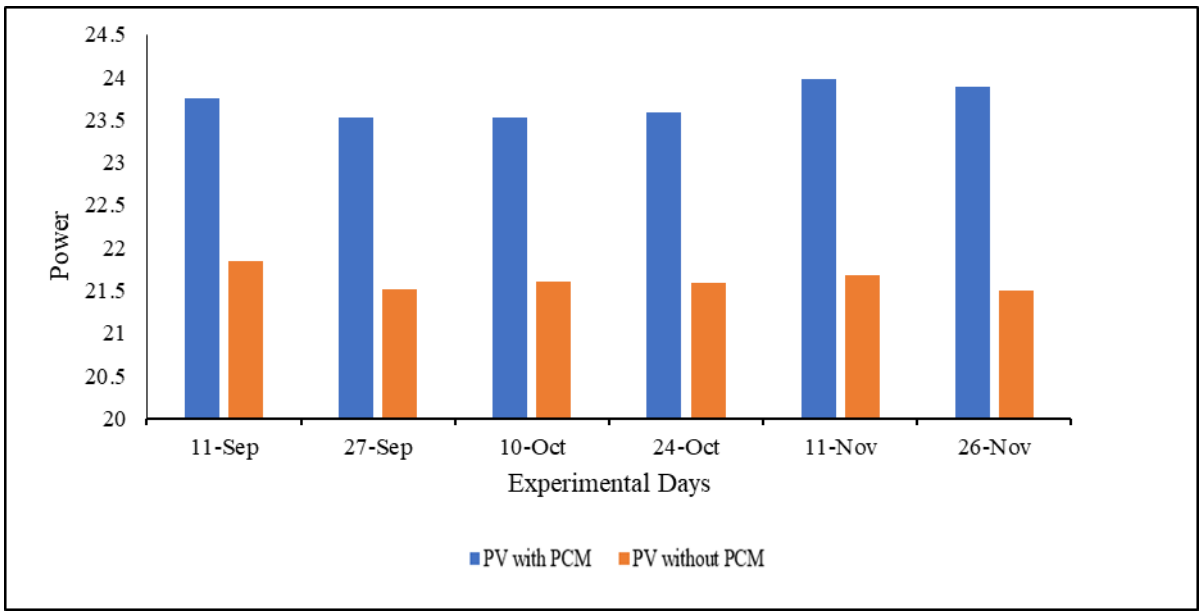

Figure VII. Power from PV panels

Figure 8 illustrates the relationship between current and voltage for both PV panels. The IV curve shows the power obtained from the PV-PCM system and the PV system without PCM. The extreme power gotten from the PV-PCM system is 21.51 W, whereas the PV system without PCM produces 19.4 W. This indicates a clear surge in the electrical

power of the PV module when Soya Wax is used as PCM for cooling. At the points corresponding to the maximum power, the PV-PCM system has a current of 1.23 A and a voltage of 17.49 V, while the PV system without PCM has a current of 1.18 A and a voltage of 16.44 V. The results further confirm the effectiveness of Soya Wax as PCM in enhancing the electrical effectiveness and power production of the PV plate. The cooling provided by the PCM enables the PV-PCM plate to operate at higher power levels compared to the plate without PCM cooling, leading to an overall improvement in the performance and effectiveness of the PV plate.

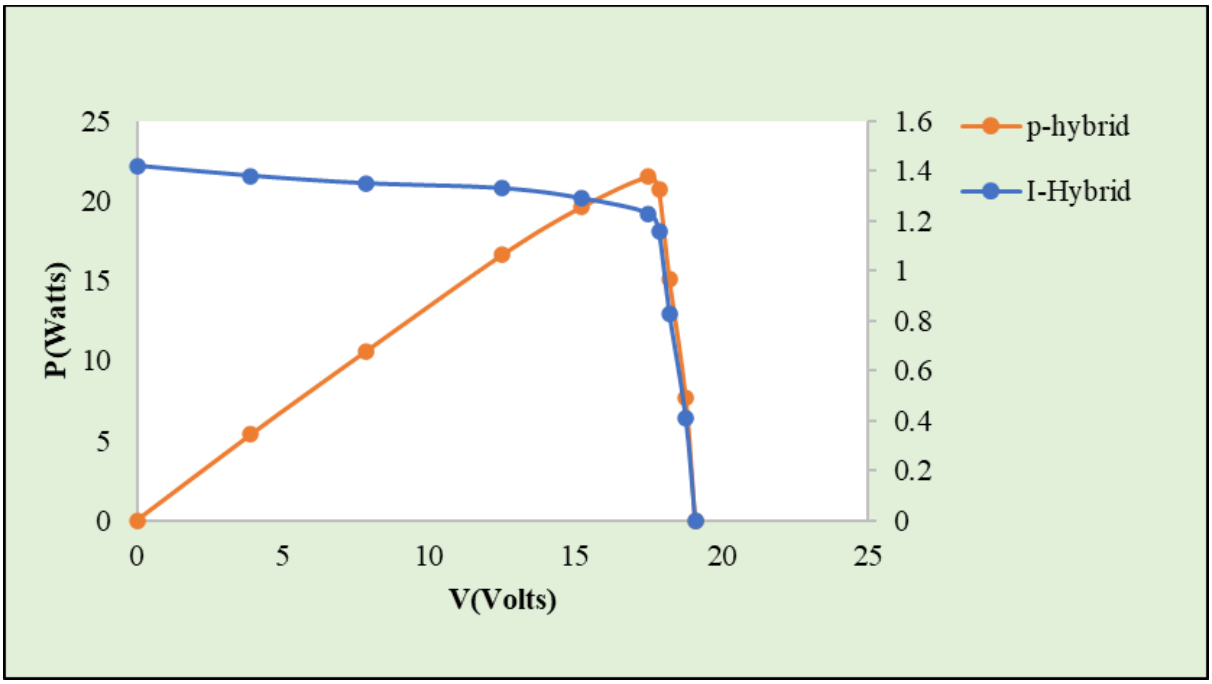

Figure VIII. (a) IV curve of PV-PCM with Voltage, current, and power profile

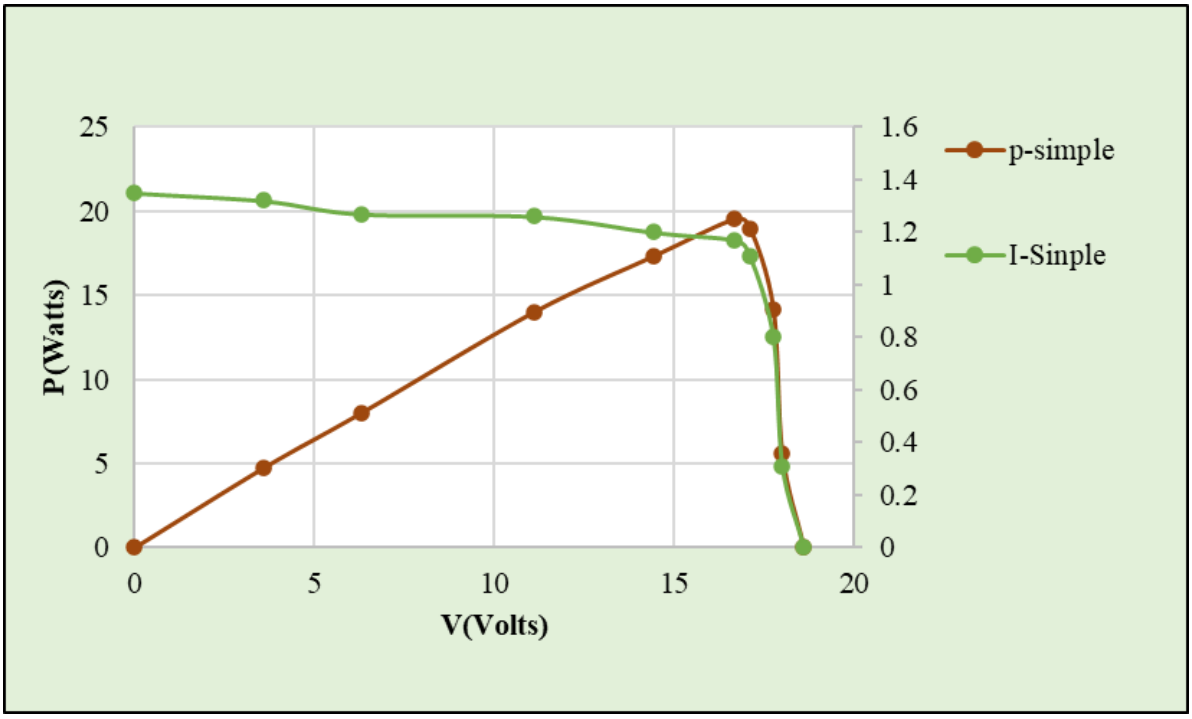

Figure VIII. (b) IV curve of PV-Simple with Voltage, current, and power profile

4. Conclusion. - This study aimed to explore the effectiveness of using PCM as a coolant to adjust the cell temperature of PV modules. Two different configurations of PV panels were considered for the experiments. One panel was kept simple, while the second configuration integrated PCM to provide cooling. The PCM used in the experiment was Soya wax. As the solar panels absorbed heat, the soya wax began to melt, transitioning from a solid to a liquid state. This

heat absorption significantly improved the electric power production capability of solar panels. The results revealed a remarkable 31.25% reduction in solar cell temperature, from 64°C in the panel without PCM to 44°C in the panel with PCM cooling. This drop in cell temperature resulted in the maximum electric power outputs of 21.5 W and 19.4 W for the PV-Hybrid and PV-simple configurations, respectively. Data was collected for different ten days, and it was observed that PV with PCM constantly produced more electrical power when compared with the simple PV plate. The integration of PCM to absorb thermal energy from the solar plate backplane effectively lowered the panel's surface temperature, leading to an increase in electric power output. This technical evaluation of the hybrid PVT system demonstrated that employing PCM at the panel's backside is a promising approach to boost power outputs while also lowering the cell temperature. Overall, the study highlights the significant impact of soya wax in enhancing the effectiveness and power generation of PV modules, presenting a viable and theoretically possible solution to progress the performance of PV plates.

References

[1] M. A. Sheikh, “Renewable energy resource potential in Pakistan,” *Renew. Sustain. Energy Rev.*, vol. 13, no. 9, pp. 2696–2702, 2009, doi: 10.1016/j.rser.2009.06.029.

[2] A. A. Naqvi, A. Ahmed, T. Bin Nadeem, L. A. Khan, and I. U. Ahad, “Energy and stress analysis of a hybrid photovoltaic thermal module,” *Case Stud. Therm. Eng.*, vol. 47, no. January, p. 103114, 2023, doi: 10.1016/j.csite.2023.103114.

[3] A. A. Naqvi, T. Bin Nadeem, A. Ahmed, M. Uzair, and S. A. A. Zaidi, “Techno-economic design of a grid-tied Photovoltaic system for a residential building,” *Adv. Energy Res.*, vol. 8, no. 1, pp. 59–71, 2021, doi: 10.12989/eri.2021.8.1.059.

[4] A. A. Naqvi, T. Bin Nadeem, A. Ahmed, and A. Ali Zaidi, “Designing of an off-grid Photovoltaic system with battery storage for remote location,” *Tecciencia*, vol. 16, no. 31, pp. 15–28, 2021, doi: 10.18180/tecciencia.2021.31.2.

[5] Y. Jia, G. Alva, G. F.-R. and S. E. Reviews, and U. 2019, “Development and applications of photovoltaic–thermal systems: A review,” *Elsevier*, 2019.

[6] M. Ahmed, A.; Naqvi, A. A.; Bin, T.; Uzair, “Experimental Investigation of Dust Accumulation on the Performance of the Photovoltaic Modules : a Case Study of Karachi , Pakistan,” *Appl. Sol. Energy*, vol. 57, no. 5, pp. 370–376, 2021, doi: 10.3103/S0003701X21050029.

[7] A. A. Naqvi, A. Ahmed, M. Jamal, A. Majeed, A. Khizar, and B. Shaheer, “Performance Evaluation of Hybrid PVT Air Collector. A Comparative Approach,” *GMSARN Int. J.*, vol. 16, no. 2, pp. 121–127, 2022.

[8] A. N. Asad, A. Ahmed, and T. Bin Nadeem, “Efficiency Improvement of Photovoltaic Module by Air Cooling,” *Appl. Sol. Energy (English Transl. Geliotekhnika)*, vol. 57, no. 6, pp. 517–522, 2021, doi: 10.3103/S0003701X21060049.

[9] E. Skoplaki and J. A. Palyvos, “On the temperature dependence of photovoltaic module electrical performance: A review of efficiency/power correlations,” *Sol. Energy*, vol. 83, no. 5, pp. 614–624, 2009, doi: 10.1016/j.solener.2008.10.008.

[10] P. M. Kumar, R. Anandkumar, D. Sudarvizhi, K. B. Prakash, and K. Mylsamy, “Experimental investigations on thermal management and performance improvement of solar PV panel using a phase change material,” *AIP Conf. Proc.*, vol. 2128, 2019, doi: 10.1063/1.5117935.

[11] M. A. Muhammad Uzair, Asad A. Naqvi, “Statistical Approach to select the Best Suitable Solar Model for Global Radiation : Case Study of Karachi , Pakistan,” *Tecciencia*, vol. 17, no. 32, pp. 17–28, 2022.

[12] M. Uzair, A. A. Naqvi, and S. U. H. Kazmi, “Estimation of the Diffused Solar Irradiation on the Tilted Plane of Photovoltaic Solar Panels Estimación de la Irradiación Solar Difusa en el Plano Inclinado de Paneles Solares Fotovoltaicos Estimativa da Irradiação Solar Difusa no Plano Inclinado de Pain,” vol. 24, pp. 37–52, 2023.

[13] A. A. N. Uzair, Muhammad and M. Uzair, “Numerical investigation to determine the optimal tilt angle of single slope solar still during summer season,” *Tecciencia*, vol. 17, no. 32, pp. 29–40, 2022.

[14] J. H. Kim, S. H. Park, and J. T. Kim, “Experimental performance of a photovoltaic-thermal air collector,” *Energy Procedia*, vol. 48, pp. 888–894, 2014, doi: 10.1016/j.egypro.2014.02.102.

[15] S. Diwania, A. S. Siddiqui, S. Agrawal, and R. Kumar, “Performance assessment of PVT-air collector with V-groove absorber: A theoretical and experimental analysis,” *Heat Mass Transf. und Stoffuebertragung*, vol. 57, no. 4, pp. 665–679, 2021, doi: 10.1007/s00231-020-02980-0.

[16] N. Aste, F. Leonforte, and C. Del Pero, “Design, modeling and performance monitoring of a photovoltaic-thermal (PVT) water collector,” *Sol. Energy*, vol. 112, pp. 85–99, 2015, doi: 10.1016/j.solener.2014.11.025.

[17] M. M. Sardouei, H. Mortezapour, and K. Jafari Naeimi, “Temperature distribution and efficiency assessment of different PVT water collector designs,” *Sadhana - Acad. Proc. Eng. Sci.*, vol. 43, no. 6, pp. 1–13, 2018, doi: 10.1007/s12046-018-0826-x.

[18] J. Yazdanpanahi, F. Sarhaddi, and M. Mahdavi Adeli, "Experimental investigation of exergy efficiency of a solar photovoltaic thermal (PVT) water collector based on exergy losses," *Sol. Energy*, vol. 118, pp. 197–208, 2015, doi: 10.1016/j.solener.2015.04.038.

[19] A. K. Hamzat, A. Z. Sahin, M. I. Omisanya, and L. M. Alhems, "Advances in PV and PVT cooling technologies: A review," *Sustain. Energy Technol. Assessments*, vol. 47, no. June, p. 101360, 2021, doi: 10.1016/j.seta.2021.101360.

[20] H. M. Ali, "Recent advancements in PV cooling and efficiency enhancement integrating phase change materials based systems – A comprehensive review," *Sol. Energy*, vol. 197, no. November 2019, pp. 163–198, 2020, doi: 10.1016/j.solener.2019.11.075.

[21] K. Velmurugan, S. Kumarasamy, T. Wongwuttanasatian, and V. Seithtanabutara, "Review of PCM types and suggestions for an applicable cascaded PCM for passive PV module cooling under tropical climate conditions," *J. Clean. Prod.*, vol. 293, p. 126065, 2021, doi: 10.1016/j.jclepro.2021.126065.

[22] M. Tao, L. Zhenpeng, and Z. Jiaxin, "Photovoltaic panel integrated with phase change materials (PV-PCM): technology overview and materials selection," *Renew. Sustain. Energy Rev.*, vol. 116, no. September, p. 109406, 2019, doi: 10.1016/j.rser.2019.109406.

[23] H. M. T. Al-Najjar *et al.*, "Improving the Melting Duration of a PV/PCM System Integrated with Different Metal Foam Configurations for Thermal Energy Management," *Nanomaterials*, vol. 12, no. 3, 2022, doi: 10.3390/nano12030423.

[24] A. Hasan, S. J. McCormack, M. J. Huang, and B. Norton, "Evaluation of phase change materials for thermal regulation enhancement of building integrated photovoltaics," *Sol. Energy*, vol. 84, no. 9, pp. 1601–1612, 2010, doi: 10.1016/j.solener.2010.06.010.

[25] Y. S. Indartono, A. Suwono, and F. Y. Pratama, "Improving photovoltaics performance by using yellow petroleum jelly as phase change material," *Int. J. Low-Carbon Technol.*, vol. 11, no. 3, pp. 333–337, 2016, doi: 10.1093/ijlct/ctu033.

[26] R. Stropnik and U. Stritih, "Increasing the efficiency of PV panel with the use of PCM," *Renew. Energy*, vol. 97, pp. 671–679, 2016, doi: 10.1016/j.renene.2016.06.011.

[27] H. Xu, N. Wang, C. Zhang, Z. Qu, and F. Karimi, "Energy conversion performance of a PV/T-PCM system under different thermal regulation strategies," *Energy Convers. Manag.*, vol. 229, no. December 2020, p. 113660, 2021, doi: 10.1016/j.enconman.2020.113660.

[28] G. M. Masters, *Renewable and Efficient Electric Power Systems.* John Wiley & Sons Inc., 2004.

Nota contribución de los autores:

1. Concepción y diseño del estudio
2. Adquisición de datos
3. Análisis de datos
4. Discusión de los resultados
5. Redacción del manuscrito
6. Aprobación de la versión final del manuscrito

MF ha contribuido en: 1, 2, 3, 4, 5 y 6.
AAN ha contribuido en: 1, 2, 3, 4, 5 y 6.
MU ha contribuido en: 1, 2, 3, 4, 5 y 6.

Nota de aceptación: Este artículo fue aprobado por los editores de la revista Dr. Rafael Sotelo y Mag. Ing. Fernando A. Hernández Gobertti.

Fatigue Life Estimation for Different Geometrical Configuration of Load-Carrying Cruciform Joint using ABAQUS and Fe-Safe

Estimación del Tiempo de Fatiga para Diferentes Configuraciones Geométricas de Juntas Cruciformes Portadoras de Carga utilizando ABAQUS y Fe-Safe

Estimativa do Tempo de Fadiga para Diferentes Configurações Geométricas de Juntas Cruciformes Portantes usando ABAQUS e Fe-Safe

Zulqarnain Mukhtar Mahmood[1], Muhammad Asif[2(*)], Syed Asad Ali Zaidi[3]

Recibido: 03/02/2024 Aceptado: 29/03/2024

Summary. - This research paper focuses on the fatigue analysis of load-carrying cruciform joints made up of thick plates, which are crucial components in ship structures. The study investigates the fatigue life of fillet welded cruciform joints using both 2D and 3D geometries. Various loading conditions and boundary conditions are considered, and an elastic-plastic finite element analysis is conducted using ABAQUS 2021. The number of cycles to failure is estimated using Fe-Safe and the strain-based Brown Miller Morrow model. The results, presented through contour plots, Log Life repeats, and Load Range vs. Number of Cycles graphs, reveal the fatigue behavior and failure locations. Additionally, the methodology is validated against experimental data from literature, demonstrating its applicability. The findings provide insights into the fatigue characteristics of load-carrying cruciform joints in thick plates, contributing to enhanced design and reliability in the shipbuilding industry.

Keywords: Load-carrying Cruciform joint, Fatigue analysis, Elastic-Plastic FEA, ABAQUS, Fe-Safe, 2D and 3D Cruciform geometries.

(*) Corresponding Author

[1] Bachelor of Engineering, Department of Naval Architecture, Pakistan Navy Engineering College, National University of Sciences and Technology (Pakistan), zulqarnainmukhtar622@gmail.com, ORCID iD: https://orcid.org/0009-0003-4412-0477

[2] Assistant Professor, Department of Naval Architecture, Pakistan Navy Engineering College, National University of Sciences and Technology (Pakistan), muhammadasif@pnec.nust.edu.pk, ORCID iD: https://orcid.org/0000-0003-4318-8253

[3] Assistant Professor, Department of Mechnaical Engineering, Faculty of Engineering, Islamic University of Madinah (Saudi Arabia), Sali@iu.edu.sa, ORCID iD: https://orcid.org/0000-0001-5457-5684

Memoria Investigaciones en Ingeniería, núm. 26 (2024). pp. 98-124
https://doi.org/10.36561/ING.26.7
ISSN 2301-1092 • ISSN (en línea) 2301-1106 – Universidad de Montevideo, Uruguay

Resumen. - *Este trabajo de investigación se centra en el análisis de fatiga de uniones cruciformes portadoras de carga formadas por placas gruesas, que son componentes cruciales en las estructuras de los barcos. El estudio investiga la vida a fatiga de uniones cruciformes soldadas en ángulo utilizando geometrías 2D y 3D. Se consideran varias condiciones de carga y condiciones de contorno, y se realiza un análisis de elementos finitos elástico-plástico utilizando ABAQUS 2021. El número de ciclos hasta la falla se estima utilizando Fe-Safe y el modelo Brown Miller Morrow basado en deformaciones. Los resultados, presentados a través de gráficos de contorno, repeticiones de registro de vida y gráficos de rango de carga versus número de ciclos, revelan el comportamiento de fatiga y las ubicaciones de falla. Además, la metodología está validada con datos experimentales de la literatura, lo que demuestra su aplicabilidad. Los hallazgos proporcionan información sobre las características de fatiga de las uniones cruciformes que soportan carga en placas gruesas, lo que contribuye a mejorar el diseño y la confiabilidad en la industria de la construcción naval.*

Palabras clave: *Unión cruciforme portadora de carga, Análisis de fatiga, FEA Elástico-Plástico, ABAQUS, Fe-Safe, Geometrías cruciformes 2D y 3D.*

Resumo**. -** *Este trabalho de pesquisa concentra-se na análise de fadiga de juntas cruciformes de suporte de carga compostas por placas espessas, que são componentes cruciais em estruturas de navios. O estudo investiga a vida à fadiga de juntas cruciformes soldadas em ângulo usando geometrias 2D e 3D. Várias condições de carregamento e condições de contorno são consideradas, e uma análise de elementos finitos elástico-plásticos é conduzida usando ABAQUS 2021. O número de ciclos até a falha é estimado usando Fe-Safe e o modelo Brown Miller Morrow baseado em deformação. Os resultados, apresentados através de gráficos de contorno, repetições de log de vida útil e gráficos de faixa de carga versus número de ciclos, revelam o comportamento da fadiga e os locais de falha. Adicionalmente, a metodologia é validada frente a dados experimentais da literatura, demonstrando sua aplicabilidade. As descobertas fornecem informações sobre as características de fadiga das juntas cruciformes de suporte de carga em chapas grossas, contribuindo para melhorar o design e a confiabilidade na indústria de construção naval.*

Palavras-chave: *Junta cruciforme portante, análise de fadiga, geometrias elástico-plásticas FEA, ABAQUS, Fe-Safe, 2D e 3D cruciformes.*

1. Introduction. - The construction of ships involves various types of connections, including stiffener joints and plate joints, which are predominantly formed through welding processes. Cruciform joints are used to link longitudinal and transverse structural parts of ships, such as the keel, its frames, and bulkheads. These joints are essential for transmitting and distributing loads across the ship's hull, ensuring the vessel's structural integrity and strength. The load-carrying ability of cruciform joint is critical for the ship to endure the numerous forces encountered during operation, such as waves, the currents, and impacts loads. The proper design and construction of cruciform joints is critical to preventing stress concentrations of fatigue, and structural failure.

The intersection of longitudinal and transverse elements of structure in a cruciform joint generates a complicated stress field, with high stress concentrations located in the weld's toe and root. Geometric discontinuities, weld flaws, and residual stresses induced during the fabrication procedure can all contribute to higher stress concentrations. Welding plays a crucial role in the shipbuilding industry, but it also poses the risk of failures occurring in these joints during the ship's commissioned life. Among the significant joints in ship structures are the cruciform welded joints or connections. These joints experience high loads and are critical to the structural integrity of the ship. Therefore, it is essential to conduct a comprehensive fatigue analysis to ensure their reliability and longevity.

Traditional fatigue evaluation techniques, such as nominal stress and hot-spot stress methods, frequently rely on simpler stress estimations that may not adequately represent the intricate stress distributions found in cruciform joints. Furthermore, empirical relationships based on limited data from experiments, like S-N curves or as notch factor methods, may not sufficiently account for the distinctive geometric and material properties of a particular cruciform joints design, potentially leading to discrepancies in fatigue life estimates.

Benefits of FEA include detailed stress analysis include a more in-depth and accurate assessment of the stress distribution inside a cruciform joint, taking into account the intricate geometry, the properties of the material, loading conditions, and weld-specific characteristics like the weld profile, residual stresses, as well as the presence of defects. Engineers can also undertake parametric studies to optimize the joint's design and material properties, and the findings can be tested versus experimental evidence, allowing for the improvement and validation of the models used for analysis to assure better fatigue life forecasts.
The present research paper focuses on the fatigue analysis of fillet welded load-carrying cruciform joints made up of thick plates. The study involves both 2D and 3D geometries, considering various boundary conditions. The analysis is performed using elastic-plastic finite element analysis (FEA) conducted in ABAQUS 2021. The number of cycles to failure is estimated using Fe-Safe and the strain-based Brown Miller Morrow model. To accurately model the behavior of the joints, the material properties of SAE1045 steel are considered.

The findings of this research have significant implications for the shipbuilding industry. Understanding the fatigue behavior of load-carrying cruciform joints in thick plates enables engineers and designers to make informed decisions regarding their design, fabrication, and maintenance. By identifying critical areas prone to fatigue damage and optimizing the joint configurations, the structural integrity and longevity of ships can be enhanced.

Moreover, the research contributes to the broader field of fatigue analysis and structural engineering. The methodology employed in this study can be extended to other types of joints and structures, providing a framework for evaluating fatigue life and enhancing the reliability of various engineering applications. The specific objectives include:

a) Investigating the fatigue behavior of cruciform joints under various loading conditions.
b) Assessing the influence of 2D and 3D geometry and different boundary conditions to investigate the fatigue characteristics, failure locations, and stress distributions within the joints.
c) Estimating the number of cycles to failure using elastic-plastic FEA and the strain-based Brown Miller Morrow model.
d) Validating the proposed methodology by comparing the simulated results with experimental data from the literature.

The contribution of this research is three-fold. Firstly, to analyze the fatigue life of the cruciform joint through the 3D geometry under varying load magnitudes ranging from 480 to 680 MPa. Secondly, to investigate the fatigue performance of the joint through the 2D geometry under different boundary conditions, including axial loading, vertical loading, bending, and combined axial-bending loading. Lastly, to validate the methodology employed in this study by comparing the simulation results with experimental data from the literature.

The significance of this research lies in its contribution to the understanding of fatigue behavior in load-carrying

cruciform joints of thick plates. The findings will aid in the development of more reliable and durable joint designs for ship structures, thereby improving the overall structural integrity and safety of vessels. Furthermore, the research methodology and insights gained can be extended to other applications that involve welded connections subjected to cyclic loading conditions.

The organization of this paper is as follows: Section 2 provides a literature review on fatigue analysis of welded joints and previous studies related to load-carrying cruciform joints. Section 3 describes the methodology employed, including the finite element modeling techniques, material properties, and numerical simulations. Section 4 presents the results and discussions, including contour plots, Log Life repeats, and Load Range vs. Number of Cycles graphs. Section 5 focuses on the validation study by comparing the simulated results with experimental data from the literature. Finally, Section 6 concludes the paper and discusses the implications of the research findings, along with suggestions for future work.

Fatigue refers to the processes that occur when a material is subjected to cyclic stress, resulting in accumulated degradation and, finally, final fracture. Waves produced in oceans are seen as cyclic excitations applied on a ship while it is at sea. These loads have the potential to cause fatigue damage in structures of ships. The forces generated by the ship's movement (such as rolling and pitching), wind movement, and green water motion are eventually transferred to the ship hull through the lashing bridge structure [1]. Modern ship’s structure face serious fatigue damage concerns due to increased ship's tonnage capacity and substantial usage of strong steel [2]. As histories and subsequent service experiences have revealed, fatigue and fracture are key failure causes of ships [3]. The most typical problems in marine vessel's structures during operational activities include fatigue fractures, panel's buckling, indents, and rusting. Fatigue damages, in particularly, play a vital role in ship structures [4]. See **Error! Reference source not found.** for phases of fatigue life.

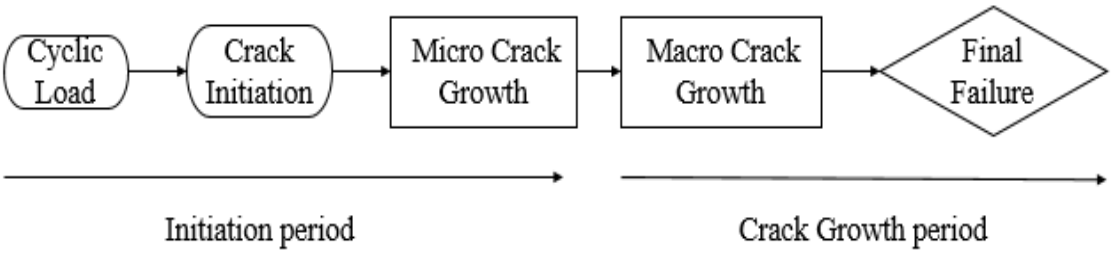

Figure I. Fatigue Life Phases

The plate is a flat structural component having a thin thickness in comparison to its surface size and dimensions. When working with plates, it is common to be perplexed by the subject of how to describe thin or thick plate, or which plate is regarded thicker. According to [5] ratio of thickness to width or thickness to a length less than 10% is regarded as a thin plate, while a ratio higher than 10% is called a thick plate. Thicknesses of thin plates range from $0.1 > t > 0.01$ and thick plates have a thickness (t) higher than 0.01 [6].

Welding is a widely used manufacturing process in shipbuilding, and they are roughly divided into two types: (1) Welding which relies only on heat source, such as fusion welding. (2) Welding which combines heat and pressure sources, such as forge welding [7]. As welding is a fundamental connecting procedure in shipyards, this procedure resulted in welding deformities, which caused numerous issues during the manufacturing of ships [8]. Welding errors can occur because of a welder's inexperience, the use of wrong substances or faulty welding processes, and environmental circumstances [9]. As a large quantity of corrected work is needed, welding imperfections lower the fabrication quality of the ship's hull blocks and lead to poor productive performance [10].

The welded load-carrying cruciform joints (LCJs) are one of the most common connection types in shipbuilding or maritime engineering projects, and fatigue failure to these is a serious hazard to welded constructions [11]. When cruciform joints are exposed to continually changing stresses, they become fatigued [12]. Many types of research have been performed related to fatigue assessment load-carrying cruciform joint (LCJ) and non-load carrying cruciform joint (NLCJ) in literature. This joint is one of the important welded joints for ship structure during ship’s construction [13].

Work done by [14] examined the quality of weld and fatigue of NLCJs made by VAG laser and MAG Hybrid welding to produce four lots for testing and find stress concentration factors by applying finite element models with the help of defined parameters of the local geometry of weld. Fatigue of LCJs contain incomplete weld penetration and under-

matching strength of weld deposit and base metal were studied by [15] performing experiments of high and low cycle fatigue on specimens. Research was performed by [16] to analyze fatigue strength affected by the size of cruciform welded joints exposed axial as well as bending stresses. The research in [17] investigates the fatigue modeling or simulation of high-performing steel joints formed by welding by utilizing notched stress and strain-based methods, linear elastic fracture mechanics (LEFM), and SED (strain energy density).

For location of fatigue failure, a study by [18] consider notch stress intensity concept based on William's explanation in LEFM as well as ponder the weld size, transverse plate thickness, incomplete penetration, and plate thickness.

Three geometrically multifarious structural details of the ship were studied and analyzed [19] to estimate their fatigue life using local approaches. All details have communal characteristics like Cruciform joints (two plates crossing each other). A comparative study for fatigue behavior of high cycle fatigue, applied on steel LCJs made by welding was performed by [20] at weld toe and root using PSM (peak stress method) and notch SIF (stress intensity factor). Experimental and theoretical work has been done by [21] to study the effect of cooling and welded bead profile made by shielded metal arc welding process for fatigue life of cruciform joint formed by 8 mm thick plates made up steel ASTM A36 HR.

Some researchers [22] used relationship of RSG (relative stress gradient) and SCF to Notch factor ratio to study the effect caused by the thickness of plates, the radius of weld toe, and bead profile for fatigue of cruciform welded joints. A parametric study for the calculation of notch SCF using spline shape weld model during finite element analyses had performed by [23] for cruciform welded joints experiencing unalike loading scenarios. The research of [24] propose new formulas for SCFs for cruciform joints containing fillet welds subjected to bending loads after employing extended numerical solutions of finite element methods. To study the penetration of weld (full and incomplete) for both fillet welded LCJs and NLCJs had done by [25] with the help of 3D FEM. Strain energy density (SED) approach was used by [26] to investigate parameters like scale effect, bead penetration, length of weld leg, and dimensions of plates for cruciform joints.

Fatigue of fillet welded LCJs made up of austenitic stainless steel investigated by [27] using SN curve, fatigue crack growth, and shape along with prediction method of fatigue life. An evaluation was proposed in [28] to find full fatigue (crack initiation + crack propagation) of cruciform joint prepared by 7005 aluminum alloy considering residual stresses produced after welding. The research work of [29] proposed new equations for SIF at the crack of weld toe for welded LCJ with help of 3D finite element analysis to identify the failure site. To inspect LCF and HCF, a novel energy analytical solution for weld toe and root of welded LCJs made up of 10CrNi3MoV steel was studied in [30] considering the effects of weldment's plasticity and mechanical heterogeneity based on Neuber's Fictitious Notch Rounding concept. The paper [31] re-analyzed the fillet welded LCJs for which failing occur at weld roots and compare results of nominal and notch stress methods for fatigue strength. Some key findings of related research are listed in **Table I**.

Study	Fatigue Analysis Approach	Key Findings
Wei Song et al. [20]	PSM and Notch SIF	A comparative study for fatigue behavior of HCF, applied on steel welded LCJs at weld toe and root.
Oscar and Nelson [21]	Experimental and Theoratical	Find fatigue life due to effect of cooling and welded bead profile made by shielded metal arc welding process.
Toru and Naoki [22]	RSG, SCF and Notch Factor	Study the effects caused by the thickness of plates, the radius of weld toe, and bead profile for fatigue of LCJ
Yixun Wang et al. [23]	Finite Element Analysis	A parametric study for the calculation of notch SCF for fatigue of cruciform joints.
Wang Sub Shin et al. [25]	3D Finite Element Model	Fatigue on the penetration of full and incomplete welded LCJs and NLCJs

Pietro Foti et al. [26]	Strain energy density	Investigate parameters like scale effect, bead penetration, weld leg length, and dimensions of plates for cruciform joints.
Yang Peng et al. [27]	Fatigue life Prediction Method	Fatigue of fillet welded LCJs investigated by using SN curve, fatigue crack growth, and shape.
Jianxiao Ma et al. [28]	Residual Stress Approach	Find full fatigue (crack initiation + crack propagation) of cruciform joint
Haisheng Zhao et al. [29]	3D Finite Element Analysis	Identify the fatigue failure site for welded LCJ.
Wei Song et al. [30]	Neuber's Fictitious Notch Rounding Concept	Inspect LCF and HCF for weld toe and root of welded LCJs made up of 10CrNi3MoV.

Table I. Key Findings of Related Research

The proposed research aims to build upon the existing body of knowledge by conducting a fatigue analysis of load-carrying cruciform joints in thick plates. By employing both 2D and 3D geometries, the study seeks to provide a comprehensive understanding of the fatigue behavior, failure locations, and fatigue life of these joints under various loading conditions. The research findings will contribute to the design and optimization of load-carrying cruciform joints in ship structures, enhancing their fatigue resistance and structural integrity.

2. Methodology. - This section contains the details about what methodology has been used for the present study and it has been applied. It will discuss the joint and software used for the research. It has the following details:

2.1 ABAQUS. - Abaqus, originally known as ABAQUS, was built in 1978 as a simulation software package for studying complex problems utilizing FEA simulations as well as models and designs made with the help of a computer called computer-aided engineering or CAE. This software suite is composed of five core program applications.
Complete ABAQUS Environment (cae) is an application that is employed to make models of physical bodies and investigation of machine-driven parts and systems. It is mostly used for pre-processing designs and models for simulation as well as viewing the results of finite element analysis.
Standard or Implicit, is a common purpose analyzer for finite element analysis using an implicit type of integration strategy. It is a traditionally used tool.
Explicit, used for the distinctive purpose of analyzing finite element problems that investigates highly non - linear problems with several complicated connections under transient loading using an explicit integration approach.
Computational Fluid Dynamics (CFD) is an application used for problems related to fluid dynamics that deliver innovative CFD competencies considering significant pretreatment and post-processing provision.
Electromagnetic, a software tool that is used for computer-based electromagnetic problems that address sophisticated electromagnetic theoretical problems.
ABAQUS is a popular and robust software suite for finite element analysis (FEA) that provides extensive modeling capabilities. Cruciform joints, which frequently display intricate stress distributions and distortion patterns, are a good fit for this analysis method because of its ability to handle non-linear materials, complicated geometries, and a wide range of loading situations. Predicting the fatigue behavior of a joint requires the software to be able to capture the impacts of weld profiles, residual stresses, and various other manufacturing-related parameters on the stress distribution inside the joint. **Figure II** depicts the general solution procedure in ABAQUS.

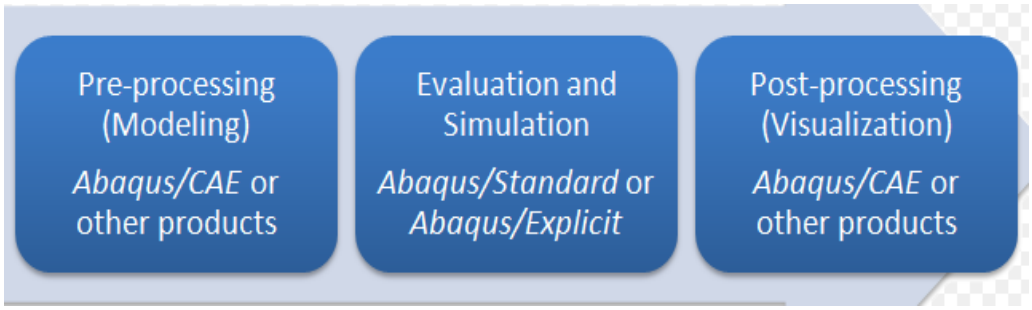

Figure II. ABAQUS General Solution Sequence

2.2 Fe-Safe. - Fe-safe is the industry's first market accessible fatigue analysis program that focuses on current multi-axial strain-based failure methodologies. It is known for its correctness, efficiency, and simplicity of use when analyzing metals, rubber, thermo-mechanical, creep-fatigue, and the welded joints. Fe-Safe is a robust, all-inclusive, and user-friendly package of failure analysis software for models of finite elements. It is used in conjunction with commercialized FEA software packages to determine:

- Occurrence of fatigue cracks
- Estimating the commencing of fatigue cracks
- To find Working stress safety factors
- The chance of survival and persistence at various working lives
- Cracks propagation probability

Fe-Safe will spontaneously select the most suited analytical approach for engineers who may not be fatigue specialists and will approximate material characteristics if test results are not provided. **Figure III** depicts a general fatigue analysis scheme in Fe-Safe.

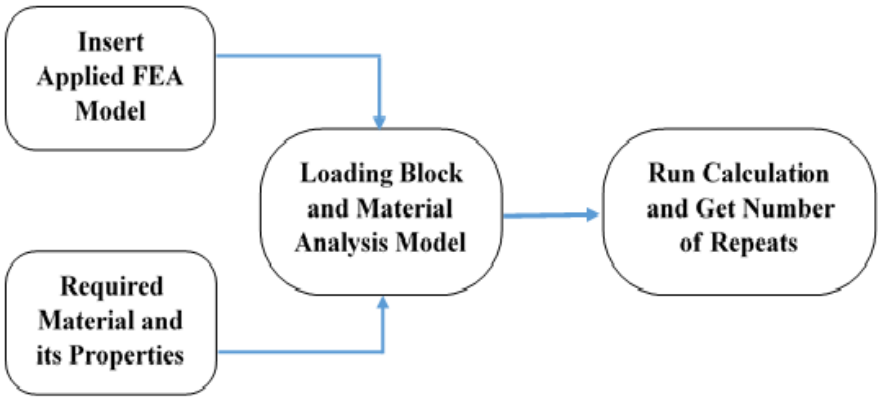

Figure III Fe-Safe Fatigue Analysis General Scheme

2.3 Geometry Used (3D and 2D). - For the investigation, two types of cruciform joint geometry were explored. [25] Gives the dimensions for 3D geometry. **Figure IV** shows an example of this. This geometry includes a 6 mm convex-shaped fillet weld. SolidWorks was used to create a whole (plates + welds) 3D solid model. **Figure V** depicts a SolidWorks model.

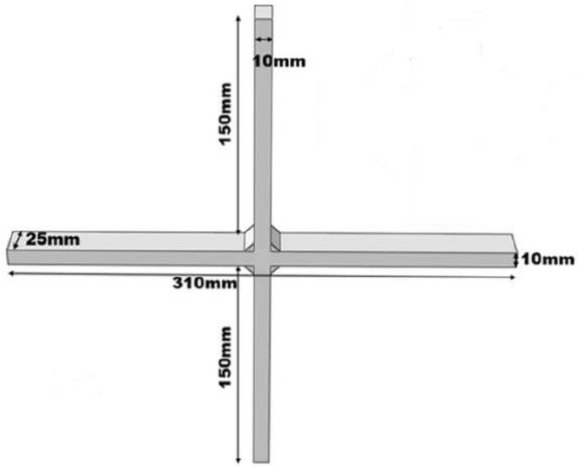

Figure IV. Cruciform Joint 3D Dimensions [25]

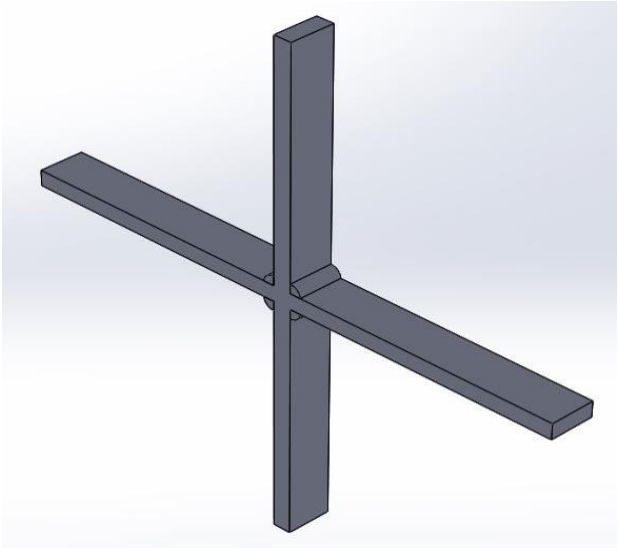

Figure *V.* 3D Model made by SolidWorks.

Dimensions for the 2D geometry of the joint are derived from [32]. **Figure VI** shows an example of this. This shape includes an 8 mm flat fillet weld.

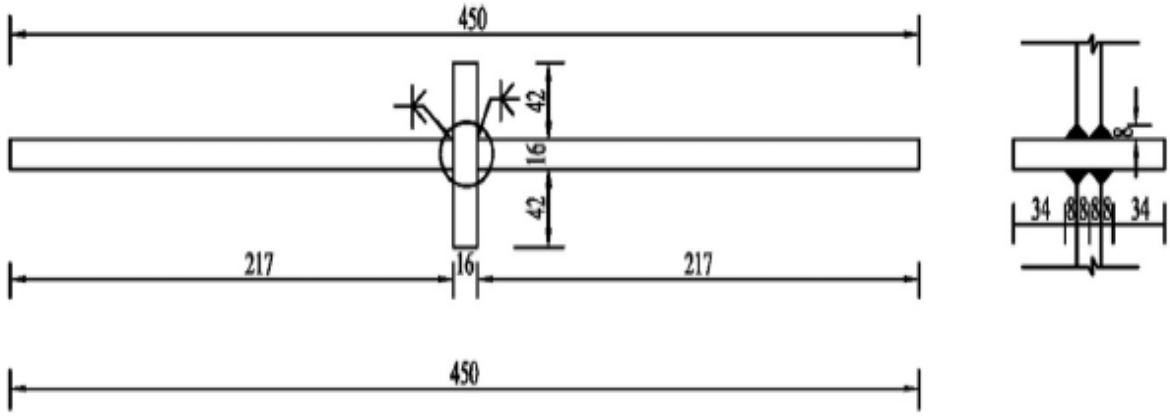

Figure VI. Cruciform Joint 2D Dimensions

This 2D geometry was created in ABAQUS using the part creation feature. 1/4th of geometry was made for axial and vertical loading cases. The rest of the cases are studied on half of the geometry. **Figures 7** and **Figure 8** show ABAQUS 2D models.

Figure VII. 1/4th of the geometry made by ABAQUS.

Figure VIII. Half of the Geometry made by ABAQUS.

2.4 Material for Cruciform Joint. - SAE 1045 is the material used in this study. It is mild carbon steel that is widely utilized in a variety of industries. Axles, bolts, connecting rods, pins, studs, shafts, spindles, and other similar uses are common. It is obvious that these parts are frequently subjected to repeated loading. As a result, increasing the fatigue resistance of SAE 1045 appears to be necessary. SAE 1045's chemical composition is obtained from [33] and is presented in **Table II**.

Constituents	Carbon	Silicon	Manganese	Phosphorus	Sulfur	Iron
Weight %	0.423	0.20	0.56	0.008	0.02	rest

Table II. SAE 1045 Chemical Composition

The monotonic characteristics are achieved [34] by utilizing a 25 KN servo-hydraulic machinery to perform a uniaxial cycle test with a stress ratio of R = -1. During the test, a 2-mm strain gauge was affixed to the specimen to gather strain events. See Figure 3.8 for servo-hydraulic machinery and **Table III** for SAE 1045 monotonic properties.

Properties	Values
Ultimate Tensile Stress (σ_u) (UTS)	798 MPa
Yield Stress (σ_y)	414 MPa
Young's Modulus (E)	198 MPa

Table *III.* SAE 1045 Monotonic Properties

Following that, a cycle test [34] was performed at various percentages of UTS (ultimate tensile strength) acquired from the preceding tensile test. The percentages used are 60, 65, 70, 80, and 85 percent. As a result, five various stress values were used to capture failure time and strain range readings. See Table 3.3 for more information.

Applied Stress (MPa)	Strain Ranges ($\boldsymbol{\mu\varepsilon}$)
480 (60 % of UTS)	2294

520 (65 % of UTS)	3200
570 (70 % of UTS)	4059
640 (80 % of UTS)	4565
680 (85 % of UTS)	5800

Table IV. Applied Stresses for Cyclic Test and Strain Ranges

2.5 Elastic-Plastic FEA. - ABAQUS is used for elastic-plastic finite element analysis. First, a 3D model made by SolidWorks is loaded into ABAQUS, and the 2D geometry of a cruciform joint is created in ABAQUS using the Sketch and Feature tools. Static General STEP is built for plastic analysis after specifying the elastic and plastic material characteristics of SAE 1045. As previously stated, two configurations are being investigated. As a result, for 3D geometry, one type of boundary condition along with axial loadings of 480, 520, 570, 640, and 680 MPa are investigated. One side is fixed, upper and lower face of cruciform joint is allowed to move and the side opposite to fixed side is subjected to axial loading. For more information, see **Figure X**. In the current study, 2D geometry is subjected axial loading for same loading values as of 3D geometry and boundary conditions. For Meshing, an 8-node biquadratic plain strain element CPE8R with reduced integration is utilized. After the work is completed, the findings are taken in the form of stress and deformation contours. The whole flow diagram of elastic-plastic FEA may be found in **Figure IX**.

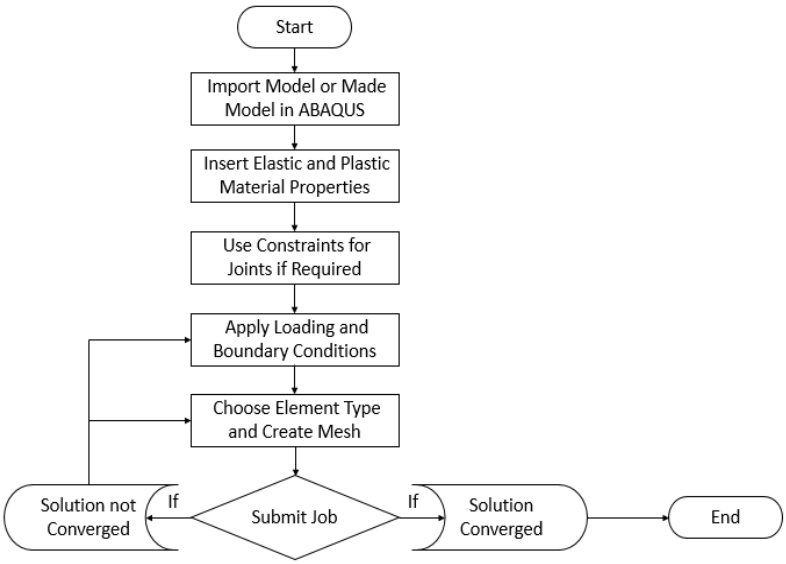

Figure IX. Elastic-Plastic FEA Flowchart

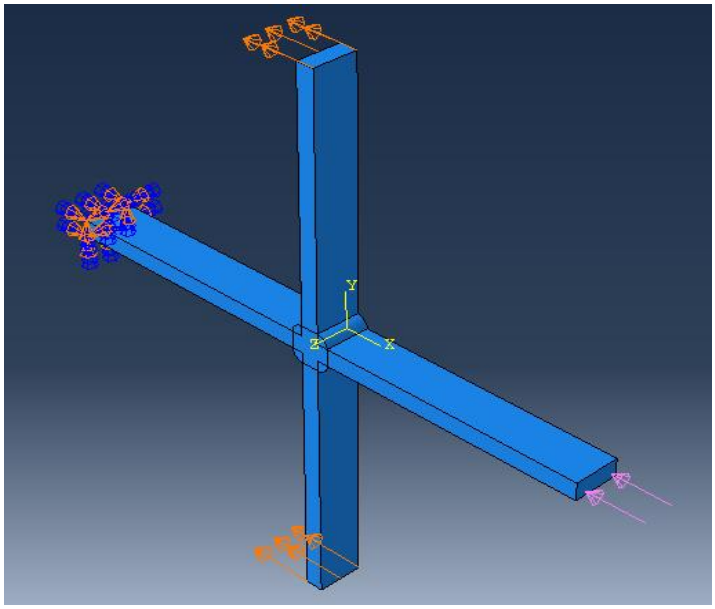

Figure X. Loading Scenario and Boundary Condition for 3D Geometry

2.6 Strain Based Brown Miller Morrow. - According to the Brown-Miller model, much fatigue impairment happens on that plane or surface which is under the influence of the maximum amplitude value of shear strain, and the impairment or failure is an accumulation of both; the shear strain and the strain perpendicular to that plane [35]. See **Figure XI**.

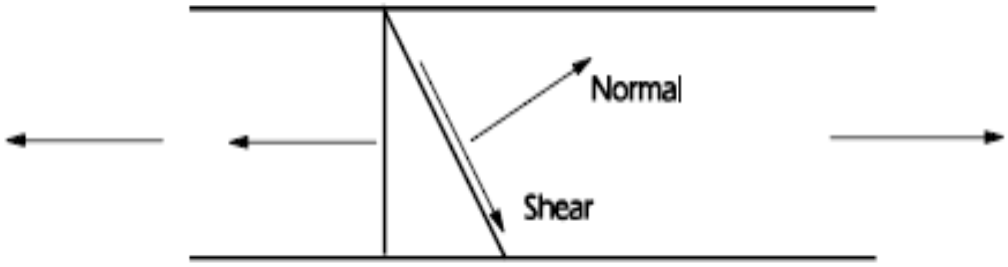

Figure *XI.* Normal and Shear Strain Description [35]

The Brown-Miller model offers the most accurate life predictions for ductile metals but is less accurate for brittle metals. It is a critical plane-based multi-axial fatigue processing algorithm that employs surfaces or planes at a right angle to the surface as well as planes at 45º to the surface. This model focuses on the plane within the material where the likelihood of crack initiation is the highest. It has following key limitations:

- It does not consider non-proportional loadings for fatigue life.
- It lacks to consider mean stress effects on fatigue life.
- It does not explicitly consider progressively accumulation of damage during fatigue.

For materials, it is assumed that the materials are ductile that exhibits plastic deformation before failure. Material is homogenous and isotropic which means that their properties are uniform and does not change direction of loading.

An elastic FEA's stress results are required for this algorithm. To estimate elastic-plastic analysis-based stress strains outcomes from the source of elastic FEA stresses, multi-axial type elastic-plastic based corrections are employed [36].

If

$$\gamma_{max} = Maximum\ Shear\ Strain$$
$$\varepsilon_n = Strain\ Normal\ to\ Maximum\ Shear\ Strain$$

Then from the strain circle of Mohr

$$\frac{\gamma_{max}}{2} = \frac{\varepsilon_1 - \varepsilon_3}{2}$$

And

$$\varepsilon_n = \frac{\varepsilon_1 + \varepsilon_3}{2}$$

In case of uniaxial plain stress

$$\varepsilon_1 = -\upsilon\varepsilon_3$$

And

$$\varepsilon_3 = -\upsilon\varepsilon_1$$

Then

$$\gamma_{max} = \varepsilon_1 - \varepsilon_3 = (1+\upsilon)\varepsilon_1$$

And

$$\varepsilon_n = \frac{\varepsilon_1 + \varepsilon_3}{2} = \frac{(1-\upsilon)\varepsilon_1}{2}$$

But, the conservative strain life prediction equation is

$$\frac{\Delta\varepsilon}{2} = \frac{\sigma_f'}{E}(2N_f)^b + \varepsilon_f'(2N_f)^c$$

It can be re-written by considering the amplitudes of shear and normal strains on the left-hand side as

$$\frac{\Delta\gamma_{max}}{2} + \frac{\Delta\varepsilon_n}{2} = C_1\frac{\sigma_f'}{E}(2N_f)^b + C_2\varepsilon_f'(2N_f)^c$$

Elastic **Plastic**

For elastic stress cases, the Poisson ratio is

$$\upsilon_e = 0.3$$

Then

$$\gamma_{max} = (1+\upsilon_E)\varepsilon_1 = 1.3\,\varepsilon_1$$

Also

$$\varepsilon_n = \frac{(1-\upsilon_E)\varepsilon_1}{2} = 0.35\,\varepsilon_1$$

Then the constant C_1will be

$$C_1 = 1.3 + 0.35 = 1.65$$

And similarly, for a plastic case, the Poisson ratio is

$$\upsilon_p = 0.5$$

Then

$$\gamma_{max} = (1+\upsilon_p)\varepsilon_1 = 1.5\,\varepsilon_1$$

And

$$\varepsilon_n = \frac{(1-\upsilon_p)\varepsilon_1}{2} = 0.25\,\varepsilon_1$$

So, the constant C_2will be

$$C_2 = 1.5 + 0.25 = 1.75$$

Hence, the complete Brown Miller equation for strain life will become

$$\frac{\Delta\gamma_{max}}{2} + \frac{\Delta\varepsilon_n}{2} = 1.65\frac{\sigma_f'}{E}(2N_f)^b + 1.75\varepsilon_f'(2N_f)^c$$

The researchers Kandil, Brown, and Miller created this version of the Brown-Miller parameter.
The strain-life equation is changed for mean stress correction proposed by Morrow:

$$\frac{\Delta\gamma}{2} + \frac{\Delta\varepsilon_n}{2} = 1.65\frac{\sigma_f'}{E}(2N_f)^b + 1.75\varepsilon_f'(2N_f)^c$$

This approach may also be used to analyze the fatigue of elastic-plastic FEA data [36].

2.7 Fatigue Analysis Using Fe-Safe. - Fe-safe is the industry's first commercially accessible fatigue analysis program that focuses on current multiaxial strain-based fatigue methodologies.

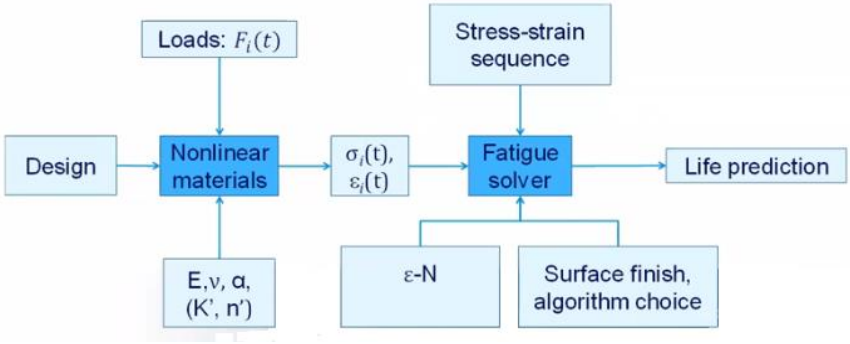

Figure XII. Combined ABAQUS and Fe-Safe Flowchart for Fatigue Analysis

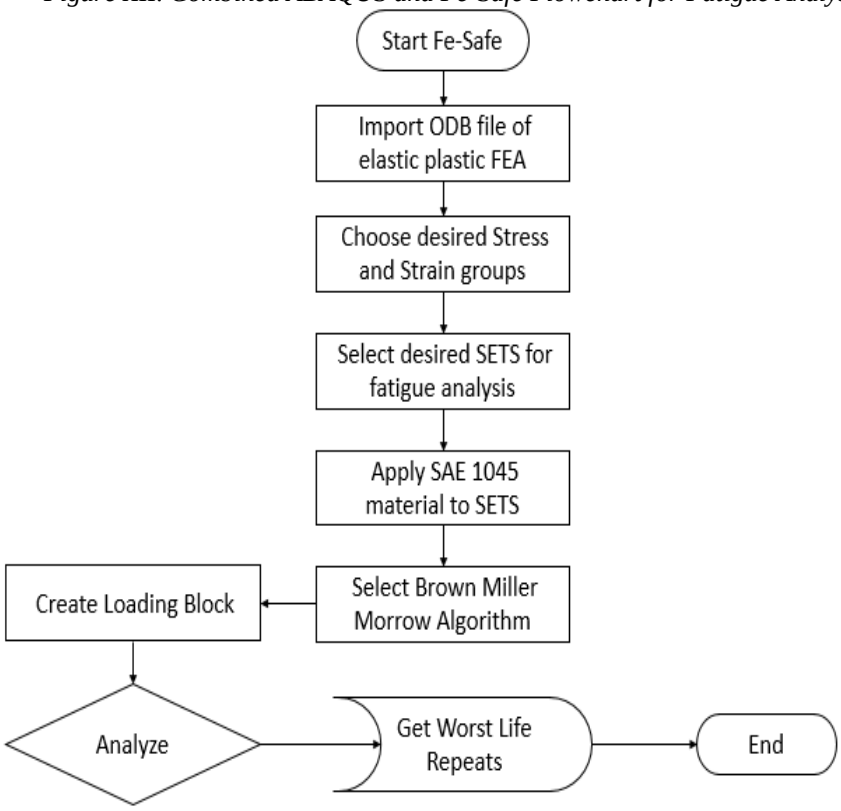

Figure XIII. Fe-Safe Fatigue Life Prediction Flow Chart

The schematic illustration of fatigue analysis utilizing ABAQUS and Fe-Safe is shown in **Figure XII**. It is known for its accuracy, speed, and ease of use when analyzing metals, rubber, thermo-mechanical and creep fatigue, and welded joints. Fe-Safe is a robust, all-inclusive, and user-friendly packages of fatigue analysis tools for finite element models [37]. The flowchart for Fe-Safe working is shown in **Figure XIII**. The worst life repeats represent the number of cycles to failure for estimation of fatigue life of joint.

3. Results & Discussion. - This chapter includes the results and discussions of outcomes obtained from the above-mentioned methodologies. Results are shown in the form of contours, tables, graphs, or curves. First, the 3D geometry of Load-carrying Cruciform Joint (LCJ) is discussed and then after that, the loading scenarios and boundary conditions for 2D are detailed.

3.1 Results of 3D Geometry. - As mentioned in the previous chapter that this geometry has been studied for five different loadings and only one type of boundary condition. This was done to understand the fatigue analysis process using ABAQUS and Fe-Safe to perform a detailed study on different loading and boundary conditions for 2D geometry. In this context, five loadings are applied on 3D geometry ranging from 480 to 680, and the contour shown in **Figure XIV** is for the last loading value i.e., 680 MPa. **Figure XV** shows the results of fatigue life obtained by Fe-Safe.

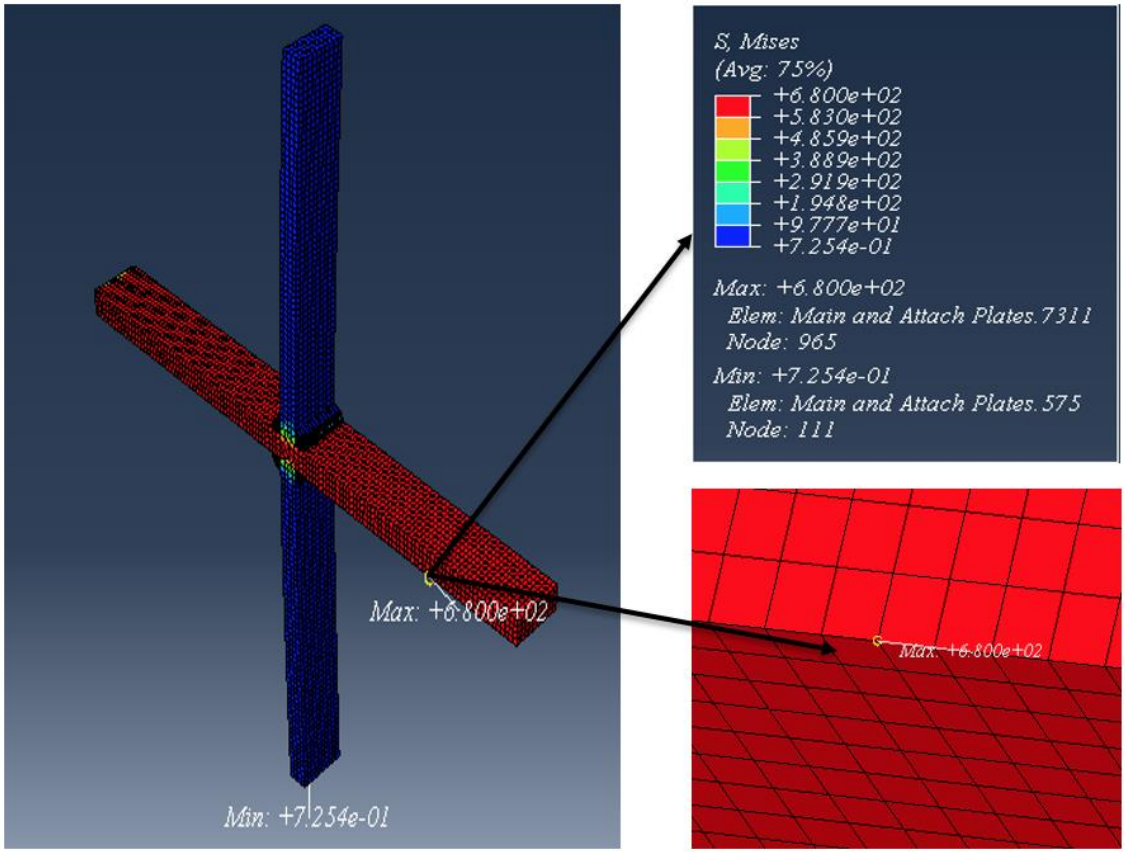

Figure 1: Contour of 3D Geometry for 680 MPa from ABAQUS

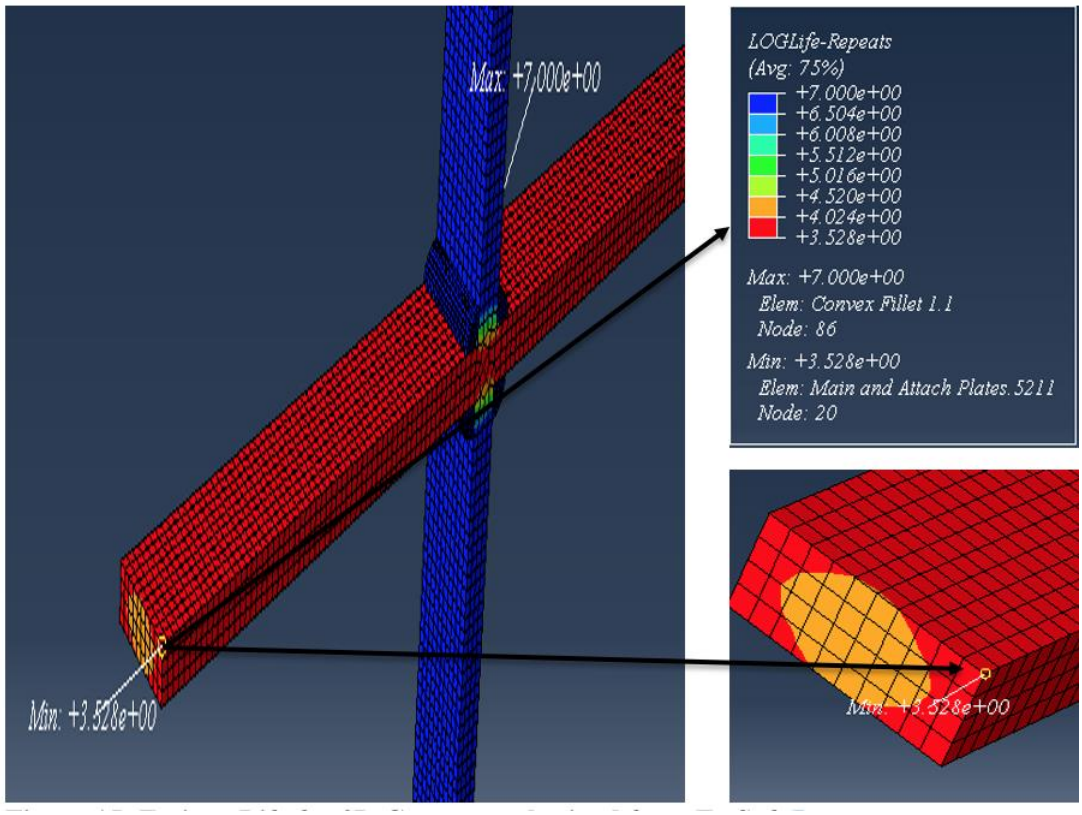

Figure 2: Fatigue Life for 3D Geometry obtained from Fe-Safe

3.2 Discussion. - Linear hexahedral elements of type C3D8R are used for the Meshing of 3D geometry. The total number of elements and nodes are 12640 and 17613. The boundary conditions are applied in such a way that the plate end opposite to the applied load is fixed while the other top and bottom ends are allowed to move in the direction of applied stress regarding **Figure 10**. From **Figure 14**, the most crucial region exists on the main plate where the value of Von Mises stress is 680 MPa. It is on element 7311 having node 965. So, one can say that a joint failure will occur on that element. But it is not on the same element as shown by **Figure 15**. According to this, element 5211 with node 20 has minimum Log Life which means that failure occurs on that element, not on element 7311. This element lies in the fixed end region as is clear in **Figure 15**. Log Life repeats are used for representing the number of cycles to failure. The minimum value of Log Life shows that such element or region will fail earlier than other elements or regions of a structure. Hence, as a result, structure damage occurs after a certain number of repetitions of the applied load. **Table 5** contains outcomes for each applied load.

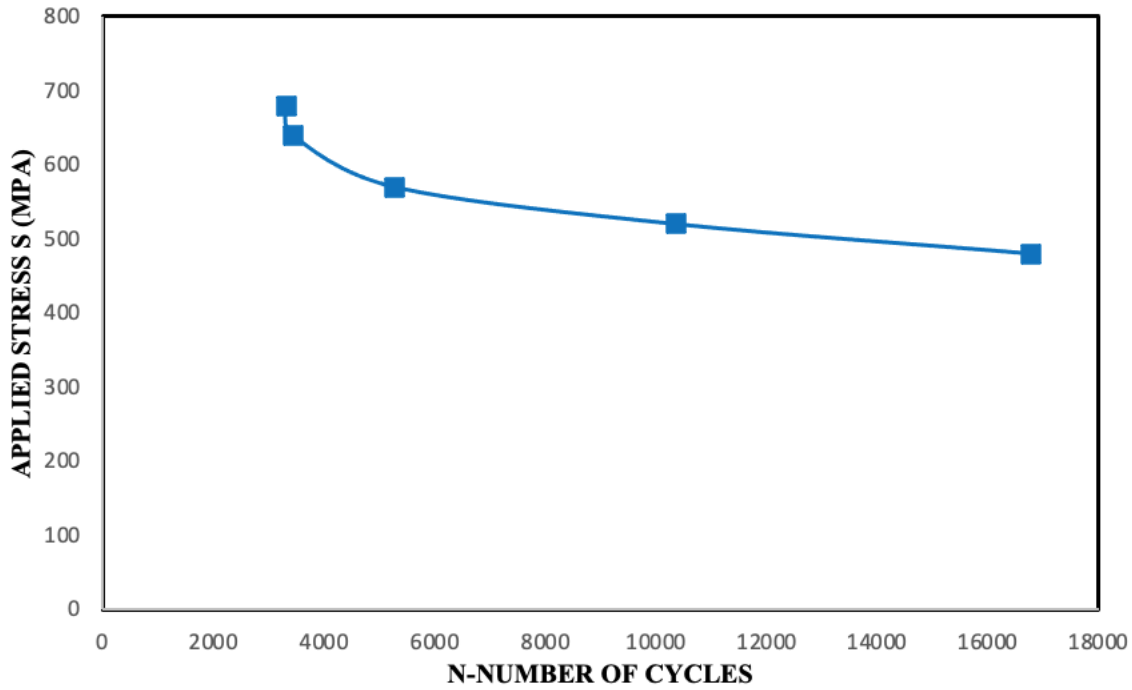

Figure XVI. SN-Curve for 3D Geometry of Joint

Results for 3D Geometry	
Applied Stress (MPa)	No. of Repeats
480	16773.326
520	10354.495
570	5281.393
640	3448.218
680	3318.614

Table V. Number of Repeats for each Applied Load on 3D Geometry

Using values of **Table V**, a graph is made to represent SN-Curve for 3D geometry of Cruciform joint. See **Figure XVI**.

3.3 Results of 2D Geometry. - For 2D geometry, the axial load applied ranges from 100 to 500 MPa with an equal difference of 100 MPa. But, for each case, only the outcomes obtained after applying maximum load i.e. 500 MPa are shown in the following figures. It is chosen because, at maximum value, it is better to study the structural changes occurred in the joint to show extreme behavior at higher loading condition. See **Figure XVII** for results obtained from elastic-plastic FEA in ABAQUS and **Figure XVIII** for the number of cycles got from Fe-Safe.

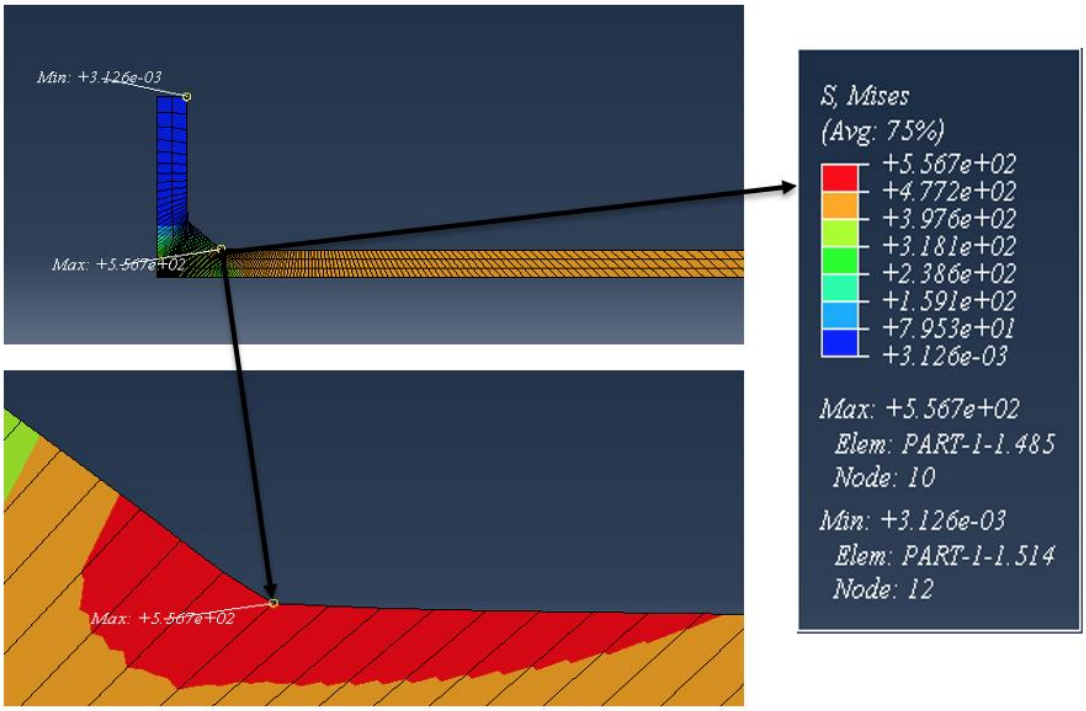

Figure XVII. Contour of Axial Load of 500 MPa from ABAQUS

3.4 Discussion. - Quadratic quadrilateral elements of type CPE8R are used for the Meshing of 2D geometry. The total number of elements and nodes are 547 and 2036. The boundary condition type 1 is such that in which 1/4th of 2D geometry is considered due to symmetry for elastic-plastic FEA and in which attached plate end opposite to applied stress is allowed to move in the vertical direction and the lower end of main plate is allowed to move in the horizontal direction. From **Figure XVII**, the most critical area exists on fillet weld toe where the value of Von Mises stress is 556.2 MPa. It is on element 485 having node 10. So, it is obvious to say that joint damage will occur to that element. And it is the same element as shown in **Figure XVIII**. According to this, element 485 with node 10 has minimum Log Life repeats which means that failure occurs on that element. This element lies in the weld toe region as is clear in **Figure XVIII**. Log Life repeats are used for signifying the number of cycles to failure. **Table VI** contains the results for each applied axial load.

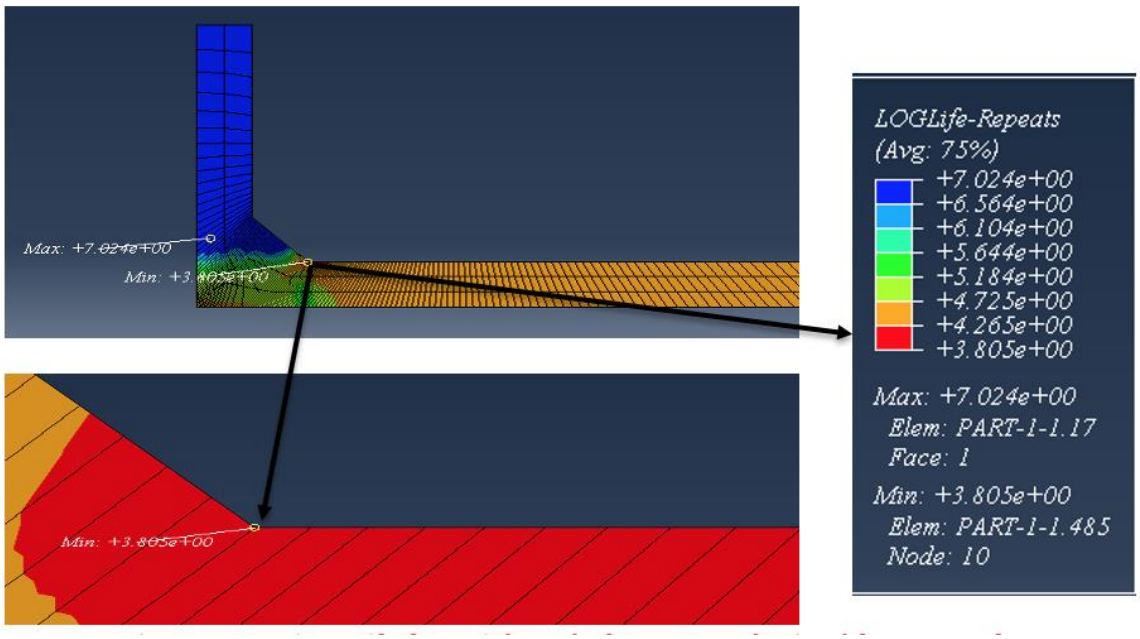

Figure XVIII. Fatigue Life for Axial Load of 500 MPa obtained from Fe-Safe

Results for Axial loading	
Applied Stress (MPa)	**No. of Repeats**
480	432123.5
520	347315.469
570	21706.598
640	6183.626
680	6141.355

Table VI. Number of Repeats for Axial Load on 2D Geometry

Using values of **Table VI**, SN-Curve for axial loading is made. See **Figure XIX**.

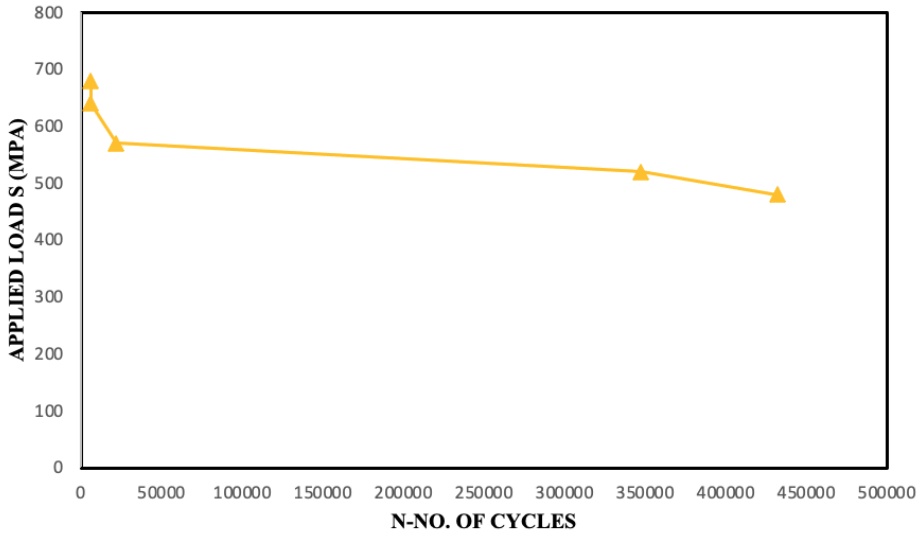

Figure XIX. SN-Curve for Axial loading applied 2D Geometry.

3.5 Comparison of Results (3D & 2D Geometry). - Comparison of results for 3D and 2D geometry is shown in **Figure XX** for better understanding of the trends of SN-curves. At load 480 MPa, there is large difference between number of cycles of both geometry and when becomes closer to 600 MPa, the curves for both begin coinciding with each other. It means both geometries show the same fatigue behavior at higher loadings when consider strain-based Brown Miller Model for fatigue estimation.

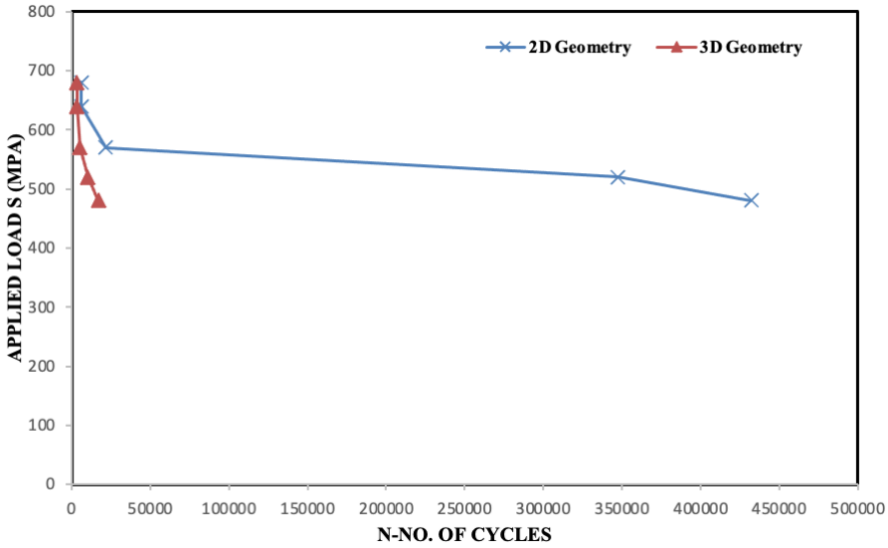

Figure 3: Comparison of Results

4. Validation Study. - For validation study of methodology, the data are taken from [38]. The data is composed of eight different geometrical configurations of welded Cruciform joints. Each joint has four welds with different horizontal and vertical dimensions. See **Figure XXI** for a 3D geometry description.

Dimensions of each weld detail for eight samples are given **Table VII**. The sample numbers used in that table are the same as in **Table II** of [11]. The width of the main plate is denoted by "L" and the thickness of the attached plates is indicated by "t". All the dimensions are in millimeters (mm).

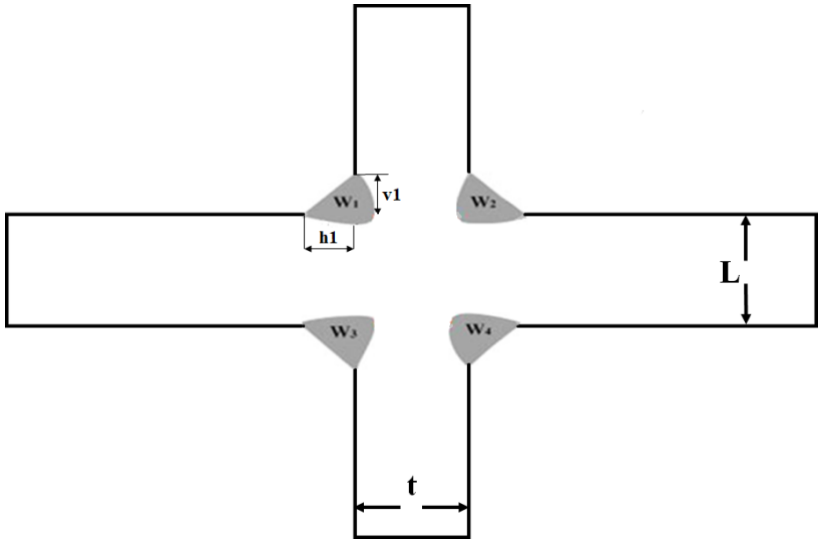

Figure XXI. Description of symbols used for geometry.

Sample No.	Weld 1 (mm)		Weld 2 (mm)		Weld 3 (mm)		Weld 4 (mm)		L	t
	h1	v1	h2	v2	h3	v3	h4	v4	(mm)	(mm)
19	8.13	8.52	7.25	8.6	8.5	8.62	7.8	9.63	35	12
6	10.27	10.36	9.82	11.56	9.9	11.9	8.85	10.21	35	12
5	10.57	10.52	10.11	12.94	10.08	12.08	9.05	9.87	35	12
4	10.19	10.21	10.56	11.89	10.49	11.38	8.82	9.9	35	12
18	8.89	12.33	6.91	10.94	10.49	11.1	10.8	11.93	35	12
3	10.27	10.36	9.82	11.56	9.9	11.9	8.85	10.21	35	12
2	10.57	10.52	10.11	12.94	10.08	12.08	9.05	9.87	35	12
1	10.19	10.21	10.56	11.89	10.49	11.38	8.82	9.9	35	12

Table VII. Details of Eight Samples used for the validation study

4.1 Experimental Data. - Experimental data contain the number of fatigue cycles, location of the fracture, and applied loads concerning each sample mentioned in **Table VII**. Experimental data are given in **Table VIII**.

Sample Number	Cases	Applied Load (MPa)	Fatigue Cycles	Fracture Location
19	C1	100	320500	Weld Root
6	C2	200	224700	Weld Toe
5	C3	240	129600	Weld Toe
4	C4	280	56580	Weld Toe

18	C5	305	53500	Weld Toe
3	C6	320	46800	Weld Toe
2	C7	360	37800	Weld Toe
1	C8	400	21500	Weld Toe

Table VIII. Experimental data detail

A 250-KN electro-hydraulic servo testing machine MTS 809 coupled with a load-control condition was used to conduct higher cycle fatigue experimentations of load-carrying Cruciform joint.

4.2 Material for Joint. - The SAE 1045 is the material used in this study. It is mild carbon steel that is widely utilized in a variety of industries. Axles, bolts, connecting rods, pins, studs, shafts, spindles, and other similar uses are common. It is obvious that these parts are frequently subjected to repeated loading. As a result, increasing the fatigue resistance of SAE 1045 appears to be necessary. SAE 1045's chemical composition is obtained from [33] and is presented in **Table IX**.

Constituents	Carbon	Silicon	Manganese	Phosphorus	Sulfur	Iron
Weight %	0.423	0.20	0.56	0.008	0.02	rest

Table IX. SAE 1045 Chemical Composition

The monotonic characteristics are achieved [34] by utilizing a 25 KN servo-hydraulic machinery to perform a uniaxial cycle test with a stress ratio of R = -1. During the test, a 2-mm strain gauge was affixed to the specimen to gather strain events. See **Table X** for SAE 1045 monotonic properties.

Properties	**Values**
Ultimate Tensile Stress (σ_u)	798 MPa
Yield Stress (σ_y)	414 MPa
Young's Modulus (E)	198 MPa

Table X. SAE 1045 Monotonic Properties

Following that, a cycle test [34] was performed at various percentages of UTS (ultimate tensile strength) acquired from the preceding tensile test. The percentages used are 60, 65, 70, 80, and 85 percent. As a result, five various stress values were used to capture failure time and strain range readings. See **Table XI** for more information.

Applied Stress (MPa)	**Strain Ranges ($\mu\varepsilon$)**
480 (60 % of UTS)	2294
520 (65 % of UTS)	3200
570 (70 % of UTS)	4059
640 (80 % of UTS)	4565
680 (85 % of UTS)	5800

Table XI. Applied Stresses for Cyclic Test and Strain Ranges

4.3 Conducting Elastic-Plastic FEA. - ABAQUS is used for elastic-plastic finite element analysis. First, the 3D geometry of a cruciform joint is created in ABAQUS using the Sketch and Feature tools. Static General STEP is built for plastic analysis after specifying the elastic and plastic material characteristics of SAE 1045. In the current case, eight distinct types of geometrical configurations are investigated for fatigue cycles, for loading values of 100, 200, 240, 280, 305, 320, 360, and 400 for the same boundary condition. For Meshing, an 8-node linear hexahedral element of type C3D8R with reduced integration is utilized. The whole flow diagram of boundary and loading conditions can be seen in **Figure XXII**. The right and left ends are allowed to move in x, y and z direction while all rotations are forbidden. On the upper and lower end of the joint load is applied. The loading nature is cyclic tensile, and zero weld penetration is considered because of the technique of wire electrode cutting [11]. All eight configurations were made separately keeping the other dimensions constant.

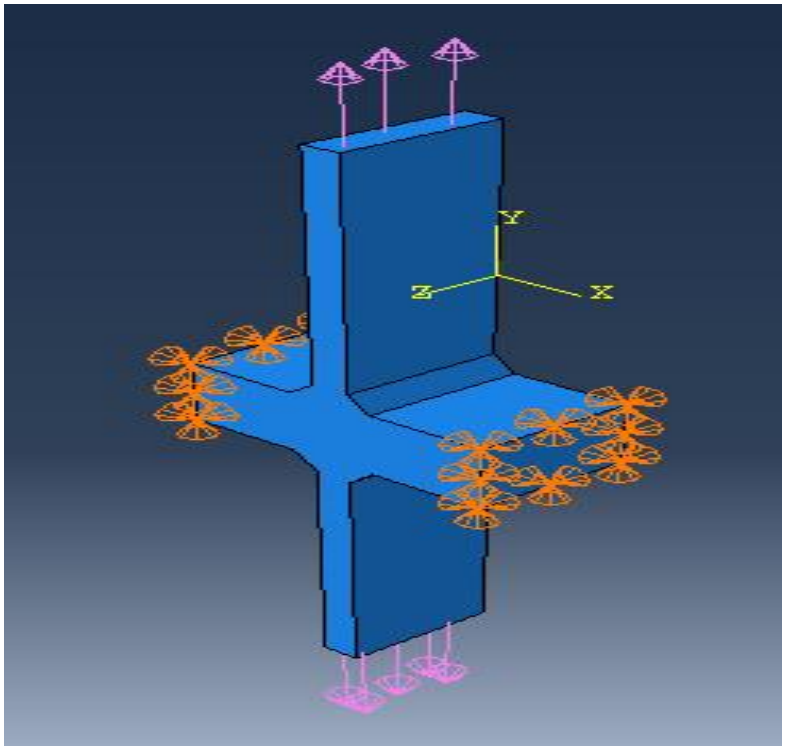

Figure XXII. Loading and boundary conditions on cruciform joint.

4.4 Fatigue Analysis Using Fe-Safe. - Fe-safe is the industry's first commercially accessible fatigue analysis program that focuses on current multiaxial strain-based fatigue methodologies. The schematic illustration of fatigue analysis utilizing ABAQUS and Fe-Safe is shown in **Figure XXIII**. It is known for its accuracy, speed, and ease of use when analyzing metals, rubber, thermo-mechanical and creep fatigue, and welded joints. Fe-Safe is a robust, all-inclusive, and user-friendly packages of fatigue analysis tools for finite element models [37]. The worst life repeats represent the number of cycles to failure for estimation of fatigue life of joint.

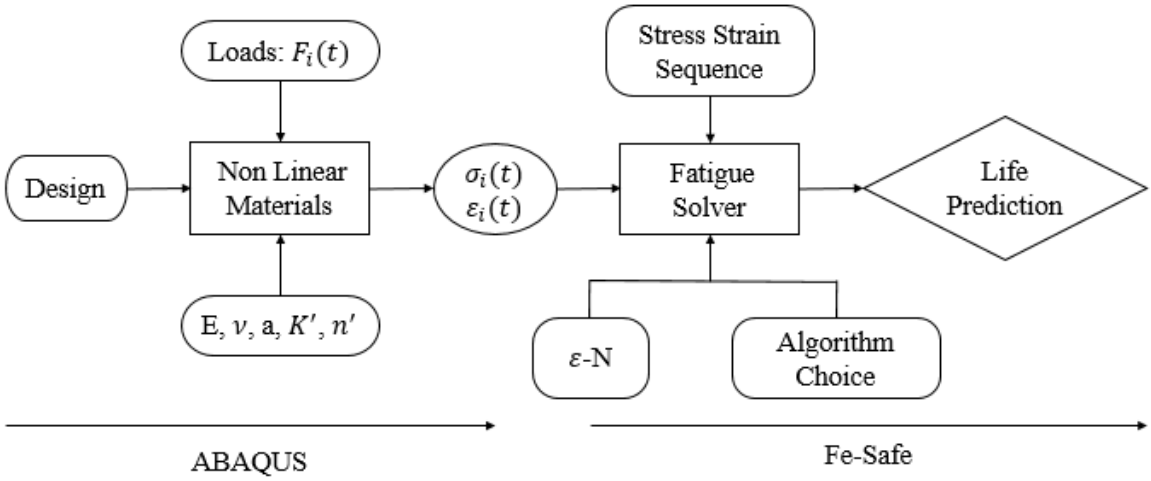

Figure XXIII. Fatigue analysis using ABAQUS and Fe-Safe

4.5 Simulation Results. - The simulated results are shown in the form of Log Life repeats contours. **Figure XXIV** contains contours of each eight configurations for their respective loadings i.e., 100, 200, 240, 280, 305, 320, 360, 400 MPa. Each contour indicated the region in which minimum Log Life repeats occur with a highlighted area. For all cases, the fatigue damage location is not the same because of the irregular or nonlinear plastic nature of the material. After that, **Table XII** is made to show the differences between the simulated and experimental number of cycles, percentage errors, and the failure locations for eight samples. Finally, **Figure XXV** shows a graph representing both simulated and experimental curves.

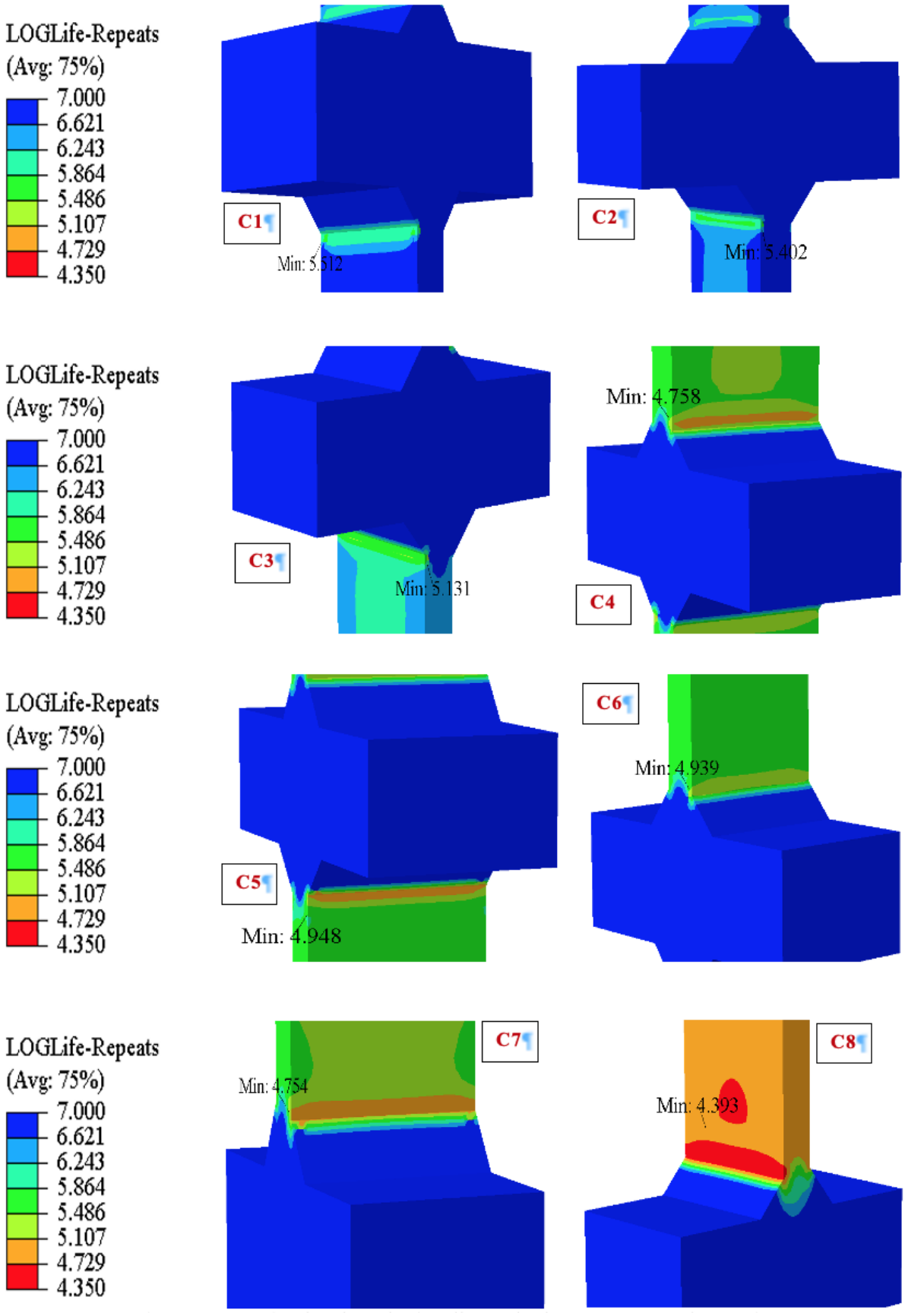

Figure XXIV. Simulated results for all samples by ABAQUS and Fe-Safe

Sample Number	Applied Load (MPa)	Simulated Cycles	Experimental Cycles	% Error	Fracture Location
19	100	324776	320500	1.316	Weld 3 Toe on the lower plate
6	200	234804	224700	4.303	A little bit below of Weld 4 Toe on the lower plate
5	240	135127	129600	4.090	Weld 4 Toe on the lower plate
4	280	57215	56580	1.109	On upper Plate above Weld 2
18	305	56794	53500	5.799	Lower Plate below weld 3
3	320	50186	46800	6.746	The backside of the upper plate above weld 1
2	360	38610	37800	2.097	The backside of the upper plate above weld 1
1	400	21648	21500	0.683	Near to back end on the upper plate

Table XII. Detail of Simulations for Eight samples.

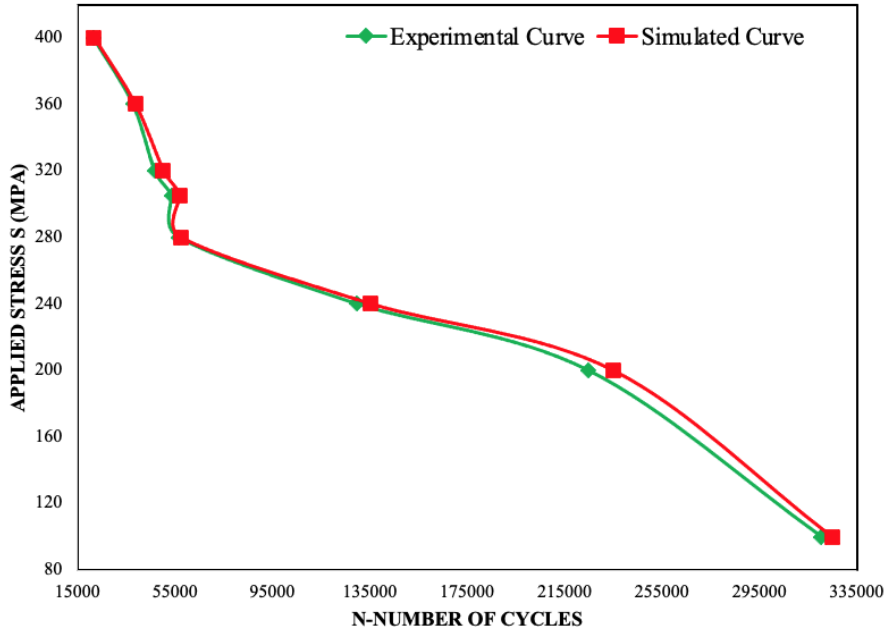

Figure XXV. Simulated and Experimental SN-Curve

5. Conclusions. - The conclusions for 3D geometry, 2D geometry and validation study are as follows:

5.1 3D Geometry. –

- The fatigue failure occurs on that element that did not lie on the lower surface of the main plate. Rather, it lied on the fixed end of the main plate.
- Although the whole plate is under extreme loading as shown in **Figure XIV**, the accumulated effect of applied load cause failure only on the element of the fixed end side.
- As stated, earlier results of only the higher loadings were displayed, so, it may be possible that in other cases the element of failure would not be the same.

- The SN-Curve for 3D geometry shows large differences in the number of repeats for small loading values i.e., from 480 to 640 MPa.
- When the load of 680 MPa was applied, the fatigue damage occurred rapidly after a few repeats showing a very small difference as compared to previous values.
- The abrupt fatigue failure due to large load is also making the sense of corresponding to larger load applications.

5.2 2D Geometry. –

- The applied load causes tension in the weld joint; opposite to the case of 3D geometry, in which applied load cause compression.
- The most affected zone due to tension is at the weld toe. The same region is also highlighted by Fe-Safe results.
- The SN-Curve for this case showed huge differences between the number of repeats when the applied loads were small.
- The difference became small as the load exceeded 500 MPa indicating the occurrence of fatigue damage after a few thousand repeats as compared to small loads.
- This is true because higher loads cause faster plastic deformation accompanied by large strains.

5.3 Validation Study. - Following are the key findings with reference to **Table XII** and **Figure XXV**:

- The simulated results show that the fracture locations are different for most of the samples from the region obtained by experimental results.
- The number of cycles attained after the simulation is greater than the experimental for each sample.
- Most of the fracture locations are identified near the weld toes region except for toes of weld 3 and weld 4.
- No weld root failure has been identified for any weld and no failure occurs for toes of weld 1 and weld 2.
- The lower plate is in a severe situation because weld 3 and weld 4 are located on lower plate, joining the main plate.
- Since no fracture occurred on weld 1 and weld 2, the most crucial region for upper plate is the backside of the plate.
- No fracture occurred on the main plate and toes of welds situated on the main plate because loading is tensile causing fracture on weld toes situated on upper & lower plates and on the lower & upper plates separately.
- The graph in **Figure 25** shows that at higher loads, fatigue failure occurs after few thousand repeats due to abrupt plasticity behavior in material and for lower loads, it takes more than 3 lacs repeats.
- The lowest % error is 0.683 for Sample 1 with 400 MPa load and maximum % error is 6.746 for Sample 3 with 320 MPa load after simulation.
- As the % error is less than 10 % for all cases, it shows that the simulated results by ABAQUS and Fe-Safe are in acceptable range.

6. Recommendations. - Recommendations for improving designs of load carrying cruciform joints (LCJs) and for future research directions are as follows:

6.1 Improving Design of Load Carrying Cruciform Joints. -

- Increasing the radius of the weld toe helps minimize stress concentration, which is a typical site for fracture development.
- Adjusting weld leg length helps equally distribute loads throughout the joint and reduce localized stress concentrations.
- Weld reinforcement, like thicker welds or fillet connections, can improve joint strength.
- High-quality welding techniques, including joint preparation, weld parameters that are and post-weld examination, can reduce weld faults that cause stress.
- Applying post-weld procedures, such as peening or thermal treatment, can lower residual stresses in the connecting surfaces and prevent early fatigue cracks.

6.2 Future Research Directions. -

- Consider using modern materials like high-strength steels, aluminum alloys, as well as fiber-reinforced composites to manufacture cruciform joints.
- Investigate how material parameters, which include the tensile strength, yield strength, and resistance to fatigue, affect joint load-carrying capability and fatigue life.
- Incorporate more complicated loading situations, such as coupled axial, bending, as well as torsional loads, that ship constructions often face.
- Use sophisticated fatigue analysis approaches, such as critical plane techniques or energy-based theories, to properly simulate joint performance for multi-axial fatigue loading.
- Investigate how environmental factors such corrosive sea environments, temperature changes, and weathering impact the functionality and endurance of cruciform joints.
- Understand how additive manufacturing (AM) methods, such 3D printing, may be used to create cruciform joints with customizable attributes and increased geometric complexity.
- Investigate how AM-specific factors, including roughness of the surface and residual stresses, affect joint's mechanical efficiency and fatigue life.

References

[1] D. W. a. J. L. Chuntong Li, "Numerical analysis and experimental study on the scaled model of a container ship lashing bridge," Ocean Engineering, vol. 201, no. March, p. 107095, 2020.

[2] K. Y. L. P. a. Y. G. Jingxia Yue, "A frequency-time domain method for ship fatigue damage assessment," Ocean Engineering, vol. 220, no. August 2020, p. 108154, 2021.

[3] W. Fricke, "Fatigue and Fracture of Ship Structures," Encyclopedia of Maritime and Offshore Engineering, pp. 1-12, 2017.

[4] A. P. MSP. Raju, "A Study on Common Ship Structural Failures," International Journal of Mechanical Engineering and Technology, vol. 9, no. 7, pp. 746-754, 2018.

[5] K. H. Yang, "Chapter 2 - Meshing, Element Types, and Element Shape Functions," in Basic Finite Element Method as Applied to Injury Biomechanics, K. Yang, Ed., Academic Press, 2018, pp. 51-109.

[6] S. V. B. P. Shwetha K, "Comparison Between Thin Plate And Thick Plate From Navier Solution Using Matlab Software," International Research Journal of Engineering and Technology, vol. 05, no. 06, pp. 2675-2680, June 2018.

[7] A. Risitano, "Welded Joints," in Mechanical Design, CRC Press, 2011, pp. 463-486.

[8] J. K. Janusz Kozak, "The Influence of Manufacturing Oversizing on Postwelding Distortions of the Fillet Welded Joint," Polish Maritime Research, vol. 22, no. 4, pp. 59-63, 2015.

[9] S. Chakraborty, "Common Welding Methods And Weld Defects In Shipbuilding Industry," Marine Insight, 9 July 2021. [Online]. Available: https://www.marineinsight.com/naval-architecture/common-welding-methods-weld-defects-shipbuilding-industry/.

[10] B.-S. J. a. S.-W. K. Tae-Jun Kim, "Welding Deformation Analysis Based on Improved Equivalent Strain Method to Cover External Constraint During Cooling Stage," International Journal of Naval Architecture and Ocean Engineering, vol. 7, no. 5, pp. 805-816, 2015.

[11] X. L. a. S. R. Wei Song, "Fatigue assessment of steel load-carrying cruciform welded joints by means of local approaches," Fatigue & Fracture of Engineering Materials and Structures, vol. 41, no. 12, pp. 2598-2613, 2018.

[12] Wikipedia, "Welding Joint," 1 January 2021. [Online]. Available: https://en.wikipedia.org/wiki/Welding_joint#cite_note-7.

[13] N. T. T. Y. A. T. a. A. Y. Iwata Toshiaki, "Thickness effect on fatigue strength of welded joint improved by HFMI," Yosetsu Gakkai Ronbunshu/Quarterly Journal of the Japan Welding Society, vol. 34, no. 4, pp. 249-259, 2016.

[14] J. S. Zuheir Barsoum, "Fatigue assessment of cruciform joints welded with different methods," Steel Research International, vol. 77, no. 12, pp. 882-888, 2006.

[15] T. a. C. K.Saiprasertkit, "Experimental study of load-carrying cruciform joints containing incomplete penetration and strength under-matching in low and high cycle fatigue regions," Procedia Engineering, vol. 14, pp. 572-581, 2011.

[16] T. O. a. Y. K. Kazuki Tatsuta, "A study on the size effect of cruciform joint for fatigue strength subjected to bending and axial stress," in Japan Society of Naval Architects Lecture Proceedings No. 22, 2016.

[17] P. G. J. J. J. R. a. P. L. Heikki Remesa, "Fatigue strength modelling of high-performing welded joints," International Journal of Fatigue, vol. 135, no. February, p. 105555, 2020.

[18] X. F. P. a. H. W.Song, "Fatigue failure transition analysis in load-carrying cruciform welded joints based on strain energy density approach," Fatigue and Fracture of Engineering Materials and Structures, vol. 40, no. 7, pp. 1164-1177, 2017.

[19] W. a. C. C.Fischer, "Fatigue assessment of web-stiffened corners in plated structures by local approaches," Ship Technology Research, vol. 65, no. 2, pp. 69-78, 2018.

[20] X. L. Wei Song, "High cycle fatigue assessment of steel load-carrying cruciform welded joints: An overview of

recent results," Frattura ed Integrita Strutturale, vol. 12, no. 46, pp. 94-101, 2018.

[21] N. A. Oscar Araque, "Weld magnification factor approach in cruciform joints considering postwelding cooling medium and weld size," Materials, vol. 11, no. 81, pp. 1-18, 2018.

[22] N. O. Toru Shiratsuchia, "Investigation of thickness and bead profile effects on fatigue strength of welded joints based on relative stress gradient," International Journal of Fatigue, vol. 134, no. February, p. 105520, 2020.

[23] Y. L. a. S. T. Yixun Wang, "Parametric formula for stress concentration factor of fillet weld joints with spline bead profile," Materials, vol. 13, no. 9, p. 4639, 2020.

[24] P. T. a. G. G. Krzysztof L.Molski, "Stress concentration at cruciform welded joints under axial and bending loading modes," Welding in the World, vol. 64, no. 11, pp. 1867-1876, 2020.

[25] K.-H. C. a. S. M. Wang Sub Shin, "Fatigue analysis of cruciform welded joint with weld penetration defects," Engineering Failure Analysis, vol. 120, no. November 2020, 2021.

[26] D. S. G. R. F. B. Pietro Foti, "Fatigue assessment of cruciform joints Comparison between Strain Energy Density predictions and current standards and recommendations," Engineering Structures, vol. 230, no. November 2020, 2021.

[27] Z. D. J. C. X. J. J. D. Yang Peng, "Fatigue behaviour of load-carrying fillet-welded cruciform joints of austenitic stainless steel," Journal of Constructional Steel Research, vol. 2021, 2021.

[28] P. W. a. H. F. Jianxiao Ma, "Fatigue life of 7005 aluminum alloy cruciform joint considering welding residual stress," Materials, vol. 14, no. 5, pp. 1-20, 2021.

[29] X. L. a. S. T. L. Haisheng Zhao, "Fracture analysis of load-carrying cruciform welded joint with a surface crack at weld toe," Engineering Fracture Mechanics, vol. 241, no. July 2020, pp. 1-21, 2021.

[30] X. L. G. Z. S. W. D. S. M. H. a. F. B. Wei Song, "Notch energy-based low and high cycle fatigue assessment of load-carrying cruciform welded joints considering the strength mismatch," International Journal of Fatigue, vol. 151, p. 106410, 2021.

[31] M. D. A. A. a. T. B. Hamidreza Rohani Raftar, "Re-evaluation of weld root fatigue strength for load-carrying fillet welded joints using the notch stress concept," International Journal of Fatigue, vol. 144, no. November 2020, 2021.

[32] W. W. R. F. P. Z. a. Y. D. Zhiyu Jie, "Stress intensity factor and fatigue analysis of cracked cruciform welded joints strengthened by CFRP sheets considering the welding residual stress," Thin Walled Structures, vol. 154, 2020.

[33] N. Y. A. E. Sasan Yazdani, "Enhancement of fatigue strength of SAE 1045 steel by tempering treatment and shot peening," Materials Science Forum, Vols. 561-565, no. PART 1, pp. 41-44, 2007.

[34] S. A. N. J. O. I. Mazian Mohammad, "Fatigue life assessment of SAE 1045 carbon steel under strain events using the Weibull distribution," Journal of Mechanical Engineering, vol. 5, no. Specialissue 1, pp. 165-180, 2018.

[35] D. S. SIMULIA, "Chapter 7 - Biaxial Fatigue," in Fatigue Theory Reference Manual, Dasault Systems, 2021, pp. 1-57.

[36] D. S. SIMULIA, "Chapter 14 - Fatigue Analysis of Elastic FEA Results," in Fe-Safe 2019 User Guide, Dasault Systems, 2018, pp. 1-26.

[37] D. S. SIMULIA, "Chapter 1 - Introduction," in Fe-Safe 2019 User Guide, Dasault Systems, 2018, pp. 1-6.

[38] X. L. S. Wei Song, "Fatigue assessment of steel load-carrying cruciform welded joints by means of local approaches," Fatigue and Fracture of Engineering Materials and Structures, vol. 41, no. 12, pp. 2598-2613, 2018.

Nota contribución de los autores:

1. Concepción y diseño del estudio
2. Adquisición de datos
3. Análisis de datos
4. Discusión de los resultados
5. Redacción del manuscrito
6. Aprobación de la versión final del manuscrito

ZMM ha contribuido en: 1, 2, 3, 4, 5 y 6.
MA ha contribuido en: 1, 2, 3, 4, 5 y 6.
SAAZ ha contribuido en: 1, 2, 3, 4, 5 y 6.

Nota de aceptación: Este artículo fue aprobado por los editores de la revista Dr. Rafael Sotelo y Mag. Ing. Fernando A. Hernández Gobertti.

Efectos Del Envejecimiento Estructural durante la Vida Útil de Edificios: Caso de Estudio de un Edificio Educativo

Effects of Structural Aging during the Useful Life of Buildings: Case Study of an Educational Building

Efeitos do Envelhecimento Estrutural durante a Vida Útil dos Edifícios: Estudo de Caso de um Edifício Educacional

Fernando Aguirre Camacho[1], Fernando Treviño Montemayor[2], Carlos Alberto Hoyos Castellanos[3(*)], Martín Eduardo García Avilanes[4]

Recibido: 21/02/2024 Aceptado: 08/03/2024

Resumen. - Este artículo presenta los resultados desarrollados en el Instituto Tecnológico de Tepic con el propósito de realizar un dictamen estructural del edificio "Q". Su finalidad fue evaluar las condiciones estructurales del edificio generadas por el uso de este, las cuales pueden ser causal para comprometer la seguridad del edificio, y por lo tanto del personal del Instituto y sus estudiantes como sus usuarios cotidianos. Se discute la culminación del periodo de su vida útil y las características de su envejecimiento. El inmueble en cuestión fue construido en el año 1976, su diseño original fue a base de marcos rígidos de acero estructural, con columnas a base de placas en sección cajón de diversos calibres, utilizando soldaduras en las uniones de los elementos estructurales. Este inmueble corresponde a un modelo de edificio "tipo" diseñado en el año 1966 para el Comité Administrador del Programa Federal de Construcción de Escuelas (CAPFCE).

En el análisis de las condiciones del edificio se emplearon diversas técnicas para determinar deformaciones, asentamientos, y deterioros en general de los materiales que comprenden la estructura del edificio, encontrando a simple vista alteraciones en algunos elementos estructurales. Se concluye finalmente que a pesar de que el edificio estructuralmente se puede conservar realizando algunas acciones de reparación y mantenimiento, su diseño estructural no cumplía las especificaciones de las normativas actuales, por lo que el organismo responsable de la construcción de la infraestructura educativa determinó que la única solución viable era la demolición total del inmueble y su construcción nueva.

Palabras clave: Envejecimiento de edificios, Seguridad Estructural, Dictamen estructural, Vida útil.

(*) Autor Corresponsal

[1] Maestro en Ingeniería línea terminal en construcción. Tecnológico Nacional de México, plantel Instituto Tecnológico de Tepic, faguirre@ittepic.edu.mx ORCID: https://orcid.org/0000-0001-5965-1375

[2] Maestro en Estructuras. Tecnológico Nacional de México, plantel Instituto Tecnológico de Tepic, ftrevino@ittepic.edu.mx, ORCID: https://orcid.org/0000-0003-3924-7660

[3] Maestro en Ciencias en Ciencias Computacionales. Tecnológico Nacional de México, plantel Instituto Tecnológico de Tepic, hoyoscarlos@ittepic.edu.mx, ORCID: https://orcid.org/0000-0001-5965-1375

[4] Ingeniero Civil. Tecnológico Nacional de México, plantel Instituto Tecnológico de Tepic, mgarciaa@ittepic.edu.mx ORCID: https://orcid.org/0009-0008-5238-5033

Memoria Investigaciones en Ingeniería, núm. 26 (2024). pp. 125-142
https://doi.org/10.36561/ING.26.8
ISSN 2301-1092 • ISSN (en línea) 2301-1106 – Universidad de Montevideo, Uruguay

Summary. - *This article presents the results developed at the Instituto Tecnológico de Tepic with the purpose of carrying out a structural opinion of the "Q" building. Its purpose was to evaluate the structural conditions of the building generated by its use, which may be a cause for compromising the safety of the building, and therefore of the Institute's staff and its students as its daily users. The culmination of the period of its useful life and the characteristics of its aging are discussed. The property in question was built in 1976, its original design was based on rigid structural steel frames, with columns based on box section plates of various calibers, using welding at the joints of the structural elements. This property corresponds to a "type" building model designed in 1966 for the Administrative Committee of the Federal School Construction Program (CAPFCE).*

In the analysis of the conditions of the building, various techniques were used to determine deformations, settlements, and general deterioration of the materials that comprise the structure of the building, finding alterations in some structural elements with the naked eye. It is finally concluded that although the building can be structurally preserved by carrying out some repair and maintenance actions, its structural design did not meet the specifications of the current regulations, so the body responsible for the construction of the educational infrastructure determined that the The only viable solution was the total demolition of the property and its new construction.

Keywords: *Aging of buildings, Structural Safety, Structural opinion, Useful life.*

Resumo *. - Este artigo apresenta os resultados desenvolvidos no Instituto Tecnológico Tepic com o objetivo de realizar um parecer estrutural do edifício "Q". Seu objetivo foi avaliar as condições estruturais do edifício geradas pela sua utilização, que podem ser causa de comprometimento da segurança do edifício e, portanto, dos funcionários do Instituto e de seus alunos como seus usuários diários. Discute-se o culminar do período da sua vida útil e as características do seu envelhecimento. O imóvel em questão foi construído em 1976, seu projeto original era baseado em pórticos estruturais rígidos de aço, com pilares assentes em placas de seção caixão de diversos calibres, utilizando soldagem nas juntas dos elementos estruturais. Este imóvel corresponde a um modelo de edifício "tipo" projetado em 1966 para o Comitê Gestor do Programa Federal de Construção de Escolas (CAPFCE).*

Na análise das condições do edifício foram utilizadas diversas técnicas para determinar deformações, recalques e deterioração geral dos materiais que compõem a estrutura do edifício, encontrando a olho nu alterações em alguns elementos estruturais. Conclui-se, por fim, que embora o edifício possa ser preservado estruturalmente através da realização de algumas ações de reparação e manutenção, o seu projeto estrutural não atendeu às especificações da regulamentação em vigor, pelo que o órgão responsável pela construção da infraestrutura educativa determinou que o único A solução viável foi a demolição total do imóvel e sua nova construção.

Palavras-chave: *Envelhecimento de edifícios, Segurança Estrutural, Parecer estrutural, Vida útil.*

1. Introducción. - En este dictamen técnico se muestran los resultados de la investigación realizada para determinar aptitud estructural para continuar en servicio del inmueble de dos niveles, denominado Edificio "Q", ubicado dentro de las instalaciones del Instituto Tecnológico de Tepic, con la finalidad de recabar la información necesaria para evaluar si este en su conjunto, o alguno de sus elementos estructurales llegaron al fin de su vida útil.
La vida útil es entendida como el periodo después de la construcción y/o instalación durante el cual el edificio y sus partes cumplen o exceden los requerimientos de rendimiento para lo cual fueron diseñados y construidos [5].
Con el paso del tiempo los edificios sufren deterioros, sus materiales se degradan y consumen su vida útil, este proceso depende de la calidad estructural y constructiva, así como de su mantenimiento, sin dejar a un lado el uso que se le dé y a las condiciones externas a que sea sometido.
Los factores principales que intervienen en el envejecimiento de los edificios pueden clasificarse en factores constructivos, mantenimiento y agentes ambientales exteriores e internos.
Dentro de la investigación para determinar las características del envejecimiento del edificio Q, se realizaron una serie de inspecciones a los elementos estructurales del inmueble, incluyendo las condiciones del acero y sus soldaduras en columnas y vigas, calidad y resistencia del concreto, y evaluaciones en búsqueda de deformaciones y asentamientos.
Cabe destacar la importancia que tiene una oportuna evaluación de manera exhaustiva de las condiciones estructurales del edificio en cuestión, pues conlleva la seguridad de al menos mil personas entre estudiantes, docentes y trabajadores administrativos que a diario hacen uso de este inmueble.

1.1 Descripción del inmueble. - El inmueble se encuentra ubicado dentro de las instalaciones del Tecnológico Nacional de México, plantel Instituto Tecnológico de Tepic, con dirección Avenida Tecnológico #2595, Colonia Lagos del Country, Tepic, Nayarit., México. C.P. 63175.
Se tiene el registro que el edificio en cuestión se construyó en el año de 1976, lo cual representa una vida útil de 47 años al tiempo de las inspecciones.

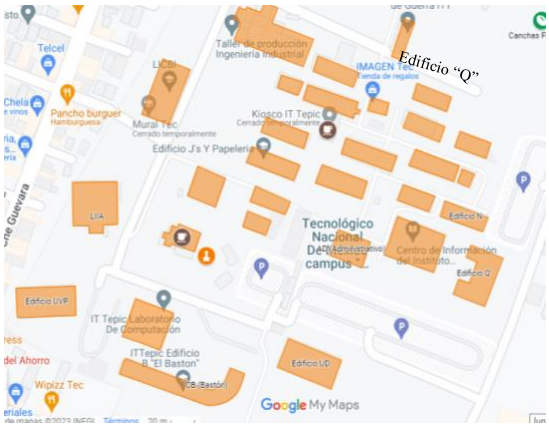

Figura I. Ubicación del edificio dentro de las instalaciones del I. T. Tepic

Figura II. Edificio Q.

Es una construcción de dos niveles, estructura prefabricada consistente en marcos rígidos de acero armado a base de placas en sección cajón, con claros longitudinales de 3.05 m, uno de 4.00 m para el entre eje de escalera y un claro transversal de 8.00 m con voladizos de 2.10 y 0.80 metros en planta baja para andador y marquesina, y de 2.10 metros en la azotea como marquesinas. Las secciones de columnas, trabes y cerramientos son de diseño especial, en cajas formadas con placas de acero de diversos calibres. En nodos, las uniones son soldadas en su perímetro a todo alrededor. Las columnas en su parte inferior se unen a los dados de concreto por medio de anclas y tuercas. La losa de entrepiso y la cubierta de azotea son losas llenas de concreto reforzado, en donde esta última es a dos aguas, con una ligera pendiente del 3%. Los muros son de mampostería de tabique de barro, los cuales actúan como divisorios.
El último registro de mantenimiento que se tiene del edificio fue en el año 2019. Dentro de los conceptos realizados se llevó a cabo la limpieza e impermeabilización de azotea, así como el cambio de puertas multipanel y el recubrimiento con pintura de elementos estructurales, muros divisorios y losa del edificio.

2. Metodología. - Para evaluar el estado estructural y físico del edificio, se realizaron una serie de actividades de revisión al interior y exterior del inmueble evaluando sus condiciones estructurales para conocer el estado real y valorar el grado de riesgo en el que se encontraba la edificación. Se revisó la estructura del edificio, losas, trabes, columnas, pisos y muros.

2.1 Verificación física ocular. - Por las características del método, se buscaron signos evidentes de daño, tales como deflexiones, pandeos, colapsos parciales, inclinaciones, caída de pretiles, agrietamientos severos, entre otros efectos

del envejecimiento del edificio. En adición, se buscaron evidencias de fallas y peligros geotécnicos, como agrietamiento del suelo, asentamientos o indicios de movimiento de laderas, como lo sugieren las normas técnicas de INIFED. [1]

Se identificó el edificio, y se inició con un recorrido alrededor de la estructura con el fin de identificar daños previos a simple vista, como muros con posibles inclinaciones o peligro de desprendimiento, examinando si existen discontinuidades verticales, signos de daño en muros de fachada, fisuras y grietas, deflexiones, asentamientos o emergencias en la cimentación.
En la inspección dentro del edificio se buscaban las zonas visibles del sistema estructural, en especial daños a columnas, trabes, muros y losas. Se buscaron evidencias de columnas deformadas, desplomadas o con signos de daño, incluyendo la verificación de signos de daño en marcos, como pandeo local, general o fallas de conexiones en la unión viga columna.

2.2 Deformación en losas de concreto. - Las deformaciones que se producen dentro de una losa de concreto están determinadas por las condiciones de apoyo y por la posición relativa entre el plano medio y la dirección de las cargas. [3], junto con las cuantías y posición del acero de refuerzo y la calidad del concreto, aunado al historial de cargas permanentes.
Para determinar las deformaciones de las losas de concreto se identificaron los puntos de apoyo de las losas y su plano de deformación. En este caso los tramos de losa estudiados eran losas rectangulares con un volado de 3.06 metros.
Por medio de una estación total marca Leica TS02 se registraron los niveles de las losas en sus apoyos y su parte central (Fig. III), para detectar su deflexión por diferencia de niveles.

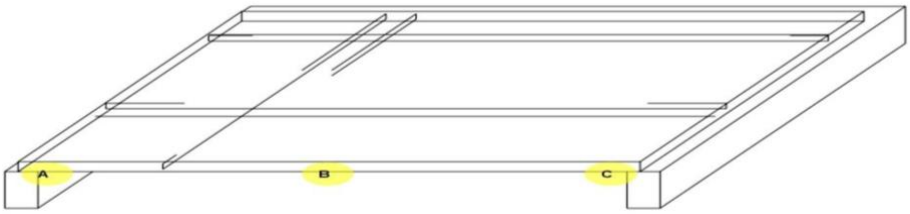

Figura III. Niveles de losa.

De acuerdo con la ACI 318S-05 referente a los Requisitos de Reglamento para Concreto Estructural se calcula la deflexión permisible, tomando en cuenta los criterios de la tabla de deflexión máxima admisible calculada. Utilizando la fórmula:

$$\frac{l}{240}$$

La cual refiere a un sistema de entrepiso o cubierta que soporte o esté ligado a elementos no estructurales no susceptibles de sufrir daños debido a deflexiones grandes, donde comprende la parte de la deflexión total que ocurre después de la unión de los elementos no estructurales (la suma de la deflexión a largo plazo debida a todas las cargas permanentes, y la deflexión inmediata debida a cualquier carga viva adicional).

Las losas presentan 306 centímetros de claro por lo que la deflexión máxima admisible presentada es:

$$\frac{l}{240} = \frac{306}{240} = 1.275cm$$

2.3 Asentamientos. - Para obtener un diagnóstico de asentamientos del edificio, se realizó un levantamiento topográfico donde se recabaron los niveles de diversos puntos representativos con el fin de buscar las diferencias entre ejes, los que se supone deberían encontrarse en la misma cota.

Se tomó a las columnas como punto referente para la toma de 3 diferentes niveles sobre estas, el primero a nivel de banqueta, el segundo en la axila que se genera en el entrepiso por el encuentro trabe columna y finalmente el tercero en la axila generada por trabe columna de la azotea (Fig. III). Este proceso se repitió en cada uno de los ejes de las columnas tanto en la parte frontal y posterior del edificio.

Al finalizar con la captura de datos se realizó un registro de diferencias de nivel entre los 3 diferentes grupos de cotas horizontales. Tomando en cuenta las normas técnicas complementarias sobre criterios y acciones para el diseño estructural de las edificaciones de la Ciudad de México se observó que los hundimientos diferenciales no excedieran los 2 cm.

Como criterio final se realizó una relación de la distorsión diferencial tolerable la cual refiere a la inclinación que experimenta un elemento estructural, utilizando como permisible para marcos de acero y tomando en cuenta el número de pisos del edificio:

$$Distorsión\ permisibles = 0.006(1.255 - 0.0636n)$$

n= número de pisos

$$Distorsión\ permisibles = 0.006(1.255 - 0.0636 * 2) = 0.0068$$

Y las distorsiones se calcularon a partir de:

$$Distorsión\ angular = \frac{Hundimiento\ diferencial}{Distancia\ entre\ cotas}$$

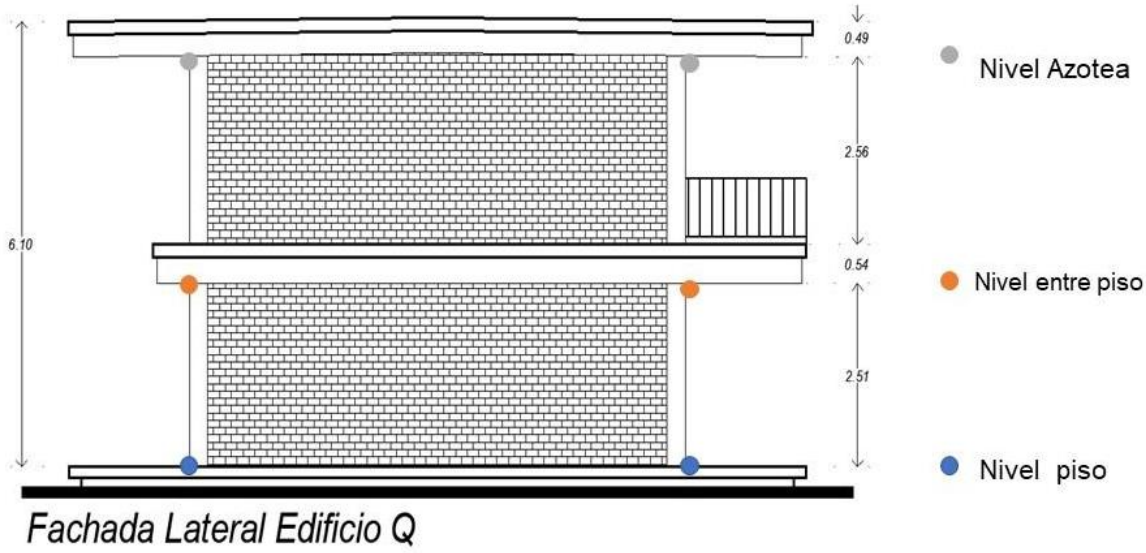

Figura IV. Cotas del edificio.

2.4 Resistencia del concreto. - A partir de la norma ASTM C42, se extrajeron dos núcleos de concreto (muestras, núcleos o corazones) directamente de la losa de entrepiso a través de un equipo de extracción mediante una broca hueca con borde diamantado, las muestras extraídas fueron dos cilindros con 20 centímetros de altura y cuatro pulgadas de diámetro.

Se determinó mediante el apoyo de pruebas de laboratorio la resistencia a la compresión del concreto (f'c), de acuerdo con la norma ASTM C39, este método de ensayo consistió en la aplicación de una carga de compresión uniaxial a los cilindros moldeados o núcleos a una velocidad de carga especificada (0.25 ± 0.05 MPa/s).

La máquina de ensayo se equipó con dos bloques de carga de acero, con caras endurecidas, una de las cuales es un bloque con asiento esférico y se apoyó en la parte superior del espécimen, y la otra fue un bloque sólido en el cual descansa el espécimen. Las caras de carga de los bloques tienen una dimensión mínima al menos 3 % mayor que el diámetro del espécimen a ser ensayado. Se cabecearon las dos caras de los corazones con un mortero de azufre fundido nivelado y perpendicular al eje del espécimen.

Durante la compresión se aplicó carga continuamente y sin impacto, hasta que el espécimen falló. Se tomó nota de la carga máxima soportada por el espécimen durante el ensayo, detectando tipo de falla y apariencia del concreto, para después realizar los cálculos necesarios para obtener el esfuerzo resistente a compresión de los especímenes a través de la relación de carga máxima soportada por el espécimen durante el ensayo entre el área de la sección transversal promedio determinada.


Figura V. Ensayo del primer espécimen.


Figura VI. Ensayo del segundo espécimen.

2.5 Carbonatación del concreto. - Se realizaron pruebas químicas al concreto hidráulico de la losa de entrepiso, en base a la NMX-C-515-ONNCCE-2016 se utilizó fenolftaleína al 1% en alcohol con el objetivo de determinar la calidad del concreto de las losas de entrepiso. La carbonatación en el concreto determina la pérdida de pH que ocurre cuando el dióxido de carbono atmosférico reacciona con la humedad dentro de los poros del concreto; dicho fenómeno puede causar problemas de corrosión del refuerzo incluso en un concreto de alta calidad. El ensayo consiste en aplicar el indicador a la superficie de la muestra de concreto, y dejar secar unos minutos, para posteriormente determinar la profundidad de la carbonatación. La reacción que se produce al entrar en contacto la fenolftaleína con el concreto es una coloración rosa oscura cuando está en presencia de un medio básico o de PH alto.

Figura VII. Muestras de concreto

Figura VIII. Solución de fenolftaleína

La prueba del indicador de fenolftaleína es recomendada sólo para establecer un estimado de la profundidad que ha alcanzado la carbonatación. Para llegar a una confirmación de este alcance es preciso la microscopía óptica o bien, la microscopía electrónica, incluso a profundidades superiores a las que evidencia la prueba cualitativa de la fenolftaleína. A través del microscopio se reconoce el fenómeno de carbonatación en el concreto por la presencia de cristales de calcita, y la ausencia de hidróxido de calcio, etringita y granos de cemento deshidratados. Cabe decir que la prueba del indicador de fenolftaleína resulta muy útil como un medio de hacer una evaluación inicial de la presencia de carbonatación en el concreto; es rápida, fácil de ejecutar y ampliamente utilizada en la actualidad. Algunas investigaciones sugieren que en el caso de un concreto más poroso y permeable, en cuya mezcla se haya utilizado una elevada relación agua/cemento, el fenómeno de la carbonatación puede presentarse a razón de hasta 5 mm por año [6]. La parte que toma el color rosáceo no está carbonatada, en cambio la zona que no cambia de color está invadida de carbono.


Figura IX. Aplicación de fenolftaleína al 1% en alcohol en muestras de concreto.

2.6 Oxidación por diferencia de pesos. - Para determinar el daño que se tenía en el acero de refuerzo, en este caso varillas de 3/8" de diámetro (0.95 cm); se obtuvieron muestras de varillas provenientes del concreto armado de la edificación. Se clasificaron a simple vista en varillas sanas (que son las que no contaban con un porcentaje elevado de óxido), y varillas con óxido (varillas oxidadas). Posterior a esto se cortaron en longitudes de 21.43 y 21.8 cm cada una, 9 probetas de acero de varillas sanas y 9 de varillas oxidadas, para un total de 18. Seguido a esto, se obtuvieron los pesos de ambas clasificaciones teniendo así que las varillas sanas pesaban 1,069.7 gr, mientras que las varillas corroídas tuvieron un peso de 1,089.3 gr.

Se dejaron, posteriormente, en una solución de vinagre con bicarbonato sódico por un periodo aproximado de 72 horas con el objetivo de remover la capa corroída de la varilla. Transcurrido ese tiempo, se sacaron las probetas para lavarlas, secarlas y se limpiaron con un cepillo de alambre para retirar el óxido de cada una hasta dejar metal blanco. Una vez terminado el proceso anterior, se volvieron a obtener los pesos de ambas clasificaciones para así determinar el porcentaje en la diferencia de peso.

Figura X. Recolección de muestras de varillas.

Figura XI. Corte y preparación de probetas.

Figura XII. Probetas sumergidas en la solución.

Figura XIII. Limpieza de las probetas

Figura XIV. Clasificación de probetas limpias

Figura XV. Pesaje final de las probetas limpias.

2.7 Sanidad de las soldaduras. - Se empleó la técnica de inspección por el método de líquidos penetrantes con base a la norma AWS D1.1 – 20, para verificación de sanidad de las soldaduras entre trabes y columnas del edificio. La inspección por líquidos penetrantes (PT) es una técnica versátil y de simple aplicación para una gran variedad de materiales y diseños que permite localizar defectos o grietas superficiales. El método se basa en los principios básicos de la acción capilar, y la capacidad de humectación de un líquido de baja viscosidad, propiedades que permiten que éste penetre por hendiduras o grietas imperceptibles a la vista para resaltarlas y evidenciarlas. [2].

Para ello se limpió la superficie a inspeccionar, para liberar de impurezas, polvo, pinturas, recubrimientos, residuos de material, grasas y cualquier otro tipo de sustancia o material que pudiera interferir en la evaluación. Posteriormente se aplicó el líquido penetrante en forma directa sobre la superficie que se desea evaluar. La dosificación se realizó con una brocha o rociado según la zona a aplicar. Una vez aplicado el líquido penetrante, fue necesario dar tiempo para que se infiltre en las grietas e imperfecciones. El tiempo típico fue de hasta 3 horas.

Figura XVI. Soldaduras limpias.

Se procedió a retirar o limpiar de la superficie de la pieza todo el excedente del líquido penetrante, con el fin de evidenciar lo que llegó a infiltrarse por las grietas o defectos. La remoción debe ser antes de que el penetrante seque, pues de lo contrario no va a actuar el revelador, volviéndose necesario reiniciar todo el proceso. [2]

Enseguida se aplica el revelador el cual permaneció sobre la superficie el mismo tiempo que el penetrante, con el objetivo de reaccionar con el líquido penetrante (únicamente presente en las grietas o defectos) para colorear y resaltar las áreas en las que éste se encuentre, es decir, en las que hubo infiltración.
Una vez concluida una inspección con líquidos penetrantes, se limpió la superficie ya que éstos tienden a retener humedad, incrementando el riesgo de corrosión, o bien afectando el uso posterior de la pieza.

Podemos resaltar a manera de resumen que en algunos parámetros obtenidos después de haber realizado las pruebas anteriormente citadas y compararlas con los criterios admisibles, se observa que, por ejemplo, que las de deformaciones de alginas losas de entrepiso son mayores que las permisibles por las normas, asimismo, los asentamientos en algunos de los apoyos apenas cumplen con las normativas aplicables. En relación a la calidad o resistencia a la compresión del concreto hidráulico de la losa de entrepiso, los resultados obtenidos manifestaron que estas son menores a los de las normas aplicables. Estos son los hallazgos más relevantes encontrados.

3. Resultados. - Después de realizar los trabajos descritos, se obtuvieron los siguientes resultados.

3.1 Deformación en losas de concreto. –

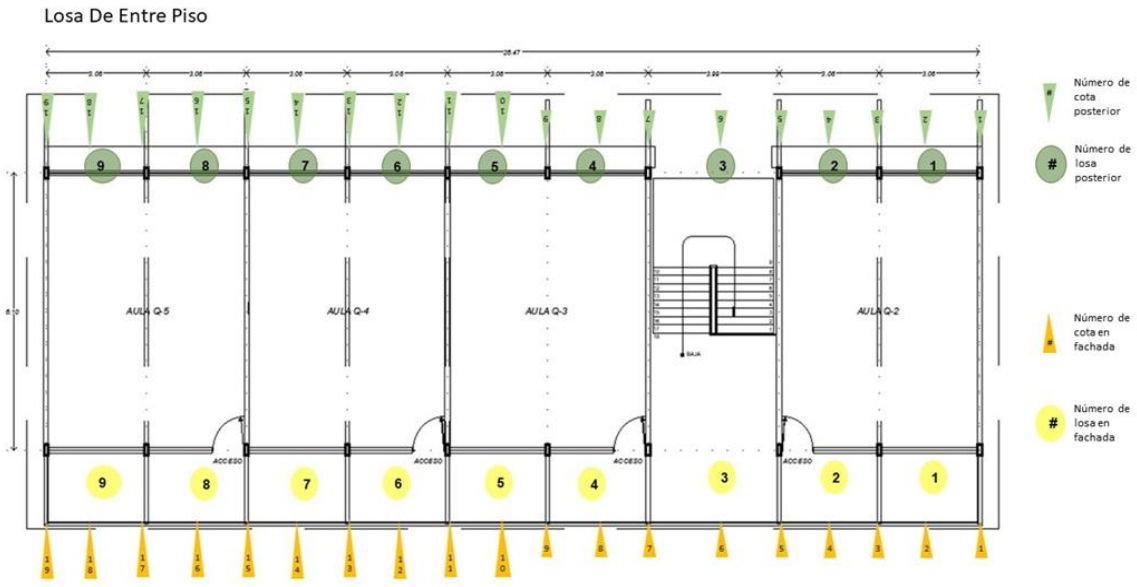

Figura XVII. Ubicación en planta de los puntos de niveles.

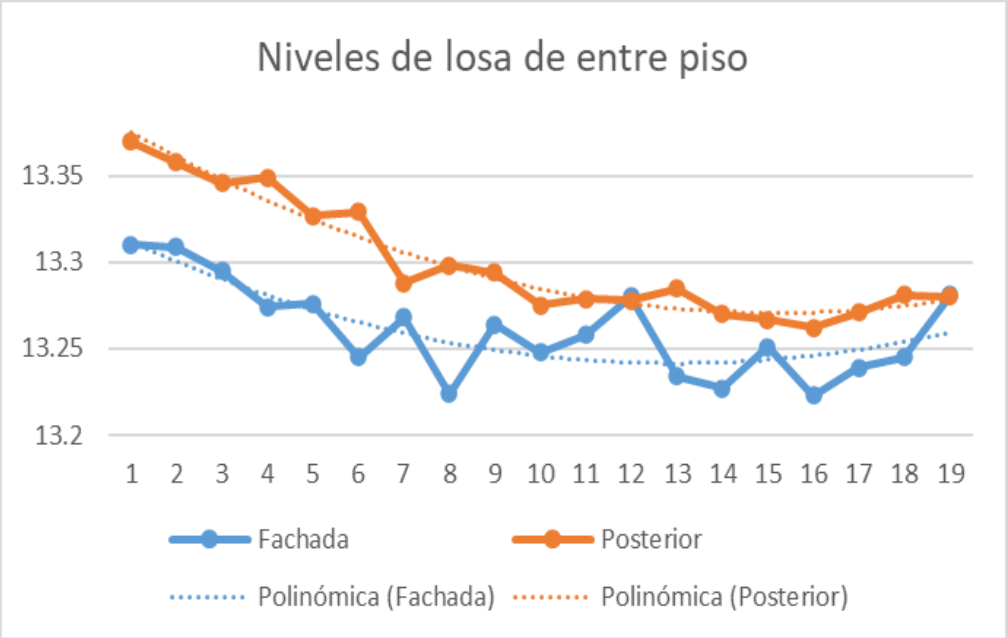

Figura XVIII. Detallado de los niveles de losa detectados

En la siguiente tabla se muestran las diferencias entre el nivel en los apoyos y el centro de la losa representado en metros, el dato superior representando la diferencia respecto al apoyo derecho y el dato inferior la diferencia respeto al apoyo izquierdo, y se marca a los que superan los 0.01275 metros.

	NIVEL DE COTAS (m)		
	Número	Fachada	Posterior
	1	13.31	13.37
LOSA 1	2	13.309	13.358
	3	13.295	13.346
LOSA 2	4	13.274	13.349
	5	13.276	13.327
LOSA 3	6	13.245	13.329
	7	13.268	13.288
LOSA 4	8	13.224	13.298
	9	13.264	13.294
LOSA 5	10	13.248	13.275
	11	13.258	13.279
LOSA 6	12	13.28	13.278
	13	13.234	13.285
LOSA 7	14	13.227	13.27
	15	13.251	13.267
LOSA 8	16	13.223	13.262
	17	13.239	13.271
LOSA 9	18	13.245	13.281
	19	13.281	13.28

Tabla I. Nivel de cotas de cada losa considerada.

Diferencia entre cota de apoyo al centro de losa (m)		
No. De losa	Fachada	Posterior
LOSA 1	0.001	0.012
	-0.014	-0.012
LOSA 2	0.021	-0.003
	0.002	-0.022
LOSA 3	0.031	-0.002
	0.023	-0.041
LOSA 4	0.044	-0.01
	0.04	-0.004
LOSA 5	0.016	0.019
	0.01	0.004
LOSA 6	-0.022	0.001
	-0.046	0.007
LOSA 7	0.007	0.015
	0.024	-0.003
LOSA 8	0.028	0.005
	0.016	0.009
LOSA 9	-0.006	-0.01
	0.036	-0.001

Tabla II. Diferencias entre el nivel en los apoyos y el centro de la losa.

3.2 Asentamientos. -

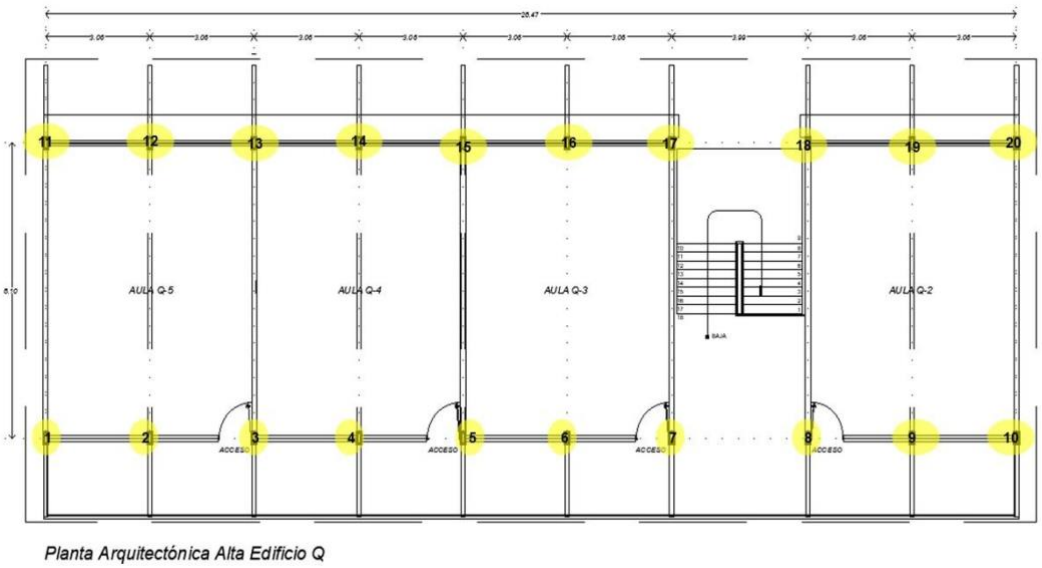

Figura XIX. Localización en planta de los puntos de nivelación de la losa

Niveles del edificio			
FRONTAL			
	A	B	C
1	1585.2	1274.1	1027
2	1583.3	1269.3	1027.8
3	1582.1	1270.2	1023.8
4	1578.8	1265.7	1022.7
5	1578.6	1266	1022
6	1579.3	1264.6	1020.9
7	1580.5	1264.6	1018.3
8	1578.5	1262.3	1018.1
9	1577.5	1263.1	1017.6
10		1261.2	1017.7

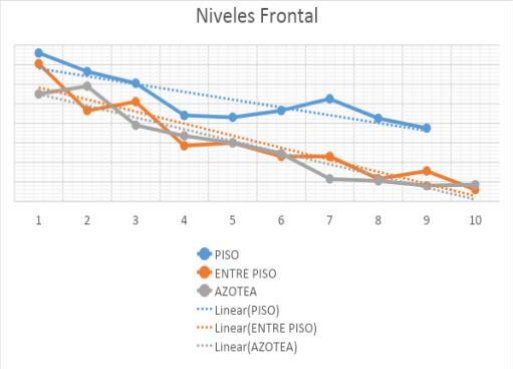

Figura XX. Cotas de la losa en la parte frontal del edificio

Niveles del edificio			
POSTERIOR			
	A	B	C
11	1590.1	1275.8	1039.1
12	1588.8	1276.6	1037.8
13	1588.2	1276.4	1037.1
14	1584.9	1269.3	1035.6
15	1588.3	1270.7	1037.4
16	1585	1269.8	1030.7
17	1584.8	1269.1	1029
18	1583.6	1266.5	1028.7
19	1584.3	1268.5	1029.5
20	1583.6	1265.4	1030

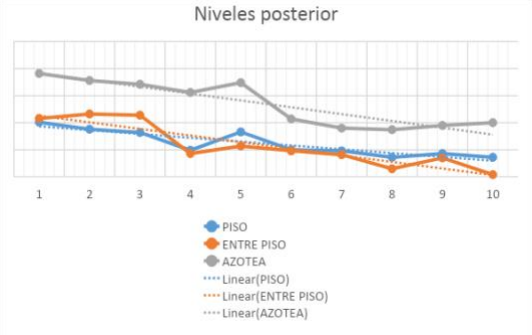

Figura XXI. Cotas de la losa en la parte posterior del edificio

Diferencias en niveles de fachada			
COTAS	PISO	ENTRE PISO	AZOTEA
1--2	1.9	4.8	0.8
2--3	1.2	0.9	4
3--4	3.3	4.5	1.1
4--5	0.2	0.3	0.7
5--6	0.7	1.4	1.1
6--7	1.2	0	2.6
7--8	2	2.3	0.2
8--9	1	0.8	0.5
9--10		1.9	0.1

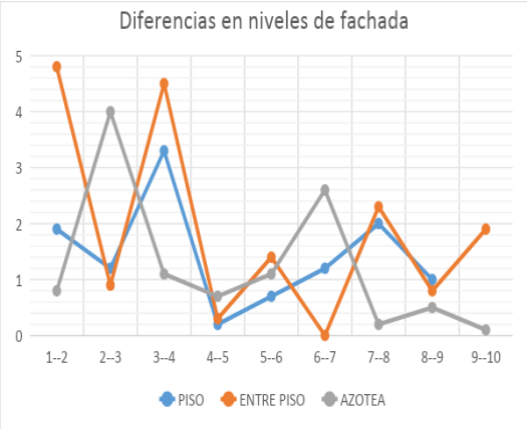

Figura XXII. Hundimiento diferencial en niveles frontales del edificio (en centímetros)

Diferencias en niveles en posterior			
COTAS	PISO	ENTRE PISO	AZOTEA
11--12	1.3	0.8	1.3
12--13	0.6	0.2	0.7
13--14	3.3	7.1	1.5
14--15	3.4	1.4	1.8
15--16	3.3	0.9	6.7
16--17	0.2	0.7	1.7
17--18	1.2	2.6	0.3
18--19	0.7	2	0.8
19--20	0.7	3.1	0.5

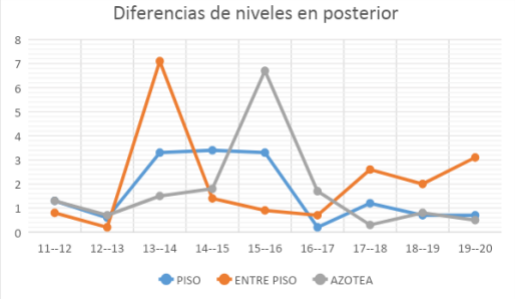

Figura XXIII. Hundimientos diferenciales en niveles posteriores del edificio (en centímetros)

Distorsión angular de niveles frontales			
COTAS	PISO	ENTRE PISO	AZOTEA
1--2	0.00620915	0.01568627	0.00261438
2--3	0.00392157	0.00294118	0.0130719
3--4	0.01078431	0.01470588	0.00359477
4--5	0.00065359	0.00098039	0.00228758
5--6	0.00228758	0.00457516	0.00359477
6--7	0.00392157	0	0.00849673
7--8	0.00501253	0.00576441	0.00050125
8--9	0.00326797	0.00261438	0.00163399
9--10	0	0.00620915	0.0003268

Distorsión angular de niveles posteriores			
COTAS	PISO	ENTRE PISO	AZOTEA
11--12	0.00424837	0.00261438	0.00424837
12--13	0.00196078	0.00065359	0.00228758
13--14	0.01078431	0.02320261	0.00490196
14--15	0.01111111	0.00457516	0.00588235
15--16	0.01078431	0.00294118	0.02189542
16--17	0.00065359	0.00228758	0.00555556
17--18	0.00300752	0.00651629	0.00075188
18--19	0.00228758	0.00653595	0.00261438
19--20	0.00228758	0.01013072	0.00163399

Figura XXIV. Distorsión angular en niveles frontal y posterior del edificio

3.3 Resistencia del concreto. - En el primer núcleo, corazón o muestra resultó de 174.42 kg/cm2 y el segundo de 137.35 kg/cm2, muy por debajo de lo que estipula la norma que es de un mínimo de 250 kg/cm2.

Figura XXV. Ensaye de 1er espécimen dando una resistencia de 174.42 kg/cm^2

Figura XXVI. Ensaye de 2do espécimen dando una resistencia de 137.35 kg/cm^2

3.4 Carbonatación del concreto. - Los fragmentos de muestra más representativos fueron los que tenían el espesor de la losa completos y presentaron lo siguiente:

3.4.1 Muestra 1. - Este fragmento pertenece a un cilindro extraído de la losa de entrepiso del salón Q5 del edificio el cual contaba con una losa llena de 16 centímetros de espesor.
La muestra logra rescatar 13 centímetros de la losa y se muestra que en su parte central 9 centímetros presentan coloración rosácea lo que nos indica que esta zona no se encuentra carbonatada.

Figura XXVII. Muestra 1 de concreto, estudio de carbonatación.

3.4.2 Muestra 2. - Este fragmento pertenece a un cilindro extraído de la losa del pasillo de entrepiso del salón Q2 del edificio el cual contaba con una losa llena de 10 centímetros de espesor.
La muestra de la losa se rescató en su espesor total y se muestra que en su parte central 7.5 centímetros presentan coloración rosácea lo que nos indica que esta zona no se encuentra carbonatada.

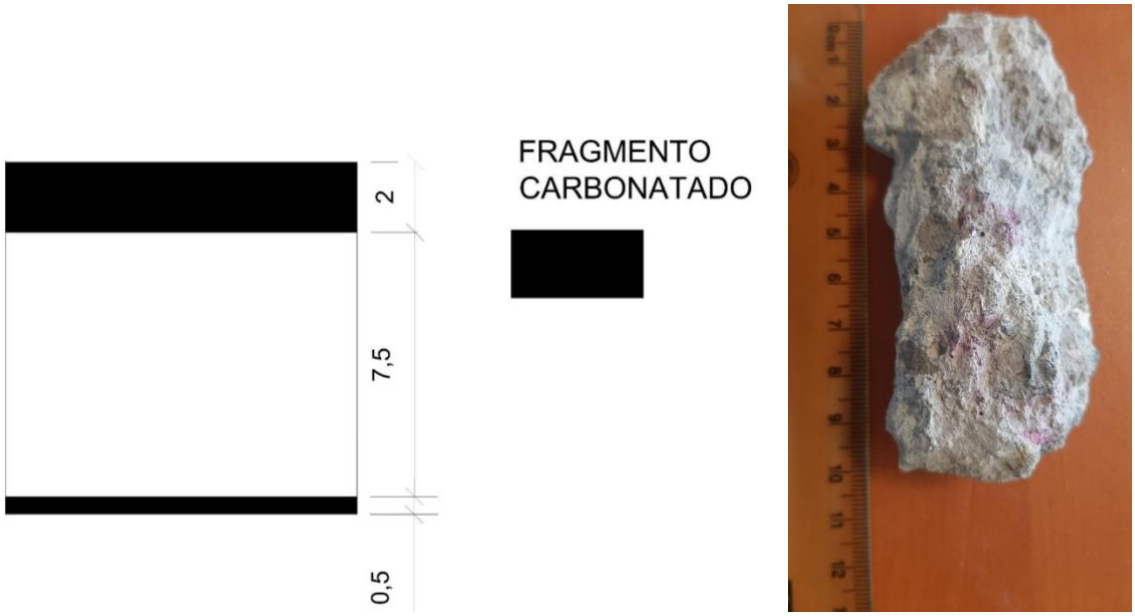

Figura XXVIII. Muestra 2 de concreto, estudio de carbonatación.

3.5 Oxidación por diferencia de pesos. - Dentro de la tabla 1.1 se puede observar la diferencia de pesos presentada en cada conjunto de muestras. Las varillas que se presentaban con óxido perdieron un 2.27% de pérdida de peso, mientras las varillas más sanas solo un 0.22% de pérdida.

Peso total de las probetas	
Varillas sin óxido (sanas)	
Antes de remoción de óxido	1069.7 gr
Después de la remoción de óxido	1067.3 gr
Diferencia	2.4 gr
Varillas con óxido	
Antes de la remoción de óxido	1089.3 gr
Después de la remoción de óxido	1064.6 gr
Diferencia	24.7 gr

Tabla III. Pérdida de peso por oxidación.

3.6 Sanidad de las soldaduras. - Se aprecia aplicación de soldadura de manera irregular, así como áreas con defectos de soldadura tales como: socavación, falta de fusión y cráteres, esto posiblemente por la inadecuada calibración de maquinaria y/o habilidad del soldador. Dichos defectos se presentan de manera general en todos los cordones de soldadura aplicada en conexiones existentes entre trabes y columnas.

Se presentan áreas en las cuales se omitió la aplicación de soldadura, esto de manera general en las que se encuentran los marcos de ventanas en conexiones entre trabes y columnas. Cabe mencionar que este laboratorio desconoce el motivo de dicha omisión de soldadura, puesto que la misma no obstruía ni generaba problemas para el injerto de dichos marcos de ventana.

Se observan áreas en las cuales se encuentran residuos de material, esto posiblemente por elementos los cuales fueron utilizados como provisionales para el izaje o montaje de los elementos estructurales.

Se presentan áreas en las cuales existen principios de oxidación de material base.

Las áreas mencionadas con anterioridad fueron señaladas físicamente por el laboratorio “Cárdenas Inspectores en Soldaduras” ubicada en Guadalajara, Jalisco, la cual notificó al personal correspondiente quedando de manera pendiente su reparación.

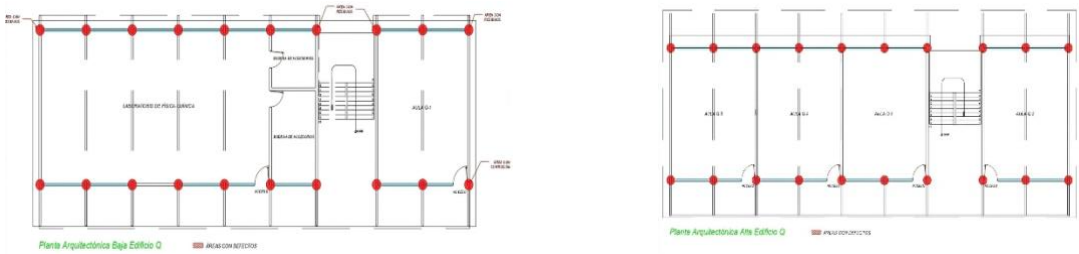

Figura XXIX. Plantas arquitectónicas del edificio Q.

4. Conclusiones. –

4.1 Deformación de las losas. - La mayoría de las losas del pasillo de la fachada, es decir de la losa de entrepiso, superan la deformación máxima permisible en la losa. Esto se podía observar a simple vista en el edificio y se verificó con los resultados de diferencia de niveles entre sus apoyos y el centro de losa. Es notoria la presencia de deflexiones positivas en el centro de la marquesina posterior del entrepiso, pues al ser tan corto el voladizo, adyacente a un tablero grande, los efectos hiperestáticos se alcanzaron a manifestar en varios entre ejes.

Todo esto no sólo representa un impacto en la estética del edificio, pues además de afectar la funcionalidad por la apreciación de los usuarios, tanto de la deformación como de la flexibilidad, se reduce la reserva de capacidad estructural.

Se puede deducir que el tiempo de vida de la estructura estaba en su límite de seguridad, ya que las deformaciones observadas hacen inferir que el material usado ya había cumplido su utilidad, lo que originó que se perdiera la confiabilidad estructural del edificio. Al ser un plantel educativo, usado por un gran número de jóvenes durante todo el día, no era posible tomar el riesgo de seguir usando el edificio de manera segura.

4.2 Asentamientos. - Más notorio que las deformaciones de las losas de tablero a tablero, es la distribución de los niveles de la estructura del edificio. Las cotas tanto de piso en planta baja, como de la estructura en primero y segundo piso, confirman una tendencia de asentamientos totales crecientes de izquierda a derecha.
En cuanto a los asentamientos diferenciales, se evaluaron las diferencias entre los niveles de las cotas citadas tomando en cuenta que no sobrepasan los 2 cm de diferencias entre ellas y se corroboró por medio de la distorsión angular que esta irregularidad se presentaba en las mismas cotas, este fenómeno es perceptible en las cotas 3-4 y 13-14 las cuales se encuentran en el mismo eje transversal y presentan la mayor distorsión angular.

4.3 Resistencia del concreto. - Los dos especímenes de concreto se encontraron por debajo de los resultados esperados y al ser un parámetro crítico en la estructura ve reducida, aunque de manera local, la seguridad e integridad del edificio. La resistencia actual del concreto es muy baja, reduciendo la capacidad de carga de las losas, poniendo en peligro la seguridad de los usuarios y las actividades que se realizan en la estructura. Además de que es un indicador de ser más propenso a la corrosión, la erosión y otros tipos de deterioro, lo que reduce la vida útil de la estructura.

4.4 Carbonatación. - Se concluye que existe carbonatación de las capas superficiales superior e inferior de la losa en espesor variable entre 25% y 44% de su espesor, deteriorando la capacidad pasivadora de la corrosión del acero de refuerzo por el concreto.

En suma, la baja resistencia del concreto, la potencial corrosión del acero estructural dentro del concreto que ya se ha iniciado conlleva a la aparición de fisuras y grietas, pérdida de adherencia entre concreto y refuerzo, concluyendo en la reducción de la vida útil, integridad y seguridad de la losa.

4.5 Oxidación del acero de refuerzo estructural. - Las varillas con óxido experimentaron una pérdida de peso del 2.27%, mientras que las varillas en mejores condiciones solo mostraron una pérdida del 0.22%. Esta diferencia sugiere que el óxido presente en las varillas afecta negativamente su peso, su sección transversal y su integridad estructural. Estos hallazgos indican la importancia de mantener protegida la estructura y monitorear periódicamente las varillas, tomar acciones para prevenir problemas relacionados con la corrosión, garantizar su rendimiento y seguridad a largo plazo.

4.6 Sanidad de las soldaduras. - En resumen, se han identificado varios problemas en las conexiones existentes entre trabes y columnas en relación con la soldadura y la integridad estructural en un sitio o estructura. Estos problemas incluyen, soldadura irregular y defectuosa, estos problemas pueden deberse a una inadecuada calibración de maquinaria y/o a la falta de habilidad por parte del soldador durante el proceso constructivo; también la omisión de soldadura en algunas áreas, aunque se ha señalado que no obstruía ni generaba problemas para el montaje de los marcos de ventana; así como residuos de material por elementos provisionales, lo que en conjunto puede afectar la integridad de la estructura. Por último, se presentaron principios de corrosión en el metal base, lo que es preocupante, ya que la corrosión puede comprometer la resistencia estructural del conjunto con el tiempo.

Es importante abordar estos problemas de manera adecuada para garantizar la seguridad y la integridad estructural a largo plazo.

4.7 Conclusión General. - En general, y de acuerdo con las conclusiones de cada una de las secciones de este estudio, se propone demoler todas las losas de entrepiso y azotea, y en virtud de que los muros divisorios están desplantados sobre la primera, demolerlos igualmente para posteriormente complementar los cordones de soldadura interrumpidos en la estructura de acero y colar nuevas losas, desplantando sobre ellas los muros divisorios.

El deterioro de las estructuras puede ser acelerado por factores como la falta de mantenimiento y la exposición a cargas excesivas, por lo que es importante que se realice un mantenimiento regular y adecuado de la estructura para prevenir el envejecimiento y detectar cualquier problema temprano.

En base a la norma NMX-R-079-SCFI-2015, relativa a los requisitos de seguridad estructural de la infraestructura física educativa, no se cumplen los que deben considerarse para evaluar la seguridad estructural de una edificación como la deformabilidad, los defectos e irregularidades en la estructura y la cimentación, así como el riesgo inherente a su ubicación, la calidad del mantenimiento y el uso para el cuál esté destinado.

Además, el mantenimiento adecuado no sólo conserva la estética del edificio, sino que también garantiza su seguridad. La inversión en mantenimiento es una inversión en el futuro del edificio. Al realizar acciones preventivas y correctivas, se prolonga la vida útil de los materiales, se reduce la necesidad de reemplazos completos y se minimizan los costos a largo plazo.

El edificio Q no cumple con lo establecido en la norma NMX-R-021-SCFI-2013 [4], relativa a los requisitos de calidad de la infraestructura física educativa, y en particular al capítulo 9 sección E sobre los daños en elementos estructurales: asentamientos totales, asentamientos diferenciales, corrosión del acero estructural en perfiles y en acero de refuerzo del concreto armado, deflexiones y vibración en losas, concreto de baja resistencia.
El Volumen 7 Tomo 2 del INIFE se refiere a la conservación de estructuras, aborda aspectos relacionados con la conservación y mantenimiento de estructuras, incluyendo las de acero, en el contexto de la infraestructura educativa. En última instancia, la decisión de demoler y construir un nuevo edificio depende de una evaluación completa de factores financieros, técnicos, de seguridad y funcionales, así como de las regulaciones locales y las necesidades del entorno en el que se encuentra el edificio.

Como resultado de los trabajos realizados durante la inspección y realización de diversos estudios y pruebas aplicados a los diferentes elementos estructurales del edificio citado, por parte de las autoridades responsables de la infraestructura educativa de los inmuebles del sector público y por parte de los participantes especialistas en estructuras, asimismo, debido a factores como el deterioro evidente debido a la edad y además de otros como los climatológicos, se concluyó que la estructura de acero no cumplía con las normativas actuales y representaba un riesgo para la seguridad de los usuarios como estudiantes, docentes y personal administrativo.

Por esta razón, se tomó la decisión de demoler completamente la estructura existente y construir un nuevo edificio con las mismas características arquitectónicas, pero cumpliendo las normativas actuales de construcción y estructuración, en su posición original. Esta medida garantizará que el nuevo edificio cumpla con las normativas vigentes, brindando un entorno seguro para los ocupantes y minimizando cualquier riesgo potencial asociado con la estructura anterior.

Responsable del estudio
M.C. Fernando Aguirre Camacho.

Colaboradores
M.I. Fernando Treviño Montemayor, M.C. Carlos Alberto Hoyos Castellanos, Ing. Martín Eduardo García Avilanes,

Alumnos participantes
Noelia Ortega Bobadilla, Karen Guadalupe Montaño Pelayo, Jonatan Rodríguez Nonato, Estudiantes de Ingeniería Civil del TecNM Instituto Tecnológico de Tepic

Referencias

[1] Alcocer Martínez de Castro, S. M., Valencia Ronquillo, G. A., & Bautista Monroy, R. (2021). Evaluación postsísmica de la infraestructura física educativa de México Volumen 1: Metodología. *Instituto Nacional de la Infraestructura Física Educativa, en Liquidación*, 95-104. Obtenido de https://www.inifed.gob.mx/tecnica/tiv/Evaluacion_Metodologia_VF_DIGITAL_130221.pdf

[2] Carrión Viramontes, F. J., Lomelí González, M. G., Quintana Rodríguez, J. A., & Martínez Madrid, M. (2003). La evaluación no destructiva de materiales estructurales y puentes. (C. y. Secretaría de Infraestructura, Ed.) (Publicación Técnica no. 231), 44-52. Obtenido de https://www.imt.mx/archivos/publicaciones/publicaciontecnica/pt231.pdf

[3] Schinca, J., Lassus, O., & Fernández, M. (2007). Estabilidad de las construcciones III Losas 1, Casos de losas aisladas. 17-20.

[4] Secretaría de Economía. (2013). NMX-R-021-SCFI-2013 Escuelas - Calidad de la Infraestructura Física Educativa - Requisitos. México, Mpexico. Obtenido de https://www.gob.mx/cms/uploads/attachment/file/104914/NMX-R-021_Calidad_de_la_INFE_requisitos.pdf

[5] Universidad Tecnológica de la Mixteca. (2014). Planeación de l a Vida Útil en Proyectos Arquitectónicos. *Temas de Ciencia y Tecnología*, *18*(53), 53-58. Obtenido de https://www.utm.mx/edi_anteriores/temas53/index.html

[6] Vidaud, I. y. (2012). La carbonatación en el concreto reforzado. *Construcción y Tecnología en concreto*, 20-23. Obtenido de https://www.imcyc.com/revistacyt/enero2013/pdfs/ingenieria.pdf

Nota contribución de los autores:

1. Concepción y diseño del estudio
2. Adquisición de datos
3. Análisis de datos
4. Discusión de los resultados
5. Redacción del manuscrito
6. Aprobación de la versión final del manuscrito

FAC ha contribuido en: 1, 2, 3, 4, 5 y 6.

FTM ha contribuido en: 1, 2, 3, 4, 5 y 6.

CAHC ha contribuido en: 1, 2, 3, 4, 5 y 6.

MEGA ha contribuido en: 1, 2, 3, 4, 5 y 6.

Nota de aceptación: Este artículo fue aprobado por los editores de la revista Dr. Rafael Sotelo y Mag. Ing. Fernando A. Hernández Gobertti.

Análisis comparativo de las metodologías de predimensionamiento para columnas en una edificación de seis niveles sin sótano

Comparative analysis of methodologies for column pre-sizing in a six-level building without basement

Análise comparativa de metodologias de pré-dimensionamento de colunas em edifício de seis níveis sem cave

Marcos Josue Rupay Vargas[1(*)], Regner Raul Parra Lavado[2], Jorge Santiago Lopez Yarango[3]

Recibido: 22/02/2024 Aceptado: 15/03/2024

Resumen. - Los tipos de metodologías para poder asignar o calcular el predimensionamiento de una determinada estructura permite conocer los comportamientos de los elementos estructurales a lo largo del tiempo de vida útil lo cual se podrá observar y analizar cuando se realice el análisis sísmico estático y dinámico a la edificación. Para poder predimensionar una edificación se debe tener en consideración el número de niveles de pisos, el ancho de luz entre vigas y columnas, y el cálculo del metrado de carga para cada elemento estructural. El objetivo principal de esta investigación es poder analizar cuáles son los efectos que se producen en el predimensionamiento de los elementos estructurales verticales (columnas) en cuanto a las derivas de una edificación de 6 niveles sin sótano bajo los parámetros de la Normativa Peruana Cargas E. 020, Diseño Sismorresistente E. 030 y Concreto Armado E. 060. Los resultados finales permitirán demostrar que método empleado fue el adecuado para el diseño de la edificación y esto influirá en los costos de su construcción. Para la investigación se concluye que el método sísmico es la metodología más adecuada para el cálculo de predimensionamiento de los elementos estructurales.

Palabras clave: Columnas 1, Derivas 2, Edificación 3, Predimensionamiento 4, Vigas 5.

(*) Autor Corresponsal

[1] Docente Universitario, Área Estructuras de la Escuela Profesional de Ingeniería Civil de la facultad de Ingeniería de la Universidad Nacional Intercultural de la Selva Central Juan Santos Atahualpa (Perú), mrupay@uniscjsa.edu.pe, ORCID iD: https://orcid.org/0000-0002-7891-1838

[2] Docente Universitario, Área Transportes de la Escuela Profesional de Ingeniería Civil de la Facultad de Ingeniería de la Universidad Nacional Intercultural de la Selva Central Juan Santos Atahualpa (Perú), rparra@uniscjsa.edu.pe, ORCID iD: https://orcid.org/0000-0002-3564-4637

[3] Docente Universitario, Área Estructuras de Facultad de Ingeniería Civil de la Universidad Nacional del Centro (Perú), jlopez@uniscjsa.edu.pe, ORCID iD: https://orcid.org/0009-0008-8216-4928

Memoria Investigaciones en Ingeniería, núm. 26 (2024). pp. 143-155
https://doi.org/10.36561/ING.26.9
ISSN 2301-1092 • ISSN (en línea) 2301-1106 – Universidad de Montevideo, Uruguay

Summary. - *The types of methodologies to be able to assign or calculate the pre-sizing of a certain structure allow us to know the behaviors of the structural elements throughout their useful life, which can be observed and analyzed when the static and dynamic seismic analysis of the building is carried out. In order to pre-size a building, the number of floor levels, the span width between beams and columns, and the calculation of the load metering for each structural element must be taken into consideration. The main objective of this research is to be able to analyze the effects that occur in the pre-sizing of the vertical structural elements (columns) in terms of the drifts of a 6-story building without a basement under the parameters of the Peruvian E-Loads Regulations. 020, Earthquake Resistant Design E. 030 and Reinforced Concrete E. 060. The final results will demonstrate that method used was appropriate for the design of the building and this will influence the costs of its construction. For the investigation, it is concluded that the seismic method is the most appropriate methodology for calculating the pre-sizing of structural elements.*

Keywords: *Columns 1, Drifts 2, Building 3, Pre-sizing 4, Beams 5.*

Resumo. ***-*** *Os tipos de metodologias para poder atribuir ou calcular o pré-dimensionamento de uma determinada estrutura permitem-nos conhecer os comportamentos dos elementos estruturais ao longo da sua vida útil, que podem ser observados e analisados quando se realiza a análise sísmica estática e dinâmica do edifício. é realizada. Para pré-dimensionar uma edificação deve-se levar em consideração o número de níveis de piso, a largura do vão entre vigas e pilares e o cálculo da dosagem de carga para cada elemento estrutural. O objetivo principal desta pesquisa é poder analisar os efeitos que ocorrem no pré-dimensionamento dos elementos estruturais verticais (pilares) em termos dos deslocamentos de um edifício de 6 andares sem subsolo sob os parâmetros da E peruana. -Regulamento de Cargas 020, Projeto Resistente a Terremotos E. 030 e Concreto Armado E. 060. Os resultados finais demonstrarão que método utilizado foi adequado ao projeto da edificação e isso influenciará nos custos de sua construção. Pela investigação conclui-se que o método sísmico é a metodologia mais adequada para o cálculo do pré-dimensionamento de elementos estruturais.*

Palavras-chave: *Pilares 1, Derivações 2, Edifício 3, Pré-dimensionamento 4, Vigas 5.*

1. Introducción. - Se conoce que en el área de las estructuras y los edificios es donde los ingenieros civiles ponen su mayor empeño en cuanto a ver las condiciones de una edificación y es que esta cumpla con la servicialidad para la cual se construyó y los años de vida útil ideal que deberían tener. Se debe saber que el predimensionamiento es el primer paso para poder saber cuáles son las medidas de los elementos estructurales ya que en base a ello se definen todos las cuales comprenden las placas, losas, columnas, vigas, etc. [13].

Cuando se predimensionan los elementos estructurales verticales o columnas para una edificación, el ingeniero especialista o proyectista deberá contar con la seguridad, experiencia y criterio técnico para poder saber si las dimensiones que se asignan o se van a tomar en consideración son las óptimas y tendrán un buen desempeño estructural.

Según [10] la funcionalidad de una estructura siempre va a depender de los elementos estructurales y también del tipo de estructura que se tendrá en consideración ya que puede ser una de pórticos, albañilería confinada, mixta, etc.; entonces las condiciones frente a las que estaremos van a variar y tendremos que efectuar un análisis estructural óptimo.

Finalmente, se debe recalcar que cuando vamos a realizar el predimensionamiento de las columnas para poder ver si cumple entonces se aplicara el poder realizarle el análisis dinámico a la edificación sin espectros de sismo ya que si empleamos estos espectros entonces tendríamos que quizás sobredimensionar y no se vería cual es la función que cumplen las columnas directamente porque ahí tendríamos que optar por considerar placas.

Entonces ante este problema que nos encontramos lo que se busca con la redacción del artículo científico es que se puedan analizar el efecto de los predimensionamiento de las columnas mediante tres métodos diferentes de cálculo, aplicado a una estructura o edificación de seis niveles sin sótano y con un sistema estructural de pórticos.

2. Materiales y métodos. – Para el desarrollo se consideró poder trabajar con una edificación de un sistema estructural de pórticos, la cual cuenta con seis niveles ubicada en el distrito y provincia de Chanchamayo, en la región Junín.
Para iniciar con la obtención de los resultados se tuvo que emplear los planos de la estructura en el software AutoCAD versión del año 2020 tal como se puede apreciar en la Figura I, que se emplearan para el predimensionamiento de los elementos estructurales verticales o columnas aplicando tres metodologías distintas para ver cuál es la variación en las dimensiones.

Para poder llegar al objetivo planteado se debe plantear dos variables distintas, las cuales son que las derivas finales del análisis estructural que van a depender directamente de la aplicación de las metodologías de predimensionamiento con las cuales se van a trabajar.

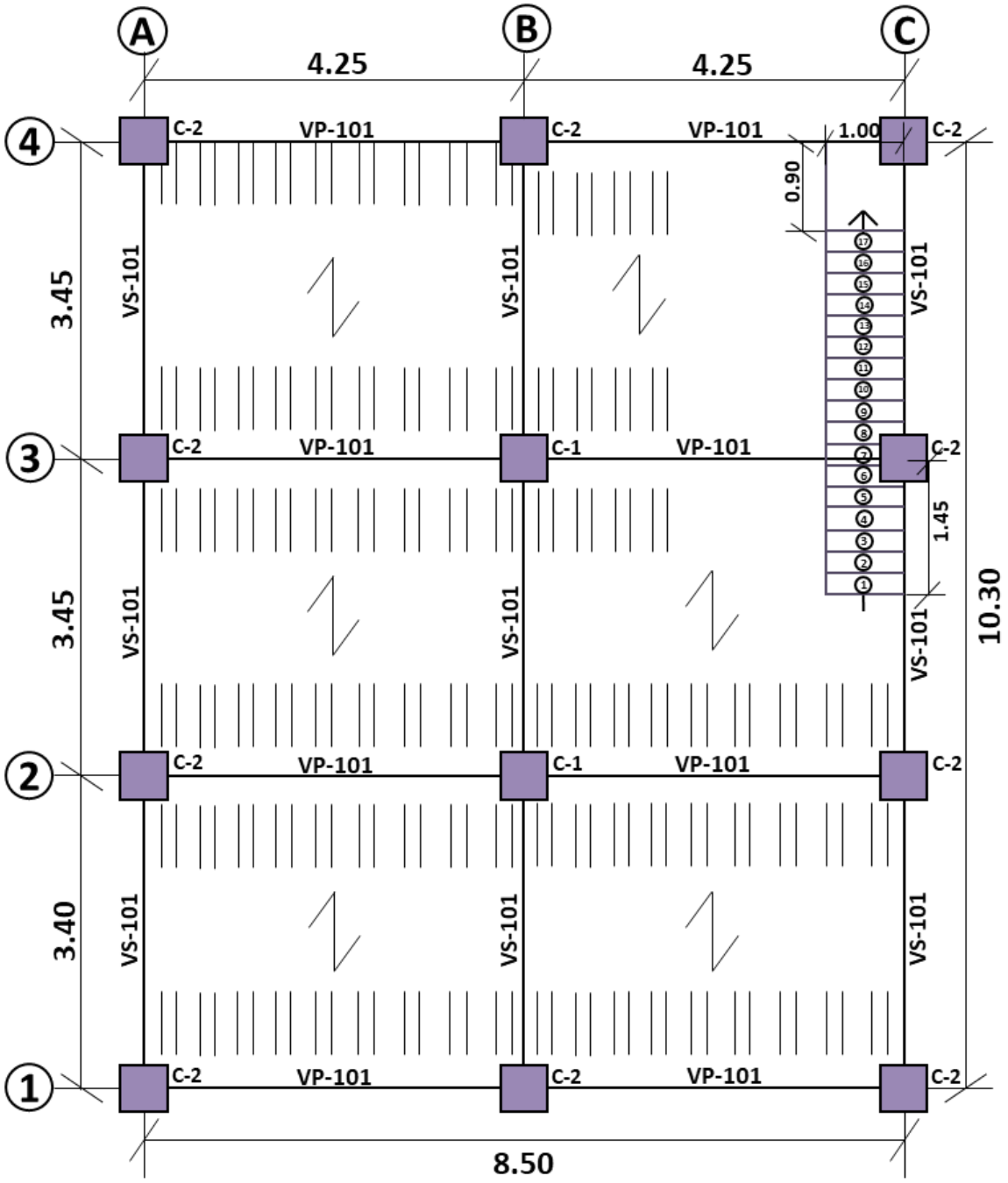

Figura I: Plano de estructuración de la edificación. Fuente: Elaboración propia (2024).

Se elaboraron los planos de vista en planta para la edificación la cual consta de seis niveles en la cual se detallan las longitudes que se tienen entre ejes tanto lateral y frontal, sentido de la losa que en este caso será aligerada bidireccional ya que la división entre la luz mayor del eje X e Y son menores a 2. También se detallan en qué sentido están las vigas principales y secundarias ya que esto también tendrá influencia en su análisis estructural debido a los diafragmas que se crearan.

2.1. Predimensionamiento por la metodología de gravedad. - Cuando se desarrolla la metodología para aplicar el predimensionamiento por gravedad lo que se llega a producir es que existirá un esfuerzo axial de deformaciones máximas en toda el área de la columna la cual será afectada directamente. (Vásquez Bustamante, 2019)

En este tipo de metodología para poder realizar el predimensionamiento de aplica la siguiente formula $[\text{S} * \text{PG}/(\text{n} * F'\text{c})] = \text{b} * \text{D}$, el cual se ha detallado en la siguiente tabla:

Tipo de columna
Céntricas (para el primer nivel)
Céntricas (para los ultimo niveles)
Excéntricas
Esquineras

Tabla 1. Coeficientes para predimensionamiento de columnas aplicando metodología por gravedad. [13]

Nota: En referencia al número de los niveles de la edificación y su ubicación de cada columna es que los coeficientes van a ir variando. Estos coeficientes son los que se observan en la Tabla I.

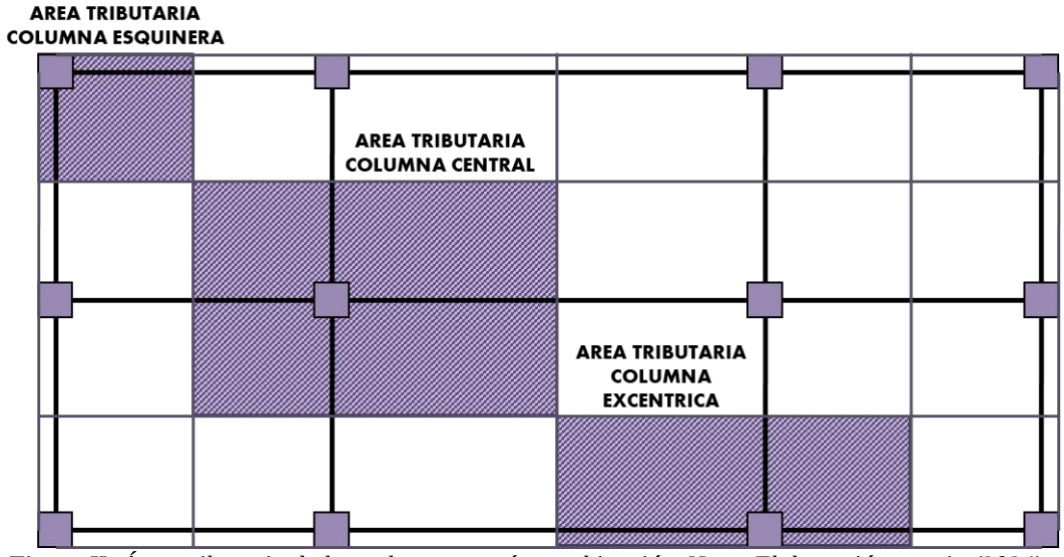

Figura II: Área tributaria de las columnas según su ubicación. Nota: Elaboración propia (2024)

El área tributaria de una columna varia en base a la ubicación en los ejes y también según su posición ya que debido a ello es que se puede determinar las longitudes correspondientes para cada uno de estos elementos estructurales.

			Área Tributaria (m2)	**N° niveles**	**n**	**f´c**	**Método 01**
		ℵ		6		280	
C 1	E	1.50	3.72		0.20	25.8766	30 x 30
C 2	L	1.25	7.41		0.25	29.8195	30 x 30
C 3	E	1.50	3.72		0.20	25.8766	30 x 30
C 4	L	1.25	7.22		0.25	29.4347	30 x 30
C 5	C	1.10	14.43		0.30	35.6348	40 x 40
C 6	L	1.25	7.22		0.25	29.4347	30 x 30
C 7	L	1.25	7.44		0.25	29.8798	30 x 30
C 8	C	1.10	14.86		0.30	36.1619	40 x 40
C 9	L	1.25	7.44		0.25	29.8798	30 x 30
C 10	E	1.50	3.50		0.20	25.0998	30 x 30
C 11	L	1.25	7.00		0.25	28.9828	30 x 30
C 12	E	1.50	3.72		0.20	25.8766	30 x 30

Tabla II. Predimensionamiento de las columnas de la estructura por el Método de Gravedad. Fuente: *Elaboración propia (2024)*

Nota: n, ℵ = coeficientes para cada columna según su ubicación en los ejes, Método 01 = Método por gravedad

2.2. Predimensionamiento por la metodología del American Concrete Institute. - Cuando nos referimos al poder trabajar aplicando la metodología del American Concrete Institute nos centramos en poder aplicar a cada una de las secciones de la columna un esfuerzo axial directo utilizando la teoría de que el esfuerzo de servicio se debería aplicar cuando este sea menor al 0.45 * f'c. [3]

Según el (American Concrete Institute, 2014) existe unas limitaciones para poder analizar en cuanto a las derivas según el propio código del ACI ya que especifica y a la vez muestra una asociación de que la deformación máxima cuando se somete este elemento estructural a compresión solo debe ser de un 3%.

Cuando se aplica la fórmula anterior mencionada se debe tener en consideración dos aspectos de que 0.45 es para columnas centrales y 0.35 para las columnas laterales. (American Concrete Institute, 2014)

Donde:

$$PS = P * Área\ Tributaria\ de\ la\ Columna * Número\ de\ Niveles \quad (1)$$

PS = Peso de servicio

Donde P asume los siguientes valores en relación con la categoría o cuan esencial es la edificación con la que se está trabajando.

Parámetros del American Concrete Institute	
Columnas Centrales	Área columna = PS / (0.45 * f'c)
Columnas Excéntricas	Área columna = PS / (0.35 * f'c)
Columnas Esquineras	

Tabla III. – Coeficientes para el predimensionamiento de columnas aplicando la metodología del A.C.I
Fuente: Adaptado de [7]

Nota: Se debe tener en consideración cual es el f'c = fuerza de compresión del concreto al momento de aplicar el cálculo en el predimensionamiento de las dimensiones de la columna porque mientras mayor sea este dato menor serán las dimensiones.

Categoría			**N° niveles**	**PS**	**f'c**	**ACI**	**Método 02**
	A	Área Tributaria (m2)	6		280		
C 1	1500	3.72		33480		0.35	25 x 25
C 2	1500	7.41		66690		0.35	30 x 30
C 3	1500	3.72		33480		0.35	25 x 25
C 4	1500	7.22		64980		0.35	30 x 30
C 5	1500	14.43		129870		0.45	35 x 35
C 6	1500	7.22		64980		0.35	30 x 30
C 7	1500	7.44		66960		0.35	30 x 30
C 8	1500	14.86		133740		0.45	35 x 35
C 9	1500	7.44		66960		0.35	30 x 30
C 10	1500	3.50		31500		0.35	25 x 25
C 11	1500	7.00		63000		0.35	30 x 30
C 12	1500	3.72		33480		0.35	25 x 25

Tabla IV. Predimensionamiento de las columnas de la estructura por el Método A.C.I.
Fuente: Elaboración propia (2024). Nota: Método 02 = Método del ACI

2.3. Predimensionamiento por la metodología del factor sismo. - Según [9] lo que se debe tener en consideración es que para el predimensionamiento mediante esta metodología se debe aplicar el factor de zona sísmica en donde se va a construir la edificación, además de las condiciones climáticas y topográficas del propio medio, ya que, es muy importante para poder realizar un análisis dinámico y espectral de una determinada edificación.

$$L\ columna = W \times [(0.25 * Vs * h\ 1er\ Piso * 1002)/(0.007 * G)] * 0.25 \quad (3)$$

Donde:

Vs = Z * U * C * S* (WFINAL01 + WFINAL02)
PE = Vs * (Área tributaria de la columna)
Módulo cortante para el concreto G = E / (2 * (1 + v)) = 0.417 * E

Abreviatura	Descripción
(f´c)	Resistencia a la compresión del concreto
(Fy)	Valor de fluencia del acero
(#PisosTOTAL)	# de niveles
(S/C SIN AZOTEA)	Sobrecarga de todos los niveles sin considerar la azotea
(S/C CON AZOTEA)	Sobrecarga solo de la azotea
(PP. Col)	Peso de la columna
(PP. Vig)	Peso de la viga
(PP. Alig)	Peso del aligerado
(PP. Tab)	Peso de la tabiquería
(Acb + PP. Col + PP. Vig + PP. Alig +PP. Tab)	Carga Muerta (CM 1)
(Acb + PP. Col + PP. Vig + PP. Alig)	Carga Muerta (CM 2)
S/C SIN AZOTEA	Carga Viva (CV 1)
S/C CON AZOTEA	Carga Viva (CV 2)
E = 150000 * ((f´c) ^ 0.5)	Módulo de elasticidad del concreto

Tabla V- Parámetros especificados para el predimensionamiento de columnas aplicando la metodología del factor sísmico. [13]

Nota: La metodología aplicada para poder realizar el predimensionamiento por el factor sismo en una edificación requiere poder considerar varios factores los cuales se extraen de la Norma Técnica Peruana E 0.30 para poder considerar ciertos parámetros los cuales serán de vital importancia y que se han detallado en la Tabla V previamente vista.

Predimensionamiento		**Estructuración Simétrica**				
Tipo de Columna	**AT (m2)**	**VS (Kg)**	**b x D**	**Si b = D (cm)**	**b x D**	**Emplear**
C 1	3.72	25,958.16	956.24	30.92	1,050	30 x 35
C 2	7.41	51,706.98	1,349.60	36.74	1,400	35 x 40
C 3	3.72	25,958.16	956.24	30.92	1,050	30 x 35
C 4	7.22	50,381.16	1,332.19	36.50	1,400	35 x 40
C 5	14.43	100,692.54	1,883.34	43.40	2,025	45 x 45
C 6	7.22	50,381.16	1,332.19	36.50	1,400	35 x 40
C 7	7.44	51,916.32	1,352.33	36.77	1,400	35 x 40

C 8	14.86	103,693.08	1,911.20	43.72	2,025	45 x 45
C 9	7.44	51,916.32	1,352.33	36.77	1,400	35 x 40
C 10	3.50	24,423.00	927.54	30.46	1,050.00	30 x 35
C 11	7.00	48,846.00	1,311.73	36.22	1,400.00	35 x 40
C 12	3.72	25,958.16	956.24	30.92	1,050.00	30 x 35

Tabla VI. - Predimensionamiento de las columnas de la estructura por el Método de Sismo. Fuente: Elaboración propia (2024)
Nota: AT= área tributaria, VS= cortante basal, b = base de la columna, D = peralte de la columna

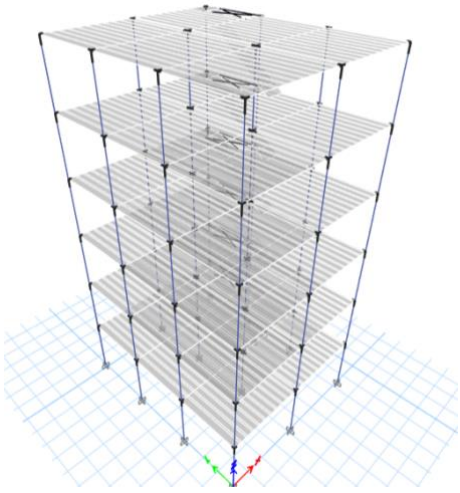

Figura III: Software ETABS V 19.0.0. Nota: Elaboración propia (2024)

Las dimensiones de las columnas obtenidas aplicando las metodologías se insertaron y ejecutaron en el software Etabs, la cual permitió obtener los desplazamientos o drifts para poder ver con que dimensiones la estructura presenta un mejor comportamiento elástico.

Cálculo de derivas	
Regularidad estructural	Regular
Coeficiente de desplazamiento lateral (C1)	1
Coeficiente de reducción sísmica (R)	8
Altura de entrepiso (cm)	280 cm
Máxima desplazamiento en Y-Y	Etabs
Máxima desplazamiento real en Y-Y	Etabs
Máxima deriva de piso en Y-Y (MDP y-y)	Etabs
Revisión máxima deriva en dirección Y-Y	(C1) * (R) * (MDP y-y) < = 0.007

Tabla VII. Cálculo de las derivas de cada nivel de la estructura. Fuente: Adaptado de [12]

Nota: Luego de realizar el predimensionamiento aplicando los tres métodos y al ejecutar en el software se procederá a realizar la verificación en base a las derivas obtenidas haciendo una referenciación con la Tabla IV.
Estas derivas no deben exceder en 1% a la altura de cada nivel que se consideró en la estructura que en este caso fue de 280 cm.

3. Resultados. - Cuando se ejecutó el predimensionamiento de cada una de las columnas aplicando las tres metodologías que se mencionaron en la introducción de este articulo científico, se ha optado por considerar y detallar en la Tabla VIII cuales serán esas dimensiones para cada uno de los métodos, pero también se han distribuido en tres tipos de columnas tanto como son las centrales, esquineras y laterales las cuales como sabemos tienen un diferente comportamiento estructural.

Las dimensiones utilizadas se detallan a continuación:

Características	Método 01	Método 02	Método 03
Columnas centrales (C 1)	40 x 40	35 x 35	45 x 45
Columnas laterales (C 2)	30 x 30	30 x 30	40 x 35
Columnas esquineras (C 3)	30 x 30	25 x 25	35 x 30

Tabla VIII. Predimensionamiento de las columnas obtenidas de los métodos aplicados.
Fuente: Elaboración propia (2024)

Nota: Seguido de realizar los modelados de la edificación de seis niveles se aplicó también el poder crear un espectro de sismo el cual se efectúa utilizando las condiciones propias del suelo, tipo de edificación y otros aspectos esenciales más. Estos factores se extrajeron de la Norma Técnica Peruana E 0.30; de este proceso se obtienen el producto que se buscaba que son las derivas que se obtienen de la edificación.

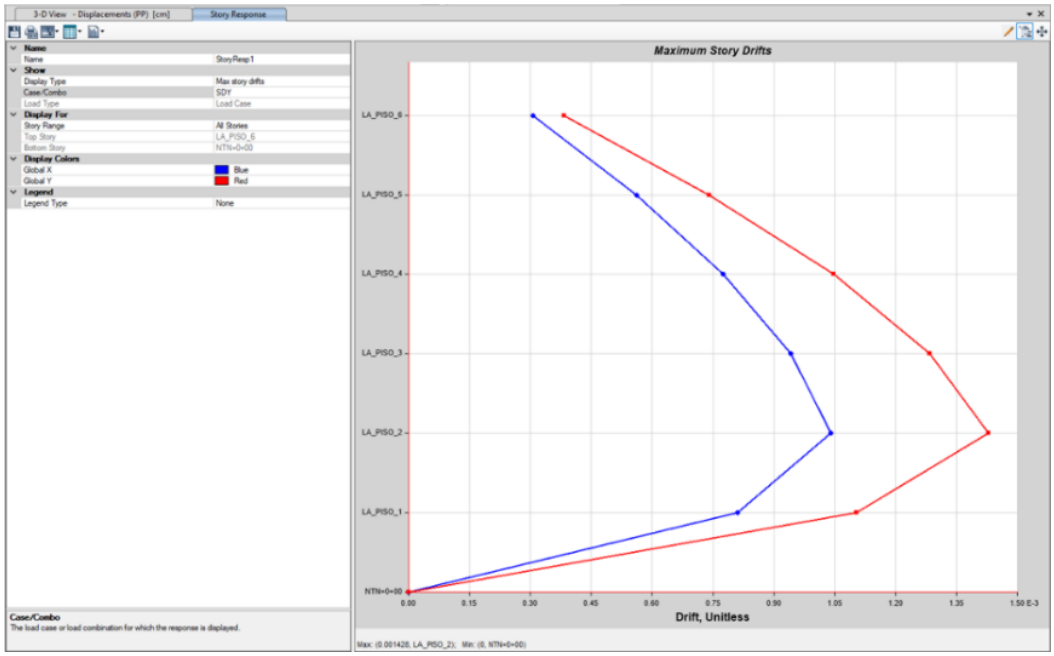

Figura IV: Diagrama de interacción de la columna más crítica aplicando el Método 01.
Nota: *Elaboración propia (2024)*

De los resultados obtenido cuando se aplicó el Método 01, nos arrojó que la columna en la dirección de sentido Y – Y se obtiene un 0.001428 cm tal como se observa en la Figura IV, seguido de ello se verifica propiamente como se detalló en el aspecto teórico a que este valor no debe superar el 0.007 cm.

Luego de ello verificamos la Tabla IX donde la deriva máxima aplicada tiene un valor de 0.0086 cm, la cual de acuerdo con la norma E 0.30 no cumple al cálculo máximo de la verificación de la deriva.

Verificación de la deriva producida con el Método 01	
Regularidad Estructural	Regular
Coeficiente para el Desplazamiento Lateral (C1)	0.75
Coeficiente de Reducción Sísmica (R)	8
Altura de entrepiso (cm)	280 cm
Desplazamiento Máximo en Y-Y	1.76 cm
Desplazamiento Máximo Real en Y-Y	10.56 cm
Verificación de la deriva en dirección y-y	0.0086 <= 0.007 (NO)

Tabla IX. Verificación de la deriva utilizando el método 01. Fuente: Elaboración propia (2024)
Nota: MDP y-y = Deriva máxima.

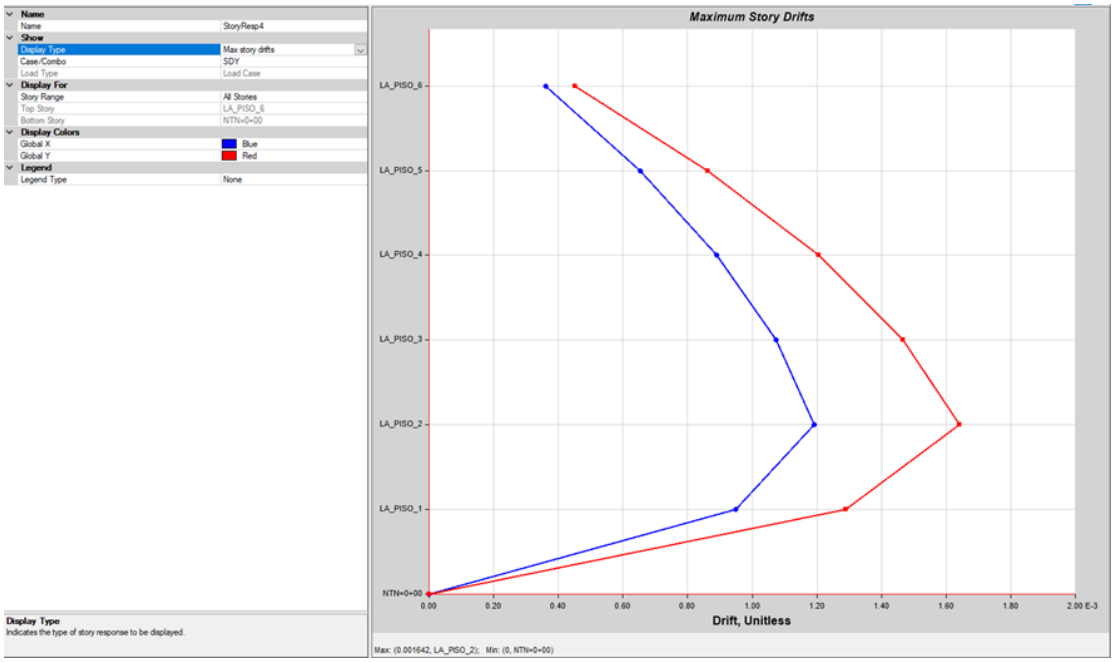

Figura V. Diagrama de interacción de la columna más crítica aplicando el Método 02.
Nota: Elaboración propia (2024)

De los resultados obtenido cuando se aplicó el Método 02, nos arrojó que la columna en la dirección de sentido Y – Y se obtiene un 0.001642 cm tal como se observa en la Figura V, seguido de ello se verifica propiamente como se detalló en el aspecto teórico a que este valor no debe superar el 0.007 cm.

Luego de ello verificamos la Tabla X donde la deriva máxima aplicada tiene un valor de 0.0099 cm, la cual de acuerdo con la norma E 0.30 no cumple al cálculo máximo de la verificación de la deriva.

Verificación de la deriva producida con el Método 02	
Regularidad Estructural	Regular
Coeficiente para el Desplazamiento Lateral (C1)	0.75
Coeficiente de Reducción Sísmica (R)	8
Altura de entrepiso (cm)	280 cm
Desplazamiento Máximo en Y-Y	2.02 cm
Desplazamiento Máximo Real en Y-Y	12.10 cm
Verificación de la deriva en dirección y-y	0.0099 <= 0.007 (NO)

Tabla X. - Verificación de la deriva utilizando el método 02
Fuente: Elaboración propia (2024). Nota: MDP y-y = Deriva máxima

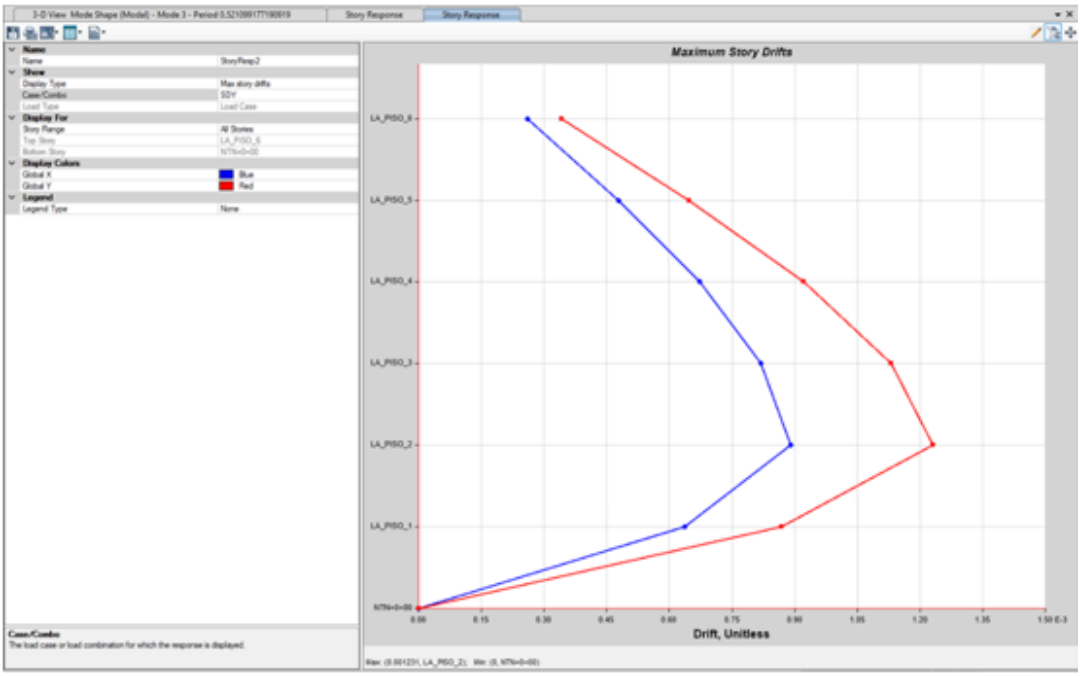

Figura VI. Diagrama de interacción de la columna más crítica aplicando el Método 03
Nota: *Elaboración propia (2024)*

De los resultados obtenido cuando se aplicó el Método 02, nos arrojó que la columna en la dirección de sentido Y – Y se obtiene un 0.001231 cm tal como se observa en la Figura VI, seguido de ello se verifica propiamente como se detalló en el aspecto teórico a que este valor no debe superar el 0.007 cm.

Luego de ello verificamos la Tabla XI donde la deriva máxima aplicada tiene un valor de 0.0069 cm, la cual de acuerdo con la norma E 0.30 no cumple al cálculo máximo de la verificación de la deriva.

Verificación de la deriva producida con el Método 03	
Regularidad Estructural	Regular
Coeficiente para el Desplazamiento Lateral (C1)	0.75
Coeficiente de Reducción Sísmica (R)	8
Altura de entrepiso (cm)	280 cm
Desplazamiento Máximo en Y-Y	1.52 cm
Desplazamiento Máximo Real en Y-Y	9.10 cm
Verificación de la deriva en dirección y-y	0.0074 <= 0.007 (NO)

Tabla XI. - Verificación de la deriva utilizando el método 03
Fuente: Elaboración propia (2024). Nota: MDP y-y = Deriva máxima.

4. Discusión. - El presente articulo científico ha permitido poder ver y realizar la comparativa de los resultados obtenidos en cuanto a las dimensiones de las columnas de una edificación y verificar cual es la variación de los desplazamientos de la estructura.

Según [4] los métodos de predimensionamiento siempre presentan diferentes condiciones de aplicación y que esto puede verse en el resultado final. Las variaciones finalmente se pudieron observar en las derivas ya que en cuanto a las dimensiones siempre el área total del elemento estructural será el mismo.

Cabe mencionar que para esta comparativa de las derivas o distorsiones que se producen en los entrepisos se utiliza la Tabla N° 11 de la normativa previamente mencionada.

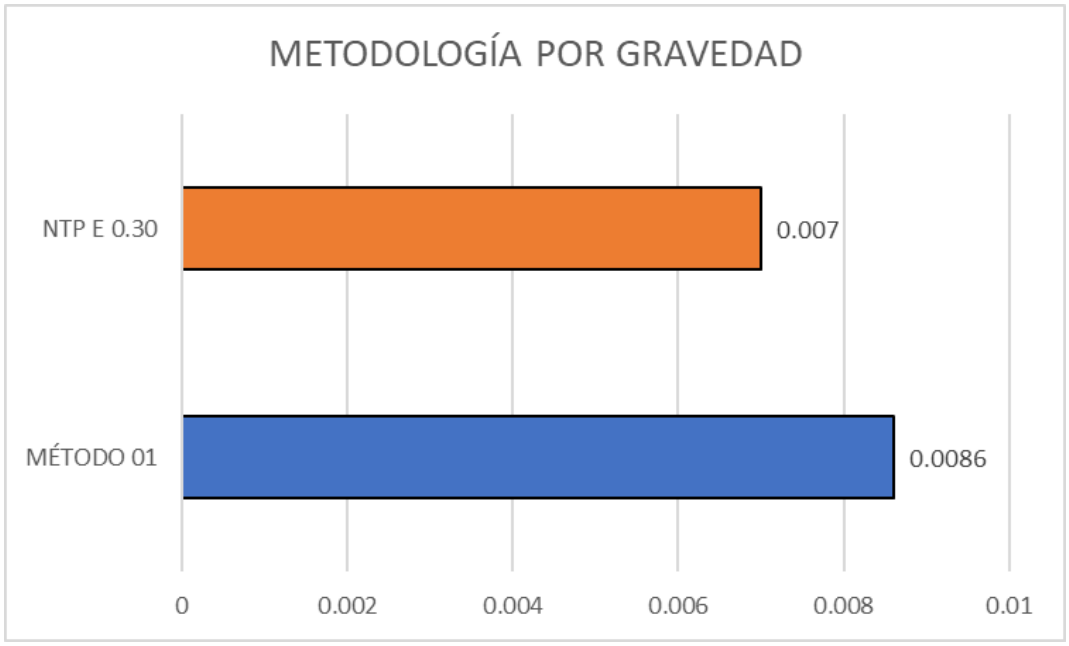

Figura VII. Comparación de la deriva obtenida con el primer método aplicado. Nota: Elaboración propia (2024)

Al momento de aplicar el método por gravedad se obtuvo como resultado que el valor máximo que fue producido en el eje Y-Y, con un valor de 0.0016 cm, en la cual la Figura VII representa casi en exceso a un 22.85 % con lo que respecta al valor que nos menciona la Norma Técnica Peruana E 0.30.

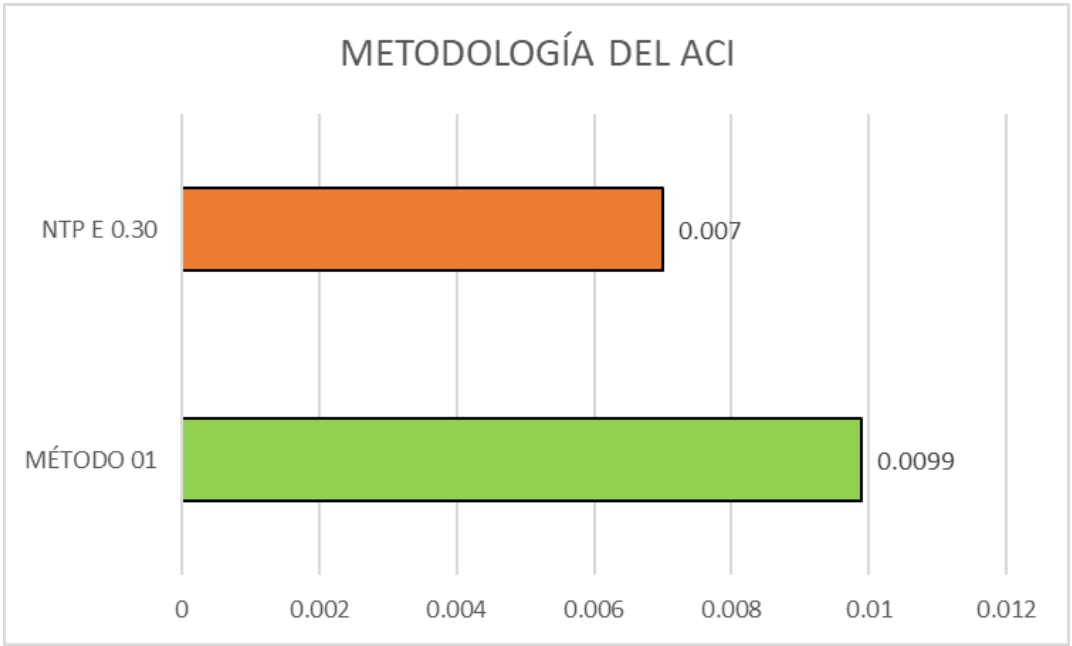

Figura VIII. Comparación de la deriva obtenida con el segundo método aplicado. Nota: Elaboración propia (2024)

Al momento de aplicar el método del ACI se obtuvo como resultado que el valor máximo que fue producido en el eje Y-Y, con un valor de 0.0029 cm, en la cual la Figura VIII representa casi en exceso a un 41.43 % con lo que respecta al valor que nos menciona la Norma Técnica Peruana E 0.30.

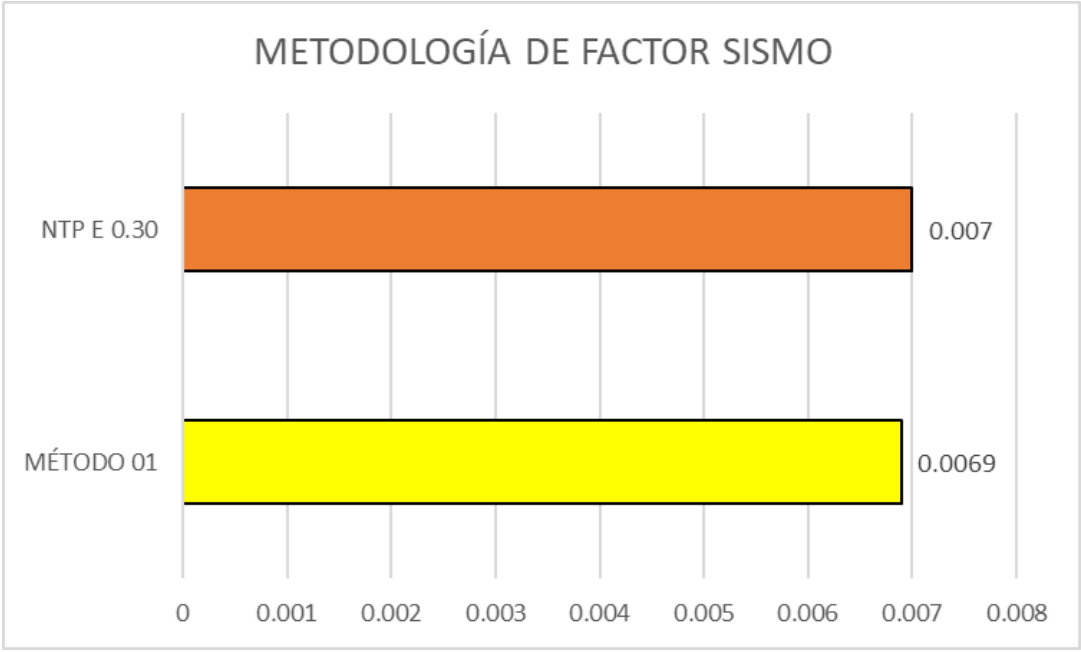

Figura IX. Comparación de la deriva obtenida con el segundo método aplicado. Nota: Elaboración propia (2024)

Al momento de aplicar el método por el factor sismo se obtuvo como resultado que el valor máximo que fue producido en el eje Y-Y, con un valor de 0.0004 cm, en la cual la Figura IX representa casi en exceso a un 5.71 % con lo que respecta al valor que nos menciona la Norma Técnica Peruana E 0.30.

5. Conclusiones. - Cuando se realizó el predimensionamiento de las columnas para la edificación con la que se está trabajando se aplicaron las metodologías tales como son la de gravedad, American Concrete Institute y el de factor sismo; esto nos permite poder realizar la precisión de que en todos los casos se ha podido observar una mayor distorsión en el segundo nivel debido a que es donde la estructura comienza a fallar.

De los tres métodos que se emplearon en el predimensionamiento con el que mejor resultados se obtuvieron en cuanto a las derivas que arrojo el análisis dinámico con espectro fue el tercer método el cual es del factor sismo teniendo una deriva de 0.0074 la cual como sabemos supera la distorsión máxima permitida, pero entre todos fue el menor.

Al emplear las metodologías de predimensionamiento en la estructuración para poder ejecutar las verificaciones se pudo observar que las dimensiones de las columnas por un hecho directo que mientras más niveles tenga la edificación mayor serán las medidas pero lo que también se pudo concluir es que las columnas rectangulares trabajan de mejor manera estructuralmente en comparación a las cuadradas ya que su centro de gravedad o centroide no trabajara de forma directa con las cargas que se calculan en el metrado de cargas.

Finalmente, de los resultados obtenidos se pudo obtener que con el primer método aplicado la deriva fue de 0.0086, con el segundo método el valor obtenido fue de 0.0099 y con el ultimo método se obtuvo de 0.0074; se puede afirmar que en el tercer método se aplicó una columna rectangular en el elemento que produce el mayor desplazamiento en comparación con los otros métodos que casi las dimensiones de esas columnas tanto en ancho y peralte fueron casi iguales.

Las mayores derivas producidas cuando se aplicaron los tres métodos de predimensionamiento para poder comparar las derivas fueron producidos en el eje Y y esto hace referencia a que quizás la longitud entre luces de ese lado es menor ya que el comportamiento estructural de la edificación afectara más en esa zona. [5]

Referencias

[1] American Concrete Institute, A. (2014). Requisito de Reglamento para Concreto Estructural (ACI 318S - 14). Always advancing.

[2] Barbat, A. H., Vargas, Y. F., Pujades, L. G., & Hurtado, J. E. (2016). Evaluación probabilista del riesgo sísmico de estructuras con base en la degradación de rigidez. ScienceDirect, XXXII, 39-47. Recuperado el Enero de 2024, de https://www.sciencedirect.com/science/article/pii/S0213131515000073

[3] Blanco, A. (1996). Estructuración y Diseño de Estructuras de concreto Armado.

[4] Calderón, R. J. (1996). Predimensionamiento de columnas en edificaciones de concreto armado.

[5] Chávez, A., & Ascencios, H. (2015). Análisis estructural y diseño sísmico de un edificio de 9 pisos con semisótano.

[6] Espinosa Cazarín, E. F., Terán Gilmore, A., Zúñiga Cuevas, O., & Jean Perilliat, R. (Junio de 2014). Consideraciones para el diseño sísmico de edificios altos de mampostería confinada ubicados en zonas sísmicas. SCIELO(90), 88-109. Recuperado el 01 de 2024, de https://www.scielo.org.mx/scielo.php?script=sci_arttext&pid=S0185-092X2014000100004&lang=es

[7] Gauri G., K., & Mundhada, D. (2017). Comparative Study of Static and Dynamic Seismic Analysis of. International Journal of Engineering Research, VII, 06-10. doi:10.9790/9622-0705050610

[8] Luévanos, A. (2012). A comparative study of two models for the seismic analysis of buildings. SCIELO, XXXII(3), 37-41. Recuperado el Enero de 2024

[9] Ortiz, E. L. (2012). Diseño estructural sismo-resistente de los edificios de departamentos de hormigón armado “Limburg Platz" de la ciudad de Quito, para garantizar la seguridad de los ocupantes (Bachelor's thesis).

[10] Trinches Boscardin, J., Yepes, V., & Kripka, M. (2019). Optimization of reinforced concrete building frames with automated. ICITECH, 1.

[11] Vásquez Bustamante, O. (2019). Reglamento Nacional de Edificaciones E 0.30. Lima.

[12] Vasquez, O. (2019). Reglamento Nacional de Edificaciones E 0.30.

[13] Vivar Q., A. (2021). Ingenieria en Edificaciones Aplicando la NTE E 0.20. Lima: Draft S.A.C Ingenieros.

[14] Wahane, R. M., & Phuke, R. M. (Junio de 2017). Comparative Study of Various Seismic Analysis Methods for Rc. Journal of Engineering Research and Application, VII, 30-36. doi:10.9790/9622-0706033036

Nota contribución de los autores:

1. Concepción y diseño del estudio
2. Adquisición de datos
3. Análisis de datos
4. Discusión de los resultados
5. Redacción del manuscrito
6. Aprobación de la versión final del manuscrito

MPRV ha contribuido en: 1, 2, 3, 4, 5 y 6.
RRPL ha contribuido en: 1, 2, 3, 4, 5 y 6.
JSLY ha contribuido en: 1, 2, 3, 4, 5 y 6.

Nota de aceptación: Este artículo fue aprobado por los editores de la revista Dr. Rafael Sotelo y Mag. Ing. Fernando A. Hernández Gobertti.

Análisis y diseño sísmico de una edificación multifamiliar de diez niveles y dos sótanos aplicando la interacción suelo-estructura con un sistema dual y platea de cimentación

Seismic Analysis and Design of a Ten-Story, Two-Basement Multifamily Building Using Soil-Structure Interaction with a Dual System and Foundation Slab

Análise comparativa de metodologias de pré-dimensionamento de colunas em edifício de seis níveis sem cave

Bladimir Quispe[1], Edson Carcausto[2], Genner Villarreal[3(*)]

Recibido: 23/02/2024 Aceptado: 20/04/2024

Resumen. - La presente investigación se desarrolla con la finalidad de determinar la influencia de la interacción sísmica en una edificación con respecto a una edificación con suposición de base fija. El edificio a modelar es de concreto armado con un sistema dual, cuya estructura está conformada por 10 niveles y dos sótanos, y una platea de cimentación la cual está ubicada en la ciudad de Arequipa, distrito de Yura.

Generalmente al realizar los análisis sísmicos de diferentes edificaciones se asume una suposición de base fija. Esta constituye particularmente adecuada siempre y cuando el tipo de suelo sea el de un tipo de roca dura a diferencia de otros tipos de suelos que no presentarían estas cualidades para un análisis con suposición de base fija. En la investigación se evalúa la influencia de la interacción suelo – estructura, es por esto que para la realización del modelamiento se utiliza el programa ETABS 2016, se procede a realizar un modelamiento de la edificación y a su vez esta cumpla lo establecido en la Norma Técnica E.030 de Diseño Sismorresistente. Posterior a esto se analiza la estructura, tomando en consideración la aplicación de los modelos dinámicos de D.D. Barkan – O.A. Savinov, Norma Rusa SNIP 2.02.05-87, A.E. Sargsian y N.G. Shariya.

Finalmente se concluye que, de los resultados obtenidos al realizar el análisis con la suposición de base fija versus el modelo de interacción suelo-estructura, los periodos fundamentales, el desplazamiento en las direcciones X e Y, las distorsiones, los esfuerzos cortantes en la base, las fuerzas internas de los elementos estructurales sufren un impacto en el resultado de cada uno de ellos.

Palabras clave: Análisis sísmico, suposición de base fija, sistema dual, interacción suelo – estructura.

(*) Autor Corresponsal

[1] Ingeniero Civil. Universidad de San Martin de Porres (Perú), bladimir_quispe@usmp.pe, ORCID iD: https://orcid.org/0009-0005-5741-0769

[2] Ingeniero Civil. Universidad de San Martin de Porres, edson_carcausto@usmp.pe, ORCID iD: https://orcid.org/0009-0004-3262-0279

[3] PhD. Universidad de San Martin de Porres, gvillarrealc@usmp.pe, ORCID iD: https://orcid.org/0000-0003-1768-646X

Memoria Investigaciones en Ingeniería, núm. 26 (2024). pp. 158-187
https://doi.org/10.36561/ING.26.10
ISSN 2301-1092 • ISSN (en línea) 2301-1106 – Universidad de Montevideo, Uruguay

Summary. - *The present investigation is developed with the purpose of determining the influence of the seismic interaction in a building with respect to a building with perfect embedment. The building to be modeled is a reinforced concrete building with a dual system, whose structure consists of 10 levels and two basements, and a foundation slab which is located in the city of Arequipa, district of Yura.*

Generally, when performing seismic analysis of different buildings, a perfect embedment is assumed. This is particularly adequate as long as the type of soil is hard rock or very stiff soils, as opposed to other types of soils that would not present these qualities for a perfect embedment analysis. In this investigation, the influence of soil-structure interaction is evaluated, which is why the ETABS 2016 program is used to perform the modeling, and the building is modeled to comply with the provisions of the Technical Standard E.030 of Seismic Resistant Design. Subsequently, the structure is analyzed, taking into consideration the application of the dynamic models of D.D. Barkan - O.A. Savinov, Russian Standard SNIP 2.02.05-87, A.E. Sargsian and N.G. Shariya.

Finally, it is concluded that, from the results obtained when carrying out the analysis with the assumption of a fixed base versus the soil-structure interaction model, the fundamental periods, the displacement in the X and Y directions, the distortions, the shear stresses in the base, the internal forces of the structural elements, suffer an impact on the result of each of them.

Keywords: *Seismic analysis, fixed base assumption, dual system, soil-structure interaction.*

Resumo*. -* *A presente investigação desenvolve-se com o objectivo de determinar a influência da interacção sísmica num edifício relativamente a um edifício com hipótese de base fixa. O edifício a modelar é de concreto armado de sistema duplo, cuja estrutura é composta por 10 níveis e dois subsolos, e uma laje de fundação que está localizada na cidade de Arequipa, distrito de Yura.*

Geralmente, ao realizar análises sísmicas de diferentes edifícios, assume-se uma suposição de base fixa. Isto é particularmente adequado desde que o tipo de solo seja um tipo de rocha dura, ao contrário de outros tipos de solo que não apresentariam estas qualidades para uma análise com uma suposição de base fixa. Na pesquisa é avaliada a influência da interação solo-estrutura, por isso é utilizado o programa ETABS 2016 para realizar a modelagem. O edifício é modelado e por sua vez atende ao disposto na Norma Técnica E.030. -Design resistente. Depois disso, a estrutura é analisada, levando em consideração a aplicação dos modelos dinâmicos de D.D. Barkan – O.A. Savinov, padrão russo SNIP 2.02.05-87, A.E. Sargsian e N.G. Sharia.

Por fim, conclui-se que, a partir dos resultados obtidos ao realizar a análise com pressuposto de base fixa versus modelo de interação solo-estrutura, foram identificados os períodos fundamentais, o deslocamento nas direções X e Y, as distorções, as tensões de cisalhamento na base, as forças internas dos elementos estruturais impactam no resultado de cada um deles.

Palavras-chave: *Análise sísmica, suposição de base fixa, sistema dual, interação solo-estrutura.*

1. Introducción. - El análisis de Interacción Suelo – Estructura es un método nuevo de análisis sísmico, el cual conecta a la Ingeniería Estructural con la Ingeniería Geotécnica, esta unión se da en la interacción de la base de la edificación con el suelo de fundación. En los últimos años los programas de software estructural tienen el desarrollo de capacidades que permiten varios tipos de estructuras, las cuales consideran la interacción que se da con el suelo de fundación de la base de la edificación.

En nuestra actualidad existen varios softwares como SAP2000, ETABS, STAAD Pro, ROBOT STRUCTURAL, Oasys GSA, entre otros, en las cuales nos permiten hacer modelamientos de cualquier tipo de estructuras, considerando el efecto de la interacción suelo-estructura.

Los softwares estructurales que incorporan capacidades SSI (Interacción suelo-estructura) son herramientas poderosas para el análisis y diseño de estructuras complejas, por ejemplo:

SAP2000: Es un software ampliamente utilizado para el análisis y diseño de estructuras civiles. Incorpora capacidades SSI que permiten modelar y analizar sistemas estructurales con subestructuras independientes. SAP2000 es conocido por su versatilidad y robustez en el análisis de estructuras de diferentes tipos y materiales.

ETABS: Similar a SAP2000, ETABS es otro software líder en el análisis y diseño de estructuras. Además de sus capacidades avanzadas para modelar y analizar edificios de varios pisos, ETABS también incorpora funcionalidades SSI para el análisis de sistemas estructurales complejos.

STAAD.Pro: Desarrollado por Bentley Systems, STAAD.Pro es una herramienta de análisis estructural que permite modelar y analizar una amplia variedad de estructuras, desde simples hasta muy complejas. STAAD.Pro incluye capacidades SSI que facilitan el análisis de sistemas con subestructuras independientes.

ROBOT STRUCTURAL Analysis Professional: Este software de Autodesk es utilizado para el análisis y diseño de estructuras de acero, concreto y madera. Incorpora capacidades SSI que permiten modelar y analizar sistemas estructurales complejos, como puentes y edificios de múltiples niveles con elementos estructurales independientes.

Oasys GSA (General Structural Analysis): Oasys GSA es un software de análisis estructural que ofrece capacidades avanzadas para el modelado y análisis de estructuras complejas. Incorpora funcionalidades SSI que permiten analizar sistemas con subestructuras independientes de manera eficiente.

Estos son solo algunos ejemplos de software estructural que incorporan capacidades SSI. Cada uno de estos programas tiene sus propias características y ventajas, por lo que la elección del software adecuado dependerá de las necesidades específicas del proyecto y de las preferencias del usuario.
Al observar las actuales tendencias de modelamiento estructural referidas a la SSI, se puede inferir que es posible modelar esta edificación donde los sistemas de apoyos consideren la presencia física de las cimentaciones y el suelo donde se apoya. Este tipo de modelamiento permite acercarnos al real comportamiento de los sistemas de apoyo en las estructuras y, por lo tanto, a una respuesta más próxima de la edificación frente a las acciones de gravedad y principalmente de sismo.

Existen dos métodos de realización de la interacción suelo-estructura, el método geotécnico que modela la estructura, la cimentación y el suelo de fundación con elementos sólidos incorporando sus propiedades físico-mecánicas y el método estructural, que modela la interacción suelo-estructura, incorporando los coeficientes de rigidez equivalente [23].

En la actualidad, existen dos formas de considerar la interacción suelo-estructura por el método estructural, una es la forma directa, aplicando los coeficientes de rigidez equivalente y otra es la forma inversa, generando un nuevo espectro para su diseño [24].

En la presente investigación se aplicó la forma directa del método estructural, la cual goza de gran popularidad y aplicación en muchos códigos de diseño a nivel mundial.

2. Análisis Sísmico. –

2.1. Análisis estático o de fuerzas estáticas equivalentes. - El presente análisis estático representa las solicitaciones sísmicas mediante fuerzas que actúan en el centro de masa de cada nivel de la edificación.

El artículo 28.1.2. de la Norma de Diseño Sismorresistente del Perú (E030), para el análisis mediante este procedimiento se pueden tomar estructuras regulares o irregulares ubicadas en la zona sísmica 1, en las otras zonas sísmicas puede emplearse este procedimiento para las estructuras clasificadas como regulares, según el artículo 19, de no más de 30 m de altura y de no más de 15 m de altura para las estructuras con muros portantes de concreto armado y albañilería confinada.

Según lo descrito en el artículo 28.1.2. la edificación en estudio no cumple con este artículo, por tal motivo se identifica que la edificación tiene una altura mayor a 30 m y es por ello que no es necesario el análisis estático en la edificación.

2.1.1. Consideraciones y limitaciones:

a) Linealidad de la respuesta: Este método asume que la respuesta de la estructura es lineal ante las cargas estáticas aplicadas. Sin embargo, en estructuras altamente no lineales, como aquellas sujetas a grandes deformaciones o comportamiento plástico, este enfoque puede no ser adecuado.

b) No considera efectos dinámicos: El análisis estático no tiene en cuenta los efectos dinámicos del comportamiento estructural, como la redistribución de cargas debido a la inercia y la rigidez dinámica.

c) Sensibilidad a la selección de cargas de diseño: La precisión del análisis estático depende en gran medida de la selección adecuada de las cargas de diseño y de su distribución en la estructura. Una mala elección puede conducir a resultados inexactos.

d) Limitaciones en estructuras irregulares: En el caso de estructuras altamente irregulares en planta o en elevación, el análisis estático puede subestimar o sobrestimar la respuesta sísmica debido a la falta de consideración de los efectos dinámicos.

2.2. Análisis dinámico modal espectral. - El análisis del edificio se realiza mediante el método de combinación modal espectral, dependientes de las masas que se aplican en el centro de masas, la rigidez de la estructura y el espectro de diseño, de acuerdo a la Norma de Diseño Sismorresistente E030. Los resultados esperados son los períodos de vibración, número de modos, estudio de formas de vibrar, alabeo en losas, desplazamiento lateral, distorsión de entrepisos y fuerzas internas de diseño por sismo, verificando las irregularidades y el cortante dinámico mínimo.

2.2.1. Consideraciones y limitaciones:

a) Linealidad de las propiedades modales: El análisis modal espectral asume que las propiedades modales de la estructura son lineales y que las formas modales se pueden superponer linealmente para obtener la respuesta total de la estructura. En estructuras altamente no lineales, este supuesto puede no ser válido.

b) Sensibilidad a la selección de modos: La precisión del análisis modal espectral depende en gran medida de la selección adecuada de los modos de vibración a considerar. Una mala selección puede conducir a resultados inexactos, especialmente en estructuras con modos de vibración significativamente diferentes.

c) Limitaciones en estructuras con múltiples direcciones de excitación: El análisis modal espectral puede tener limitaciones en estructuras con múltiples direcciones de excitación sísmica, ya que solo considera la respuesta en las direcciones modales principales.

d) No considera la interacción entre modos: El análisis modal espectral no tiene en cuenta la interacción entre los modos de vibración, lo que puede ser importante en estructuras con modos cercanos en frecuencia.

2.2.2. Parámetros de sitio. - De acuerdo a la Norma de Diseño Sismorresistente E030, los factores de zona sísmica, uso y suelo son los indicados en las tablas I, II y III.

Factor de zona (Z)

Zona	Factor Z
3	0.35

Tabla I. Factor de zona de la edificación.

Factor de uso (U)

Categoría	Descripción	Factor U
Edificaciones Comunes "C"	Vivienda Multifamiliar	1,0

Tabla II. Categoría de la edificación.

Factor de suelo (S)

Factor de suelo "S"	S3
Z3	1,2

Tabla III. Factor de suelo de la edificación

2.2.3. Aceleración espectral

$$S_a = \frac{Z \,.\, U \,.\, C \,.\, S}{R} \,.\, g$$

Donde:

Z: Factor zona $Z_3 = 0{,}35$

U: Factor de uso (Categoría de las edificaciones) $U = 1{,}00$
C: Factor de amplificación sísmica $C = 2{,}5$
S: Factor de suelo $S_3 = 1{,}20$
R: Coeficiente de reducción sísmica (sistema dual) $R_x = R_y = 7$
g: Gravedad $g = 9.71$ m/s2

Aceleración espectral

$$S_{ax} = S_{ay} = \frac{0.35 * 1{,}00 * 2.5 * 1{,}20}{7} * 9.71 \frac{m}{s2}$$

$S_{ax} = S_{ay} = 1.457$

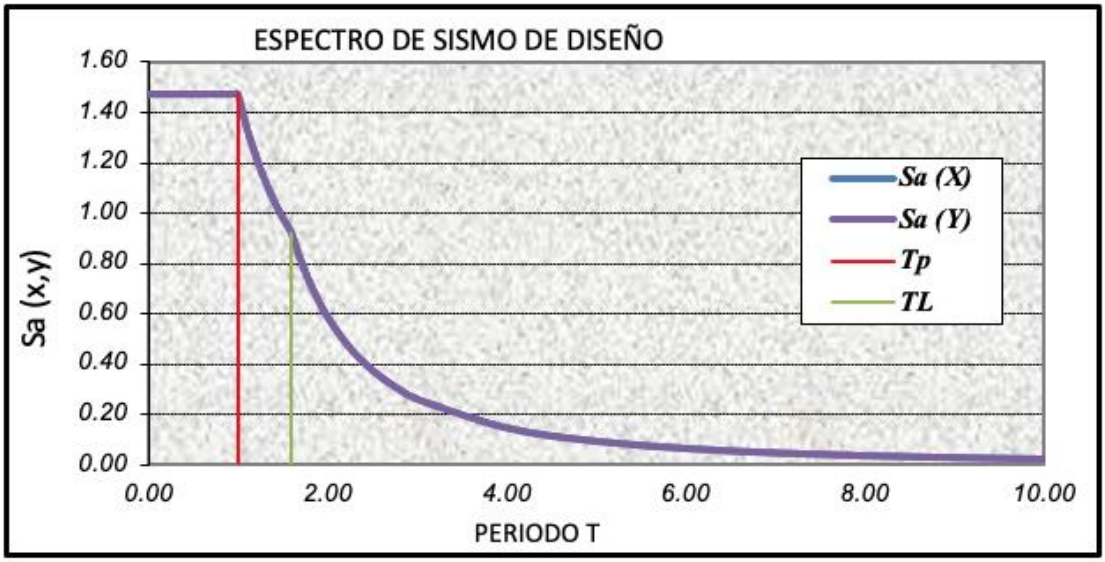

Figura I.- Espectro de aceleración.

Luego de la realización del análisis sísmico dinámico modal espectral, procedemos a realizar la verificación de las irregularidades en altura y planta, de acuerdo a la Norma de Diseño Sismorresistente E030.

2.2.4. Irregularidades en altura

Irregularidad de rigidez – piso blando:

Piso Blando en X-X (0.75)

Table: Story Stiffness				Irregularidad de Rigidez		
Story	**Stiffness X**	**Rigidez lateral de entrepiso (ki)**	**70% x ki**	**Irregularidad**	**80% x (promedio ki)**	**Irregularidad**
	tonf/m	**tonf/m**	**tonf/m**	**no/si**	**tonf**	**no/si**
tanque elevado	12705.986	12705.986	8894.1902	NO existe	10164.7888	NO existe
10° piso	74036.909	61330.923	42931.6461	NO existe	29614.7636	NO existe
9° piso	125146.214	51109.305	35776.5135	SI existe	33372.3237	SI existe
8° piso	154455.762	29309.548	20516.6836	SI existe	37799.9403	SI existe
7° piso	172004.082	17548.32	12283.824	NO existe	26124.5795	SI existe
6° piso	184447.113	12443.031	8710.1217	NO existe	15813.5731	SI existe
5° piso	195509.808	11062.695	7743.8865	NO existe	10947.7456	NO existe
4° piso	208647.885	13138.077	9196.6539	NO existe	9771.6808	NO existe
3° piso	227845.995	19198.11	13438.677	NO existe	11573.0352	NO existe
2° piso	255501.812	27655.817	19359.0719	NO existe	15997.8677	NO existe
1° piso	282049.82	26548.008				

Tabla IV. Verificación de la irregularidad de rigidez sísmica en "X".

Piso Blando en Y-Y (0.75)						
Table: Story Stiffness				**Irregularidad de Rigidez**		
Story	**Stiffness Y**	**Rigidez lateral de entrepiso (ki)**	**70% x ki**	**Irregularidad**	**80% x (promedio ki)**	**Irregularidad**
	tonf/m	**tonf/m**	**tonf/m**	**No/Si**	**tonf**	**No/Si**
Tanque elevado	8995.484	8995.484	6296.839	NO existe	5037.471	NO existe
10° Piso	58009.13	49013.646	34309.552	NO existe	16242.556	NO existe
9° Piso	101295.681	43286.551	30300.586	SI existe	18908.527	NO existe
8° Piso	129979.17	28683.489	20078.442	NO existe	22583.621	SI existe
7° Piso	150975.844	20996.674	14697.672	NO existe	17353.787	SI existe
6° Piso	168196.584	17220.74	12054.518	NO existe	12488.169	NO existe
5° Piso	183660.449	15463.865	10824.706	NO existe	10020.505	NO existe
4° Piso	199652.92	15992.471	11194.73	NO existe	9086.388	NO existe
3° Piso	222126.009	22473.089	15731.162	NO existe	10066.826	NO existe
2° Piso	251961.555	29835.546	20884.882	NO existe	12749.54	NO existe
1° Piso	287288.179	35326.624				

Tabla V. Verificación de la irregularidad de rigidez sísmica en "Y".

Realizada las verificaciones se determina que la estructura no presenta irregularidad por piso blando por lo cual le corresponde por norma, una estimación de valor de:

$$I_a = 1$$

Irregularidad de resistencia - piso débil:

Piso Débil en X-X (0.75)				
Table: Story Stiffness			**Irregularidades de Resistencia**	
Story	**Shear X**	**Resistencia de Entrepiso (ri)**	**80% x ri**	**Irregularidad**
	tonf	**tonf/m**	**tonf/m**	**No/Si**
Tanque elevado	9.539	9.539	7.6312	NO existe
10° Piso	75.8323	75.8323	60.6658	NO existe
9° Piso	151.8801	151.8801	121.5041	NO existe
8° Piso	218.6852	218.6852	174.9482	NO existe
7° Piso	277.1993	277.1993	221.7594	NO existe
6° Piso	327.8672	327.8672	262.2938	NO existe
5° Piso	370.8733	370.8733	296.6986	NO existe
4° Piso	406.1565	406.1565	324.9252	NO existe
3° Piso	433.4499	433.4499	346.7599	NO existe
2° Piso	452.532	452.532	362.0256	NO existe
1° Piso	463.4632	463.4632		

Tabla VI. Verificación de la irregularidad de piso débil en "X"

Piso Débil EN X-X (0.75)				
Table: Story Stiffness			Irregularidades de Resistencia	
Story	**Shear Y**	**Resistencia de Entrepiso (Ri)**	**80% x Ri**	**Irregularidad**
	tonf	**tonf/m**	**tonf/m**	**No/Si**
Tanque elevado	9.539	9.539	7.6312	NO existe
10° Piso	75.8323	75.8323	60.6658	NO existe
9° Piso	151.8801	151.8801	121.5041	NO existe
8° Piso	218.6852	218.6852	174.9482	NO existe
7° Piso	277.1993	277.1993	221.7594	NO existe
6° Piso	327.8672	327.8672	262.2938	NO existe
5° Piso	370.8733	370.8733	296.6986	NO existe
4° Piso	406.1565	406.1565	324.9252	NO existe
3° Piso	433.4499	433.4499	346.7599	NO existe
2° Piso	452.532	452.532	362.0256	NO existe
1° Piso	463.4632	463.4632		

Tabla VII. Verificación de la irregularidad de piso débil en "Y"

De la verificación la edificación el sistema estructural es discontinuo en los pisos 1 y 2 y el resto de pisos es típico, se deduce que, no presenta irregularidad por piso débil, por lo cual le corresponde por norma el valor de:

$$I_a = 1$$

Irregularidad de masa o peso:

Irregularidad Estructural en Altura				
Table: Story Forces			Irregularidad de Masa o Peso (0.90)	
Story	**P**	**Peso/nivel**	**1.5 x Peso/nivel**	**Irregularidad**
	tonf	**tonf**	**tonf**	**No/Si**
Tanque elevado	64.918	64.918		
10° Piso	458.4575	393.5395		
9° Piso	929.2815	470.824	706.236	NO existe
8° Piso	1400.1055	470.824	706.236	NO existe
7° Piso	1870.9294	470.8239	706.2359	NO existe
6° Piso	2341.7534	470.824	706.236	NO existe
5° Piso	2812.5774	470.824	706.236	NO existe
4° Piso	3283.4014	470.824	706.236	NO existe
3° Piso	3754.2254	470.824	706.236	NO existe
2° Piso	4230.1074	475.882	713.823	NO existe
1° Piso	4746.3555	516.2481	774.3722	NO existe
Sótano 01	5425.8409	679.4854		
Sótano 02	6166.6046	740.7637		
		4746.3555		

Tabla VIII. Verificación de irregularidades de masa

Realizada las verificaciones se determina que la estructura no presenta irregularidades por masa o peso, por lo cual le corresponde por norma, una estimación de valor de:

$$I_a = 1$$

Irregularidad geométrica vertical:

De la verificación la edificación el sistema estructural es discontinuo en los pisos 1 y 2 y el resto de pisos es típico, se deduce que, no presenta irregularidad geométrica vertical, por lo cual le corresponde por norma el valor de:

$$I_a = 1$$

Discontinuidad de los sistemas resistentes:

De la verificación la edificación el sistema estructural es discontinuo en los pisos 1 y 2 y el resto de pisos es típico, se deduce que, no presenta irregularidad en los sistemas resistentes, por lo cual le corresponde por norma el valor de:

$$I_a = 1$$

2.2.5. Irregularidades en planta. –

Irregularidad torsional:

Torsión en X-X				
Table: Diafragma Deriva máxima/media			**I. Torsional**	**I. Torsional Extrema**
Story	**Desviación Máxima**	**Relación**	**Irregularidad**	**Irregularidad**
			>1.3	**>1.5**
10° Piso	0.0023	1.186	NO existe	NO existe
9° Piso	0.0027	1.201	NO existe	NO existe
8° Piso	0.0032	1.218	NO existe	NO existe
7° Piso	0.0037	1.235	NO existe	NO existe
6° Piso	0.0042	1.249	NO existe	NO existe
5° Piso	0.0045	1.26	NO existe	NO existe
4° Piso	0.0046	1.27	NO existe	NO existe
3° Piso	0.0046	1.276	NO existe	NO existe
2° Piso	0.0042	1.28	NO existe	NO existe
1° Piso	0.0031	1.266	NO existe	NO existe

Tabla IX. Verificación de la irregularidad torsional sismo en "X"

Torsión en Y-Y				
Table: Diafragma Deriva máxima/media			**I. Torsional**	**I. Torsional Extrema**
Story	**Desviación Máxima**	**Ratio**	**Irregularidad**	**Irregularidad**
			>1.3	**>1.5**
10° Piso	0.003	1.021	NO existe	NO existe
9° Piso	0.0034	1.008	NO existe	NO existe
8° Piso	0.0038	1	NO existe	NO existe
7° Piso	0.0041	1.005	NO existe	NO existe
6° Piso	0.0044	1.01	NO existe	NO existe
5° Piso	0.0046	1.014	NO existe	NO existe
4° Piso	0.0047	1.02	NO existe	NO existe
3° Piso	0.0046	1.03	NO existe	NO existe
2° Piso	0.0042	1.046	NO existe	NO existe

1° Piso	0.0031	1.08	NO existe	NO existe

Tabla X. Verificación de la irregularidad torsional sismo en "Y"

Irregularidad por esquinas entrantes:

Debido a las diferentes dimensiones en planta que presenta nuestra edificación no se presenta esquinas entrantes, por lo cual le corresponde por norma una estimación de valor de:

$$I_p = 1{,}00$$

Irregularidad por discontinuidad de diafragma:

El presente proyecto no cuenta con aberturas significativas en las losas y estas aberturas son constantes a partir de piso 3, por lo cual no presenta irregularidad por discontinuidad de diafragma, por lo cual le corresponde por norma una estimación de valor de:

$$I_p = 1{,}00$$

Irregularidad por sistemas no paralelos:

El presente proyecto por su geometría no cuenta con irregularidades por sistemas no paralelos, por lo cual le corresponde por norma una estimación de valor de:

$$I_p = 1{,}00$$

Posterior de la realización de las verificaciones de las diferentes irregularidades tanto en altura y planta, así como en sismo dinámico "X" e "Y", se obtiene como resultado que la edificación es regular en altura y regular en planta, de los diferentes valores obtenidos se deberá tomar los menores y se obtendrá el coeficiente de reducción sísmica (R):

$$R = R_0 . I_a . I_P = 7 \text{ x } 1 \text{ x } 1 = 7.00$$

3. Análisis dinámico del edificio con suposición de base fija

3.1 Modos de vibración. -

Modos de Vibración				
TABLE: Modal Participating Mass Ratios				
Case	**Mode**	**Period**	**UX**	**UY**
Modal	1	0.639	0.0015	0.7214
Modal	2	0.593	0.4645	0.0004
Modal	3	0.51	0.2666	0.001
Modal	4	0.18	0.0005	0.1282
Modal	5	0.174	0.0636	0.0002
Modal	6	0.15	0.0591	0.003
Modal	7	0.09	0.001	0.0281
Modal	8	0.088	0.0183	0.0088
Modal	9	0.077	0.0203	0.003
Modal	10	0.058	0.0001	0.0129
Modal	11	0.055	0.0086	0.0029
Modal	12	0.05	0.0087	0.0014

Tabla XI. Masas participativas en los modos de vibración

- El primer modo de vibración es de traslación en el eje “X”, teniendo un resultado de 0.639 segundos.
- El segundo modo de vibración es de traslación en el eje “Y”, teniendo un resultado de 0.593 segundos.
- El tercer modo de vibración es de rotación alrededor del eje “Z”, teniendo un resultado de 0.510 segundos.

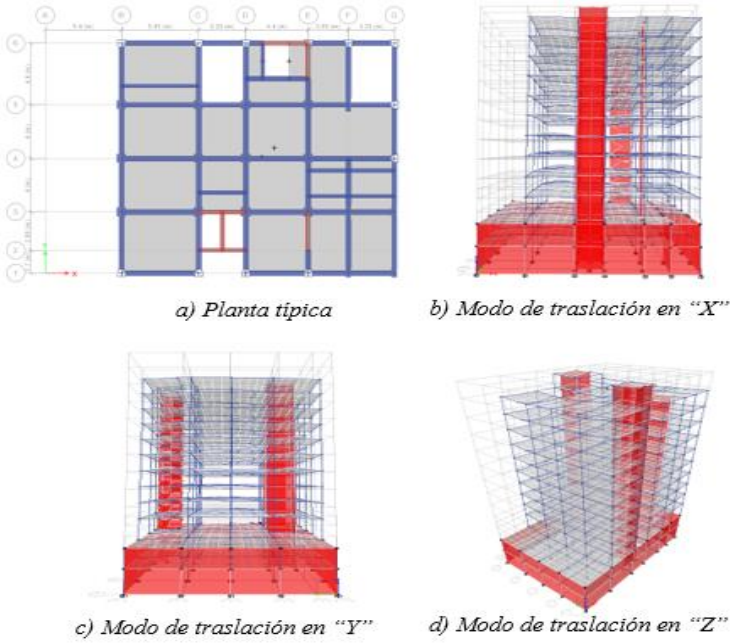

Figura II.- Planta típica, modos de vibración Software ETABS 2016.

3.2. Distorsión de entrepisos. –

Distorsión X-X					
Table: Story Drifts					
Story	**Direction**	**Drift**	**Desplazamiento Relativo**	**Desplazamiento**	**Cumple**
			(cm)	**cm**	> 0.007
Tanque elevado	X	0.0021	0.504	11.148	SI
10° Piso	X	0.00228	0.638	10.643	SI
9° Piso	X	0.00273	0.765	10.006	SI
8° Piso	X	0.00323	0.906	9.241	SI
7° Piso	X	0.00373	1.045	8.335	SI
6° Piso	X	0.00416	1.165	7.291	SI
5° Piso	X	0.00448	1.255	6.126	SI
4° Piso	X	0.00465	1.301	4.871	SI
3° Piso	X	0.0046	1.287	3.57	SI
2° Piso	X	0.00425	1.19	2.282	SI
1° Piso	X	0.00312	1.092	1.092	SI

Tabla XII. Distorsión de entrepisos en “X”.

Distorsión Y-Y					
Table: Story Drifts					
Story	**Drift**	**Label**	**Desplazamiento Relativo (cm)**	**Desplazamiento**	**Cumple**
				cm	> 0.007
Tanque elevado	0.003118	105	0.748	12.164	SI
10° Piso	0.003005	16	0.841	11.416	SI
9° Piso	0.003382	162	0.947	10.575	SI
8° Piso	0.003758	162	1.052	9.628	SI
7° Piso	0.004142	111	1.16	8.575	SI
6° Piso	0.004443	111	1.244	7.416	SI
5° Piso	0.004633	111	1.297	6.172	SI
4° Piso	0.004686	111	1.312	4.874	SI
3° Piso	0.004576	111	1.281	3.562	SI
2° Piso	0.00423	167	1.184	2.281	SI
1° Piso	0.003133	167	1.097	1.097	SI

Tabla XIII. Distorsión de entrepisos en "Y".

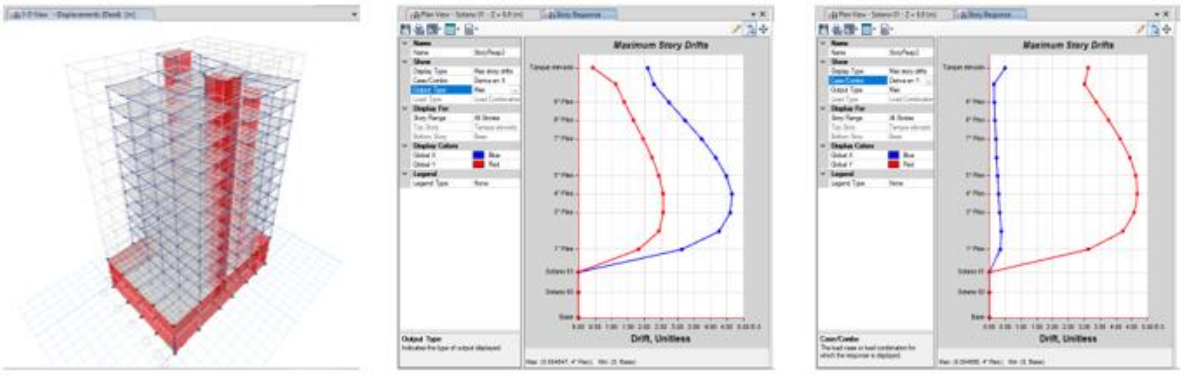

a) Vista 3D del modelo *a) Desplazamientos máximos en "X"* *a) Desplazamientos máximos en "Y"*

Figura III.- Distorsiones de entrepisos en X e Y Software ETABS 2016

- Se observa que cumple con las distorsiones de entrepiso para el sismo en las direcciones "X" e "Y", siendo su valor menor al indicado en la tabla 11 de la Norma de Diseño Sismorresistente E.030.

3.3. Cortante dinámico mínimo

	Cortante Estático	**Cortante Dinámico**	**FA**
X	711.953	463.463	1.229
Y	711.953	555.759	1.025

Tabla XIV. Factor de amplificación del cortante dinámico en ambas direcciones.

De acuerdo con el artículo 29.4.1. se debe de realizar la verificación para que las estructuras regulares alcancen por lo menos el 80% del cortante estático y para estructuras irregulares, no debe de ser menor que el 90%.

4. Análisis dinámico del edificio con Interacción Suelo-Estructura. -

4.1. Consideraciones para el diseño. - Para el presente cálculo del modelo dinámico de la edificación, se debe de tener en cuenta las diferentes características, así como las del suelo.

Características de la edificación

- Resistencia a la compresión del concreto $f'c = 2800$ Ton/m2
- Módulo de elasticidad del concreto $Ec = 2509980$ Ton/m2
- Coeficiente de Poisson del concreto $\mu_C = 0.2$
- Losa de techo aligerada de espesor $e = 0.25$
- Platea de cimentación con dimensiones 26 m x18 m x1.15 m
- Profundidad de desplante Mayor a 1.8 m

Características del suelo

- Tipo de suelo arena arcillosa de baja plasticidad
- Módulo de elasticidad del suelo $Es = 20$MPa ó 2000 Ton. m2
- Densidad del suelo $\rho_S = 0.1$ T.s^2/m^4
- Coeficiente de Poisson del suelo $\mu_C = 0.35$
- Capacidad portante del suelo $q_a = 1.94$ kg/cm^2
- Pesos por piso:

NIVEL	PESO (Ton)
Tanque elevado	64.92
10° Piso	393.54
9° Piso	470.82
8° Piso	470.82
7° Piso	470.82
6° Piso	470.82
5° Piso	470.82
4° Piso	470.82
3° Piso	470.82
2° Piso	475.88
1° Piso	516.25
Sótano 01	679.49
Sótano 02	740.76
TOTAL	**6166.6046**

Tabla XV. Distribución de peso por piso.

4.2. Cálculo de masas de la platea. - Las masas traslacionales respecto a los ejes centroidales X, Y, Z y las masas rotacionales respecto a los ejes de contacto con el suelo-platea, indicamos como X', Y', Z'. Se calculan con las siguientes fórmulas.

$$M_t = M_x = M_y = M_z = \frac{2.4 * 26 * 18 * 1.15}{9.81} = 131.67\ (T.s^2/m)$$

$$M_{\varphi x'} = 131.67 * \left(\frac{1.15}{2}\right)^2 + \frac{131.67 * 18^2}{12} = 3598.62\ (T.s^2/m)$$

$$M_{\varphi y'} = 131.67 * \left(\frac{1.15}{2}\right)^2 + \frac{131.67 * 26^2}{12} = 7460.93\ (T.s^2/m)$$

$$M_{\varphi z'} = \frac{131.67(26^2 + 18^2)}{12} = 10972.48\ (T.s^2/m)$$

M_x $(T.s^2/m)$	M_y $(T.s^2/m)$	M_z $(T.s^2/m)$	$M_{\varphi x'}$ $(T.s^2/m)$	$M_{\varphi y'}$ $(T.s^2/m)$	$M_{\varphi z'}$ $(T.s^2/m)$
131.67	131.67	131.67	3598.62	7460.93	10972.48

Tabla XVI. Masas de la platea.

4.3. Cálculo de coeficientes de rigidez

4.3.1. Modelo dinámico D.D. Barkan – O.A. Savinov. - Para la investigación se utilizó el libro Interacción sísmica suelo-estructura en edificaciones con plateas de cimentación del Dr. Genner Villarreal Castro, asumiendo un valor de:

$C_o = 0.8\ Kg/cm^2$ (arena arcillosa de baja plasticidad).

Calculamos la magnitud de la presión estática del suelo "ρ" para la platea:

$$\rho = \frac{6{,}166.60 + 2.4 * 26 * 18 * 1.15}{26 * 18} = 15.94\ \left(\frac{Ton}{m^2}\right)$$

Se procede a calcular D_o por la siguiente formula:

$$D_o = \frac{1-\mu}{1-0.5\mu} * C_o = \frac{1-0.35}{1-0.5*0.35}(800) = 630.30\ \left(\frac{Ton}{m^3}\right)$$

Luego, se calculan los coeficientes $C_x, C_z, C_{\varphi x}, C_{\varphi y}$ por las fórmulas:

$$C_x = D_o * \left[1 + \frac{2(a+b)}{\Delta * A}\right] * \sqrt{\frac{\rho}{\rho_o}}$$

$$C_x = 630.30 * \left[1 + \frac{2(26+18)}{1*468}\right] * \sqrt{\frac{15.94}{2}} = 2{,}113.78\frac{ton}{m^3}$$

$$C_z = C_o * \left[1 + \frac{2(a+b)}{\Delta * A}\right] * \sqrt{\frac{\rho}{\rho_o}}$$

$$C_z = 800 * \left[1 + \frac{2(26+18)}{1*468}\right] * \sqrt{\frac{15.94}{2}} = 2{,}682.88\frac{ton}{m^3}$$

$$C_{\varphi x} = C_o * \left[1 + \frac{2(a+3b)}{\Delta * A}\right] * \sqrt{\frac{\rho}{\rho_o}}$$

$$C_{\varphi x} = 800 * \left[1 + \frac{2(26+3*18)}{1*468}\right] * \sqrt{\frac{15.94}{2}} = 3{,}030.30\frac{ton}{m^3}$$

$$C_{\varphi y} = C_o * \left[1 + \frac{2(b+3a)}{\Delta * A}\right] * \sqrt{\frac{\rho}{\rho_o}}$$

$$C_{\varphi y} = 800 * \left[1 + \frac{2(18+3*26)}{1*468}\right] * \sqrt{\frac{15.94}{2}} = 3{,}184.71\frac{ton}{m^3}$$

Ahora se determinan los coeficientes de rigidez $K_x, K_y, K_z, K_{\varphi x}, K_{\varphi y}$ con las siguientes fórmulas:

$$K_x = K_y = C_x * A = 2113.78 * 26 * 18 = 989{,}249.27 \left(\frac{T}{m}\right)$$

$$K_z = C_z * A = 2{,}682.88 * 26 * 18 = 1{,}255{,}585.61 \left(\frac{T}{m}\right)$$

$$K_{\varphi x} = C_{\varphi x} * I_x = 3{,}030.30 * \frac{26 * 18^3}{12} = 38{,}290{,}844.63 \ (T.m)$$

$$K_{\varphi y} = C_{\varphi y} * I_y = 3{,}184.71 * \frac{18 * 26^3}{12} = 83{,}961{,}642.10 \ (T.m)$$

4.3.2. Modelo dinámico Norma Rusa SNIP 2.02.05-87. - El coeficiente de compresión elástica uniforme lo calculamos con la siguiente fórmula:

$$C_z = b_o * E * \left(1 + \sqrt{\frac{A_{10}}{A}}\right) = 1.2 * 2000 * \left(1 + \sqrt{\frac{10}{468}}\right) = 2750.82 \frac{ton}{m^3}$$

- ✓ Si $b_o = 1.2$ (Arenas arcillosas)
- ✓ Si $A_{10} = 10\ m^2$

Luego, determinamos los coeficientes de desplazamiento elástico uniforme, compresión elástica no uniforme y desplazamiento elástico no uniforme y lo calculamos con las siguientes fórmulas:

$$C_x = 0.7 * C_z = 0.7 * 2750.823 = 1925.58 \left(\frac{T}{m^3}\right)$$

$$C_{\varphi x} = C_{\varphi y} = 2 * C_z = 2 * 2750.823 = 5501.65 \left(\frac{T}{m^3}\right)$$

$$C_{\varphi z} = C_z = 2750.82 \left(\frac{T}{m^3}\right)$$

Calculamos los coeficientes de rigidez con las siguientes fórmulas:

$$K_x = K_y = C_x * A = 1925.58 * 468 = 901{,}169.68 \left(\frac{T}{m}\right)$$

$$K_z = C_z * A = 2750.82 * 468 = 1{,}287{,}385.26 \left(\frac{T}{m}\right)$$

$$K_{\varphi x} = C_{\varphi x} * I_x = 5501.65 * \frac{26 * 18^3}{12} = 69{,}518{,}804.11 \ (Ton.m)$$

$$K_{\varphi y} = C_{\varphi y} * I_y = 5501.65 * \frac{18 * 26^3}{12} = 145{,}045{,}406.10 \ (Ton.m)$$

$$K_{\varphi z} = C_{\varphi z} * I_z = 2750.82 * \left(\frac{18 * 26^3}{12} + \frac{26 * 18^3}{12}\right) = 107{,}282{,}105.10 \ (Ton.m)$$

Ahora determinamos las características de la amortiguación relativa para las vibraciones verticales β_z con la siguiente formula:

$$\beta_z = 2 * \sqrt{\frac{E}{C_z * p_m}} = 2 * \sqrt{\frac{2000}{2750.82 * 19.4}} = 0.387$$

Donde:

$$p_m = 1 * 1.94 \left(\frac{kg}{cm^2}\right) = 19.4 \left(\frac{Ton}{m^2}\right)$$

Luego calculamos las amortiguaciones relativas para las vibraciones rotacionales y verticales con las siguientes fórmulas:

$\beta_x = 0.6 * \beta_z = 0.6 * 0.387 = 0.232$
$\beta_{\varphi x} = \beta_{\varphi y} = 0.5 * \beta_z = 0.5 * 0.387 = 0.194$
$\beta_{\varphi z} = 0.3 * \beta_z = 0.3 * 0.387 = 0.116$

Posteriormente calculamos las características de amortiguamiento con las siguientes fórmulas:

$B_x = B_y = 2 * \beta_x * \sqrt{K_x * M_x} = 2 * 0.232 * \sqrt{901{,}169.68 * 131.67}$
$B_x = B_y = 5{,}061.05\ (T.s^2/m)$
$B_z = 2 * \beta_z * \sqrt{K_z * M_z} = 2 * 0.387 * \sqrt{1{,}287{,}385.26 * 131.670}$
$B_z = 10{,}081.84\ (T.s^2/m)$
$B_{\varphi x} = 2 * \beta_{\varphi x} * \sqrt{K_{\varphi x} * M_{\varphi x'}} = 2 * 0.194 * \sqrt{69{,}518{,}804.11 * 3598.62}$
$B_{\varphi x} = 193{,}656.32\ (T.s^2/m)$
$B_{\varphi y} = 2 * \beta_{\varphi y} * \sqrt{K_{\varphi y} * M_{\varphi y'}} = 2 * 0.194 * \sqrt{145{,}045{,}406.10 * 7460.93}$
$B_{\varphi y} = 402{,}773.79\ (T.s^2/m)$
$B_{\varphi z} = 2 * \beta_{\varphi z} * \sqrt{K_{\varphi z} * M_{\varphi z'}} = 2 * 0.116 * \sqrt{107{,}282{,}105.10 * 10972.48}$
$B_{\varphi z} = 252{,}046.12\ (T.s^2/m)$

En las presentes tablas se muestra los coeficientes de rigidez y características de amortiguamiento para los dos modelos dinámicos.

Modelo dinámico	$\mathbf{K_x}$ $(\mathbf{T/m})$	$\mathbf{K_y}$ $(\mathbf{T/m})$	$\mathbf{K_z}$ $(\mathbf{T/m})$	$\mathbf{K_{\varphi x}}$ $(\mathbf{T/m})$	$\mathbf{K_{\varphi y}}$ $(\mathbf{T/m})$	$\mathbf{K_{\varphi z}}$ $(\mathbf{T/m})$
Barkan	989,249.27	989,249.27	1,255,585.61	38,290,844.63	83,961,642.10	-
Norma Rusa	901,169.68	901,169.68	1,287,385.26	69,518,804.11	145,045,406.10	107,282,105.10

Tabla XVII. Coeficientes de rigidez.

Modelo dinámico	$\mathbf{B_x}$ $(\mathbf{T.s^2/m})$	$\mathbf{B_y}$ $(\mathbf{T.s^2/m})$	$\mathbf{B_z}$ $(\mathbf{T.s^2/m})$	$\mathbf{B_{\varphi x}}$ $(\mathbf{T.s^2/m})$	$\mathbf{B_{\varphi y}}$ $(\mathbf{T.s^2/m})$	$\mathbf{B_{\varphi z}}$ $(\mathbf{T.s^2/m})$
Norma Rusa	5,061.05	5,061.05	10,081.84	193,656.32	402,773.79	252,046.12

Tabla XVIII. Coeficientes de amortiguamiento.

4.4. Asignación de punto en el centro de la platea. - Se realiza la asignación de un punto en el centroide de la platea, lugar donde se colocarán las masas calculadas. Luego, se le asignará un resorte con los coeficientes de rigidez calculados, estos simulan las características elásticas del suelo.

4.4.1. Modelo Dinámico D.D. Barkan – O.A. Savinov

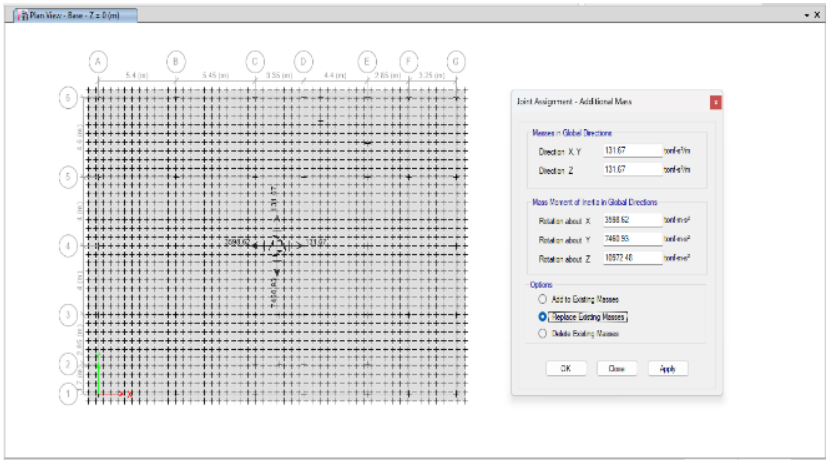

Figura IV.- Asignación de masas

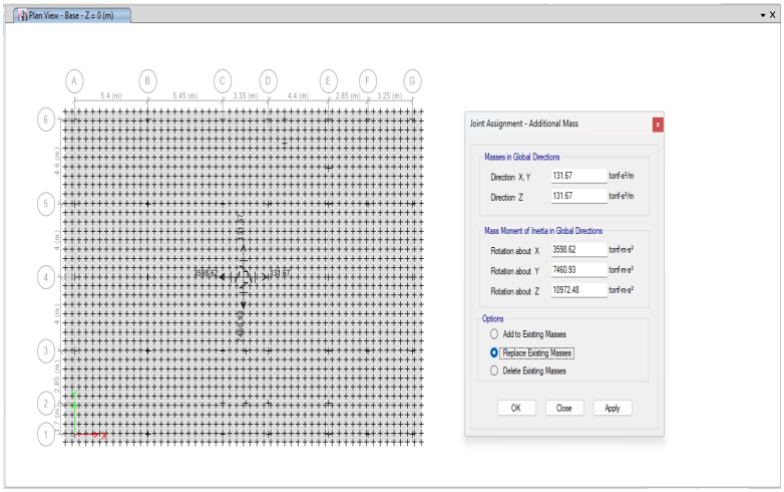

Figura V.- Asignación de coeficientes de rigidez

4.4.2. Modelo Dinámico Norma Rusa SNIP 2.02.05-87

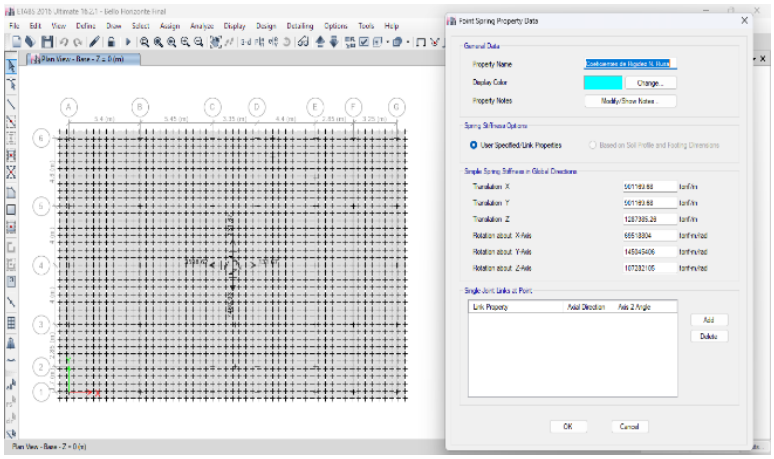

Figura VI. - Asignación de masas

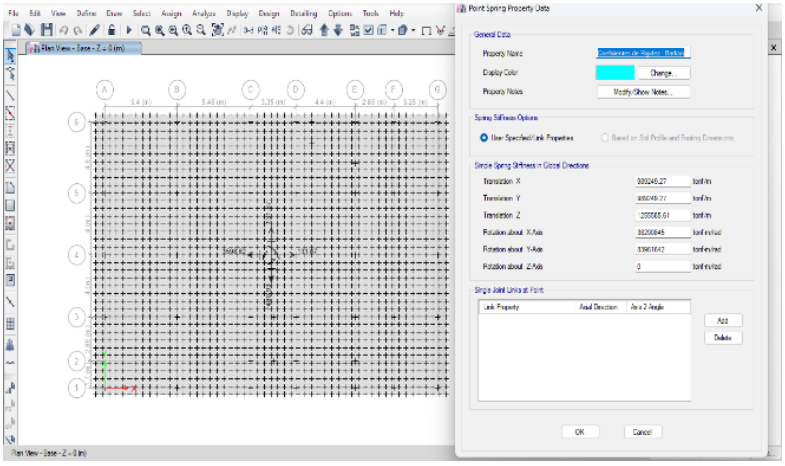

Figura VII.- Asignación de coeficientes de rigidez

5. Análisis y discusión de resultados

5.1. Periodos de vibración. - Como se muestra en la tabla XIX de comparación de periodos de los modelos utilizados y esta a su vez se encuentra graficada en la figura VIII, los periodos se han incrementado en los modelos Barkan y Norma Rusa. Cabe recordar que en estos dos se ha considerado la flexibilidad del suelo de fundación, en el modo 1 se puede observar que el modelo empotrado tiene un periodo de 0.639 segundos, el modelo Barkan tiene un periodo de 0.674 segundos y el modelo de la Norma Rusa, un periodo de 0.667 segundos.

Modo	Comparación de Periodos		
	Empotrado	Barkan	Norma Rusa
1	0.639	0.674	0.667
2	0.593	0.612	0.608
3	0.51	0.522	0.52
4	0.18	0.18	0.18
5	0.174	0.174	0.174
6	0.15	0.15	0.15
7	0.09	0.09	0.09
8	0.088	0.088	0.088
9	0.077	0.077	0.077
10	0.058	0.058	0.058
11	0.055	0.055	0.055
12	0.05	0.05	0.05
13	0.043	0.043	0.043
14	0.041	0.041	0.041
15	0.038	0.038	0.038
16	0.035	0.035	0.035
17	0.032	0.032	0.032
18	0.029	0.029	0.029
19	0.028	0.028	0.028
20	0.026	0.026	0.026
21	0.024	0.024	0.024
22	0.023	0.023	0.023
23	0.023	0.023	0.023
24	0.022	0.022	0.022
25	0.02	0.02	0.02
26	0.02	0.02	0.02

27	0.02	0.02	0.02
28	0.02	0.02	0.02
29	0.018	0.018	0.018
30	0.018	0.018	0.018
31	0.018	0.018	0.018
32	0.018	0.018	0.018
33	0.017	0.017	0.017
34	0.017	0.017	0.017
35	0.016	0.016	0.016
36	0.013	0.015	0.015

Tabla XIX. Comparación de periodos de los modelos dinámicos.

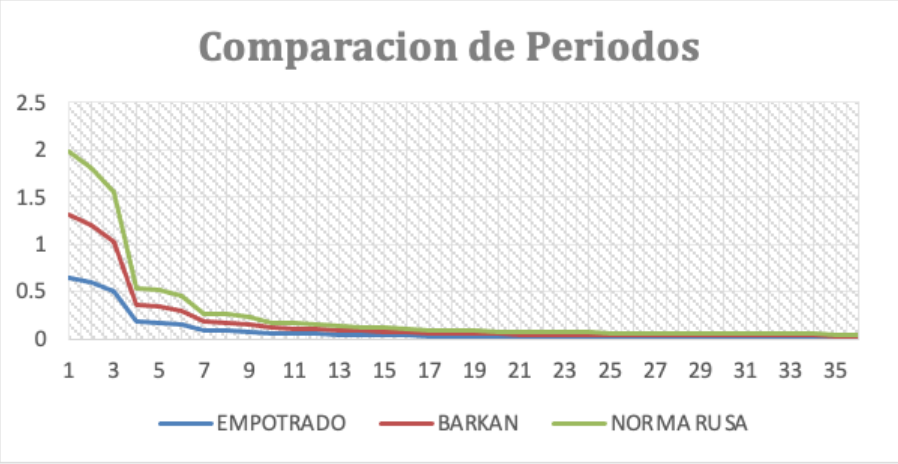

Figura VIII.- Comparación de periodos con los modos de vibración.

5.2. Desplazamientos.

5.2.1 Modelo de suposición de base fija. - Se observa un desplazamiento máximo de 11.148 cm en la dirección "X", y un desplazamiento máximo de 11.945 cm en dirección "Y".

Dirección X-X		**Dirección Y-Y**	
Pisos	**Desplazamiento (cm)**	**Pisos**	**Desplazamiento (cm)**
Tanque elevado	11.148	Tanque elevado	11.945
10° Piso	10.643	10° Piso	11.197
9° Piso	10.006	9° Piso	10.355
8° Piso	9.241	8° Piso	9.408
7° Piso	8.335	7° Piso	8.356
6° Piso	7.291	6° Piso	7.196
5° Piso	6.126	5° Piso	5.952
4° Piso	4.871	4° Piso	4.655
3° Piso	3.570	3° Piso	3.343
2° Piso	2.282	2° Piso	2.062
1° Piso	1.092	1° Piso	0.877

Tabla XX. Desplazamientos modelo de suposición de base fija

5.2.2 Modelo dinámico D.D. Barkan – O.A. Savinov. - Se observa un desplazamiento máximo de 12.684 cm en la dirección "X", y un desplazamiento máximo de 13.604 cm en dirección "Y".

Dirección X-X		Dirección Y-Y	
Pisos	**Desplazamiento (cm)**	**Pisos**	**Desplazamiento (cm)**
Tanque elevado	12.684	Tanque elevado	13.604
10° Piso	12.067	10° Piso	12.735
9° Piso	11.300	9° Piso	11.753
8° Piso	10.399	8° Piso	10.667
7° Piso	9.349	7° Piso	9.474
6° Piso	8.154	6° Piso	8.174
5° Piso	6.833	5° Piso	6.792
4° Piso	5.421	4° Piso	5.359
3° Piso	3.964	3° Piso	3.914
2° Piso	2.528	2° Piso	2.505
1° Piso	1.207	1° Piso	1.202

Tabla XXI. Desplazamientos modelo D.D. Barkan – O.A. Savinov.

5.2.3 Modelo Dinámico Norma Rusa SNIP 2.02.05-87. - Se observa un desplazamiento máximo de 12.416 cm en la dirección "X", y un desplazamiento máximo de 13.311 cm en dirección "Y".

Dirección X-X		Dirección Y-Y	
Pisos	**Desplazamiento (cm)**	**Pisos**	**Desplazamiento (cm)**
Tanque elevado	12.416	Tanque elevado	13.311
10° Piso	11.820	10° Piso	12.467
9° Piso	11.078	9° Piso	11.514
8° Piso	10.201	8° Piso	10.457
7° Piso	9.178	7° Piso	9.293
6° Piso	8.009	6° Piso	8.022
5° Piso	6.715	5° Piso	6.668
4° Piso	5.330	4° Piso	5.262
3° Piso	3.899	3° Piso	3.844
2° Piso	2.488	2° Piso	2.461
1° Piso	1.188	1° Piso	1.181

Tabla XXII. Desplazamientos modelo Norma Rusa 2.02.05-87.

En la Figura IX se observan los desplazamientos en X, de los diferentes modelos utilizados, teniendo mayor desplazamiento el modelo Barkan a comparación del modelo Empotrado y el modelo de la Norma Rusa.

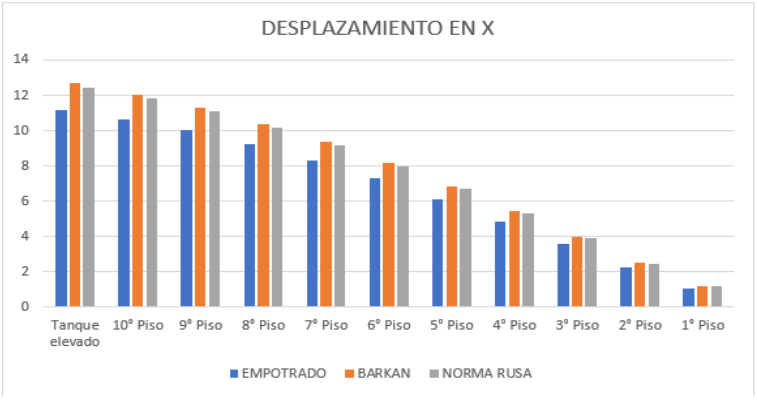

Figura IX.- Comparación de desplazamientos con los modelos dinámicos en "X"

En la Figura X se observa los desplazamientos en Y, de los diferentes modelos utilizados, teniendo mayor desplazamiento el modelo Barkan a comparación del modelo Empotrado y el modelo de la Norma Rusa.

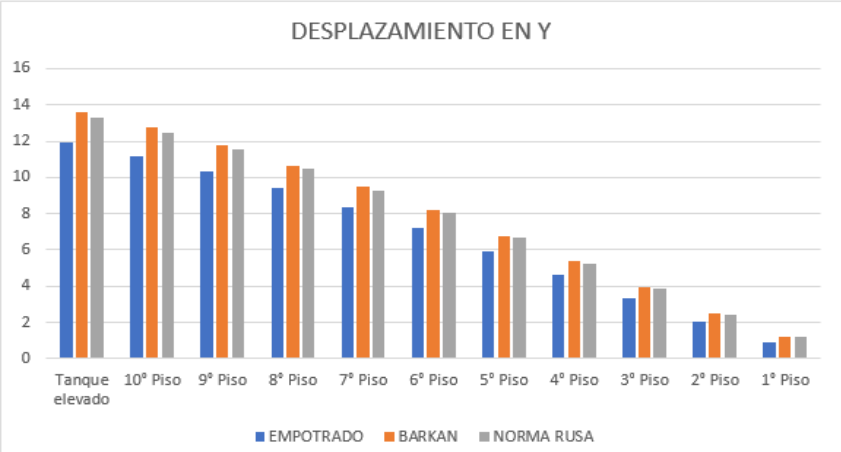

Figura X.- Comparación de desplazamientos con los modelos dinámicos en "Y"

5.3. Distorsiones de entrepisos. -

5.3.1 Modelo de suposición de base fija.

Dirección X-X			
Table: Story Drifts			
Story	**Drift**	**Lim 0.007**	**Cumple**
Tanque elevado	0.00210	0.007	SI
10° Piso	0.00228	0.007	SI
9° Piso	0.00273	0.007	SI
8° Piso	0.00323	0.007	SI
7° Piso	0.00373	0.007	SI
6° Piso	0.00416	0.007	SI
5° Piso	0.00448	0.007	SI
4° Piso	0.00465	0.007	SI
3° Piso	0.00460	0.007	SI
2° Piso	0.00425	0.007	SI
1° Piso	0.00312	0.007	SI

Tabla XXIII. Distorsión en "X" modelo de suposición de base fija.

Dirección Y-Y			
Table: Story Drifts			
Story	**Drift**	**Lim 0.007**	**Cumple**
Tanque elevado	0.00312	0.007	SI
10° Piso	0.00301	0.007	SI
9° Piso	0.00338	0.007	SI
8° Piso	0.00376	0.007	SI
7° Piso	0.00414	0.007	SI
6° Piso	0.00444	0.007	SI
5° Piso	0.00463	0.007	SI
4° Piso	0.00469	0.007	SI

3° Piso	0.00458	0.007	SI
2° Piso	0.00423	0.007	SI
1° Piso	0.00313	0.007	SI

Tabla XXIV. Distorsión en "Y" modelo de suposición de base fija.

Se aprecia en las tablas XXIII y XXIV que la distorsión máxima se da en el 4° piso con una distorsión de 0.00448 en la dirección X y 0.00469 en la dirección Y, cumpliendo en ambas direcciones con la distorsión máxima permitida por la Norma de Diseño Sismorresistente E030.

5.3.2 Modelo dinámico D.D. Barkan – O.A. Savinov.

Dirección X-X			
Table: Story Drifts			
Story	**Drift**	**Lim 0.007**	**Cumple**
Tanque elevado	0.00257	0.007	SI
10° Piso	0.00274	0.007	SI
9° Piso	0.00322	0.007	SI
8° Piso	0.00375	0.007	SI
7° Piso	0.00427	0.007	SI
6° Piso	0.00472	0.007	SI
5° Piso	0.00505	0.007	SI
4° Piso	0.00520	0.007	SI
3° Piso	0.00513	0.007	SI
2° Piso	0.00472	0.007	SI
1° Piso	0.00345	0.007	SI

Tabla XXV. Distorsión en "X" modelo dinámico Barkan.

Dirección Y-Y			
Table: Story Drifts			
Story	**Drift**	**Lim 0.007**	**Cumple**
Tanque elevado	0.00362	0.007	SI
10° Piso	0.00351	0.007	SI
9° Piso	0.00388	0.007	SI
8° Piso	0.00426	0.007	SI
7° Piso	0.00464	0.007	SI
6° Piso	0.00494	0.007	SI
5° Piso	0.00512	0.007	SI
4° Piso	0.00516	0.007	SI
3° Piso	0.00503	0.007	SI
2° Piso	0.00465	0.007	SI
1° Piso	0.00344	0.007	SI

Tabla XXVI. Distorsión en "Y" modelo dinámico Barkan.

Se aprecia en las tablas XXV y XXVI que la distorsión máxima se da en el 4° piso con una distorsión de 0.00520 en la dirección X y 0.00516 en la dirección Y, cumpliendo en ambas direcciones con la distorsión máxima permitida por la Norma de Diseño Sismorresistente E.030

5.3.3 Modelo Dinámico Norma Rusa SNIP 2.02.05-87.

Dirección X-X			
Table: Story Drifts			
Story	**Drift**	**Lim 0.007**	**Cumple**
Tanque elevado	0.00248	0.007	SI
10° Piso	0.00265	0.007	SI
9° Piso	0.00313	0.007	SI
8° Piso	0.00366	0.007	SI
7° Piso	0.00417	0.007	SI
6° Piso	0.00462	0.007	SI
5° Piso	0.00495	0.007	SI
4° Piso	0.00511	0.007	SI
3° Piso	0.00504	0.007	SI
2° Piso	0.00464	0.007	SI
1° Piso	0.00340	0.007	SI

Tabla XXVII. Distorsión en "X" modelo dinámico Norma Rusa

Dirección Y-Y			
Table: Story Drifts			
Story	**Drift**	**Lim 0.007**	**Cumple**
Tanque elevado	0.00352	0.007	SI
10° Piso	0.00340	0.007	SI
9° Piso	0.00378	0.007	SI
8° Piso	0.00416	0.007	SI
7° Piso	0.00454	0.007	SI
6° Piso	0.00484	0.007	SI
5° Piso	0.00502	0.007	SI
4° Piso	0.00506	0.007	SI
3° Piso	0.00494	0.007	SI
2° Piso	0.00457	0.007	SI
1° Piso	0.00338	0.007	SI

Tabla XXVIII Distorsión en "Y" modelo dinámico Norma Rusa.

Se aprecia en las tablas XXVII y XXVIII que la distorsión máxima se da en el 4° piso con una distorsión de 0.00511 en la dirección X y 0.00506 en la dirección Y, cumpliendo en ambas direcciones con la distorsión máxima permitida por la Norma de Diseño Sismorresistente E.030

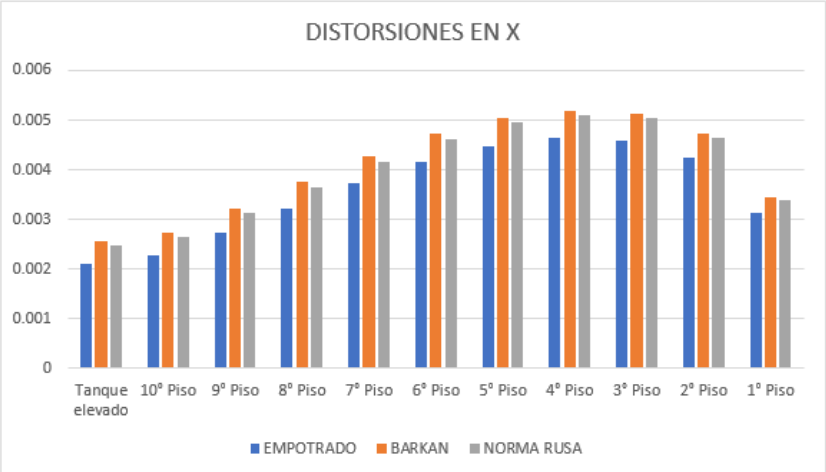

Figura XI.- Comparación de distorsiones con los modelos dinámicos en "X"

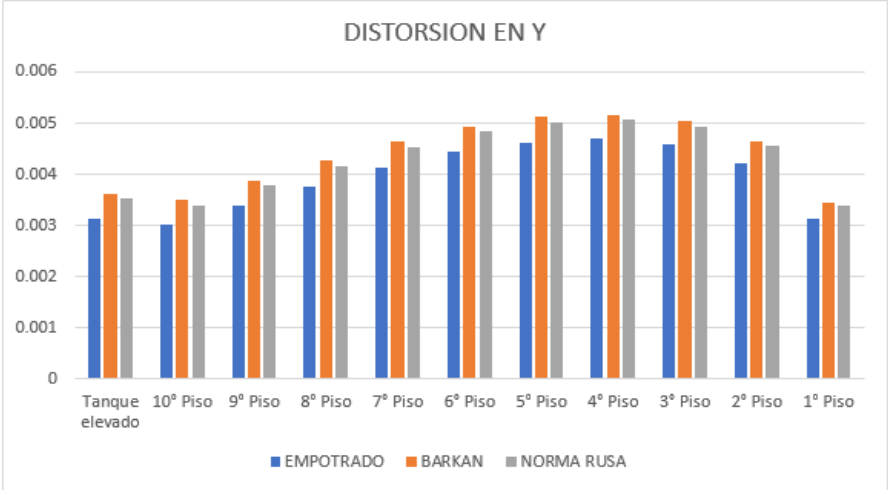

Figura XII.- Comparación de distorsiones con los modelos dinámicos en "Y"

Como se aprecia en las figuras XI y XII, las distorsiones de entrepiso en X e Y, siendo el mayor valor con el modelo dinámico Barkan, seguido de la Norma Rusa y el menor valor con el modelo empotrado en la base.

5.4. Fuerzas cortantes. - Se realiza la comparación de resultados de fuerzas cortantes de los modelos analizados.

Dirección	Modelo Empotrado (tonf)	Modelo Barkan (tonf)	Modelo Norma Rusa (tonf)
X	463.4632	489.5136	484.2614
Y	555.7586	554.0225	554.3393

Tabla XXIX. Fuerza Cortante.

Figura XIII. Comparación de las fuerzas cortantes con los modelos dinámicos en "X"

En la Figura XIII se aprecia un incremento de la fuerza cortante en la dirección X en el modelo Barkan y en el modelo de la Norma Rusa.

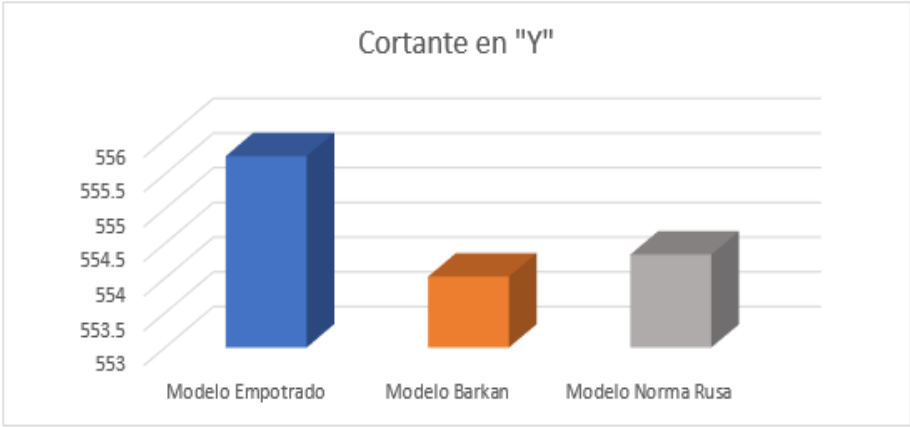

Figura XIV.- Comparación de las fuerzas cortantes con los modelos dinámicos en "Y"

En la Figura XIV se aprecia una reducción de la fuerza cortante en la dirección Y en el modelo Barkan y en el modelo de la Norma Rusa.

5.5. Momento flector

Dirección	Modelo Empotrado (tonf)	Modelo Barkan (tonf)	Modelo Norma Rusa (tonf)
X	468.6993	346.0116	371.7405
Y	448.3551	329.5101	354.5755

Tabla XXX. Momento flector.

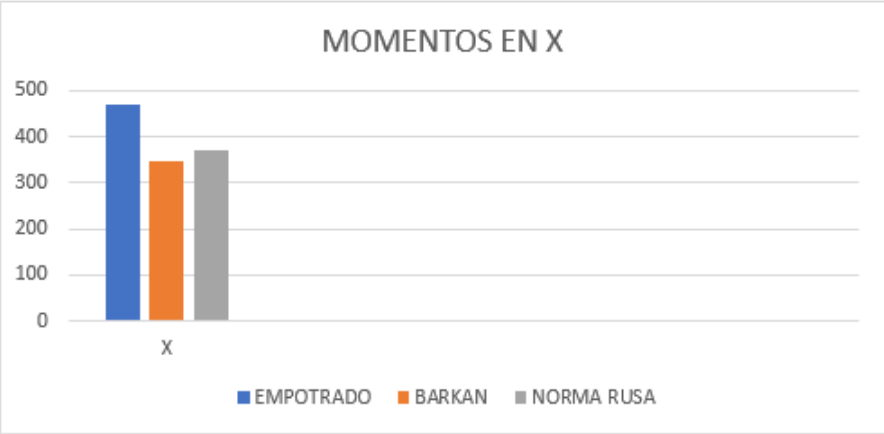

Figura XV.- Comparación de momentos con los modelos dinámicos en "X"

En la Figura XV se aprecia una reducción de momentos en la dirección X en los modelos dinámicos Barkan y Norma Rusa, a comparación con el modelo de suposición de base fija.

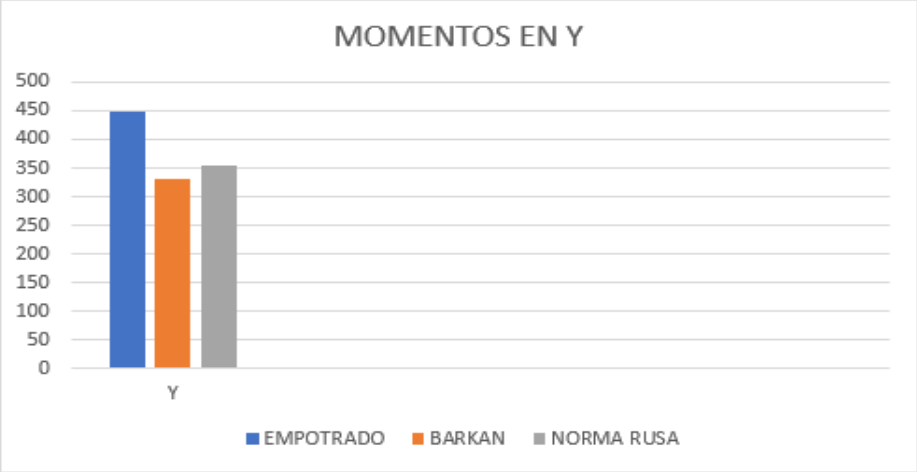

Figura XVI.- Comparación de momentos con los modelos dinámicos en "Y"

En la Figura XVI se aprecia una reducción de momentos en la dirección Y en los modelos dinámicos Barkan y Norma Rusa, a comparación con el modelo de suposición de base fija.

6. Conclusiones

- Se concluye que, al realizar un análisis de interacción suelo-estructura con los modelos dinámicos Barkan y Norma Rusa, los periodos fundamentales Tx y Ty se incrementan, esto frente a un análisis con la suposición de base fija.
    - Se obtiene que los periodos Tx en el modelo empotrado presenta un valor de 0.593 seg., mientras que en el modelo Barkan es de 0.612 segundos y en el modelo Norma Rusa es de 0.608 segundos.
    - Se obtiene que los periodos Ty en el modelo empotrado presenta un valor de 0.639 seg., mientras que en el modelo Barkan es de 0.674 segundos y en el modelo Norma Rusa es de 0.667 segundos.
- Se concluye que, al realizar un análisis de interacción suelo-estructura con los modelos dinámicos Barkan y Norma Rusa, los desplazamientos en las direcciones X e Y se incrementan, esto frente a un análisis con la suposición de base fija.

  - Se obtiene que los desplazamientos máximos en la dirección X, el modelo empotrado presenta 11.148 cm., mientras que en el modelo Barkan es de 12.684 cm. y en el modelo Norma Rusa es de 12.416 cm.
  - Se obtiene que, los desplazamientos máximos en la dirección Y, el modelo empotrado presenta 11.945 cm., mientras que en el modelo Barkan es de 13.604 cm. y en el modelo Norma Rusa es de 13.311 cm.
- Se concluye que, al realizar un análisis de interacción suelo-estructura con los modelos dinámicos Barkan y Norma Rusa, las distorsiones máximas en las direcciones X e Y se incrementan, esto frente a un análisis con la suposición de base fija.
  - Se obtiene que, la deriva máxima en la dirección X se da en el 4° Piso, el modelo empotrado presenta 0.00465, mientras que en el modelo Barkan es de 0.00520 y en el modelo Norma Rusa es de 0.00511.
  - Se obtiene que, la deriva máxima en la dirección Y, se da en el 4° Piso, el modelo empotrado presenta 0.00469, mientras que en el modelo Barkan es de 0.00516 y en el modelo Norma Rusa es de 0.00506.
- Se concluye que, al realizar un análisis de interacción suelo-estructura con los modelos dinámicos Barkan y Norma Rusa, las fuerzas cortantes en la base Vx se incrementan y las fuerzas cortantes Vy disminuyen, esto frente a un análisis con la suposición de base fija.
  - Se obtiene que, las fuerzas cortantes en la base en la dirección X, el modelo empotrado presenta 463.4632 tonf, mientras que en el modelo Barkan es de 489.5136 tonf y en el modelo Norma Rusa es de 484.2614 tonf.
  - Se obtiene que, las fuerzas cortantes en la base en la dirección Y, el modelo empotrado presenta 555.7586 tonf, mientras que en el modelo Barkan es de 554.0225 tonf y en el modelo Norma Rusa es de 554.3393 tonf.
- Se concluye que, teniendo en cuenta las fuerzas cortantes en la base mencionados líneas arriba, el sistema estructural la cual conforma la presente edificación es de un Sistema Dual y en todos los modelos analizados las cortantes en la base de las placas en las direcciones X e Y, son mayores al 60% y menores al 80%.
  - Se obtiene que, las fuerzas cortantes de las placas en la base en la dirección X, el modelo empotrado presenta una cortante en las placas de 343.6504 tonf siendo un 74.148 % respecto a la cortante principal de 463.4632 tonf.
  - Se obtiene que, las fuerzas cortantes de las placas en la base en la dirección Y, el modelo empotrado presenta una cortante en las placas de 334.3892 tonf siendo un 60.168 % respecto a la cortante principal de 555.7586 tonf.
  - Se obtiene que, las fuerzas cortantes de las placas en la base en la dirección X, el modelo Barkan presenta una cortante en las placas de 342.6288 tonf siendo un 69.994 % respecto a la cortante principal de 489.5136 tonf.
  - Se obtiene que, las fuerzas cortantes de las placas en la base en la dirección Y, el modelo Barkan presenta una cortante en las placas de 335.0546 tonf siendo un 60.477 % respecto a la cortante principal de 554.0225 tonf.
  - Se obtiene que, las fuerzas cortantes de las placas en la base en la dirección X, el modelo Norma Rusa presenta una cortante en las placas de 342.7141 tonf siendo un 70.770 % respecto a la cortante principal de 484.2614 tonf.
  - Se obtiene que, las fuerzas cortantes de las placas en la base en la dirección Y, el modelo Norma Rusa presenta una cortante en las placas de 334.7704 tonf siendo un 60.391 % respecto a la cortante principal de 554.3393 tonf.

Referencias

[1] Abanto Oblitas R., Cisneros Meneses L., Gómez Córdova G., Díaz Esquivel C., Rojas Peralta P. (2020). Propuesta preliminar del método de análisis de interacción suelo-estructura para suelos peruanos. Repositorio de Tesis PUCP. Obtenido de https://hdl.handle.net/20.500.12404/18127

[2] Araca F., Gómez L., Cahui A., Martin G. (2020). Influencia de la interacción suelo-estructura en el comportamiento de las viviendas aporticadas con zapatas aisladas en la ciudad de Juliaca. Revista Cientifica de la UCSA, 7(2), 70-81. https://doi.org/http://scielo.iics.una.py/scielo.php?script=sci_arttext&pid=S2409-87522020000200070&lng=es&nrm=iso&tlng=es

[3] Arancibia A. (2020). Estudio del efecto de la interacción suelo-estructura en edificios bajos de albañilería. Repositorio Académico de la Universidad de Chile. https://doi.org/https://repositorio.uchile.cl/handle/2250/177340

[4] Arellano María, Cavallin Johana (2018). Estudio del comportamiento dinámico en edificaciones irregulares considerando interacción suelo-estructura. Revista Ingeniería, 2(2), 28-36. https://doi.org/ https://doi.org/10.33996/revistaingenieria.v2i2.12

[5] Calderin F., Almenarez D., Boada D. (2020). Consideración del fenómeno interacción suelo-estructura en edificio prefabricado. Obtenido de https://www.redalyc.org/journal/1813/181366194007/html/

[6] Castro C., Pérez G. (2020). Análisis de la interacción suelo - estructura estática para una edificación regular de hormigón armado y 3 tipos de suelos. Ecuador: Universidad Politécnica Salesiana. Obtenido de https://dspace.ups.edu.ec/handle/123456789/18193

[7] Falcón N. (2024). Evaluación de la respuesta sísmica de un edificio aporticado considerando la interacción suelo-estructura. Obtenido de https://preprints.scielo.org/index.php/scielo/preprint/view/8016/14974

[8] Fernández Limés A., Fernández Lorenzo I., Cobelo Cristiá W. (2023). Influencia de la interacción suelo-estructura estática en edificio de 100 metros de altura. Revista Ingeniería y Desarrollo, 2(2), 213-232. https://doi.org/10.14482/inde.41.02.201.456

[9] García N., Jaramillo Y., Sarmiento P. (2023). Evaluación de la influencia de la interacción suelo - estructura en la respuesta sísmica de una edificación tipo comercial en Ecuador. Guayaquil: Escuela Superior Politécnica del Litoral. Obtenido de https://www.dspace.espol.edu.ec/handle/123456789/59581

[10] Guanchez Edinson (2019). Aspectos sismo-geotécnicos considerados en el diseño de cimentaciones (Parámetros dinámicos e interacción suelo-estructura). Obtenido de Prontubeam: https://www.prontubeam.com/articulos/2019-08-22-Aspectos-sismo-geotecnicos-considerados-en-el-diseno-de-cimentaciones

[11] Hervas D., Villavicencio E. (2021). Influencia de la respuesta estructural en una edificación de 5 pisos de hormigón reforzado resistente a momentos, mediante la interacción suelo-estructura variando el tipo de cimentación, en suelos tipo D. Manabí: Universidad Estatal del Sur de Manabí. Obtenido de https://repositorio.unesum.edu.ec/handle/53000/2725?mode=full

[12] Jines R. (2017). Interacción sísmica suelo-estructura en edificaciones de sistema dual en la ciudad de Moquegua. Universidad Privada de Tacna. Obtenido de https://repositorio.upt.edu.pe/bitstream/handle/20.500.12969/412/Jines-Cabezas-Ruth-Mercedes.pdf?sequence=1

[13] Pinto-Vega Francisco, Ledezma Christian (2019). Interacción suelo-estructura en edificios de gran altura con subterráneos en Santiago, Chile. Obras y proyectos (25), 66-75. https://doi.org/http://dx.doi.org/10.4067/S0718-28132019000100066

[14] Puente D., Vilcamich E., Castro J., Andrade J., Cuadros L. (2023). Interacción suelo-estructura en un edificio con sótanos: consideraciones para el análisis sísmico. Lima: Pontificia Universidad Católica del Perú. Obtenido de https://tesis.pucp.edu.pe/repositorio/handle/20.500.12404/26315

[15] Ramírez Cabrera W., Quispillo Morocho K. (2022). Análisis comparativo de la respuesta estructural y del nivel de desempeño de una edificación de hormigón armado, considerando dos opciones: base rígida e interacción suelo-estructura. Universidad Técnica de Ambato. Obtenido de

https://doi.org/https://repositorio.uta.edu.ec/handle/123456789/34107

[16] Reglamento Nacional de Edificaciones (2020). Norma E020 (cargas). Lima: Servicio Nacional de Capacitación para la Industria de la Construcción – SENCICO. Obtenido de https://drive.google.com/file/d/1g8gduNJSHHRkBp0Ls08sC8pk4Sizucav/view

[17] Reglamento Nacional de Edificaciones (2020). Norma E030 (Diseño sismorresistente). Lima: Servicio Nacional de Capacitación para la Industria de la Construcción – SENCICO. Obtenido de https://drive.google.com/file/d/1W14N6JldWPN8wUZSqWZnUphg6C559bi-/view

[18] Reglamento Nacional de Edificaciones (2020). Norma E050 (Suelos y cimentaciones). Lima: Servicio Nacional de Capacitación para la Industria de la Construcción – SENCICO. Obtenido de https://drive.google.com/file/d/1XdLUkwUqDXsuIQgSbFsJ-J9BTt4u3Hp5/view

[19] Reglamento Nacional de Edificaciones (2020). Norma E.060 (Concreto armado). Lima: Servicio Nacional de Capacitación para la Industria de la Construcción – SENCICO. Obtenido de https://drive.google.com/file/d/19EYUVMgwvm6rDs47GV374avco2ylU5Kz/view

[20] Romero E., Almache L. (2022). Evaluación estructural de la iglesia patrimonial El Tambo considerando base rígida e interacción dinámica suelo-estructura. Cuenca: Universidad Católica de Cuenca. Obtenido de https://dialnet.unirioja.es/servlet/articulo?codigo=9227615

[21] Tena Colunga, A. (2019). Interacción suelo-estructura. Reflexiones sobre su importancia en la respuesta dinámica de estructuras durante sismos. Revista Internacional de Ingeniería de Estructuras, 24(2), 141-165. https://journal.espe.edu.ec/ojs/index.php/riie/article/view/1282

[22] Velaña Carcelén L. (2022). Diseño sismorresistente de una estructura mixta de 4 niveles, con interacción suelo-estructura y diagonales rigidizadoras, para uso administrativo, enfocado a un suelo con características tipo E. Ecuador: Universidad Estatal del Sur de Manabí. Obtenido de https://repositorio.unesum.edu.ec/handle/53000/3486

[23] Villarreal Castro, G. (2017). Interacción sísmica suelo-estructura en edificaciones con plateas de cimentación. Lima: Editora & Imprenta Gráfica Norte S.R.L.

[24] Villarreal Castro G. (2020). Interacción suelo estructura en edificaciones con zapatas aisladas. Revista Internacional de Ingeniería de Estructuras, 25(3), 311-332. Obtenido de https://ia801900.us.archive.org/34/items/articulo-13-interaccion-suelo-estructura/Art%C3%ADculo%2013%20Interacci%C3%B3n%20Suelo%20Estructura.pdf

[25] Villarreal Castro G., Águila Gómez C. (2021). Interacción suelo-estructura y su influencia en la respuesta sísmica de edificios de concreto armado. Revista Internacional de Ingeniería de Estructuras, 25(3), 426-471. Obtenido de https://journal.espe.edu.ec/ojs/index.php/riie/article/view/2336/1775

[26] Villarreal Castro G., Cerna Vásquez M., Espinoza Torres C. (2021). Interacción sísmica suelo-estructura en edificaciones con muros de ductilidad limitada sobre plateas de cimentación. Revista Internacional de Ingeniería de Estructuras, 26(1), 153-178. https://journal.espe.edu.ec/ojs/index.php/riie/article/view/1967

Nota contribución de los autores:

1. Concepción y diseño del estudio
2. Adquisición de datos
3. Análisis de datos
4. Discusión de los resultados
5. Redacción del manuscrito
6. Aprobación de la versión final del manuscrito

BQ ha contribuido en: 1, 2, 3, 4, 5 y 6.
EC ha contribuido en: 1, 2, 3, 4, 5 y 6.
GV ha contribuido en: 1, 2, 3, 4, 5 y 6.

Nota de aceptación: Este artículo fue aprobado por los editores de la revista Dr. Rafael Sotelo y Mag. Ing. Fernando A. Hernández Gobertti.

Impactos de la transición energética en pequeñas comunidades fuera de red

Impacts of the energy transition in small off-grid communities

Impactos da transição energética em pequenas comunidades fora da rede

Estefany Garces[1 (*)], Carlos J. Franco[2]

Recibido: 25/02/2024 Aceptado: 20/04/2024

Resumen. - La transición energética es un asunto prioritario que concierne a todos, desde las grandes ciudades y sus sectores intensivos en electricidad hasta pequeñas comunidades rurales remotas cuyo suministro eléctrico se produce mediante sistemas de generación descentralizados que, en muchos casos, se abastecen parcial o totalmente de combustibles fósiles. En Colombia, más del 90% de estas comunidades rurales generan su electricidad utilizando plantas diésel, lo que hace relevante el estudio de la transición energética en las mismas. Así, el objetivo de esta investigación es mostrar los impactos de la transición energética en estas comunidades y cómo, a largo plazo, la transición puede garantizar el acceso a una electricidad fiable, asequible, sostenible y moderna para todos. Para lograr este objetivo, se usó una metodología mixta que incluyó trabajo de campo y simulaciones en computador. A través del trabajo de campo, se identificaron múltiples impactos de la transición a renovables, por ejemplo, impactos sociales en cuanto mejores condiciones para la educación, impactos ambientales como la reducción de emisiones de CO2 e impactos económicos como la posibilidad de desarrollar nuevas actividades productivas. Los resultados de las simulaciones muestran que, a largo plazo, la transición a sistemas de generación descentralizados 100% renovables es factible y garantizaría a los habitantes de estas pequeñas comunidades un suministro eléctrico sostenible, fiable y asequible; sin embargo, para lograrlo es necesario superar varios retos, siendo uno de los más relevantes el diseño y planificación de microrredes cuya expansión con renovables pueda perpetuarse en el tiempo. Finalmente, los hallazgos de esta investigación podrían aplicarse, haciendo adaptaciones según cada caso, a pequeñas comunidades fuera de red en el mundo.

Palabras clave: Comunidades fuera de red; Transición energética; Generación descentralizada; Tecnologías renovables; Colombia.

(*) Autor Corresponsal

[1] Investigador posdoctoral. Departamento de Ciencias de la Computación y de la Decisión, Facultad de Minas, Universidad Nacional de Colombia, Sede Medellín (Colombia), egarces@unal.edu.co, ORCID iD: https://orcid.org/0000-0002-4134-1130.

[2] Profesor Titular. Departamento de Ciencias de la Computación y de la Decisión, Facultad de Minas, Universidad Nacional de Colombia, Sede Medellín (Colombia), cjfranco@unal.edu.co, ORCID iD: https://orcid.org/0000-0002-7750-857X.

Memoria Investigaciones en Ingeniería, núm. 26 (2024). pp. 188-201
https://doi.org/10.36561/ING.26.11
ISSN 2301-1092 • ISSN (en línea) 2301-1106 – Universidad de Montevideo, Uruguay

Summary. - *The energy transition is a priority issue that concerns everyone, from big cities and their electricity-intensive sectors to small, remote, rural communities whose electricity supply is produced through decentralized generation systems that, in many cases, are partially or entirely supplied with fossil fuels. In Colombia, more than 90% of these rural communities generate their electricity using diesel plants, which makes it relevant to study the energy transition in these communities. Thus, the aim of this research is to show the impacts of the energy transition on these communities and how, in the long term, the transition can ensure access to reliable, affordable, sustainable, and modern electricity for all. To achieve this objective, it is necessary to use a mixed methodology that includes fieldwork and computer simulations. Through the fieldwork, multiple impacts of the transition to renewables were identified, for example, social impacts in terms of better conditions for education, environmental impacts such as the reduction of CO2 emissions and economic impacts such as the possibility of developing new productive activities. The results of the simulations show that, in the long term, the transition to 100% renewable decentralized generation systems is feasible and would guarantee the inhabitants of these small communities a sustainable, reliable and affordable electricity supply; however, to achieve this, several challenges must be overcome, one of the most relevant being the design and planning of microgrids whose expansion with renewables can be perpetuated over time. Finally, the findings of this research could be applied, with adaptations on a case-by-case basis, to small off-grid communities around the world.*

Keywords: *Off-grid communities; Energy transition; Decentralized generation; Renewable technologies; Colombia.*

Resumo. ***-*** *A transição energética é uma questão prioritária que diz respeito a todos, desde as grandes cidades e seus setores com uso intensivo de eletricidade até as pequenas e remotas comunidades rurais cujo fornecimento de eletricidade é feito por sistemas de geração descentralizados que, em muitos casos, são parcial ou totalmente alimentados por combustíveis fósseis. Na Colômbia, mais de 90% dessas comunidades rurais geram sua eletricidade usando usinas a diesel, o que torna relevante o estudo da transição energética nessas comunidades. Assim, o objetivo desta pesquisa é mostrar os impactos da transição energética nessas comunidades e como, a longo prazo, a transição pode garantir o acesso à eletricidade confiável, acessível, sustentável e moderna para todos. Para atingir este objetivo, é necessária a utilização de uma metodologia mista que inclui trabalho de campo e simulações computacionais. Por meio do trabalho de campo, foram identificados vários impactos da transição para energias renováveis, por exemplo, impactos sociais em termos de melhores condições de educação, impactos ambientais, como a redução das emissões de CO2, e impactos econômicos, como a possibilidade de desenvolver novas atividades produtivas. Os resultados das simulações mostram que, no longo prazo, a transição para sistemas de geração descentralizada 100% renováveis é viável e garantiria aos habitantes dessas pequenas comunidades um fornecimento de eletricidade sustentável, confiável e acessível; no entanto, para isso, é necessário superar vários desafios, sendo um dos mais relevantes o projeto e o planejamento de microrredes cuja expansão com renováveis possa ser perpetuada ao longo do tempo. Por fim, as descobertas desta pesquisa poderiam ser aplicadas, com adaptações caso a caso, a pequenas comunidades fora da rede em todo o mundo.*

Palavras-chave: *Comunidades fora da rede; Transição energética; Geração descentralizada; Tecnologias renováveis; Colômbia.*

1. Introducción.- La transición energética es esencial a la hora de abordar los desafíos asociados con la seguridad energética, el cambio climático, impulsar el crecimiento económico y fomentar la innovación tecnológica, convirtiéndola en un asunto impostergable si se quiere garantizar el bienestar de la población mundial e impulsar el cumplimiento de los Objetivos de Desarrollo Sostenible (ODS), en especial el ODS7 con el cual tiene un estrecho vínculo [1]. A través del ODS7 se establece que se debe "garantizar el acceso a una energía asequible, fiable, sostenible y moderna para todos" [2], por ende, es relevante investigar cómo la transición energética favorece el logro de las metas planteadas en este ODS, tanto en las grandes ciudades como en las pequeñas comunidades rurales remotas de cada país.

Los gobiernos han tomado medidas para lograr este objetivo y en la última década se han valido principalmente del uso de sistemas de generación descentralizados como las microrredes, minirredes y los sistemas solares domésticos (SHS por sus siglas en inglés); y de las tecnologías renovables como la solar fotovoltaica (PV), las pequeñas centrales hidroeléctricas (PCH), la eólica y la biomasa, para dar respuesta y satisfacer las necesidades energéticas de aquellas comunidades que aún no tienen acceso a electricidad, las cuales se concentran en zonas rurales remotas de países en desarrollo [3], [4]. La selección del tipo de sistema se asocia con el tamaño y densidad de la población, mientras que la selección de la tecnología depende en mayor medida de los recursos de generación disponibles en la zona [5]. A pesar de los avances y esfuerzos multilaterales, tanto la Agencia Internacional de Energías Renovables (IRENA) como la Agencia Internacional de Energía (IEA), concuerdan que al año 2030 no se alcanzará la meta de acceso universal [1], [4] – de acuerdo con el informe sobre los progresos en el logro del ODS7, elaborado por la IEA, para el 2030 sólo se alcanzará un 92% del objetivo de universalización [4].

Este informe indica que el ritmo del progreso en la electrificación se ha desacelerado en los últimos años, en parte por la crisis mundial generada por el Covid-19, pero principalmente por la creciente complejidad de llegar a poblaciones sin servicio eléctrico más remotas y pobres, las cuales se concentran en la región de África subsahariana, siendo Nigeria, República Democrática del Congo y Etiopia los países con mayor cantidad de personas sin acceso a la electricidad en el mundo; así mismo, dentro de los primeros 20 países que afrontan esta problemática están Myanmar, Pakistán e India [4]. Estas poblaciones suelen estar ubicadas en lugares con características geográficas complejas, por ejemplo: islas, desiertos, asentamientos montañosos, franjas de bosque, claros de selva, entre otros; lo cual influye en que sean comunidades de difícil o muy difícil acceso, pobre infraestructura, con condiciones sociales y económicas desfavorables, y en ocasiones con pocos habitantes y/o baja densidad poblacional [5]–[8]. Este informe también menciona que si se quiere garantizar el acceso de la forma como lo establece el ODS7, es indispensable un despliegue acelerado del uso de energías renovables [4], es decir, acelerar la transición energética [1].

Colombia no es ajena a esta situación, y a pesar de que la tasa de acceso a electricidad en el país asciende al 96.9% [9], en sus comunidades rurales de más difícil acceso, las cuales en su mayoría comparten las características antes mencionadas, aún se deben afrontar tres retos en cuanto a la provisión de un servicio eléctrico asequible, fiable, sostenible y moderno para todos sus habitantes [10], [11].

El primer reto es llevar electricidad al 3.1% de la población que aún carece de este servicio [9]–[11]. Esta población en su mayoría vive en zonas rurales remotas donde no es posible llevar las redes de transmisión y distribución del Sistema Interconectado Nacional (SIN) [7], [10], estas zonas se conocen en Colombia como Zonas No Interconectadas (ZNI) y en la literatura como comunidades fuera de red [12], [13]. El gobierno de Colombia ha tomado acciones frente a este reto, y una de sus hojas de ruta es el Plan Indicativo de Expansión de Cobertura Eléctrica (PIEC) 2019-2023, en el cual se establecen tres mecanismos para lograr la universalización de la electricidad en el país: 1) la interconexión a la red, para aquellas comunidades en que sea factible; 2) la instalación de sistemas individuales fotovoltaicos, en comunidades dispersas y de menos de 25 usuarios; y 3) la construcción de microrredes híbridas que incluyen plantas térmicas diésel, generación solar fotovoltaica y bancos de baterías [14].

Los retos dos y tres consisten en aumentar las horas de prestación del servicio eléctrico y mejorar su calidad y asequibilidad [11], retos que conciernen a las comunidades ZNI que ya cuentan con acceso a la electricidad y donde la transición energética juega un papel fundamental ya que la generación en estas comunidades depende en gran medida de plantas diésel [10], [11] , en efecto de 280.38 MW de capacidad instalada en las ZNI en 2019, sólo 14.10 MW eran renovables [15, p. 38], [16]. La mayoría de estos sistemas descentralizados de generación con diésel fueron instalados hace más de 20 años, pues en ese entonces eran la solución de electrificación más viable dados los inasequibles costos de las soluciones renovables [5], [17]. Como consecuencia de la generación eléctrica con diésel, los habitantes de estas comunidades quedan expuestos a diversos contaminantes, entre ellos el dióxido de carbono (CO_2), lo cual puede afectar su salud; y a otras molestias como la polución sonora [10]. Además, el diésel hace que el servicio eléctrico sea costoso y este limitado a unas pocas horas al día, ya que el precio del combustible en estas zonas suele ser muy elevado y los usuarios, generalmente de bajos ingresos, no están en capacidad de pagar por más horas de suministro, únicamente las que el gobierno subsidia, haciendo que estas pequeñas comunidades ZNI permanezcan atrapadas en situación de

pobreza energética [5], [10], [11], [18], [19].

Considerando lo anterior, el objetivo de este artículo se divide en dos partes: 1) analizar los impactos que genera la transición energética en comunidades ZNI cuyo servicio eléctrico ha dependido de plantas diésel y evidenciar cómo a través de la transición a renovables se puede hacer frente a los retos dos y tres, es decir, aumentar las horas de prestación del servicio eléctrico y mejorar su calidad y asequibilidad; y 2) identificar los impactos futuros de continuar o no con esta transición, teniendo como premisa que a través del uso de tecnologías renovables estas comunidades podrían mantener en el tiempo un suministro eléctrico confiable, asequible, sostenible y moderno como lo establece el ODS7 [11]. Para lograr lo planteado, en la Sección 2 se detalla la metodología utilizada. Luego, en la Sección 3, se muestran los resultados obtenidos a través del trabajo de campo y las simulaciones por computador, y finalmente se discute en torno a los impactos de la transición energética en comunidades fuera de red. Por último, en la Sección 4, se presentan las conclusiones de este trabajo.

2. Metodología.- Esta investigación se hizo en 4 etapas: 1) seleccionar una comunidad ZNI que fuera adecuada para los propósitos de la investigación, 2) visitar la comunidad seleccionada y realizar entrevistas y encuestas, 3) seleccionar una herramienta de simulación que permitiera reproducir los comportamientos del sistema estudiado, y 4) parametrizar el modelo seleccionado en la etapa 3 de acuerdo con la información recopilada en la etapa 2 para así poder simular comportamientos futuros de la comunidad bajo estudio.

2.1. Etapa 1: Identificar la comunidad caso de estudio. - El primer paso fue la selección de una comunidad fuera de red en Colombia. Para ello, y con el propósito de identificar un caso de estudio adecuado, se tuvieron en cuenta los siguientes criterios: una comunidad no interconectable al SIN, que la comunidad hubiera tenido un sistema de generación descentralizado únicamente diésel, que dicho sistema hubiera sido repotenciado a través de la instalación de capacidad de generación renovable, y que al momento de la visita el sistema estuviera funcionando adecuadamente. También se tuvieron en cuenta otros criterios como el tamaño de la comunidad y que sus habitantes estuvieran dispuestos recibir una visita y compartir información. Para determinar las posibles comunidades a visitar se llevaron a cabo entrevistas semi estructuradas a personas que han participado en proyectos de electrificación rural en el país, entre ellos: investigadores, funcionarios del gobierno y de empresas públicas y privadas – el guion de las entrevistas y sus resultados se reportan en [10], [20].

A través de esta etapa se identificó la comunidad El Vergel como potencial caso de estudio. Esta comunidad ZNI está ubicada en el departamento del Amazonas en Colombia, a aproximadamente 2,5 horas río arriba desde su capital Leticia (ver Figura I).

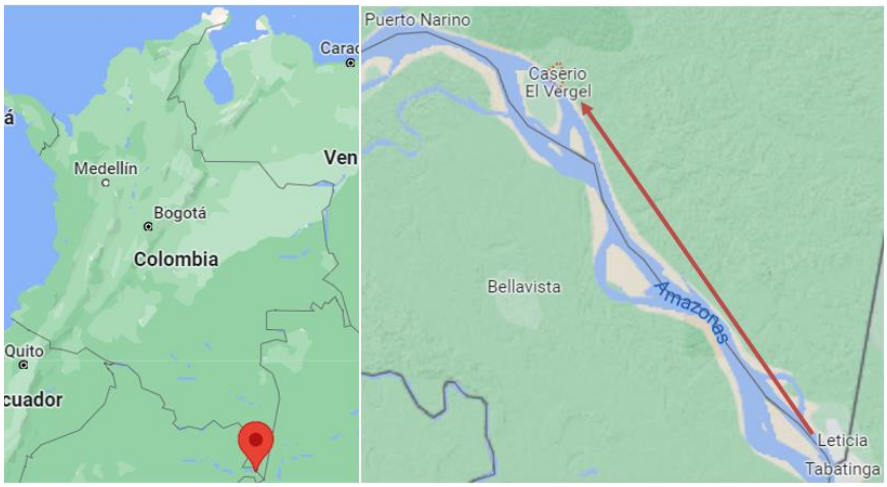

Figura I.- Ubicación y acceso a la comunidad El Vergel. Fuente: Elaboración propia con imágenes de Google maps. Datos del mapa: @2023 Google, INEGI 200 km y 10 km

2.2. Etapa 2: Realizar visita a la comunidad y entrevistas. - Fue necesario visitar la comunidad y a la empresa de servicios públicos (ESP) encargada de su suministro eléctrico, ya que en la literatura y en las páginas del gobierno es poca la información con respecto al caserío El Vergel y su microrred híbrida. Las visitas se hicieron con el fin de recolectar información respecto al proceso de hibridación que experimentó su microrred diésel, los impactos que esta transición trajo y la caracterización de sus usuarios y demanda eléctrica.

Como primer paso se contactó y acordó una reunión con uno de los ingenieros de la ESP de la zona, es decir, la empresa Energía para el Amazonas S.A. E.S.P (ENAM), la cual se ocupa de la prestación del servicio eléctrico en el municipio de Leticia y demás asentamientos del departamento del Amazonas en Colombia [21]. A través de la reunión con el ingeniero se confirmó que la ENAM se hizo cargo de la instalación del sistema renovable en el caserío El Vergel y que ellos se ocupan de supervisar su operación, generar la facturación (es una sola factura para toda la comunidad) y mantener en buen estado el sistema de generación y distribución de la microrred, ocupándose principalmente de la planta diésel, las redes de distribución eléctrica y las baterías. Posteriormente, se visitó la comunidad, en donde se llevaron a cabo encuestas a los usuarios, para ello se tuvo presente que las personas entrevistadas fueran mayores de edad y preferiblemente encargadas de la toma de decisiones en el núcleo familiar. Finalmente, se realizó una entrevista a uno de los operarios de la microrred, quien es un líder comunitario elegido por los habitantes del caserío para esta gestión y que fue capacitado por ENAM para apoyar cuestiones como la recolección del dinero de la factura, apoyar algunas actividades de mantenimiento como la limpieza de los paneles y reportar anomalías en el funcionamiento de la microrred. Las encuestas y entrevistas utilizadas se reportan en el Anexo B de [20] y dentro del grupo de las personas que las llevaron a cabo estuvieron los dos autores de este artículo.

2.3. Etapa 3: Seleccionar una herramienta de simulación. - Esta etapa es necesaria en relación con la identificación de los futuros impactos de dar continuidad o no a la transición energética en comunidades fuera de red, cuestión que hace parte del objetivo de esta investigación. Para ello, se utiliza un modelo de simulación, reportado en [11], [20], cuya hipótesis se fundamenta en que las comunidades fuera de red podrían mantener en el tiempo un suministro eléctrico confiable, asequible, sostenible y moderno a través de la instalación de nueva capacidad de generación renovable y aprovechando la rápida disminución de los costos de estas tecnologías – la instalación de nueva capacidad está supeditada al crecimiento de la demanda eléctrica y la selección de la tecnología a los recursos de generación disponibles en la zona [3], [5], [11], [20]. En el modelo se asume como fuente primaria de energía renovable la tecnología solar fotovoltaica por varias razones, entre ellas: su disponibilidad, ya que la energía solar es un recurso disponible en todo el mundo; su alta modularidad, lo cual la hace muy atractiva para la electrificación de comunidades fuera de red; su facilidad de instalación y adaptabilidad, que posibilita incorporar nueva capacidad de generación sobre sistemas ya existentes; y su bajo costo, pues se le ha considerado una de las tecnologías renovables más baratas y competitivas en cuanto a costos de generación [22]–[25]. Asimismo, considerar la solar fotovoltaica como fuente primaria en el caso de estudio es un supuesto adecuado, ya que: 1) es la fuente que actualmente utilizan, y 2) es la que se prevé continuarán utilizando, ya que la energía solar es el recurso de mayor disponibilidad en el caserío El Vergel – durante la visita se observó que la zona no cuenta con un adecuado régimen de vientos ni tampoco dispone de condiciones adecuadas para instalar una PCH o una planta de generación con biomasa [10], [20].

Este modelo también asocia otros supuestos y requiere de algunos insumos específicos para que a través de las simulaciones se puedan identificar los impactos futuros de dar o no continuidad a la transición energética. Por ejemplo, para el pronóstico de la demanda se considera el crecimiento poblacional, la capacidad adquisitiva de los habitantes y el aumento en las horas de suministro eléctrico (ver [20, pp. 87–91]), en este sentido se modela la dinámica poblacional, la relación entre el consumo eléctrico per cápita y el PIB, y se proponen escalones de crecimiento de la demanda de acuerdo con la cantidad de horas de electricidad disponible desde 4 hasta 24 horas – para esto último se utilizan los posibles consumos energéticos de comunidades fuera de red en Colombia reportados en el PIEC 2019-2023 [14]. En cuanto a la estimación de los costos de las tecnologías se incluyen las curvas de aprendizaje de los costos de un sistema solar fotovoltaico, para los años 2019 al 2040, y de baterías de litio, para los años 2018 al 2040 – estos rangos de años se consideran apropiados ya que las reposiciones y repotenciaciones no requieren fechas anteriores [20, pp. 183–184]. Otros parámetros tecnológicos y de costos que se consideran dentro del modelo de simulación son los siguientes: factor de emisiones de CO_2 de una planta diésel, vida útil de un sistema solar fotovoltaico, vida útil de las baterías de litio, tasa de degradación anual de la capacidad instalada solar y de la capacidad de almacenamiento de las baterías, costo de generación diésel, OPEX fijo de operar una planta diésel, OPEX fijo de una planta solar con baterías, entre muchos otros – todos los parámetros usados en el modelo de simulación se detallan en [20, pp. 176–184].

A través de este modelo es posible determinar cómo proporcionar en comunidades fuera de red un suministro eléctrico sostenible y fiable que se mantenga en el tiempo, integrando y midiendo aspectos medioambientales, tecnológicos, institucionales, económicos y sociales [11]. El modelo consta de tres bloques principales: 1) Demanda Eléctrica, 2) Capacidad Instalada, y 3) Flujos de Caja [20]. En la Figura II se resumen los principales componentes incorporados en el modelo de simulación y las ecuaciones matemáticas más representativas de cada uno de los bloques.

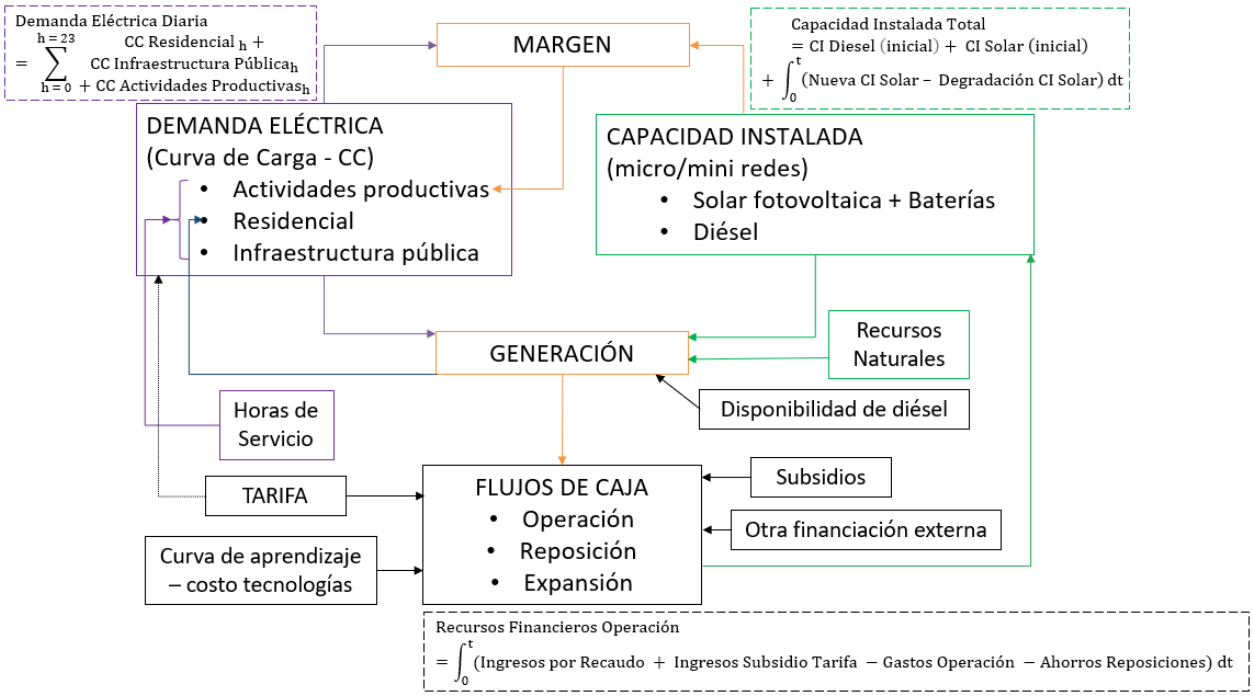

Figura II.- Principales componentes del modelo de simulación y sus ecuaciones. Fuente: Elaboración a partir de [11], [20].

2.4. Etapa 4: Parametrizar la herramienta de simulación. - En la Tabla I se resumen los parámetros que corresponden únicamente a la comunidad El Vergel, los demás parámetros utilizados en el modelo se reportan en la Tabla C.1 del Apéndice C de [11] y en el Anexo D de [20].

Parámetro	Valor	Referencia
Capacidad instalada diésel	36 kW	[20]
Factor de potencia planta diésel	0.8	[20]
Horas de subsidio diésel ASE	5 horas	[26]
Capacidad instalada solar	13.5 kW	[20]
Radiación solar promedio	3.5 a 4.0 kW h/m^2	[20]
Consumo Subsistencia ASE	50 kWh/mes-usuario	[26]
% Subsidio tarifario	80.35%	[20]

Tabla I.- Parámetros correspondientes al caserío El Vergel.

La simulación comienza en el año 2012, ya que en ese año se llevó a cabo la hibridación de la planta de generación diésel, y se extiende por 21 años. Se selecciona este horizonte de tiempo ya que a través del modelo se quiere validar el comportamiento del sistema, en por lo menos un ciclo de vida completo, considerando los remplazos y repotenciaciones de la tecnología renovable, en este caso paneles solares y baterías, lo que se traduce en mínimo 20 años [27], [28]. Las simulaciones se realizaron mediante el software Powersim Studio 10 y utilizando un paso de simulación anual.

3. Resultados y discusión.- En esta sección se presentan los resultados del estudio de la siguiente manera: 1) los resultados obtenidos a través de la visita a la comunidad y las entrevistas y encuestas realizadas; 2) los resultados obtenidos a través del modelo de simulación de dinámica de sistemas; y 3) una discusión en torno a los resultados y los impactos de la transición energética y cómo a través de esta se puede hacer frente a los retos dos y tres planteados en la introducción, y cómo la transición a renovables posibilita un suministro eléctrico confiable, asequible y sostenible para estas comunidades.

3.1 Resultados obtenidos a través de la visita a la comunidad y las entrevistas. - A través de la entrevista al funcionario de la ENAM, se pudo corroborar que antes del año 2012, la prestación del servicio eléctrico en la comunidad El Vergel dependía totalmente de una microrred con una planta de generación diésel de 36 kW. En la Figura III se puede ver que el caserío es poco disperso, lo que facilitó la instalación de la microrred diésel. En la Figura III también se muestran algunos de sus componentes: poste de luz, cuadro de mando de la planta de generación diésel y el tanque donde se almacena el combustible.

Figura III.- Comunidad El Vergel, microrred y algunas componentes del sistema de generación diésel. Fuente: Fotografías de los autores.

El funcionario de ENAM también confirmó que en el año 2012 repotenciaron la microrred diésel de El Vergel con la instalación de una central de generación fotovoltaica con una capacidad nominal de 13.5 kW, constituida por 45 módulos solares y 24 baterías (ver Figura IV). La instalación de la capacidad de generación renovable se llevó a cabo gracias a un contrato de concesión de exclusividad denominado Área de Servicio Exclusivo (ASE), firmado entre ENAM y el Ministerio de Minas y Energía [29]. En dicho contrato ENAM se comprometió a aumentar y mejorar la cobertura del servicio de energía eléctrica a través de la instalación de centrales de generación constituidas por tecnologías renovables [30].

Figura IV.- Central de generación fotovoltaica y sus componentes. Fuente: Fotografías de los autores.

Mediante la visita a la comunidad y las encuestas realizadas a sus habitantes se pudo constatar que la instalación de la central de generación fotovoltaica ha mejorado la calidad de vida de sus habitantes, quienes ahora disponen de 16 horas de suministro eléctrico diario, de las 6 am a las 10 pm, servicio que los lugareños consideran suficiente y que les ha facilitado el uso de aparatos eléctricos que antes no podían utilizar como congeladores, compresores de pintura, computadores, ventiladores, entre otros. Asimismo, a través de la visita se pudo observar que con la instalación de la central fotovoltaica la comunidad ha podido desarrollar nuevas actividades económicas en torno al turismo. Al momento de la visita la comunidad contaba con un eco hotel en funcionamiento y dos más en proceso de construcción. Además, algunos lugareños han instalado tiendas donde pueden ofrecer a los visitantes alimentos fríos y congelados como gaseosas, agua, cervezas y helados, y algunos otros se han dedicado a la fabricación de artesanías.

Finalmente, a través de la entrevista con el operario de la microrred se indaga si la instalación de la central de generación fotovoltaica ha impactado a la comunidad El Vergel y el comportamiento de su demanda eléctrica. De acuerdo con el operario, antes de esta instalación, la microrred diésel se ponía en funcionamiento de 4 a 6 horas al anochecer – dependiendo del combustible disponible. El operario también detalla que, en el año 2012, justo antes que el sistema diésel fuera repotenciado, los 32 usuarios de ese momento disponían cada uno de 3 puntos de iluminación que generaban un único pico de demanda en las noches de aproximadamente 4 a 5 kW. El operario también indica que gracias a la instalación de la central fotovoltaica a finales de 2013 se incorporaron nuevos usos eléctricos con la compra de 4 televisores y 3 congeladores. Y a finales de julio de 2019, momento en que se realizó la visita, la microrred híbrida contaba con 4 nuevos usuarios, es decir, 38 en total. Además, la demanda aumentó y cambió sus patrones, presentando dos picos de demanda, uno a medio día y el más alto en las noches, el cual estaba entre los 9 a 10 kW (esta información se sintetiza en la Figura V).

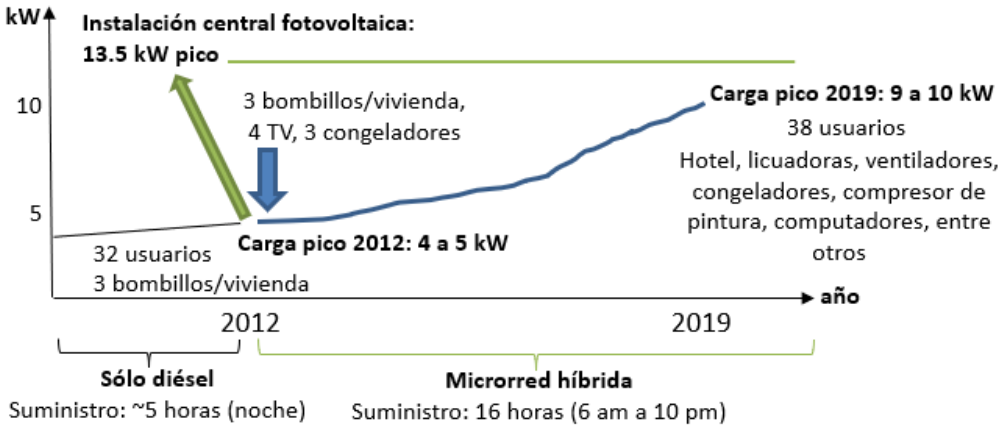

Figura V.- Crecimiento de la demanda eléctrica comunidad El Vergel. Fuente: Elaboración propia.

La disminución del margen entre la capacidad instalada de la central fotovoltaica y la demanda pico de la comunidad (ver Figura V), ha incidido en el aumento del uso de la planta diésel en las noches. De acuerdo con el operario durante los primeros años de funcionamiento de la central fotovoltaica era casi nulo el uso de la planta diésel y para el momento de la visita la misma se estaba usando en promedio dos horas durante la noche. Esta situación se debe a varios factores, por un lado, se tiene el crecimiento de la demanda y por otro el deterioro de las baterías, lo cual hace que durante horas nocturnas la energía almacenada en estas sea insuficiente para abastecer toda la demanda y se deba recurrir al encendido de la planta diésel. El operario también menciona que el aumento del uso de la planta diésel ha incidido en aumentos en el costo de la electricidad, lo cual genera malestar entre los usuarios. La disminución del margen también podría incidir en otras problemáticas en un futuro no muy lejano, ya que, si la demanda supera la capacidad de generación, se podrían presentar fallas del sistema y apagones por sobrecarga, lo que deja en evidencia la necesidad de instalar nueva capacidad de generación fotovoltaica y baterías.

3.2 Resultados obtenidos a través del modelo de simulación. - Para obtener los resultados aquí presentados se realizaron dos tareas: 1) parametrizar el modelo de simulación de acuerdo con la información recopilada de la comunidad El Vergel, y 2) validar el modelo de simulación al reproducir lo mencionado por el operario para los años 2012 y 2019 – al respecto, en la Figura VI se puede ver que el modelo es capaz de reproducir las curvas de carga antes y después de la hibridación del sistema, es decir, con la microrred diésel se observa un único pico de demanda en la noche de 4.38 kW, valor dentro del rango dado por el operario; y al 2019, con la microrred híbrida, se pueden ver dos picos de demanda, siendo mayor el de la noche con un valor de 9.46 kW – también dentro del rango dado.

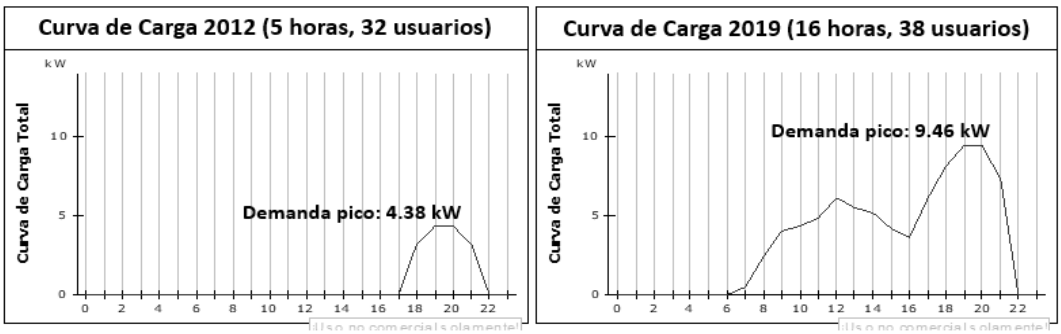

Figura VI.- Simulación del comportamiento de la demanda antes y después de la hibridación de la microrred. Fuente: Elaboración propia.

Una vez se garantiza que el modelo de simulación es capaz de reproducir comportamientos conocidos, se pasa a la simulación de dos posibles escenarios:

- Escenario 1: la microrred híbrida sigue operando con las condiciones actuales, es decir, no se instala nueva capacidad de generación renovable.
- Escenario 2: la microrred híbrida crece, es decir, se le instala nueva capacidad de generación fotovoltaica y baterías de forma paulatina, a medida que la demanda lo requiera, y se incluye un plan de disminución de uso de diésel del 5.9% anual. El servicio eléctrico se sigue prestando durante 16 horas al día.

Bajo el Escenario 1, las simulaciones muestran que la generación eléctrica a través de la planta diésel supera la generación solar fotovoltaica en el año 2023 (ver Figura VII – Generación), lo cual incide en un comportamiento

incremental de los gastos de operación (OPEX) como se puede observar en la Figura VII – Gastos. En la Figura VII – Gastos, también se pude observar que no hay inversión en nueva capacidad instalada – el gasto de capital (CAPEX) permanece en cero durante toda la simulación; y que se hacen dos gastos importantes en reposiciones, el primero corresponde al banco de baterías y el segundo a los demás competentes de la central fotovoltaica instalada en el 2012. Considerando todos los gastos bajo el Escenario 1 (OPEX y Reposiciones), el costo total del sistema durante los 21 años de simulación asciende a $181,728.39 USD.

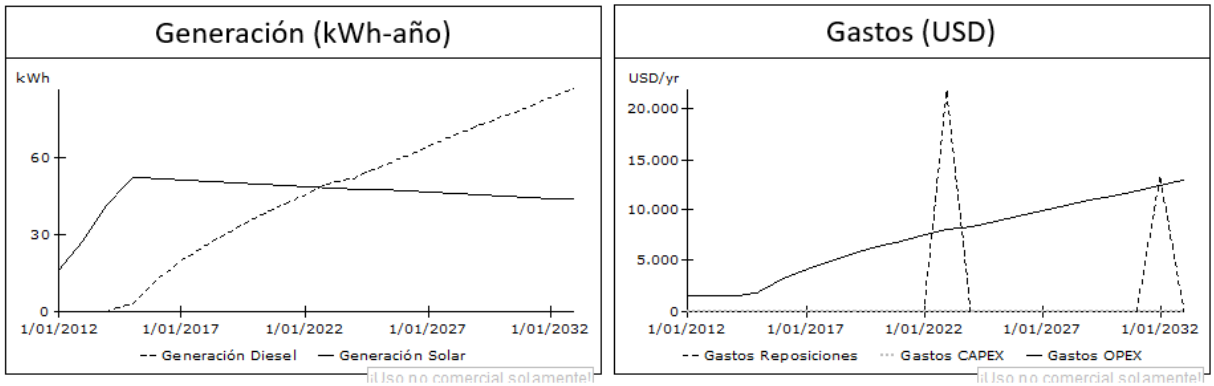

Figura VII.- Resultados Escenario 1. Fuente: Elaboración propia.

Bajo el Escenario 2, se puede observar en la Figura VIII – Generación, que para el año 2023 se debería empezar a incorporar nueva capacidad de generación renovable ya que, al estrecharse el margen entre la oferta y la demanda, el modelo indica que es necesario repotenciar el sistema de generación y se hace a través de capacidad instalada solar fotovoltaica. En la Figura VIII – Generación, también se puede ver como el uso de diésel va disminuyendo a medida que se tiene más capacidad instalada renovable y al final de la simulación el uso de diésel es cero. Además, en la Figura VIII – Gastos, se puede ver como disminuyen los gastos OPEX a medida que se disminuye el uso de la planta diésel y se repotencia el sistema con más capacidad de generación fotovoltaica - a estas repotenciaciones se asocian los gastos CAPEX. Asimismo, se ven nuevamente los dos gastos en reposiciones mencionados para el Escenario 1. Considerando todos los gastos bajo el Escenario 2 (OPEX; Reposiciones y CAPEX), el costo total del sistema durante los 21 años de simulación asciende a $175,222.81 USD.

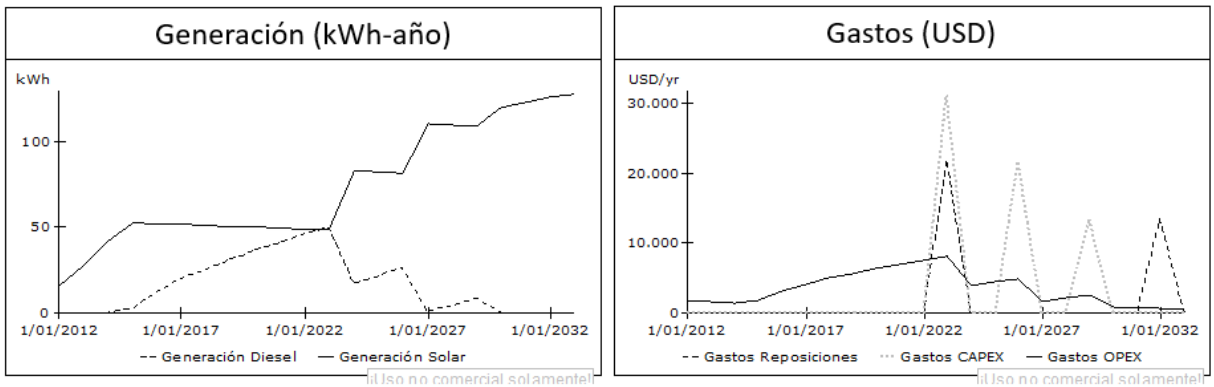

Figura VIII.- Resultados Escenario 2. Fuente: Elaboración propia.

Comparando el costo total del sistema del Escenario 1 ($181,728.39 USD) vs el Escenario 2 ($175,222.81 USD), es claro que desde el punto de vista económico es mejor continuar repotenciando el sistema a través de renovables e incorporar un plan de disminución de uso de diésel, que esperar saturar la componente renovable de la microrred y tener que aumentar las horas de uso de la planta diésel. También es notorio el beneficio ambiental, ya que bajo el Escenario 1 se generan 232.7 toneladas de CO2, mientras que bajo el Escenario 2 el CO2 generado es de 90.4 toneladas. Finalmente, se observan efectos positivos en términos sociales, ya que el porcentaje de actividades productivas pasa de cero cuando solo estaba la microrred diésel a 12% con el sistema híbrido. Además, se incentiva el crecimiento de la demanda y su suministro se garantiza a través de tecnologías menos contaminantes y costosas.

Finalmente, reconociendo y abordando las incertidumbres asociadas con los parámetros de simulación y su impacto potencial en los resultados, se hace un análisis de sensibilidad sobre la radiación y el CAPEX. Por un lado, se disminuye la radiación a 3.5 kW h/m^2 y se aumenta el CAPEX en un 20%, los resultados obtenidos bajo el Escenario 1 muestran que las emisiones y el costo total del sistema aumentan, pues al tener menos radiación se debe hacer mayor uso de la

planta diésel. Algo similar ocurre con el Escenario 2, aunque en este hay un efecto adicional y se da por el aumento del CAPEX, haciendo que el costo total del sistema se incremente considerablemente ($207,622.3 USD). En ambos escenarios el % de las actividades productivas permanecen iguales. Por otro lado, al aumentar la radiación a 4 kW h/m^2 y disminuir el CAPEX en un 20% se observa que bajo el Escenario 1 el costo total del sistema y las emisiones disminuyen levemente, ya que al tener más radiación se usará un poco menos la planta diésel. Asimismo, ocurre con el Escenario 2, es decir, las emisiones y el costo total del sistema disminuyen; sin embargo, la disminución del costo total del sistema en este caso es más notorio ($159,669.5 USD) dada la disminución en el CAPEX. Además, el % de actividades productivas se incrementa levemente. Estos resultados evidencian la sensibilidad del sistema a la variación de estos dos parámetros y validan que el modelo funciona adecuadamente, pues estos son coherentes con los resultados que se esperan según las variaciones realizadas.

3.3 Discusión de los resultados. - Los resultados obtenidos a través de la reunión con el funcionario de ENAM, la visita a la comunidad, la entrevista al operario de la microrred, y las encuestas realizadas a los habitantes de El Vergel, evidencian que la transición a fuentes renovables trae consigo múltiples beneficios. De acuerdo con la información recolectada, la instalación de la central fotovoltaica posibilitó el incremento del número de horas de suministro eléctrico, pasando de 5 a 16 horas diarias. Además, la instalación de la central de generación fotovoltaica en la microrred diésel ha permitido mejorar la calidad del servicio eléctrico. Esto indica que la transición energética permite hacer frente a los retos dos y tres que se mencionan en la introducción y que afrontan las pequeñas comunidades fuera de red que actualmente son abastecidas a través de plantas de generación diésel, en otras palabras, la hibridación de las plantas de generación diésel haciendo uso de tecnologías renovables, como la solar fotovoltaica, facilita el aumento en las horas de suministro eléctrico y mejora la calidad y asequibilidad a este servicio.

Asimismo, se hace evidente que la incorporación de la central fotovoltaica a la microrred diésel también trajo consigo impactos económicos y sociales. Desde el punto de vista económico uno de los elementos que más resalta es el desarrollo de actividades productivas en torno al turismo, pues como se pudo observar durante la visita, cerca de la comunidad se construyó un eco hotel que empezó a operar una vez la microrred podía suministrar 16 horas de electricidad, dicha iniciativa la llevaron a cabo personas del municipio de Leticia, sin embargo, la comunidad se ha visto beneficiada por los empleos que allí se generan y también porque esto ha motivado a sus habitantes a construir sus propios eco hoteles. Además, la actividad económica del turismo también ha incentivado algunos emprendimientos locales como la venta de comestibles y la fabricación de artesanías. Desde el punto de vista social se observó que los habitantes han podido mejorar su calidad de vida al poder refrigerar sus alimentos y hacer uso de ventiladores. También se han favorecido las condiciones para la educación pues al contar con electricidad durante el día la escuela permanece iluminada, se pueden conectar computadores y acceder a internet. Por último, también se identificaron beneficios en aspectos como el acceso a información y entretenimiento, ya que algunos habitantes han adquirido televisores, radios y celulares que pueden usar durante 16 horas o más.

Los resultados obtenidos mediante el modelo de simulación evidencian que es totalmente necesario continuar con la transición energética, instalando nueva capacidad de generación renovable y disminuyendo el uso de las plantas de generación diésel, si se quiere prestar un suministro eléctrico sostenible en el tiempo. Al comparar los resultados obtenidos en los dos escenarios, queda claro que si a la microrred híbrida no se le incorpora nueva capacidad de generación renovable el uso de la planta de generación diésel será cada vez mayor, lo cual repercute en el aumento del costo de generación, en que la comunidad deba disminuir su demanda eléctrica y en una mayor contaminación ambiental. Para evitar esta situación la ESP debe sortear diferentes tipos de desafíos. Desde el punto de vista técnico, y dado que la comunidad abordada no se puede integrar con las principales redes de distribución del país, es un reto para la ESP continuar ampliando la capacidad de generación de la microrred a través de renovables, a fin de poder atender el crecimiento de la demanda y evitar el uso de la planta diésel. Otro gran desafío es conseguir los recursos financieros para cubrir los costos de la instalación de nueva capacidad de generación renovable, pues sin la expansión con renovables el uso de la planta diésel continuará y será cada vez mayor, lo cual en si ya es un problema, pues ni la ESP ni la comunidad está en capacidad de solventar su operación, de hecho, El Vergel recibe un subsidio tarifario del 80.35%. Finalmente, otro reto para la ESP es lograr que los habitantes adquieran mayor conocimiento en cuanto a la gestión y mantenimiento de sus microrredes, pues al ser una comunidad pequeña y aislada, las personas tienen una formación limitada que obstaculiza el desarrollo de nuevas capacidades.

De forma global, los resultados corroboran que la transición energética es el camino para garantizar que las pequeñas comunidades fuera de red, cuya generación eléctrica depende total o parcialmente de plantas diésel, tengan un suministro eléctrico confiable, asequible, sostenible y moderno en el tiempo. Para lograr esto se deben considerar por lo menos dos pasos: 1) convertir las microrredes diésel en microrredes híbridas - entre más pronto mejor; y 2) repotenciar las microrredes híbridas y convertirlas en 100% renovables - esto último implicaría la implementación de dos estrategias. La primera, es instalar paulatinamente nueva capacidad de generación renovable - de acuerdo con las señales dadas por el crecimiento de la demanda. La segunda, es establecer un plan de disminución del uso de la planta

de generación diésel con miras a su eliminación - esta estrategia debe aplicarse gradualmente, a medida que haya mayor capacidad de generación renovable, y sin descuidar los mantenimientos para evitar cortes de suministro. Sumado a estas estrategias, la ESP también debe continuar con el desarrollo de competencias técnicas acorde con las capacidades de los habitantes, por ejemplo, apoyar asuntos administrativos y llevar a cabo mantenimientos sencillos como limpiar los paneles, monitorear el agua de las baterías, e informar de forma temprana cualquier anormalidad. Por último, la ESP debería aprovechar como parte de su estrategia de sostenibilidad financiera la disminución de los precios de algunas tecnologías renovables como la solar fotovoltaica, y deberían considerar reflejar este beneficio a los usuarios con una disminución de la tarifa en cuanto sea posible.

4. Conclusiones. - La hibridación de microrredes diésel a través del uso de tecnologías renovables, como la solar fotovoltaica y baterías, trae efectos favorables a comunidades fuera de red cuyo suministro eléctrico en la actualidad depende únicamente de plantas de generación diésel. Por un lado, el efecto inmediato del aumento de las horas de prestación de servicio eléctrico, y, por otro lado, un efecto paulatino en el crecimiento de la demanda eléctrica que se vincula a nuevos usos eléctricos y la posibilidad de desarrollar actividades productivas, de formación y entretenimiento.

La expansión gradual de la capacidad de generación de la microrred híbrida a través de la instalación de tecnologías renovables conjugado con la disminución paulatina del uso del diésel trae múltiples beneficios a estas comunidades – como se muestra a través de los resultados del modelo de simulación. Estos beneficios se pueden ver desde las tres principales dimensiones de sostenibilidad, es decir, desde la dimensión económica, con un costo total inferior (incluyendo OPEX, reposiciones y CAPEX); desde la dimensión ambiental, con una disminución sustancial de emisiones de CO2; y desde la dimensión social, con un servicio eléctrico lo suficientemente amplio como para desarrollar actividades productivas, de formación y entretenimiento a través de un sistema de generación menos contaminante y costoso. En este sentido, las ESP deberían anticiparse con el diseño e instalación de sistemas de electrificación fuera de red que puedan ser repotenciados haciendo uso de tecnologías renovables y de forma paulatina – a medida que el crecimiento de la demanda lo requiera.

Las simulaciones también indican que es posible lograr, en el largo plazo, un suministro eléctrico continuo y totalmente renovable en pequeñas comunidades fuera de red. En este sentido es relevante señalar algunas recomendaciones de política que ayudarían a cumplir con esta visión. La primera es que el gobierno debería promover que toda nueva capacidad de generación que se instale en estas comunidades sea en su totalidad o en mayor medida renovable. La segunda es que el gobierno debería exigir a las ESP escenarios de crecimiento de la demanda eléctrica y los respectivos planes de expansión de sus sistemas de generación a través del uso de tecnologías renovables. Como tercera recomendación está un control más estricto por parte del gobierno en cuanto a que las ESP presten un servicio eléctrico confiable todo el tiempo. Una cuarta recomendación es que el gobierno debería establecer metas de instalación de tecnologías renovables y de disminución del uso de plantas diésel con miras a proporcionar un servicio eléctrico 100% renovable en el largo plazo. Sumado a las políticas, se requiere un esfuerzo continuo por parte de las ESP y las comunidades en cuanto al monitoreo de sus sistemas de generación, su mantenimiento y adecuado uso. Por ejemplo, que las ESP acojan las políticas planteadas, capaciten periódicamente personas de la comunidad para apoyar algunas actividades de administración y mantenimiento, y que proporcionen información a los habitantes sobre el uso eficiente de la energía. También es necesario que los habitantes se comprometan con un buen uso del recurso eléctrico y que lo aprovechen en actividades productivas y de formación que promuevan el desarrollo económico y social de sus comunidades.

Finalmente, a través del artículo se confirma que la transición energética es deseable y necesaria si se quiere garantizar un suministro eléctrico confiable, asequible, sostenible y moderno en estas comunidades. De acuerdo con la información recopilada y los resultados arrojados por el modelo de simulación, la transición energética trae consigo múltiples beneficios y posibilita un suministro eléctrico sostenible tanto en el ámbito ambiental como en el social y económico. Sin embargo, llevar a cabo esta transición vincula diferentes tipos de desafíos, algunos de ellos mencionados en la discusión de los resultados, lo cual indica que es necesario continuar investigando para realmente lograr que las pequeñas comunidades fuera de red cuenten con un suministro eléctrico acorde con lo establecido en el ODS7.

Disponibilidad de datos: El conjunto de datos que apoya los resultados de este estudio no se encuentran disponibles.

Financiación: Este trabajo fue financiado por el Departamento Administrativo de Ciencia, Tecnología e Innovación del Gobierno de Colombia COLCIENCIAS ahora Ministerio de Ciencia, Tecnología e Innovación, como parte del proyecto doctoral “Alternativas de gestión para el suministro eléctrico sostenible en Zonas No Interconectadas” a través de la Convocatoria 727 de 2015 - Doctorados Nacionales con contrato FP44842-130-2017.

Referencias

[1] IRENA, “World Energy Transitions Outlook 2022: 1.5°C Pathway,” Abu Dhabi, 2022. Accessed: Jan. 31, 2023. [Online]. Available: https://www.irena.org/publications/2022/Mar/World-Energy-Transitions-Outlook-2022

[2] United Nations, “THE 17 GOALS - Sustainable Development Goals,” 2016. https://sdgs.un.org/goals (accessed Feb. 02, 2023).

[3] IRENA, “Off-grid renewable energy solutions to expand electricity access: An opportunity not to be missed,” 2019. [Online]. Available: https://www.irena.org/publications/2019/Jan/Off-grid-renewable-energy-solutions-to-expand-electricity-to-access-An-opportunity-not-to-be-missed

[4] IEA, “Tracking SDG7: The Energy Progress Report, 2022,” Paris, 2022. [Online]. Available: https://www.iea.org/reports/tracking-sdg7-the-energy-progress-report-2022

[5] E. Terrado, A. Cabraal, and I. Mukherjee, “Designing Sustainable Off-Grid Rural Electrification Projects: Principles and Practices,” Washington, D.C., 2008. doi: 10.1596/1813-9450-5193.

[6] S. Mandelli, J. Barbieri, R. Mereu, and E. Colombo, “Off-grid systems for rural electrification in developing countries: Definitions, classification and a comprehensive literature review,” Renew. Sustain. Energy Rev., vol. 58, pp. 1621–1646, May 2016, doi: 10.1016/j.rser.2015.12.338.

[7] A. Haghighat Mamaghani, S. A. Avella Escandon, B. Najafi, A. Shirazi, and F. Rinaldi, “Techno-economic feasibility of photovoltaic, wind, diesel and hybrid electrification systems for off-grid rural electrification in Colombia,” Renew. Energy, vol. 97, pp. 293–305, 2016, doi: 10.1016/j.renene.2016.05.086.

[8] J. Tomei et al., “Forgotten spaces: How reliability, affordability and engagement shape the outcomes of last-mile electrification in Chocó, Colombia,” Energy Res. Soc. Sci., vol. 59, no. March 2019, 2020, doi: 10.1016/j.erss.2019.101302.

[9] IEA, “SDG7: Data and Projections,” Paris, 2022. Accessed: Jan. 29, 2023. [Online]. Available: https://www.iea.org/reports/sdg7-data-and-projections

[10] E. Garces, J. Tomei, C. J. Franco, and I. Dyner, “Lessons from last mile electrification in Colombia: Examining the policy framework and outcomes for sustainability,” Energy Res. Soc. Sci., vol. 79, Sep. 2021, doi: 10.1016/j.erss.2021.102156.

[11] E. Garces, C. J. Franco, J. Tomei, and I. Dyner, “Sustainable electricity supply for small off-grid communities in Colombia : A system dynamics approach,” Energy Policy, vol. 172, 2023, doi: 10.1016/j.enpol.2022.113314.

[12] Congreso de Colombia, Ley 855 de 2003 - Por la cual se definen las Zonas No Interconectadas. Colombia: Sistema Único de Información Normativa, 2003. [Online]. Available: http://www.suin-juriscol.gov.co/viewDocument.asp?id=1669722

[13] H. Louie, Off-Grid Electrical Systems in Developing Countries. Seattle: Springer International Publishing, 2018. doi: 10.1007/978-3-319-91890-7.

[14] UPME, “Plan Indicativo de Expansión de Cobertura de Energía Eléctrica PIEC 2019-2023,” 2019. [Online]. Available: http://www.upme.gov.co/Siel/Siel/Portals/0/Piec/Informacion_Base_PIEC_Dic302019.pdf

[15] IPSE, “Informe de gestión IPSE 2018,” Bogotá D.C. – Colombia, 2019. [Online]. Available: http://www.ipse.gov.co/transparencia-y-acceso-a-informacion-publica/informacion-de-interes2/noticias/551-informe-de-gestion-2018

[16] IPSE, “Informe de Gestión IPSE 2019,” pp. 1–92, 2020, [Online]. Available: http://www.ipse.gov.co/ipse/informes-de-gestion/category/359-informe-de-gestion-2019#

[17] D. F. Barnes and W. M. Floor, “Rural energy in developing countries: A Challenge for Economic Development,” Annu. Rev. Energy Environ., vol. 21, no. 1, pp. 497–530, 1996, doi: 10.1146/annurev.energy.21.1.497.

[18] SSPD, “Zonas No Interconectadas - ZNI: Diagnóstico de la Prestación del Servicio de Energía Eléctrica 2017,” Bogotá, 2017. [Online]. Available: https://www.superservicios.gov.co/sites/default/archivos/Publicaciones/Publicaciones/2018/Dic/diag_zni_2018_7122018.pdf

[19] MME, “Resolución 182138 de 2007 - Por la cual se expide el procedimiento para otorgar subsidios del sector eléctrico en las Zonas No Interconectadas.” Ministerio de Minas y Energía, pp. 1–4, 2007. [Online]. Available: http://energuaviare.com/sites/default/files/RESOLUCION_MME_182138_2007.pdf

[20] E. Garces, “Alternativas de gestión para el suministro eléctrico sostenible en Zonas No Interconectadas,” Universidad Nacional de Colombia, 2021. [Online]. Available: https://repositorio.unal.edu.co/handle/unal/80271

[21] ENAM, “ENAM Energía para el Amazonas S.A. E.S.P.” http://www.enam.com.co/

[22] IRENA, “Electricity storage and renewables: Costs and markets to 2030,” Abu Dhabi, 2017. Accessed: Aug. 11, 2020. [Online]. Available: https://www.irena.org/costs/Electricity-Storage

[23] R. Jimenez, “Barriers to electrification in Latin America: Income, location, and economic development,” Energy Strateg. Rev., vol. 15, pp. 9–18, 2017, doi: 10.1016/j.esr.2016.11.001.

[24] J. P. Viteri and F. Henao, “A human-centered approach to regional off-grid electrification budgeting: the Colombian case,” Sustain. Sci. Pract. Policy, vol. 19, no. 1, p., 2023, doi: 10.1080/15487733.2023.2217043.

[25] REN21, “Renewables 2022 Global Status Report,” Paris, 2022. [Online]. Available: https://www.ren21.net/gsr-2022/

[26] MME, Resolución 181272 de 2011 - Por la cual se ajusta el procedimiento para otorgar subsidios del sector eléctrico en las áreas de servicio exclusivo de las zonas no interconectadas continentales y se deroga la Resolución 180195 de 2011. Bogotá, 2011. [Online]. Available: http://legal.legis.com.co/document/Index?obra=legcol&document=legcol_aa41c3358d910134e0430a0101510134

[27] F. Huneke, J. Henkel, J. A. Benavides González, and G. Erdmann, “Optimisation of hybrid off-grid energy systems by linear programming,” Energy. Sustain. Soc., vol. 2, no. 1, p. 7, 2012, doi: 10.1186/2192-0567-2-7.

[28] A. Vides-Prado et al., “Techno-economic feasibility analysis of photovoltaic systems in remote areas for indigenous communities in the Colombian Guajira,” Renew. Sustain. Energy Rev., vol. 82, no. September 2015, pp. 4245–4255, Feb. 2018, doi: 10.1016/j.rser.2017.05.101.

[29] CREG, Resolución CREG-067 de 2009. Colombia, 2009. [Online]. Available: http://apolo.creg.gov.co/Publicac.nsf/2b8fb06f012cc9c245256b7b00789b0c/618b3f69976a25ea0525785a007a715c/$FILE/Creg067-2009.pdf

[30] CREG, Documento CREG-057 de 2009. Colombia, 2009. [Online]. Available: http://apolo.creg.gov.co/Publicac.nsf/2b8fb06f012cc9c245256b7b00789b0c/618b3f69976a25ea0525785a007a715c/$FILE/D-057-09 ÁREAS DE SERVICIO EXCLUSIVO ZNI VAUPÉS.pdf

Nota contribución de los autores:

1. Concepción y diseño del estudio
2. Adquisición de datos
3. Análisis de datos
4. Discusión de los resultados
5. Redacción del manuscrito
6. Aprobación de la versión final del manuscrito

EG ha contribuido en: 1, 2, 3, 4 y 5.
CJF ha contribuido en: 1, 2, 3, 4 y 6.

Nota de aceptación: Este artículo fue aprobado por los editores de la revista Dr. Rafael Sotelo y Mag. Ing. Fernando A. Hernández Gobertti.

Towards Sustainable Energy Storage: A Low-Cost IoT Solution for Real-time Monitoring of Lead-Acid Battery Health

Hacia el almacenamiento de energía sostenible: una solución de IoT de bajo costo para el monitoreo en tiempo real del estado de las baterías de plomo-ácido

Rumo ao armazenamento de energia sustentável: uma solução IoT de baixo custo para monitoramento em tempo real da saúde da bateria de chumbo-ácido

Sadiq Ur Rehman[1(*)], Halar Mustafa[2], Muhammad Ahsan Shaikh[3], Shahzor Memon[4]

Recibido: 13/03/2024 Aceptado: 20/05/2024

Summary. - This research article introduces a microcontroller-based prototype system called the Battery Health Monitoring System (BHMS), designed to evaluate the health and condition of lead-acid batteries. The focus of the study is on utilizing the Internet of Things (IoT) for real-time battery monitoring. The system incorporates various sensors to track and record critical parameters such as current, voltage, power drain, state of charge (SOC), temperature, and overall battery health. These sensors are configured to trigger an alert when any monitored parameters fall below predefined values. The study aims to validate the effectiveness of the proposed low-cost system in real-time monitoring of lead-acid batteries.

Keywords: Lead-acid battery, Temperature, IoT, ESP8266.

(*) Corresponding Author
[1] Ph.D., Assistant Professor, FEST, Hamdard University (Pakistan), sadiq.rehman@hamdard.edu.pk,
ORCID iD: https://orcid.org/0000-0002-6308-450X
[2] M.E, Lecturer, FEST, Hamdard University (Pakistan), halar.mustafa@hamdard.edu.pk,
ORCID iD: https://orcid.org/0000-0002-7021-5010
[3] Ph.D., Lecturer, FEST, Hamdard University (Pakistan), muhammad.ahsan@hamdard.edu.pk,
ORCID iD: https://orcid.org/0000-0003-2408-5689
[4] M.E. Assistant Professor, FEST, Hamdard University (Pakistan) Shahzor.memon@hamdard.edu.pk,
ORCID iD: https://orcid.org/0000-0003-3555-628X

Memoria Investigaciones en Ingeniería, núm. 26 (2024). pp. 202-212
https://doi.org/10.36561/ING.26.12
ISSN 2301-1092 • ISSN (en línea) 2301-1106 – Universidad de Montevideo, Uruguay

Resumen. - *Este artículo de investigación presenta un sistema prototipo basado en microcontrolador llamado Sistema de monitoreo del estado de la batería (BHMS), diseñado para evaluar la salud y el estado de las baterías de plomo-ácido. El objetivo del estudio es utilizar el Internet de las cosas (IoT) para monitorear la batería en tiempo real. El sistema incorpora varios sensores para rastrear y registrar parámetros críticos como corriente, voltaje, consumo de energía, estado de carga (SOC), temperatura y estado general de la batería. Estos sensores están configurados para activar una alerta cuando algún parámetro monitoreado cae por debajo de los valores predefinidos. El estudio tiene como objetivo validar la eficacia del sistema de bajo coste propuesto en el seguimiento en tiempo real de baterías de plomo-ácido.*

Palabras clave: *Batería de plomo-ácido, Temperatura, IoT, ESP8266.*

Resumo. ***-*** *Este artigo de pesquisa apresenta um protótipo de sistema baseado em microcontrolador denominado Battery Health Monitoring System (BHMS), projetado para avaliar a saúde e a condição de baterias de chumbo-ácido. O foco do estudo está na utilização da Internet das Coisas (IoT) para monitoramento da bateria em tempo real. O sistema incorpora vários sensores para rastrear e registrar parâmetros críticos, como corrente, tensão, consumo de energia, estado de carga (SOC), temperatura e integridade geral da bateria. Esses sensores são configurados para disparar um alerta quando algum parâmetro monitorado cair abaixo dos valores predefinidos. O estudo visa validar a eficácia do sistema de baixo custo proposto no monitoramento em tempo real de baterias de chumbo-ácido.*

Palavras-chave: *Bateria de chumbo-ácido, Temperatura, IoT, ESP8266.*

1. Introduction. - Batteries are critical in various applications, including automotive, renewable energy, and telecommunication systems [1]. The failure of batteries can lead to significant consequences, including power outages, equipment damage, and economic losses. Therefore, it is essential to monitor the health of batteries in real time to ensure their optimal performance and prevent failure. Figure I show the market demand for lead acid batteries in the general market.

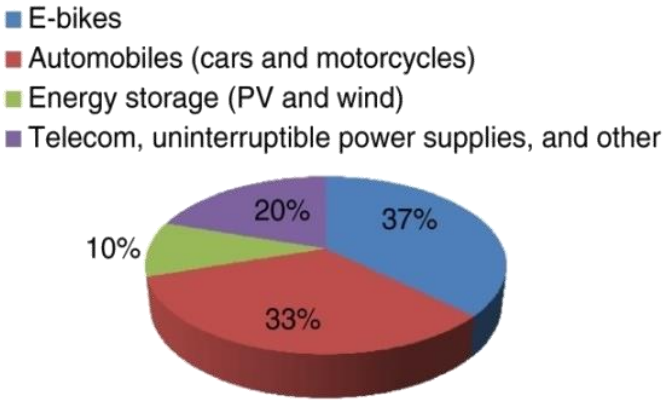

Figure I. Market Distribution of Lead Acid Battery[2]

In lead-acid batteries, State of Charge (SOC), describes how charged the battery is right now about its maximum capacity [3]. Usually, it is stated as a percentage, where 100% denotes a fully charged battery and 0% denotes a fully discharged battery. For the battery to operate at its best and last as long as possible, it is imperative to monitor its state of charge (SOC). A typical formula for calculating a 12V lead-acid battery's SOC can be written as;

$$\text{SoC}= \frac{Remaining\ Capacity}{full\ charge\ capacity\ (Temperature,\ \ Present\ charge\ or\ discharge\ rate)} \qquad \text{Eq (1)}$$

The opposite of the SOC, the State of Discharge (SOD) in lead-acid batteries indicates how much of the battery's capacity has been utilized.

$$\text{SOD}=100\%-\text{SOC} \qquad \text{Eq (2)}$$

With the advent of the Internet of Things (IoT) [4-5], battery health monitoring systems can now be designed and implemented at low costs with increased efficiency.

This research paper focuses on designing and implementing a low-cost battery health monitoring system using IoT for real-time monitoring of lead-acid batteries. Since lead acid batteries have high reliability and low maintenance requirements, they are widely used in various applications. The major issue with lead-acid batteries is the problem of sulfation [6], water loss, and corrosión. Careful monitoring of these batteries is required to prevent failure and enhance lifespan. In this article, we proposed the battery health monitoring system consists of IoT based system that collects data from various sensors attached to the lead-acid batteries. The sensors are responsible for calculating the parameters like temperature, voltage, current, and electrolyte level, to provide the status of the battery's health. Collected data is then transmitted to the IoT platform for real-time monitoring and analysis.
In the proposed system, we have used all the components that are easily available in the market to reduce cost. Even the IoT platform (ThinkSpeak) is used as open-source software. The real-time monitoring features of the system allow users to recognize possible battery problems and take preventative measures before damage is done.

2. Literature Review.- Lead acid batteries are one of the essential power sources that are extensively used in various industries, these industries include automotive, telecommunications, power generation, distribution, etc [7]. Hence it is important to have an effective battery system. The problem with lead acid batteries is rated to their cost (expensive), and their continuous usage may cause performance degradation. There is also a recycling process issue with the lead acid batteries which cause damage to the environment [8]. As a result, it is important to keep vigilant in the management and handling of lead acid batteries to minimize adverse effects and increase their lifespan.

There has been a lot of research work done in the field of monitoring the health of lead-acid batteries. Extensive work is presently related to the battery management systems (BMS) required for lead acid batteries. Authors in [9]

demonstrate how to calculate the state of charge (SoC) and introduce the concept of the battery management system (BMS) that is used for systems like uninterruptible power supplies (UPS), hybrid electric vehicles (HEVs), and electric cars (EVs). No concept of real-time monitoring was present in this research work. The work on the accuracy of battery monitoring circuits for portable communication devices is proposed in [10]. However, this system's accuracy is subject to debate because when all the parameters are considered, it produces an error margin of up to 10%. Working on parameters like temperature, voltage, current, and SoC was done in [11] with the analysis of battery discharging parameters. This research provided the key importance of monitoring all batteries in a battery bank to keep the ideal operating levels and circumstances. Discussion and development tendencies of electric vehicle (EV) batteries were done in [12], in these articles author emphasizes the importance of the BMS in both electric and hybrid vehicles. This study describes how BMS features including cell balancing, charge management, and state monitoring are combined to guarantee dependable and safe battery operation. However, again in this work, real real-time monitoring feature was not included. In [13], the authors address the present issues with BMS and emphasize the significance of assessing a battery's condition, including its longevity, health, and charge. Through an examination of the most recent methods for battery condition evaluation, it also addresses upcoming issues and possible fixes for BMS.

Today's electric vehicles prefer lithium-ion (Li-ion) batteries for energy storage due to their high energy density, strong output, extended lifespan, low self-discharge rate, and lack of memory effect [14]. However, a well-designed BMS is crucial to ensuring safety, dependability, performance optimization, and cost-effectiveness while lowering manufacturing complexity and weight [15]. Table 1 represents the guide for the common battery used worldwide.

The transfer of data between controllers and sensors has led to the development of wireless Battery Management Systems (WBMSs). These systems alleviate wiring issues and allow for more flexible placement of battery modules. Utilizing 5G or 4G networks [16-18] along with an IoT gateway, WBMSs employ IoT protocols (such as those in energy management systems or converters) to directly connect with cloud support servers for tasks like fault diagnostics and battery state monitoring.

	PROS	CONS	COMMON APPLICATION
LEAD ACID	Rechargable, Extremely Common, High Power Density, Durable, Wide Temperature Range	Low Energy Density, Very Heavy, Large in Size	High Current Demand Applications, Car Batteries, Large Scale Battery Banks
ALKALINE	Extremely Common, Cheap, Decent Power Density, Low cost	Susceptible to Natural Rupture, Generally Non-Rechargable, Short Lifetime	Non-Rechargable Consumer Electronics, Flashlights, Toys, Household Items
NICKEL-METAL HYDRIDE	High Current Ability, Less Susceptible to Memory Issues, Lower Cost	Short Storage Life, Susceptible to Overcharge	Power Tools, RC Airplanes and Drones, Portable Systems
LITHIUM ION	Very High Energy Density, Limited Memory Effect, Long Life, Low Maintenance, Rechargable	High cost, Vunerable to Stress (and Exploding!), Require Lots of Protection	Space Constrained Products, Weight Constrained Products, Cell Phones, IoT Devices, Electronic Watches

Table I. Pros and cons of common battery

In this paper, an IoT-based prototype model for real-time lead acid battery monitoring is provided. The objective is accomplished by taking into account variables like temperature, voltage, current, power, and SOC, which are the indicators of the battery's state of health. It is important to note that the proposed prototype is designed to accommodate various capacities of 12V lead acid batteries, allowing versatility in its application.

3. Proposed system model.- The proposed system monitors the voltage, current, power utilized, state of charge (SoC), health, and temperature of a lead-acid battery. The gathered data is sent to the IoT platform Thingspeak using the ESP8266 [19] module, which is programmed with Arduino software. Arduino [20] is used to store and handle the data generated by sensors. A voltage division circuit is used with an ACS712 sensor [21] to measure the voltage; it divides the 12V from the lead-acid battery into 8.7V and 3.3V, with the 3.3V input going to the ESP8266 module.

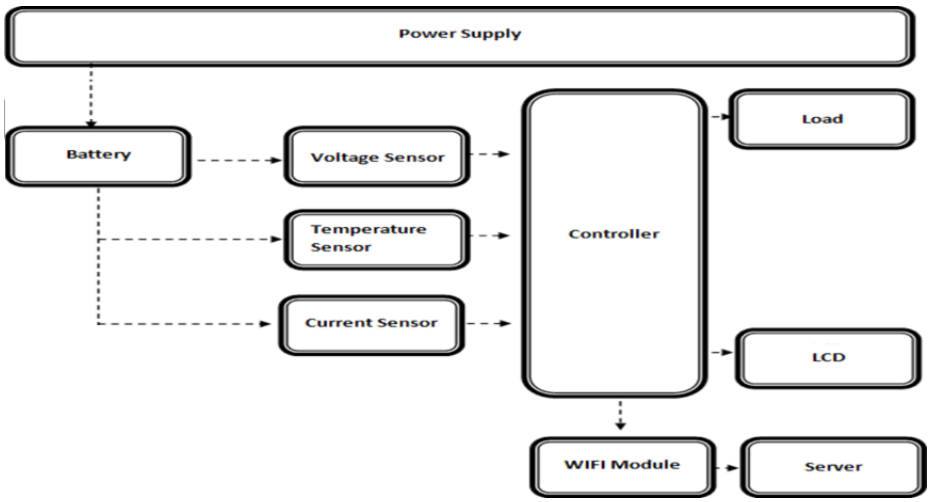

Figure II. System Block Diagram

The battery's voltage can be converted to a percentage to calculate the State of Charge (SoC). Since it is difficult to measure the battery's interior temperature, the external temperature is instead monitored. A DHT 11 sensor [22] is used for this. Thingspeak is used to monitor all of these characteristics, and updates are made in real-time every 15 seconds. This proposed system can be put in remote locations, reducing the need for periodic power management system maintenance. To achieve the claimed functionality, the component used in the proposed system model can be seen in Figure III.

Figure III. Components for the prototype model

The voltage method used in this proposed prototype uses voltage analysis rather than current measurements to indirectly derive the State of Charge (SoC). Thingspeak provides temperature, current, voltage, battery health, and state of charge (SoC) data of the battery in a graphical format, facilitating remote monitoring via an IoT platform. In this model, the load attached to the battery is a 12V DC fan.

4. Results.- After installing the Arduino software, the libraries for the DHT 11 sensor, ZMPT101B, ACS712, and ESP8266 were downloaded. The coding for the proposed system model was completed using the Arduino software, incorporating mathematical formulas to determine the SOC% from voltage data. Additionally, the calculation of power utilized was performed using the formula provided in equation (3).

$$\text{Power} = \text{Voltage} \times \text{Current} \qquad \text{Eq (3)}$$

The ESP8266 transmits all the sensor data to Thingspeak, an IoT platform, for monitoring. When there is a change in battery current and voltage due to the load of a 12V DC fan, these changes can be observed in the graphs.

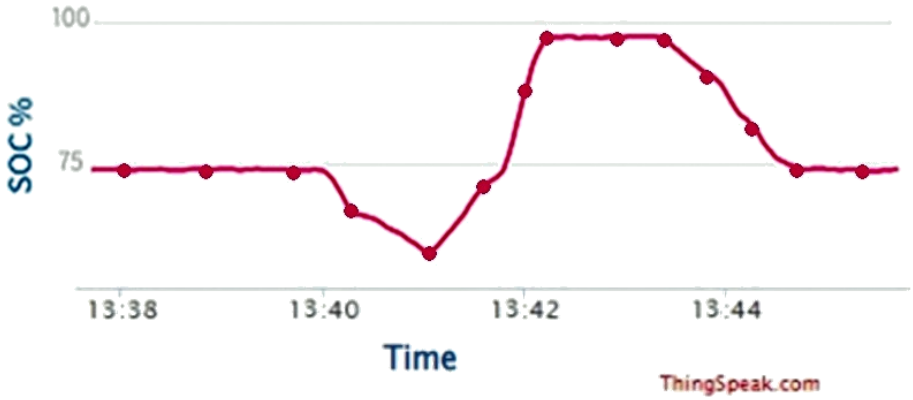

Figure IV. Battery Charge Status.

Figure IV shows that battery charge status, readings were recorded at 10-minute intervals from 13:37 to 13:47. The state of charge (SOC) indicates that 75% of the battery's charge remains when no load is connected. At 13:40, a 12V DC fan was used as a load, causing the SOC graph to drop. Once the charge in the battery drops to 55%, the charging circuit activates and increases the SOC to 98%. When the battery reaches this charge level, the charging stops, resulting in a constant SOC graph as the DC fan is switched off at this time. After 1 minute, the fan switches on again, causing the SOC to drop from 98%. Figure V shows the change in voltage due to the resistive load. Notably, when the voltage level drops to 10V at 21:10, the battery starts charging and remains in charging mode until it reaches 11.6V. The variation in voltage drop is due to the DC fan speed, which consumes more current, as shown in Figure VI.

Our proposed system works perfectly and matches the theoretical results of power utilization in mW with the simulation results obtained from Figures V and VI, as seen in Figure VII.

Figure V. Change in battery voltage concerning the resistive load.

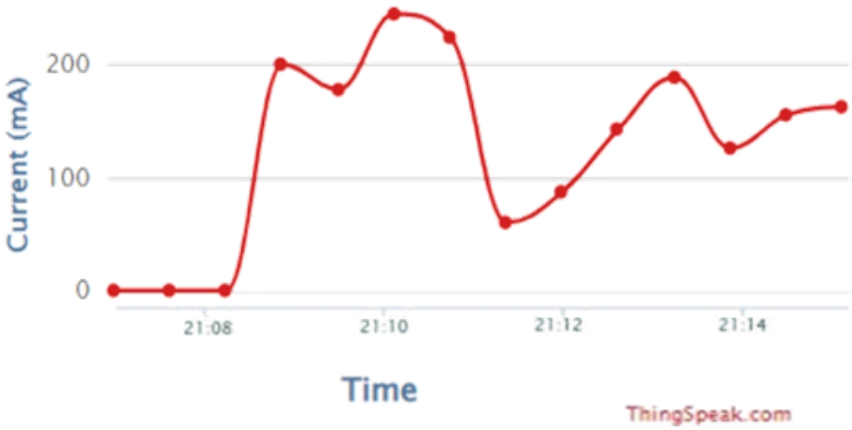

Figure VI. Change in battery Current concerning the resistive load.

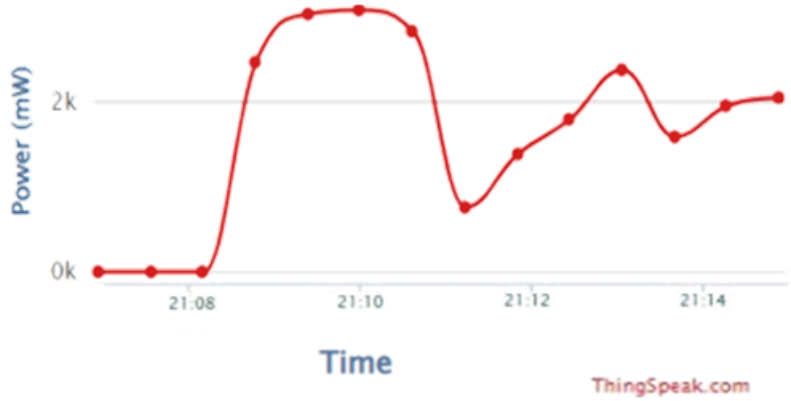

Figure VII. Power is drawn from the battery.

Figure VIII. Change in battery surface temperature due to change in current.

Figure VIII illustrates the variation in the surface temperature of the battery during charging and discharging. This temperature change results from fluctuations in the temperature of the acid inside the battery that stores the charges. Additionally, as the temperature rises, the battery's health deteriorates, as depicted in Figure IX. The battery's health is determined using the formula provided in equation (4).

$$\text{SoH} = \frac{full\ charge\ capacity\ (25C,\ \ Design\ Capacity\ charge\ or\ discarge\ rate)}{Design\ Capacity} \qquad \text{Eq (4)}$$

Figure IX. Change in battery health.

There were some limitations encountered while testing this proposed system. One of the main challenges was synchronizing data with the cloud. Additionally, obtaining a clear graph during variations in DC fan speed proved difficult. The room temperature also affected the monitoring of the battery's surface temperature during charging and discharging.

5. Conclusion.- Monitoring battery health is crucial for lead-acid batteries, and with the rise of wireless technology, IoT has become a widely utilized feature in this prototype model. This functionality allows users to monitor lead-acid battery parameters remotely and at any time. The proposed system model consists of basic components readily available in local markets, and sensor coding to interface with the microcontroller is easily accessible online. Results obtained from the model include State of Charge (SoC), voltage, current, power drained, surface temperature, and battery health.

It's important to note that the performance of the proposed system may vary among different brands of lead-acid batteries due to their unique discharge signatures. A notable aspect of the system is a 15-second delay before data is uploaded to the cloud. It should be acknowledged that the system's accuracy may be compromised when dealing with series and parallel combinations of batteries in power banks, as its optimization is geared toward single batteries. Additionally, incorporating control features could be considered for future enhancements to this proposed system.

References

[1] Vangapally, N., Penki, T.R., Elias, Y., Muduli, S., Maddukuri, S., Luski, S., Aurbach, D. and Martha, S.K., "Lead-acid batteries and lead–carbon hybrid systems: A review", Journal of Power Sources, 579, p.233312, 2023. https://doi.org/10.1016/j.jpowsour.2023.233312

[2] Van der Kuijp, T.J., Huang, L. and Cherry, C.R. "Health hazards of China's lead-acid battery industry: a review of its market drivers, production processes, and health impacts", Environmental Health, 12, pp.1-10, 2013. https://doi.org/10.1186/1476-069X-12-61

[3] Kebede, A.A., Coosemans, T., Messagie, M., Jemal, T., Behabtu, H.A., Van Mierlo, J. and Berecibar, M, "Techno-economic analysis of lithium-ion and lead-acid batteries in stationary energy storage application", Journal of Energy Storage, 40, p.102748, 2021. https://doi.org/10.1016/j.est.2021.102748

[4] Shakir, M., Karim, S., Memon, S., Rehman, S.U. and Mustafa, H, "An improvement in IoT-based smart trash management system using Raspberry Pi", International Journal of Computational Vision and Robotics, 14(2), pp.191-201, 2024. https://doi.org/10.1504/IJCVR.2024.136997

[5] Rehman, S.U. and Khan, A., "Integrating IoT Technology for Improved Distribution Transformer Monitoring and Protection", Electrical, Control, and Communication Engineering, 19(1), pp.22-28, 2023. https://doi.org/10.2478/ecce-2023-0004

[6] Mahrous, Y.S., Shenouda, A.Y., Ali, A.A. and Barakat, M.A, "Novel insight into the behavior of carbon in the positive active material of the lead-acid battery", Diamond and Related Materials, 140, p.110498, 2023. https://doi.org/10.1016/j.diamond.2023.110498

[7] Olabi, A.G., Wilberforce, T., Sayed, E.T., Abo-Khalil, A.G., Maghrabie, H.M., Elsaid, K. and Abdelkareem, M.A., "Battery energy storage systems and SWOT (strengths, weakness, opportunities, and threats) analysis of batteries in power transmission". Energy, 254, p.123987, 2022. https://doi.org/10.1016/j.energy.2022.123987

[8] Lopes, P.P. and Stamenkovic, V.R, "Past, present, and future of lead-acid batteries". Science, 369(6506), pp.923-924, 2020. https://doi.org/10.1126/science.abd335

[9] Chang, W.Y., "The state of charge estimating battery methods: A review". International Scholarly Research Notices, 2013. https://doi.org/10.1155/2013/953792

[10] Kodgirwar, S., Chandrachood, A., Vyas, S. and Kodgirwar, V., "Design of Signal Conditioning Circuit for Biomedical Sensors and Battery Monitoring Circuit for a Portable Communication System", American Journal Of Engineering Research (AJER), (6), pp.100-107, 2016.

[11] Wahyuddin, M.I., Priambodo, P.S. and Sudibyo, H., "August. State of charge (SoC) analysis and modeling battery discharging parameters". 4th International Conference on Science and Technology (ICST), pp. 1-5, IEEE, 2018. https://doi.org/10.1109/ICSTC.2018.8528631

[12] Song, Y., Yang, Y. and Hu, Z., "Present status and development trend of batteries for electric vehicles". Dianwang Jishu/Power System Technology, 35(4), pp.1-7, 2011.

[13] Liu, K., Li, K., Peng, Q. and Zhang, C., "A brief review on key technologies in the battery management system of electric vehicles". Frontiers of mechanical engineering, 14, pp.47-64, 2019. https://doi.org/10.1007/s11465-018-0516-8

[14] Dinger, A., Martin, R., Mosquet, X., Rabl, M., Rizoulis, D., Russo, M. and Sticher, G., "Batteries for electric cars: Challenges, opportunities, and the outlook to 2020". The Boston Consulting Group, 7, p.2017, 2010.

[15] Li, J., Zhou, S. and Han, Y. eds., "Advances in battery manufacturing, service, and management systems". John Wiley & Sons, 2016.

[16] Rehman, S.U., Hussain, A., Hussain, F. and Mannan, M.A., "A comprehensive study: 5G wireless networks and emerging technologies". International Electrical Engineering Conference (IEEC), Vol. 5, pp. 25-32, 2020.

[17] Rehman, S.U., Ahmad, J., Manzar, A. and Moinuddin, M., "Beamforming techniques for mimo-noma for 5g and

beyond 5g: Research gaps and future directions". Circuits, Systems, and Signal Processing, 43(3), pp.1518-1548, 2024. https://doi.org/10.1007/s00034-023-02517-w

[18] Ur Rehman, S., "Outage probability and ergodic capacity analysis of MIMO-NOMA heterogeneous network for 5G system". Journal of Independent Studies and Research Computing, 20(2), 2022. https://doi.org/10.31645/JISRC.22.20.2.3

[19] Rehman, S.U., Khan, I., Rehman, N.U. and Hussain, A., "Low-Cost Smart Home Automation System with Advanced Features". Quaid-E-Awam Univ. Res. J. Eng. Sci. Technol. Nawabshah, 20(01), pp.74-82, 2022. https://doi.org/10.52584/QRJ.2001.10

[20] Rehman, S.U., Raza, M.H. and Khan, A.R., "Delta 3D printer: metal printing". Journal of Electrical Engineering, Electronics, Control and Computer Science, 5(3), pp.19-24, 2019.

[21] Rumpa, L.D., Ambabunga, Y.A. and Pineng, M., "Optimization of ACS712 Sensor Current Measurement in Solar Power System through Regression Modeling". Journal of Applied Informatics and Computing, 7(2), pp.198-201, 2023. https://doi.org/10.30871/jaic.v7i2.6511

[22] Indu, A. and Kumar, S.M., "An Approach for Implementing Innovative Weather Monitoring System with DHT11 Sensor and Arduino Uno Tool based on IoT". Sixth International Conference on I-SMAC (IoT in Social, Mobile, Analytics, and Cloud)(I-SMAC), pp. 274-278, IEEE, 2022. https://doi.org/10.1109/I-SMAC55078.2022.9987289

Nota contribución de los autores:

1. Concepción y diseño del estudio
2. Adquisición de datos
3. Análisis de datos
4. Discusión de los resultados
5. Redacción del manuscrito
6. Aprobación de la versión final del manuscrito

SUR ha contribuido en: 1, 2, 3, 4 y 5.
HM ha contribuido en: 5 y 6.
MAS ha contribuido en: 5 y 6.
SM ha contribuido en: 5 y 6.

Nota de aceptación: Este artículo fue aprobado por los editores de la revista Dr. Rafael Sotelo y Mag. Ing. Fernando A. Hernández Gobertti.

Modos de vibración traslacional de un edificio mediante métodos iterativos y verificación con uso de softwares Mathcad y Etabs

Translational vibration modes of a building through iterative methods and verification using Mathcad and Etabs software

Modos de vibração translacional de uma edificação através de métodos iterativos e verificação utilizando os softwares Mathcad e Etabs

Marcos Josue Rupay Vargas[1 (*)], Regner Raúl Parra Lavado[2], Juan Percy Espejo Castilla[3], Juan Miguel Quispe Llantay[4]

Recibido: 15/03/2024 Aceptado: 09/04/2024

Resumen. - Esta investigación se centra en calcular los modos de vibración traslacional de un edificio de pórticos de tres niveles, con el fin de determinar sus periodos y forma de vibrar, la evaluación se llevó a cabo mediante métodos interactivos de Stodola y Holzer, el método numérico de Jacobi, y los resultados obtenidos se verificaron utilizando funciones del vector eigenvals y matriz eigenvecs del software Mathcad, Además, se realizó una verificación con un modelamiento en el software Etabs, siguiendo las propiedades establecidas por la Norma Técnica E.030 de Diseño Sismorresistente del Reglamento Nacional de Edificaciones (RNE).

A lo largo de la investigación, se obtuvieron resultados precisos por medio de los cálculos manuales como con las verificaciones con el uso de los softwares Mathcaf y ETABS. En cada instancia, se determinó que estos métodos representan la vía más apropiada para obtener valores aproximados con respecto a la verificación realizada con su periodo y forma de vibrar. Estos resultados confiables subrayan la eficacia de las herramientas y métodos empleados, destacando la comprensión profunda de las características dinámicas de la edificación analizada.

Palabras clave: Modos de vibración; Método de Stodola; Método de Holzer; Método de Jacobi; Función Eigenvals y Eigenvecs.

(*) Autor Corresponsal

[1] Doctorado en Ingeniería Civil. Universidad Nacional Intercultural de la Selva Central “Juan Santos Atahualpa” (Perú), mrupay@uniscjsa.edu.pe, ORCID iD: https://orcid.org/0000-0002-7891-1838

[2] Maestro en Ingeniería Civil. Universidad Nacional Intercultural de la Selva Central “Juan Santos Atahualpa” (Perú), rparra@uniscjsa.edu.pe, ORCID iD: https://orcid.org/0000-0002-3564-4637

[3] Estudiante de Ingeniería Civil. Universidad Nacional Intercultural de la Selva Central “Juan Santos Atahualpa” (Perú), 77023708@uniscjsa.edu.pe, ORCID iD: https://orcid.org/0009-0008-8494-9278

[4] Estudiante de Ingeniería Civil. Universidad Nacional Intercultural de la Selva Central “Juan Santos Atahualpa” (Perú), 73383929@uniscjsa.edu.pe, ORCID iD: https://orcid.org/0009-0000-7813-5712

Summary. - *This research focuses on calculating the translational vibration modes of a three-level frame building, in order to determine its periods and way of vibrating, the evaluation was carried out using interactive methods of Stodola and Holzer, the numerical method of Jacobi, and the results obtained were verified using functions of the eigenvals vector and eigenvecs matrix of the Mathcad software. In addition, a verification was carried out with modeling in the Etabs software, following the properties established by the Technical Standard E.030 for Seismic-Resistant Design of the Reglamento Nacional de Edificaciones (RNE).*

Throughout the investigation, accurate results were obtained through manual calculations as well as verifications with the use of Mathcaf and ETABS software. In each instance, it was determined that these methods represent the most appropriate way to obtain approximate values with respect to the verification carried out with its period and way of vibrating. These reliable results underline the effectiveness of the tools and methods used, highlighting the deep understanding of the dynamic characteristics of the analyzed building.

Keywords: *Vibration Modes; Stodola Method; Holzer Method; Jacobi Method; Function Eigenvals and Eigenvecs.*

Resumo. ***-*** *Esta pesquisa tem como foco o cálculo dos modos de vibração translacional de um edifício com pórtico de três níveis, a fim de determinar seus períodos e forma de vibrar, a avaliação foi realizada utilizando métodos interativos de Stodola e Holzer, o método numérico de Jacobi, e os resultados obtidos foram verificados utilizando funções do vetor de autovals e matriz de eigenvecs do software Mathcad.Além disso, foi realizada uma verificação com modelagem no software Etabs, seguindo as propriedades estabelecidas pela Norma Técnica E.030 para Projeto Resistente a Sísmicos do Reglamento Nacional de Edificaciones (RNE).*

Ao longo da investigação, resultados precisos foram obtidos através de cálculos manuais, bem como verificações com o uso dos softwares Mathcaf e ETABS. Em cada caso, determinou-se que estes métodos representam a forma mais adequada para obter valores aproximados no que diz respeito à verificação realizada com o seu período e forma de vibração. Estes resultados fiáveis sublinham a eficácia das ferramentas e métodos utilizados, destacando a profunda compreensão das características dinâmicas do edifício analisado.

Palavras-chave: *Modos de Vibração; Método Stodola; Método Holzer; Método Jacobi; Função Eigenvals e Eigenvecs.*

1. Introducción. – En el ámbito de la ingeniería Antisismica, la comprensión de los modos de vibración traslacional de edificios es esencial para garantizar su seguridad y resistencia ante cargas dinámicas, especialmente en zonas sísmicas. En este contexto, la presente investigación se centra en el análisis de un edificio aporticado de tres niveles, con el propósito fundamental de calcular sus modos de vibración traslacional, determinar sus periodos y caracterizar sus formas de vibrar.

Para alcanzar estos objetivos, se emplearán métodos iterativos bien establecidos, como el método de Stodola, el método de Holzer y el método numérico de Jacobi. La verificación de los resultados se llevará a cabo mediante el uso de las funciones del vector eigenvals y matriz eigenvecs del software Mathcad. Además, se realizará una validación adicional utilizando el software Etabs, siguiendo las normativas establecidas por la Norma Técnica E.030 de Diseño Sismorresistente del Reglamento Nacional de Edificaciones (RNE).

Esta investigación busca no solo calcular los modos de vibración, sino también demostrar la eficacia de los métodos empleados, tanto a través de cálculos manuales como del uso de herramientas computacionales avanzadas. La aplicación de estos enfoques proporcionará información valiosa para comprender las características dinámicas de la estructura analizada, contribuyendo así al avance de la ingeniería estructural y al diseño sismorresistente de edificaciones.

2. Materiales y métodos. – Nos enfocamos en un modelo estructural conocido como "edificio simple", el cual se caracteriza por la ausencia de rotaciones en los elementos horizontales a nivel de los pisos. En esta configuración, el edificio simple, cuando se ve sometido a excitaciones que provocan desplazamientos horizontales, comparte numerosas similitudes con una viga en voladizo deformada únicamente por esfuerzo cortante. Para obtener esta deformación, es necesario aceptar las siguientes premisas: la masa de la estructura se concentra por completo en el nivel de los pisos, y las vigas en cada piso son considerablemente más rígidas que las columnas. Esta primera premisa simplifica el problema al convertir un sistema con un número infinito de grados de libertad (GDL) en uno con tantos GDL como masas concentradas a nivel de los pisos.

Los modos de vibración de la edificación, junto con sus frecuencias, periodos y formas de vibración, se calcularán mediante el método iterativo de Stodola y de Holzer, el método numérico de Jacobi, y se verificarán utilizando las funciones del vector eigenvals y matriz eigenvecs del software Mathcad. Además, se realizará una verificación adicional mediante el software Etabs.

La figura I ilustra la configuración de un edificio simple de 3 niveles con un eje de simetría. En donde el módulo de elasticidad del concreto (E) es de 2.20×10^6 tonf/m^2. Las cargas de los dos primeros niveles y de la azotea son de 1.20 y 0.80 tonf/m^2, respectivamente. Las dimensiones de las columnas varían entre 40 x 40 y 40 x 60 cm según el plano en planta. Dada la rigidez significativa de las vigas, se asume un modelo de corte. La aceleración de la gravedad se establece en 9.81 m/s^2.

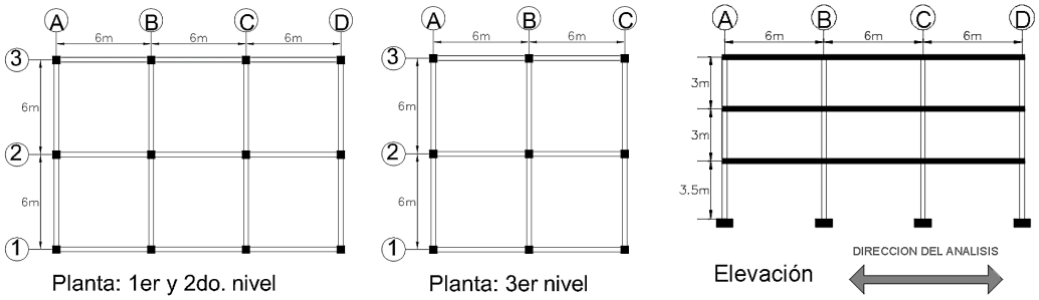

Figura I.- Edificio simple de tres niveles con un eje de simetría

El proceso para cada uno de los métodos comienza con la obtención de la matriz de rigidez lateral y la matriz de masa.

- **Matriz de rigidez lateral. -** Para simplificar el cálculo de modos traslacionales, se emplea un modelo de corte. Sin embargo, es crucial recordar que esto implica una simplificación significativa del modelo. A continuación, se detallan las rigideces de cada entrepiso, junto con la matriz de rigidez lateral.

$$I_c = \frac{b \times h^3}{12}$$

$$k_{ent} = \frac{12EI}{h_1^3}$$

$$K = \begin{bmatrix} k_1 + k_2 & -k_2 & 0 \\ -k_2 & k_2 + k_3 & -k_3 \\ 0 & -k_3 & k_3 \end{bmatrix} = \begin{bmatrix} 105384.8699 & -64663.7037 & 0 \\ -64663.7037 & 113161.4815 & -48497.7778 \\ 0 & -48497.7778 & 48497.7778 \end{bmatrix}$$

- **Matriz de masa. -** La masa de cada entrepiso se obtiene multiplicando la carga por el área y dividiéndolo entre la aceleración de la gravedad.

$$M_i = \frac{P_i}{g}$$

$$M = \begin{bmatrix} M_1 & 0 & 0 \\ 0 & M_2 & 0 \\ 0 & 0 & M_3 \end{bmatrix} = \begin{bmatrix} 27.9095 & 0 & 0 \\ 0 & 27.9095 & 0 \\ 0 & 0 & 12.5390 \end{bmatrix}$$

2.1. Método iterativo de Stodola. – Es un método numérico para hallar la primera frecuencia y la forma de vibrar de un sistema mecánico o estructural. Consiste en suponer un vector inicial de desplazamientos y aplicar una serie de operaciones matriciales para obtener un vector mejorado, que se acerca al modo de vibración buscado [4].

- **Primer modo de vibración** :

Matriz dinámica : $D_1 = K^{-1} \times M = \begin{bmatrix} 0.6854 & 0.6854 & 0.3079 \\ 0.6854 & 1.1170 & 0.5018 \\ 0.6854 & 1.1170 & 0.7604 \end{bmatrix} \times 10^{-3}$

Forma de vibrar asumida : $\phi_{asumida} = \begin{bmatrix} 0.4 \\ 0.7 \\ 1 \end{bmatrix}$

Primera iteración : $\phi'_1 = D_1 \times \phi_{asumida} = \begin{bmatrix} 0.001062 \\ 0.001558 \\ 0.001816 \end{bmatrix}$

Forma normalizanda : $\phi_1 = \frac{\phi'_1}{\phi'_{1_3}} = \begin{bmatrix} 0.584577 \\ 0.857661 \\ 1 \end{bmatrix}$

Segunda iteración : $\phi'_1 = D_1 \times \phi_1 = \begin{bmatrix} 0.001296 \\ 0.001860 \\ 0.002119 \end{bmatrix} \rightarrow \phi_1 = \frac{\phi'_1}{\phi'_{1_3}} = \begin{bmatrix} 0.61179 \\ 0.87799 \\ 1 \end{bmatrix}$

Seguimos iterando hasta que las variaciones entre las formas normalizadas seguidas sean las mismas.

Última iteración : $\phi'_1 = D_1 \times \phi_1 = \begin{bmatrix} 0.001333 \\ 0.001907 \\ 0.002166 \end{bmatrix} \rightarrow \phi_1 = \frac{\phi'_1}{\phi'_{1_3}} = \begin{bmatrix} 0.6156 \\ 0.8806 \\ 1 \end{bmatrix}$

Frecuencia y periodo : $\omega_1 = \sqrt{\frac{1}{\phi'_{1_3}}} = 21.4869\ rad/s \rightarrow T_1 = \frac{2\pi}{\omega_1} = 0.2924\ s$

- **Segundo modo de vibración :**

Matriz identidad : $I = \begin{bmatrix} 1 & 0 & 0 \\ 0 & 1 & 0 \\ 0 & 0 & 1 \end{bmatrix}$

Masa generalizada : $M^* = {\phi_1}^T \times M \times \phi_1 = 44.760694$

Matriz de barrido : $\beta = I - \frac{\phi_1 \times {\phi_1}^T \times M}{M^*} = \begin{bmatrix} 0.7637 & -0.3380 & -0.1725 \\ -0.3380 & 0.5164 & -0.2467 \\ -0.3839 & -0.5491 & 0.7199 \end{bmatrix}$

Matriz dinámica : $D_2 = D_1 \times \beta = \begin{bmatrix} 1.735 & -0.468 & -0.656 \\ -0.468 & 0.696 & -0.325 \\ -1.460 & -0.723 & 1.536 \end{bmatrix} \times 10^{-4}$

Primera iteración : $\phi'_2 = D_2 \times \phi_{asumida} = \begin{bmatrix} -2.896 \times 10^{-5} \\ -2.4859 \times 10^{-6} \\ 4.45579 \times 10^{-5} \end{bmatrix}$

Forma normalizanda : $\phi_2 = \frac{\phi'_2}{\phi'_{2_3}} = \begin{bmatrix} -0.650015 \\ -0.055767 \\ 1 \end{bmatrix}$

Seguimos iterando hasta que las variaciones entre las formas normalizadas seguidas sean las mismas.

Última iteración : $\phi'_2 = D_2 \times \phi_2 = \begin{bmatrix} -0.000196 \\ 0.000003 \\ 0.000262 \end{bmatrix} \rightarrow \phi_2 = \frac{\phi'_2}{\phi'_{2_3}} = \begin{bmatrix} -0.7486 \\ 0.0132 \\ 1 \end{bmatrix}$

Frecuencia **y** periodo : $\omega_2 = \sqrt{\frac{1}{\phi'_{2_3}}} = 61.7799\ rad/s \rightarrow T_2 = \frac{2\pi}{\omega_2} = 0.1017\ s$

- **Tercer modo de vibración** :

Matriz inversa dinámica : $D_3 = M^{-1} \times K = \begin{bmatrix} 3775.95 & -2316.91 & 0 \\ -2316.91 & 4054.59 & -1737.68 \\ 0 & -3867.74 & 3867.74 \end{bmatrix}$

Primera iteración : $\phi'_3 = D_3 \times \phi_{asumida} = \begin{bmatrix} -111.4548 \\ 173.7681 \\ 1160.3226 \end{bmatrix}$

Forma normalizanda : $\phi_3 = \frac{\phi'_3}{\phi'_{3_3}} = \begin{bmatrix} -0.096055 \\ 0.149758 \\ 1 \end{bmatrix}$

Seguimos iterando hasta que las variaciones entre las formas normalizadas seguidas sean las mismas.

Última iteración : $\phi'_3 = D_3 \times \phi_3 = \begin{bmatrix} 4332.776 \\ -6814.330 \\ 7419.846 \end{bmatrix} \rightarrow \phi_3 = \frac{\phi'_3}{\phi'_{3_3}} = \begin{bmatrix} 0.5839 \\ -0.9184 \\ 1 \end{bmatrix}$

Frecuencia **y** periodo : $\omega_3 = \sqrt{\phi'_{3_3}} = 86.1385\ rad/s \rightarrow T_3 = \frac{2\pi}{\omega} = 0.0729\ s$

2.2. Método iterativo de Holzer. – Se fundamenta en la repetición de un conjunto de expresiones matriciales que detallan la evolución dinámica del sistema [3].

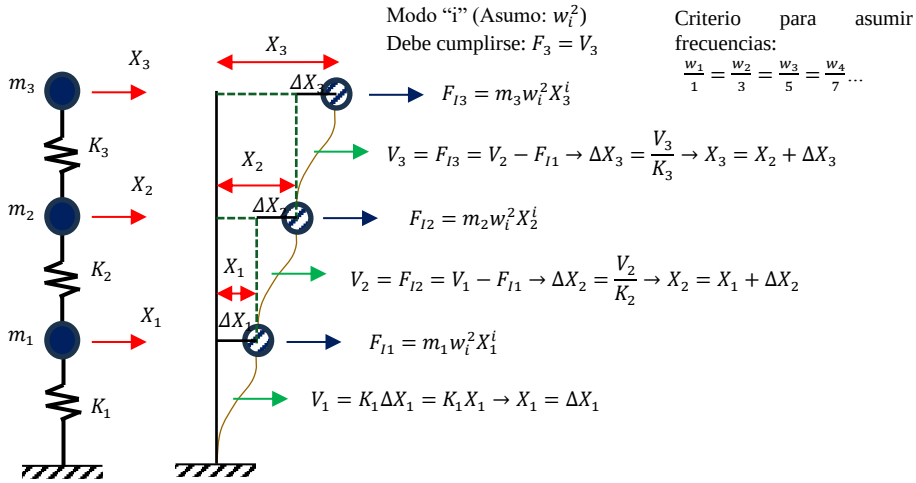

Figura I.- Esquema del método de Holzer

- **Primer modo de vibración** :

Frecuencia circular y periodo : $\omega_1 = 21.4869\ rad/s \rightarrow T_1 = \frac{2\pi}{\omega_1} = 0.2924\ s$

Nivel 1 : $X_1 = \Delta X_1 = 1 \rightarrow V_1 = k_1 \times \Delta X_1 = 40721.1662$

: $F_1 = M_1 \times X_1 \times w_1^2 = 12885.3923$

Nivel 2 : $V_2 = V_1 - F_1 = 27835.7739$

: $\Delta X_2 = \frac{V_2}{k_2} = 0.4305 \rightarrow X_2 = X_1 + \Delta X_2 = 1.4305$

: $F_2 = M_2 \times X_2 \times w_1^2 = 18432.1650$

Nivel 3 : $V_3 = V_2 - F_2 = 9403.6089$

: $\Delta X_3 = \frac{V_3}{k_3} = 0.1939 \rightarrow X_3 = X_2 + \Delta X_3 = 1.6244$

: $F_3 = M_3 \times X_3 \times w_1^2 = 9403.6089 \rightarrow V_3 - F_3 = 0$

Forma normlizada : $D_1 = \begin{bmatrix} X_1 \\ X_2 \\ X_3 \end{bmatrix} = \begin{bmatrix} 1 \\ 1.4305 \\ 1.6244 \end{bmatrix} \rightarrow \phi_1 = \frac{D_1}{D_{1_3}} = \begin{bmatrix} 0.6156 \\ 0.8806 \\ 1 \end{bmatrix}$

- **Segundo modo de vibración** :

Frecuencia circular y periodo : $\omega_2 = 61.7799\ rad/s \rightarrow T_2 = \frac{2\pi}{\omega_2} = 0.1017\ s$

Nivel 1 : $X_1 = \Delta X_1 = 1 \rightarrow V_1 = k_1 \times \Delta X_1 = 40721.1662$

: $F_1 = M_1 \times X_1 \times w_2^2 = 106523.5692$

Nivel 2 : $V_2 = V_1 - F_1 = -65802.4030$

: $\Delta X_2 = \frac{V_2}{k_2} = -1.0176 \rightarrow X_2 = X_1 + \Delta X_2 = -0.0176$

: $F_2 = M_2 \times X_2 \times w_2^2 = -1875.8331$

Nivel 3 : $V_3 = V_2 - F_2 = -63926.5699$

: $\Delta X_3 = \frac{V_3}{k_3} = -1.3181 \rightarrow X_3 = X_2 + \Delta X_3 = -1.3357$

: $F_3 = M_3 \times X_3 \times w_2^2 = -63926.5699 \rightarrow V_3 - F_3 = 0$

Forma normlizada : $D_2 = \begin{bmatrix} X_1 \\ X_2 \\ X_3 \end{bmatrix} = \begin{bmatrix} 1 \\ -0.0176 \\ -1.3357 \end{bmatrix} \rightarrow \phi_2 = \frac{D_2}{D_{2_3}} = \begin{bmatrix} -0.7486 \\ 0.0132 \\ 1 \end{bmatrix}$

- **Tercer modo de vibración** :

Frecuencia circular y periodo : $\omega_3 = 86.1385\ rad/s \rightarrow T_3 = \frac{2\pi}{\omega_3} = 0.0729\ s$

Nivel 1 : $X_1 = \Delta X_1 = 1 \rightarrow V_1 = k_1 \times \Delta X_1 = 40721.1662$

: $F_1 = M_1 \times X_1 \times w_3^2 = 207084.0565$

Nivel 2 : $V_2 = V_1 - F_1 = -166362.8903$

: $\Delta X_2 = \frac{V_2}{k_2} = -2.5727 \rightarrow X_2 = X_1 + \Delta X_2 = -1.5727$

: $F_2 = M_2 \times X_2 \times w_3^2 = -325689.3574$

Nivel 3 : $V_3 = V_2 - F_2 = 159326.4671$

: $\Delta X_3 = \frac{V_3}{k_3} = 3.2852 \rightarrow X_3 = X_2 + \Delta X_3 = 1.7125$

: $F_3 = M_3 \times X_3 \times w_3^2 = 159326.4671 \rightarrow V_3 - F_3 = 0$

Forma normlizada : $D_3 = \begin{bmatrix} X_1 \\ X_2 \\ X_3 \end{bmatrix} = \begin{bmatrix} 1 \\ -1.5727 \\ 1.7125 \end{bmatrix} \rightarrow \phi_3 = \frac{D_3}{D_{3_3}} = \begin{bmatrix} 0.5839 \\ -0.9184 \\ 1 \end{bmatrix}$

2.3. Método numérico de Jacobi. – Se fundamenta en la repetición de un conjunto de expresiones en forma de matrices que detallan la dinámica del sistema a lo largo del tiempo [1].

Matriz diagonal inferior : $L = \sqrt{M} = \begin{bmatrix} 5.2829 & 0 & 0 \\ 0 & 5.2829 & 0 \\ 0 & 0 & 3.5411 \end{bmatrix}$

Matriz dinámica : $D = L^{-1} \times K \times (L^{-1})^T$

$$D = \begin{bmatrix} 3775.9525 & -2316.9082 & 0 \\ -2316.9082 & 4054.5894 & -2592.4703 \\ 0 & -2592.4703 & 3867.7419 \end{bmatrix}$$

Ciclos de rotación : $\{1,2,3\} = p, q\{\{1,2\},\{1,3\},\{2,3\}\}$

- **Primera iteración** : $Tan(2\theta) = \frac{2D_{(p,q)}}{(D_{(p,p)} - D_{(q,q)})} \rightarrow \theta = 0.5 ArcTan\left(\frac{2D_{(p,q)}}{(D_{(p,p)} - D_{(q,q)})}\right)$

$D_n = (R_n)^T \times D_{n-1} \times R_n$

1ra rotación : eliminando el término, $d_{1,2}$ $(p = 1, q = 2)$

: $\theta_1 = 0.5 ArcTan\left(\frac{2D_{(1,2)}}{(D_{(1,1)} - D_{(2,2)})}\right) = 0.7554$

$$: R_1 = \begin{bmatrix} \cos\theta_1 & -sen\ \theta_1 & 0 \\ sen\ \theta_1 & \cos\theta_1 & 0 \\ 0 & 0 & 1 \end{bmatrix} = \begin{bmatrix} 0.7280 & -0.6856 & 0 \\ 0.6856 & 0.7280 & 0 \\ 0 & 0 & 1 \end{bmatrix}$$

$$: D_1 = (R_1)^T \times D \times R_1 = \begin{bmatrix} 1594{,}178 & 0 & -1777.287 \\ 0 & 6236.364 & -1887.367 \\ -1777.287 & -1887.367 & 3867.742 \end{bmatrix}$$

2da rotación : $d_{1,3}$ $(p = 1, q = 3)$

: $\theta_2 = 0.5 ArcTan\left(\frac{2D_{(1,3)}}{(D_{(1,1)} - D_{(3,3)})}\right) = 0.5009$

$$: R_2 = \begin{bmatrix} \cos\ \theta_2 & 0 & -sen\ \theta_2 \\ 0 & 1 & 0 \\ sen\ \theta_2 & 0 & \cos\ \theta_2 \end{bmatrix} = \begin{bmatrix} 0.8772 & 0 & -0.4802 \\ 0 & 1 & 0 \\ 0.4802 & 0 & 0.8772 \end{bmatrix}$$

$$: D_2 = (R_2)^T \times D_1 \times R_2 = \begin{bmatrix} 621.216 & -906.305 & 0 \\ -906.305 & 6236.364 & -1655.526 \\ 0 & -1655.526 & 4840.704 \end{bmatrix}$$

3ra rotación : $d_{3,2}$ $(p = 2, q = 3)$

$$: \theta_3 = 0.5 ArcTan\left(\frac{2D_{(2,3)}}{(D_{(3,3)} - D_{(2,2)})}\right) = 0.5859$$

$$: R_3 = \begin{bmatrix} 1 & 0 & 0 \\ 0 & \cos(\theta_3) & sen(\theta_3) \\ 0 & -sen(\theta_3) & \cos(\theta_3) \end{bmatrix} = \begin{bmatrix} 1 & 0 & 0 \\ 0 & 0.8332 & 0.5530 \\ 0 & -0.5530 & 0.8332 \end{bmatrix}$$

$$: D_3 = (R_3)^T \times D_2 \times R_3 = \begin{bmatrix} 621.216 & -755.127 & -501.171 \\ -755.127 & 7335.123 & 0 \\ -501.171 & 0 & 3741.945 \end{bmatrix}$$

- **Segunda iteración** : se realiza el mismo proceso que en la 1ra iteración.

$$D_4 = \begin{bmatrix} 537.333 & 0 & -498.108 \\ 0 & 7419.006 & 55.332 \\ -498.108 & 55.332 & 3741.945 \end{bmatrix};\ D_5 = \begin{bmatrix} 461.695 & 8.307 & 0 \\ 8.307 & 7419.006 & 54.705 \\ 0 & 54.705 & 3817.583 \end{bmatrix};$$

$$D_6 = \begin{bmatrix} 461.695 & 8.306 & -0.126 \\ 8.306 & 7419.837 & 0 \\ -0.126 & 0 & 3816.752 \end{bmatrix}$$

- **Tercera iteración** : se realiza el mismo proceso que en la 1ra iteración.

$$D_7 = \begin{bmatrix} 461.685 & 0 & -0.126 \\ 0 & 7419.846 & 55.332 \\ -0.126 & 55.332 & 3816.752 \end{bmatrix};\ D_8 = \begin{bmatrix} 461.685 & 0 & 0 \\ 0 & 7419.846 & 0 \\ 0 & 0 & 3816.752 \end{bmatrix};$$

$$D_9 = \begin{bmatrix} 461.685 & 0 & 0 \\ 0 & 7419.846 & 0 \\ 0 & 0 & 3816.752 \end{bmatrix}$$

Se realizará el número de iteración que sea conveniente a fin de que todos los datos de la matriz sean proximos a cero con excepción de los valores de la diagonal principal.

Frecuencias y periodos:

$$: w_1 = \sqrt{D_{6(1,1)}} = 21.4869\ rad/s \rightarrow T_1 = \frac{2\pi}{w_1} = 0.2924\ \text{s}$$

$$: w_3 = \sqrt{D_{6(2,2)}} = 86.1385\ rad/s \rightarrow T_3 = \frac{2\pi}{w_2} = 0.0729\ \text{s}$$

$$: w_2 = \sqrt{D_{6(3,3)}} = 61.7799\ rad/s \rightarrow T_2 = \frac{2\pi}{w_3} = 0.1017\ \text{s}$$

- **Formas de vibración** $: U = R_1 \times R_2 \times R_3 \times R_4 \times R_5 \times R_6 \times R_7 \times R_8 \times R_9$

$$U = \begin{bmatrix} 0.4861 & -0.4569 & -0.7450 \\ 0.6954 & 0.7185 & 0.0131 \\ 0.5293 & -0.5244 & 0.6670 \end{bmatrix}$$

$$: D = (L^{-1})^T \times U = \begin{bmatrix} 0.0920 & -0.0865 & -0.1410 \\ 0.1316 & 0.1360 & 0.0025 \\ 0.1495 & -0.1481 & 0.1884 \end{bmatrix}$$

- **Formas de vibración normalizado:**

$$: d_1 = \begin{bmatrix} 0.0920 \\ 0.1316 \\ 0.1495 \end{bmatrix} \rightarrow \phi_1 = \frac{d_1}{d_{1_3}} = \begin{bmatrix} 0.6156 \\ 0.8806 \\ 1 \end{bmatrix}$$

$$d_3 = \begin{bmatrix} -0.0865 \\ 0.1360 \\ -0.1481 \end{bmatrix} \rightarrow \phi_3 = \frac{d_3}{d_{3_3}} = \begin{bmatrix} 0.5839 \\ -0.9184 \\ 1 \end{bmatrix}$$

$$d_2 = \begin{bmatrix} -0.1410 \\ 0.0025 \\ 0.1884 \end{bmatrix} \rightarrow \phi_2 = \frac{d_2}{d_{2_3}} = \begin{bmatrix} -0.7486 \\ 0.0132 \\ 1 \end{bmatrix}$$

2.4. Empleando la función del vector eigenvals y matriz eigenvecs del software Mathcad. – El software Mathcad tiene funciones integradas para calcular los valores y vectores propios de una matriz, que son eigenvals y eigenvecs, respectivamente. Estas funciones devuelven un vector con los valores propios y una matriz con los vectores propios, ordenados de menor a mayor [2].

Matriz dinámica

$$: A = K^{-1} \times M = \begin{bmatrix} 0.6854 & 0.6854 & 0.3079 \\ 0.6854 & 1.1170 & 0.5018 \\ 0.6854 & 1.1170 & 0.7604 \end{bmatrix} \times 10^{-3}$$

Función del vector eigenvals $: \delta = \text{eigenvals}(A) = \begin{bmatrix} 0.002166 \\ 0.000262 \\ 0.000135 \end{bmatrix}$

Frecuencias y periodos $: \lambda = \frac{1}{\delta} \rightarrow w = \sqrt{\lambda} = \begin{bmatrix} 21.4869 \\ 61.7799 \\ 86.1385 \end{bmatrix} \frac{rad}{s} \rightarrow \text{T} = \frac{2\pi}{w} = \begin{bmatrix} 0.2924 \\ 0.1017 \\ 0.0729 \end{bmatrix} s$

Función de la matriz eigenvecs $: \phi' = \text{eigenvecs}(A) = \begin{bmatrix} -0.4194 & -0.5993 & 0.3951 \\ -0.6000 & 0.0106 & -0.6214 \\ -0.6813 & 0.8005 & 0.6766 \end{bmatrix}$

Formas de vibración normalizado:

$$: \phi'_1 = \begin{bmatrix} -0.4194 \\ -0.6000 \\ -0.6813 \end{bmatrix} \rightarrow \phi_1 = \frac{\phi'_1}{\phi'_{1_3}} = \begin{bmatrix} 0.6156 \\ 0.8806 \\ 1 \end{bmatrix}$$

$$: \phi'_2 = \begin{bmatrix} -0.5993 \\ 0.0106 \\ 0.8005 \end{bmatrix} \rightarrow \phi_2 = \frac{\phi'_2}{\phi'_{2_3}} = \begin{bmatrix} -0.7486 \\ 0.0132 \\ 1 \end{bmatrix}$$

$$: \phi'_3 = \begin{bmatrix} 0.3951 \\ -0.6214 \\ 0.6766 \end{bmatrix} \rightarrow \phi_3 = \frac{\phi'_3}{\phi'_{3_3}} = \begin{bmatrix} 0.5839 \\ -0.9184 \\ 1 \end{bmatrix}$$

2.5. Empleando el Software Etabs. – La determinación de los modos de vibración implica un análisis que cuidadosamente tiene en cuenta las características de rigidez y la distribución de masas en la estructura.
En cada dirección de análisis, se seleccionan los modos de vibración cuya suma de masas efectivas represente al menos el 90% de la masa total. Se da prioridad a los tres primeros modos predominantes en la dirección de análisis, asegurando así una representación significativa de la respuesta dinámica de la estructura.

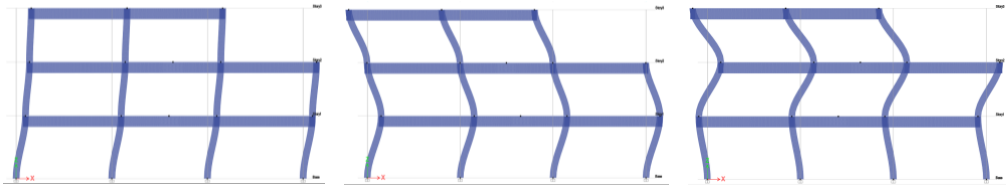

Modo 1: ϕ'_1, T_1 Modo 2: ϕ'_2, T_2 Modo 1: ϕ'_3, T_3

Figura I.- Modos de vibración traslacional de un edificio de 3 niveles

- **Periodos de vibración** $: T_1 = 0.2924\ s \quad T_2 = 0.1017\ s \quad T_3 = 0.0729\ s$

Case	Mode	Period sec	UX	UY	UZ	SumUX	SumUY	SumUZ	RX	RY	RZ	SumRX
Modal	1	0.407089	0	0.963595	0	0	0.963595	0	0.034575	0	0.000514	0.034575
Modal	2	0.292467	0.963594	0	0	0.963594	0.963595	0	0	0.034576	0	0.034575
Modal	3	0.141588	0	0.03311	0	0.963594	0.996705	0	0.959954	0	0.024059	0.994529
Modal	4	0.10172	0.033111	0	0	0.996705	0.996705	0	0	0.959952	0	0.994529
Modal	5	0.101549	0	0.003295	0	0.996705	1	0	0.005471	0	0.010832	1
Modal	6	0.072955	0.003295	0	0	1	1	0	0	0.005472	0	1
Modal	7	7.6E-05	0	0	0	1	1	0	0	0	0.915637	1
Modal	8	2.7E-05	0	0	0	1	1	0	0	0	0.047118	1
Modal	9	2E-05	0	0	0	1	1	0	0	0	0.001842	1

Figura I.- Periodos de vibración de un edificio de 3 niveles

- **Formas de vibración:**

Story	Diaphragm	Output Case	Case Type	Step Type	Step Number	UX mm	UY mm	RZ rad	Point	X mm	Y mm	Z mm
Story3	D3	Modal	LinModEigen	Mode	2	0.047722	0	0	1	6000	6000	9500
Story2	D2	Modal	LinModEigen	Mode	2	0.042025	0	0	2	9000	6000	6500
Story1	D1	Modal	LinModEigen	Mode	2	0.029379	0	0	3	9000	6000	3500

Figura I.- Primera forma de vibrar de un edificio de 3 niveles

Story	Diaphragm	Output Case	Case Type	Step Type	Step Number	UX mm	UY mm	RZ rad	Point	X mm	Y mm	Z mm
Story3	D3	Modal	LinModEigen	Mode	4	-0.060138	0	0	1	6000	6000	9500
Story2	D2	Modal	LinModEigen	Mode	4	-0.000793	0	0	2	9000	6000	6500
Story1	D1	Modal	LinModEigen	Mode	4	0.045022	0	0	3	9000	6000	3500

Figura I.- Segunda forma de vibrar de un edificio de 3 niveles

Story	Diaphragm	Output Case	Case Type	Step Type	Step Number	UX mm	UY mm	RZ rad	Point	X mm	Y mm	Z mm
Story3	D3	Modal	LinModEigen	Mode	6	-0.047283	0	0	1	6000	6000	9500
Story2	D2	Modal	LinModEigen	Mode	6	0.043424	0	0	2	9000	6000	6500
Story1	D1	Modal	LinModEigen	Mode	6	-0.02761	0	0	3	9000	6000	3500

Figura I.- Tercera forma de vibrar de un edificio de 3 niveles

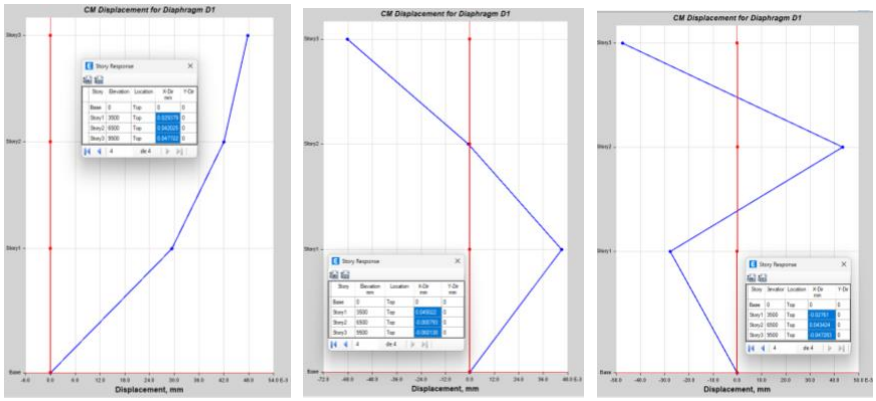

Modo 1: ϕ'_1 Modo 2: ϕ'_2 Modo 1: ϕ'_3

Figura I.- Formas de vibrar de un edificio de 3 niveles

$$\phi'_1 = \begin{bmatrix} 0.029379 \\ 0.042025 \\ 0.047722 \end{bmatrix} mm \quad \phi'_2 = \begin{bmatrix} 0.045022 \\ -0.000793 \\ -0.060138 \end{bmatrix} mm \quad \phi'_3 = \begin{bmatrix} -0.027610 \\ 0.043424 \\ -0.047283 \end{bmatrix} mm$$

- **Formas de vibrar normalizadas** **:** Estos valores normalizados son hallados mediante la division del ultimo valor sobre si mismo, ya que se asume que el ultimo valor que puede tener en la parte superior es 1.

$$\Phi_1 = \frac{\phi'_1}{\phi'_{1_3}} = \begin{bmatrix} 0.6156 \\ 0.8806 \\ 1 \end{bmatrix} \quad \Phi_2 = \frac{\phi'_2}{\phi'_{2_3}} = \begin{bmatrix} -0.7486 \\ 0.0132 \\ 1 \end{bmatrix} \quad \Phi_3 = \frac{\phi'_3}{\phi'_{3_3}} = \begin{bmatrix} 0.5839 \\ -0.9184 \\ 1 \end{bmatrix}$$

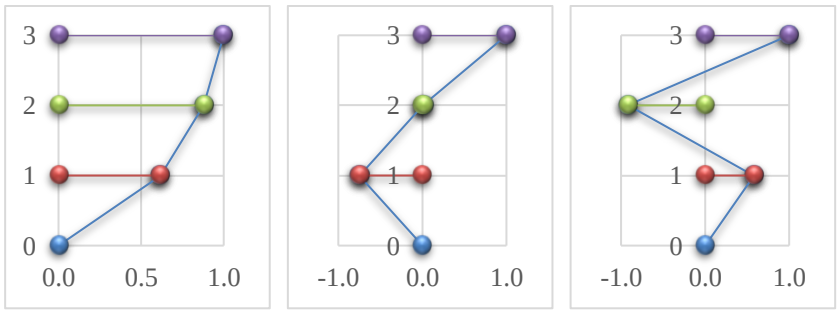

Modo 1: ϕ'_1 Modo 2: ϕ'_2 Modo 1: ϕ'_3

Figura I.- Formas de vibrar normalizadas de un edificio de 3 niveles

3. Resultados. – Los resultados se presentan en las siguientes tablas, permitiendo la comparación entre los métodos iterativos y las respuestas proporcionadas por los programas Mathcad y Etabs.

1ra forma	Método de Stodola	Método de Holzer	Método de Jacobi	Funciones de Mathcad	Etabs
$\boldsymbol{\phi_{1_1}}$	0.6156	0.6156	0.6156	0.6156	0.6156
$\boldsymbol{\phi_{1_2}}$	0.8806	0.8806	0.8806	0.8806	0.8806

ϕ_{1_3}	1	1	1	1	1

Tabla I.- Comparación de la primera forma de vibrar normalizada

2da forma	Método de Stodola	Método de Holzer	Método de Jacobi	Funciones de Mathcad	Etabs
ϕ_{2_1}	-0.7486	-0.7486	-0.7486	-0.7486	-0.7486
ϕ_{2_2}	0.0132	0.0132	0.0132	0.0132	0.0132
ϕ_{2_3}	1	1	1	1	1

Tabla II.- Comparación de la segunda forma de vibrar normalizada

3ra forma	Método de Stodola	Método de Holzer	Método de Jacobi	Funciones de Mathcad	Etabs
ϕ_{3_1}	0.5839	0.5839	0.5839	0.5839	0.5839
ϕ_{3_2}	-0.9184	-0.9184	-0.9184	-0.9184	-0.9184
ϕ_{3_3}	1	1	1	1	1

Tabla III.- Comparación de la tercera forma de vibrar normalizada

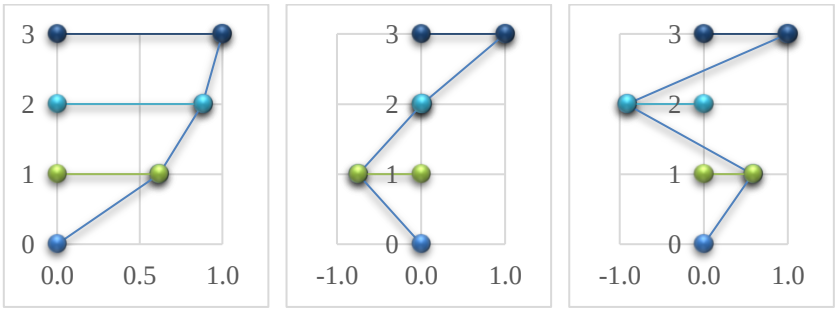

Periodo	Método de Stodola	Método de Holzer	Método de Jacobi	Funciones de Mathcad	Etabs
T_1	0.2924	0.2924	0.2924	0.2924	0.2924
T_2	0.1017	0.1017	0.1017	0.1017	0.1017
T_3	0.0729	0.0729	0.0729	0.0729	0.0729

Tabla IV.- Comparación de los periodos de vibración

4. Discusión. –

- La presente investigación se centra en el cálculo de modos de vibración traslacional de un edificio simple mediante métodos iterativos para calcular su periodo y forma de vibrar. Además, de la verificación con los softwares Mathcad y Etabs.
- En relación con lo obtenido en el Etabs, los periodos 1, 2 y 3 para la estructura son de 0.2924, 0.1017 y 0.0729 segundos, respectivamente. Todos los métodos nos entregaron valores iguales.
- En cuanto a las formas de vibrar, los valores obtenidos en cada método son iguales a los resultados del programa Etabs en una aproximación de 4 decimales.

5. Conclusiones. –

- Los métodos de Stodola, Holzer, Jacobi, y Eigenvals y Eigenvecs demostraron ser efectivos en la determinación del periodo y forma de vibrar de la estructura de concreto armado de tres niveles.
- La comparación entre los resultados obtenidos manualmente y a través del software ETABS valida la precisión de los métodos empleados, lo que sugiere que son herramientas confiables para el análisis dinámico de estructuras.
- Las variaciones de los valores se deben al número de iteraciones que se realizan en cada método, siendo así el método de Stodola el que requiere de mayores iteraciones para obtener valores próximos.

Referencias

Aguilar Falconi, R. (2012). Dinámica de estructuras con CEINCI-LAB (2 ed.). (C. d. Científicas, Ed.) https://www.researchgate.net/publication/279914782_Dinamica_de_Estructuras_con_CEINCI-LAB

[2] De Dios Ochoa, D. J., & Maldonado, H. (s.f.). Métodos de calculo de Modos de Vibración. Universidad Nacional De San Cristobal De Huamanga, 10. https://es.scribd.com/document/450940362/Modos-pdf

[3] Muñoz Peláez, A. (2002). Ingeniería Sismorresistente (1 ed.). https://www.elsolucionario.org/ingenieria-sismorresistente-alejandro-munoz-pelaez-1ra-edicion/

[4] Santana Tapia, R. D. (2013). Ingeniería Antisísmica principios básicos y aplicaciones (1 ed.). Santana Tapia, Ronald Daniel. http://isbn.bnp.gob.pe/catalogo.php?mode=detalle&nt=60371

[5] Zelaya Jara, V. (2011). Análisis sísmico (1 ed.). Zelaya Jara, Víctor Antonio. http://isbn.bnp.gob.pe/catalogo.php?mode=detalle&nt=96379

Nota contribución de los autores:

1. Concepción y diseño del estudio
2. Adquisición de datos
3. Análisis de datos
4. Discusión de los resultados
5. Redacción del manuscrito
6. Aprobación de la versión final del manuscrito

MJRV ha contribuido en: 1, 2, 3, 4, 5 y 6.
RRPL ha contribuido en: 1, 2, 3, 4, 5 y 6.
JPEC ha contribuido en: 1, 2, 3, 4, 5 y 6.
JMQL ha contribuido en: 1, 2, 3, 4, 5 y 6.

Nota de aceptación: Este artículo fue aprobado por los editores de la revista Dr. Rafael Sotelo y Mag. Ing. Fernando A. Hernández Gobertti.

Evaluation of preheating impact on weld residual stresses in AH-36 steel using Finite Element Analysis

Evaluación del impacto del precalentamiento sobre las tensiones residuales de soldadura en acero AH-36 mediante análisis de elementos finitos

Avaliação do impacto do pré-aquecimento nas tensões residuais de solda no aço AH-36 utilizando Análise de Elementos Finitos

Atif Shazad [1(*)], Muhammad Asif [2], Najam Siddiqui[3], Muhammad Uzair[4], Asad A Zaidi[5]

Recibido: 18/03/2024 Aceptado: 20/05/2024

Summary. - Shipbuilding industry is a valuable and profit earning industry which plays a vital role in country's economic development. Ships have crucial impact on country's trade due to necessary support for maritime transportation. Moreover, ships can be utilized for protecting coastal area. Steel chiefly utilized for ships construction due to its good strength and durability. This study emphasizes on residual stress analysis of AH-36 shipbuilding steel. Abaqus software is utilized for finite element analysis to evaluate residual stresses. Mitigation of these residual stresses is very essential; hence preheating technique is discussed in this study. Preheating was conducted at three temperatures i.e., 100ºC,150ºC and 200ºC. Results indicate that Von Mises stresses were decreased effectively due to preheating. 12.6%, 21% and 45.6% reduction were observed at preheating temperatures 100ºC, 150ºC and 200ºC respectively. Further evaluation of stresses revealed that due to preheating of base plate, longitudinal stresses reduced to 21.3%, 44% and 52.4% by increasing preheating temperature from 100ºC,150ºC and 200ºC, respectively. Mitigation of thermal gradient between weld zone and base plate resulted in reduction in overall stresses of base plate.

Keywords: Mitigation; AH-36; Abaqus; residual stresses; finite element analysis.

(*) Corresponding Author

[1] PhD Scholar, Department of Mechanical Engineering, NED University of Engineering and Technology (Pakistan), atifshahzad2717@gmail.com, ORCID iD: https://orcid.org/0000-0002-3277-7901

[2] Assistant Professor, Department of Engineering Sciences, PN Engineering College, National University of Sciences and Technology, Karachi, Pakistan, muhammadasif@pnec.nust.edu.pk, ORCID iD: https://orcid.org/0000-0003-4318-8253

[3] Engineer, Department of Engineering Sciences, PN Engineering College, National University of Sciences and Technology, Karachi, Pakistan, najam.siddiqui@gmail.com, ORCID iD: https://orcid.org/0009-0004-3086-5715

[4] Associate Professor, Department of Mechanical Engineering, NED University of Engineering and Technology (Pakistan), uzair@neduet.edu.pk, ORCID iD: https://orcid.org/0000-0002-2033-6244

[5] Associate Professor, Department of Mechanical Engineering, Islamic University of Madinah (KSA), sali@iu.edu.sa, ORCID iD: https://orcid.org/0000-0001-5457-5684

Memoria Investigaciones en Ingeniería, núm. 26 (2024). pp. 225-243
https://doi.org/10.36561/ING.26.14
ISSN 2301-1092 • ISSN (en línea) 2301-1106 – Universidad de Montevideo, Uruguay

Resumen. - *La industria de la construcción naval es una industria valiosa y rentable que desempeña un papel vital en el desarrollo económico del país. Los barcos tienen un impacto crucial en el comercio del país debido al apoyo necesario para el transporte marítimo. Además, los barcos pueden utilizarse para proteger la zona costera. Acero utilizado principalmente para la construcción de barcos debido a su buena resistencia y durabilidad. Este estudio hace hincapié en el análisis de tensiones residuales del acero de construcción naval AH-36. El software Abaqus se utiliza para el análisis de elementos finitos para evaluar tensiones residuales. La mitigación de estas tensiones residuales es muy esencial; por lo tanto, en este estudio se analiza la técnica de precalentamiento. El precalentamiento se realizó a tres temperaturas, es decir, 100 ºC, 150 ºC y 200 ºC. Los resultados indican que las tensiones de Von Mises disminuyeron efectivamente debido al precalentamiento. Se observaron reducciones del 12,6%, 21% y 45,6% a temperaturas de precalentamiento de 100ºC, 150ºC y 200ºC respectivamente. Una evaluación adicional de las tensiones reveló que, debido al precalentamiento de la placa base, las tensiones longitudinales se redujeron al 21,3%, 44% y 52,4% al aumentar la temperatura de precalentamiento de 100ºC, 150ºC y 200ºC, respectivamente. La mitigación del gradiente térmico entre la zona de soldadura y la placa base dio como resultado una reducción de las tensiones generales de la placa base.*

Palabras clave: *Mitigación; AH-36; Ábaco; tensiones residuales; análisis de elementos finitos.*

Resumo**.** ***-*** *A indústria da construção naval é uma indústria valiosa e lucrativa que desempenha um papel vital no desenvolvimento económico do país. Os navios têm um impacto crucial no comércio do país devido ao apoio necessário ao transporte marítimo. Além disso, os navios podem ser utilizados para proteger a área costeira. Aço utilizado principalmente na construção de navios devido à sua boa resistência e durabilidade. Este estudo enfatiza a análise de tensões residuais do aço para construção naval AH-36. O software Abaqus é utilizado para análise de elementos finitos para avaliar tensões residuais. A mitigação destas tensões residuais é muito essencial; portanto, a técnica de pré-aquecimento é discutida neste estudo. O pré-aquecimento foi realizado em três temperaturas, ou seja, 100ºC, 150ºC e 200ºC. Os resultados indicam que as tensões de Von Mises diminuíram efetivamente devido ao pré-aquecimento. Foram observadas reduções de 12,6%, 21% e 45,6% nas temperaturas de pré-aquecimento 100ºC, 150ºC e 200ºC respectivamente. Uma avaliação mais aprofundada das tensões revelou que, devido ao pré-aquecimento da placa de base, as tensões longitudinais foram reduzidas para 21,3%, 44% e 52,4% aumentando a temperatura de pré-aquecimento de 100ºC, 150ºC e 200ºC, respectivamente. A mitigação do gradiente térmico entre a zona de solda e a placa de base resultou na redução das tensões globais da placa de base.*

Palavras-chave: *Mitigação; AH-36; Abaqus; tensões residuais; análise de elementos finitos.*

1. Introduction. –

1.1 Residual Stresses Generation. - Residual stresses are internal stresses that remain in a material even after external forces are removed. These stresses often occur due to uneven heating, especially in welding processes. In welding, localized heating leads to non-uniform temperature distribution, causing structural and metallurgical changes. The base metal and the heat-affected zone usually have higher temperatures compared to the weld metal [3, 22]. As the weld cools, the stress in the weld area increases, potentially reaching the base metal's yield point. Sequential welding creates additional complexities [18]. The solidified parts of the weld resist shrinkage of subsequent beads, causing longitudinal stress in earlier welded sections. In butt joints, the preparation limits transverse movement, leading to transverse residual stress. Similarly, in fillet welds, tensile stress develops along the length of the weld [7].

Residual stress in welded structures can result in two primary outcomes: premature failure or distortion, or a combination of both. Distortion occurs when the area around a heated weld cools and contracts unevenly, causing one part of the weld to shrink and placing uneven stress across the weld's cross-section [24]. This leads to elastic contraction in the weldment. Such non-uniform contraction manifests as visible distortions. Therefore, predicting the post-welding behavior of materials and adjusting design and construction methods accordingly is crucial. This approach is essential to mitigate distortions and residual stresses, which commonly affect the dimensional precision of structures [19].

1.2 Variations in Residual Stresses. - The impact of residual stresses varies based on their application; they can be either beneficial or detrimental. In some designs, residual stresses are deliberately employed for advantageous purposes. For example, through a process known as laser peening, compressive residual stresses are introduced on the surface of an object. This method is used to strengthen brittle surfaces or enhance the durability of thin sections [23]. However, more often, residual stresses have negative consequences. They can compromise the structural integrity of a product, and manufacturers may not become aware of them until they have already caused considerable deformation [14].

Finite element analysis was implemented to model the welding process and to anticipate stresses in butt welding of two similar carbon steel plates. Research findings indicate that the axial residual stress calculated using this finite element approach aligns closely with the results obtained from experimental observations [12]. [11] conducted a study focusing on FEA of welded structures. Their objective was to develop a reliable method for optimizing the strength of weld joints and predicting their thermal behavior. The study's results highlighted that the critical metallurgical area is the cooling metal adjacent to the weld pool.

[1] conducted a study to evaluate the effectiveness of weld-bonded connections, study also examined joints formed through adhesive bonding by utilizing the finite element method. This involved creating models for spot welding, adhesive bonding, and weld bonding, each complete with specific constraints, stress scenarios, and appropriate material characteristics.

Principal stresses generated due to spot welding were found greater than major principal stresses produced in adhesive bonded joint, and weld bonded joint [2, 16] employed the finite element method for replication of a fusion welded joint. Their developed model incorporated dynamic heat transfer, elastoplastic behavior, a shifting heat source, and

temperature-sensitive thermophysical properties. Fatigue properties of welded joints were evaluated by [13], finite element method was used to assess the fatigue strength. Fracture locations and forecast about lifespan before failure of welded joint were main attributes of this research.

Detail modelling of welded joint was performed by [6] in FEA, digital recreation of physical dynamics of welding process was main objective of this research. Model's accuracy against computational time was required to be balanced, the results of this study revealed comprehensive insight into the mechanical properties of joints. The sequence of welding process significantly impacted the peaks of longitudinal stress. [9] studied impact of multi-pass welded joint in pipes, a three-dimensional thermo-mechanical model was developed to investigate the effect of welding procedures on the residual stress field in a multi-pass welded pipe.

Mitigation of residual stresses and distortions, [4] investigated post welding method for degradation of residual stresses. Different clamping situations studied by [20] positively influenced the residual stress distribution in T-Joint. [8] performed multi-beam preheating process to abate structural deformations. Reduction in compressive stresses in weld area was observed after implanting this method. [25] performed study to assess the influence on cold spraying on Friction stir welded AA 2219 alloy residual stresses. Impact of shot peening due to cold spray enhanced mechanical properties and degraded residual stress.

Manufacturing induced residual stresses were studied by [10] to figure out number of residual stresses in specific areas of T joint weld configuration. High peaks of residual stresses adjacent to the weld areas indicated greater quantity of residual stresses. Cruciform fillet joints were examined by [17] to evaluate distortions and residual stresses by utilizing Simufact welding software. Numerical methods and experimental work were compared to evaluate behavior of joints and validation of results.

[26] conducted research regarding influence of residual stress on bending resistance of welding joints. It was observed that residual stresses influenced negatively on bending resistance by degrading its stiffness more than 10%. Residual stress generation in double welded rib to deck joints were investigated by [8], research aim was focused on enhancement of fatigue strength of streel bridges. Ultrasonic impact treatment was utilized to mitigate deleterious effects of residual stresses and advantageous compressive stresses were induced for improvement in fatigue strength.

2. Motivation. - After an extensive review of existing literature, it has been noted that a substantial amount of research has been dedicated to Finite Element Method (FEM) simulations of welding processes, especially in relation to the formation of residual stresses. Despite this, there remains a noticeable gap in the literature regarding the stress analysis of materials used in the maritime industry a sector vital to global trade and the economic stability of nations. This study seeks to address this gap by focusing on AH-36, a material commonly used in shipbuilding, to investigate the residual stresses that develop during its welding process. Although FEM is providing good results but with certain limitations like constant material properties, Point heat source, Transient thermal behavior, Simplified geometries and Phase transformations etc.

3. Methodology. - The methodology of this research was focused on simulations performed in ABAQUS software. Two types of simulations were performed on welding joint, thermal analysis of the joint and structural analysis of the joint to evaluate influence of residual stresses. Welding analysis in other software's is time consuming and model settings are difficult, however ABAQUS/CAE plug is recently created in Abaqus Welding Interface (AWI) to eliminate this deficiency. Graphical user interface was provided by this software for setting cross-sectional simulation of welding in ABAQUS. Model tree as shown in Figure I illustrate details like weld passes and controls etc.

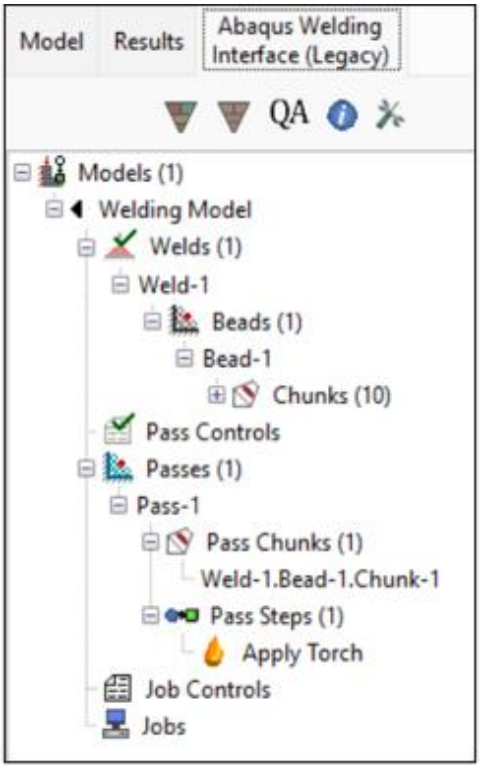

Figure I. Model Tree in Abaqus.

This involved first looking at temperature changes, then examining the stress caused by these changes. The heat source was identified based on how temperature spread and the material's ability to expand when heated. In stress analysis, the same mesh was used for both heat and stress analysis. This demonstrates a very fine mesh in the heat-affected zone and weld region, while larger mesh sizes are used farther from the heat-affected zone as shown in Figure 2. The plates can move freely. The temperature data from the heat analysis is used as input for the stress model, which is created using the AWI plugin. Since the heat model uses temperatures higher than the melting point, stress analysis limits temperatures to below the melting point using a simple subroutine. Material AH-36 was used for this analysis due to its significant importance in shipbuilding industry. Mechanical and thermophysical properties of AH-36 represent in Figure 3. These values were briefly explained by Dragi et al in his research about FEA of butt joint [5]. In this study, the parent metal was preheated to temperatures 100ºC, 150ºC and 200ºC to investigate impact on residual stresses.

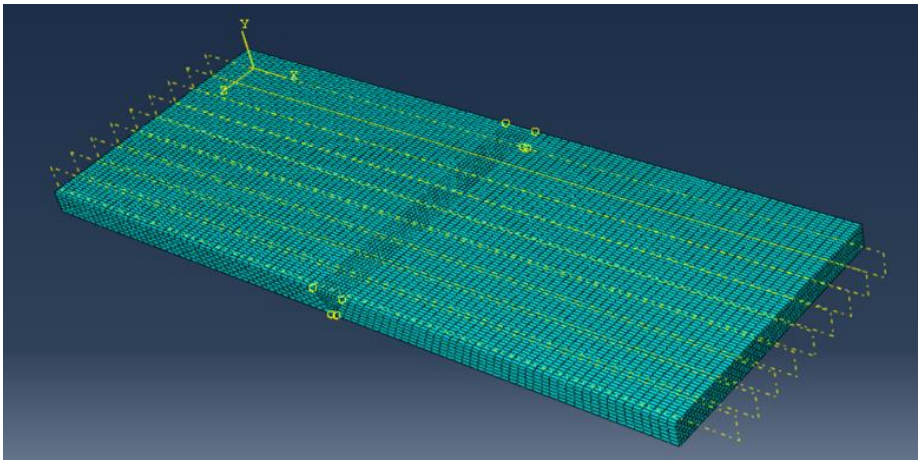

Figure II. Meshing.

A welding torch was utilized, set to a very high temperature of 1500ºC, which is slightly above the liquidus temperature of 1482ºC. This precise temperature setting is crucial as it ensures the material reaches a molten state, necessary for effective welding. The torch was moved at a controlled speed, taking 15 seconds for each section, highlighting the importance of torch speed in achieving uniform heat distribution and consistent weld quality. During the process, the temperature was elevated to the required level for most of the time the torch was operational, ensuring thorough heating of the material. For the final part of the process, the temperature was maintained at this level to stabilize the weld and prevent any potential defects.

Temperature (°C)	Specific heat (J/kg°C)	Conductivity (W/m°C)	Density (kgm-3)	Yield stress (MPa)	Thermal expansion coefficient (10-5/°C)	Young´s modulus (GPa)	Poisson´s ratio
0	480	60	7880	380	1.15	210	0.3
100	500	50	7880	340	1.2	200	0.3
200	520	45	7800	315	1.3	200	0.3
400	650	38	7760	230	1.42	170	0.3
600	750	30	7600	110	1.45	80	0.3
800	1000	25	7520	30	1.45	35	0.3
1000	1200	26	7390	25	1.45	20	0.3
1200	1400	28	7300	20	1.45	15	0.3
1400	1600	37	7250	18	1.45	10	0.3
1550	1700	37	7180	15	1.45	10	0.3

Figure III. Mechanical and Thermophysical properties of AH-36 steel.

4. Validation study. - In validation process, analysis results were compared with the experimental data from [15] as shown in Figure 5. The geometry of the weld joint, illustrated in Figure 4, was modelled after the referenced study to ensure accurate validation. Thermal histories were recorded using thermocouples placed at specific locations on both the left and right plates during welding. Thermocouples were located at 125mm along the weld line. For this thermal analysis, we used Stainless Steel 304 as the material. We accounted for latent heat effects, with a melting range between

2600°F (solidus) and 2700°F (liquidus), and a latent heat value of 118 BTU/lb. Throughout the analysis, we maintained a constant material density of 0.283 lb/in³.

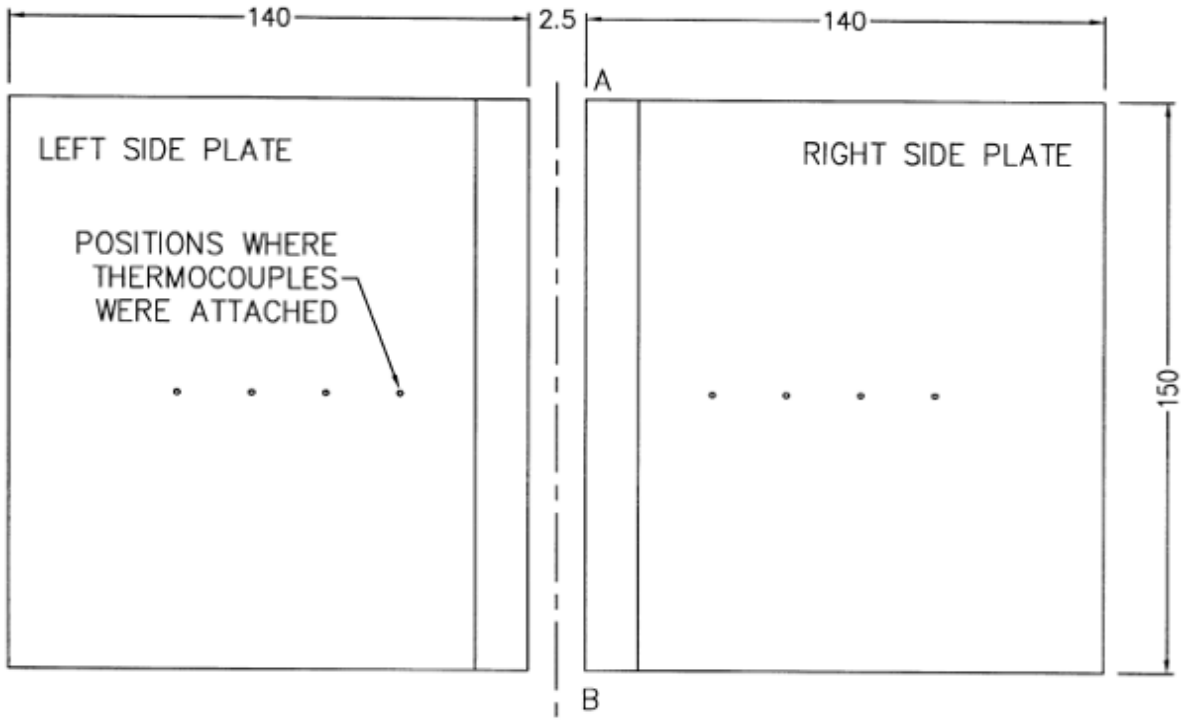

Figure IV. Geometry for validation.

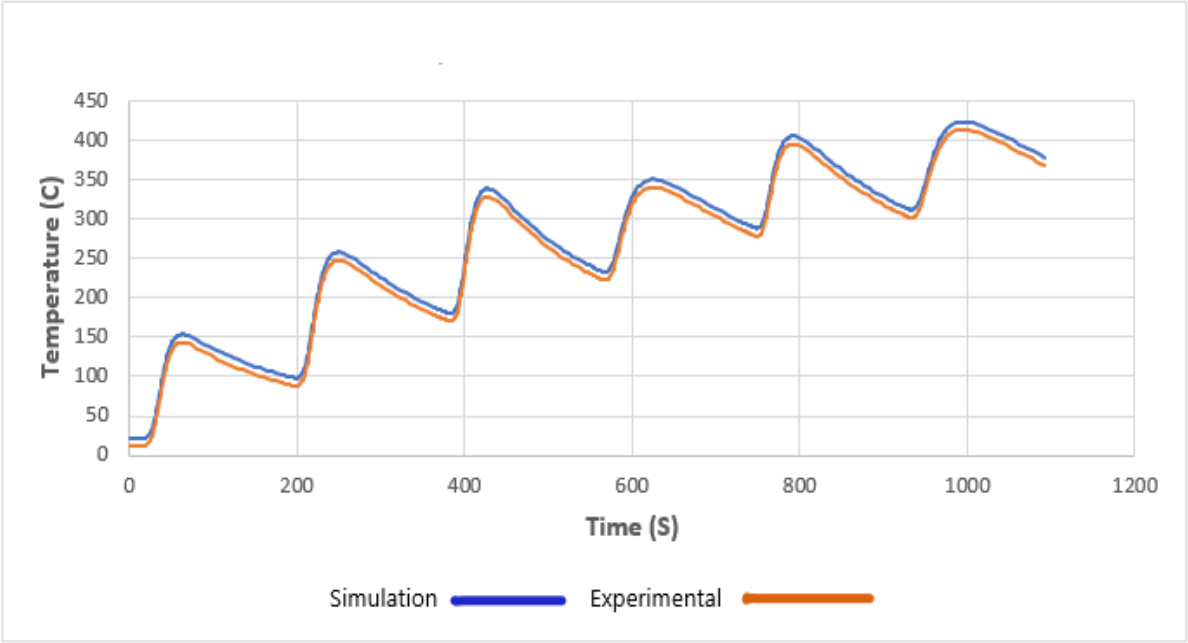

Figure V. Temperature distributions Curves for Validation.

In ABAQUS, setting the right boundary conditions is key for getting accurate results. For this problem, two main boundary conditions were used: the surrounding air temperature and thermal convection. The thermal convection was set at 0.025mW/mm^{2}K. The air around the model was kept at 21ºC. The analysis didn't consider any phase change.

The Automated Welding Interface sets the weld bead's temperature to 1500ºC during the welding process. Figure 6 shows the boundary condition of the weld bead has been created during pass.

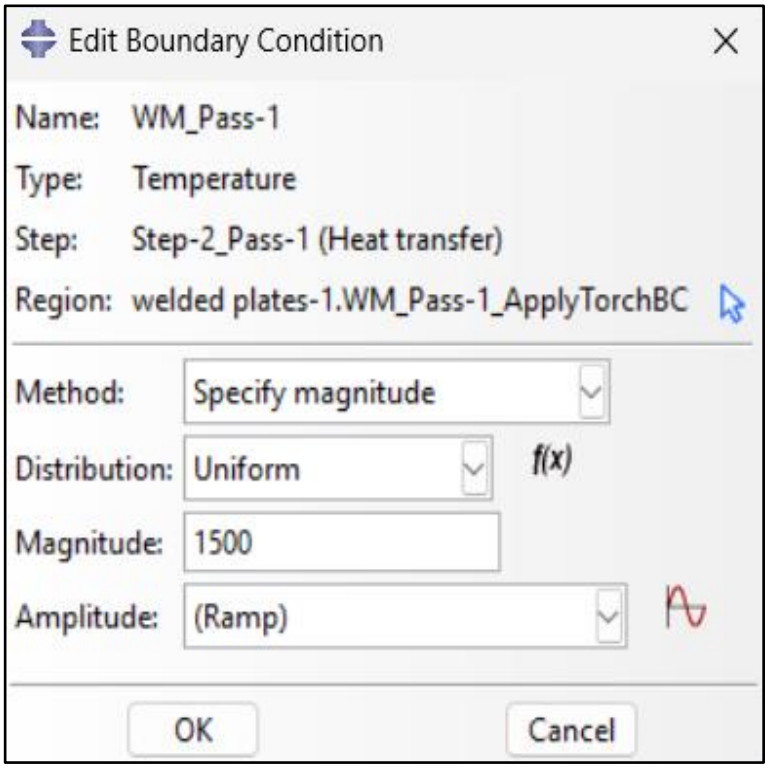

Figure VI. Boundary Conditions during pass creation.

5. Results and Discussions. -

5.1 Results of Parent Model Analysis. - The AH-36 material was chosen for this study. Comparative study of temperature distributions and residual stresses before and after preheating was performed to investigate impact on properties. The results were presented in the form of graphs and contour maps. To determine the residual stresses caused by welding, we assessed the results of thermal and structural analyses using the contour plots from both studies.

5.1.1 Temperature distributions for Parent Model. - Figure VII illustrates the temperature distribution on the welded plates after thermal analysis. The initial temperature of parent material and surrounding atmosphere both set to 21ºC with the coefficient of heat convection 0.025mW/mm^{2}K while value of emissivity maintained at 0.9. The maximum temperature can be seen as 1500ºC which is greater than the liquidus temperature (1482ºC) of the AH-36 steel.

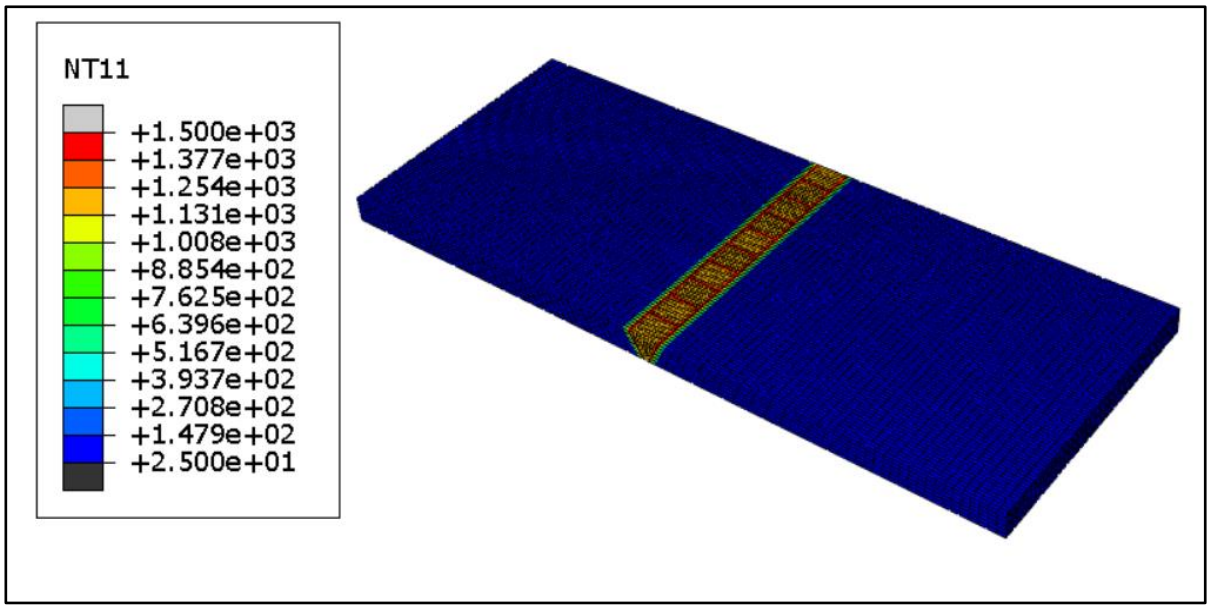

Figure VII. Temperature Distributions for Parent Model.

5.1.2 Von Mises Stress Distributions before Preheating. - Figure VIII represents Von Mises stress intensity map which demonstrates that stresses were building up in the heat affected zone (HAZ) area around the weld zone (WZ). Due to concentration of stresses in HAZ, failure of joint inclined to this particular region. Any microcrack amplify the stress concentration and results in deterioration as well as enlargement of crack. Therefore, additional safety measures like heat treatment might be used in that region to lessen the degree of stress concentration. It was observed that the maximum stress generated in the middle of the weld along its path as shown in Figure 9, so this was location of interest. The region parallel to that mid plane were faced large compressive stresses due to the expansion of weld region, hence inclined to high residual stresses. HAZ was susceptible to failure due to large residual stresses.

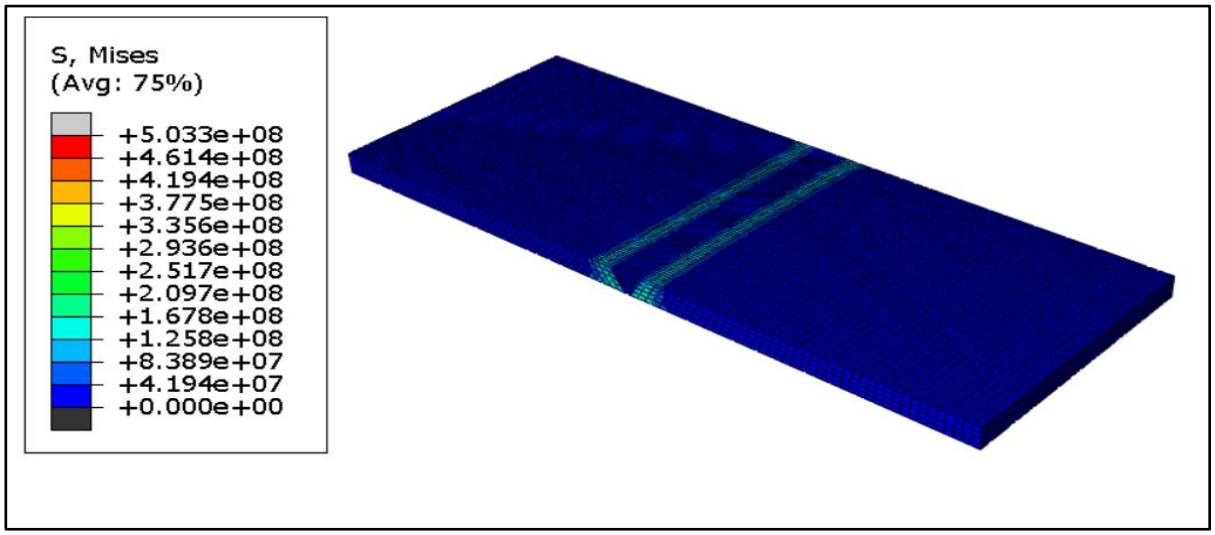

Figure VIII. Von Mises stress distribution.

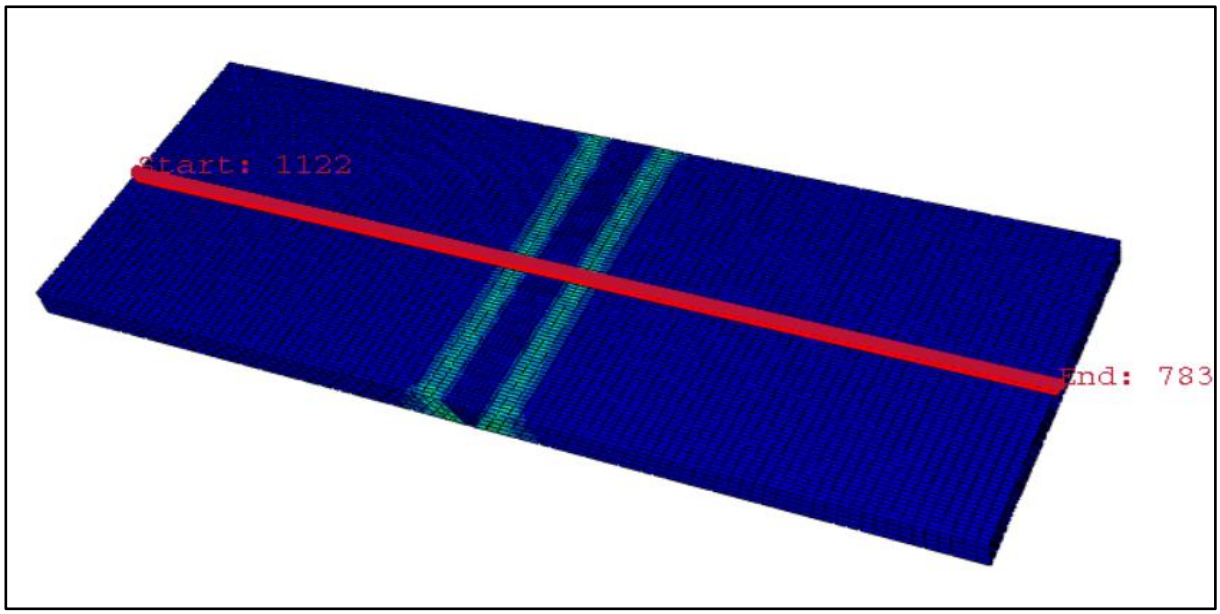

Figure IX. Mid Plane for Maximum Stress.

Stress distribution was found out in the welded plates along the path as shown in Figure 10. The maximum value of the stress distribution came out to be 103 MPa at the root of the weld at the distance of 122mm and 140mm from the start of the path, the value drops to 0.28MPa at the end of the welded plates.

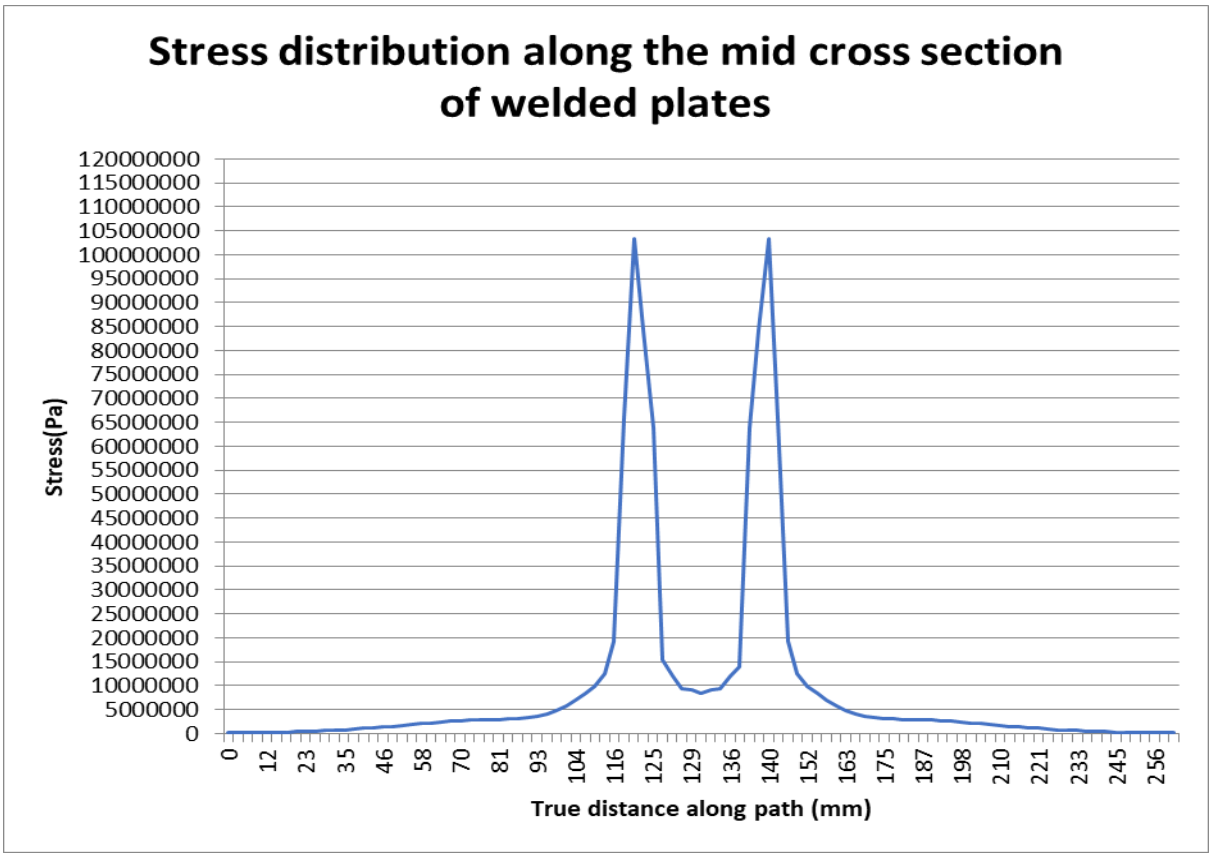

Figure X. Stress distribution along path length.

Figure XI illustrates the axial stresses impacting the plate along the Z axis, originating from the tensile tension of the welding line. A compressive stress peak, quantified at -313 MPa, contrasts with the highest tensile stresses reaching 355 MPa. Exceeding the tensile strength threshold in certain areas can lead to deformation. Notably, the cooling method employed significantly influences the reduction in axial stress values during the plate's cooling phase.

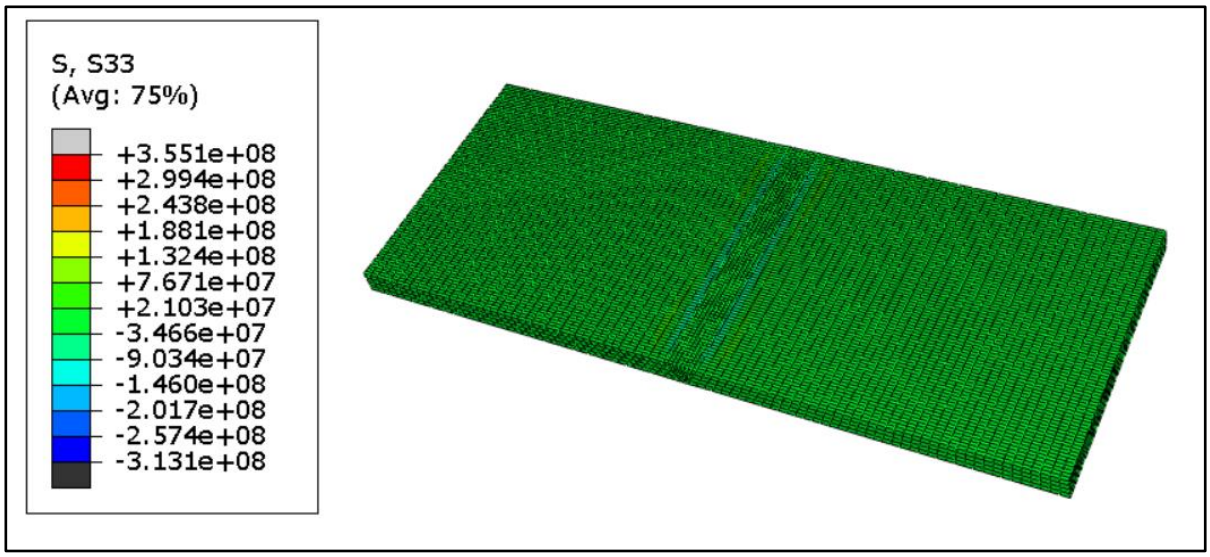

Figure XI. Stresses Parallel to weld direction (S33).

In Figure XII, the illustration of S33 stress distribution, aligned parallel to the weld line, unfolds a nuanced observation. Adjacent to the WZ, the material undergoes a phase of compressive stresses, which gracefully diminish with increased distance from the weld line. Notably, the apex of these stresses is characterized by a compressive nature, reaching a significant magnitude of -54.5 MPa.

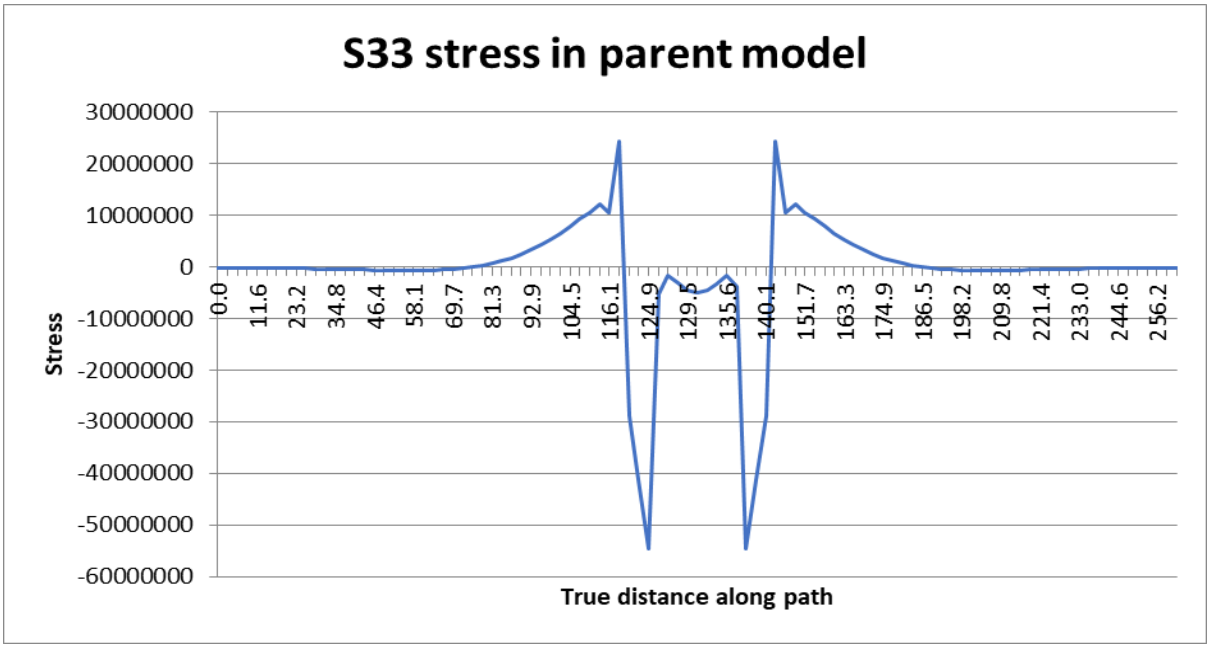

Figure XII. Stresses along weld line.

Figure XIII elegantly captures the stress distribution extending across the plate's length. Within the region of the weld area, the plate is subjected to pronounced tensile stresses, a stark contrast to the surrounding weld metal, where compressive stresses show their dominance. Beyond these zones, the narrative shifts as the rest of the plate exhibits stresses of a markedly lower magnitude.

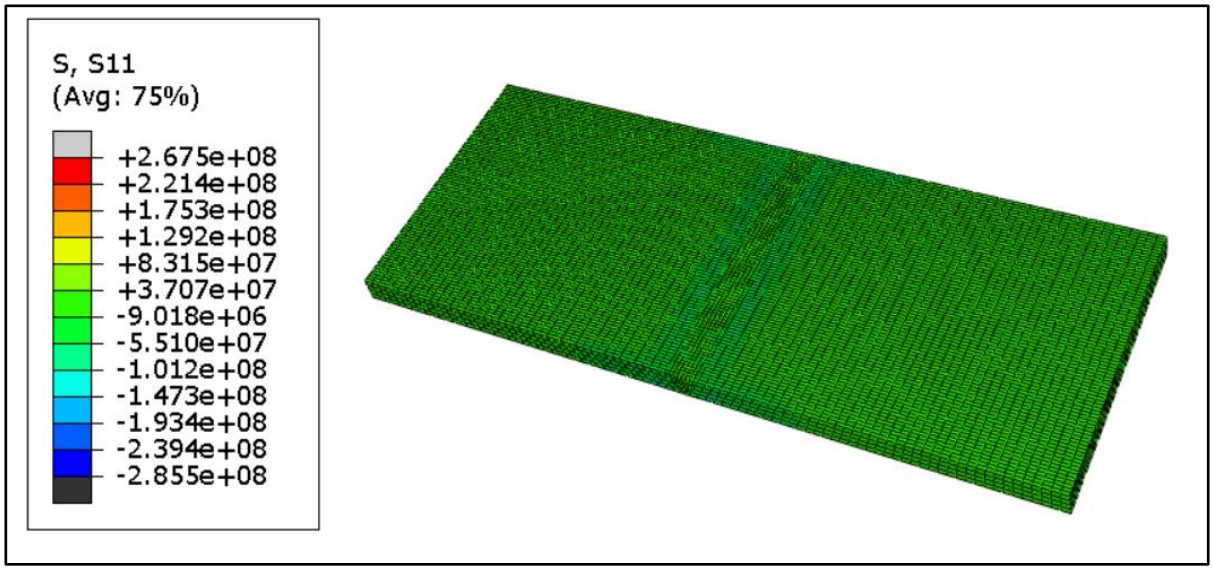

Figure XIII. Stresses along length of Plate (S11).

5.2 Preheating of Parent metal. - Preheating technique was utilized to investigate impact of preheating on residual stresses of AH-36 steel. Results achieved after mitigation of residual stresses by preheating were compared with the results of simulation before preheating. Non uniform distribution in welding is a primary source of distortions and residual stresses. Preheating is a process used to raise the parent metal temperature before welding to minimize the temperature differential. The parent metal was warmed in this investigation to temperatures of 100°C, 150°C and 200°C. The residual stresses or distortions were significantly reduced.

5.2.1 Von mises Stress Distributions. - The base metal was preheated to temperatures of 100ºC,150ºC and 200ºC to reduce the temperature gradient between WZ and parent metal. Figure XIII illustrate the overall von mises stress distribution in the welded plates. It was observed in Figure XIV (a) that maximum stresses at distance of 122mm and 140mm from WZ was reduced from 103MPa to 90MPa due to preheating of base plate at 100ºC. 12.6% reduction was achieved due to preheating which ultimately decrease the thermal gradient. Similarly Figure 14(b) and 14(c) illustrate familiar reduction pattern in Von mises stresses due to preheating of the base plate at 150ºC and 200ºC.

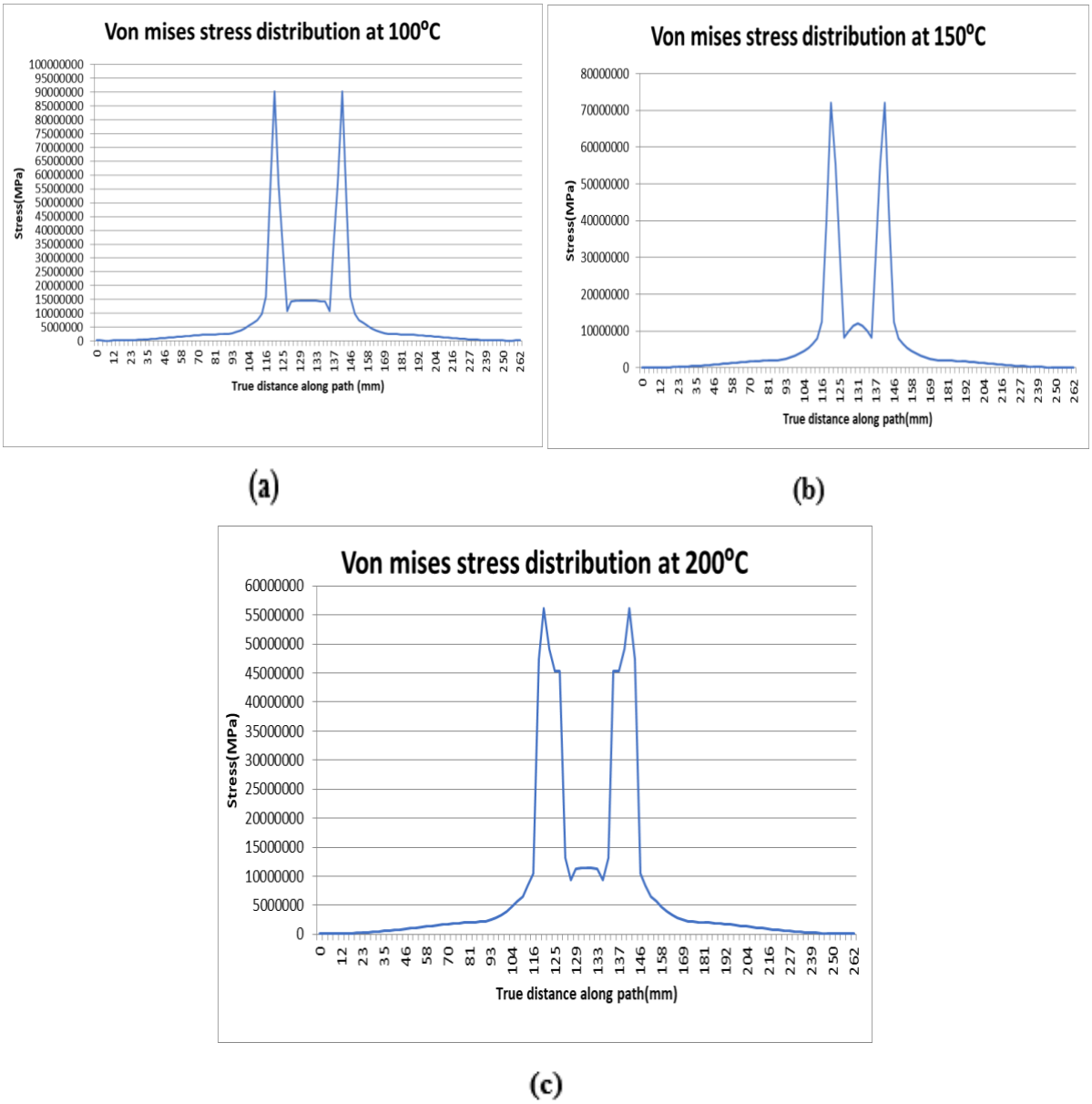

Figure XIV. Von Mises Stresses (a) Preheating at 100ºC (b) Preheating at 150ºC (c) Preheating at 200ºC

Reduction in thermal gradient was obvious due to preheating of base plate, hence stresses were further mitigated from 90MPa to 72MPa at preheating temperature 150ºC. Further increment in preheating temperature to 200ºC, Von mises stresses reduced from 72MPa to 56MPa. Reductions observed due to 150ºC and 200ºC temperature were 21% and 45.6% respectively.

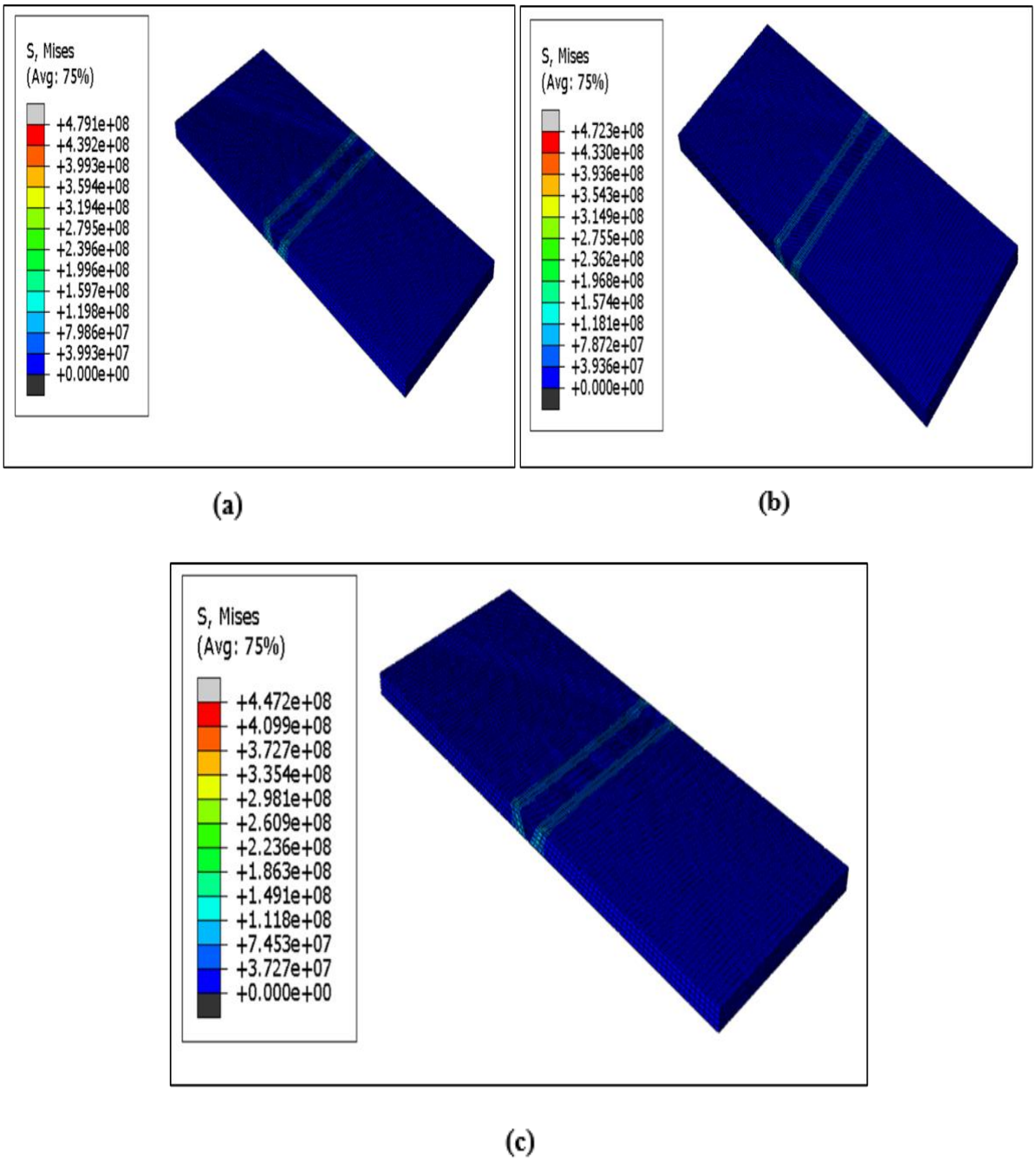

Figure XV. Simulations of Von Mises stress distributions (a) Preheating at 100ºC (b) Preheating at 150ºC (c) Preheating at 200ºC

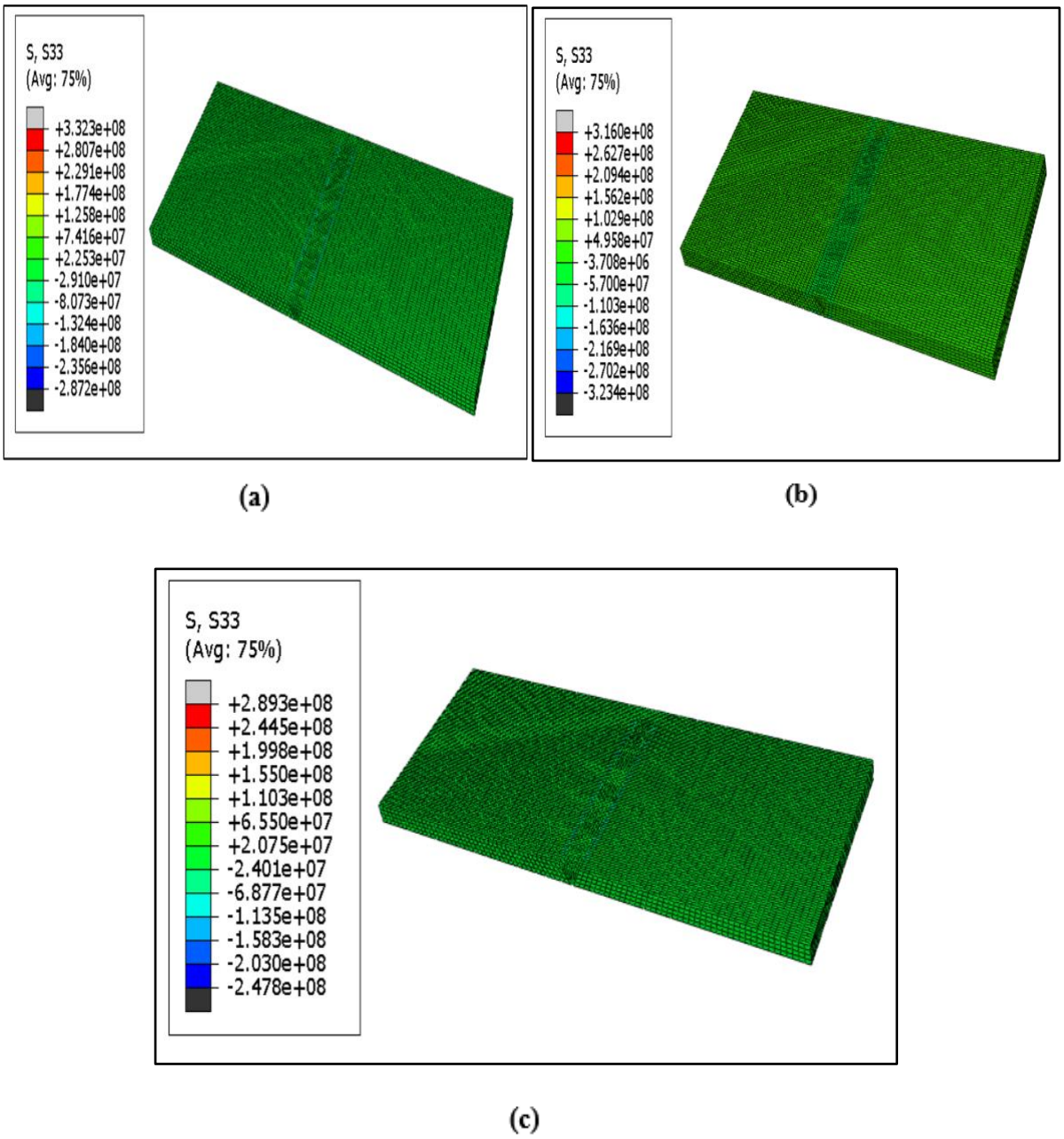

Figure XVI. Stress Distributions along weld Line (Longitudinal stresses S33) (a) Preheating at 100ºC (b) Preheating at 150ºC (c) Preheating at 200ºC

Figure XV have shown reduction in Von mises stresses due to preheating of base plate, significant reduction in overall stresses of base plate was observed because of degradation in thermal gradient. Distortions were reduced ultimately due to preheating of base plate. Increment in preheating temperature from 100ºC to 200ºC resulted in degradation on overall stresses and deformations. Joint strength may be affected due to variations in HAZ area and chance of weld joint failure get reduced due to elimination of thermal cracking. Stresses along weld path was evaluated in Abaqus and it was revealed that preheating mitigation technique applied for residual stresses was very effective. It was shown in Figure 11 that maximum stress along weld path (S33) was 355MPa, however this longitudinal stress was significantly abated due to preheating method. Figure XVI(a) revealed notable degradation in maximum longitudinal stress from

355MPa to 332MPa because of preheating base plate at 100ºC. 21.3% reduction in longitudinal stresses was observed when base plate temperature maintained at 100ºC. Increment in preheating temperature will inversely be related with longitudinal stresses, so ultimately decrease residual stresses along weld path. Further degradation in longitudinal stresses was observed in Figure XVI(b) at preheating temperature 150ºC, stresses were reduced from 355MPa to 316MPa. 44% reduction in stresses was achieved due to increment in preheating temperature. Longitudinal stresses were further decreased as shown in Figure XVI(c) from 355MPa to 289MPa due to further increase in preheating temperature from 150ºC to 200ºC. Implementation of this mitigation method reduced longitudinal stresses from 44% to 52.4%.

6. Conclusion. - This study focused on analyzing the impact of thermal processes and preheating on the residual stresses and structural integrity of AH-36 steel welded plates. Thermal analysis declared a maximum temperature of 1500ºC was achieved during welding, which is greater than the liquidus temperature of AH-36 steel. Due to large thermal gradient between base plate and WZ, thermal stresses produced which ultimately results in high residual stresses. The study identified High stress concentrations were identified in the Heat Affected Zone around the weld zone. The maximum stress was observed along the weld line, indicating a critical area for potential failure due to microcrack formation and stress amplification. Significant variations in stresses were noted in Z axis direction, with a peak compressive stress of -313 MPa and a peak tensile stress of 355 MPa. This variation could lead to deformation if the tensile strength threshold is exceeded. Compressive stresses were prominent along weld path due to expansion and contraction of weld zone due to large temperature difference. Compressive stresses have shown negative pattern with increasing distance from the weld line. Overall analysis of stress distribution across the plate's length showed pronounced tensile stresses in the base plate contrasting with compressive stresses in the surrounding metal. Mitigation method was utilized to lower residual stresses, Preheating the base metal to 100ºC, 150ºC, and 200ºC right before welding significantly reduced the temperature gradient. Reduction in thermal gradient mitigated residual stresses and distortions as well. Notably, preheating at 200ºC reduced Von Mises stresses from 103 MPa to 56 MPa. Longitudinal stresses were substantially reduced with preheating. Preheating at 200ºC decreased these stresses from 355 MPa to 289 MPa, highlighting the effectiveness of preheating in mitigating residual stresses. The findings highlighted the significant potential of preheating as a mitigation technique for residual stresses in welded joints. Future research could explore the optimization of preheating temperatures and durations for different materials and welding conditions. Additionally, integrating preheating with other stress mitigation techniques, such as post-weld heat treatment or advanced welding processes, could further enhance the structural integrity and lifespan of welded structures.

References

[1] Al-Samhan, A., & Darwish, S. M. H. (2003). Finite element modelling of weld-bonded joints. Journal of materials processing technology, 142(3), 587-598.

[2] Anca, A., Cardona, A., & Fachinotti, V. (2008). Finite element modeling of welded joints. Mecánica Computacional, (19), 1445-1470.

[3] Colegrove, P., Ikeagu, C., Thistlethwaite, A., Williams, S., Nagy, T., Suder, & Pirling, T. (2009). Welding process impact on residual stress and distortion. Science and technology of welding and joining, 14(8), 717-725.

[4] Cozzolino, L. D., Coules, H. E., Colegrove, P. A., & Wen, S. (2017). Investigation of post-weld rolling methods to reduce residual stress and distortion. Journal of Materials Processing Technology, 247, 243-256.

[5] Dragi, S. & V. Ivana (2009). "Finite element analysis of residual stress in butt welding two similar plates." J. Scientific Technical Review. 1(1), 57–60.

[6] Garipova, N., Batigün, C., & Gür, C. H. (2014). Numerical and Experimental Determination of the Residual Stress State in Multipass Welded API 5L X70 Plates. Materials Testing, 56(10), 831-836.

[7] Gannon, L., Liu, Y., Pegg, N., & Smith, M. (2010). Effect of welding sequence on residual stress and distortion in flat-bar stiffened plates. Marine Structures, 23(3), 385-404.

[8] Han, S. H., Cui, C., Zheng, Q. S., Zhang, Q. H., & Bu, Y. Z. (2023). Effect of ultrasonic impact treatment on welding residual stress and fatigue resistance of doubly-welded rib-to-deck joints in OSD. Journal of Constructional Steel Research, 211, 108157.

[9] Jiang, W., & Yahiaoui, K. (2012). Effect of welding sequence on residual stress distribution in a multipass welded piping branch junction. International Journal of Pressure Vessels and Piping, 95, 39-47.

[10] Kollár, D., Völgyi, I., & Joó, A. L. (2023). Assessment of residual stresses in welded T-joints using contour method. Thin-Walled Structures, 190, 110966.

[11] Kurtz. G. W. "Finite Element Analysis of Welded Structures," Welding Research Supplement, 1978.

[12] Kassab, R. K., Champliaud, H., Van Lê, N., Lanteigne, J., & Thomas, M. (2012). Experimental and finite element analysis of a T-joint welding. Journal of Mechanics engineering and automation, 2(7), 411-421.

[13] Marin, T., & Nicoletto, G. (2009). Fatigue design of welded joints using the finite element method and the 2007 ASME Div. 2 Master curve. Frattura ed Integrità Strutturale, 3(9), 76-84.

[14] Malikoutsakis, M., & Savaidis, G. (2009). An approach to the effective notch stress concept to complex geometry welds focusing on the Fe modeling of weld ends. Aristotle University of Thessaloniki, Greece.

[15] Murugan, S., Kumar, P. V., & Raj, B. (1998). Temperature distribution during multipass welding of plates. International journal of pressure vessels and piping, 75(12), 891-905.

[16] Perić, M., Garašić, I., Nižetić, S., & Dedić-Jandrek, H. (2018). Numerical analysis of longitudinal residual stresses and deflections in a T-joint welded structure using a local preheating technique. Energies, 11(12), 3487.

[17] Raftar, H. R., Ahola, A., Lipiäinen, K., & Björk, T. (2023). Simulation and experiment on residual stress and deflection of cruciform welded joints. Journal of Constructional Steel Research, 208, 108023.

[18] Reed, R. C., & Bhadeshia, H. K. D. H. (1994). A simple model for multipass steel welds. Acta metallurgica et materialia, 42(11), 3663-3678.

[19] Ramos, H. M. E., Tavares, S. M. O., & de Castro, P. M. S. T. (2018). Numerical modelling of welded T-joint configurations using SYSWELD. Science and Technology of Materials, 30, 6-15.

[20] Schenk, T., Richardson, I. M., Kraska, M., & Ohnimus, S. (2009). A study on the influence of clamping on welding distortion. Computational Materials Science, 45(4), 999-1005.

[21] Shazad, A., Jadoon, J., Uzair, M., & Muzammil, M. (2023). Material Modelling and Failure Study of Different

Fiber Reinforced Composites for Pressure Vessel. Memoria Investigaciones en Ingeniería, (24), 92-104.

[22] Shazad, A., Jadoon, J., Uzair, M., Akhtar, M., Shakoor, A., Muzamil, M., & Sattar, M. (2022). Effect of composition and microstructure on the rusting of MS rebars and ultimately their impact on mechanical behavior. Transactions of the Canadian Society for Mechanical Engineering, 46(4), 685-696.

[23] Stamenković, D., & Vasović, I. (2009). Finite element analysis of residual stress in butt welding two similar plates. Scientific technical review, 59(1), 57-60.

[24] Tabatabaeian, A., Ghasemi, A. R., Shokrieh, M. M., Marzbanrad, B., Baraheni, M., & Fotouhi, M. (2022). Residual stress in engineering materials: a review. Advanced engineering materials, 24(3), 2100786.

[25] Yang, X., Meng, T., Su, Y., Qi, Z., Wu, D., Vairis, A., & Li, W. (2023). Study on relieving residual stress of friction stir welded joint of 2219 aluminium alloy using cold spraying. Materials Characterization, 206, 113417.

[26] Yan, R., Yu, Z., Wang, S., & Liu, J. (2023). Influence of welding residual stress on bending resistance of hollow spherical joints. Journal of Constructional Steel Research, 208, 108004.

Nota contribución de los autores:

1. Concepción y diseño del estudio
2. Adquisición de datos
3. Análisis de datos
4. Discusión de los resultados
5. Redacción del manuscrito
6. Aprobación de la versión final del manuscrito

NS ha contribuido en: 1, 2, 3, 4 y 5.
MA ha contribuido en: 5 y 6.
MU ha contribuido en: 5 y 6.
AS ha contribuido en: 5 y 6.
AAZ ha contribuido en: 5 y 6.

Nota de aceptación: Este artículo fue aprobado por los editores de la revista Dr. Rafael Sotelo y Mag. Ing. Fernando A. Hernández Gobertti.

Design of a low-cost portable electrocardiograph for telemedicine application

Evaluación del impacto del precalentamiento sobre las tensiones residuales de soldadura en acero AH-36 mediante análisis de elementos finitos

Avaliação do impacto do pré-aquecimento nas tensões residuais de solda no aço AH-36 utilizando Análise de Elementos Finitos

Hólger Santillán[1(*)], Angelo Mantilla[2], David Cárdenas[3], Peregrina Wong [4]

Recibido: 24/03/2024 Aceptado: 31/05/2024

Summary. - This paper presents the design of a portable electrocardiograph designed to provide community health care. The AD8232 main sensor has multiple options for displaying cardiac activity. The first option uses the serial plotter in the Arduino IDE, while the second employs LabVIEW, allowing additional observation of the patient's blood pressure via block coding. In addition, the Arduino cloud is integrated to process the information captured by the ESP32, enabling visualization on any device with internet access. Through this platform, it is possible to download the studies performed in different periods (1 hour, 1 day, 7 days, and 15 days), with an efficiency percentage of 4.11%.

Keywords: Portable Electrocardiograph; Healthcare; IoT; Community; Cardiac Activity.

(*) Corresponding Author

[1] Master en Telecomunicaciones. Universidad Politécnica Salesiana, Grupo de Investigación en Sistemas de Telecomunicaciones – GISTEL, Universidad de las Palmas de Gran Canaria, hsantillan@ups.edu.ec holger.santillan101@alu.ulpgc.es, ORCID iD: https://orcid.org/0000-0003-4803-7016

[2] Ingeniero en Telecomunicaciones. Universidad Politécnica Salesiana, Grupo de Investigación en Sistemas de Telecomunicaciones - GISTEL, amantillam1@est.ups.edu.ec , ORCID iD: https://orcid.org/0009-0000-2163-8714

[3] Master Universitario en Tecnologías y s\Sistemas de Comunicación. Universidad Politécnica Salesiana, Grupo de Investigación en Sistemas de Telecomunicaciones - GISTEL, dcardenasv@ups.edu.ec , ORCID iD: https://orcid.org/0000-0003-4241-9929

[4] Ingeniera electrónica. Universidad Politécnica Salesiana, Grupo de Investigación en Sistemas de Telecomunicaciones – GISTEL, Universidad de las Palmas de Gran Canaria, peregrina.wong101@alu.ulpgc.es ORCID iD: https://orcid.org/0000-0003-1290-7729

https://doi.org/10.36561/ING.26.15
ISSN 2301-1092 • ISSN (en línea) 2301-1106 – Universidad de Montevideo, Uruguay

Resumen. - *El presente trabajo presenta el diseño de un electrocardiógrafo portátil diseñado para proporcionar asistencia médica comunitaria. Se emplea el sensor principal AD8232, con múltiples opciones de visualización de la actividad cardíaca. La primera opción utiliza el serial plotter en el IDE de Arduino, mientras que la segunda emplea LabVIEW, permitiendo la observación adicional de la presión arterial del paciente mediante codificación de bloques. Además, se integra la nube de Arduino para procesar la información capturada por el ESP32, lo que posibilita la visualización en cualquier dispositivo con acceso a internet. A través de esta plataforma, se pueden descargar los estudios realizados en distintos lapsos de tiempo (1 hora, 1 día, 7 días y 15 días), con un porcentaje de eficacia del 4.11%.*

Palabras clave: *Electrocardiógrafo portátil; Asistencia Sanitaria; IoT; Comunidad; Actividad Cardiaca*.

Resumo. ***-*** *Este artigo apresenta o projeto de um eletrocardiógrafo portátil projetado para prestar cuidados de saúde comunitários. O sensor principal AD8232 possui múltiplas opções para exibir a atividade cardíaca. A primeira opção utiliza o plotter serial no Arduino IDE, enquanto a segunda utiliza o LabVIEW, permitindo observação adicional da pressão arterial do paciente por meio de codificação em bloco. Além disso, a nuvem Arduino está integrada para processar as informações captadas pelo ESP32, possibilitando a visualização em qualquer dispositivo com acesso à internet. Através desta plataforma é possível baixar os estudos realizados em diferentes períodos (1 hora, 1 dia, 7 dias e 15 dias), com percentual de eficiência de 4,11%.*

Palavras-chave: *Eletrocardiógrafo Portátil; Assistência médica; IoT; Comunidade; Atividade Cardíaca.*

1. Introduction. - The electrocardiogram is known as a non-invasive medical test that records the electrical activity of the patient's heart. It is used to evaluate the health of the most important organ, the heart, and to detect possible cardiovascular problems. During an electrocardiogram, electrodes are attached to the skin at different locations on the human body, such as the chest and upper and lower extremities [1], [2].

During the pandemic or situations in which it has been difficult for patients to approach a medical center to review the information or know the status of the study has been a limiting factor either physical, personal, or environmental conditions and this has severely affected humanity during this health crisis [3], [4].

At present, there is a solution to this problem, which consists of the use of medical equipment capable of connecting to the network and sending the information obtained in real time, which will be stored in a cloud and can be viewed by anyone who requires it [5], [6].

The use of the IoT (Internet of Things) connection in medical equipment has the purpose of improving the quality of service both to better process the studies and to provide the doctor with the facility to visualize the information to perform an analysis anywhere on the planet. This has represented a great improvement in the field of health, allowing Telecommunications and Medicine to work together [7], [8].

IoT communication is based on a device that acts as a transmitting antenna, in our case the ESP32, which receives the processed signal through its ports and proceeds to send it to the Arduino cloud. This device is one of the main options to consider when making an IoT connection due to its advantages over other components that do not have this capability [9], [10].

In the design of this article, Arduino Uno is used as the receiver and will be the one to process the information from the AD8232 sensor which captures the cardiac signal in analog form. The Arduino transforms the analog signal to digital for easy reading and sends the data to the other stages of the design, sending the COM port to the LabVIEW software which through the LINX library helps to make the connection of the system [11], [12].

At this stage the LabVIEW software provides a plus to the design since the blood pressure is displayed along with the graph of the cardiac activity of the heart, normally in other mostly analog equipment this result is displayed every minute, but through the formula for the prediction of blood pressure (equation 1), the prediction is obtained every 15 seconds which provides a much faster response to conventional [13], [14].

The final and most important step of this design is to send the information to the Arduino ESP32 Wi-Fi module which is previously linked to the Arduino cloud where, through its interface, the cardiac activity can be observed in real-time and this collection of information can be downloaded through an Excel file in comma delimited format for processing [15], [16].

The tracing shown in Figure I is the result of a simulation performed using BTL Cardiopoint software. This software is used as an electrocardiogram (ECG) simulator, allowing various clinical conditions and scenarios to be accurately recreated. The graphical representation provides detailed information about the electrical activity of the heart and is useful for medical education and cardiovascular research. This tracing, generated using the aforementioned software, provides a valuable tool for the analysis and interpretation of cardiac activity in controlled settings. In addition, it facilitates the practice of ECG interpretation, helping to improve the diagnostic and patient management skills of healthcare professionals [17], [18].

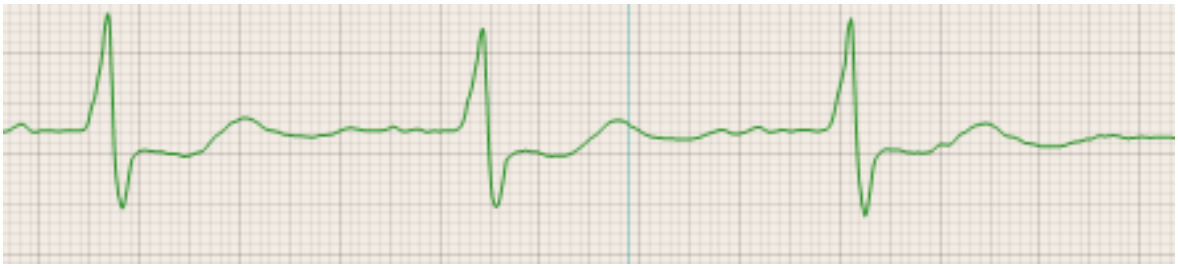

Figure I. Simulation of an ECG using Cardiopoint software.

1.1 Related Work. - The authors of the article [16] mention that currently, many people die of cardiac arrest, due to a poor check and control of the state of their cardiovascular system. They propose a solution to this problem through their design, which is based on the realization of a cardiac activity monitor using the AD8232 sensor and an ESP32 that serves as a microprocessor and the device responsible for the connection to the cloud using Ubidots and Thingspeak [19], [20].

The authors of the article [5] designed an ECG that focuses on making the cost as low as possible, and at the same time they implemented a system to detect any anomaly in the outlets, in the case of any, they will send an alert message to the doctor or the person in charge. The design has a Bluetooth connection system that covers a distance of 100 meters. It is concluded that its design is a great advance for society and a great alternative for people or entities that need to start in the cardiovascular care of their patients because the manufacturing cost of the proposed design is significantly lower than other models previously considered [21], [22].

The authors of the article [3] state that cardiovascular care awareness has now increased due to the emergence of COVID-19, since during the pandemic period, the number of deaths due to cardiac arrest increased considerably. They point out that the speed of detection time is crucial to avoid irreparable damage to human life.

They concluded that the design will be very useful because it can accommodate the information collected through unique record codes that will facilitate the search of the records [23], [24].

The authors mention that about 30% of the population in rural areas of Bangladesh lives in poverty. Due to the lack of modern medical technology in these areas, medical care and diagnostic services are limited for rural residents. As a result, adequate medical care is inaccessible to the rural population. In this context, modern technology could be implemented to address their health problems. For example, electrocardiogram (ECG) sensing tools connected to the human body can be used to collect essential cardiovascular data through Internet of Things (IoT) devices [22].

The authors of the article mention that, in recent times, several researchers have explored the connection between emotions and people's physical well-being. This research interest has intensified due to the rapid progress of computer technology, especially in the biomedical field. In the field of engineering, there is a focus on understanding how emotions affect the human body, which motivates researchers to conduct studies in this area. It should be noted that this design does not have an information storage system, nor does it have the function of sending the information to the cloud, it only focuses on the analysis and visualization during the ECG [1].

The aforementioned authors presented their devices to the world, some of them stand out in some particular quality depending on the case. But they all fulfill their general purpose, to provide a tool for the care and prevention of cardiovascular problems in humans, these articles were of great help in guiding which direction could focus the analysis of this study and what other issues to innovate as evidenced in the implementation of the pressure gauge in LabVIEW, therefore this article has great advantages to take into consideration as shown in the results section.

1.2 **Arterial prediction formula implemented in LabVIEW. -** The equation for blood pressure prediction (1) used in LabVIEW is as follows:

$$W = \left(\frac{P}{4}\right) * t \quad (1)$$

Where:

$$W \rightarrow Pulse\ prediction\ every\ (t)\ time \quad [bpm]$$
$$P \rightarrow Arterial\ pulses\ captured\ by\ the\ sensor \quad [bpm]$$
$$t \rightarrow Time\ at\ which\ data\ will\ be\ predicted \quad [s]$$

Equation 1 is used to calculate blood pressure using radial pulse-taking techniques, whereby, if the pulse during the first 15 seconds is continuous, the value obtained is multiplied by 4, resulting in an accurate prediction of the value that would be obtained if the pulse were taken for a full minute. One of the great advantages of using this method is that physicians can know in advance the blood pressure coming from the individual under study.

2. Method. - For the design of the electrocardiograph, first of all, the placement of the electrodes and the type of data obtained through the AD8232 sensor are identified and coded using Arduino. The information obtained is analyzed locally using the Serial plotter in the Arduino IDE. Then, using LabVIEW, a graphical interface is created to visualize the electrical activity of the heart and make a blood pressure prediction, which is obtained every 15 seconds as opposed to the manual method, which is obtained every minute. Finally, the Arduino cloud is used to open the doors to the world of IoT, it is observed by any device with internet access and as an additional benefit, the report of the data received is downloaded as a text file [25], [26].

The advantage of using the AD8232 sensor is its ease concerning its size, which allows it to make cases, thus facilitating its portability with the patient. This sensor handles 3.3 volts, obtained through the Arduino, which is powered with 5V. This also facilitates the use of portable batteries with which the portability of the prototype is enhanced [27], [28].

It is important to mention the advantage of downloading the information containing the studies performed on each patient in a comma delimited file that can be opened by Excel and obtain the details every second of the reading of the data of the electrical activity of the heart, this information needs to be processed as shown below. With the information already processed, a more in-depth analysis is performed in the cardiovascular area.

Below, in Figure II, a scheme is presented to explain more simply the stages of processing and analysis of the prototype.

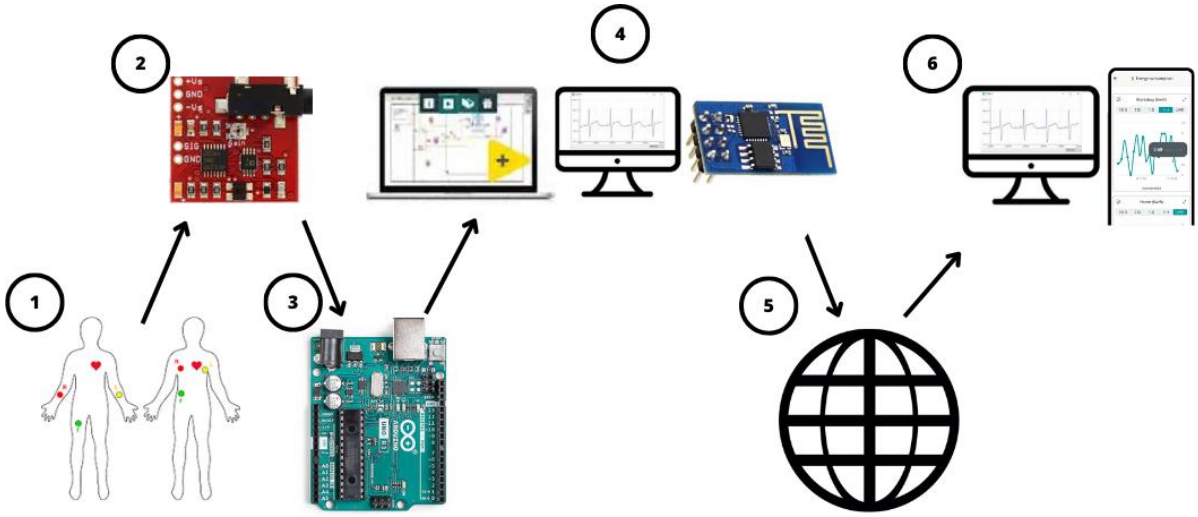

Figure II. Outline of the proposed design.

Where:

1. Placement of the electrodes on the patient.
2. Recording of electrical measurements of the heart using the AD8232 module.
3. Processing of the measurements taken by the Arduino.
4. Visualization of the cardiac activity on the monitor through Arduino and LabVIEW.
5. Sending the data of the measurements to the cloud.
6. Remote viewing of the analysis performed.

The most important materials used in the development of this design are the following:

-Arduino UNO.

-AD8232 sensor.

-ESP32.

-Cables to interconnect the devices with each other.

Figure III shows the physically assembled prototype circuit, which represents the design of a portable electrocardiograph intended to provide medical assistance to the community. The circuit incorporates the use of the AD8232 as the primary sensor for accurate detection of cardiac activity. In addition, it offers three options for displaying the heart rate graph, allowing for versatile monitoring that is adaptable to the user's needs. This innovative design seeks to provide an affordable and effective solution for cardiac monitoring in medical and community settings, thus contributing to improving cardiovascular health and quality of life.

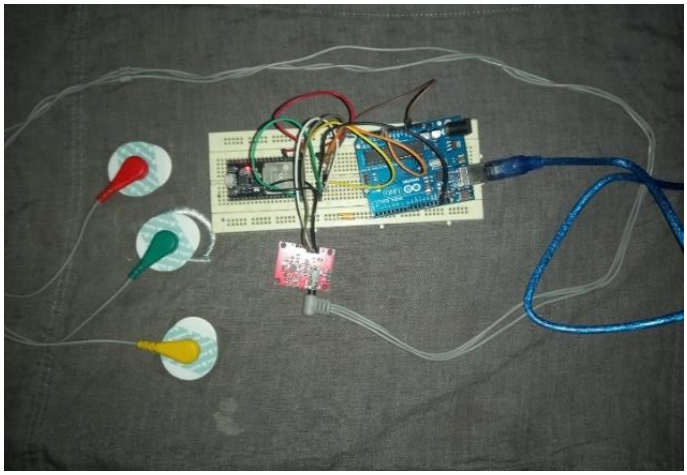

Figure III. Physically assembled circuit.

Figure IV shows the torso of a patient with the electrode arrangement of the prototype circuit of a portable electrocardiograph. These electrodes, essential for accurate detection of the heart rhythm, are strategically placed following standard medical guidelines as follows.

- Red electrode: located on the right side of the right torso on the lateral side (1).
- Yellow electrode: located on the left side of the torso at the level of the heart (2).
- Green electrode (Neutral): located under the last rib on the right side of the torso (3).

This innovative approach to electrocardiograph design reflects a significant advance in medical technologies, as it enables effective, noninvasive cardiac rhythm monitoring in clinical and community settings. The correct arrangement of the electrodes on the patient's torso ensures accurate and reliable measurements, which is critical for informed medical decision-making and cardiovascular health care.

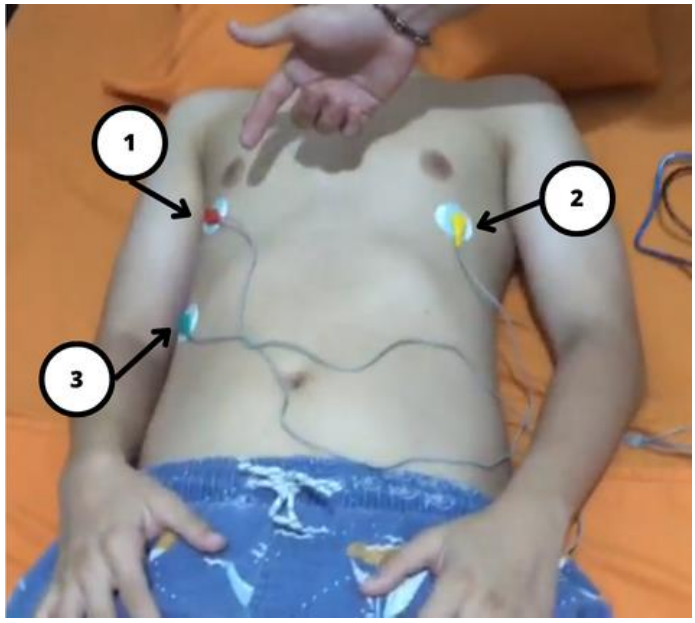

Figure IV. Placement of electrodes on the patient.

2.1 LabVIEW Block Diagram Configuration. - Next, each of the steps related to the configuration of the block diagram used in LabVIEW, as shown in Figure V, are detailed. In this comprehensive analysis, each of the components and connections of the diagram are addressed, explaining their function and their contribution to the overall system operation. In addition, the design decisions made during the creation of the block diagram are described, highlighting their relevance to the success of the project.

This detailed approach provides a thorough understanding of the configuration process in LabVIEW, allowing readers to become familiar with the techniques used and their application in the specific context of the project. This detailed explanation seeks to provide clarity and facilitate replication of the process by other researchers or practitioners interested in using LabVIEW for similar projects.

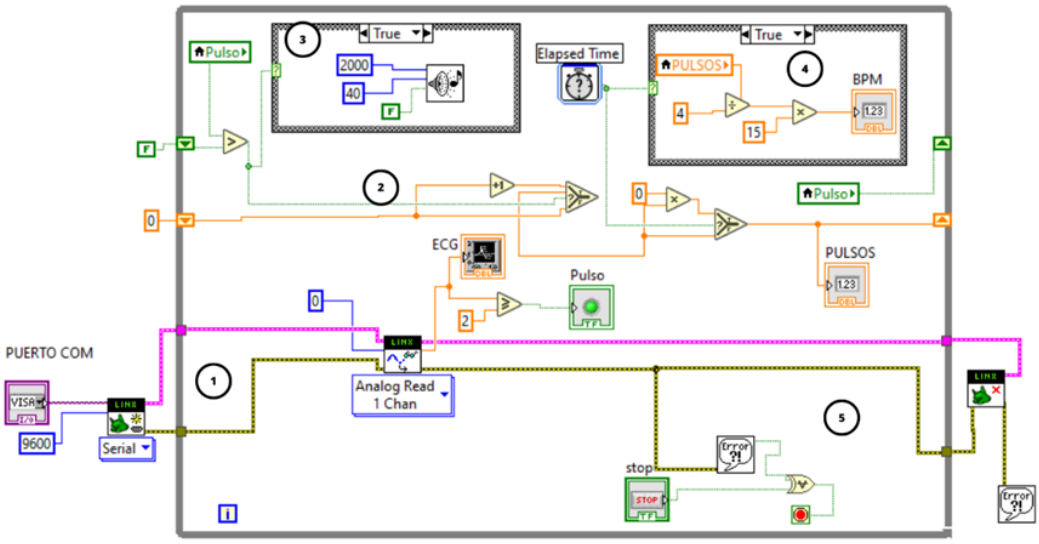

Figure IV. Configure Design in LabVIEW.

2.2 Configuration LabVIEW with Arduino. - In Figure VI, we initially present the COM port block, which is in charge of reading the information through the COM ports of our PC. This information is sent to the Linx Open. vi file, where the baud rate is set to 9600 to ensure optimal data transmission speed to the system.

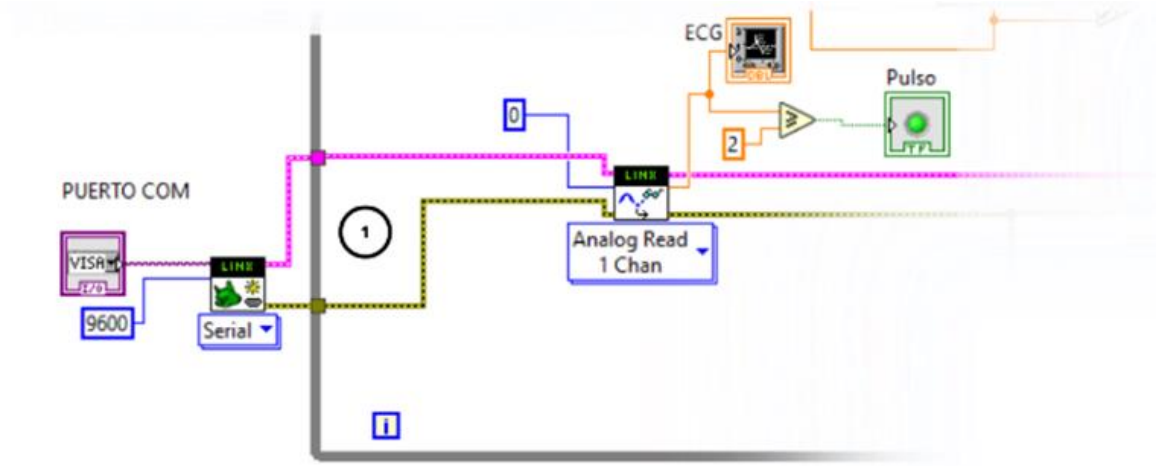

Figure VI. Arduino communication block.

After establishing communication with the Arduino, an analog reading is made, because the information processed by the sensor is of this type. It is established that the pin of the Arduino to which the reading is being made will be the A0, after this process the acquired data is sent to be displayed on a display, which will also trigger an LED that will show the heartbeat obtained.

2.2 Comparator Processing. - Figure VII shows the comparator process, highlighting a gradual increment to reach the set value. Once this requirement is met, a multiplication by zero is performed to reset the counter and return to the initial loop. This cycle continues iteratively to ensure consistent and efficient operation of the system. The visual representation provides a clear understanding of how the comparators are managed in the process, making it easy to optimize and adjust parameters appropriately as needed.

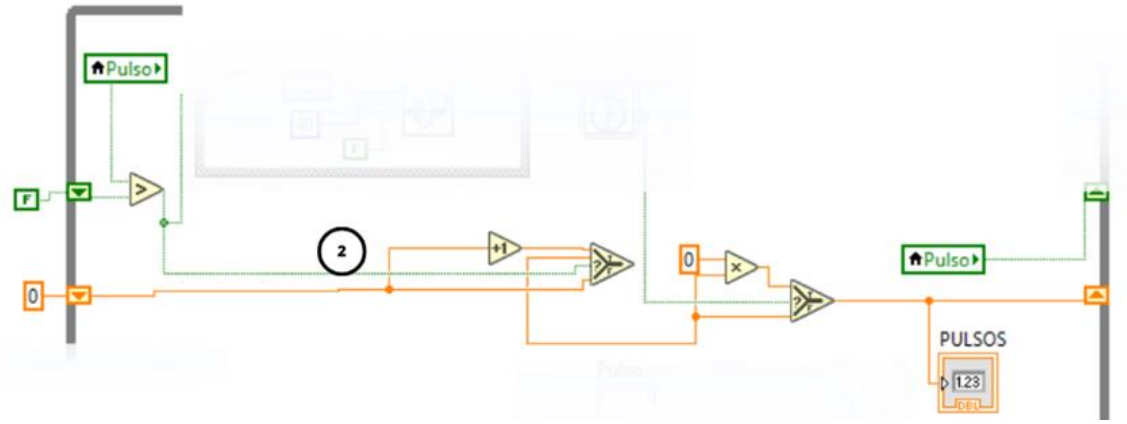

Figure VII. Data Processing Block.

2.3 Audible Heartbeat Indicator. - In this section, the implementation of a horn to notify the detection of a heartbeat by the proposed prototype is incorporated. Figure VIII clearly shows how this component is integrated into the heart rate measurement system. The addition of the horn enables instant audible feedback, which improves usability and user experience during cardiac monitoring. This additional functionality is critical for alerting the user to the detection of a heartbeat and can be useful in a variety of clinical and personal care settings.

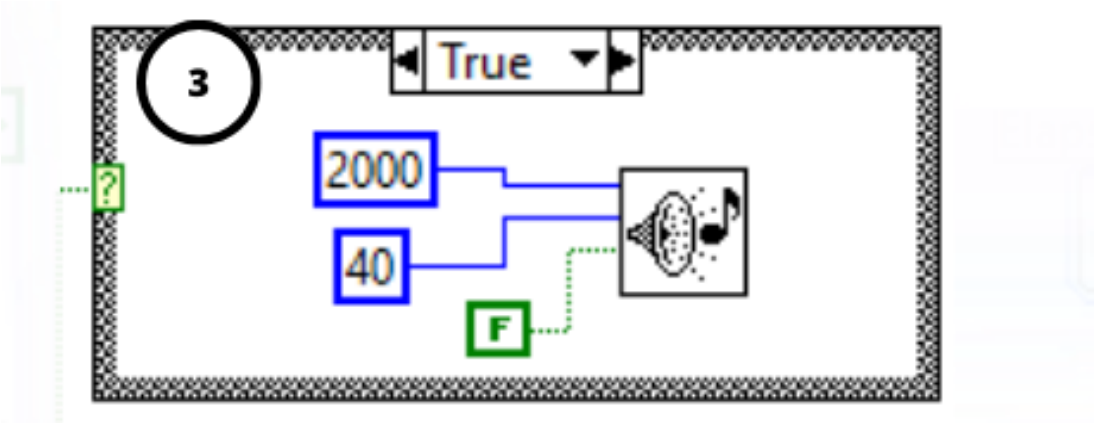

Figure VIII. Beats the sound indicator block.

2.4 Blood Pressure Prediction Programming. - In this section, there is an "Elapsed Time" which will act as the equipment clock and allows to set the time unit in milliseconds. The coding of the pressure prediction system is located inside the loop. The formula for the calculation of the blood pressure prediction is used, to know the cardiac pressure data the pulsations must be taken during one minute, but with this formula, it will be able to make a prediction in only 15 seconds and show it more efficiently as shown in Figure IX.

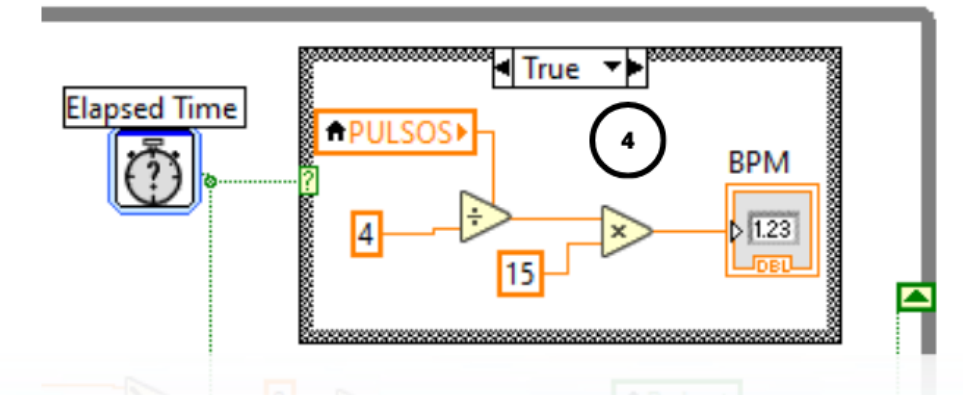

Figure IX. Heartbeat prediction block.

2.5 Stop Configuration. - In Figure X, you can see the section corresponding to the stop button, which is designed to initiate the block that completes the communication between LabVIEW and Arduino. This function is crucial to ensure proper and controlled termination of the data exchange process between the devices. The inclusion of this button provides the user with a convenient means to stop communication quickly and safely when necessary. In addition, its integration into the overall system interface makes it easy to access and use during the operation of the control system.

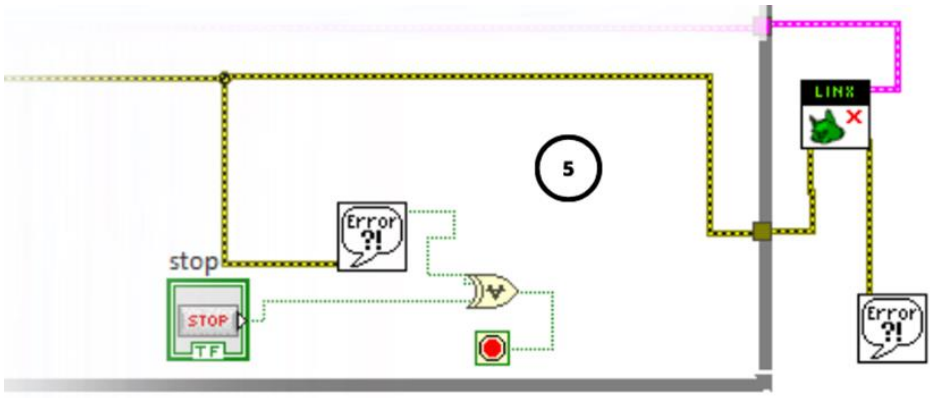

Figure VIII. Stop Configuration Block.

The code used to perform the processing through the ESP32 and its subsequent sending to the Arduino cloud is presented below:

```
#include "thingProperties.h"
void setup() {
  Serial.begin(9600);
  delay(1500);
  initProperties();
  // Connect to Arduino IoT Cloud
  ArduinoCloud.begin(ArduinoIoTPreferredConnection);
  setDebugMessageLevel(2);
  ArduinoCloud.printDebugInfo();
}

void loop() {
  ArduinoCloud.update();
  analogData();
}
void analogData() {
pulso_cardiaco= analogRead(34);
Serial.println(pulso_cardiaco);
delay(200);
}
```

2.6 Cloud Configuration. - Regarding the creation of an Arduino cloud user for real-time monitoring of a portable electrocardiograph system, designed to provide medical assistance to the community, a specific process is followed. This process involves the use of the AD8232 as the main sensor and provides real-time cardiac activity display options. To create a user in the Arduino cloud, the user must provide information such as email, username, and password. This process is shown in detail in Figure XI.

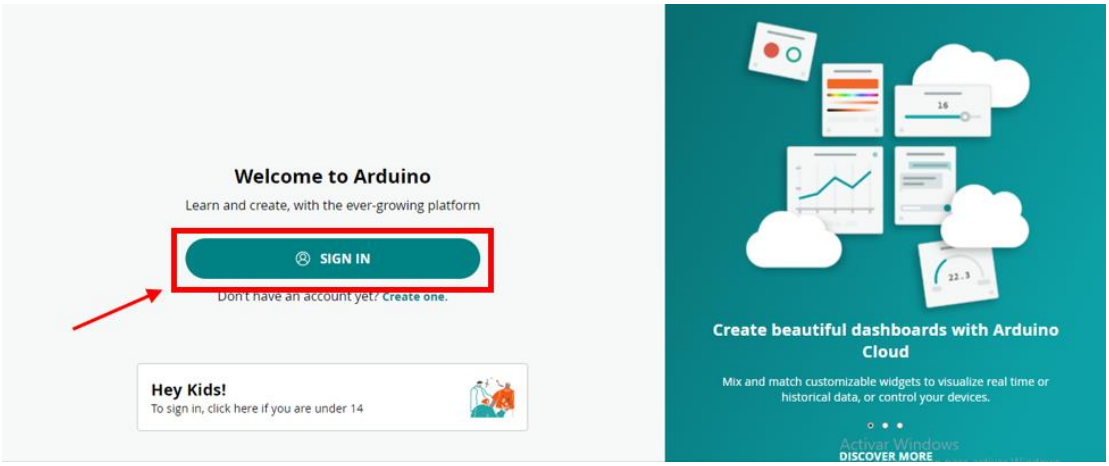

Figure XI. Account Registration on Arduino.

In addition, the appropriate boxes must be checked according to the privacy preferences and acceptance of terms. Once these steps are completed, click "Sign Up" to finalize the Arduino cloud registration. Creating a user in the Arduino cloud allows access to additional functionalities, such as data storage and analysis in the cloud, which facilitates remote monitoring and efficient management of the electrocardiography system.

Once the measurement information from the portable electrocardiograph circuit has been successfully sent, users can access it in real-time from the "Dashboard" section. To do so, they should click on the specific control panel created for this purpose, as shown in detail in Figure XII below.

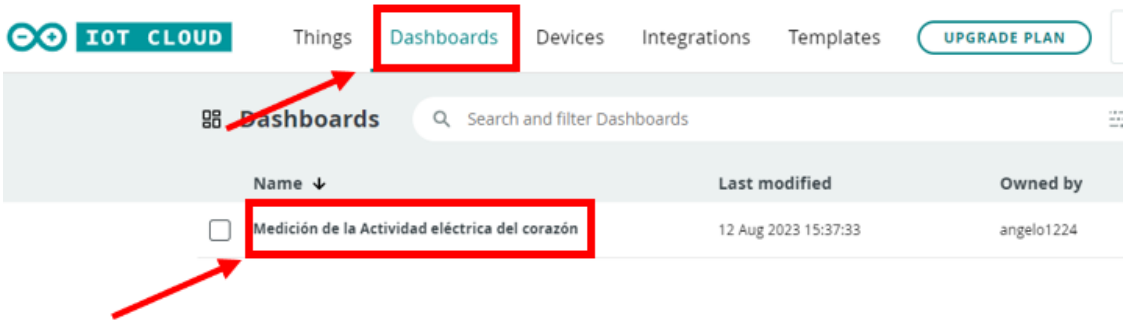

Figure XII. Accessing the Dashboard on Arduino IoT Cloud.

Real-time visualization of the data facilitates the tracking and continuous monitoring of the heart rhythm, which is crucial for the early detection of any irregularity or medical emergency. In addition, access to this real-time information from any location provides greater flexibility and responsiveness for medical professionals and caregivers, enabling them to make informed decisions and provide more timely and effective medical care to patients.

2.7 Equipment Cost. - The estimated cost of the system is $74, broken down as follows: Arduino Uno $20, Arduino AD8283 Module $19, Arduino Wifi Module $15, and other consumables totaling $20.
However, it is important to note that this cost could increase significantly if a desktop computer and the necessary software licenses are not available. The acquisition of these additional items could add approximately $800 to the total cost of the project, resulting in a final value of $874.

Considering the importance of cost minimization as one of the main design parameters, the idea of mass-producing the electrocardiograph is encouraged. This not only benefits educational institutions but also private or public companies looking for cost-effective solutions for cardiac monitoring.

Thanks to this cost-effective approach, our design can successfully compete with other similar products on the market. In addition, by offering an easily accessible portable electrocardiograph at an affordable price, we are contributing to improving the accessibility of medical care and cardiovascular health monitoring for a wide range of users from interested parties.

3. Results. - Table I below compares the data collected from the proposed prototype with the data simulated in the simulator. This analysis provides a comparative contrast between the two data sets, revealing that, on average, there is a margin of error of 5.81%. This level of discrepancy is considered considerably low, indicating a satisfactory correspondence between the data obtained in practice and the simulated data.

This result reinforces the validity and accuracy of the proposed prototype for heart rate measurement. Furthermore, it suggests that the simulation model used is effective in predicting the behavior of the system under real conditions. This finding is encouraging as it demonstrates the reliability of the prototype in practical settings, supporting its potential application in medical and health monitoring applications.

Sensed data (R) mV	Simulated data (S) mV	% error
1210	1180	2,5
1120	1215	7,8
1300	1195	8,8
1120	1205	7,1
1520	1180	11,9
1210	1165	3,9
1180	1195	1,3
1163	1185	1,9
1012	1170	13,5
1201	1190	0,9
1321	1160	13,9
1210	1195	1,3
1150	1175	2,1
1310	1180	11,0
1180	1205	2,1
1050	1195	12,1
1210	1180	2,5
1186	1200	1,2
1283	1215	5,6
1112	1195	6,9
1090	1200	9,2
1123	1175	4,4
1168	1190	1,8
Average error %		5,813

Table I. Sensed data compared with simulation.

As was carried out in the analysis presented in Table I above, a scenario study was performed with 53 additional patients under similar test conditions. The results obtained were averaged and contrasted with the simulated data, thus calculating the error of the proposed prototype.

The purpose of this scenario was to analyze the level of discrepancy present in the measurement of the electrical activity of the heart. Table II, which contains the information collected from these 53 additional patients, is presented below.

Table II shows three columns with information, the first column is the average value of the patient's 2-hour ECG study, and the second column contains the average value of a simulated ECG with the patient's data (age, weight, height, etc.) using Cardiopoint software, and the third column corresponds to the average value of the two columns mentioned above [29], [30].

	ECG (R) mV	ECG (S) mV	% error
Patient 1	1192,56	1188,91	5.81
Patient 2	1245,70	1190,65	8,10
Patient 3	1271,87	1196,87	9,01
Patient 4	1251,30	1191,04	5,63
Patient 5	1248,74	1188,83	5,54
Patient 6	1230,13	1174,57	4,75
Patient 7	1229,13	1174,22	4,70
Patient 8	1224,22	1173,22	4,37
Patient 9	1236,30	1174,35	5,31
Patient 10	1172,43	1190,61	2,36
Patient 11	1172,65	1123,48	5,60
Patient 12	1173,00	1137,43	4,73
Patient 13	1173,83	1115,65	6,44
Patient 14	1168,57	1151,96	8,83
Patient 15	1157,87	1133,91	8,48
Patient 16	1160,74	1127,83	9,46
Patient 17	1142,39	1120,22	8,11
Patient 18	1155,91	1098,91	6,31
Patient 19	1163,48	1128,04	4,70
Patient 20	1151,26	1130,00	4,23
Patient 21	1174,35	1138,04	4,95
Patient 22	1147,57	1133,48	2,70
Patient 23	1166,04	1130,43	4,17
Patient 24	1144,87	1134,78	3,62
Patient 25	1159,00	1132,83	4,43
Patient 26	1130,22	1188,91	4,93
Patient 27	1216,13	1133,70	7,29
Patient 28	1134,26	1175,87	4,02
Patient 29	1306,52	1244,13	5,07
Patient 30	1098,30	1112,17	3,81
Patient 31	1230,43	1265,00	3,50
Patient 32	1344,39	1410,43	4,83
Patient 33	1353,91	1370,87	2,77
Patient 34	1113,04	1102,83	1,97

Patient 35	1410,43	1370,87	3,00
Patient 36	1095,17	1116,96	1,97
Patient 37	1261,13	1278,87	1,97
Patient 38	1095,48	1114,96	1,91
Patient 39	1111,39	1127,83	1,65
Patient 40	1259,52	1266,00	1,67
Patient 41	1183,52	1214,17	2,87
Patient 42	1235,17	1253,57	1,75
Patient 43	1207,87	1201,35	1,77
Patient 44	1214,87	1231,26	1,91
Patient 45	1171,48	1191,39	2,05
Patient 46	1192,09	1225,74	2,81
Patient 47	1159,65	1179,17	2,21
Patient 48	1227,48	1237,83	1,45
Patient 49	1309,22	1320,17	1,04
Patient 50	1124,35	1135,48	1,44
Patient 51	1196,48	1215,57	1,60
Patient 52	1311,91	1269,30	3,37
Patient 53	1341,43	1373,04	2,57
Average	1202,83	1190,71	4,11

Table II. Table of results from conducted studies.

This extended analysis provides a more comprehensive evaluation of the prototype's accuracy and reliability in a variety of clinical scenarios. The results obtained will help to further validate the clinical utility of the proposed device and provide valuable information for future improvements and refinements of the system.

Table III presents the average value obtained from each of the studies performed. These data were collected over 2 hours using the proposed prototype for cardiac measurement of the Patients in the test scenarios. Subsequently, this set of values is downloaded from the cloud in .csv format for further processing.

	ECG (R) mV
Patient 1	1192,56
Patient 2	1245,70
Patient 3	1271,87
Patient 4	1251,30
Patient 5	1248,74
Patient 6	1230,13
Patient 7	1229,13
Patient 8	1224,22
Patient 9	1236,30
Patient 10	1172,43

Patient 11	1172,65
Patient 12	1173,00
Patient 13	1173,83
Patient 14	1168,57
Patient 15	1157,87
Patient 16	1160,74
Patient 17	1142,39
Patient 18	1155,91
Patient 19	1163,48
Patient 20	1151,26
Patient 21	1174,35
Patient 22	1147,57
Patient 23	1166,04
Patient 24	1144,87
Patient 25	1159,00
Patient 26	1130,22
Patient 27	1216,13
Patient 28	1134,26
Patient 29	1306,52
Patient 30	1098,30
Patient 31	1230,43
Patient 32	1344,39
Patient 33	1353,91
Patient 34	1113,04
Patient 35	1410,43
Patient 36	1095,17
Patient 37	1261,13
Patient 38	1095,48
Patient 39	1111,39
Patient 40	1259,52
Patient 41	1183,52
Patient 42	1235,17
Patient 43	1207,87
Patient 44	1214,87
Patient 45	1171,48
Patient 46	1192,09
Patient 47	1159,65
Patient 48	1227,48

Patient 49	1309,22
Patient 50	1124,35
Patient 51	1196,48
Patient 52	1311,91
Patient 53	1341,43
Averages	1202,83

Table III. Summary of simulations.

The collected data are subjected to a conversion process using the table hosted in Table IV. This table is used to subtract 1800 from the value extracted from the .csv file, followed by a multiplication by 1.8 conversion necessary to express it in millivolts.

This method allows us to obtain a standard measure of cardiac activity, thus providing a clearer picture of the reliability of the proposed design. The calculation of the average of these samples is essential to assess the consistency of the data obtained and to ensure the accuracy of the device as a whole.

In addition, the presentation of these effectively processed data facilitates communication with the professionals responsible for the diagnosis and analysis of the cardiac studies performed.

Conversion factors		
Obtained data	Data – 1800	x1.8 (mV)
2500	700	1260
2400	600	1080
2450	650	1170
2491	691	1243,8
2501	701	1261,8
2486	686	1234,8
2512	712	1281,6
2502	702	1263,6
2415	615	1107

Table IV. Conversion table.

The integration of the Arduino cloud with the help of the ESP32 allows the establishment of an IoT connection that makes it possible to view the data collected by the heart rate monitoring prototype from any location. This solution offers the advantage of accessing the information received at predefined time intervals, such as hourly, daily, weekly, and fortnightly.

Additionally, the facility is provided to download this data into a comma-delimited Excel (.csv) file, as shown in Figure XIII. This ability to remotely view and download data in Excel format offers additional flexibility in the analysis and management of the information obtained from cardiac monitoring, which is especially useful for medical professionals and research teams.

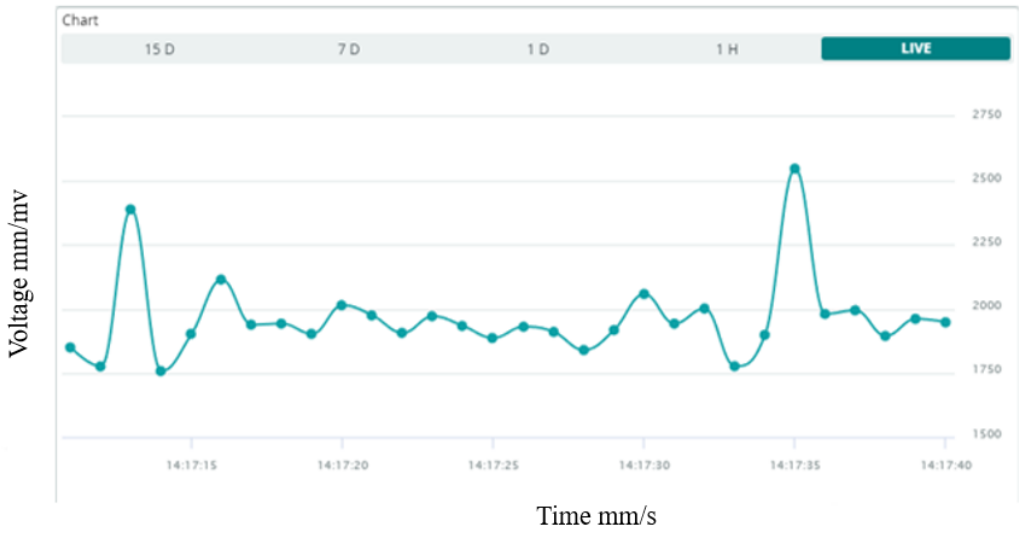

Figure IXIII. Real-time visualization of collected data.

The graphs generated locally using the Arduino serial plotter are presented below. These plots visually display the data collected by the heart rate monitoring prototype and are detailed in Figure XIV. The graphical representation of this data provides a clear and detailed visualization of the heart rate over time, making it easy to identify patterns and anomalies in the Patient's cardiac activity. These graphs provide an invaluable tool for the analysis and interpretation of the results obtained, both for healthcare professionals and researchers in the field of cardiology.

Figure XIV. Graphs were obtained using the Arduino Serial Plotter.

Figure XV shows the measurements collected over one hour in the system, obtained from the data recorded by the heart rate monitoring prototype and linked to the IoT platform. This visual representation provides a detailed snapshot of the heart rate over a specific period, allowing an accurate assessment of the Patient's cardiac activity over that interval.

These measurements provide valuable information about heart rate variability and can help identify potential irregularities or patterns of interest for clinical analysis. Analysis of these measurements can provide meaningful insights for the assessment of the Patient's cardiovascular health and contribute to informed medical decision-making.

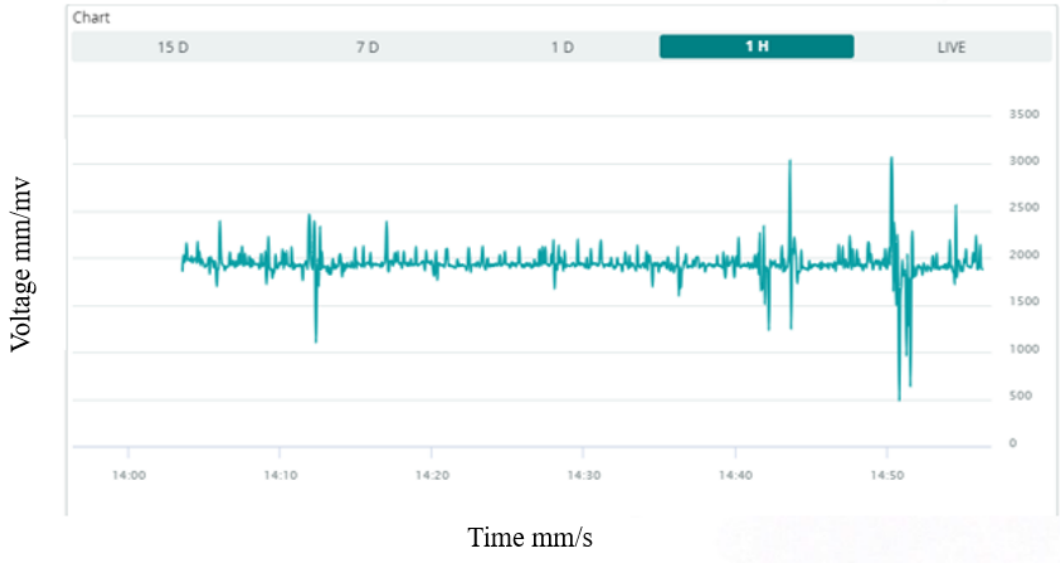

Figure XIV. Displaying measurements in real time over a 1-hour period.

4. Discussion. - The authors of the article [16], made a design of a remote monitoring of heartbeat and ECG signal using the SP32 with which they obtained graphs using the Arduino serial plotter.
The results obtained for comparison are determined by analyzing the graphs obtained, it is considered that the metric used in that design is performed every 60 seconds (1 minute), unlike our design in which every 15 seconds a prediction is made which allows obtaining a much faster and reliable measurement.

The authors performed an electrocardiogram that hosts the information in the cloud through MySQL which allows it to manage display screens much more friendly to the end user, thus allowing the characteristic ease and accessibility, in that aspect presents an improvement with the design presented in this article, a clear particularity that can be polished and added in subsequent works to enhance the present design.
Something notorious in the article is the lack of a margin of error study of the values obtained by the AD8232, which is necessary to evaluate the reliability of the data presented [3].

In [5] made a similar design to the one presented in this thesis, although they use the same sensors, they do not contemplate obtaining the blood pressure, they only focus on obtaining the ECG graphs, they use the Ubidots cloud to visualize the information sent by the ESP32. In addition, they make a comparison between the different forms of connection either by Bluetooth, wifi, or ZigBee but do not present a comparison of the quality of the transmitted data, which marks a notable difference compared to the present article.

The development of this design provides a very accurate analysis of the electrical activity of the heart, facilitating the study and analysis of cardiovascular patterns in patients. A great advantage compared to the design of the researchers in the article [16] is the improvement and implementation of the predictive analysis of blood pressure no longer every 60 seconds but every 15 seconds, providing an advantage for the prediction of possible tachycardias or bradycardias, which can be correctly detected by health professionals, providing a very valuable tool for those who use this design.

The following Table V compares the related works, showing the strengths of each one of them, and showing which one's present improvements compared to others. It is concluded that the proposed design, despite the 4.11% error rate, offers a wider range of characteristics compared to other designs, reducing the error rate may be the objective to be achieved in future research from already established bases.

	ECG	Cloud	ABPM	Census info	% Error
Proposed	✓	✓	✓	✓	4.11
Art. [16]	✓	✓	✓	✓	X
Art. [5]	✓	✓	X	✓	X
Art. [3]	✓	✓	X	X	X

Art. [22]	✓	✓	✓	X	0.41
Art. [1]	✓	X	X	X	X

Table V. Comparison table of related items

The design of the portable electrocardiograph system outlined in this paper presents several notable advantages. Firstly, the system offers detailed blood pressure information, enhancing the comprehensive assessment of a patient's cardiovascular health. Additionally, it features a visual indicator that records each detected heartbeat, facilitating precise monitoring of cardiac activity.

A standout feature of the system is its capability to transmit collected information to the cloud. This functionality allows users to access data from any internet-connected device, providing increased flexibility and accessibility in monitoring heart health. Furthermore, the system offers the option to download information as an XML file, streamlining further processing for analysis and storage purposes.

Measured values, such as an Average ECG (R) of 1202.83 mV and simulated Average ECG (S) values of 1190.71 mV, reveal a margin of error of 4.11%. Despite this small margin, the prototype demonstrates acceptable reliability in measuring cardiac activity. These results underscore the effectiveness and practicality of the developed portable electrocardiograph system, underscoring its potential for integration into clinical and community settings.

5. Conclusions. - After a thorough evaluation of the performance of the portable electrocardiograph designed to provide community healthcare, 1-3 hour study scenarios were conducted to verify the reliability of the information captured and transmitted through our cloud platform. During this process, a margin of error of 4.11% was observed.

However, the presence of a certain level of noise was detected in the measurements shared with the Arduino cloud, suggesting that this interference could explain part of the error and the slight distortion in the received signal. These findings highlight areas of improvement for future research, where techniques could be implemented to mitigate the noise and thereby improve the quality of the transmitted signal.

The design of the portable electrocardiograph system makes a valuable contribution to community medical knowledge, opening the door for further exploration in this field through additional research. This design lays the foundation for the future development of devices aimed at improving the quality of life of both students and society in general, representing a significant advance for human welfare. In this sense, the ability to provide quality medical care at the community level is strengthened with the implementation of this innovative technology.

Furthermore, it is important to highlight that the successful implementation of this portable electrocardiograph in community settings could have a significant impact on the early detection of cardiac problems and the prevention of serious complications. By facilitating more accessible and continuous monitoring of patients' cardiac health, it could improve preventive medical care and reduce the burden on healthcare systems, especially in remote or underserved areas. This would not only benefit individuals at risk for heart disease but would also contribute to health promotion and overall community well-being. Ultimately, the portable electrocardiograph represents not only a technological advance in the medical field, but also a vital tool for improving quality of life and public health at the community level.

References

[1] L. Dioren Rumpa, S. Suluh, I. Hendrika Ramopoly, and W. Jefriyanto, "Development of ECG sensor using Arduino uno and e-health sensor platform: Mood detection from heartbeat," in Journal of Physics: Conference Series, Institute of Physics Publishing, Jun. 2020. https://doi.org/10.1088/1742-6596/1528/1/012043

[2] M. Bansal and B. Gandhi, "IoT Big Data in Smart Healthcare (ECG Monitoring)," in Proceedings of the International Conference on Machine Learning, Big Data, Cloud and Parallel Computing: Trends, Perspectives and Prospects, COMITCon 2019, 2019. https://doi.org/10.1109/COMITCon.2019.8862197

[3] A. Qtaish and A. Al-Shrouf, "A Portable IoT-cloud ECG Monitoring System for Healthcare," IJCSNS International Journal of Computer Science and Network Security, vol. 22, no. 1, 2022

[4] P. Kamble and A. Birajdar, "IoT Based Portable ECG Monitoring Device for Smart Healthcare," in 5th International Conference on Science Technology Engineering and Mathematics, ICONSTEM 2019, 2019. https://doi.org/10.1109/ICONSTEM.2019.8918776

[5] P. Singh and A. Jasuja, "IoT-based low-cost distant patient ECG monitoring system" 2017 International Conference on Computing, Communication and Automation (ICCCA), Greater Noida, India, 2017, pp. 1330-1334, https://doi.org/10.1109/CCAA.2017.8230003

[6] E. Kim, J. Kim, J. Park, H. Ko, and Y. Kyung, "TinyML-Based Classification in an ECG Monitoring Embedded System," Computers, Materials and Continua, vol. 75, no. 1, 2023, https://doi.org/10.32604/cmc.2023.031663

[7] N. Misran, M. S. Islam, G. K. Beng, N. Amin, and M. T. Islam, "IoT Based Health Monitoring System with LoRa Communication Technology," in Proceedings of the International Conference on Electrical Engineering and Informatics, 2019. https://doi.org/10.1109/ICEEI47359.2019.8988869

[8] A. D. Acharya and S. N. Patil, "IoT based Health Care Monitoring Kit," in Proceedings of the 4th International Conference on Computing Methodologies and Communication, ICCMC 2020, 2020 https://doi.org/10.1109/ICCMC48092.2020.ICCMC-00068

[9] H. Santillán, M. Suárez, and D. Cárdenas, "Desarrollo de una herramienta IoT para optimizar el control de la humedad en el cultivo de cacao," Memoria Investigaciones en Ingeniería, vol. 25, Dec. 2023, https://doi.org/10.36561/ING.25.14

[10] H. Santillán Carranza, J. O. Enríquez Sandoval, y J. F. Bonilla Castro, «Development of a Raspberry Pi-Based Wireless Educational Tool», INGENIO, vol. 7, n.º 1, pp. 13–22, feb. 2024. https://doi.org/10.29166/ingenio.v7i1.5630

[11] Y. He, B. Fu, J. Yu, R. Li, and R. Jiang, "Efficient learning of healthcare data from IoT devices by edge convolution neural networks," Applied Sciences (Switzerland), vol. 10, no. 24, 2020, https://doi.org/10.3390/app10248934

[12] E. G. Bertogna, F. M. Machado, and M. A. Sovierzoski, "An optimized ECG android system using data compression scheme for cloud storage," Health Technol (Berl), vol. 10, no. 5, 2020, https://doi.org/10.1007/s12553-020-00464-z

[13] Md. O. F. et al. Altaf C., "Low Power IoT based Implementation ECG & Health Monitoring System.," Proceeding International Conference on Science and Engineering, vol. 11, no. 1, 2023, https://doi.org/10.52783/cienceng.v11i1.319

[14] Q. N. and A. F., "Design Health care system using Raspberry Pi and ESP32," Int J Comput Appl, vol. 177, no. 36, 2020, https://doi.org/10.5120/ijca2020919863

[15] J. Lakshmi Prasanna, S. V. Aswin Kumer, M. Ravi Kumar, M. Sangeetha Lakshmi, P. Srilaxmi, and C. Santhosh, "Low-cost ECG and Heart Monitoring System Using Ubidot Platform," in Lecture Notes in Networks and Systems, 2022. https://doi.org/10.1007/978-981-19-0976-4_19

[16] M. A. Rahman, Y. Li, T. Nabeed, and M. T. Rahman, "Remote monitoring of heart rate and ECG signal using ESP32," in Proceedings - 2021 4th International Conference on Advanced Electronic Materials, Computers and

Software Engineering, AEMCSE 2021, 2021. https://doi.org/10.1109/AEMCSE51986.2021.00127

[17] B. Sugandi, M. H. Satria, H. Arif, N. Nelmiawati, and I. H. Mulyadi, "LOW COST WIRELESS ECG PATCH USING ESP32," JURNAL INTEGRASI, vol. 12, no. 1, 2020, https://doi.org/10.30871/ji.v12i1.1764

[18] V. K. Patil, V. R. Pawar, S. P. Kulkarni, T. A. Mehta, and N. R. Kharea, "Real Time Emotion Recognition with AD8232 ECG Sensor for Classwise Performance Evaluation of Machine Learning Methods," International Journal of Engineering, Transactions B: Applications, vol. 36, no. 6, 2023, https://doi.org/10.5829/ije.2023.36.06c.02

[19] A. Bushnag, "A Wireless ECG Monitoring and Analysis System Using the IoT Cloud," Intelligent Automation and Soft Computing, vol. 33, no. 1, 2022, https://doi.org/10.32604/iasc.2022.024005

[20] K. J. P. Ortiz, J. P. O. Davalos, E. S. Eusebio, and D. M. Tucay, "IoT: Electrocardiogram (ECG) monitoring system," Indonesian Journal of Electrical Engineering and Computer Science, vol. 10, no. 2, 2018, https://doi.org/10.11591/ijeecs.v10.i2.pp480-489

[21] L. R. Yeh et al., "Integrating ECG monitoring and classification via iot and deep neural networks," Biosensors (Basel), vol. 11, no. 6, 2021, https://doi.org/10.3390/bios11060188

[22] M. O. Rahman et al., "Internet of Things (IoT) based ECG System for Rural Health Care," International Journal of Advanced Computer Science and Applications, vol. 12, no. 6, 2021, https://doi.org/10.14569/IJACSA.2021.0120653

[23] G. Xu, "IoT-Assisted ECG Monitoring Framework with Secure Data Transmission for Health Care Applications," IEEE Access, vol. 8, 2020, https://doi.org/10.1109/ACCESS.2020.2988059

[24] P. W. Rusimamto, Endryansyah, L. Anifah, R. Harimurti, and Y. Anistyasari, "Implementation of arduino pro mini and ESP32 cam for temperature monitoring on automatic thermogun IoT-based," Indonesian Journal of Electrical Engineering and Computer Science, vol. 23, no. 3, 2021, https://doi.org/10.11591/ijeecs.v23.i3.pp1366-1375

[25] Y. Liu, "Artificial intelligence-based neural network for the diagnosis of diabetes: Model development," JMIR Med Inform, vol. 8, no. 5, 2020, https://doi.org/10.2196/18682

[26] H. Hamil et al., "Design of a secured telehealth system based on multiple biosignals diagnosis and classification for IoT application," Expert Syst, vol. 39, no. 4, 2022, https://doi.org/10.1111/exsy.12765

[27] A. Mishra, B. Chakraborty, D. Das, and P. Bose, "AD8232 based Smart Healthcare System using Internet of Things (IoT)," International Journal of Engineering Research & Technology (IJERT), vol. 7, no. April, 2018.

[28] Z. Annisa, P. C. Nugraha, and M. R. Makruf, "An Advanced Holter Monitor Using AD8232 and MEGA 2560," Jurnal Teknokes, vol. 14, no. 2, 2021, https://doi.org/10.35882/teknokes.v14i2.6

[29] L. I. Skora, J. J. A. Livermore, and K. Roelofs, "The functional role of cardiac activity in perception and action," Neuroscience and Biobehavioral Reviews, vol. 137. 2022. https://doi.org/10.1016/j.neubiorev.2022.104655

[30] S. Villamil, C. Hernández, and G. Tarazona, "An overview of internet of things," Telkomnika (Telecommunication Computing Electronics and Control), vol. 18, no. 5, pp. 2320–2327, Oct. 2020, https://doi.org/10.12928/TELKOMNIKA.v18i5.15911

Nota contribución de los autores:

1. Concepción y diseño del estudio
2. Adquisición de datos
3. Análisis de datos
4. Discusión de los resultados
5. Redacción del manuscrito
6. Aprobación de la versión final del manuscrito

HS ha contribuido en: 1, 2, 3, 4, 5 y 6.
AM ha contribuido en: 1, 2, 3, 4, 5 y 6.
DC ha contribuido en: 1, 2, 3, 4, 5 y 6.
PW ha contribuido en: 1, 2, 3, 4, 5 y 6.

Nota de aceptación: Este artículo fue aprobado por los editores de la revista Dr. Rafael Sotelo y Mag. Ing. Fernando A. Hernández Gobertti.

Improving the Improvement

Mejorando la Mejora

Melhorando a Melhoria

Darío Alentorn[1(*)]

Recibido: 06/06/2024 Aceptado: 28/06/2024

Summary. - This work reflects on the benefits of applying risk-based thinking for improvement in a quality management system.

Based on the crucial role of theory and on the belief that conceptual accuracy and clarity are the main key to an effective practice, this work studies and analyzes the state-of-the-art core concepts of improvement and risk management, through international and national standards, including ISO 9000, ISO 31000 and ANSI-PMI Standards, among others. Consequently, reformulations of the main definitions about improvement are proposed, with the contribution of risk-based thinking concepts, in order to provide a wider perspective of the knowledge platform that has been built.

The structure of this paper consists of: Summary, Introduction, Framework, Analysis and Discussion, Conclusions and References.

Keywords: Quality; Risk; Improvement; ISO 9001, ISO 31000.

(*) Corresponding Author

[1] Structural Civil Engineer, PMP. Universidad de Montevideo, Uruguay, dalentorn@correo.um.edu.uy, ORCID iD: https://orcid.org/0009-0001-7726-9396

Memoria Investigaciones en Ingeniería, núm. 26 (2024). pp. 265-274
https://doi.org/10.36561/ING.26.16
ISSN 2301-1092 • ISSN (en línea) 2301-1106 – Universidad de Montevideo, Uruguay

Resumen. - *El presente trabajo reflexiona sobre los beneficios de la aplicación del pensamiento basado en riesgos para la mejora en un sistema de gestión de calidad.*

Basado en el papel crucial de la teoría y en la creencia de que la precisión y claridad conceptual es la clave principal para una práctica efectiva, este trabajo estudia y analiza los más recientes conceptos relativos a la mejora y la gestión de riesgos, mediante la revisión de estándares internacionales y nacionales, incluyendo las Normas ISO 9000, ISO 31000 y ANSI-PMI, entre otras. En consecuencia, se propone la reformulación de las principales definiciones relativas a la mejora, enriquecidas con el aporte del pensamiento basado en riesgos, permitiendo ver más allá y con mayor perspectiva, la plataforma de conocimiento construida.

La estructura del trabajo consta de: Resumen, Introducción, Marco Conceptual, Análisis y Discusión, Conclusiones y Referencias.

Palabras clave: *Calidad; Riesgos; Mejora; ISO 9001, ISO 31000.*

Resumo. ***-*** *Este trabalho reflete sobre os benefícios da aplicação do pensamento baseado no risco para a melhoria de um sistema de gestão da qualidade.*

Baseado no papel crucial da teoria e na crença de que a precisão e a clareza conceptual são a chave principal para uma prática eficaz, este trabalho estuda e analisa os conceitos mais recentes relacionados com a melhoria e a gestão de riscos, através da revisão de normas internacionais e nacionais, incluindo a ISO 9000, ISO 31000 e ANSI-PMI, entre outros. Consequentemente, propõe-se a reformulação das principais definições relacionadas com a melhoria, enriquecida com o contributo do pensamento baseado no risco, permitindo-nos ver mais longe e com maior perspectiva, a plataforma de conhecimento construída.

A estrutura do trabalho é composta por: Resumo, Introdução, Estrutura Conceitual, Análise e Discussão, Conclusões e Referências.

Palavras-chave: *Qualidade; Riscos; Melhoria; ISO 9001; ISO 31000.*

1. Introduction. - Although the 2015 version of ISO 9001 [1] promotes the risk-based thinking approach, highlighting its benefits, it is partially applied to the Improvement chapter.

Despite the close link between improvement and risk-based thinking, there is only one mention to risks in the 10. Improvement chapter of ISO 9001 [1]. This mention is in 10.2 Nonconformity and corrective action part e): "When a nonconformity occurs, including any arising from complaints, the organization shall:(…) e) update risks and opportunities determined during planning, if necessary…".

This point of view focuses on the planning process, coherently with ISO 9001 requirements related to risks (6. Planning, 6.1 Actions to address risks). But the Improvement requirements can get much more benefits from a risk-based thinking approach.

The objective of this work is to provide guidance for the best application of risk-based thinking to the continuous improvement process as well as inputs for a future review of the ISO 9000 series standards. For this, definitions from different sources are compiled and revised. An analysis of their strengths and weaknesses is also done. As a result of the analysis carried out, a redefinition of the terms corrective action, preventive action and correction is proposed in order to widen them, facilitating the application of risk-based thinking.

2. Framework: definition of key concepts for the analysis. -

2.1 Preventive action [2]

"action to eliminate the cause of a potential nonconformity or other potential undesirable situation.
Note 1 to entry: There can be more than one cause for a potential nonconformity. Note 2 to entry: Preventive action is taken to prevent occurrence whereas corrective action is taken to prevent recurrence".

2.2 Corrective action [2]

"action to eliminate the cause of a nonconformity and to prevent recurrence.
Note 1 to entry: There can be more than one cause for a nonconformity. Note 2 to entry: Corrective action is taken to prevent recurrence whereas preventive action (3.12.1) is taken to prevent occurrence. "

2.3 Correction [2]

"action to eliminate a detected nonconformity.
Note 1 to entry: A correction can be made in advance of, in conjunction with or after a corrective action. Note 2 to entry: A correction can be, for example, rework or regrade".

2.4 Improvement [2]

"activity to enhance performance.
Note 1 to entry: The activity can be recurring or singular".

2.5 Continual improvement [2]

"recurring activity to enhance performance.
Note 1 to entry: The process of establishing objectives and finding opportunities for improvement is a continual process through the use of audit findings and audit conclusions, analysis of data, management reviews or other means and generally leads to corrective action or preventive action."

2.6 Performance [2]

"measurable result
Note 1 to entry: Performance can relate either to quantitative or qualitative findings.
Note 2 to entry: Performance can relate to the management of activities, processes, products, services, systems or organizations".

2.7 Risk-related terms.

2.7.1 Risk [2]

"effect of uncertainty.
Note 1 to entry: An effect is a deviation from the expected — positive or negative.
Note 2 to entry: Uncertainty is the state, even partial, of deficiency of information related to, understanding or knowledge of, an event, its consequence, or likelihood.
Note 3 to entry: Risk is often characterized by reference to potential events (as defined in ISO Guide 73:2009, 3.5.1.3)

and consequences (as defined in ISO Guide 73:2009, 3.6.1.3), or a combination of these.
Note 4 to entry: Risk is often expressed in terms of a combination of the consequences of an event (including changes in circumstances) and the associated likelihood (as defined in ISO Guide 73:2009, 3.6.1.1) of occurrence.
Note 5 to entry: The word "risk" is sometimes used when there is the possibility of only negative consequences".

2.7.1.1 Risk, Risk Source. [3]
Risk: "effect of uncertainty on objectives
Note 1 to entry: An effect is a deviation from the expected. It can be positive, negative or both, and can address, create or result in opportunities and threats.
Note 2 to entry: Objectives can have different aspects and categories and can be applied at different levels.
Note 3 to entry: Risk is usually expressed in terms of risk sources, potential events, their consequences and their likelihood".
Risk source: element which alone or in combination has the potential to give rise to risk.

2.7.2 Risk, Threat, Opportunity.

2.7.2.1 Approach according to PMI-PMBOK [4]
"Risk. An uncertain event or condition that, if it occurs, has a positive or negative effect on one or more project objectives" [4] P. 248
"Threat. A risk that would have a negative effect on one or more project objectives" [4] P. 251
"Opportunity. A risk that would have a positive effect on one or more project objectives." [4] P. 243

2.7.2.2 Approach according to ANSI/PMI 08-002-2024 [5]
"A risk is an uncertain event or condition that, if it occurs, has a positive or negative effect on one or more program objectives. Risks can have both positive and negative impacts on programs. Negative risks, often referred to as threats, affect the implementation of programs and realization of benefits. Positive risks, usually referred to as opportunities help foster effective, efficient program implementation and increased realization of benefits."

2.7.2.3 Approach according to ANSI/PMI 99-001-2021 [6]
"A risk is an uncertain event or condition that, if it occurs, can have a positive or negative effect on one or more objectives. Identified risks may or may not materialize in a project…Project teams seek to maximize positive risks (opportunities) and decrease exposure to negative risks (threats)".

2.7.3 Risk, Threat, Opportunity, Cause. [7]
Risk. "An individual risk is an uncertain event or condition that, if it occurs, has a positive or negative effect on one or more objectives."
Opportunities. "Opportunities are risks that have a positive effect on one or more objectives".
Threats. "Threats are risks that would have a negative effect on one or more objectives."
Cause "events or circumstances that currently exist or are certain to exist in the future, which might give rise to risks". [7] Risk management in Organizations, P. 11
X6.2 As a result of cause, risk may occur, which would lead to effect" [7] Identify Risks, P. 129 (Appendix X6 Techniques for the Risk management framework.

2.7.4 Threat, Opportunity

2.7.4.1 Threat, Opportunity according to IEC 31010 [8]
Threat: potential source of danger, harm, or another undesirable outcome
Note 1 to entry: A threat is a negative situation in which loss is likely and over which one has relatively little control.
Note 2 to entry: A threat to one party may pose an opportunity to another.
Opportunity: combination of circumstances expected to be favorable to objectives
Note 1 to entry: An opportunity is a positive situation in which gain is likely and over which one has a fair level of control.
Note 2 to entry: An opportunity to one party may pose a threat to another.
Note 3 to entry: Taking or not taking an opportunity are both sources of risk.

2.7.4.2 Threat, Opportunity according to ISO Online browsing platform [14]
Opportunity: risk occurrence that would have a favorable impact
Threat: risk occurrence that would have a negative impact

3. Analysis and Discussion.

3.1 Prevention.

3.1.1 Relationship between preventive and corrective actions with risk-based thinking. - The ISO 9001:2015 Standard [1], Annex A, Clause A.4 Risk-based Thinking, establishes: “One of the key purposes of a quality management system is to act as a preventive tool. Consequently, this International Standard does not have a separate clause or subclause on preventive action. The concept of preventive action is expressed through the use of risk-based thinking in formulating quality management system requirements.”

This shows prevention as associated with preventive actions, but it is then worth questioning whether corrective actions are included in the concept of prevention.

Considering ISO definitions for preventive and corrective actions (see 2.1 and 2.2), it is concluded that preventive actions are intended to prevent the occurrence of a nonconformity and corrective actions are, in turn, intended to prevent the recurrence of a nonconformity . Therefore, the concept of prevention should include both. Likewise, from the cited paragraph, preventive actions have been replaced by risk-based thinking, but it is restricted to "formulating requirements for the quality management system." It should be noted that, by definition, preventive action not only refers to this, but also to preventing the occurrence of any non-conformity, for example of a product or a process. Suppose that a negative trend of a process is observed, which is below the minimum acceptable quality level, the maintenance of the trend would result in a non-compliant value. A preventive action to solve this is not the formulation “of quality management system requirements”, but it is a common type of preventive action.

Therefore, the current ISO concept of preventive action (see 2.1) is limiting and the same applies to corrective action, since it has not been interpreted from a risk-based thinking perspective. According to its current definition, it would be appropriate to do so as an action taken to eliminate the risk of recurrence of a nonconformity, just as preventive action should be interpreted as an action taken to eliminate the risk of the occurrence of a nonconformity.

On the other hand, although a similar treatment is observed in the ISO definitions of preventive actions and corrective actions, the concept of preventive action is more comprehensive than that of corrective action, as it includes not only the elimination of a cause of nonconformity , but also that of “another potential undesirable situation.” This approach is much more aligned with risk-based thinking and should be incorporated into the concept of corrective action, to include the elimination of the cause of other real undesirable situations, for which there is a risk of recurrence.

3.1.2 Prevention and Improvement. - In Note 1 to the continual improvement definition (see 2.5), it is established that “generally leads to corrective action or preventive action”. The word “generally” refers to other types of improvement actions that are not corrective or preventive actions as defined by ISO (see 2.1 and 2.2). In fact, this is where risk-based thinking again contributes to improving the improvement concepts, allowing to consider those actions that, without eliminating the cause of real or potential non-conformities, reduce the risk associated with recurrence or occurrence respectively.

Reviewing the meanings of prevention in English and Spanish languages, there are important differences. In English [13] the main meaning is “the action of keeping from happening or making impossible an anticipated event or intended act”. So, this concept is only related to negative effects, that is why the action is to make impossible the event. But in Spanish [9] the main meaning is "to prepare, harness and arrange in advance what is needed for a purpose" . This concept is more comprehensive in Spanish, because it could be related also to events with positive consequences on the purpose. Thus, this kind of action should be included in the concept of preventive action, from the risk-based thinking perspective, not only considering the negative effects on the objectives (undesirable situations or potential non-conformities) but also the positive effects. Prevention and improvement are not only related to negative effects on the objectives. Continuing with risk-based thinking, suppose an event or condition that, if it occurs, will have a positive effect on the objectives. Suppose a strategy to increase its likelihood and/or its positive impacts. In this case, we would be taking an action that does not respond to the prevention of the occurrence of a negative impact, but to the promotion of the positive impacts.

3.2 Improvement and Cost of Quality. - The Prevention-Appraisal-Failure (PAF) quality cost model is defined [10] as “a methodology that allows an organization to determine the extent to which its resources are used for activities that prevent poor quality, that appraise the quality of the organization’s products or services, and that result from internal and external failures.” This methodology considers conformance costs (prevention and appraisal) and nonconformance costs (internal and external failures).

Internal and external failure costs are considered poor quality costs, which means a loss for the organization. They include the costs of correction, rework or rectification. On the other hand, prevention and appraisal costs are considered costs of good quality, meaning investment, due to their contribution to profits. The first ones because they avoid the appearance of non-conformities and the second ones, because they reduce poor quality costs, avoiding or reducing the non-conformities delivered to clients.

"Quality improvement is synonymous with a reduction in the cost of poor quality" [11]. Prevention costs are incurred to prevent or avoid quality problems and they include the costs for preventive and corrective actions (improvement). "The Prevention category is defined as the experience gained from the identification and elimination of specific causes of failure cost to prevent the recurrence of the same or similar failures in other products or services" [11]. "Internal failure costs have been defined to include basically all costs required to evaluate, dispose of, and either correct or replace nonconforming products or services prior to delivery to the customer ..." [11].

The Note to subclause 10.1 Generalities in clause 10. Improvement of ISO 9001 [1] establishes that:
"Examples of improvement can include correction, corrective action, continual improvement, breakthrough change, innovation and re-organization".

But, based on the PAF model's main concepts summarized before, correction (see 2.3) should not be considered an example of improvement, because it leads to poor quality costs (loss), and it should not be considered an investment (improvement costs). From the quality point of view, the common instruction is "get it right first time, every time" but correction seeks to eliminate a detected nonconformity, whenever the minimum acceptable quality level is not reached.

The ISO definition of preventive action (see 2.1) considers the ideal situation for managing a potential nonconformity or a potential unfavorable situation, which is to eliminate its cause to avoid its occurrence. From the quality costs' point of view, this is also the ideal situation, with an entirely effective action that leads the cost of future losses to zero. Unfortunately, the definition does not consider the actions aiming at reducing the effects of the nonconformity and/or the likelihood of its occurrence, even though both paths lead to reduce the costs that the nonconformity would generate in case of occurrence (losses), which should also be considered prevention.

The ISO 9000 corrective action's definition (see 2.2) emphasizes the importance of searching for the root cause of an existing nonconformity in order to prevent recurrence. Similarly, this concept does not contemplate the cases in which neither the cause, nor the actions to avoid recurrence can be found. In these cases, actions can be taken to reduce the effects of the nonconformity and/or the likelihood of its recurrence. Both paths lead to reducing the costs that the non-conformity would generate in case of recurrence, and that is why they should be included in the definition of corrective action to make it more comprehensive (see 3.3.3).

3.3 Improvement and Risk-based thinking. -

3.3.1 PMI Risk management concepts. - The PMI Standard for Risk Management (see 2.7.3) recommends describing each risk using a three-part statement which includes cause-risk effect. This approach facilitates the relationship with the traditional quality management point of view of corrective and preventive actions. In fact, studying the risk associated with the occurrence or recurrence of a nonconformity implies the identification of the cause in order to eliminate it. This kind of risk response is called "avoid" in this standard, and it consists of eliminating a threat or protecting an activity from its impact. So preventive and corrective actions correspond to the avoid strategy of risk-based thinking.

But there are other kinds of responses as "Mitigate" which consist of actions taken to reduce the probability of occurrence and/or impact of a threat. Once again, risk-based thinking feeds the Improvement classical concepts of preventive and corrective actions, widening them, by the consideration of these type of actions that, while not eliminating the cause, may reduce the risk. This concept is aligned with the Cost of Quality methodology, as shown in 3.2.

All PMI Standards (see 2.7.2 and 2.7.3) classify risks based on their effects. If they are positive, they are called opportunities and if they are negative, they are called threats. Risk management seeks "to maximize positive risks (opportunities) and decrease exposure to negative risks (threats)".

3.3.2 ISO Risk-based thinking. - The ISO Risk Management Standard defines risk, but its expression (see 2.7.1.1, Note 3) does not mention the cause of the risk (as PMI Standards do), but the source of the risk. Thus, in ISO 31000:2018 [3] "6.5.2 Selection of risk treatment options" one of them is eliminating the risk source, and others are changing the likelihood or consequences. These concepts are very similar to the ones described before, in 3.3.1.

Opportunities and threats are mentioned in Note 1 to the risk definition, though they are not defined in this standard [3] but linked (see 2.7.4.1).

In ISO 9001:2015 [1] "risks and opportunities" are mentioned systematically, but if the risk concept includes the positive effects on the objectives, it is not clear the reason for the explicit reference to opportunities. This may be caused by the association of the word risk only to negative effects, against its own definition.

In the same standard [1], Note 2 to 6.1.2 (6.1 Actions to address risks and opportunities) establishes that: "Actions to address risks can include avoiding risk, taking risk in order to pursue an opportunity, eliminating the risk source, changing the likelihood or consequences, sharing the risk, or retaining risk by informed decision". Thus, the "Actions to address risks" are similar to the "Risk response" in PMI standards.

3.3.3 The failure mode and effects analysis (FMEA). - This classic quality management tool provides a method to calculate the risk associated with the occurrence or recurrence of non-conformities (replacing the failure concept). It helps to identify potential failure modes in a system as well as their causes and effects. The potential failures are prioritized according to how serious their consequences are (S), how frequently they occur (O), and how difficult it is to detect failure before the user becomes aware (D). The purpose of the FMEA is to take actions to eliminate or reduce failures, starting with the top-priority ones.

There is a risk for each potential failure, and this is calculated by the Risk Priority Number (RPN), as a product of three previously mentioned factors Severity, Occurrence, and Detection (RPN = SxOxD). Each of these three factors goes from 1 to 10. Eliminating the cause would be equivalent to obtaining a probability of occurrence of 1 (which, for example, could be associated with 1 in 1.500.000) [12].

This tool is especially helpful to understand the mitigation actions to address risks, because the actions to be taken should decrease the RPN. In fact, it emphasizes the importance of considering actions that do not eliminate the cause of the nonconformity but reduce the probability of occurrence or recurrence and/or their impact. Subclause 5.3.7.1 of IEC 60812:2018 [15] establishes: "Understanding how the failure occurs is useful in order to identify the best way to reduce the likelihood of failure or its consequences.". This leads to a reinforcement of the concept of preventive and corrective actions that should not be limited to eliminating the cause of non-conformities, but that also includes those that mitigate the risk of occurrence or recurrence.

4. Conclusions. - The main characteristics that the definitions of the terms related to improvement should be included were compiled and reformulated.

As in ISO 9000 [2], the criterium to establish a definition is describing only those characteristics that are crucial to identify the concept. Information concerning the concept which is important but not essential to its description is put in one or more notes to the definition.

Based on the above, a reformulation of improvement core concepts is proposed, ending up in a formulation of an Improvement Principle.

Preventive action,
action to eliminate the cause of a potential nonconformity or other undesirable potential situation (threat), or else to reduce the probability and/or the negative effects of its occurrence or to increase the likelihood and/or the positive impacts of an opportunity.

Note 1: The treatment of the risk of occurrence of a potential nonconformity or other potential undesirable situation, as well as that of a potential desirable situation, are equivalent to taking a preventive action.
Note 2: The greatest effectiveness of a preventive action is obtained when the risk of occurrence is eliminated, whereas that of corrective action is obtained by eliminating the risk of recurrence.
Note 3: When the cause cannot be identified, or actions to eliminate it cannot be visualized, the risk can be mitigated by reducing the likelihood and/or negative effects of its occurrence.
Note 4: There can be more than one cause for a potential nonconformity.
Note 5: Preventive action is an improvement action.
Note 6: From the quality cost's point of view, the costs to take preventive action are considered an investment.

Corrective action,
action to eliminate the cause of a detected nonconformity or other undesirable situation, or else to reduce or mitigate the likelihood and/or the negative effects of its recurrence.

Note 1: The treatment of the risk of recurrence of a nonconformity or other potential undesirable situation is equivalent to taking a corrective action.
Note 2: The greatest effectiveness of a corrective action is obtained when the risk of recurrence is eliminated, whereas that of preventive action is obtained by eliminating the risk of its occurrence.
Note 3: When the cause cannot be identified, or actions to eliminate it cannot be visualized, the risk can be mitigated by reducing the likelihood and/or negative effects of its occurrence.
Note 4: There can be more than one cause for a detected nonconformity.
Note 5: Corrective action is an improvement action.
Note 6: From the quality cost's point of view, the costs to take corrective action are considered an investment.

Correction,
action to eliminate a detected nonconformity or other undesirable situation.

Note 1: Correction is not an improvement action.
Note 2: From the quality cost's point of view, the correction costs are considered loss.
Note 3: A correction can be made in conjunction with a corrective action.
Note 4: A correction can be, for example, to rework or regrade.

The new definitions of corrective and preventive actions include all the possibilities for avoiding causes or reducing likelihood or effects of undesirable events, besides considering positive risks, their causes, probability of occurrence and impact. This includes all the possibilities related to negative or positive risks, allowing to formulate the following Improvement Principle:

Any improvement action can be interpreted as a preventive or a corrective action.

References

[1] ISO 9001:2015, Quality management systems - Requirements, 2015, Edition 5.

[2] ISO 9000:2015, Quality management systems - Fundamentals and vocabulary, 2015, Edition 4.

[3] ISO 31000:2018, Risk management - Guidelines, 2018, Edition 2.

[4] ANSI-PMI Combined Glossary for the Standard of Project Management and A Guide for the Project Management Body of Knowledge (PMBOK Guide) – 2021, Seventh Edition.

[5] ANSI/PMI 08-002-2024, The Standard for Program Management, 2024, Fifth Edition. 2 Program Management Principles - 2.7 Risk, p. 58

[6] ANSI/PMI 99-001-2021, The Standard for Project Management, 2021, Seventh Edition. 3 Project Management Principles – 3.10 Optimize Risks Responses, p. 53

[7] PMI The Standard for Risk Management in Portfolios, Programs, and Projects, 2019.

[8] IEC 31010:2019, Risk management - Risk assessment techniques, 2019, Edition 2.

[9] Real Academia Española, Diccionario de la Lengua Española. Available: https://dle.rae.es [Accessed June 5, 2024].

[10] American Society for Quality (ASQ), Cost of Quality. Available: https://asq.org/quality-resources/cost-of-quality [Accessed June 5, 2024].

[11] Besterfield, D. Quality Control, 2001, Sixth Edition. Prentice Hall

[12] Besterfield, D. Total Quality Control, 2003, Third Edition. Prentice Hall

[13] Oxford University, Oxford English Dictionary. Available: https://www.oed.com/.

[Accessed June 5, 2024].

[14] ISO Online browsing platform. Available https://www.iso.org/obp/ui, from ISO 21500:2021. [Accessed June 5, 2024].

[15] IEC 60812:2018, Failure modes and effects analysis (FMEA and FMECA), 2018, Edition 3.0.

Nota contribución de los autores:

1. Concepción y diseño del estudio
2. Adquisición de datos
3. Análisis de datos
4. Discusión de los resultados
5. Redacción del manuscrito
6. Aprobación de la versión final del manuscrito

DA ha contribuido en: 1, 2, 3, 4, 5 y 6.

Nota de aceptación: Este artículo fue aprobado por los editores de la revista Dr. Rafael Sotelo y Mag. Ing. Fernando A. Hernández Gobertti.

Lista de Autores – Memoria Investigaciones en Ingeniería (Número 26).

List of Authors – Memoria Investigaciones en Ingenieria (Volume 26).

MIIUM26-08: Revitalizing Comfort: Designing an Energy–Efficient HVAC System for the University Auditorium.

Prof. Abdul Samad Khan, NED University of Engineering and Technology (Pakistan)
Prof. Muhammad Ehtesham ul Haque, NED University of Engineering and Technology
Prof. Adeel Ahmed Khan, NED University of Engineering and Technology (Pakistan)
Eng. Syed Izhar ul haque, NED University of Engineering and Technology (Pakistan)
Eng. Syed Obaidullah, NED University of Engineering and Technology (Pakistan)
Eng. Muhammad Umer Khan, NED University of Engineering and Technology (Pakistan)

MIIUM26-09: Reducing Energy Consumption of Refrigerator Compressor using Aluminum Oxide Nanoparticles.

Prof. Adeel Ahmed Khan, NED University of Engineering and Technology (Pakistan)
Prof. Muhammad Ehtesham ul Haque, NED University of Engineering and Technology
Farjad Siddiqui, NED University of Engineering and Technology (Pakistan)
Syed Muhammad Taha Nasir, NED University of Engineering and Technology (Pakistan)
Talha Shafique, NED University of Engineering and Technology (Pakistan)
Hassan Khalid, NED University of Engineering and Technology (Pakistan)

MIIUM26-12: Utilization of Sawdust Ash as an additive of cement in concrete and study of its mechanical properties.

Prof. Ifrah Asif, NED University of Engineering and Technology (Pakistan)
Muhammad Ubair Hussain, NED University of Engineering and Technology (Pakistan)
Abdul Arham Khan, NED University of Engineering and Technology (Pakistan)
Muhammad Ashar, NED University of Engineering and Technology (Pakistan)
Muhammad Usman, NED University of Engineering and Technology (Pakistan)
Prof. Zain Shahid, NED University of Engineering and Technology (Pakistan)

MIIUM26-13: Diseño de un sistema de control para el tratamiento de aguas de enfriamiento de un formador de azufre.

Prof. Urimare Campo, Universidad de Oriente (Venezuela)
Prof. Yordy González-Rondón, Universidad de Oriente (Venezuela)

MIIUM26-14: Use of Phase Change Material to enhance the Effectiveness of the Photovoltaic Module.

Muhammad Farhan, NED University of Engineering and Technology (Pakistan)
Prof. Asad A. Naqvi, NED University of Engineering and Technology (Pakistan)
Prof. Muhammad Uzair, NED University of Engineering and Technology (Pakistan)

MIIUM26-15: Fatigue Life Estimation for Different Geometrical Configuration of Load-Carrying Cruciform Joint using ABAQUS and Fe-Safe.

Eng. Zulqarnain Mukhtar Mahmood, National University of Sciences and Technology (Pakistan)
Prof. Muhammad Asif, National University of Sciences and Technology (Pakistan)
Prof. Syed Asad Ali Zaidi, Islamic University of Madinah (Saudi Arabia)

MIIUM26-16: Efectos Del Envejecimiento Estructural durante la Vida Útil de Edificios: Caso de Estudio de un Edificio Educativo.

Mag. Fernando Aguirre Camacho, Tecnológico Nacional de México (México)
Mag. Fernando Treviño Montemayor, Tecnológico Nacional de México (México)
Mag. Carlos Alberto Hoyos Castellanos, Tecnológico Nacional de México (México)
Ing. Martín Eduardo García Avilanes, Tecnológico Nacional de México (México)

MIIUM26-17: Análisis comparativo de las metodologías de predimensionamiento para columnas en una edificación de seis niveles sin sótano.

Mag. Ing. Regner Raul Parra Lavado, Universidad Nacional Intercultural de la Selva (Perú)
Mag. Ing. Jorge Santiago Lopez Yarango, Universidad Nacional Intercultural de la Selva (Perú)
Mg Ing. Marcos Josue Rupay Vargas, Universidad Nacional Intercultural de la Selva (Perú)

MIIUM26-18: Análisis y diseño sísmico de una edificación multifamiliar de diez niveles y dos sótanos aplicando la interacción suelo-estructura con un sistema dual y platea de cimentación.

Ing. Bladimir Quispe, Universidad de San Martin de Porres (Perú)
Ing. Edson Carcausto, Universidad de San Martin de Porres (Perú)
Dr. Genner Villarreal, Universidad de San Martin de Porres (Perú)

MIIUM26-19: Impactos de la transición energética en pequeñas comunidades fuera de red.

Dr. Estefany Garces, Universidad Nacional de Colombia (Colombia)
Prof. Carlos J. Franco, Universidad Nacional de Colombia (Colombia)

MIIUM26-20: Towards Sustainable Energy Storage: A Low-Cost IoT Solution for Real-time Monitoring of Lead-Acid Battery Health.

Dr. Sadiq Ur Rehman, Hamdard University (Pakistan)
Prof. Halar Mustafa, Hamdard University (Pakistan)
Dr. Muhammad Ahsan Shaikh, Hamdard University (Pakistan)
Prof. Shahzor Memon, Hamdard University (Pakistan)

MIIUM26-21: Modos de vibración traslacional de un edificio mediante métodos iterativos y verificación con uso de softwares Mathcad y Etabs.

Dr. Marcos Josue Rupay Vargas, Universidad Nacional Intercultural de la Selva (Perú)
Mag. Regner Raúl Parra Lavado, Universidad Nacional Intercultural de la Selva (Perú)
Juan Percy Espejo Castilla, Universidad Nacional Intercultural de la Selva (Perú)
Juan Miguel Quispe Llantay, Universidad Nacional Intercultural de la Selva (Perú)

MIIUM26-22: Evaluation of preheating impact on weld residual stresses in AH-36 steel using Finite Element Analysis.

Dr. Atif Shazad, National University of Sciences and Technology (Pakistan)
Prof. Muhammad Asif, NED University of Engineering and Technology (Pakistan)
Eng. Najam Siddiqui, NED University of Engineering and Technology (Pakistan)
Prof. Muhammad Uzair, National University of Sciences and Technology (Pakistan)
Prof. Asad A Zaidi, Islamic University of Madinah (Saudi Arabia)

MIIUM26-24: Design of a low-cost portable electrocardiograph for telemedicine application.

Mag. Hólger Santillán, Universidad Politécnica Salesiana (Ecuador)
Ing. Angelo Mantilla, Universidad Politécnica Salesiana (Ecuador)
Mag. David Cárdenas, Universidad Politécnica Salesiana (Ecuador)
Prof. Peregrina Wong, Universidad Politécnica Salesiana (Ecuador)

MIIUM26-41: Improving the Improvement.

Prof. Darío Alentorn, Universidad de Montevideo (Uruguay)

Lista de Revisores – Memoria Investigaciones en Ingeniería (Número 26).

List of Reviewers – Memoria Investigaciones en Ingenieria (Volume 26).

Dr. Zhen Hong Ban, University College of Chemistry and Chemical Engineering (Malaysia)
Dr. Ahsan Ahmed, NED University of Engineering and Technology (Pakistan)
Dr. Hassan Liaquat, Auckland University of Technology (New Zealand)
Dr. Muhammad Asif, National University of Science and Technology (Pakistan)
Prof. Peregrina Wong, Universidad Politécnica Salesiana (Ecuador)
Prof. Muhammad Uzair, NED University of Engineering and Technology (Pakistan)
Dr. Fidel Germán Sagástegui Plasencia, Universidad Privada Antenor Orrego (Perú)
Dr. Alexis Tejedor, Universidad Tecnológica de Panamá (Panamá)
Dr. Ernesto Chagoyén Méndez, Universidad Central "Marta Abreu" de las Villas (Cuba)
Dr. Eduardo Miranda, Instituto Tecnológico de Educación Superior de Monterrey (México)
Dr. Genner Villarreal Castro, Universidad Privada Antenor Orrego (Perú)
Dr. Ricardo Oviedo Sarmiento, Universidad Nacional Federico Villarreal (Perú)
Dra. Natalia Rudeli, Universidad de Montevideo (Uruguay)
Dra. Ana Luz Quintanilla Montoya, Universidad de Colima (México)
Dr. Vinod Yadav, Maulana Azad National Institute of Technology (India)
Dr. Daniel Lovera Davila, Universidad Nacional de San Marcos (Perú)
Prof. Angie Tatiana Ortega Ramírez, Universidad de América (Colombia)
Mag. Fabricio José Cedeño Castro, Instituto Superior Tecnológico Simón Bolívar (Ecuador)
Mag. Nelson Layedra, Escuela Superior Politécnica del Litoral (Ecuador)
Dr. Waldo Hasperué, Universidad Nacional de La Plata (Argentina)
Dr. Alfonso Fernández, Instituto Politécnico Nacional (México)
Mag. Harvey Charles Dávila Lavi, Universidad César Vallejo (Perú)
Prof. Hernán Lara Saavedra, Universidad Técnica Particular de Loja (Ecuador)
Dr. Carlos Francisco Javierre Lardies, Universidad de Zaragoza (España)
Dr. Jorge Limón Romero, Universidad Autónoma de Baja California (México)
Dr. Mahdi Hassan, Quaid e Awam University of Engineering Science and Technology (Pakistan)
Dr. Ahsanullah Soomro, Quaid e Awam University of Engineering Science and Technology
Ing. Mariela Medina, Universidad de la República UDELAR (Uruguay)
Ing. Claudio López Merlino, Universidad de la República UDELAR (Uruguay)
Ing. Daniel Ferrari, Universidad de la República UDELAR (Uruguay)